ERCOFTAC Series

Jochen Fröhlich
Hans Kuerten
Bernard J. Geurts
Vincenzo Armenio *Editors*

Direct and Large-Eddy Simulation IX

Springer

Direct and Large-Eddy Simulation IX

ERCOFTAC SERIES

VOLUME 20

Series Editor

Bernard Geurts
Faculty of Mathematical Sciences, University of Twente, Enschede, The Netherlands

Aims and Scope of the Series

ERCOFTAC (European Research Community on Flow, Turbulence and Combustion) was founded as an international association with scientific objectives in 1988. ERCOFTAC strongly promotes joint efforts of European research institutes and industries that are active in the field of flow, turbulence and combustion, in order to enhance the exchange of technical and scientific information on fundamental and applied research and design. Each year, ERCOFTAC organizes several meetings in the form of workshops, conferences and summerschools, where ERCOFTAC members and other researchers meet and exchange information.

The ERCOFTAC Series will publish the proceedings of ERCOFTAC meetings, which cover all aspects of fluid mechanics. The series will comprise proceedings of conferences and workshops, and of textbooks presenting the material taught at summerschools.

The series covers the entire domain of fluid mechanics, which includes physical modelling, computational fluid dynamics including grid generation and turbulence modelling, measuring-techniques, flow visualization as applied to industrial flows, aerodynamics, combustion, geophysical and environmental flows, hydraulics, multiphase flows, non-Newtonian flows, astrophysical flows, laminar, turbulent and transitional flows.

More information about this series at http://www.springer.com/series/5934

Jochen Fröhlich · Hans Kuerten
Bernard J. Geurts · Vincenzo Armenio
Editors

Direct and Large-Eddy Simulation IX

Springer

Editors
Jochen Fröhlich
Institut für Strömungsmechanik
Technische Universität Dresden
Dresden
Germany

Hans Kuerten
Department of Mechanical Engineering
Eindhoven University of Technology
Eindhoven
The Netherlands

Bernard J. Geurts
Faculty EEMCS, Multiscale Modeling and Simulation
University of Twente
Enschede
The Netherlands

Vincenzo Armenio
Dipartimento di Ingegneria Civile ed Ambientale
Università di Trieste
Trieste
Italy

ISSN 1382-4309
ERCOFTAC Series
ISBN 978-3-319-14447-4 ISBN 978-3-319-14448-1 (eBook)
DOI 10.1007/978-3-319-14448-1

Library of Congress Control Number: 2014959198

Springer Cham Heidelberg New York Dordrecht London

Printed on acid-free paper

Springer International Publishing AG Switzerland is part of Springer Science+Business Media (www.springer.com)

Preface

Representing turbulence by a small number of quantities, such as intensity and length scale, for example, is appropriate and efficient in many engineering situations. Resolving most of or even all turbulent motion by means of Large-Eddy Simulation (LES) or Direct Numerical Simulation (DNS), respectively, provides much more information but is computationally very demanding. Recent years have witnessed an ever-increasing availability of computer power so that the approach can now be applied by many researchers. Indeed, a minimum number of operations, determined by the grid size and the required time steps, needs to be executed to obtain sound separation of length and timescales between the smallest and the largest resolved ones.[1] During recent years, the required performance threshold is met by more and more computer systems. Also, discretization methods and solution algorithms have improved as a result of decades of scientific activities in this field. As a consequence, meaningful DNS and LES can now be performed for more and more applications. For the same reason, a central issue of LES, subgrid-scale modelling, has become less critical today as the grid scales are further away from the resolved scales than before. Still, these methods present lots of pitfalls, and a cost-effective simulation requires optimal models. Much work has been done on improving discretization schemes, subgrid-scale models and other model contributions such as generation of inflow turbulence. On this basis, the development and application of these methods and models continues to be a very active field of research. More and more data sets from DNS nowadays provide detailed and accurate reference for improved understanding and development of physical models.

"Direct and Large-Eddy Simulation 9" was organized in Dresden, Germany, with a local team from the Institute of Fluid Mechanics at TU Dresden and the Helmholtz Center Dresden Rossendorf. This ninth edition took place almost two decades after the start of this ERCOFTAC workshop series in 1994. The first event, DLES1, had been organized by Peter Voke at the University of Surrey and seen 25

[1] S.B. Pope, New J. Phys. 6:35, 2004.

papers, almost equally partitioned into four sessions, turbulent structures and round jets, subgrid-scale modelling, stratified and atmospheric flows and transition. The papers mainly came from those European countries in possession of large computers, six from Great Britain, four from France, the Netherlands and Germany, each, two from Italy and Sweden, one from Switzerland and Norway and two from overseas, USA and Japan, all attributed according to the first author.

During the 20 years since then, the workshop has substantially increased in size and has been tracing the development of the subject from an exclusive one to a broadly applied and fast developing area of research. DLES9 in 2013 so far was the biggest event of the series with 86 contributed talks and 23 poster presentations, selected after a careful reviewing process. Naturally, the range of session topics has become much broader compared to DLES1. Beyond the traditional core subjects of DLES, LES modelling, numerics, turbulent structures, transition and environmental flows, they have been spreading to further applications, among which reactive flows and combustion together with multiphase flows being the larges ones, in terms of the number of papers. Certain methodological topics which have come up over recent years were also featured at DLES9, such as quality of LES and extension to hybrid LES/RANS methods, while other sessions dealt with developments and results in further application areas. A special session on MHD turbulence was put together by HZDR. In addition to the regular contributions, nine keynote presentations provided overviews of recent developments and state of the art for transition (Dan Henningson), cavitation (Stefan Hickel), marine boundary layers (Peter Sullivan), combustion (Heinz Pitsch), LES modelling (Roel Verstappen), MHD turbulence (Annick Pouquet), multiphase flow (Alfredo Soldati), jet noise (Tim Colonius) and applications to industrial flows (Florian Menter).

Most of the invited and contributed papers have been submitted for inclusion in the Proceedings of DLES9 and after a careful review procedure most of these can be found in this volume. The papers are grouped into themes, mostly along the order of the sessions of the workshop. These contributions give a good overview of the most important current issues and application areas in DNS and LES. Fundamental issues related to the usage of LES and the development of the various models required for LES are still an important research topic. The applications to various research questions show that LES and DNS have become important tools for fundamental research able to generate substantial physical insight into numerous phenomena related to various and diverse turbulent flows.

The organization of the ERCOFTAC DLES9 Workshop and the preparation of these proceedings would not have been possible without the support of many. We thank the members of the Scientific Committee for their contribution to the reviewing process and the numerous helpers involved in preparing and managing the event as well as handling the proceedings. We also gratefully acknowledge financial support from the J.M. Burgerscentrum, ANSYS Germany, Innius GTD, Howden Germany, DFG priority programme MetStröm, Gesellschaft der Freunde

und Förderer der TU Dresden and Helmholtz-Zentrum Dresden Rossendorf. The European Research Community on Flow, Turbulence and Combustion, ERCOFTAC, supported the attendance and contribution of young scientists to DLES9 by making available scholarships to Ph.D. students.

Dresden, May 2014

Jochen Fröhlich
Hans Kuerten
Bernard J. Geurts
Vincenzo Armenio

Committees

Local Organizing Committee

Jochen Fröhlich, TU Dresden, Germany
Andre Giesecke, HRZD Dresden, Germany
Frank Rüdiger, TU Dresden, Germany
Jörg Stiller, TU Dresden, Germany
Uta Strempel, TU Dresden, Germany

Scientific Committee

B.J. Boersma, TU Delft, The Netherlands
D. Borello, University of Rome, Italy
M. Breuer, Helmut-Schmidt-University, Hamburg, Germany
L. Davidson, Chalmers University of Technology, Sweden
S. Elghobashi, University of California, Irvine, USA
R. Friedrich, TU Munich, Germany
K. Fukagata, Keio University, Japan
M. García-Villalba, Universidad Carlos III de Madrid, Spain
W.P. Jones, Imperial College, London, Great Britain
T. Kempe, TU Dresden, Germany
L. Kleiser, ETH Zurich, Switzerland
E. Lamballais, PPRIME Poitiers, France
C. Meneveau, Johns Hopkins University, USA
J. Meyers, University Leuven, Belgium
U. Piomelli, Queens University, Kingston, Canada
S.B. Pope, Cornell University, USA
M.-V. Salvetti, University of Pisa, Italy
S. Sarkar, University of California, San Diego, USA

W. Schröder, RWTH Aachen, Germany
J. Sesterhenn, TU Berlin, Germany
S. Sherwin, Imperial College London, Great Britain
F. Stefani, HZDR, Dresden, Germany
D. Thévenin, Universität Magdeburg, Germany
A. Tomboulides, Aristotle University of Thessaloniki, Greece
F. Toschi, TU Eindhoven, The Netherlands
M. Uhlmann, Karlsruhe Institute of Technology, Germany
L. Vervisch, Coria, Rouen, France

Contents

Part V Stability and Transition

Part VI Turbulence

Part IX Aerodynamics and Fluid-Structure Interaction

Part X Environmental Flows

Part XIV Multiphase Flows

Part I
LES Modelling

On Scale Separation in Large Eddy Simulations

Roel Verstappen

1 Large Eddy Simulation

Since the larger eddies in turbulent flow cannot reach a near equilibrium between the rate at which energy is supplied and the rate at which energy is dissipated (by the action of viscosity), they break up, transferring their energy to somewhat smaller scales. The smaller scales undergo a similar break-up process, and transfer their energy to yet smaller scales. The energy cascade continues until the scale becomes so small that dissipation is getting predominant. The entire spectrum—ranging from the scales where the flow is driven to the smallest, dissipative scales—is to be resolved numerically when turbulence is computed directly. In most applications, however, we can only resolve the larger eddies, and certainly not the small scales where the dissipation takes place. Therefore, finding a coarse-grained description is one of the main challenges to turbulence research. Large eddy simulation (LES) seeks to predict the dynamics of spatially filtered turbulent flows. Therefore a spatial filter is applied to the incompressible Navier-Stokes (NS) equations,

$$\partial_t \overline{u} + C(\overline{u},\overline{u}) + D(\overline{u}) + \nabla \overline{p} = C(\overline{u},\overline{u}) - \overline{C(u,u)} = -\nabla \cdot \left(\overline{u \otimes u} - \overline{u} \otimes \overline{u}\right) \quad (1)$$

where it is assumed that the filter $u \mapsto \overline{u}$ commutes with linear differential operators in the NS-equations. This applies for example to the diffusive operator $D = -\nu\nabla^2$. The main problem is that the filter does not commute with the nonlinear, convective operator $C(u, v) = (u \cdot \nabla)v$.

The right-hand side in Eq. (1) represents the effects of the residual scales on the larger eddies (the part of the fluid motion with velocity $\overline{u}$). It depends on both u and $\overline{u}$, due to the nonlinearity. To remove the dependence on u the commutator of C and the filter is replaced by a closure model $-\nabla \cdot \tau(\overline{u})$. The motion of the larger eddies is then governed by

R. Verstappen (✉)
Johann Bernoulli Institute for Mathematics and Computer Science,
University of Groningen, Groningen, The Netherlands
e-mail: r.w.c.p.verstappen@rug.nl

J. Fröhlich et al. (eds.), *Direct and Large-Eddy Simulation IX*,
ERCOFTAC Series 20, DOI 10.1007/978-3-319-14448-1_1

$$\partial_t v + C(v,v) + D(v) + \nabla q = -\nabla \cdot \tau(v). \tag{2}$$

Here the variable name is changed from $\overline{u}$ to v to stress that the solution of the equation above differs from that of Eq. (1), because the closure model is not exact. The inequality $\nabla \cdot \tau(\overline{u}) \neq \nabla \cdot \left(\overline{u \otimes u} - \overline{u} \otimes \overline{u}\right)$ is crucial, since information is to be lost: the solution v of Eq. (2) must possess less scales of motion (degrees of freedom) than the Navier-Stokes solution u; see also Guermond et al. [1]. Finding a closure model that is both inexact (to reduce the complexity of the flow) and accurate (to approximate the dynamics of the larger eddies well) represents the main difficulty to LES. Because turbulence is so far from being completely understood, there is a wide range of closure models, mostly based on heuristic, ad hoc arguments that cannot be derived from the NS-equations, see for example [2] and the references therein.

2 Scale Truncation

The very essence is of LES is that the solution v of Eq. (2) contains only scales of size $\geq \delta$, where δ is the user-chosen length of the filter $u \mapsto \overline{u}$. This property enables us to solve (2) numerically when it is not feasible to compute the full turbulent field u numerically. Therefore we view the closure model τ as a function of v that is designed such that it stops the production of small scales of motion from continuing at the filter scale. Here the filtering operator $u \mapsto \overline{u}$ is defined by

$$\overline{u} = \frac{1}{|\Omega_\delta|} \int\limits_{\Omega_\delta} u(x,t)\, dx$$

where the domain Ω_δ has diameter δ. This filter is known as a box or top-hat filter. Furthermore, we suppose that Ω_δ is a periodic box, so that boundary terms resulting from integration by parts (in the computations to come) vanish. It may be emphasised here that the periodicity conditions are applied to v, not to u, and δ is supposed to be the smallest scale in v.

Poincaré's inequality states that there exists a constant C_δ, depending only on Ω_δ, such that for every function v in the Sobolev space $W^{1,2}(\Omega_\delta)$,

$$\int\limits_{\Omega_\delta} ||v - \overline{v}||^2\, dx \;\leq\; C_\delta \int\limits_{\Omega_\delta} ||\nabla v||^2\, dx \tag{3}$$

The optimal constant C_δ - the Poincaré constant for the domain Ω_δ - is the inverse of the smallest (non-zero) eigenvalue of the dissipative operator $-\nabla^2$ on Ω_δ. Payne and Weinberger [3] have shown that the Poincaré constant is given by $C_\delta = (\delta/\pi)^2$ for convex domains Ω_δ. It may be stressed here that the upper bound given by Poincaré's inequality is sharp: the equality sign in Eq. (3) holds if v is fully aligned with the eigenfunction of $-\nabla^2$ on Ω_δ that is associated to the eigenvalue $1/C_\delta$.

The residual field $v' = v - \overline{v}$ contains eddies of size smaller than δ. These small scales are produced by the nonlinear, convective term in Eq. (2). The closure model must keep them from becoming dynamically significant. Poincaré's inequality (3) shows that the $L^2(\Omega_\delta)$ norm of the residual field v' is bounded by a constant (independent of v) times the $L^2(\Omega_\delta)$ norm of ∇v. Consequently, we can confine the dynamically significant part of the motion to scales $\geq \delta$ by controlling the velocity gradient. To see how the evolution of the $L^2(\Omega_\delta)$ norm of ∇v is to be restrained by the closure model, we consider the residual field v' first:

$$\frac{\mathrm{d}}{\mathrm{d}t}\int\limits_{\Omega_\delta} \tfrac{1}{2}||v'||^2\,dx \;=\; \int\limits_{\Omega_\delta}\Big(-\nu||\nabla v'||^2 \;+\; T\left(\overline{v},v'\right) \;+\; \tau'(v):\nabla v'\Big)\,dx \tag{4}$$

The middle term in the right-hand side stands for the energy transfer from $\overline{v}$ to v'; the last term represents the eddy dissipation, i.e., the dissipation resulting from the closure model. Equation (2) should not produce residual scales, i.e., the eddy dissipation has to balance the energy transfer at the scale set by the filter. Now suppose that the closure model is taken such that the last two terms in (4) cancel each other out. Then,

$$\frac{\mathrm{d}}{\mathrm{d}t}\int\limits_{\Omega_\delta} \tfrac{1}{2}||v'||^2\,dx \;=\; -\nu\int\limits_{\Omega_\delta}||\nabla v'||^2\,dx \tag{5}$$

This equation shows that the evolution of the energy of v' is not depending on $\overline{v}$. Stated otherwise, the energy of residual scales dissipates at a natural rate, without any forcing mechanism involving scales larger than δ. With the help of the Poincaré inequality (3) and the Gronwall lemma, we obtain from Eq. (5) that the energy of the residual scales decays at least as fast as $\exp(-\nu t/C_\delta)$, for any filter length δ. Applying Poincaré's inequality and Gronwalls lemma to

$$\frac{\mathrm{d}}{\mathrm{d}t}\int\limits_{\Omega_\delta} \tfrac{1}{2}||\nabla v||^2\,dx = -\nu\int\limits_{\Omega_\delta}||\nabla^2 v||^2\,dx \tag{6}$$

results into the same rate of decay. So, we can keep the residual v' under control by imposing (6). The left-hand side in Eq. (6) can be rewritten with the help of Eq. (2). This yields (after integration by parts with vanishing boundary terms),

$$\frac{\mathrm{d}}{\mathrm{d}t}\int\limits_{\Omega_\delta} \tfrac{1}{2}||\nabla v||^2\,dx = \int\limits_{\Omega_\delta}\Big(-\nu||\nabla^2 v||^2 \;-\; \nabla\left((v\cdot\nabla)v\right):\nabla v \;-\; \tau(v):\nabla\nabla^2 v\Big)\,dx$$

Thus we see that Eq. (6) holds if the contributions of the last two terms in the right-hand side above cancel each other out. Since the convective derivative is skew-symmetric,

$$(v\cdot\nabla)^* = -(v\cdot\nabla), \tag{7}$$

we have $\int_{\Omega_\delta} \nabla((v\cdot\nabla)v) : \nabla v\,dx = \int_{\Omega_\delta} \nabla v^{\mathrm{T}} \nabla v : \nabla v\,dx$. Consequently, the energy of the residual scales decays at least as fast as $\exp(-\nu t/C_\delta)$, for any filter length δ if

$$\int_{\Omega_\delta} \tau(v) : S(\nabla^2 v)\,dx = \int_{\Omega_\delta} \Big(A^2(v) - S^2(v)\Big) : S(v)\,dx \tag{8}$$

where we have split the velocity gradient into its symmetric $S(v) = \frac{1}{2}(\nabla v + \nabla v^{\mathrm{T}})$ and skew-symmetric part $A(v)$. In addition, τ is supposed to be symmetric.

Condition (8) can also be derived with the help of the vorticity $\omega = \nabla \times v$, since

$$\int_{\Omega_\delta} ||\omega||^2\,dx = \int_{\Omega_\delta} ||\nabla v||^2\,dx$$

By taking the curl of Eq. (2) we find the vorticity equation and from that we obtain

$$\frac{\mathrm{d}}{\mathrm{dt}} \int_{\Omega_\delta} \tfrac{1}{2}||\omega||^2\,dx = \int_{\Omega_\delta} \Big(-\nu||\nabla\omega||^2 + \omega\cdot S(v)\omega + \tau(v) : \nabla(\nabla\times\omega)\Big)\,dx$$

In the right-hand side we recognise the vortex stretching term that can produce smaller scales of motion and the eddy dissipation that should counteract the production of smaller scales at the scale δ. As before, the net contribution of these terms should vanish. Now, by comparing this condition and our previous condition term-by-term we obtain the equality

$$\int_{\Omega_\delta} \omega\cdot S(v)\omega\,dx = \int_{\Omega_\delta} \Big(A^2(v) - S^2(v)\Big) : S(v)\,dx$$

Furthermore, the (point-wise) identity $\omega\otimes\omega = 4\,A^2(v) + ||\omega||^2\,\mathrm{I}$ yields $\omega\cdot S(v)\,\omega = \omega\otimes\omega : S(v) = 4A^2(v) : S(v)$. In this way we find that $\int_{\Omega_\delta} A^2(v) : S(v)\,dx = -\frac{1}{3}\int_{\Omega_\delta} S^2(v) : S(v)\,dx$. Consequently, the right-hand side in Eq. (8) can be expressed in terms of the third invariant,

$$r(v) = -\tfrac{1}{3}\mathrm{tr}(S^3(v)) = -\det(S(v)),$$

of the strain rate tensor S. This leads to the following condition

$$\int_{\Omega_\delta} \tau(v) : S(\nabla^2 v)\, dx \;=\; 4 \int_{\Omega_\delta} r(v)\, dx \tag{9}$$

which guarantees that scales of size smaller than δ are not produced.

3 Modelling Consistency

Ideally we want to meet Eq. (9) for a closure model that represents the effects of the residual scales on the larger eddies accurately, i.e., $\tau(\overline{u}) \;\approx\; \overline{u \otimes u} - \overline{u} \otimes \overline{u}$. The closure error can be estimated for a convolution filter with a Gaussian kernel, e.g. This is typically done in Fourier space. There the Gaussian filter reads

$$\overline{u}(k) \;=\; \exp\left(-\frac{\delta^2}{4\gamma}\,|k|^2\right) u(k) \tag{10}$$

where γ is the shape parameter. Equation (10) can be inverted since the exponential is nonzero. However, the inversion is not stable, because $1/\exp(-|k|^2\delta^2/4\gamma) \to \infty$ as the wavenumber $|k|$ goes to infinity. Therefore Eq. (10) is inverted inexactly. By omitting terms of the order of δ^4, we get the approximation $u' = -(\alpha\delta)^2\,\nabla^2 u$. The coefficient $\alpha^2 = 1/(4\gamma)$ depends on choice of the shape parameter in the kernel. The lowest order approximation $u' = -(\alpha\delta^2)\,\nabla^2 u$ is generic for symmetric filters, i.e., applies to our box filter too. Any convolution filter satisfies Young's inequality which states that the energy of the filtered field $\overline{u}$ is less than (or at most equal to) the energy of the full, unfiltered field u. For a box filter with the approximation $u' = -(\alpha\delta)^2\,\nabla^2 u$, we have

$$\begin{aligned} \tfrac{1}{2}\int_{\Omega_\delta} ||\overline{u}||^2\, dx = \tfrac{1}{2}\int_{\Omega_\delta} ||u||^2 - 2(\alpha\delta)^2||\nabla u||^2 + ||u'||^2\, dx \;\overset{(3)}{\leq}\; \\ \tfrac{1}{2}\int_{\Omega_\delta} ||u||^2 + (C_\delta - 2(\alpha\delta)^2)||\nabla u||^2\, dx \;\leq\; \tfrac{1}{2}\int_{\Omega_\delta} ||u||^2\, dx \end{aligned} \tag{11}$$

provided $C_\delta - 2(\alpha\delta)^2 \leq 0$. Often, γ is taken equal to 6, which results into $\alpha^2 = 1/24$. Since this choice of γ violates Young's inequality, we take

$$u' = -\tfrac{1}{2} C_\delta\, \nabla^2 u \tag{12}$$

This approximation results into $\tau(\overline{u}) = C_\delta \, \nabla \overline{u}^{\mathrm{T}} \, \nabla \overline{u} \, + \, \mathscr{O}(\delta^4)$. The leading term

$$\tau(v) \;\; = \;\; C_\delta \, \nabla v^{\mathrm{T}} \, \nabla v \tag{13}$$

is known as the Clark model [4], where we have modified the coefficient so that Young's inequality is satisfied. The Clark model is notorious for its unstable behaviour. Again this illustrates the conflicting demands between which we compromise; here: modelling consistency versus stability.

4 Forward Transfer: Eddy Viscosity

In this section, we consider the closure problem in the case that the third invariant $r(v)$ of the rate-of-strain tensor $S(v)$ is nonnegative. This corresponds to forward transfer of energy at the scale δ set by the filter; the other possibility (backward transfer) will be dealt with in the next section. In case that $r > 0$, the larger eddies lose energy by interacting with the smaller scales of motion. This loss can be described by an eddy viscosity model,

$$\tau(v) - \tfrac{1}{3}\mathrm{tr}(\tau)\mathrm{I} \;\; = \;\; -2 \, \nu_t \, S(v) \tag{14}$$

where ν_t denotes the eddy viscosity. The classical Smagorinsky model reads $\nu_t = C_S^2 \, \delta^2 \, \sqrt{4q}$ in which

$$q(v) = \tfrac{1}{2}\mathrm{tr}(S(v)^2)$$

is the second invariant of the strain rate tensor $S(v)$. For the eddy viscosity model (14) the scale separation condition (9) reads

$$2\nu_t \int\limits_{\Omega_\delta} S(v) : S(-\nabla^2 v) \, dx \;\; = \;\; 4 \int\limits_{\Omega_\delta} r(v) \, dx \tag{15}$$

where we have taken ν_t constant in Ω_δ. The symmetric differential operator $-\nabla^2$ is positive definite on Ω_δ. The eigenvalues μ_i of $-\nabla^2$ can be ordered. The inverse of the Poincaré constant is the smallest: $0 < 1/C_\delta = \mu_1 < \mu_2 < \mu_3 < \cdots$ Hence,

$$\int\limits_{\Omega_\delta} S(v) : S(-\nabla^2 v) \, dx \;\; \geq \;\; \frac{1}{C_\delta} \int\limits_{\Omega_\delta} S(v) : S(v) \, dx \;\; = \;\; \frac{2}{C_\delta} \int\limits_{\Omega_\delta} q(v) \, dx$$

where the equality sign applies if v is fully aligned with the eigenfunction associated with the smallest eigenvalue $\mu_1 = 1/C_\delta$. Thus we obtain the lowerbound

$$\nu_t \;\geq\; C_\delta \,\frac{\overline{r(v)}}{\overline{q(v)}} \tag{16}$$

where the bar denotes the box filter, i.e., the average over Ω_δ.

It has not been established, thus far, that taking the minimal amount of eddy viscosity, that is

$$\nu_t \;=\; C_\delta \,\frac{\overline{r(v)}}{\overline{q(v)}}, \tag{17}$$

will adequately model the subfilter contributions to the evolution of the filtered velocity. Projecting both the eddy viscosity model (14–17) and the Clark model (13) onto the tensor $-S(v)$ leads to the following consistency question

$$2C_\delta \,\frac{\overline{r(v)}}{\overline{q(v)}} \int\limits_{\Omega_\delta} S(v) : S(v)\, dx \;\stackrel{?}{=}\; -C_\delta \int\limits_{\Omega_\delta} \nabla v^{\mathrm{T}} \nabla v : S(v)\, dx.$$

In Sect. 2 it was shown that the right-hand side equals $4C_\delta \int_{\Omega_\delta} r(v)\, dx$. That is, $r(v)$ provides a measure of the alignment of the Clark model and $S(v)$. By definition we have $S : S = 2q$. So, the eddy viscosity model given by Eq. (17) coincides with the projection of the Clark model. Stated differently, the eddy viscosity model (17) yields as much dissipation as the Clark model, i.e., the eddy viscosity model (17) is consistent in that sense. The overall situation is sketched in Fig. 1. The horizontal axis in this figure represents all possible eddy viscosity models; the axis is spanned by $-2S(v)$ and parameterised by the eddy viscosity. The shaded part of the horizontal axis in Fig. 1 depicts the subset of eddy viscosities that satisfy the scale separation condition (16).

To compute the eddy viscosity ν_t according to Eq. (17), we need know how q and r vary within Ω_δ. Here, we cannot simply take $\overline{q(v)} = q(\overline{v})$, because the relation between q and v is nonlinear. This problem is similar to the closure problem in LES, except that the original closure problem concerns the residual of the NS-solution u, whereas here it is about the residual of the large-eddy solution v. To recover some of the information lost in the filtering process, we make use of the approximation

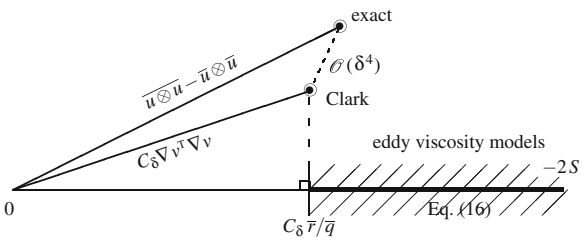

Fig. 1 Some LES-models in the space of symmetric 3×3 tensors

$$v' = -\tfrac{1}{2} C_\delta \, \nabla^2 \overline{v} \tag{18}$$

Compare Eq. (12). In homogeneous, isotropic turbulence, the ratio of r and $q^{3/2}$ scales like Re^0. This scaling law suggests to adopt the approximation

$$\nu_t \;=\; C_\delta \, \frac{r(\overline{v})}{q(\overline{v})^{3/2}} \left(\frac{\overline{q(v)}}{q(\overline{v})} \right)^{1/2} \sqrt{q(\overline{v})}$$

With the help of Eq. (18) it can be shown that $\overline{q(v)} \leq \left(\frac{3}{2}\right)^2 \, \overline{q(\overline{v})}$ where the equality-sign holds if $\overline{v}$ is fully aligned with eigenfunction of $-\nabla^2$ on Ω_δ associated with the eigenvalue $1/C_\delta$. Thus we obtain (in lowest order) the eddy viscosity model

$$\nu_t(v) \;=\; \tfrac{3}{2} \, C_\delta \, \frac{r(v)}{q(v)} \tag{19}$$

This model has the following properties: (a) $\nu_t = 0$ in any (part of the) flow where $r = 0$, i.e., the eddy viscosity vanishes if the transport to scales $< \delta$ is absent; (b) $\nu_t = 0$ in all 3D flows in which it should vanish according to Vreman [5]; (c) $\nu_t = 0$ at a wall; (d) $\nu_t \to 0$ if δ approaches the Kolmogorov scale, i.e., $\delta \propto Re^{-3/4}$; and (e) the corresponding Smagorinsky coefficient is bounded by Lilly's value: $C_S \leq 1/\sqrt{2\pi^2\sqrt{3}} \approx 0.17$ [6, 7].

5 Regularization of Backward Transfer

So far the closure model (eddy viscosity) has been determined such that the corresponding dissipation neutralises the production of scales of size smaller than δ. In case the production is negative, $r \leq 0$, the scale separation condition (15) results into a negative eddy viscosity. This is because energy is transferred from the residual scales to the larger eddies. Hence, in case of backscatter ($r < 0$) the eddy viscosity has to become negative to represent the influx of energy to the larger eddies. Since this leads to stability problems (comparable to the Clark model), we consider an alternative for the eddy viscosity model in case of backscatter. Alternatively, the computational complexity can also be reduced by replacing the nonlinearity $C(u,u)$ in the NS-equations by a regularization $\tilde{C}(u,u)$, where the regularization is to be taken such that the large scales of motion remain unaltered, whereas the tail of the modulated spectrum falls of much faster than the NS-spectrum. Examples can be found in [8, 9], e.g.

Regularization is usually applied to the NS-equations. We do something else: here a regularization is applied the filtered (!) NS-equations (1). The term $C(\overline{u},\overline{u})$

appears on both sides of the filtered NS-equations. Hence, on both sides, it can be replaced by a regularization $\widetilde{C}(\overline{u},\overline{u})$. Thus if the closure $-\nabla\cdot\tilde{\tau}(v)$ models the rhs-term $\widetilde{C}(\overline{u},\overline{u})-\overline{C(u,u)}$, we get the blend

$$\partial_t v+\widetilde{C}(v,v)+D(v)+\nabla q=-\nabla\cdot\tilde{\tau}(v) \tag{20}$$

where, as before, the solution v is supposed to approximate the filtered velocity field $\overline{u}$. Once again, the closure can be described by an eddy viscosity model:

$$\widetilde{\tau}(v)-\tfrac{1}{3}\mathrm{tr}(\widetilde{\tau})\mathrm{I}\;=\;-2\,\widetilde{\nu}_t\,S(v) \tag{21}$$

where $\widetilde{\nu}_t$ denotes the (modified) eddy viscosity. This eddy viscosity is also restricted by a scale separation condition. To determine that condition, we must first choose the regularization method.

The NS-equations conserve particular quantities (like the energy, enstropy (in 2D) and helicity) if there is no viscous dissipation. These conservation properties are a crucial factor in determining how solutions behave. For that reason, we want to preserve them under regularization. The conservation properties follow from the skew-symmetry of the convective derivative; see Eq. (7). Therefore this symmetry is preserved. As usual the regularization is based upon an self-adjoint filter $v\mapsto\widehat{v}$, which differs from the previously introduced LES-filter. The residual $v-\widehat{v}$ is denoted by $\acute{v}$. The following regularization

$$\tilde{C}(u,v)\;=\;C(u,v)\;-\;\acute{C}(\acute{u},\acute{v}) \tag{22}$$

preserves the skew-symmetry (7); see [9]. Furthermore, the regularization (22) preserves the structure of the vorticity equation. Consequently, the analysis of the production of scales of size smaller than δ (see Sect. 2) can also be performed if C is replaced by $\tilde{C}$. In this way we find that if the regularization is given by Eq. (22), the scale separation condition (9) becomes

$$\int_{\Omega_\delta}\tau(v):S(\nabla^2 v)\,dx\;=\;4\int_{\Omega_\delta}\big(r(v)-r(\acute{v})\big)\,dx \tag{23}$$

The basic idea is to blend eddy viscosity with regularization by taking the eddy viscosity model (19) if $r(v)>0$ and applying the regularization if $r(v)<0$. The regularization method can then be seen as a way to clip negative values of the eddy viscosity. To that end, the regularization is based upon the generic filter

$$\widehat{v}=v+\tfrac{1}{2}C_\varepsilon\nabla^2 v, \tag{24}$$

where C_ε is the Poincaré constant of a domain Ω_ε with diameter ε (the length of the regularization filter). Note that we again use of the generic form $\acute{v}=-\frac{1}{2}C_\varepsilon\nabla^2 v$;

cf. Eqs. (12–18). Now, we want to determine the two parameters, ν_t and C_ε, of our LES-model in such a manner that all dynamically significant scales of motion in the solution v of Eq. (20) are greater than (or equal to) δ. In case $r(v) > 0$ Eq. (23) is satisfied by taking ν_t according to Eq. (19) and $C_\varepsilon = 0$. If $r(v) \leq 0$, we take $\nu_t = 0$ and satisfy the scale separation condition (23) by determining the regularization parameter such that the right-hand side of Eq. (23) vanishes. Therefore the regularization parameter C_ε is to be solved from

$$r(v) - r(\acute{v}) = r(v) + \tfrac{1}{2} C_\varepsilon r(\nabla^2 v) = 0$$

Notice that $r(v) < 0$ implies that $r(\acute{v}) < 0$, since their difference is zero. Consequently, r does not change sign over a range of scales. Finally, it may be emphasised that we have a smooth transition between forward and backward transfer, since we have both $\varepsilon = 0$ and $\nu_t = 0$ if $r(v) = 0$.

6 First Results

As a first step the scale truncation model was tested for turbulent channel flow by means of a comparison with direct numerical simulations. This flow forms a prototype for near-wall turbulence: virtually every LES has been tested for it. The results are compared to the DNS data of [10] at $\mathrm{Re}_\tau = 590$. The dimensions of the channel are taken identical to those of the DNS of Moser et al. The computational grid used for the large-eddy simulation consists of 64^3 points. The DNS was performed on a $384 \times 257 \times 384$ grid, i.e., the DNS uses about 144 times more grid points than the present LES. The LES-results were obtained with an incompressible code that uses a fourth-order, symmetry-preserving, finite-volume discretization, see [11]. Unlike the standard Smagorinsky model (even with the relatively low value $C_S = 0.1$), the present eddy viscosity model showed an appropriate behaviour. As can be seen in Fig. 2 both the mean velocity and the root-mean-square of the fluctuating velocity are in good agreement with the DNS (Fig. 3).

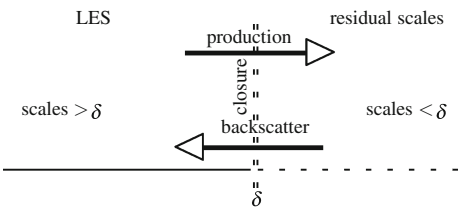

Fig. 2 Forward ($r > 0$) and backward ($r < 0$) transfer of energy at the scale δ set by the filter

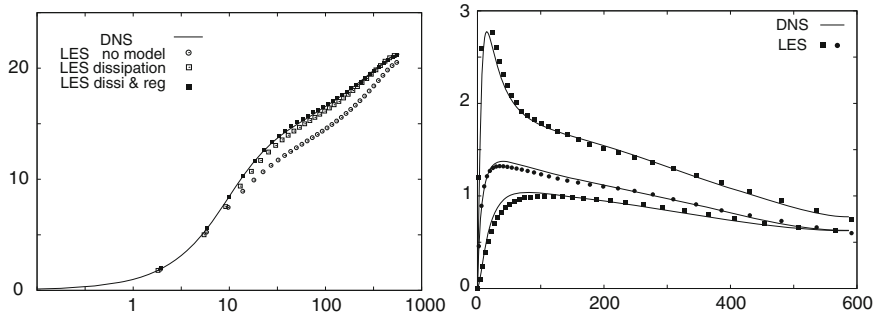

Fig. 3 The *left-hand* figure shows the mean velocity obtained with the help of the 64^3 LES and the DNS by Moser et al. Here the results obtained without any models and without regularization model are also shown for comparison. The *right-hand* figure displays the root-mean-square of the fluctuating velocities. The boxes and circles represent LES data; every symbol corresponds to data in a grid point

References

1. Guermond, J.L., Oden, J.T., Prudhomme, S.: Mathematical perspectives on large eddy simulation models for turbulent flows. J. Math. Fluid Mech. **6**, 194–248 (2004)
2. Sagaut, P.: Large Eddy Simulation for Incompressible Flows. Springer, Berlin (2001)
3. Payne, L.E., Weinberger, H.F.: An optimal Poincaré inequality for convex domains. Arch. Rat. Mech. Anal. **5**, 286–292 (1960)
4. Clark, R.A., Ferziger, J.H., Reynolds, W.C.: Evaluation of subgrid-scale models using an accurately simulated turbulent flow. J. Fluid Mech. **91**, 1–16 (1979)
5. Vreman, B.: An eddy viscosity subgrid-scale model for turbulent shear flow: Algebraic theory and applications. Phys. Fluids **16**, 3670 (2004)
6. Verstappen, R., Bose, S., Lee, J., Choi, H., Moin, P.: A dynamic eddy-viscosity model based on the invariants of the rate-of-strain. In Proceedings of the summer program 2010, Center for Turbulence Research, Stanford 183–192 (2011)
7. Verstappen, R.: When does eddy viscosity damp subfilter scales sufficiently? J. Sci. Comput. **49**, 94–110 (2011)
8. Guerts, B.J., Holm, D.D.: Regularization modeling for large-eddy simulation. Phys. Fluids **15**, L13–16 (2003)
9. Verstappen, R.: On restraining the production of small scales of motion in a turbulent channel flow. Comput. Fluids **37**, 887–897 (2008)
10. Moser, R.D., Kim, J., Mansour, N.N.: Direct numerical simulation of turbulent channel flow up to $\mathrm{Re}_\tau = 590$. Phys. Fluids **11**, 943–945 (1999)
11. Verstappen, R.W.C.P., Veldman, A.E.P.: Symmetry-preserving discretization of turbulent flow. J. Comp. Phys. **187**, 343–368 (2003)

Numerical Experiments with a New Dynamic Mixed Subgrid-Scale Model

P. Lampitella, F. Inzoli and E. Colombo

1 Introduction

One of the main drawbacks of the classical LES approach [1] is the lack of connection with its practical implementation in numerical solvers and the consequent limits in the derivation of proper subgrid-scale (SGS) models. A well known example of this comes from the implicit filtering approach; indeed, it can provide full adherence to the continuous classical LES model if performed with certain fully spectral methods, but also to a completely different one if performed with low order finite difference/volume methods. Both perform a projection of the relevant fields into a lower dimensional phase space, but for low order numerical methods the resulting LES attractor is substantially distorted by numerical artifacts. In this case, a possibility is to resort to the explicit filtering approach, but then one has to face the additional burden of the non commutation between the numerical filtering and the numerical differentiation operators. A possible approach to deal with commutation errors (CE) is to adopt higher order commuting filters, e.g., [2]. However, the divergence of the resulting SGS stress tensor is also affected and the two maintain the same scaling with respect to the filter cutoff length, showing the pivotal need for CE modeling within the classical LES approach [3]. While direct CE modeling has found various contributors, very few authors [4, 5] have considered removing CE ab initio by a proper interpretation of the LES problem.

The aim of the present work is twofold. First, previous works [4, 5] are generalized and unified in a single, more flexible, formulation allowing implicit and explicit filtering approaches; multilevel features are also exploited to extend its general applicability. Finally, a Taylor series analysis of the SGS stress tensor arising in the new framework is used to derive a consistent form of scale-similar model. Then, this is combined with a classical eddy viscosity term in a new form of dynamic procedure which is consistent with the proposed LES methodology. Model performances are assessed in the simulation of the turbulent channel flow at $\mathrm{Re}_\tau = 590$ [6].

P. Lampitella (✉) · F. Inzoli · E. Colombo
Department of Energy, Politecnico di Milano, Via Lambruschini 4, 20156 Milan, Italy
e-mail: paolo.lampitella@mail.polimi.it

J. Fröhlich et al. (eds.), *Direct and Large-Eddy Simulation IX*,
ERCOFTAC Series 20, DOI 10.1007/978-3-319-14448-1_2

2 LES Framework

As in classical LES, let us introduce the filtering operator G^i:

$$\bar{\phi}\left(\mathbf{x}, t, \Delta^i\right) = G^i * \phi\left(\mathbf{x}, t\right) = \int_{\Omega} G\left[\mathbf{x} - \xi, \Delta^i\left(\mathbf{x}\right)\right] \phi\left(\xi, t\right) \mathrm{d}\xi \tag{1}$$

where Ω is the generally finite fluid domain and G^i is a spatially varying filter kernel with width $\Delta^i(\mathbf{x})$. For future reference, we also introduce the conventions:

$$\begin{gathered} \bar{\phi}^n = G^n * \bar{\phi}^{n-1} = G^n * G^{n-1} * \cdots * G^1 * G^0 * \bar{\phi}^0 \\ G^0 * \bar{\phi}^0 = \bar{\phi}^0 = \phi \; ; \quad G^1 * \bar{\phi}^0 = \bar{\phi} \; ; \quad \tilde{\phi}^n = \overline{\rho\phi}^n / \bar{\rho}^n \end{gathered} \tag{2}$$

where the ith filter kernel G^i has an associated filter width $\Delta^i \geq \Delta^{i-1}$, which is generally different from the cutoff length of the actual filter determining $\bar{\phi}^n$, Δ_n. To remain general, we also introduced the classical Favre filtering with ρ the density of the fluid. With this notation, it is a matter of simple manipulations to express the Navier-Stokes equations at a generic filter level $n \geq 0$; limiting the discussion to the momentum equations, for the sake of conciseness, we get:

$$\begin{gathered} \frac{\partial\left(\bar{\rho}^n \tilde{u}_i^n\right)}{\partial t} + \overline{\frac{\partial}{\partial x_j}\left(\bar{\rho}^n \tilde{u}_i^n \tilde{u}_j^n + \tilde{\sigma}_{ij}^n\right)}^n = \overline{\frac{\partial}{\partial x_j}\left(\tau_{ij}^{n-0}\right)}^n \\ \tilde{\sigma}_{ij}^n = \bar{p}^n \delta_{ij} - 2\mu\left(\tilde{S}_{ij}^n - \tfrac{1}{3}\tilde{S}_{gg}^n \delta_{ij}\right) \\ \tilde{S}_{ij}^n = \tfrac{1}{2}\left(\frac{\partial \tilde{u}_i^n}{\partial x_j} + \frac{\partial \tilde{u}_j^n}{\partial x_i}\right) \\ \tau_{ij}^{n-m} = \left(\bar{\rho}^n \tilde{u}_i^n \tilde{u}_j^n - \bar{\rho}^m \tilde{u}_i^m \tilde{u}_j^m\right) + \left(\tilde{\sigma}_{ij}^n - \tilde{\sigma}_{ij}^m\right) \end{gathered} \tag{3}$$

where τ_{ij}^{n-m} with $m = 0$ is the SGS stress tensor arising in the formulation (3). With respect to classical LES formulations, we notice that: (a) no commutation with spatial derivatives is ever required, (b) there is full correspondence with the implicit filtering approach if the filter (1) is interpreted as a finite volume discretization, (c) an explicit filtering approach can be adopted if the filter (1) is effectively applied trough a numerical procedure. A classical criticism with the proposed formulation is the lack of Galilean invariance. However, it is worth noting that this is a property of any quantity which is non-uniformly filtered in space, hence it is natural that equations based on such quantities also inherit this property.

3 SGS Tensor Analysis

The main effect of reformulating the LES problem is the appearance of the SGS tensor in a different form; hence, the question of what form of SGS model should be used, naturally arises. In order to attempt an answer, we analyze the Taylor series development for τ_{ij}^{m-n} assuming that, for $m > n$, the following hold [7]:

$$\bar{\phi}^m = \bar{\phi}^n + \Delta_m^2 M_k \frac{\partial^2 \bar{\phi}^n}{\partial x_k^2} + O\left(\Delta_m^4\right) \quad \Delta_m^2 = \sum_{i=0}^{m-n} \left(\Delta^{m-i}\right)^2 \tag{4}$$

where M_k are filter dependent coefficients. Under this circumstance, and for sufficiently smooth variations of Δ_m, the following estimates are valid:

$$\bar{\rho}^m \tilde{u}_i^m \tilde{u}_j^m - \bar{\rho}^n \tilde{u}_i^n \tilde{u}_j^n = \Delta_m^2 M_k \frac{\partial^2 \bar{\rho}^n \tilde{u}_i^n \tilde{u}_j^n}{\partial x_k^2} - 2\Delta_m^2 M_k \bar{\rho}^n \frac{\partial \tilde{u}_i^n}{\partial x_k} \frac{\partial \tilde{u}_j^n}{\partial x_k} + O\left(\Delta_m^4\right) \tag{5}$$

$$\bar{p}^m - \bar{p}^n = \Delta_m^2 M_k \frac{\partial^2 \bar{p}^n}{\partial x_k^2} + O\left(\Delta_m^4\right) \tag{6}$$

$$\begin{aligned} \tilde{S}_{ij}^m - \tilde{S}_{ij}^n = {} & \frac{1}{2}\left[\frac{\partial}{\partial x_j}\left(\Delta_m^2 M_k \frac{\partial^2 \tilde{u}_i^n}{\partial x_k^2}\right) + \frac{\partial}{\partial x_i}\left(\Delta_m^2 M_k \frac{\partial^2 \tilde{u}_j^n}{\partial x_k^2}\right)\right] \\ & + \frac{1}{2}\left[\frac{\partial}{\partial x_j}\left(2\frac{\Delta_m^2 M_k}{\bar{\rho}^n}\frac{\partial \bar{\rho}^n}{\partial x_k}\frac{\partial \tilde{u}_i^n}{\partial x_k}\right) + \frac{\partial}{\partial x_i}\left(2\frac{\Delta_m^2 M_k}{\bar{\rho}^n}\frac{\partial \bar{\rho}^n}{\partial x_k}\frac{\partial \tilde{u}_j^n}{\partial x_k}\right)\right] \\ & + O\left(\Delta_m^4\right) \end{aligned} \tag{7}$$

The resulting approximation for τ_{ij}^{m-n} can then be summarized as follows:

$$\tau_{ij}^{m-n} = \Delta_m^2 f\left(\bar{\rho}^n, \tilde{u}_i^n, \tilde{u}_j^n\right) + \frac{\partial \Delta_m^2}{\partial x_j} h\left(\bar{\rho}^n, \tilde{u}_i^n\right) + \frac{\partial \Delta_m^2}{\partial x_i} h\left(\bar{\rho}^n, \tilde{u}_j^n\right) + O\left(\Delta_m^4\right) \tag{8}$$

where f and h are functional forms easily derived from Eqs. (5–7). However, when the same analysis is performed for the true SGS stress tensor τ_{ij}^{n-0}, recalling that $\bar{\phi}^m = \bar{\phi}^n + O\left(\Delta_m^2\right)$, the resulting estimate is:

$$\tau_{ij}^{n-0} = \Delta_n^2 f\left(\bar{\rho}^n, \tilde{u}_i^n, \tilde{u}_j^n\right) + \frac{\partial \Delta_n^2}{\partial x_j} h\left(\bar{\rho}^n, \tilde{u}_i^n\right) + \frac{\partial \Delta_n^2}{\partial x_i} h\left(\bar{\rho}^n, \tilde{u}_j^n\right) + O\left(\Delta_n^4\right) \tag{9}$$

Hence, even under the most simplifying assumptions, e.g., Eq. (4), a scale-similar model based on τ_{ij}^{m-n}, as originally proposed in [5], has a second order difference with respect to the true SGS stress tensor τ_{ij}^{n-0}. In order to overcome such deficiency, we propose to adopt a scaled version of scale-similar term according to the following estimate:

$$\begin{aligned}\frac{\Delta_n^2}{\Delta_m^2}\tau_{ij}^{m-n} - \tau_{ij}^{n-0} &= \Delta_n^2\left[h\left(\bar{\rho}^n, \tilde{u}_j^n\right)\beta_i + h\left(\bar{\rho}^n, \tilde{u}_i^n\right)\beta_j\right] \\ &\quad + O\left(\Delta_m^2\Delta_n^2\right) + O\left(\Delta_n^4\right) \\ \beta_i &= \frac{1}{\Delta_m^2}\frac{\partial\Delta_m^2}{\partial x_i} - \frac{1}{\Delta_n^2}\frac{\partial\Delta_n^2}{\partial x_i} = \frac{\partial}{\partial x_i}\left[\log\left(\frac{\Delta_m^2}{\Delta_n^2}\right)\right]\end{aligned} \tag{10}$$

From which it follows that, for any two couples of filter levels satisfying the scale-similarity hypothesis and the assumption (4), the proposed scale-similar tensor $\left(\Delta_n^2/\Delta_m^2\right)\tau_{ij}^{m-n}$ approximates the convective/pressure part of the tensor τ_{ij}^{n-0} with $O\left(\Delta_n^4\right)$ accuracy; if, in addition, the ratio Δ_n^2/Δ_m^2 is constant in space, the accuracy is restored also for the diffusive part.

4 Dynamic SGS Modeling

As in the computational practice some of the assumptions concerning the model derivation might be violated, we implemented the previous model in a dynamic version trough the following Germano identity, consistent with the formulation (3):

$$\tau_{ij}^{m-k} - \tau_{ij}^{n-k} = \tau_{ij}^{m-n} \tag{11}$$

It is worth noting that the lack of commutation between the filter and derivative operators results in Eq. (11) not involving any test filtered tensor. This, in turn, produces two major advantages: there is no arbitrary extraction of model constants from the test filter and no commutation property is required for the test filter. An additional advantage is the lack of filtered products of variables: for the dynamic mixed model presented below only 6 scalars need to be test filtered while for a classical dynamic Smagorinsky model the required number of filter applications is 15. Besides Eq. (11) and the cited advantages, the proposed dynamic procedure follows the classical approach. Two-parameter, mixed SGS models are introduced for the basic (n) and test (m) filter levels:

$$\begin{aligned}\tau_{ij}^{n-0} &= C_{ev}2\bar{\rho}^n\left|\tilde{S}^n\right|^\theta\left(k_{SGS}^{n-m}\right)^{\frac{1-\theta}{2}}\Delta_n^{1+\theta}\left(\tilde{S}_{ij}^n - \tfrac{1}{3}\tilde{S}_{gg}^n\delta_{ij}\right) + C_{ss}\left(\tfrac{\Delta_n}{\Delta_m}\right)^2\tau_{ij}^{m-n} \\ \tau_{ij}^{m-0} &= C_{ev}2\bar{\rho}^m\left|\tilde{S}^m\right|^\theta\left(k_{SGS}^{m-r}\right)^{\frac{1-\theta}{2}}\Delta_m^{1+\theta}\left(\tilde{S}_{ij}^m - \tfrac{1}{3}\tilde{S}_{gg}^m\delta_{ij}\right) + C_{ss}\left(\tfrac{\Delta_m}{\Delta_r}\right)^2\tau_{ij}^{r-m}\end{aligned} \tag{12}$$

with the additional test filter level r ($\Delta_r > \Delta_m > \Delta_n$) and:

$$\begin{aligned}k_{SGS}^{n-m} &= \tfrac{1}{2}\left(\tilde{u}_j^n - \tilde{u}_j^m\right)\left(\tilde{u}_j^n - \tilde{u}_j^m\right) \\ \tilde{S}^n &= \sqrt{2\tilde{S}_{ij}^n\tilde{S}_{ij}^n}\end{aligned} \tag{13}$$

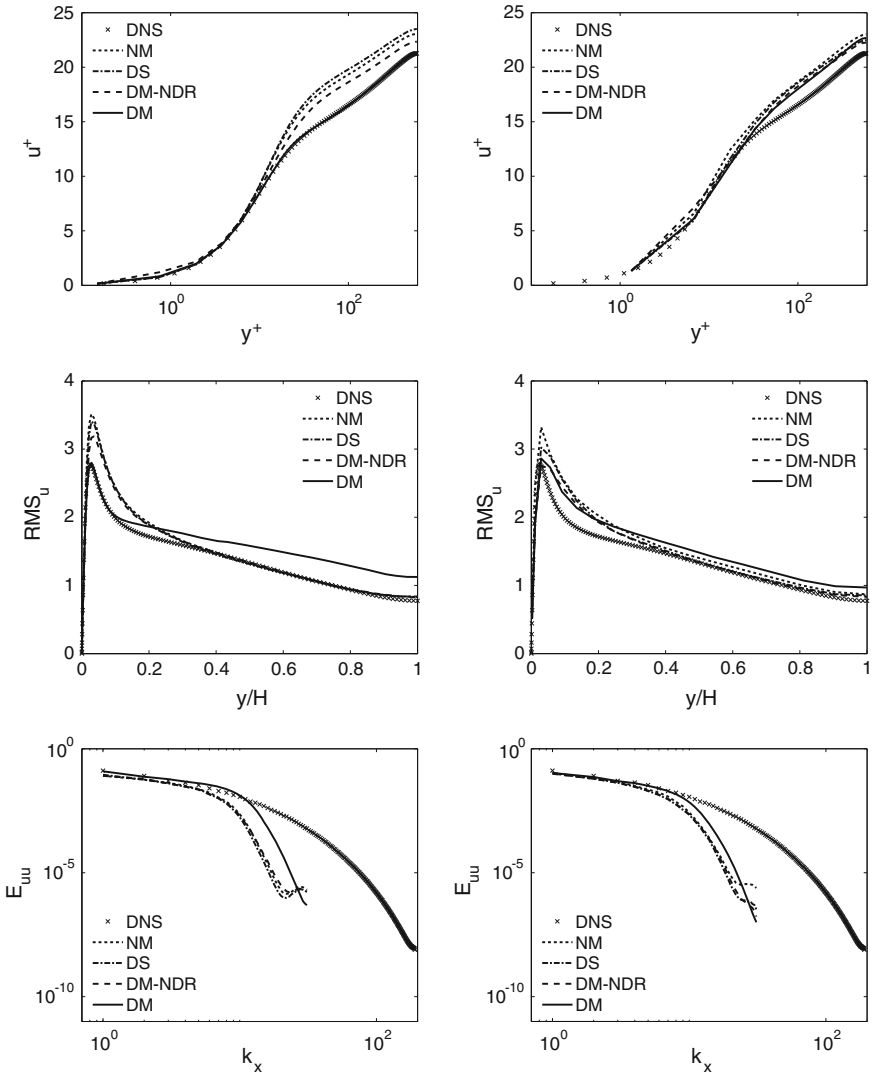

Fig. 1 Results for $\theta = 0$. *Left* fine grid, *Right* coarse grid. *Top* mean velocity, *Center* r.m.s. stream-wise velocity fluctuations, *Bottom* stream-wise spectra of stream-wise velocity at y/H=1

The dynamic constants C_{ev} and C_{ss} are then computed as in classical two parameter dynamic models [8].

5 Numerical Experiments and Discussion

The model is implemented in a commercial, unstructured, finite volume solver [9] by exploiting the implicit filtering features of the formulation. Numerical tests are performed on the turbulent channel flow at $\mathrm{Re}_\tau = 590$ [6] on a domain with extensions $L_x = 2\pi H$, $L_y = 2H$ and $L_z = \pi H$, in the stream-wise, wall-normal and span-wise directions, with H the channel half-height. Two different grids are adopted, both having 64 cells in the homogeneous directions and 33 (coarse) or 99 (fine) cells in the wall-normal direction, distributed according to a sin stretching law.

Grid effects are investigated in Fig. 1 for $\theta = 0$ (DM); results for the same model without the proposed scaling (DM-NDR), a classical dynamic Smagorinsky model (DS) and a no model computation (NM) are also reported. Major differences are evident on the fine grid. The DM model is the only one capable of recovering the mean velocity profile and the peak of the velocity fluctuation which, however, is over-predicted in the core of the channel. Notably, the DM-NDR model fails in reproducing the mean velocity profile at the first few points near the wall, where the grid stretching is higher, somehow showing the incorrect scaling. The differences are mitigated for the coarse grid, possibly because of the higher influence of the numerical error and the reduced effect of the scarcely resolved near-wall region, but the DM model is still the only one correctly reproducing the logarithmic slope of the velocity profile. Finally, on both grids, velocity spectra highlight that the present scale-similar formulation is necessary in order to recover a substantial part of the energy in the smallest resolved scales; in contrast, no actual difference is found in the spectra for the remaining modeling options. This energy recovery also allows the DM model to suppress the energy pile-up observed for the other models. This effect has been observed for different eddy-viscosity parameterizations (θ) with no substantial differences in the remaining quantities.

In conclusion, despite some grid-effect limitations arising from the implicitly filtered approach, the proposed model is found effective and necessary in removing major drawbacks of SGS closures not considering the LES framework in their derivation. Some pitfalls emerged as well, like the over-prediction of stream-wise velocity fluctuations in the core of the channel and of span-wise energy spectra (not shown); the model dependence on the Reynolds number and some preliminary tests suggest that a tensorial scale-similar dynamic constant might alleviate the problem.

References

1. Leonard, A.: Adv. Geophys. **A 18**, 237–248 (1974)
2. Vasilyev, O.V., Lund, T.S., Moin, P.: J. Comp. Phys. **146**, 82–104 (1998)
3. van der Bos, F., Geurts, B.J.: Phys. Fluids **17**, 035108 (2005)
4. Denaro, F.M., De Stefano, G.: Theor. Comput. Fluid Dyn. **25**, 315–355 (2011)
5. Vreman, A.W., Geurts, B.J.: A new treatment of commutation errors in large-eddy simulation. In: Proceedings of the IX European Turbulence Conference, Barcelona, Spain (2002)
6. Moser, R.D., Kim, J., Mansour, N.N.: Phys. Fluids **11–4**, 943–945 (1999)

7. Vreman, B., Geurts, B., Kuerten, H.: Theor. Comp. Fluid Dyn. **8**, 309–324 (1996)
8. Sarghini, F., Piomelli, U., Balaras, E.: Phys. Fluids **11–6**, 1596–1607 (1999)
9. Lampitella, P., Colombo, E. Inzoli, F.: Sensitivity analysis on numerical parameters for large eddy simulation with an unstructured finite volume commercial code. In: Proceedings of the XX AIMETA Conference, Bologna, Italy (2011)

Implicit Large-Eddy Simulation of Isotropic Turbulent Mixing

F.F. Grinstein, A.J. Wachtor, J.R. Ristorcelli and C.R. DeVore

1 Introduction

In practical turbulent flow applications exhibiting extreme geometrical complexity and a broad range of length and time scales direct numerical simulation (DNS) is prohibitively expensive and dependable large scale predictions of highly nonlinear processes must be typically achieved with under-resolved computer simulation models. In large-eddy simulation (LES) [1] large energy containing structures are resolved, smaller structures are spatially filtered out, and unresolved subgrid scale (SGS) effects are modeled; implicit LES (ILES) relies on the SGS modeling and filtering implicitly provided by *physics capturing* numerical algorithms [2]. At moderately high Reynolds number (Re) when convective time-scales are much smaller than those associated with molecular diffusion, we are primarily concerned with the numerical simulation of the convectively-driven interpenetration mixing processes (entrainment and stirring due to velocity gradient fluctuations) which can be captured with sufficiently resolved ILES. Assessing predictability of *under-resolved scalar mixing by an under-resolved turbulent velocity field* in the ILES framework is the particular focus of this paper; we investigate the performance of ILES in the context of passive scalar mixing in isotropic turbulence as function of grid-resolution dependent effective Re [3].

F.F. Grinstein (✉) · A.J. Wachtor · J.R. Ristorcelli
XCP, Los Angeles National Laboratory, MS F644, Los Alamos, NM 87545, USA
e-mail: fgrinstein@lanl.gov

A.J. Wachtor
e-mail: ajw@lanl.gov

J.R. Ristorcelli
e-mail: jrrj@lanl.gov

C.R. DeVore
NASA Goddard Space Flight Center, Greenbelt Md, USA
e-mail: c.richard.devore@nasa.gov

J. Fröhlich et al. (eds.), *Direct and Large-Eddy Simulation IX*,
ERCOFTAC Series 20, DOI 10.1007/978-3-319-14448-1_3

The mixing of a passive scalar by a fluctuating flow field is a classical problem in turbulence. Pullin [4] noted that classical scaling laws (e.g. [5]) give insights into the physics of mixing but do not provide a general means of calculating the scalar statistics in a general turbulent flow, and proposed that LES might be used in this context. Overholt and Pope [6] conducted DNS of the mixing of a passive scalar in the presence of a mean scalar gradient in one direction, by forced, spatially periodic, isotropic turbulence. In this flow, a statistically steady-state scalar variance is achieved by balancing the scalar variance production and dissipation. Pullin [4] revisited this problem and proposed a model for the flux of a passive scalar by the SGS motions. The LES results [4] predict the normalized scalar variance asymptotically approaches a nearly constant value for large Taylor Re consistent with laboratory experiments [7] also indicating essentially constant scalar variance as a function of Re for Schmidt number $Sc \sim 1$. The velocity-to-scalar dissipation time-scale ratio was also reported to be asymptotically constant in [4] but comparisons with DNS [6] available at the time were inconclusive as to whether such a result captured physical behavior. Subsequent theoretical [8] and high Re DNS [9] studies have shown that the time scale ratio should exhibit continued growth with increasing Re. The prediction of the asymptotic behavior of the scalar variance and velocity-to-scalar Taylor micro-scales ratio (which is directly proportional to the dissipation time scale ratio) are specifically investigated in this work to benchmark the performance of ILES against the previously reported work.

ILES is presently based on solving the compressible, nominally-inviscid conservation equations for mass, momentum, energy, and a passive scalar, with a well established multidimensional 4th-order FCT algorithm (e.g., [10]) suitably extended for the forced isotropic turbulence studies [3]. The simulation model effectively models high-Re, miscible (Schmidt number $Sc \sim 1$) convection-driven flow. An isotropic turbulence simulation strategy [11] was implemented by which low wave-number forcing can be enforced separately for solenoidal and dilatational components on the momentum equations. The configuration studied assumes triply-periodic boundary conditions on a cubical domain with unit box length and uniformly spaced 32^3, 64^3, 128^3, and 256^3 grids. The simulated flow is characterized by volume-time-averaged quantities: rms-velocity-fluctuation u', velocity and scalar Taylor micro-scales λ and λ_θ, and effective viscosity ν_{eff} computed as ratio of forced dissipation and squared strain-rate magnitude [12]. For a given grid resolution, and u' based turbulence Mach numbers $Ma = 0.13,\ 0.29$, effective $Re_\lambda{}^{eff} = u'\lambda/\nu_{eff}$ can be thus directly evaluated from the resolved developed simulation data.

2 Results

Figure 1 exemplifies our developed vorticity field, dominated by elongated structures characteristic of high-Re isotropic turbulence; Fig. 2 shows typical scalar visualizations for the finest resolution case. Figure 3 demonstrates scalar & velocity spectra as function of grid resolution. The scalar spectra exhibit longer inertial ranges and

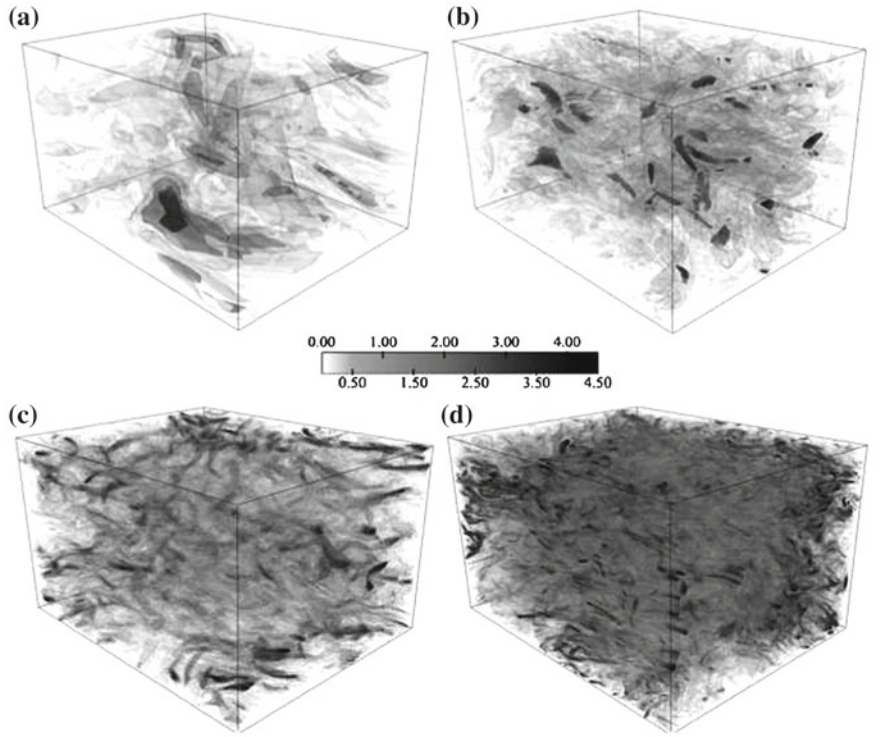

Fig. 1 Instantaneous visualizations of the vorticity magnitude; **a** 32^3, **b** 64^3, **c** 128^3, **d** 256^3

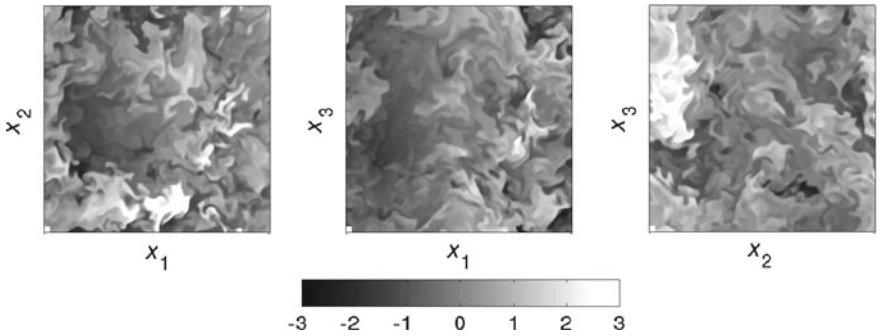

Fig. 2 Colormaps of fluctuating scalar field scaled by the *rms* of the fluctuating scalar field in mid-planes of the domain for 256^3 grid resolution; for reference, superimposed on the *lower left* of each *colormap* is a box with side length equal to the scalar Taylor micro-scale

more pronounced spectral bumps than their velocity counterparts at corresponding resolutions—consistent with [9]; the latter results directly reflect on the $(\lambda/\lambda_\theta)^2$ results discussed further below.

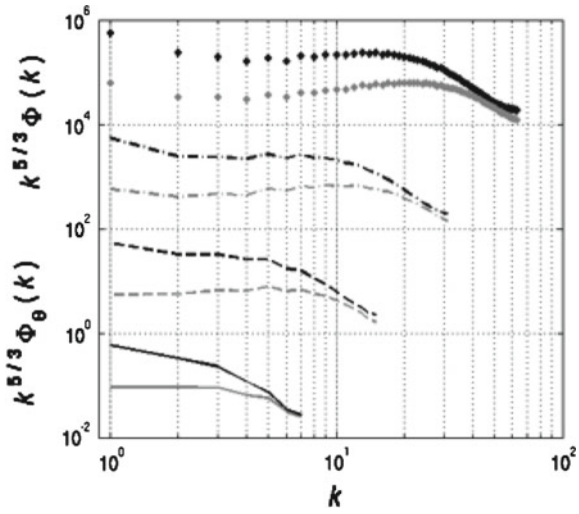

Fig. 3 Compensated velocity (*black*) and scalar variance spectra (*gray*). *Solid line* 32^3; *Dashed line* 64^3; *Dash-dot line* 128^3; *Diamond* 256^3; $Ma = 0.27$ ILES case

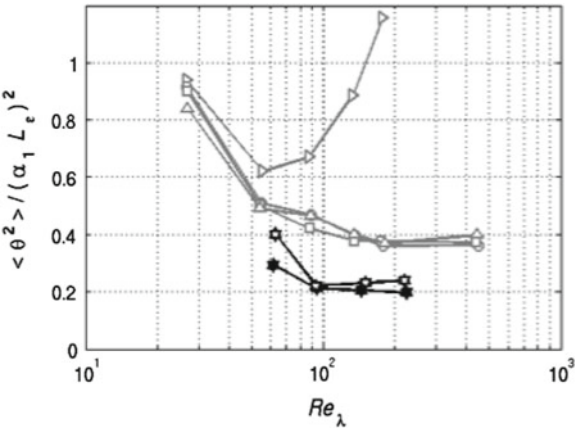

Fig. 4 Nondimensional scalar variance as a function of Re_λ. *Gray open square/triangle/circle* LES [4]; *Gray open right-triangle* LES without scalar SGS model [4]; *Black full star* ILES $Ma = 0.27$; *Black open star* ILES $Ma = 0.13$, versus Re_λ

Figure 4 compares nondimensionalized scalar variance results for present ILES with previously reported (incompressible, $Ma = 0$) scalar mixing predictions using LES [4]; ILES shows asymptotically constant scalar variance behavior as function of Re_λ attained above the mixing transition threshold $Re_\lambda \approx 100 - 140$ [13] as previously reported with LES [4] (when explicit scalar SGS model was used) and suggested by experiments [7]. Lower scalar variance predictions with present ILES are mainly attributed to differences between forcing schemes used here and in [4], and somewhat less to compressibility effects.

The ratio $(\lambda/\lambda_\theta)^2$—directly proportional to the velocity-to-scalar dissipation time-scale ratio (r) through $(\lambda/\lambda_\theta)^2 = r(5/3)Sc$—is plotted in Fig. 5 for the current ILES, the (Sc = 0.7) LES of [4], DNS [6, 9], for which $Sc = 0.7$ and $Sc = 1$, respectively. Following the theory in [8], using small scale isotropy assumptions,

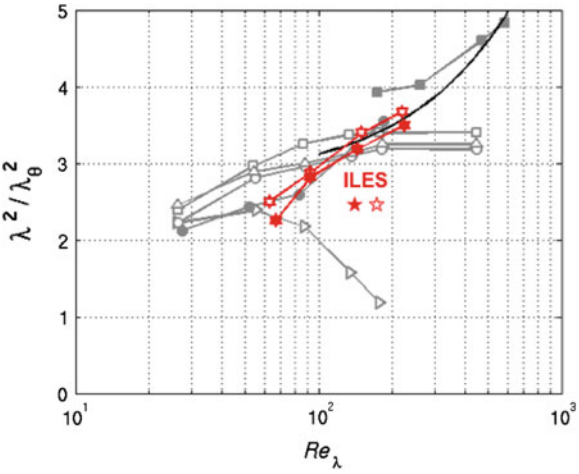

Fig. 5 $(\lambda/\lambda_\theta)^2$ as a function of Re_λ. *Gray full circle line* DNS [6]; Gray full square line: DNS [9]; Gray open square/triangle/circle LES [4]; *Gray open right-triangle* LES [4] without scalar SGS model; *full star* ILES $Ma = 0.27$; *open star* ILES $Ma = 0.13$; *full black-line* theory [8]

and rearranging the stationary forced equations for the scalar variance and scalar dissipation, we can derive an expression for $(\lambda/\lambda_\theta)^2$ [3] which exhibits its linear dependence with Re_λ for Sc = 1.0 and high Re – also plotted in Fig. 5. This result is noteworthy on several accounts. For one it shows that the ratio r—or squared ratio of Taylor micro-scales $(\lambda/\lambda_\theta)^2$—is a function of Re in developed turbulence. That the eddy turnover rate of turbulent kinetic energy and scalar variance are proportional to each other and not a function of Re has been a fundamental assumption underlying many models in turbulence phenomenology (e.g., as noted in [4]).

Early DNS results [6] showed continued growth of $(\lambda/\lambda_\theta)^2$ with increasing Re_λ, while the LES results using an explicit scalar SGS model [9] are asymptotically constant. Moreover, when the explicit scalar SGS model of [4] is turned off, the ratio rapidly decreases with Re_λ. However, the ILES simulation (also without an explicit scalar SGS term), exhibits neither decreasing nor asymptotically constant behavior, but shows continued growth over the simulated range of effective Re_λ very consistent with the early DNS [6] and the trends suggested by the more recent DNS data in [9]. The asymptotically linear dependence on Re_λ of of $(\lambda/\lambda_\theta)^2$ can thus be predicted by theory [8], and it is suggested by DNS [6, 9] and the present ILES.

3 Summary

We find that sufficiently resolved ILES can capture the fundamental aspects of the mixing transition and characteristics of developed isotropic turbulence for high Re and $Sc \sim 1$. Detailed analysis based on statistical turbulence metrics and probability distribution functions (PDFs) of velocity and scalar, including effects of Ma and grid resolution are addressed in detail in [3]. As the effective Re is increased, the SGS scalar mixing model implicitly provided by a well designed ILES numerics is

found to be adequate to consistently capture expected mixing characteristics from previously reported studies, namely, the gaussian behavior of fluctuating velocity and scalar PDFs, non-gaussian (and appropriately biased—when applicable) PDF tails of their derivatives, and asymptotically constant non-dimensional scalar variance and increasing squared-ratio of the Taylor micro-scales with Re. The results are regarded as a clear demonstration of the feasibility of predictive under-resolved simulations of high–Re turbulent scalar mixing with ILES. They strongly suggest enslavement of the small scale mixing dynamics to that of the larger scales of the flow for sufficiently large Re.

Acknowledgments This work was made possible by funding from the LANL LDRD-ER on "LES Modeling for Predictive Simulations of Material Mixing", through project number 20100441ER.

References

1. Sagaut, P.: Large Eddy Simulation for Incompressible Flows, 3rd edn. Springer, NY (2006)
2. Grinstein, F.F., Margolin, L.G., Rider, W.J., Implicit Large Eddy Simulation: Computing Turbulent Flow Dynamics. Cambridge, 2nd printing 2010
3. Wachtor, A.J., Grinstein, F.F., DeVore, C.R., Ristorcelli, J.R., Margolin, L.G.: Implicit large-eddy simulation of passive scalar mixing in statistically stationary isotropic turbulence. Phys. Fluids **25**, 025–101 (2013)
4. Pullin, D.I.: A vortex-based model for the subgrid flux of a passive scalar. Phys. Fluids **12**, 2311 (2000)
5. Tennekes, H., Lumley, J.L.: A First Course in Turbulence. MIT Press, Cambridge, MA (1972)
6. Overholt, M.R., Pope, S.B.: Direct numerical simulation of a passive scalar with imposed mean gradient in isotropic turbulence. Phys. Fluids **8**, 3128 (1996)
7. Dowling, D.R., Dimotakis, P.E.: Similarity of concentration field of gas-phase turbulent jets. J. Fluid Mech. **218**, 109–141 (1990)
8. Ristorcelli, J.R.: Passive scalar mixing: analytic study of time scale ratio, variance, and mix rate. Phys. Fluids **18**, 1–17 (2006)
9. Gotoh, T., Watanabe, T., Suzuki, Y.: Universality and anisotropy in passive scalar fluctuations in turbulence with uniform mean gradient. J. Turbulence **12**(48), 1–27 (2011)
10. Grinstein, F.F., Vortex dynamics and transition to turbulence in free shear flows, Chap. 8 in Ref. [1]
11. Petersen, M.R., Livescu, D.: Forcing for statistically stationary compressible isotropic turbulence. Phys. Fluids **22**, 1–11 (2010)
12. Fureby, C., Grinstein, F.F.: Monotonically integrated large eddy simulation of free shear flows. AIAA J. **37**, 56–544 (1999)
13. Dimotakis, P.E.: The mixing transition in turbulent flows. J. Fluid Mech. **409**, 69–98 (2000)

New Differential Operators for Large-Eddy Simulation and Regularization Modeling

F.X. Trias, A. Gorobets, A. Oliva and R.W.C.P. Verstappen

1 Introduction

We consider the numerical simulation of the incompressible Navier-Stokes (NS) equations. In primitive variables they read

$$\partial_t \mathbf{u} + \mathscr{C}(\mathbf{u}, \mathbf{u}) = \mathscr{D}\mathbf{u} - \nabla p, \qquad \nabla \cdot \mathbf{u} = 0, \tag{1}$$

where $\mathbf{u}$ denotes the velocity field, p represents the pressure, the non-linear convective term is given by $\mathscr{C}\mathbf{u}\mathbf{v} = (\mathbf{u} \cdot \nabla)\,\mathbf{v}$, and the diffusive term reads $\mathscr{D}\mathbf{u} = \nu \Delta \mathbf{u}$, where ν is the kinematic viscosity. Direct simulations at high Reynolds numbers are not feasible because the convective term produces far too many scales of motion. Hence, in the foreseeable future numerical simulations of turbulent flows will have to resort to models of the small scales. The most popular example thereof is the Large-Eddy Simulation (LES). Shortly, LES equations result from filtering the NS equations in space

$$\partial_t \overline{\mathbf{u}} + \mathscr{C}(\overline{\mathbf{u}}, \overline{\mathbf{u}}) = \mathscr{D}\overline{\mathbf{u}} - \nabla \overline{p} - \nabla \cdot \tau(\overline{\mathbf{u}})\ ; \qquad \nabla \cdot \overline{\mathbf{u}} = 0, \tag{2}$$

F.X. Trias (✉) · A. Gorobets · A. Oliva
Heat and Mass Transfer Technological Center, Technical University of Catalonia,
ETSEIAT, C/Colom 11, 08222 Terrassa, Spain
e-mail: xavi@cttc.upc.edu

A. Gorobets
e-mail: andrey@cttc.upc.edu

A. Oliva
e-mail: oliva@cttc.upc.edu

R.W.C.P. Verstappen
Johann Bernoulli Institute for Mathematics and Computing Science,
University of Groningen, P.O. Box 407, 9700 AK Groningen, The Netherlands
e-mail: R.W.C.P.Verstappen@rug.nl

J. Fröhlich et al. (eds.), *Direct and Large-Eddy Simulation IX*,
ERCOFTAC Series 20, DOI 10.1007/978-3-319-14448-1_4

where $\overline{\mathbf{u}}$ is the filtered velocity and $\tau(\overline{\mathbf{u}})$ is the subgrid stress tensor and aims to approximate the effect of the under-resolved scales, i.e. $\tau(\overline{\mathbf{u}}) \approx \overline{\mathbf{u} \otimes \mathbf{u}} - \overline{\mathbf{u}} \otimes \overline{\mathbf{u}}$. Then, the closure problem consists on replacing (approximating) the tensor $\overline{\mathbf{u} \otimes \mathbf{u}}$ with a tensor depending only on $\overline{\mathbf{u}}$ (and not $\mathbf{u}$). Because of its inherent simplicity and robustness, the eddy-viscosity assumption is by far the most used closure model

$$\tau(\overline{\mathbf{u}}) \approx -2\nu_e S(\overline{\mathbf{u}}), \tag{3}$$

where ν_e denotes the eddy-viscosity. Notice that $\tau(\overline{\mathbf{u}})$ is considered traceless without the loss of generality, because the trace can be included as part of the pressure, $\overline{p}$. Following the same notation than in [1], the eddy-viscosity can be modeled in a natural way as follows

$$\nu_e = (C_m \delta)^2 D_m(\overline{\mathbf{u}}) \tag{4}$$

where C_m is the model constant, δ is the subgrid characteristic length and D_m is a differential operator associated with the model. This provides a general framework where most of the existing eddy-viscosity models can be represented [1].

Alternatively, regularizations of the non-linear convective term basically reduce the transport towards the small scales: the convective term in the NS equations, $\mathscr{C}$, is replaced by a smoother approximation, $\tilde{\mathscr{C}}$,

$$\partial_t \mathbf{u}_\varepsilon + \tilde{\mathscr{C}}(\mathbf{u}_\varepsilon, \mathbf{u}_\varepsilon) = \mathscr{D}\mathbf{u}_\varepsilon - \nabla p_\varepsilon, \qquad \nabla \cdot \mathbf{u}_\varepsilon = 0. \tag{5}$$

The first outstanding approach in this direction goes back to Leray [2]. The Navier-Stokes-α model also forms an example thereof [3]. More recently, a family of regularization methods that exactly preserve the symmetry and conservation properties of the convective term was proposed in [4]. In this way, the production of smaller and smaller scales of motion is restrained in an unconditionally stable manner. A very recent application of this regularization approach can be found in [5].

2 Restraining the Production of Small Scales

The essence of turbulence are the smallest scales of motion. They result from a subtle balance between convective transport and diffusive dissipation. Numerically, if the grid is not fine enough, this balance needs to be restored by a turbulence model. Both regularization modeling and LES aim to do so by decreasing the non-linear transport and increasing the dissipation, respectively. Hence, in our opinion, the success of any turbulence model strongly depends on the ability to capture well this (im)balance.

Let us consider an arbitrary part of the domain flow, Ω, with periodic boundary conditions. The inner product is defined in the usual way: $(a, b) = \int_\Omega a \cdot b d\Omega$. Then, taking the L^2 inner product of (1) with—$\Delta\mathbf{u}$ leads to the enstrophy equation

$$\frac{1}{2}\frac{d}{dt}\|\omega\|^2 = (\omega, \mathscr{C}(\omega, \mathbf{u})) - \nu(\nabla\omega, \nabla\omega), \tag{6}$$

where $\|\omega\|^2 = (\omega, \omega)$ and the convective term contribution $(\mathscr{C}(\mathbf{u}, \omega), \omega) = 0$ vanishes because of the skew-symmetry of the convective operator. Following the same arguments than in [6], the vortex-stretching term can be expressed in terms of the invariant $R = -1/3tr(S^3) = -det(S)$

$$(\omega, \mathscr{C}(\omega, \mathbf{u})) = -\frac{4}{3}\int_\Omega tr(S^3)d\Omega = 4\int_\Omega R d\Omega = 4\widetilde{R}, \tag{7}$$

whereas the diffusive terms may be bounded in terms of the invariant $Q = -1/2tr(S^2)$

$$(\nabla\omega, \nabla\omega) = -(\omega, \Delta\omega) \leq -\lambda_\Delta(\omega, \omega) = 4\lambda_\Delta \int_\Omega Q d\Omega = 4\lambda_\Delta \widetilde{Q}, \tag{8}$$

where $\lambda_\Delta < 0$ is the largest (smallest in absolute value) non-zero eigenvalue of the Laplacian operator Δ on Ω and $\widetilde{(\cdot)}$ denotes the integral over Ω. However, it relies on the accurate estimation of λ_Δ on Ω. The latter may be cumbersome, especially on unstructured grids. Alternatively, it may be (numerically) computed directly from $(\nabla\omega, \nabla\omega)$ or, even easier, by simply noticing that $(\nabla\omega, \nabla\omega) = 4\int_\Omega Q(\omega)d\Omega = 4\widetilde{Q(\omega)}$. However, from a numerical point-of-view, this type of integrations are not straightforward. Instead, recalling that $\nabla \times \nabla \times \mathbf{u} = \nabla(\nabla \cdot \mathbf{u}) - \Delta\mathbf{u}$ and $\nabla \cdot \mathbf{u} = 0$, a more appropriate expression can be obtained as follows

$$(\nabla\omega, \nabla\omega) = -(\omega, \Delta\omega) = (\omega, \nabla \times \nabla \times \omega) = (\nabla \times \omega, \nabla \times \omega) = \|\Delta\mathbf{u}\|^2. \tag{9}$$

Then, to prevent a local intensification of vorticity, i.e. $\|\omega\|_t \leq 0$, the inequality $H_\Omega \leq \nu(\Delta\mathbf{u}, \Delta\mathbf{u})/(\omega, S\omega)$ must be satisfied, where H_Ω denotes the overall damping introduced by the model in the (small) part of the domain Ω. Additionally, the dynamics of the large scales should not be significantly affected by the (small) scales contained within the domain Ω, i.e. $(\omega, S\omega) < 0$. Hence, to confine the dynamics of the small scales suffices to modify the previous inequality by simply taking the absolute value of its right-hand-side. Then, from Eq. (7) and noticing that $0 < H_\Omega \leq 1$, a proper definition of the overall damping factor follows

$$H_\Omega = \min\left\{\nu\|\Delta\mathbf{u}\|^2/|\widetilde{R}|, 1\right\}. \tag{10}$$

This differential operator satisfies a list of desirable properties. Namely, it automatically switches off ($R \to 0$) for laminar flows (no vortex-stretching), 2D flows ($\lambda_2 = 0 \to R = 0$) and in the wall (the near-wall behavior of the invariants is $R \propto y^1$ and $Q \propto y^0$, where y is the distance to the wall). Notice that these features would be automatically inherit by any type of model based on this differential operator.

2.1 Regularization Modeling

Following the same notation than in [4], the action of a regularization model within the (small) part of the domain Ω (see above) can be approximated as follows

$$(\omega, \tilde{\mathscr{C}}(\omega, \mathbf{u})) \approx f_\Omega(\omega, \mathscr{C}(\omega, \mathbf{u})), \tag{11}$$

where the damping factor, f_Ω, depends on the specific regularization method and the kernel of the filter (see [4, 5], for details). Hence, the criterion proposed in Eq. (10) can be applied for regularization modeling equating f_Ω and H_Ω, i.e. $f_\Omega = H_\Omega = \min\{\nu\|\Delta\mathbf{u}\|^2/|\widetilde{R}|, 1\}$. For implementation details the reader is referred to [5].

2.2 Towards a Simple LES

An eddy-viscosity model, $\tau(\overline{\mathbf{u}}) = -2\nu_e S(\overline{\mathbf{u}})$, adds the dissipation term $(\nabla\overline{\omega}, \nu_e\nabla\overline{\omega})$ to the enstrophy equation. Then, the eddy-viscosity, ν_e, would result from a simple balance in order to prevent the local intensification of vorticity, $\|\overline{\omega}\|_t^2 \leq 0$,

$$\nu_e = 4|\widetilde{R}|/\|\Delta\overline{\mathbf{u}}\|^2. \tag{12}$$

This analysis can be extended further for other differential operators. For instance, $\tau'(\overline{\mathbf{u}}) = 2\nu_e' S(\Delta\overline{\mathbf{u}})$ and $\tau''(\overline{\mathbf{u}}) = -2\nu_e'' S(\Delta^2\overline{\mathbf{u}})$, where $\Delta^2 \equiv \Delta\Delta$ is the bi-Laplacian, lead to the following hyperviscosity terms in the enstrophy equation

$$-(\nabla\overline{\omega}, \nu_e'\nabla\Delta\overline{\omega}) \quad \text{and} \quad (\nabla\overline{\omega}, \nu_e''\nabla\Delta^2\overline{\omega}). \tag{13}$$

Then, following similar reasonings, ν_e' and ν_e'' follow

$$\nu_e' = -4|\widetilde{R}|/(\Delta\overline{\mathbf{u}}, \Delta^2\overline{\mathbf{u}}) \quad \text{and} \quad \nu_e'' = 4|\widetilde{R}|/\|\Delta^2\overline{\mathbf{u}}\|^2. \tag{14}$$

It is noticeable that, apart from the computation of R, all these models can be straightforwardly implemented by simply re-using the discrete diffusive operator.

3 Performance of $\mathscr{C}_4$-Regularization for Turbulent Buoyancy Driven Flows

The configuration adopted to illustrate the performance of the $\mathscr{C}_4$-regularization (see [4], for details) method in conjunction with the differential operator proposed in Eq. (10) corresponds to an air-filled (Pr $= 0.7$) differentially heated cavity (DHC) of aspect ratio 5 and Rayleigh number $Ra = 4.5 \times 10^{10}$ (based on the cavity height, L_3).

Table 1 The overall, the maximum and the minimum of the averaged Nusselt number

	DNS	RM1		RM2	
Mesh	$128 \times 318 \times 862$	$8 \times 20 \times 54$		$8 \times 14 \times 38$	
	$\gamma_2 = 2.0, \gamma_3 = 0.0$	$\gamma_2 = 2.0, \gamma_3 = 1.0$		$\gamma_2 = 2.3, \gamma_3 = 1.0$	
		No model	$\mathscr{C}_4$	No model	$\mathscr{C}_4$
Nu	154.5	223.8	**153.4**	207.7	**152.3**
Nu_{max}	781.5	520.6	709.4	500.4	680.0
Nu_{min}	10.5	60.4	7.1	71.0	6.1

The DNS corresponding to this configuration was carried out on the MareNostrum supercomputer using a $128 \times 318 \times 862$ mesh (the coordinate system is: x_1-spanwise, x_2-horizontal and x_3-vertical, respectively) and presented in [5] (for details about this configuration the reader is referred to this work and references therein). Firstly, we have considered two coarse meshes consisting of $8 \times 14 \times 38$ (RM2) and $8 \times 20 \times 54$ (RM1) grid points, respectively (see Table 1). The meshes are constructed keeping the same grid points distribution as for the DNS but with much coarser spatial resolution. γ_2 and γ_3 are the concentration parameters in the horizontal and vertical directions, respectively (for further details about the mesh generation the reader is referred to [5]). The domain size in the periodic direction is the same as for the DNS, i.e. $L_1/L_2 = 0.1$. In Table 1, the overall Nusselt number, Nu, together with the maximum and minimum local Nusselt numbers obtained with the coarse meshes RM1 and RM2 are compared with the DNS reference solution. Regarding the Nu, $\mathscr{C}_4$ solutions are able to provide good predictions whereas the results obtained with the same meshes but without any modeling are very far from the reference value $Nu = 154.5$. With regard to Nu_{max} and Nu_{min}, this tendency becomes even more evident. In order to confirm the reliability of the model on coarse grids, the same DHC problem has been solved on a series of 50 randomly generated meshes where the number of grid points varies within the limits: $8 \leq N_1 \leq 12$, $16 \leq N_2 \leq 28$ and $44 \leq N_3 \leq 70$, respectively. The number of grid points in each direction has been randomly generated irrespectively of the number of points in the other two directions; therefore, some of the numerical experiments correspond to highly skewed meshes. Results for the overall Nusselt and the center-line stratification are displayed in Fig. 1 (left). The very good prediction of Nu for all the tested configurations is remarkable; in contrast, the results obtained without modeling substantially differ from the reference solution. Even more important is the fairly good prediction of the stratification. Notice the inaccuracy of the results obtained with a relatively fine mesh of $32 \times 80 \times 216$ (MeshC) grid points. Similar behavior is observed in Fig. 1 (right) where the results for the maximum vertical velocity and the wall shear stress at the horizontal mid-plane, $x_3 = 0.5$, are displayed. These two quantities provide valuable information about whether the boundary layer is correctly captured by the model. The $\mathscr{C}_4$ solutions predict quite well the (0.430, 0.227) reference solution whereas both quantities are clearly under-predicted when the model is switched off.

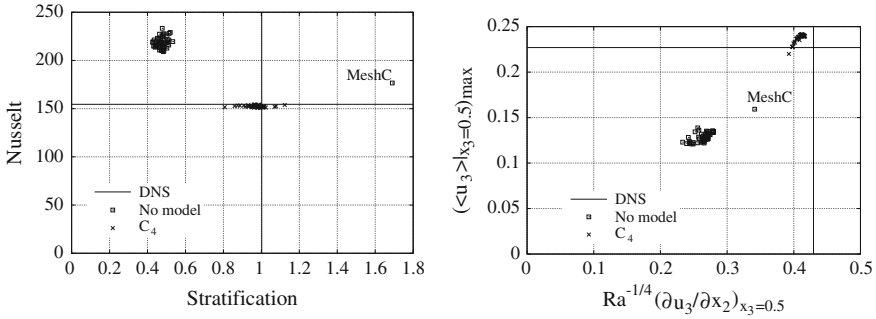

Fig. 1 *Left* The overall Nusselt number and the center-line stratification. *Right* The maximum vertical velocity and the wall shear stress scaled by $Ra^{-1/4}$ at the horizontal mid-height plane

4 Concluding Remarks and Future Research

A family of new differential operators for turbulence modeling has been derived by considering the balance between the vortex-stretching contribution and the dissipation in the enstrophy equation. They are suitable to be used for both regularization and LES modeling. In the context of LES, three eddy-viscosity-type models have been obtained. Namely, (i) $\tau(\overline{\mathbf{u}}) = -2\nu_e S(\overline{\mathbf{u}})$, (ii) $\tau'(\overline{\mathbf{u}}) = 2\nu'_e S(\Delta\overline{\mathbf{u}})$ and (iii) $\tau''(\overline{\mathbf{u}}) = -2\nu''_e S(\Delta^2\overline{\mathbf{u}})$, where ν_e, ν'_e and ν''_e are given by Eqs. (12) and (14), respectively. They can be related with already existing approaches. Firstly, the model (i) is almost the same than the recently proposed QR-model [6]. Essentially, they only differ on the calculation of the diffusive contribution to the enstrophy equation: instead of making use of the equality (9) it is bounded by means of the inequality (8); therefore, the eddy-viscosity is given by $\nu_e \propto \lambda_\Delta^{-1}|\widetilde{R}|/\widetilde{Q}$ instead of Eq. (12). Regarding the models (ii) and (iii) they can be respectively related to the well-known small-large and small-small variational multiscale methods [7] by noticing that $\mathbf{u}' = -(\varepsilon^2/24)\Delta\mathbf{u} + \mathcal{O}(\varepsilon^4)$. All these models switch off ($R \to 0$) for laminar (no vortex-stretching), 2D flows ($\lambda_2 = 0 \to R = 0$) and near the wall ($R \propto y^1$). The performance of the first differential operator has been successfully tested for a buoyancy driven turbulent flow. To test the performance of the rest of the proposed turbulence models is part of our research plans.

Acknowledgments This work has been financially supported by the *Ministerio de Ciencia e Innovación*, Spain (ref. ENE2010-17801). Also by a *Juan de la Cierva* postdoctoral contract (JCI-2009-04910) by the *Ministerio de Ciencia e Innovación*. Calculations have been performed on the IBM MareNostrum supercomputer at the Barcelona Supercomputing Centre. The authors thankfully acknowledge these institutions.

References

1. Nicoud, F., Toda, H.B., Cabrit, O., Bose, S., Lee, J.: Phys. Fluids **23**(8), 085106 (2011)
2. Leray, J.: Acta Math. **63**, 193–248 (1934)
3. Geurts, B.J., Holm, D.D.: Phys. Fluids **15**, L13–L16 (2003)
4. Verstappen, R.: Comput. Fluids **37**, 887–897 (2008)
5. Trias, F.X., Gorobets, A., Pérez-Segarra, C.D., Oliva, A.: Int. J. Heat Mass Transf. **57**, 171–182 (2013)
6. Verstappen, R.: J. Sci. Comput. **49**(1), 94–110 (2011)
7. Hughes, T.J.R., Mazzei, L., Oberai, A.A., Wray, A.A.: Phys. Fluids **13**(2), 505–512 (2001)

Assessment of Implicit Subgrid-Scale Modeling for Turbulent Supercritical Mixing

C.A. Niedermeier, S. Hickel and N.A. Adams

1 Introduction

Space transportation systems predominantly rely on cryogenic rocket combustion engines, which have successfully been used for decades. However, satisfying the increasing requirements in terms of rocket performance and reliability is very challenging due to decreasing budgets and the request for short development cycles. Therefore, the importance of computational methods in the development process increases steadily, raising the demand for computational fluid dynamics (CFD) tools that are able to simulate the flow at rocket combustor conditions.

The process of the propellant injection into a rocket combustion chamber is strongly three-dimensional and unsteady. Therefore, Large Eddy Simulation (LES) appears to be the most suitable method for future CFD tools.

Many propellants are in a supercritical state at injection, because the pressure in modern combustion chambers often exceeds 100 bar. As the fluid properties are significantly affected by molecular interactions in this high pressure environment, a real-gas equation of state and suitable relations for the transport properties have to be used for the numerical simulation.

The subgrid-scale (SGS) turbulence models of all well-established LES methods were originally designed and calibrated for incompressible or ideal gas flows. Therefore, they have to be validated and, if necessary, adjusted for the simulation of flows at supercritical pressure. We already successfully validated our in-house code INCA

C.A. Niedermeier (✉) · S. Hickel · N.A. Adams
Institute of Aerodynamics and Fluid Mechanics, Technische Universität München,
Boltzmannstr. 15, 85748 Garching B. München, Germany
e-mail: christoph.niedermeier@tum.de

S. Hickel
e-mail: sh@tum.de

N.A. Adams
e-mail: nikolaus.adams@tum.de

J. Fröhlich et al. (eds.), *Direct and Large-Eddy Simulation IX*,
ERCOFTAC Series 20, DOI 10.1007/978-3-319-14448-1_5

in terms of real-gas thermodynamics and general applicability for the simulation of supercritical flows [3, 5].

We now apply this methodology to supercritical nitrogen jet experiments of Mayer et al. [4]. The setup of the experiments, where cold, transcritical nitrogen is injected into nitrogen at supercritical temperature and pressure, reproduces the situation in a real rocket combustion chamber to a realistic extent.

2 Turbulence Modeling and Numerical Method

As an intermediate approach between Reynolds-averaged Navier-Stokes (RANS) simulations and Direct Numerical Simulations (DNS), LES resolves the large scales of turbulence while the small scales below the grid width have to be modeled. In this paper, we apply the Adaptive Local Deconvolution Method (ALDM), which follows an implicit LES (ILES) approach.

The basic idea of ILES is to combine turbulence modeling and numerical discretization of the conservation equations. ALDM is a nonlinear finite volume method and incorporates free parameters in the discretization scheme, which can be used to control the truncation error. A physically motivated implicit SGS model that is consistent with turbulence theory is obtained through parameter calibration, see Ref. [2].

ALDM is implemented in our in-house code INCA for Cartesian collocated grids and used to discretize the convective terms of the Navier-Stokes equations (see Ref. [2] for a detailed description). The diffusive terms are discretized by 2nd order centered differences and a 3rd order explicit Runge-Kutta method is used for time integration.

3 Thermodynamic Modeling and Transport Properties

All thermodynamic properties are calculated as the sum of an ideal reference value and a departure function that accounts for real gas effects. These departure functions are determined by the Peng-Robinson (PR) equation of state (EOS) [6]

$$p = \frac{RT}{V-b} - \frac{a\,(T)}{V^2 + 2Vb - b^2}\,, \tag{1}$$

where V is the molar volume and R is the universal gas constant with a value of $R = 8.314472\,\mathrm{J/(mol\,K)}$. The constants $a\,(T)$ and b are calculated from empirical relations. $a\,(T)$ accounts for attractive forces between the molecules in the fluid and is calculated from the empirical equation

$$a\,(T) = 0.457235\frac{R^2 T_c^2}{p_c}\left(1 - \kappa\left(1 - \sqrt{\frac{T}{T_c}}\right)\right)^2, \tag{2}$$

where $\kappa = 0.37464 + 1.54226\,\omega - 0.26992\,\omega^2$ is a function of the acentric factor ω. The effects of the reduction of free volume by the particular volume of the molecules are taken into account via $b = 0.077796\,RT_c/p_c$. T_c and p_c are the critical temperature and pressure of nitrogen (126.2 K/3.40 MPa). The PR EOS does not predict the density very accurately in the transcritical region. Therefore, the empirical volume correction (VC) method of Harstad et al. [1] was chosen for the final implementation.

As INCA is a density-based code, pressure and temperature have to be calculated at each timestep from internal energy and density. For ideal gases, this can be done in a straightforward manner by using the ideal gas law. For real gases, however, an iterative procedure is necessary to find the correct values for pressure and temperature. A nonlinear least squares optimization method is best suited to efficiently solve the problem. Therefore, a trust region method is used for the iterative calculation.

Viscosity and thermal conductivity are calculated according to an approach developed by Chung et al., which uses empirical correlations for dense fluids. A detailed description of this method can be found in Ref. [8].

4 Computational Setup

The test chamber used in the experiments by Mayer et al. [4] had a cross section of 60×60 mm with an adiabatic front wall and isothermal outer walls at a temperature of 298 K. In contrast to previous simulations of these experiments, where only a round, smaller section of the chamber was simulated [7, 9], we use the original width and height of the chamber for our simulations and apply the same wall boundary conditions as in the experiments. The length of our simulation domain is 80 mm with a convective outlet condition at the downstream boundary and the diameter of the jet at the inlet is D = 2.2 mm.

We performed LES for two parameter sets corresponding to case 3 and case 4 of the experimental database. The inital and boundary conditions applied in the simulations are listed in Table 1. At the inlet, a constant temperature is prescribed along with a time varying fully turbulent velocity profile resembling a turbulent pipe flow. The grid is refined near the central cutplanes of the domain in both the x-z- and the x-y-direction to improve the resolution near the centerline of the jet, see Fig. 1. The grid spacing in downstream direction is homogenenous, leading to a total number of about 3.9 million cells.

Table 1 Mean flow properties of the computed test cases

Case	3	3	4	4
Location	Inlet	Chamber	Inlet	Chamber
$\bar{u}_1$, $\frac{\mathrm{m}}{\mathrm{s}}$	4.9	0	5.4	0
ρ, $\frac{\mathrm{kg}}{\mathrm{m}^3}$	457.8	45.08	164.4	45.19
p_0, bar	39.7	39.7	39.8	39.8
T, K	126.9	298	137	298

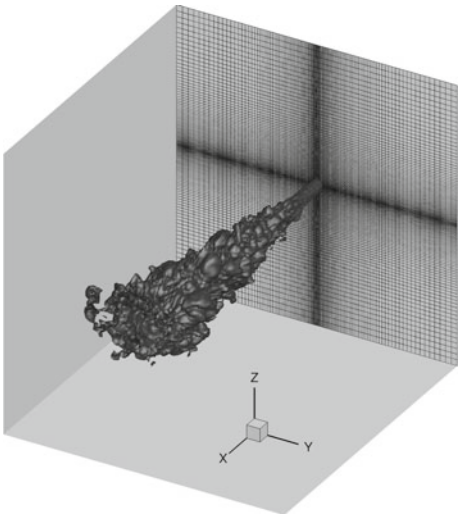

Fig. 1 Case 4—isosurface of the density 50 kg/m^3 and grid resolution in y- and z-direction

5 Results

In the following, we analyze the results for both cases in terms of flow visualizations for the velocity magnitude as well as for the temperature. Furthermore, we compare our results for the mean density along the centerline in streamwise direction with results from previous works [7, 9].

5.1 Flow Visualizations

Figure 2a, b show the velocity magnitude and the temperature for both cases in the central x-z-cutplane. It is clearly visible that the instabilities of Kelvin-Helmholtz type at the edge of the jet arise further downstream in case 3, which is the expected behaviour due to the higher density in the core region. This cold and therefore dense core region is also much longer in case 3, meaning that the main mixing process between the injected, cold nitrogen and the surrounding, warm nitrogen takes place at a later stage.

Fine structures of cold and warm packets of fluid mixing with each other and thus illustrating this process can be seen in Fig. 2b although the grid is rather coarse, meaning that ALDM is able to reproduce such flow patterns also with a low resolution. When compared to flow visualizations of Petit et al. [7], the main features of our results are very similar while being obtained on a grid with less than one third of the grid points.

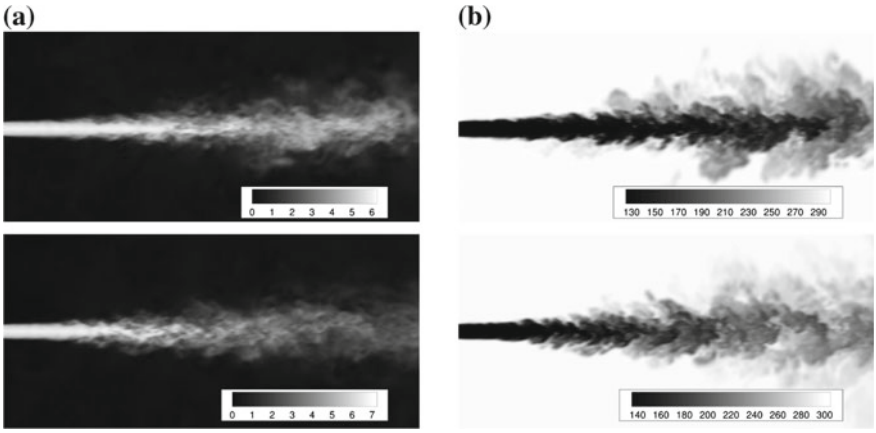

Fig. 2 **a** Velocity magnitude (m/s) in the central x-z-cutplane: case 3 (*top*), case 4 (*bottom*) **b** Temperature (K) in the central x-z-cutplane: case 3 (*top*), case 4 (*bottom*)

5.2 Centerline Density

Figure 3 shows the mean density along the centerline in x-direction for different SGS models and EOS for our simulations as well as from previous works [7, 9]. The results for both cases indicate that the well-defined density of the jet at the inlet is matched best with the thermodynamic modeling which we chose for our work, namely the PR EOS with VC. Furthermore, ALDM matches the experimental data for case 4 best. The slight deviations from the experimental data for case 3 might be caused by the coarse grid and are currently under investigation. Overall, ALDM

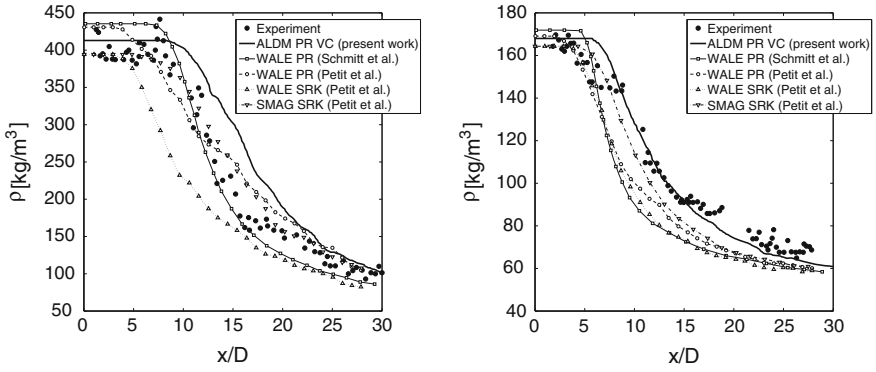

Fig. 3 Mean density along the centerline in x-direction for different SGS models (ALDM, WALE, Smagorinsky) and EOS (PR with VC, PR without VC, Soave-Redlich-Kwong) compared with experimental data: case 3 (*left*), case 4 (*right*)

delivers the best results for the combination of both test cases, especially when the coarser mesh of our simulations is taken into account.

6 Summary and Outlook

We applied the Adaptive Local Deconvolution Method to simulate supercritical nitrogen jets, resembling a realistic injection and mixing process as it is present in current rocket combustion chambers. Our results show a good agreement with the experimental data as well as with previous works, although we used a mesh which was significantly coarser than in other simulations of the same experimental setup. This means that ALDM is suitable for the simulation of realistic flows at rocket combustor conditions and therefore promising to be used in future industry-oriented CFD tools.

In the future, we will use ALDM for the simulation of multi-component coaxial injection and the subsequent mixing and combustion process of different species like Oxygen and Hydrogen or Oxygen and Methane. Our final goal is to provide an ILES methodology suitable for the design and the predictive analysis of future rocket combustors.

Acknowledgments Financial support has been provided by the German Research Foundation (Deutsche Forschungsgemeinschaft – DFG) in the framework of the Sonderforschungsbe-reich/ Transregio 40. Computational resources have been provided by the Leibniz–Rechenzentrum München (LRZ) under grant h0983.

References

1. Harstad, K., Miller, R., Bellan, J.: Efficient high-pressure state equations. AIChE J. **43**(6), 1605–1610 (1997)
2. Hickel, S., Larsson, J.: An adaptive local deconvolution model for compressible turbulence. In: Proceedings of the CTR Summer Program, pp. 85–96, (2008).
3. Jarczyk, M.M., Pfitzner, M., Niedermeier, C.A., Hickel, S., Adams, N.A.: Large eddy simulation of supercritical mixing layers. In: Proceedings of 4th European Conference for Aerospace Sciences, St. Petersburg, Russia, July 2011.
4. Mayer, W., Telaar, J., Branam, R., Schneider, G., Hussong, J.: Raman measurements of cryogenic injection at supercritical pressure. Int. J. Heat Mass Transfer **39**, 709–719 (2003)
5. Niedermeier, C.A., Hickel, S., Adams, N.A., Jarczyk, M.M., Pfitzner, M.: Large eddy simulation of oxygen/hydrogen mixing layers under supercritical conditions. In: Proceedings of 7th European Aerothermodynamics Symposium on Space Vehicles, Brugge, Belgium, May 2011.
6. Peng, D.-Y., Robinson, D.P.: A new two-constant equation of state. Ind. Eng. Chem. Fundam. **15**(1), 59–64 (1976)
7. Petit, X., Ribert, G., Domingo, P.: Large eddy simulation of supercritical fluid injection. In: Proceedings of 9th International ERCOFTAC Symposium on Engineering Turbulence Modelling and Measurements, Thessaloniki, Greece, June 2012.
8. Poling, B.E., Prausnitz, J.M., O'Connell, J.P.: The Properties of Gases and Liquids. McGraw-Hill, New York (2004)
9. Schmitt, T., Selle, L., Cuenot, B., Poinsot, T.: Large-eddy simulation of transcritical flows. C. R. Mecanique **337**(6), 528–538 (2009)

Validation of an Entropy-Viscosity Model for Large Eddy Simulation

J.-L. Guermond, A. Larios and T. Thompson

1 Introduction

A primary mainstay of difficulty when working with problems of very high Reynolds numbers is the lack of computational resources; this implies that numerical simulations in this realm are, in general, always under-resolved. That is, large gradients and eddy-phenomena, exist at the sub-grid level and cannot be correctly represented by the mesh; therefore, at the mesh scale, these solutions can be considered as behaving in a singular manner. As time progresses, these unresolved facets of the flow are likely to produce still larger gradients through the coupling of wave modes via the action of the nonlinear term; this induces an accumulation of energy at the grid scale. A solution proposed in [1] consists of monitoring the local kinetic energy balance and introducing a localized dissipation in these regions that is proportional to the violation of this balance (this is the so-called entropy viscosity). The deviation from the local energy balance (which we call the entropy residual) can be thought of as an indicator for local entropy production in analogy with entropy production for scalar conservation laws.

1.1 Motivation

Here a brief overview of the motivation for the entropy-viscosity is presented. See [1] and the references therein for a more in-depth discussion of the central ideas of the entropy-viscosity technique.

J.-L. Guermond (✉) · A. Larios · T. Thompson
Department of Mathematics, Texas A&M University,
College Station, TX 77843, USA
e-mail: guermond@math.tamu.edu

A. Larios
e-mail: alarios@math.tamu.edu

T. Thompson
e-mail: tthompson@tennessee.edu

J. Fröhlich et al. (eds.), *Direct and Large-Eddy Simulation IX*,
ERCOFTAC Series 20, DOI 10.1007/978-3-319-14448-1_6

Let (u_h, p_h) be an approximate velocity and pressure, where h denotes the grid scale, and define the numerical residual of the energy equation, $D_h(x,t)$, by

$$D_h(x,t) := \partial_t(\tfrac{1}{2}u_h^2) + \nabla\cdot((\tfrac{1}{2}u_h^2 + p_h)u_h) \\ - Re^{-1}\Delta(\tfrac{1}{2}u_h^2) + Re^{-1}(\nabla u_h)^2 - f\cdot u_h. \tag{1}$$

In a resolved flow $D_h(x,t)$ should be on the order of the consistency error of the method; a large value[1] of $|D_h(x,t)|$ is caused by under-resolution. In such situations, one would therefore wish to enforce

$$|D_h(x,t)| = 0. \tag{2}$$

However, enforcing (2) directly may over-determine the problem. In [1], the authors circumvent this difficulty by constructing a viscosity proportional to $|D_h(x,t)|$. This viscosity is called the entropy-viscosity (EV), and is defined by

$$\nu_E(x,t) := \min\left(c_{max}h(x)|u_h(x,t)|, c_E h^2(x)\frac{|D_h(x,t)|}{||u^2||_{L^\infty(\Omega)}}\right). \tag{3}$$

The momentum equation is then modified by adding the term $-\nabla\cdot(\nu_E(x,t)\nabla u)$. The entropy-viscosity[2] regularizes regions which are in violation of (2) and promotes a dissipative effect on numerical singularities.

In definition (3), the constants c_{max} and c_E are tunable parameters which depend only on the numerical method and the geometry of the mesh. For instance, in the setting of scalar conservation laws, the analogue of (3) gives $c_{max} = \frac{1}{2}$ in one space dimension with piecewise linear finite elements. Definition (3) ensures that the LES viscosity will never exceed the first-order upwind viscosity. When $h(x)$, the local grid size, is small enough so that all scales are resolved, then $|D_h(x,t)|$ is on the order of the consistency error. Hence, the LES viscosity which is proportional to $h^2(x)|D_h(x,t)|$, is far smaller than the first order upwind viscosity. The entropy-viscosity is therefore consistent, and it vanishes when all of the scales of the flow are properly resolved at the grid scale. The remainder of this paper details the context in which the entropy viscosity was tested as well as the ensuing numerical results.

2 Numerical Method

Our investigations into the efficacy of the entropy-viscosity for regularizing the Navier-Stokes equation are carried out via a well-verified periodic spectral code discussed in the context of [3, 4]. Entropy-viscosity in the setting of bounded domains,

[1] The sign of the residual has a physical interpretation discussed in [1].

[2] For a discussion of a generalized framework for definition an entropy-viscosity, presented in the context of hyperbolic conservation laws, see [2].

utilizing an ADI approach found in [5], is currently being investigated by the authors; results will appear in a forthcoming paper. The spectral code mentioned above has been well validated [3, 4, 6]. Standard 2/3's de-aliasing was utilized in a periodic box of length $L = 1$. The time-stepping scheme implemented is a fully explicit four-stage Runge-Kutta method with dynamic time-stepping respecting the CFL condition. The entropy-viscosity is formed via the canonical pseudo-spectral technique whereby derivatives are computed in spectral space and products in physical space. For this situation, $c_{max} = 0.1$ and $c_E = 0.25$ were used in (3). The entropy-viscosity, computed explicitly following (3), is formulated using the current time step in conjunction with the two time-steps prior; BDF2 is employed to compute the time derivative. The result is applied, as a regularization, for the next time-step. The action of the entropy-viscosity is not present for the first three time-steps of the simulation; in practice this has caused no stability issues, even in the case of high Reynolds numbers. Finally, the divergence free condition is enforced exactly via projection onto the space of solenoidal vector fields. All the simulations presented here are done with a low-wave number forcing designed to keep the total kinetic energy approximately constant, as described in [7].

3 Results

In this section we discuss three main results: the consistency of the entropy-viscosity (i.e., when all scales are properly resolved, there is no noticeable contribution from the entropy-viscosity), energy spectrum verification results, and the action of the entropy-viscosity in the context of under-resolved and severely under-resolved flows. Results regarding additional statistics are forthcoming.

3.1 Consistency

For a resolved flow, we expect that the contribution of the entropy-viscosity should be on the order of the local consistency error of the method. Indeed, the notion of entropy-viscosity is constructed to satisfy this requirement. It is expected that the entropy-viscosity should go to zero significantly faster than $\mathcal{O}(h^2)$.

We first test an inviscid flow with the following two-dimensional initial data: $u = \cos(8\pi x)\sin(8\pi y)$, $v = -\sin(8\pi x)\cos(8\pi y)$, $w = 0$. The flow remains two-dimensional at later times (i.e. laminar) and the total kinetic energy is constant in time. We compute the Euler solution up to $t = 4$ using the DNS code, the entropy-viscosity technique and the Smagorinsky model on various grids (32^3, 64^3, 128^3, 256^3). We show in Fig. 1a the time evolution of the kinetic energy for the entropy-viscosity solution and the Smagorinsky solution on the 32^3 grid and that of the DNS solution on the 256^3 grid. It is striking that the Smagorinsky solution loses energy fast even though the flow is laminar, whereas the entropy-viscosity solution tracks the DNS

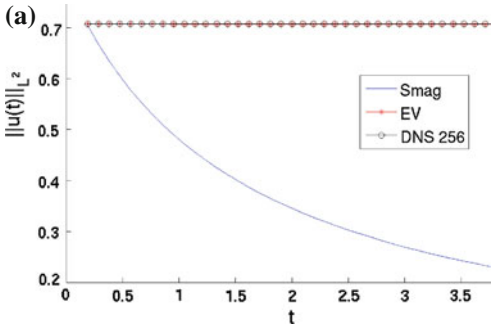

(b)

	DNS	EV	Smag.
32	4.0e-13	2.1e-06	6.8e-1
64	1.6e-16	1.1e-06	3.6e-1
128	6.5e-14	5.6e-10	1.2e-1
256	1.1e-13	8.7e-11	3.3e-2

Fig. 1 **a** Total energy versus time for Smagorinsky and EV models for an inviscid flow at 32^3. **b** Energy loss $\|\mathbf{u} - \mathbf{u}_0\|_{L^2}/\|\mathbf{u}_0\|_{L^2}$ at $t = 4$

solution rather closely. The reason why the entropy-viscosity model outperforms the Smagorinsky model is that the entropy-viscosity is very small since the flow is laminar. The entropy viscosity is significantly smaller than h^2 due to the spectral accuracy of the Fourier approximation.

We show in Fig. 1b a table displaying the relative kinetic energy loss for the DNS, entropy-viscosity, and the Smagorinsky solutions at time $t = 4$ on the four grids 32^3, 64^3, 128^3, 256^3. We observe that the DNS does not lose any energy at all the resolutions and the entropy-viscosity solution does not lose any significant amount of energy, even at low resolution. The Smagorinsky solution on the other hand has lost 68 % of the energy by time $t = 4$ on the 32^3 grid and 3.3 % on the 256^3 grid. This test confirms that contrary to the Smagorinsky method, the entropy-viscosity method does not dissipate energy in the laminar regions of the flow.

A full investigation of the consistency of the entropy viscosity method will be carried out in a forthcoming paper.

3.2 Entropy-Viscosity as an LES Model

We are interested in the applicability of the entropy-viscosity as an LES model. One expects that the entropy-viscosity should damp spurious high wave-mode contributions and resolve an otherwise unresolved flow. Therefore it is reasonable to conjuncture that entropy-viscosity is well-suited to LES.

The fundamental question of whether or not the local energy balance, being enforced via the entropy-viscosity, evinces the quintessential dynamics of resolved flow, and to what extent, is addressed; specifically the Kolmogorov $-\frac{5}{3}$ trend in the inertial range of the energy spectrum is examined.

We examine how entropy-viscosity effects the energy spectrum of under-resolved flows. In Fig. 2a–d, we show the energy spectra of simulation runs at $Re \approx 6{,}500$ for various resolutions. All runs are compared against a resolved DNS run at resolution 256^3 (called "No Model"). Each under-resolved simulation is done using the

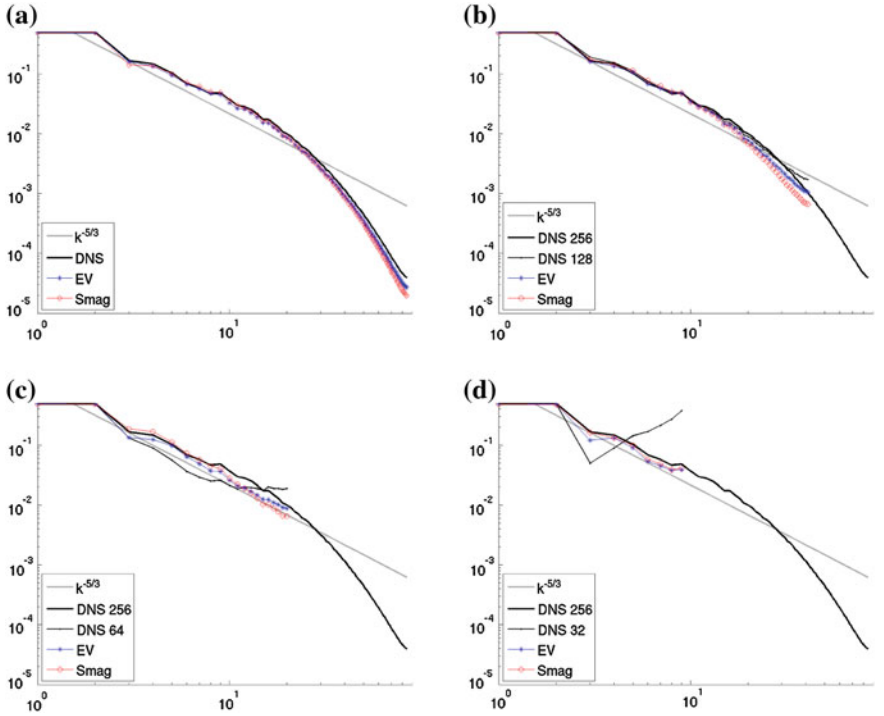

Fig. 2 **a** 256^3 resolution with entropy-viscosity (EV) and with Smagorinsky (Smag). DNS simulation included for comparison (DNS). **b** 128^3 resolution: entropy viscosity, unresolved DNS, Smagorinsky. "No Model" 256^3 DNS simulation included for comparison. **c** 64^3 resolution: entropy viscosity, unresolved DNS, Smagorinsky. "No Model" 256^3 DNS simulation included for comparison. **d** 32^3 resolution: entropy viscosity, unresolved DNS, Smagorinsky. "No Model" 256^3 DNS simulation included for comparison

entropy-viscosity model and the Smagorinsky model. One can see that unregularized ("No Model") flows fail to capture the correct spectra as expected, while the flows regularized with entropy-viscosity perform significantly better. Note also that the entropy viscosity model is always closer to the DNS spectrum than the Smagorinsky model.

3.3 Structure of the Enstropy

An important characteristic to capture in modeling isotropic turbulent flow is the structure of coherent vortex tubes, that is, the level sets of the enstropy, $|\nabla \times u(x,t)|$. We compare vortex tubes of an unresolved simulation against a simulation with exactly the same parameters, except that entropy-viscosity is added. In Fig. 3a, b, several level-surfaces with values in a range of ≈50–75 % of the maximum

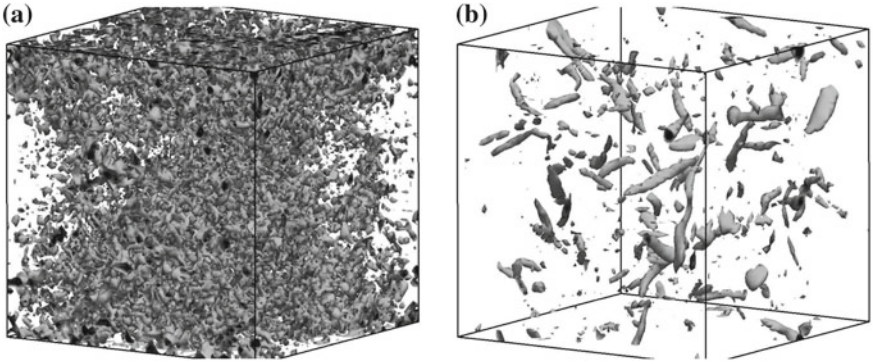

Fig. 3 **a** Surfaces of constant enstrophy for a 64^3 simulation with $Re \approx 6{,}500$ (unresolved). *Darker* surfaces indicate larger enstrophy. **b** Surfaces of constant enstrophy for a 64^3 simulation with $Re \approx 6{,}500$ with entropy-viscosity regularization at the same time step

enstrophy at the same fixed time step (taken after the flow has reached a statistical steady-state) are shown. While the enstrophy of the unresolved flow appears quite polluted (Fig. 3a), the enstrophy of the entropy-viscosity regularized flow (Fig. 3b) contains well-defined vortex tubes, and is more characteristic of turbulent flow.

References

1. Guermond, J.-L., Pasquetti, R., Popov, B.: From suitable weak solutions to entropy viscosity. J. Sci. Comput. **49**(1), 35–50 (2011). MR2831670
2. Guermond, J.-L., Pasquetti, R., Popov, B.: Entropy viscosity method for nonlinear conservation laws. J. Comput. Phys. **230**(11), 4248–4267 (2011). MR2787948 (2012h:65216)
3. Kurien, S., Taylor, M.A., Matsumoto, T.: Isotropic third-order statistic in turbulence with helicity: the 2/15-law. J. Fluid Mech. **515**, 87–97 (2004). MR2260709
4. Taylor, M.A., Kurien, S.: Recovering isotropic statistics in turbulence simulations: the Kolmogorov 4/5th law. Phys. Rev. E **68**(2), 026310 (2003). MR2010083 (2004i:76126)
5. Guermond, J.-L., Minev, P.D., Salgado, A.J.: Convergence analysis of a class of massively parallel direction splitting algorithms for the Navier-Stokes equations in simple domains. Math. Comput. **81**(280), 1951–1977 (2012). MR2945144
6. Chen, S.Y., Dhruva, B., Kurien, S., Sreenivasan, K.R., Taylor, M.A.: Anomalous scaling of low-order structure functions of turbulent velocity. J. Fluid Mech. **533**, 183–192 (2005). MR2263308 (2007d:76141)
7. Overholt, M.R., Pope, S.B.: A deterministic forcing scheme for direct numerical simulations of turbulence. Comput. Fluids **27**(1), 11–28 (1998)

A Stochastic Closure Approach for LES with Application to Turbulent Channel Flow

P. Metzner, M. Waidmann, D. Igdalov, T. von Larcher, I. Horenko, R. Klein, A. Beck, G. Gassner and C.D. Munz

1 Introduction

The integral conservation laws for mass, momentum and energy of a flow field are universally valid for arbitrary control volumes. Thus, if the associated fluxes across its bounding surfaces are determined exactly, the equations capture the underlying physics of conservation correctly and guarantee an accurate prediction of the time evolution of the integral mean values.

Starting from this concept, we model the space-time structure of the fluxes to create a discrete formulation whose justification is independent of the underly-

R. Klein · T. von Larcher (✉) · M. Waidmann
Institute of Mathematics, Freie Universität Berlin, Arnimallee 6, 14195 Berlin, Germany
e-mail: larcher@math.fu-berlin.de

R. Klein
e-mail: rupert.klein@math.fu-berlin.de

M. Waidmann
e-mail: waidmann@math.fu-berlin.de

I. Horenko · D. Igdalov · P. Metzner
Institute of Computational Science, Universita della Swizzeràitaliana,
Lugano, Switzerland
e-mail: illia.horenko@usi.ch

D. Igdalov
e-mail: dimitri.igdalov@usi.ch

A.D. Beck · G.J. Gassner · C.D. Munz
Institute of Aerodynamics and Gas Dynamics, University of Stuttgart,
Stuttgart, Germany
e-mail: beck@iag.uni-stuttgart.de

G.J. Gassner
e-mail: gassner@iag.uni-stuttgart.de

C.D. Munz
e-mail: munz@iag.uni-stuttgart.de

J. Fröhlich et al. (eds.), *Direct and Large-Eddy Simulation IX*,
ERCOFTAC Series 20, DOI 10.1007/978-3-319-14448-1_7

ing grid resolution. There are many alternatives for realizing this concept. Here, we directly aim at flux correction terms that should correct for the influence of the non-resolved small scale information. The classical closure problem would thus be reduced to the faithful reconstruction of spatio-temporal fluctuations of the fluxes across grid cell interfaces. We model those fluctuations by an advanced time series analysis approach [3], leading to mixed deterministic-stochastic model formulation.

In preparation of a new LES closure approach, the reconstruction capabilities of the data-based modeling approach are tested against 3D turbulent channel flow data computed by direct numerical simulation (DNS) for an incompressible, isothermal fluid at Reynolds number $Re_\tau = 590$ (computed by Uhlmann [7]).

In this paper, we present the outcome of our reconstruction test, and we show specifically results of the non-trivial time series data analysis rather than a simulation of the turbulent channel flow. We found, surprisingly, that the deterministic model part alone is good enough to fit the flux correction terms well. That encourages us for the ambitious attempt at dynamic LES closure along these lines.

We should like to mention that our approach particularly allows for the analysis of non-stationary and non-homogeneous data, resp., as the turbulent channel flow data are. Here, therefore, stationary/homogenous patterns, e.g. first order (Mean) and second order (Variance) statistics, often used in data analysis representations, could lead to biased results, as those moments typically do not represent the characteristics of inhomogeneous/instationary data.

2 Stochastic Subgrid Scale Approach

The stochastic subgrid scale modelling strategy is developed for application in finite volume (FV) Large Eddy Simulation (LES) codes. The approach is similar in spirit to earlier propositions by e.g., [5], but differs in terms of both the stochastic modeling ansatz as described in this paper, and in terms of the underlying discontinuous Galerkin numerical techniques as described in a companion paper [1].

Advanced methods of time series analysis for the data-based construction of stochastic models with inherently non-stationary statistical properties are used to construct stochastic surrogate models for the non-resolved fluxes from specific time series (cf. [4]). Vector-valued auto-regressive models with external influences (VARX-models) form the basis for the modeling approach (see Eq. 1). We realize non-stationary statistical properties of these models by allowing for time dependent switches between different fluctuation regimes which are represented by different, but fixed, sets of the stochastic model parameters. The LES-grid-averaged conserved quantities on the coarse grid cells in the immediate vicinity of a given LES grid cell interface are interpreted as external influences in constructing the VARX surrogate model. In this fashion the stochastic models incorporate the information available from a typical numerical discretization stencil as would be used, e.g., in formulating a classical Smagorinsky closure.

The ansatz of the VARX model reads

$$\Delta f_{t,\mathbf{x}} = \mu(t,\mathbf{x}) + A(t,\mathbf{x})\phi_1(\Delta f_{t-\tau},\ldots,\Delta f_{t-m\tau})_{\mathbf{x}} + B(t,\mathbf{x})\phi_2(u_{t,\mathbf{x}}) + \varepsilon_{t,\mathbf{x}}, \quad (1)$$

where $\Delta f_{t,\mathbf{x}}$ is the flux correction term (t as time, $\mathbf{x}$ as 3D space vector), $(\mu, A, B)(t,\mathbf{x})$ are time-dependent model parameters (m as the memory depth), ϕ_1, ϕ_2 are model ansatz functions which are generally non-linear, $u_{t,\mathbf{x}}$ denotes the external influences (here the coarse-grid stencil data), and $\varepsilon_{t,\mathbf{x}}$ is the model-data discrepancy.

The basic idea of the approach is to detect the switching processes between the fluctuation regimes and their parameters, here named $(\gamma_j(t,\mathbf{x}), \Theta_j)$ (j as the cell index), which characterize the local models. Θ_j denotes K sets of k parameters $\{\Theta_j \equiv (\Theta_1,\ldots,\Theta_k)_j\}_{j=1}^K$ representing the model parameters (μ, A, B), and γ_j are model affiliation functions with $\gamma_j(t,\mathbf{x}) \in [0,1]$ and $\sum_{j=1}^K \gamma_j(t,\mathbf{x}) = 1$. The total variation TV of γ_j is bounded

$$TV_t(\gamma_j(t,\mathbf{x})) \leq C.$$

With (k, K, C) given, the best-fit and therefore the optimal parameters are found with minimization of the model-data distance, i.e.

$$\int_t \int_{\mathbf{x}} \delta_{t,\mathbf{x}}\, d\mathbf{x}\, dt \to \min_{\gamma,\Theta} \qquad \text{where } \delta_{t,\mathbf{x}} = \sum_{j=1}^{K} \gamma_j(t,\mathbf{x}) \left\| \varepsilon_{t,\mathbf{x}}^{\Theta_j} \right\|.$$

A balance between the requirements of high representation quality and low number of free parameters (Occam's razor) is achieved by involving criteria from information theory.

3 Data Preprocessing and Numerical Flux Computation

The DNS data for the primary conserved quantities from detailed numerical turbulent channel flow simulations are averaged on a coarse LES grid which is a cartesian finite volume grid with equidistant spacing in all coordinates, hereafter referred to as *coarse-grid*.

Resolved LES-grid fluxes are determined from these averages using a straightforward finite volume approximation for the Euler equations. By subtracting these resolved fluxes from the DNS fluxes averaged over the cell faces of the LES-grid, we obtain one time series of non-resolved fluxes for each cell interface of the LES grid.

We compute a so-called exact flux (F_{ex}) based on the preprocessed DNS data, and, furthermore, a reference flux (F_{ref}) and numerical fluxes of particular order from the average velocity data on the coarse grid. Once those flux data are generated, flux correction terms are calculated as described below.

For each cell C^j and each face $a = 1,\ldots,6$ on the coarse-grid, a time series of the following LES-observables is calculated: a) the exact flux corrections $\Delta F_{ex}^{j,a}(t) \in \mathscr{R}^3$, b) the 1st order flux corrections $\Delta F_1^{j,a}(t) \in \mathscr{R}^3$, c) the 2nd order flux

corrections $\Delta F_2^{j,a}(t) \in \mathscr{R}^3$, and d) the 3rd order flux corrections $\Delta F_3^{j,a}(t) \in \mathscr{R}^3$, where

$$\Delta F_i = F_i - F_{ref},\ i = 1, 2, 3, \qquad \Delta F_{ex} = F_{ex} - F_{ref},$$

and, finally, the velocity field $V^j(t) \in \mathscr{R}^{21}$ consisting of the average velocity field of cell C^j and of the average velocity fields of all cells sharing a common face with C^j (neighbored cell).

Generally, the numerical flux function proposed by Hickel et al. [2] is used to compute fluxes of the particular order. For F_1, the cell average state value is assumed to cover the whole grid cell and, thus, the values at the cell faces are assumed to be equal to the cell center value. Consequently, no state reconstruction is needed. However, for F_2, piecewise linear state reconstruction within the grid cells is performed direction by direction based on the cell center values as in standard second order FV methods using a monotonized central limiter, [8], for slope limiting during the reconstruction. This yields higher-order accurate cell interface data. Finally, for F_3, state recovery at the cell faces is obtained via a third order WENO scheme proposed in [6]. For F_{ref}, no state reconstruction or specific numerical flux function is used but the simple flux average is calculated.

4 Results

Figure 1 shows time series of the exact flux correction data and of the raw numerical flux corrections of 1st, 2nd and 3rd order resulting from the finite volume approximation for the Euler equations. While the graphs indicate that the 3rd order

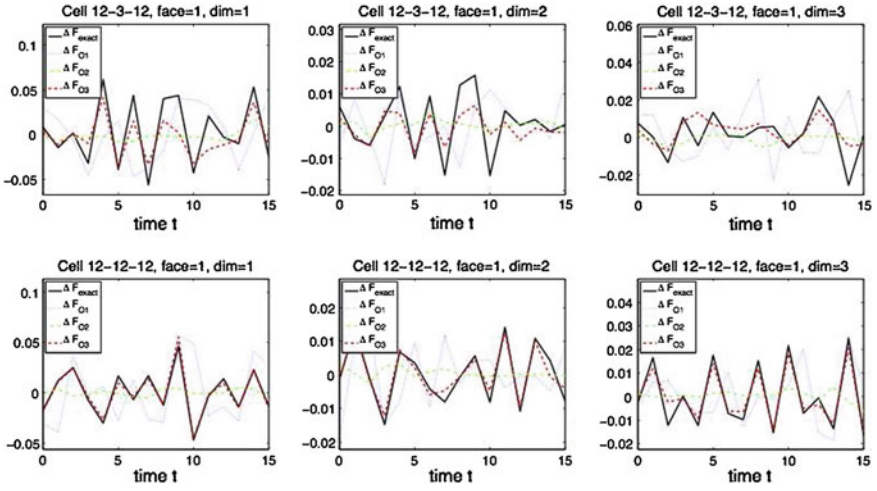

Fig. 1 Exact flux correction and raw numerical flux corrections of 1st, 2nd and 3rd order available for face 1 of two specific cells. *Upper row* near-boundary cell, *lower row* cell located in the center of the channel. From *left* to *right* x-, y-, z-component of the specific flux correction term. Note the different scaling of each figure

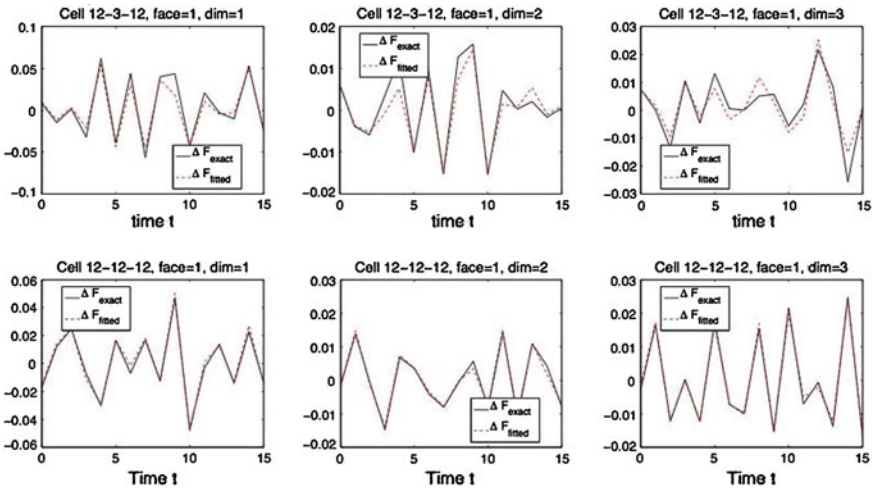

Fig. 2 As in Fig. 1 but for the fitted flux corrections available from the stochastic model framework. Note the different scaling of each figure

flux corrections generally fits the exact correction well, and noticeably well in the centered-channel case, deviations appear in the near-boundary cell [and also in cells directly adjacent to the boundary (not shown)].

Figure 2 shows time series of the model flux correction which fits the exact flux correction data remarkably well also in the near-boundary cell [which was also observed in cells directly adjacent to the boundary (not shown)].

Only two particular fluctuation regimes, a *wall model* and a *core model*, are explored by the stochastic model framework to yield such a good agreement between the exact flux correction data and the model-fit of the flux correction data (cf. Fig. 3).

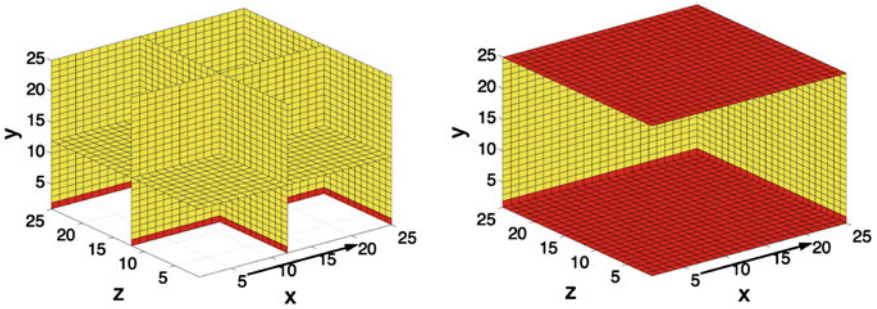

Fig. 3 Snapshot of the two fluctuation regimes, the *wall regime* (*dark grey*) and the *core regime* (*light grey*), determined by the stochastic model approach, cross-section through the channel geometry. *Left* figure highlights the grid cells with the *core model*, *right* figure the cells with the *wall model*. The *arrow* indicates the main flow x-direction

As the name already indicates, the *wall model* is assigned to the boundary cells at the rigid boundaries in y-direction and the *core model* is assigned to all other grid cells. In addition, not discussed here, the stochastic model shows no time-dependence i.e. there is no switch between those two fluctuation regimes, and one and only one of the two fluctuation regimes has been assigned to each specific cell in time.

5 Conclusions and Outlook

We have presented the application of a novel stochastic model framework, based on stencil-conditioned subgrid scale modeling of flux correction terms, as a first step towards a dynamical LES closure. The approach was tested on turbulent channel flow DNS data computed by M. Uhlmann, and we have shown results of a reconstruction test of flux correction terms.

The best-fit deterministic flux corrections agree very well despite the roughness of the coarse-grid data. This non-trivial result mentions also the role of deterministic LES closure approaches. Moreover, we find that the linear contribution to the closure uses only next neighbors on the coarse grid.

Beyond the results given here, our study reveals more remarkable features that can not be discussed in depth due to lack of space: e.g. (a) the best-fit is reached when the auto-regressive part of the stochastic model framework is not considered in the data analysis process, i.e. we have used a VX model approach instead of a VARX one, (b) when the turbulent channel flow data are coarsened to $50 \times 50 \times 50$ grid cells, a third fluctuation regime, called *transition model*, has been detected, i.e. we found resolution-dependent closure regimes, (c) our approach also captures non-stationary regimes, as we have applied the stochastic model framework to Taylor-Green-Vortex flow data showing a transition from laminar to fully turbulent flow at specific Reynolds numbers. Those results will be described in detail in an upcoming publication.

In future work, we further will make use of the stochastic approach for the analysis of local flow features, and will make a thorough comparison of the implicit-LES ansatz presented here versus explicit-LES by coupling the stochastic based flux correction model to finite volume solvers.

References

1. Gassner, G.J., Beck, A.D.: On the accuracy of high-order discretizations for underresolved turbulence simulations. Theor. Comp. Fluid Dyn. **27**, 221–237 (2013)
2. Hickel, S., Adams, N.A., Domaradzki, J.A.: And adaptive local deconvolution method for implicit LES. J. Comput. Phys. **213**, 413–436 (2006)
3. Horenko, I.: On identification of nonstationary factor models and its application to atmospherical data analysis. J. Atmos. Sci. **67**, 1559–1574 (2010)
4. Metzner, P., Putzig, L., Horenko, I.: Analysis of persistent non-stationary time series and applications. CAMCoS **7**, 175–229 (2012)

5. Scotti, A., Meneveau, C.: A fractal model for large eddy simulation of turbulent flows. Phys. D **127**, 198–232 (1999)
6. Shu, C.-W.: Essentially non-oscillatory and weighted essentially non-oscillatory schemes for hyperbolic conservation laws. Technical report, NASA Langley Research Center, 97-65 (1997)
7. Uhlmann, M.: Generation of a temporally well-resolved sequence of snapshots of the flow-field in turbulent plane channel flow. http://www-turbul.ifh.uni-karlsruhe.de/uhlmann/reports/produce.pdf (2000)
8. van Leer, B.: Towards the ultimate conservative difference scheme. II. Monotonicity and conservation combined in a second-order scheme. J. Comput. Phys. **14**, 361–370 (1974)

Comparison of URANS, PANS, LES and DNS of Flows Around Simplified Ground Vehicles with Passive Flow Manipulation

X. Han, S. Krajnović, C.-H. Bruneau and I. Mortazavi

1 Introduction

Flow control of ground vehicles has recently attracted large interest in both industry and academia. The potential in energy savings seems to be considerable and at the moment both passive and active control strategies are explored. Regardless of the choice of control strategy, numerical methods are required for our understanding of flow control processes and improvement of its performance. The present work explores applicability of whole spectra of numerical techniques from URANS, PANS to LES and DNS for prediction of two flows with an additional body.

2 Description of the Flow Cases

The first flow is that of a passive flow control around a D-shaped bluff body studied at $Re = 13000$ [1]. A small secondary body is placed behind the main D-shaped bluff body whose drag has to be reduced (see Fig. 1). The height of the main body is $D = 25\,\text{mm}$ and the free stream velocity is $U_0 = 8\,\text{m/s}$. The length in the spanwise direction is 4D and in pitchwise direction is 16D. Constant velocity is imposed

X. Han · S. Krajnović (✉)
Department of Applied Mechanics, Chalmers University of Technology, Gothenburg, Sweden
e-mail: sinisa@chalmers.se

X. Han
e-mail: xingsi@chalmers.se

C.-H. Bruneau · I. Mortazavi
INRIA Team MC2, University of Bordeaux, Bordeaux, France
e-mail: bruneau@math.u-bordeaux1.fr

I. Mortazavi
e-mail: mortaz@math.u-bordeaux1.fr

J. Fröhlich et al. (eds.), *Direct and Large-Eddy Simulation IX*,
ERCOFTAC Series 20, DOI 10.1007/978-3-319-14448-1_8

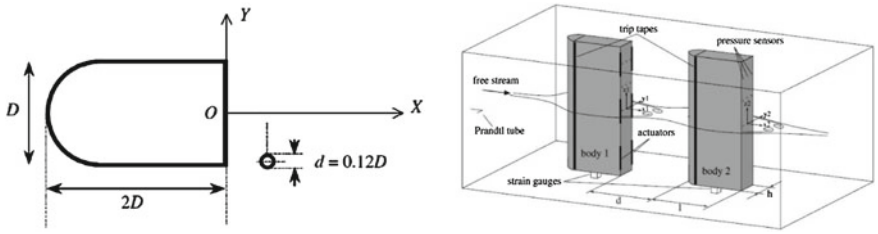

Fig. 1 The arrangement of the first case *left* main bluff body and the control cylinder in one $x\,O\,y$ plane and set-up of the second case *right* two 2D Ahmed bodies in a tandem arrangement

at the inlet, periodic conditions are used in the spanwise direction, and slip wall conditions are used on the upper and lower walls. Non-dimensional time step is $dt = 7 \times 10^{-3}\, D/U_0$.

The second case represents the so called platooning where drag reduction is obtained by placing a second vehicle in the wake of the leading one [2]. Two generic vehicles in form of 2D Ahmed bodies have a chord length $l = 181$ mm, body height $h = 50$ mm and spanwise width $w = 474$ mm. The second body is placed at a distance of $d = 5$ h behind the first body as shown in Fig. 1. The Reynolds number with respect to body height and free stream velocity is Re_h =16,200. The computational domain in both the spanwise and pitchwise directions is the same as in the experiment. Constant velocity is imposed at the inlet, periodic conditions are used in the spanwise direction, and non-slip wall conditions are used on the upper and lower walls.

3 Numerical Methods

In the present study, numerical technique from URANS to DNS will be applied. 3D PANS and LES, which are the suitable candidates for flow control problems at this stage [3] will be evaluated in the two selected cases. Partially-Averaged Navier-Stokes (PANS) is a bridging technique between RANS and DNS [4]. The new variant $\zeta - f$ PANS method [5] is used in the present simulations in which the unresolved-to-total-kinetic-energy ratio f_k is a variable parameter that depends upon the grid spacing and the integral length scale of turbulence.

URANS simulations use $\zeta - f$ turbulence model and are thus comparable with the PANS $\zeta - f$ method. In the LES studies, the SGS stress tensor $\tau_{ij} = \overline{u_i u_j} - \bar{u_i}\bar{u_j}$ is modeled by the Coherent Structure Model (CSM) [6] using the coherent structure function defined as the second invariant of the velocity gradient tensor normalized by the magnitude of a velocity gradient tensor.

The URANS, PANS and LES simulations were made with a finite volume CFD solver, AVL FIRE. A blend of central differencing scheme and upwind scheme is used for PANS and LES. The time integration is performed using the second-order implicit scheme. The SIMPLE algorithm is used to couple the velocity and pressure fields.

The DNS method uses high-order finite differences approximation with a multigrid method to solve the genuine Navier-Stokes equations in velocity-pressure [7]. The method has been used to simulate flow control around Ahmed bodies with active and passive procedures [8].

In the first case, the computational domain in the spanwise direction is $4D$ and $16D$ in the pitchwise direction. Constant velocity is imposed at the inlet, periodic conditions are used in the spanwise direction, and slip wall conditions are used on the upper and lower walls. In the second case, the computational domain in both the spanwise and pitchwise directions is the same as in the experiment. Constant velocity is imposed at the inlet, periodic conditions are used in the spanwise direction, and non-slip wall conditions are used on the upper and lower walls.

4 First Flow Case: Results and Discussions

3D URANS, PANS and LES are performed for both the natural body (NAT) and with control by an additional cylinder (CON). For all simulations, PANS and LES use the same numerical schemes and the same mesh: 6.27 million cells for NAT and 7.35 million cells for CON, while 3D URANS uses 1.38 and 0.74 million cells, respectively. The global parameters of the mean drag and lift coefficients and their RMS values on the main bluff body are shown in Table 1. It can be seen that PANS and LES predict quite close results for both NAT and CON flows, and give a drag reduction of about 28 %. 3D URANS predicts close results for NAT but higher values for CON. Figure 2 shows the iso-surfaces of the second invariant of the velocity gradient between the natural and the controlled case by LES. Similar results are produced by PANS (not shown here). The wake is significantly changed due to the presence of the control cylinder and a longer wake region is produced in the controlled case. Figures 3 and 4 show the comparisons of the predicted time-averaged streamwise velocity U/U_0 with the experiment [1] for the NAT and CON cases, respectively. The numerical predictions of PANS and LES agree well with experiment for NAT. The numerical results produce a correct tendency of the interactions of shear layer with the control cylinder but the wake regions are smaller compared with experiment.

Table 1 Global parameters of the total drag C_D, pressure drag C_{Dp} and the total lift C_L coefficients.

Case	$C_{Dp,ave}$	$C_{D,ave}$	$C_{Dp,rms}$	$C_{D,rms}$	$C_{L,rms}$	$\Delta C_{Dp,ave}$ (%)	$\Delta C_{D,ave}$ (%)
3D URANS-NAT	0.741	0.798	0.026	0.028	0.215		
PANS-NAT	0.776	0.811	0.090	0.094	0.217		
LES-NAT	0.772	0.810	0.062	0.063	0.231		
Exp.-NAT [1]	0.737	0.77	0.027	–	–		
3D URANS-CON	0.612	0.653	0.018	0.020	0.084	−17.4	−18.2
PANS-CON	0.554	0.586	0.012	0.013	0.038	−28.7	−27.8
LES-CON	0.553	0.586	0.013	0.013	0.035	−28.5	−27.6
Exp.-CON [1]	0.444	0.47	0.004	–	–	−39.7	−39.0

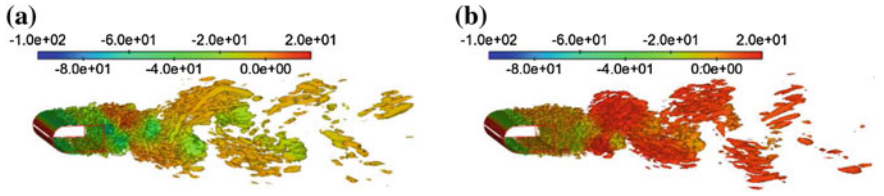

Fig. 2 Iso-surface of the second invariant of the velocity gradient ($Q = 1.0 \times 10^5$): **a** NAT by LES; **b** CON by LES, colored by pressure

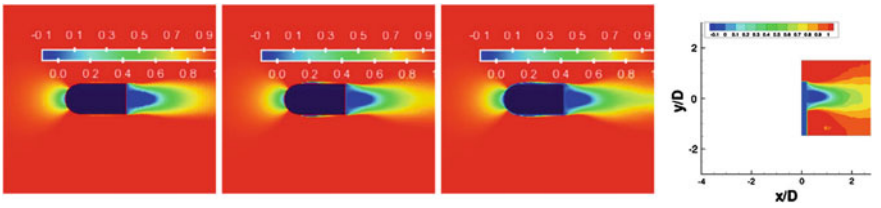

Fig. 3 Comparison of mean velocity U/U_0 between 3D URANS, PANS, LES and experiment [1] (from *left* to *right*, respectively), in the natural case

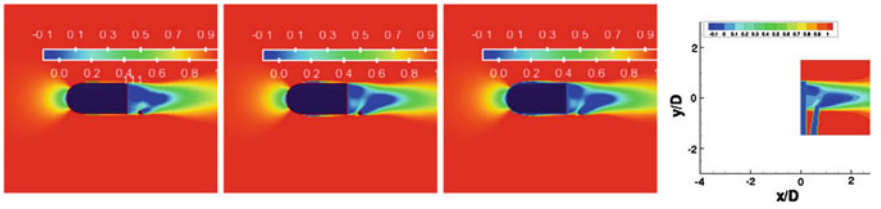

Fig. 4 Comparison of mean velocity U/U_0 between 3D URANS, PANS, LES and experiment [1] (from *left* to *right*, respectively), in the controlled case

5 Second Flow Case: Results and Discussions

D URANS, 3D URANS, PANS and LES are performed for both a single Ahmed body (C1) and two Ahmed bodies (C2). For all simulations, PANS and LES use the same numerical schemes and the same mesh: 6.36 million cells for C1 and 10.54 million cells for C2, while 2D URANS and 3D URANS use 0.043 and 1.64 million cells for C1, 2.76 and 10.54 million cells for C2. The global parameters are shown in Table 2. It can be seen that PANS and LES predict close results in same flow configurations. They produced big drag reduction up to 45.8 % for the Ahmed body in the wake. URANS simulations under-predict a lot of the Strouhal number and over-predict the mean drag for the Ahmed body in the wake. Figures 5 and 6 show the iso-surfaces of the second invariant of the velocity gradient for the natural and controlled cases, respectively, by 3D URANS, PANS and LES. Similar results are produced by PANS

Table 2 Global parameters of the Strouhal number, St, total drag C_D, and RMS drag and lift coefficients.

Ahmed body	Turbulence model	St	$C_{D,ave}$	$C_{D,rms}$	$C_{L,rms}$	$\Delta C_{D,ave}$ (%)
C1	2D URANS	0.150	0.898	0.023	0.463	–
C1	3D URANS	0.187	0.766	0.008	0.142	–
C1	PANS	0.246	0.854	0.050	0.317	–
C1	LES	0.234	0.816	0.042	0.202	–
C2-up	2D URANS	0.158	0.846	0.024	0.481	−6
C2-up	3D URANS	0.187	0.718	0.008	0.114	−6
C2-up	PANS	0.224	0.822	0.049	0.255	−4
C2-up	LES	0.228	0.793	0.033	0.295	−3
C2-down	2D URANS	0.157	0.504	0.017	0.655	−40.4
C2-down	3D URANS	0.193	0.520	0.019	0.233	−27.5
C2-down	PANS	0.224	0.388	0.048	0.485	−52.8
C2-down	LES	0.228	0.429	0.043	0.592	−45.8
C1	2D DNS		0.742		0.513	
C2-up	2D DNS		0.648		0.546	−13
C2-down	2D DNS		0.248			−67

C1 means the single body case, C2-up means the leading body in the case with two bodies and C2-down means the body in the wake

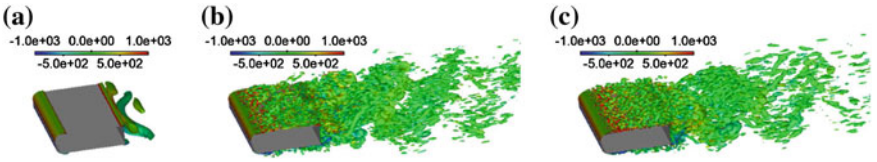

Fig. 5 Iso-surface of the second invariant of the velocity gradient ($Q = 1.0 \times 10^4$) in the single body case by: **a** 3D URANS; **b** PANS; and **c** LES, colored by pressure

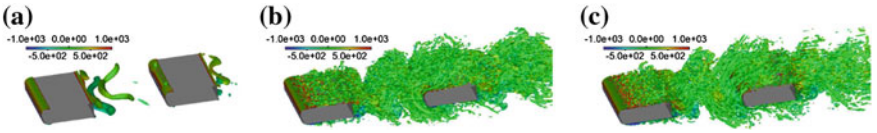

Fig. 6 Iso-surface of the second invariant of the velocity gradient ($Q = 1.0 \times 10^4$) in the two-body case by: **a** 3D URANS; **b** PANS; and **c** LES, colored by pressure

and LES. The vortex shedding from the first Ahmed body affects a lot the flow around the second Ahmed body, and thus reduces its drag substantially as observed in Table 2. Figure 7 shows comparisons of LES predictions of time-averaged streamwise velocity U/U_0 for one and two bodies respectively. The changes of flow pattern around the second Ahmed body can be observed. Figure 8 shows the RMS velocity V_{rms}/U_0 by PANS and LES. The two models produce similar flow structures

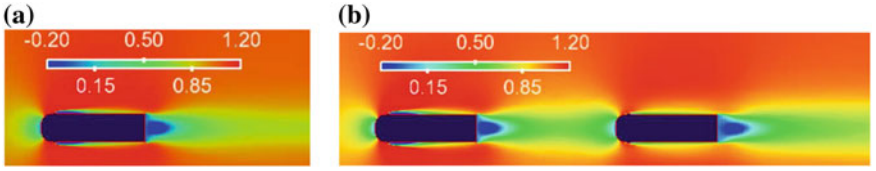

Fig. 7 Comparison of mean velocity U/U_0 in the C1 **a** and C2 **b** cases by LES

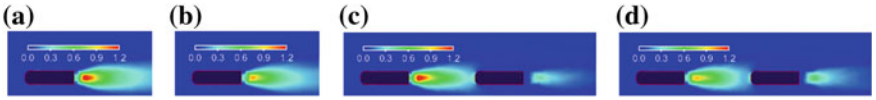

Fig. 8 Contours of RMS velocity V_{rms}/U_0 by: PANS in natural flow **a**; LES in natural flow **b**; PANS in controlled flow **c** and LES in controlled flow **d**

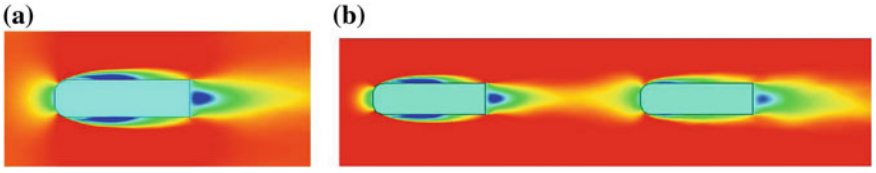

Fig. 9 Comparison of mean velocity U/U_0 in the C1 **a** and C2 **b** cases by DNS

although peak values are different. It can be seen that the RMS velocity in the wake of the second Ahmed body is depressed by large extent. The 2D DNS simulations are performed on a uniform Cartesian grid with about 15.85 million cells for C1 and 31.7 million cells for C2. Figure 9 shows comparisons of DNS predictions of time-averaged streamwise velocity U/U_0 for one and two bodies respectively. It appears clearly that the flow around the first body is very similar for cases C1 and C2 while the flow is moderated around the second body. This can be seen in particular on the drag coefficient in Table 2. The trend observed in Table 2 are confirmed by the DNS study.

6 Conclusions

The present work explores the applicability of URANS, PANS, LES and DNS for prediction of two flows with passive flow control. The results show that the presence of a body behind a first one can induce a significant drag reduction. In the case of platooning there is a tremendous change for the second body as expected but without an increase and even with a small decrease of the drag coefficient of the leading body. The results demonstrate that PANS and LES have potentials for capturing the main features of the flow and giving realistic evolution of the physical quantities.

Acknowledgments The work presented here was funded by Trafikverket and the Chalmers Sustainable Transport Initiative. The authors are grateful to AVL List GmbH for providing the licenses for the AVL FIRE solver for the project. Computation time at SNIC (the Swedish National Infrastructure for Computing) at the Center for Scientific Computing at Chalmers (C3SE) is gratefully acknowledged. The work on DNS was run on PLAFRIM platform supported by IMB University of Bordeaux and INRIA Bordeaux—Sud Ouest.

References

1. Parezanovic, V., Cadot, O.: Experimental sensitivity analysis of the global properties of a two-dimensional turbulent wake. J. Fluid Mech. **693**, 115–149 (2012)
2. Muminovic, R., Pfeiffer, J., Werner, N., King, R.: Model predictive control for a 2D bluff body under disturbed flow controls. Active Flow Control II, NNFM **108**, 257–272 (2010)
3. Krajnović, S.: Large eddy simulation of flows around ground vehicles and other bluff bodies. Phil. Trans. R. Soc. A **367**, 2917–2930 (2009)
4. Girimaji, S., Srinivasan, R., Jeong, E.: PANS turbulence models for seamless transition between RANS and LES: fixed point analyses and preliminary results. ASME paper, FEDSM2003-4336 (2003).
5. Basara, B., Krajnović, S., Girimaji, S., Pavlović, Z.: Near-wall formulation of the partially averaged Navier-Stokes turbulence model. AIAA J. **49**, 2627–2636 (2011)
6. Kobayashi, H.: The subgrid-scale models based on coherent structures for rotating homogeneous turbulence and turbulent channel flow. Phys. Fluids **17**, 045104 (2005)
7. Bruneau, Ch.-H., Saad, M.: The 2D lid-driven cavity problem revisited. Comput. Fluids **35**(3) (2006)
8. Bruneau, Ch.-H., Creusé, E., Depeyras, D., Gilliéron, P., Mortazavi, I.: Coupling active and passive techniques to control the flow past the square back Ahmed body. Comput. Fluids **38**, 1875–1892 (2010)

Variational Multiscale LES Investigation of Drag and Near-Wake Flow of an Axisymmetric Blunt-Based Body

A. Mariotti, M.V. Salvetti and G. Buresti

1 Introduction

The characterization of the relationship between the base pressure of bluff bodies and the geometrical and fluid dynamical parameters defining a certain configuration is a complex and still open problem, of interest for both fundamental research and practical applications. One of the most interesting applications concerns the development of methods for the reduction of drag, and thus of fuel consumption, of road vehicles. Indications exist in the literature that increasing the thickness of the boundary layer developing over the lateral surface of a bluff body may lead to an increase of the base pressure and to a decrease of the drag of two-dimensional or axisymmetric blunt-based bodies (see e.g. [1, 2]). Nonetheless, the physical mechanisms and flow features that are responsible for this result are not yet completely understood.

This work is part of an experimental and numerical research activity aimed at characterizing the flow features influencing the base drag of an axisymmetric blunt body. As for the experiments, it was observed in [3] that the increase of the boundary layer thickness produces a reduction of the base suctions. This is probably connected with an increase of the length of the mean recirculation region present behind the body, and with the consequent reduction of the convex curvature of the streamlines outside the boundary layer in the separation region.

In the present work, the results of Variational MultiScale (VMS) LES carried out on the same body as in the experiments are presented and analysed. Numerical simulations can give complementary information compared to the experiments, useful

A. Mariotti (✉) · M.V. Salvetti · G. Buresti
Dipartimento di Ingegneria Civile e Industriale, Università di Pisa,
via G. Caruso 8, 56122 Pisa, Italy
e-mail: alessandro.mariotti@for.unipi.it

M.V. Salvetti
e-mail: mv.salvetti@ing.unipi.it

G. Buresti
e-mail: g.buresti@ing.unipi.it

J. Fröhlich et al. (eds.), *Direct and Large-Eddy Simulation IX*,
ERCOFTAC Series 20, DOI 10.1007/978-3-319-14448-1_9

for a better comprehension of the physical mechanisms leading to drag variations on the considered body. In particular, the complete flow dynamics is available in the VMS-LES simulations, while the available experimental measurements are limited to hot-wire anemometry velocity signals, pressure distributions on the body surface and aerodynamic loads. Moreover, the flow conditions are easier to be controlled in numerical simulations. The VMS-LES approach adopted in the present work has been successfully used for the simulation of bluff-body flows in the past (see e.g. [4–6]).

2 Geometry Definition, Simulation Set-up and Numerical Method

The axisymmetric model configuration comprises a forebody with a 3:1 elliptical contour, and a cylindrical main body with a sharp-edged base perpendicular to the axis (see Fig. 1). The ratio between the diameter, d, and the overall length, l, is $d/l = 0.175$. The Reynolds number is $Re = l \cdot U/\nu = 5.5 \times 10^5$, as in the experiments. Differences are that simulations can be carried out for laminar freestream conditions, while a freestream turbulence intensity of 0.9 % is present in the experiments. Moreover, the model support present in the experiments (see [3]) is not present in the simulations.

In the numerical simulations a reduction of the boundary layer thickness is obtained by using a free-slip boundary condition over different initial portions of the body surface (see Fig. 2a, b). Conversely, in the wind tunnel tests strips of emery cloth were wrapped in various position around the body circumferences in order to anticipate boundary layer transition and, thus, to increase its thickness (see [3]). In particular, in the case NT there was natural boundary layer transition, while in the cases $T1$ and $T2$ the transition points were kept fixed at $x_t/l = 0.75$ and at $x_t/l = 0.875$, respectively.

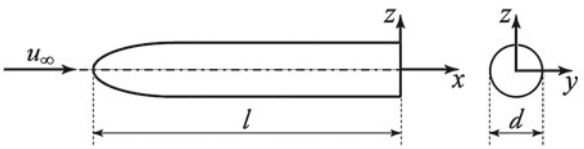

Fig. 1 Sketch of the geometry and main parameters

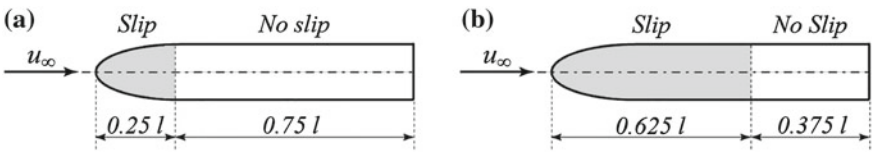

Fig. 2 **a** Case 075*l*, **b** Case 0.375*l*

Variational multiscale large-eddy simulations (VMS-LES) of the considered configuration were carried out by using AERO, an in-house developed numerical code based on a linearized implicit time advancing and on a mixed finite-volume/finite-element method, applicable to unstructured grids for space discretization (see e.g. [4]). The accuracy of the numerical method is second order both in space and time. The Smagorinsky model is used as subgrid scale model in order to close the VMS-LES equations.

The computational domain is cylindrical, with a diameter of $15d$ and a length of $50d$ ($30d$ being the distance from the body base to the outflow); it is discretized by an unstructured grid having approximately 2.4×10^6 nodes. The grid is particularly refined near the body surface and in the near wake (the wall y^+ is lower than 1). Characteristic-based boundary conditions [4] are used at the inflow, outflow and lateral surfaces of the computational domain. The boundary conditions on the body are chosen, as previously explained, in order to vary the boundary-layer thickness on the lateral surface. In particular, three simulations are presented here, which correspond to no-slip over the entire body (case l), over 75 % (case $0.75l$) and 37.5 % ($0.375l$) of the body lateral surface respectively. In all cases, no-slip is imposed on the base (see Fig. 2a, b).

3 Results

An overall impression of the main flow features is provided by the streamlines of the velocity field averaged in time and in the azimuthal direction, shown in Fig. 3 (case l). In the considered operating conditions, the boundary layer remains completely attached over the lateral surface of the model, up to the separation at the sharp-edged base contour. The flow separation at the base leads to the development of a free shear layer, to the creation of a trailing stagnation point and to a flow recirculation behind the base. The mean-velocity streamlines bend inwards after the end of the body, aside the previous mentioned recirculation zone. This mean recirculation region is usually referred to as the near-wake and it has a significant influence on base drag. Indeed, the base pressure is connected with the velocity outside the boundary layer in the separation region, which, in turn, increases with the convex curvature of the outer streamlines in the near wake.

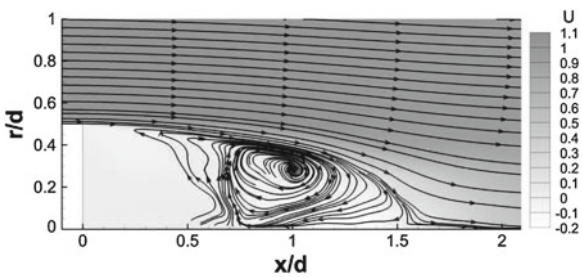

Fig. 3 Streamlines of the velocity field averaged in time and in the azimuthal direction

Table 1 Summary of the boundary layer characteristics, the length of the mean recirculation region, and the integral of the base suctions on the body base

Case	δ/d	δ^*/d	θ/d	H	l_r/d	l_r^{rms}/d	Cp_{base}	$Cp_{base}^{r\leq 0.4}$
$0.375l$	0.0306	0.0078	0.0036	2.15	1.45	1.55	−0.135	−0.136
$0.75l$	0.0411	0.0107	0.0050	2.14	1.48	1.59	−0.130	−0.131
l	0.0663	0.0146	0.0072	2.03	1.54	1.64	−0.122	−0.124

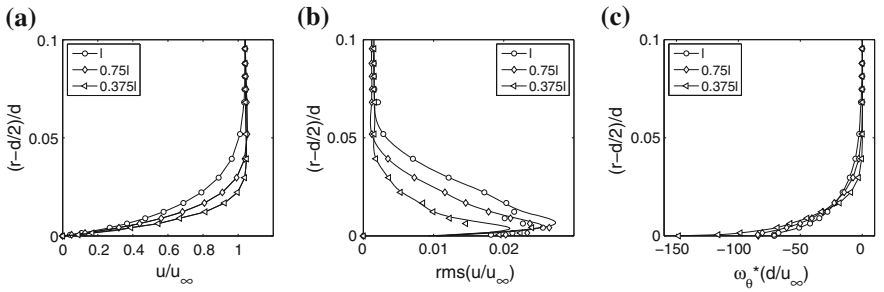

Fig. 4 **a** Profiles of x-velocity. **b** Rms of x-velocity. **c** Profiles of vorticity

As previously explained, three different boundary layer thicknesses δ/d, measured $0.1d$ from the base contour, are obtained in the simulations (see Table 1). The displacement thickness δ^*/d, the momentum thickness θ/d and the shape factor H are also summarized in Table 1. The three non-dimensional profiles of the x-velocity, of the rms of the x-velocity and of the azimuthal vorticity, ω_θ, are shown in Fig. 4a–c, respectively.

The local pressure coefficients on the base, averaged in time and in the azimuthal direction, are shown in Fig. 5 for the three considered simulations. The corresponding average values (Cp_{base}, averaged on the whole base surface) are reported in Table 1. It can be seen that the base suctions decrease with increasing boundary layer thickness. This variation is found to be connected with an increase of the length of the mean

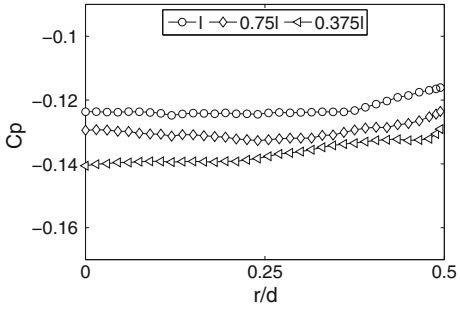

Fig. 5 Cp distribution on the base

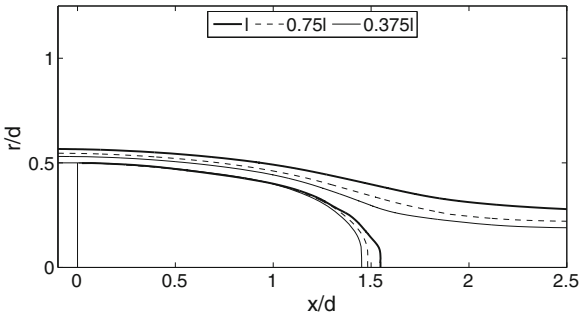

Fig. 6 Mean flow streamlines

recirculation region that is present behind the body, whose values, l_r/d, are also reported in Table 1; l_r is evaluated as the distance from the body base of the point at which the mean streamwise velocity on the axis is equal to zero. The mean flow streamlines bounding the recirculation region are shown in Fig. 6, together with the mean flow streamlines passing at the edge of the boundary layer $x/d = -0.1$. It is evident that a reduction of the length of the mean recirculation region is connected with an increase of the inward curvature of the streamlines, as suggested in [3].

In order to directly compare the present results with the experimental ones of [3], the length of the mean recirculation region was also evaluated, as done in the experiments, as the distance from the base of the point on the centreline at which the maximum of velocity fluctuations occurs; the obtained values, l_r^{rms}/d, are also reported in Table 1. Similarly, the averaged base pressure coefficient was also calculated for $r \leq 0.4$, since experimental measurements are available only inside this zone (see $Cp_{base}^{r\leq 0.4}$ in Table 1).

The effect of boundary layer thickness on the mean recirculation zone length and on the base pressure are graphically summarized in Fig. 7a, b. The momentum thickness θ/d is only shown for the sake of brevity. The experimental results are also reported. In spite of the previously outlined differences, the simulation with no-slip conditions over the full body and the experimental case with natural transition (cases l and NT) can sensibly be compared. First, it appears that the measured boundary-layer momentum thickness is slightly larger than the computed one. This difference is consistent with the fact that in the wind tunnel the oncoming flow is not perfectly smooth as in the numerical simulations and this moves the boundary-layer transition upstream, resulting in a thicker and fully-developed turbulent boundary layer at the end of the body. The different state of the boundary layer in experiments and simulations is confirmed by the values of the shape factor, H, i.e. the ratio between the displacement and the momentum thickness. In the experiments, H is equal to 1.41, which is typical of turbulent boundary layers, while the boundary layer at the end of the body in the numerical simulation seems to be still in a transitional state ($H = 2.03$). The length of the recirculation zone is definitely shorter in the experiments rather than in the simulations (see Fig. 7a). Again, this is consistent with the significant turbulence level in the experimental oncoming flow. Note, however, that

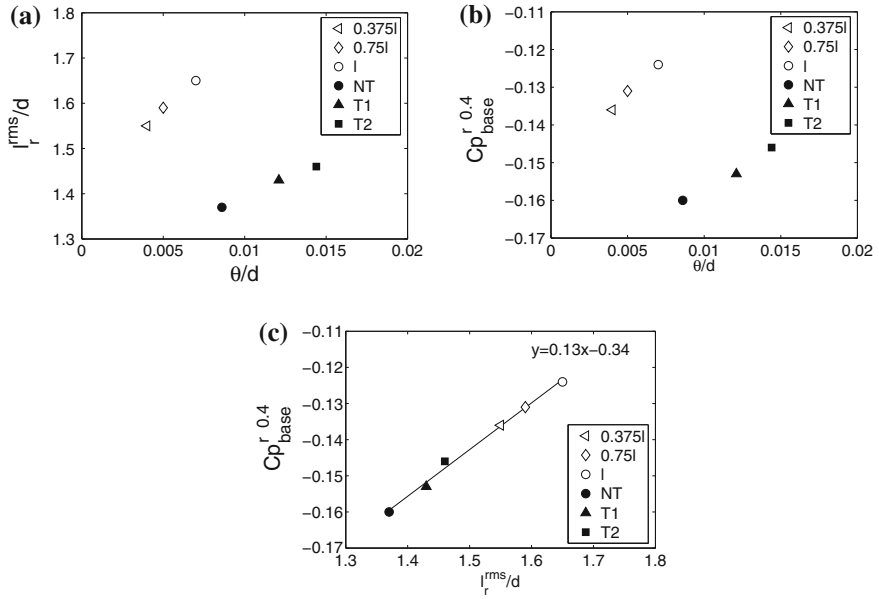

Fig. 7 **a** l_r^{rms}/d versus θ/d. **b** $Cp_{base}^{r\leq 0.4}$ versus θ/d. **c** $Cp_{base}^{r\leq 0.4}$ versus l_r^{rms}/d

the increasing trends of l_r^{rms}/d with the boundary-layer thickness θ/d are analogous for the experiments and the simulations. In the experiments larger suctions are present on the base than in the simulations (see Fig. 7b). As will be explained in the following, this is due to the shorter length of the recirculation region. Nonetheless, the dependence of the base pressure on θ/d is again similar in experiments and simulations. The connection between the length of the mean recirculation region and the base pressure is highlighted in Fig. 7c. The experimental and numerical data collapse on a single straight line, meaning that the relationship between the base pressure and l_r^{rms}/d is independent of the status of the boundary layer before separation at the body base and of the turbulence level of the oncoming flow. Additional simulations, carried out at a lower Reynolds number and not shown here for the sake of brevity, indicate that this relationship is also independent of the Reynolds number. Thus, it appears that in different flow conditions the most important parameter controlling the base drag is the length of the mean recirculation zone. On the other hand, l_r^{rms}/d can be varied by changing the boundary layer thickness, independently of the status of the boundary layer, or the freestream turbulence level. Different techniques to control l_r^{rms}/d can clearly be used, such as, for instance, blowing and suction on the body basis.

Acknowledgments The authors wish to thank Nicola Pineschi for his precious contribution in carrying out the numerical simulations.

References

1. Rowe, A., Fry, A.L.A., Motalleby, F.: Influence of boundary-layer thickness on base pressure and vortex shedding frequency. AIAA J. **39**, 754–756 (2001)
2. Porteiro, I.L.F., Przirembel, C.E.G., Page, R.H.: Modification of subsonic wakes using boundary layer and base mass transfer. AIAA J. **21**, 665–670 (1983)
3. Mariotti, A., Buresti, G.: Experimental characterization of the influence of boundary layer thickness on the base pressure and near-wake flow of a bluff body. In: Proceedings of XII National Congress of Wind Engineering, 7–10 Oct 2012, Venice, Italy (2012)
4. Camarri, S., Salvetti, M.V., Koobus, B., Dervieux, A.: A low-diffusion MUSCL scheme for LES on unstructured grids. Comput. Fluids **33**, 1101–1129 (2004)
5. Ouvrard, H., Koobus, B., Dervieux, A., Salvetti, M.V.: Classical and variational multiscale LES of the flow around a circular cylinder on unstructured grids. Comput. Fluids **39**, 1083–1094 (2004)
6. Wornom, S., Ouvrard, H., Salvetti, M.V., Koobus, B., Dervieux, A.: Variational multiscale large-eddy simulations of the flow past a circular cylinder: Reynolds number effects. Comput. Fluids **47**, 47–50 (2011)

SVV-LES and Active Control of Flow Around the Square Back Ahmed Body

Noele Peres and Richard Pasquetti

1 Introduction

This work is motivated by the need of the automotive industry to manufacture vehicles that progressively reduce and ultimately eliminate both their negative environmental impact and dependence upon oil. To this end, we focus on a simplified ground vehicle, the so-called Ahmed body [1], and try to develop an efficient and validated methodology of drag reduction (up to 10 %). This methodology will be based on active control through the implementation of synthetic MMEMS (Micro-Magneto-Electro-Mechanical-Systems) microjets. As a preliminary step, we are interested in highly resolved simulations of the Ahmed body wake flow, in view of predicting accurately the effect of microjets and minimizing the drag by optimization of their use. In order to develop new efficient strategies to reduce the aerodynamic drag force, that should be able to change locally the flow, remove or delay flow separations without constraints of design, comfort and safety, many research groups have focused on the implementation of active flow control techniques. These techniques can range from blowing, steady and pulsed jets to synthetic jets in open or closed loops [2–4]. More recently, in [5] synthetic jets, i.e. with zero-net mass-flux, are applied on an Ahmed body with slant angle $\varphi = 25°$ to decrease the aerodynamic drag between 6.5 and 8.5 %.

In the present work, the influence of both steady and synthetic microjets on the flow field are pointed out. The present active flow control technique extends the concept applied by Rouméas et al. [4], where blowing steady jets at the rear of the Ahmed

N. Peres (✉) · R. Pasquetti
Laboratoire J.A. Dieudonné, UMR CNRS *n*° 7351,
Université de Nice - Sophia Antipolis, Nice Cedex 02, 06108 Nice, France
e-mail: noele.baptista_peres@unice.fr

R. Pasquetti
e-mail: rpas@unice.fr

J. Fröhlich et al. (eds.), *Direct and Large-Eddy Simulation IX*,
ERCOFTAC Series 20, DOI 10.1007/978-3-319-14448-1_10

body are used to reduce the transverse wake section, leading to an increase of the static pressure distribution on the rear part of the vehicle and a reduction of the total pressure losses in the near-wake flow.

2 Geometry and Mathematical Modelling

The geometry of the car model proposed by Ahmed and Ramm [1] with slant angle $\varphi = 0^\circ$ is considered. The square back Ahmed body, of length $l = 1{,}044$ mm, height $h = 288$ mm, and width $w = 389$ mm, is placed at $d = 50$ mm from the ground. The computational domain, $\Omega = (-5.44\,h, 7.25\,h) \times (0, 3.2\,h) \times (-2.16\,h, 2.16\,h)$, is channel-like. The bluff body is located at the distance $1.8125\,h$ from the inlet. The blockage factor, defined as the ratio between the bluff body section to the channel one, is then $9.77\,\%$.

The Reynolds number equals $Re = Uh/\nu = 768,000$, where U is the mean upstream velocity and ν the kinematic viscosity. The boundary conditions are the following: no-slip condition at the obstacle and at the ground, free-slip condition at the top boundary of the domain and a steady boundary layer like profile at the inlet. Periodicity is assumed versus the z-spanwise direction. At the initial time the fluid is at rest.

The flow is assumed to be governed by the incompressible three-dimensional Navier-Stokes equations. The numerical method is based on a multidomain Chebyshev Fourier approximation. In the streamwise direction, the computational domain is decomposed in nonoverlapping subdomains of different lengths. At the subdomain interfaces, the C^1 continuity of the velocity components and C^0 continuity of the pressure are ensured by using an influence matrix technique [6]. In each subdomain, a collocation Chebyshev method is used in the vertical and streamwise directions, whereas a Fourier Galerkin method is used in the spanwise periodic direction. In the vertical direction a mapping is used to accumulate grid points at the roof of the car model. The discretization in time is based on a fractional step method, involving first an explicit treatment of the advection terms, then an implicit treatment of the diffusion terms using a second order backward Euler approximation (BDF2) of the time derivative and third, an incremental projection step is applied to enforce the velocity divergence free constraint, see details in [7]. The LES capability is based on the SVV stabilization technique, see [8] and references herein. The SVV dissipation term is characterized by the threshold parameter $m_N = \sqrt{N}$ and by an amplitude $\varepsilon_N = 1/N$, with N for the polynomial approximation degree in each direction. The Ahmed body is modeled using a pseudopenalization technique, that consists of a modification of the time scheme in order to approximately cancel the velocity field inside the volume of the obstacle [9]. As a result, inside the bluff body we solve the stabilized steady Stokes equations penalized with a $\alpha\mathbf{u}/\tau$ term, where $\mathbf{u}$ is the velocity field, τ the time-step and α a time scheme dependent coefficient. In case of the BDF2 scheme $\alpha = 3/2$.

The active flow control makes use of microjets located around the rear part of the body. Blowing steady and synthetic micro-jets are considered. Due to the small size of the jets, a modelling is required , see e.g. [10]. In this work the jets are, like the bluff body, modeled by pseudo-penalization, i.e., by introducing implicitly in the momentum equation an additional forcing term, $\sum_j \alpha \chi_j (\mathbf{u} - \mathbf{u}_j)/\tau$, where $\mathbf{u}_j$ stands for the velocity enforced at the grid-point location χ_j of the jet j. Note that this is done at the level of the provisional step of the projection technique. In our modelling, each jet is located at the first point out of the Ahmed body. In case of the synthetic jets the amplitude of the imposed velocity is always positive for the blowing period and zero for the suction period. Indeed, the ingested fluid has essentially an impact on the actuator device (internal flow and membrane) and a negligible one on the external flow. Moreover, setting a zero value during the suction provides a rough modeling of the actuator slot.

3 Results

The computational domain is decomposed in eight sub-domains in the x-streamwise direction. Three of them localized around the Ahmed body. In each subdomain the polynomial approximation is $40 \times 190 \times 128$, yielding about 15.7 millions of grid-points. The dimensionless time-step is taken equal to $\tau = 2.0\,10^{-3}$.

Figure 1a present visualizations of the instantaneous pressure, both in the median vertical plane and in an horizontal plane, whereas in Fig. 1b we display the mean pressure field. These visualizations highlight the low pressure regions at the rear and front of the car.

The statistics have been computed in the time interval $t \in (667, 787)$. The mean flow is visualized in Fig. 2a, which clearly points out the large spreading of the wake

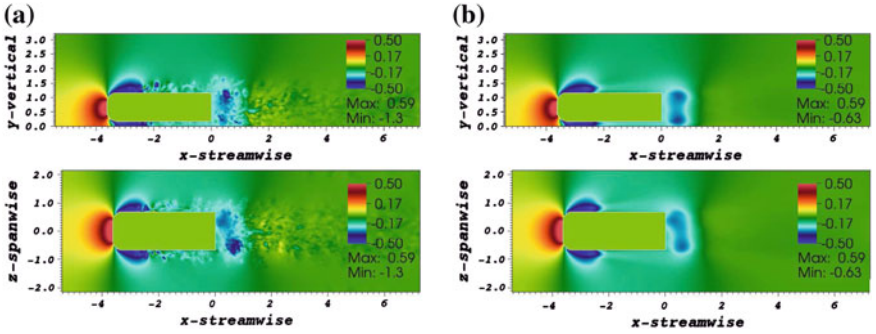

Fig. 1 **a** Instantaneous pressure in the $z = 0$ and $y = 0.58\,h$ *planes* from *top* to *bottom* respectively, **b** pressure mean field in the $z = 0$ and $y = 0.58\,h$ *planes* from *top* to *bottom* respectively

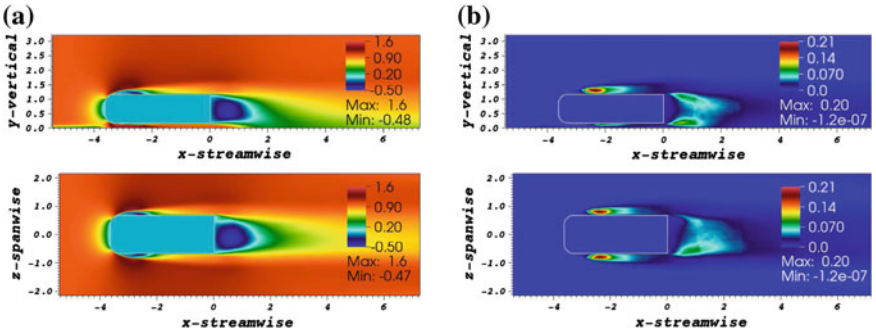

Fig. 2 **a** Mean streamwise component of the velocity in the $z = 0$ and $y = 0.58\,h$ *planes* from *top* to *bottom* respectively, **b** turbulent kinetic energy in the $z = 0$ and $y = 0.58\,h$ *planes* from *top* to *bottom* respectively

downwards of the car model, the formation of a recirculation zone at the rear of the bluff body and also the separation of the flow at the front of the car, both on the top and on the sides of the Ahmed body. Figure 2b displays the turbulent kinetic energy with extrema at the rear, and also at the top and on the sides. The slight lacks of symmetry observed with respect to the symmetry plane of the body in Figs. 1b and 2, suggests to use a longer time to compute such statistics, but this was not done for computational cost reasons.

The strategies to reduce the aerodynamic drag force presented in this work consists of reducing the transversal wake section. To achieve this goal, one uses steady or synthetic jets, located around the rear part of the Ahmed body, as sketched in Fig. 3d. The angle between each jet and the rear wall is $\theta = 45°$ inward, except in Fig. 3a where a study of its influence is carried out.

Several configurations are studied using these two techniques. Figure 3a, c represent the time evolution of the aerodynamic drag force F_x considering blowing steady jets with blowing velocity $U_{jet} = 1.5\,U$. One observes a reduction of the aerodynamic drag force up to 30 % that agrees with the results obtained by Rouméas et al. [4]. The influence of the angle θ between each jet and the rear wall is presented in Fig. 3a for $\theta = 45°$ and $\theta = 30°$, showing a weak variation of F_x between these two angles. The dependence of the number of jets on the reduction of drag is presented in Fig. 3c, where starting from a configuration where jets are localized at all the considered mesh-points, we only keep jets at one over two or one over three points.

The second technique, based on synthetic micro-jets, uses a truncated sinusoidal variation such that $U_{jet} = \max(U_{imp}\sin(2\pi f t + \varphi), 0)$, with $U_{imp} \in \{1.5\,U, 2.0\,U\}$. We have used the dimensionless frequency $f = 5$, which is much greater than the dominant one of the recirculation bubble. Moreover, a phase lagging between the successive micro-jets is implemented, i.e. $\varphi \in \{0, \pi/2, \pi, 3\pi/2\}$. Note that these choices of frequency and phase lagging are used to retrieve as much as possible

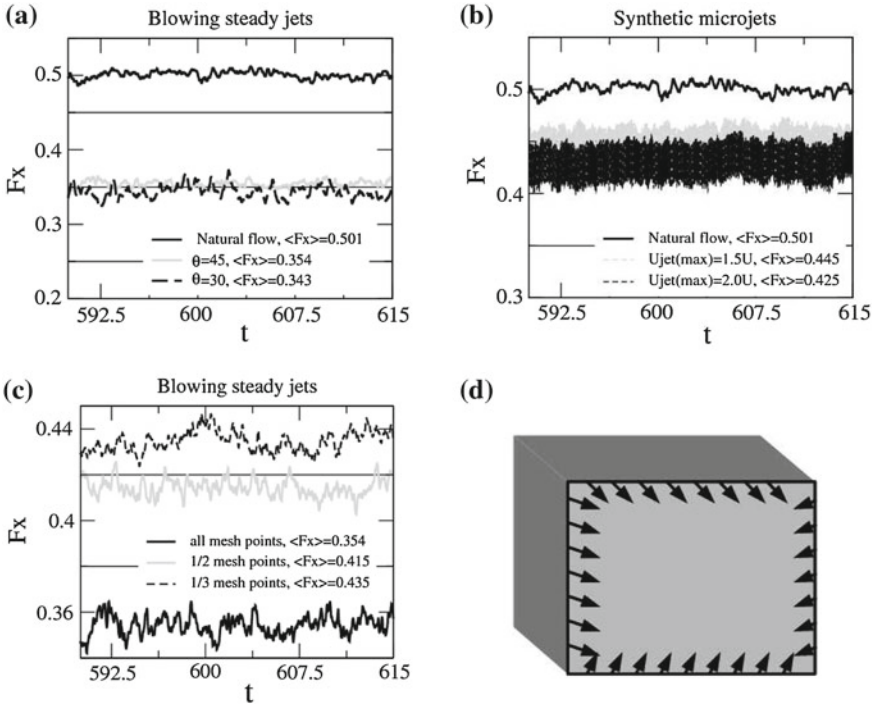

Fig. 3 **a** Time evolution of the drag force F_x, for the natural flow and the controlled flow using blowing steady jets at different angles θ, **b** time evolution of the drag force F_x, for the natural flow and the controlled flow using synthetic microjets with different velocities, **c** time evolution of the drag force F_x, and its dependence of the space distribution of the blowing steady jets, **d** jet localizations at the rear of the Ahmed body

the efficiency of the steady jet configuration. The dimensionless frequency $f = 5$ corresponds with $h = 288\,\text{mm}$ and $U = 40\,\text{ms}^{-1}$ to the realistic value 700 Hz. Figure 3b shows a reduction of the aerodynamic drag force up to 10 %, using the parameters described above. The mean values of the drag force $\langle F_x \rangle$ were computed for $t \in (590, 615)$.

Figure 4a shows the mean pressure field in the median vertical plane without control, with active flow control using synthetic micro-jets and steady jets, from top to bottom respectively. In the case of the synthetic micro-jets $U_{imp} = 1.5\,U$. Figure 4b represents the mean streamwise velocity component. These visualizations highlight the influence of the jets in the wake flow.

Future works will focus on the optimization of the drag reduction system, i.e. localization, frequency and amplitude of the micro-jets. The possibility of improving their modelling should be considered as well as the balance between the energy losses due to the microjets consumption and the profits related to the drag force reduction.

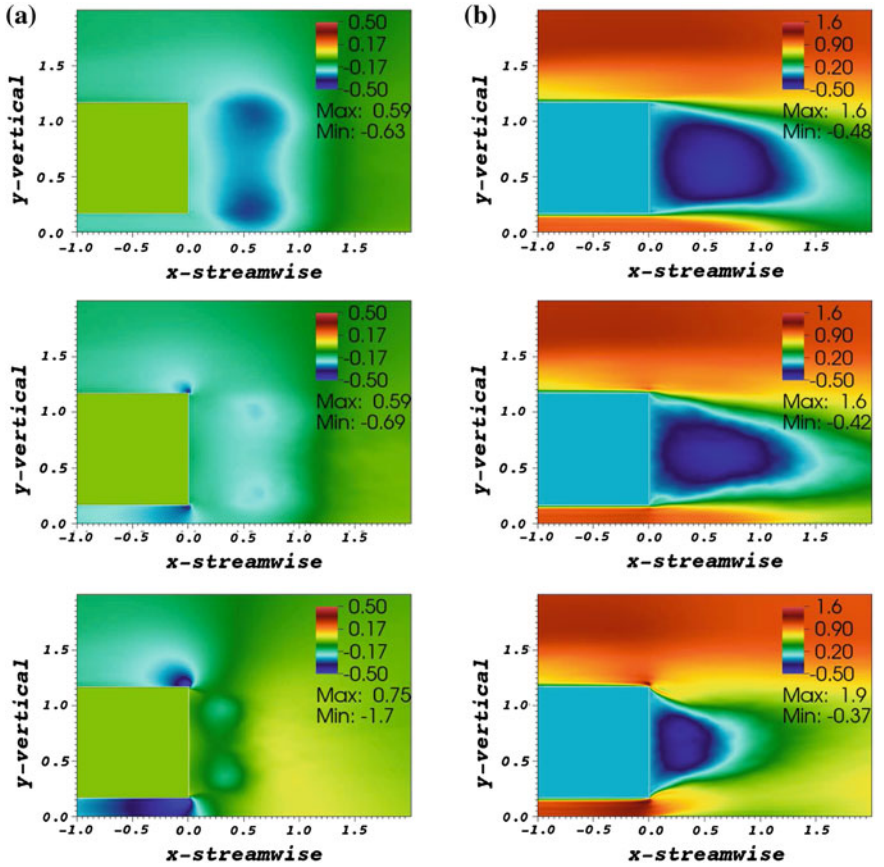

Fig. 4 **a** Mean pressure in the $z = 0$ *plane*. From *top* to *bottom* without control, with active flow control using synthetic micro-jets and using steady jets, **b** mean streamwise velocity component in the $z = 0$ *plane*. From *top* to *bottom* without control, with active flow control using synthetic micro-jets and using steady jets

Acknowledgments The work is supported by the French National Research Agency (ANR), in the frame of the project *Limitation of the impact of vehicles on the environment by means of aerodynamic control using synthetic micro-jets* (LIVE-CAMS). The calculations were carried out on the cluster of the *Centre de Calculs Interactifs* of the University of Nice Sophia Antipolis.

References

1. Ahmed, S.R., Ramm, G.: Salient features of the time-averaged ground vehicle wake. SAE paper no. 840300 (1984)
2. Bruneau, C.-H., Creusé, E., Depeyras, D., Gilliéron, P., Mortazavi, I.: Coupling active and passive techniques to control the flow past the square back Ahmed body. Comput. Fluids **39**, 1875–1892 (2010)

3. Krajnović, S., Fernandes, J.: Numerical simulation of the flow around a simplified vehicle model with active flow control. Int. J. Heat Fluid Flow **32**, 192–200 (2011)
4. Rouméas, M., Gilliéron, P., Kourta, A.: Analysis and control of the near-wake flow over a square-back geometry. Comput. Fluids **38**, 60–70 (2009)
5. Kourta, A., Leclerc, C.: Characterization of synthetic jet actuation with application to Ahmed body wake. Sens. Actuators, A **192**, 13–26 (2013)
6. Sabbah, C., Pasquetti, R.: A divergence-free multidomain spectral solver of the Navier Stokes equations in geometries of high aspect ratio. J. Comput. Phys. **139**, 359–379 (1998)
7. Cousin, L., Pasquetti, R.: High-order methods for the simulation of transitional to turbulent wakes. In: Lu, Y., Sun, W., Tang, T. (eds.) Advances in Scientific Computing and Applications, pp. 133–143. Science Press, Beijing (2004)
8. Minguez, M., Pasquetti, R., Serre, E.: High-order large-eddy simulation of flow over the Ahmed body car model. Phys. Fluids **20**, 095–101 (2008)
9. Pasquetti, R., Bwemba, R., Cousin, L.: A pseudo-penalization method for high Reynolds number unsteady flows. Appl. Numer. Math. **58**, 946–954 (2008)
10. Raju, R., Aram, E., Mittal, R., Cattafesta, L.: Simple models of zero-net mass-flux jets for flow control simulations. Int. J. Flow Control **1**(3), 179–197 (2009)

Design of High-Order Implicit Filters on Unstructured Grids for the Identification of Large-Scale Features in Large-Eddy Simulations

L. Guedot, G. Lartigue and V. Moureau

1 Motivation

Large-Eddy Simulation (LES) and Direct Numerical Simulation (DNS) are increasingly popular modeling tools for the understanding and the prediction of turbulent flows. The mesh resolution in these 3D unsteady simulations has been in a constant increase over the last decade driven by the development of massively parallel super-computers. The post-processing of the large amount of data generated by these simulations is however very challenging. The extraction of large-scale features in turbulent flows is particularly difficult because it requires to process either wide regions of the computational domain or to perform some averaging of the flow.

The extraction of large eddies in turbulent flows may be achieved using Proper Orthogonal Decomposition or Dynamic Mode Decomposition [1–3] but both methods require the storing of a large amount of snapshots, which is presently intractable for billion-cell simulations. Those methods might require to perform some temporal or spatial filtering, to remove high-frequency motions and avoid aliasing issues.

A complementary approach, which is presented in this paper, is to use high-order filters. Novel high-order filters have been developed to extract turbulent scales of a given size on unstructured grids, and they have been successfully applied in a semi-industrial swirl bruner (as presented in Sect. 5).

L. Guedot (✉) · G. Lartigue · V. Moureau
CORIA, CNRS UMR 6614, INSA, University of Rouen, Rouen, France
e-mail: lola.guedot@coria.fr

G. Lartigue
e-mail: ghislain.lartigue@coria.fr

V. Moureau
e-mail: vincent.moureau@coria.fr

J. Fröhlich et al. (eds.), *Direct and Large-Eddy Simulation IX*,
ERCOFTAC Series 20, DOI 10.1007/978-3-319-14448-1_11

2 High-order Implicit Filters

The filtering of a scalar ϕ with high-order implicit filters (HOF), as defined in [4, 5], can be written in a one-dimensional domain as

$$\overline{\phi} + \beta_p D^p \overline{\phi} = \phi \,, \textit{where } \beta_p = \frac{\Delta x^{2p}}{(-4)^p \sin^{2p}(k_c \Delta x/2)} \,, \tag{1}$$

$\overline{\phi}$ is the filtered value, D the second derivative operator, $2p$ the order of the filter, k_c the cut-off wave number, and Δx the homogeneous grid spacing.

This filter may be analyzed in the complex Fourier space assuming a monochromatic signal $\phi = A\exp(ikx)$, where A is the amplitude, k is the wave number and x the space coordinate. The filter response defined as the ratio of the filtered and unfiltered amplitudes $\overline{A}/A$ is

$$\frac{\overline{A}}{A} = \left(1 + \frac{\sin^{2p}(k\Delta x/2)}{\sin^{2p}(k_c \Delta x/2)}\right)^{-1} . \tag{2}$$

This damping function is plotted in Fig. 1 for various orders. The definition of this filter family ensures that the amplitude damping is 50 % at the cut-off wave number, i.e. where all curves intersect each other. The selectivity of a filter can be defined as its ability to damp the smallest scales while not affecting the largest ones. The higher is the order, the sharper is the filter response. The slope of the filter response at the cut-off wave number is a good estimate of the filter selectivity. The HOF shows a good selectivity which is an essential property to extract structures of a given scale from the flow.

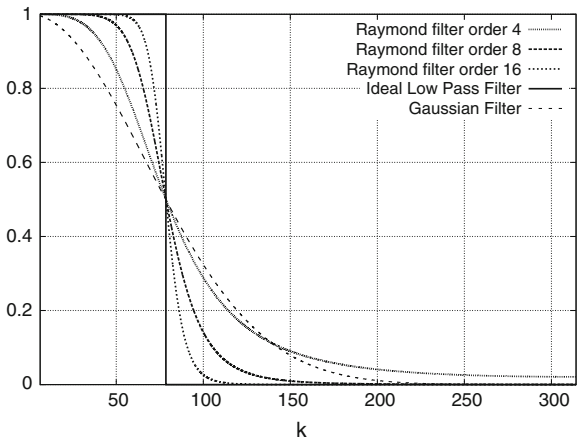

Fig. 1 Damping functions of high order filters, for order 4, 8 and 16, Gaussian filter, and low-pass filter

3 Derivation and Implementation of Raymond Filters on Unstructured Grids

A first part of the work consisted in the generalization of the filters to 3D unstructured grids with non-uniform grid spacing. In this case, the second-order derivative operator D is replaced by a node-centered Laplacian operator. Then, to ensure discrete conservative properties of the filter, the coefficient β_p is included in the Laplacian operator itself leading to a modified operator D'.

The HOF require the inversion of a symmetric matrix to find the filtered values. The linear system may be written as

$$(I + D'^{k})\overline{\phi} = \phi \tag{3}$$

where D' is the modified symmetric Laplacian operator. The algorithm used to invert the linear system and to compute $\overline{\phi}$ is a Preconditioned Conjugate Gradient (PCG).

To make this filter suitable for meshes of several millions of cells, some work has been done to accelerate the convergence and improve the robustness of the linear solver. The decomposition of the matrix of the linear system described in Eq. (3) into p complex matrices (polynomial factorization, where α_i are the complex roots of the polynomial):

$$\prod_{i=1}^{k}(I + \alpha_i \Delta')\overline{\phi} = \phi \tag{4}$$

reduces the system to p smaller systems. Each n x n complex symmetric matrix is then transformed into a 2n $\times$ 2n real symmetric matrix that can be inverted with the PCG algorithm [6].

4 Application of the Filters to Canonical Flows

4.1 Taylor Vortices

In this section, a linear combination of 2D Taylor vortices with three different sizes ($L/2$, $L/4$ and $L/8$), where L is the size of the computational domain, is considered. The mesh used in this case is a 2D cartesian grid, but the filtering is performed with an unstructured code.

The velocity field has been filtered with filter widths of $L/2$ and $L/4$. The $L/4$ filtering removes the structure of smallest size $L/8$. The $L/2$ filtering removes both $L/8$ and $L/4$ vortices, leaving only the biggest vortices. The $L/2$-filtered field can be compared to the analytical solution of Taylor Green vortices of size $L/2$ (Fig. 2 (top)). Plotting the difference between the unfiltered field and the $L/4$-filtered field enables to extract the $L/4$ vortices, which can also be compared to the exact solution

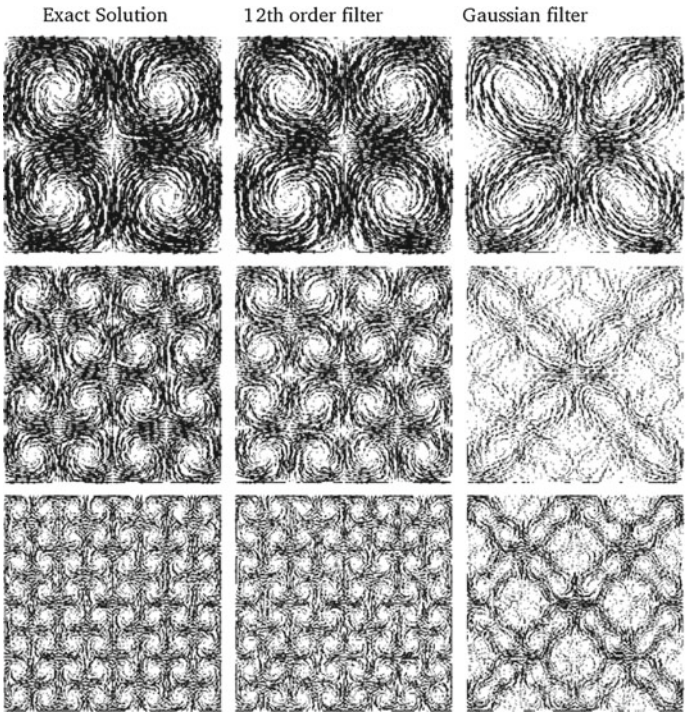

Fig. 2 Extraction of Taylor vortices with 12th order band pass filter (*center*), Gaussian band-pass filter (*right*) and comparison with exact solutions (*left*)

(Fig. 2 (center)). The same can be done for the smallest vortices (Fig. 2 (bottom)). The same was done with a Gaussian filter, and the difference between the two types of filter is clearly visible. The three types of vortices are recovered with the HOF, while Gaussian filter hardly captures the biggest vortices, and yet they are stretched and damped. For the smaller vortices, traces of the other frequencies are still visible since the Gaussian band-pass filter is not selective enough.

4.2 3D Homogeneous Isotropic Turbulence

The HOF are then applied in a 3D Homogeneous Isotropic Turbulence on a 128^3 Cartesian grid and compared to a Gaussian filter. In this case, the performances of the filter are obtained from the analysis of the Q-criterion spectrum. An example is given in Fig. 3a . The higher selectivity of the HOF is clearly visible. The spectrum fits better the unfiltered spectrum for the low wave numbers, and decreases faster after the cut-off. The HOF provide a better dissipation of the smaller scales.

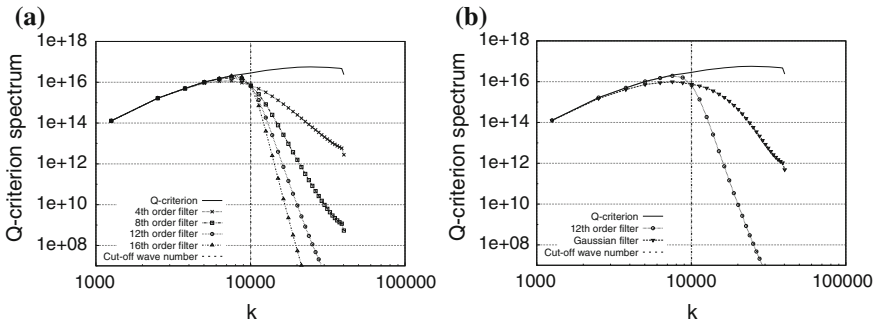

Fig. 3 **a** Influence of the order on the spectrum of filtered Q-criterion **b** Filtered and unfiltered Q criterion energy spectrum

Figure 3b compares the spectra of filtered Q-criterion with order from 4 to 16. As the order increases, the selectivity of the filter is improved. The higher is the order, the sharper is the spectrum for high wave numbers.

5 Application of the Filters to Turbulent Flows in Complex Geometries

The HOF were also applied in a complex semi-industrial swirl burner in order to assess the proper behavior of the filters on massive unstructured grids and evaluate their ability to extract large-scale features of a turbulent flow. In aeronautical swirl burners, the Precessing Vortex Core (PVC) is a well-known 3D structure which dominates the flow dynamics and part of the mixing process [7]. This kind of large coherent structure becomes hard to be extracted as the size of the mesh increases.

The Preccinsta swirl burner has been widely studied and is a challenging test for the HOF since it has been computed with several mesh resolutions from 1.7 millions of tetrahedrons to 2.6 billions [8]. On the simulation performed with the 1.7 millions mesh, Q-criterion isosurface colored by the axis distance shows the existence of a Precessing Vortex Core (helical vortex, Fig. 4a). With bigger meshes, this large structure becomes hard to post process. Large scale structures can be visualized with Q-criterion isosurfaces, but this method reveals both large and small structures regardless of their size. The bigger is the structure compared to the mesh resolution, the harder it is to be extracted. For the refined simulations (14–110 millions), Q-criterion was filtered with a 12th order filter at the approximate size of the PVC. The same isosurface is then plotted with this filtered Q-criterion (Fig. 4b–d). All the small-scale structures were removed by the filtering, leaving a big 3D helical vortex similar to the PVC observed on the 1.7 millions.

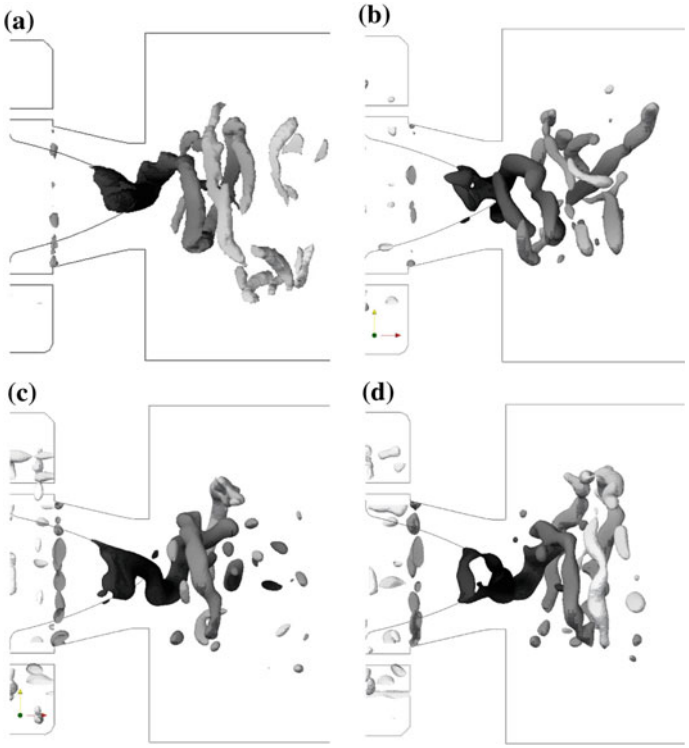

Fig. 4 **a** Isosurface of unfiltered Q-criterion on the coarse mesh. **b** Isosurface of filtered Q-criterion (12th order) on the 14 M mesh. **c** Isosurface of filtered Q-criterion (12th order) on the 41 M mesh. **d** Isosurface of filtered Q-criterion (12th order) on the 110 M mesh

6 Conclusions and Perspectives

The HOF implemented in the code show good results on canonical test cases, and were successfully applied in the PRECCINSTA semi-industrial swirl burner. The extraction of large-scale strutures with HOF in this type of burner, associated with two-phase flow simulations will enable to understand and analyse the interaction between the liquid fuel spray and the large-scale vortices.

Those filters can also be a valuable tool to interpolate data on a coarse grid and perform modal analysis (POD, DMD) with reduced computational costs.

Acknowledgments Computational time was provided by GENCI (Grand Equipement National de Calcul Intensif), and all simulations were performed on the supercomputers of IDRIS.

References

1. Lumley, J. L. (1970). Stochastic Tools in Turbulence. Academic Press.
2. Sirovich, L.: Turbulence and the dynamics of coherent structures. Q. Appl. Math. **45**, 561–590 (1987)
3. Schmid, P.: Dynamic mode decomposition of numerical and experimental data. J. Fluid Mech. **656**, 5–28 (2010)
4. Raymond, W.H.: High-order low-pass implicit tangent filters for use in finite area calculations. Mon. Weather Rev. **116**, 2132–2140 (1988)
5. Raymond, W.H.: A review of recursive and implicit filters. Mon. Weather Rev. **119**, 477–495 (1991)
6. Freund, R.W.: Conjugate gradient-type methods for linear systems with complex symmetric coefficient matrices. SIAM J. Sci. Stat. Comput. **13**(1), 425–448 (1992)
7. Syred, N.: A review of oscillation mechanisms and the role of the precessing vortex core (PVC) in swirl combustion systems. Prog. Energy. Combust. Sci. **32**, 93–161 (2006)
8. Moureau, V., Domingo, P., Vervisch, L.: From large-eddy simulation to direct numerical simulation of a lean premixed swirl flame: filtered laminar flame-PDF modelling. Comb. Flame **158**, 1340–1357 (2011)

Part II
Numerical Methods

DNS of Canonical Turbulent Flows Using the Modal Discontinuous Galerkin Method

J.-B. Chapelier, M. De La Llave Plata, F. Renac and E. Lamballais

1 Introduction

The discontinuous Galerkin (DG) method is a particular class of finite element methods which was first introduced by Reed and Hill in 1973 [1] for the treatment of the neutron transport equations. The first applications to fluid mechanics appeared two decades later with the resolution of the Euler equations [2–4], and the compressible Navier-Stokes equations [5]. This method has gained increased popularity during the last decade for CFD applications. An interesting property of DG discretizations is their arbitrarily high-order of accuracy, achieved by writing the solution in terms of a polynomial expansion of order p in each element of the computational domain. Another significant property of these methods is their ability to deal with unstructured meshes over complex geometries. Finally, a smart choice of the numerical fluxes can lead to compact discretization, which is advantageous for parallel strategies based on the MPI technique. The combination of these three properties makes the DG method interesting for the computation of turbulent flows using DNS or LES. In this paper, we present Direct numerical simulations of canonical test cases using a modal DG method. Special emphasis is placed on the interest of high-order DG discretizations for the simulation of turbulence.

J.-B. Chapelier (✉) · M. De La Llave Plata · F. Renac
ONERA - The French Aerospace Lab, Châtillon, France
e-mail: jean-baptiste.chapelier@onera.fr

E. Lamballais
PPRIME Institute, Université de Poitiers, 11 Boulevard Marie et Pierre Curie,
86962 Futuruscope Chasseneuil, France

J. Fröhlich et al. (eds.), *Direct and Large-Eddy Simulation IX*,
ERCOFTAC Series 20, DOI 10.1007/978-3-319-14448-1_12

2 Numerical Methods

We consider the compressible set of Navier Stokes equations written in conservative form. The DG discretization is based on a variational form of these equations, in which the continuity of the solution is not enforced at the interfaces between elements. The surface integrals are therefore computed by introducing a numerical flux, which takes into account the discontinuities in the solution. We consider a modal approach, for which the solution is expressed within an element as an expansion of locally orthogonal polynomials. This property is necessary to ensure that the mass matrix is diagonal. In this case, the degrees of freedom are the expansion coefficients in each element. We consider in this study a Lax Friedrichs flux for the discretization of the convective terms and the BR2 method [6] for the discretization of the viscous terms. This approach guarantees a convergence order of $p + 1$, where p is the polynomial degree of the expansion, while keeping the compacity of the method. We consider a third-order explicit Runge-Kutta method for the temporal integration. The code has been parallelized using the MPI approach. For the following studies, the meshes considered are composed of hexahedra, and the basis is composed of Legendre polynomials.

3 DNS of Canonical Flows

3.1 Collision of a Dipole Vortex with a No-Slip Wall

The first configuration considered represents the impact of a vortex-dipole on a no-slip wall. This configuration provides complex near-wall phenomena that are difficult to capture for most numerical codes. The following initialization refers to the work of Clercx [7]. We consider a square domain $\Omega = [-h, +h]^2$ with no-slip adiabatic boundary conditions at $x = \pm h$ and periodicity conditions in the y-direction. The expression of the Reynolds number is $Re = \sqrt{E_0/2}h/\nu$, where E_0 is the total kinetic energy in the domain. We consider a Reynolds number of 1,000 for comparison with the reference spectral computations of Keetels et al. [8].

We have performed a high-order DG computation using a coarse mesh (see Table 1 for the details). The associated number of degrees of freedom is low compared to reference spectral computation. Regarding the evolution of enstrophy and the isocontours of vorticity at a time after the first collision, the agreement is excellent between the two computations (see Figs. 1 and 2). This result shows the interest of high-order DG methods for the accurate resolution of vortex-based flows using coarse discretizations.

Table 1 Details of the computations for the vortex-wall collision

Computation	Order	Elements	DOFs	Δx_1
DG $p5$	6	32^2	192^2	2.5δ
Keetels et al.	–	–	2048×1024	–

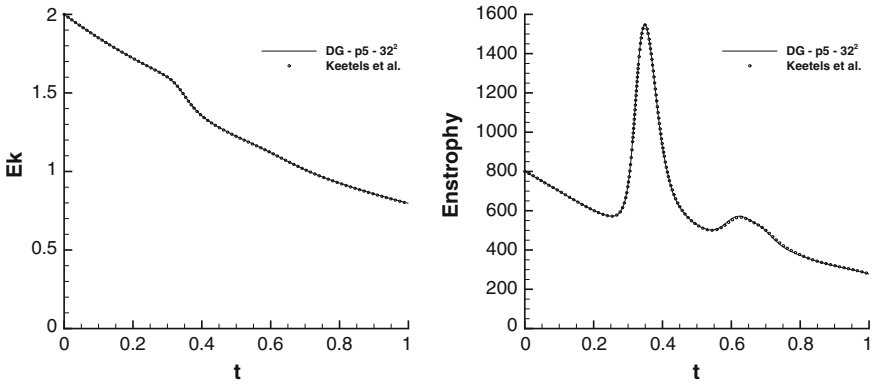

Fig. 1 Evolution of statistics for the dipole-wall collision at $Re = 1,000$

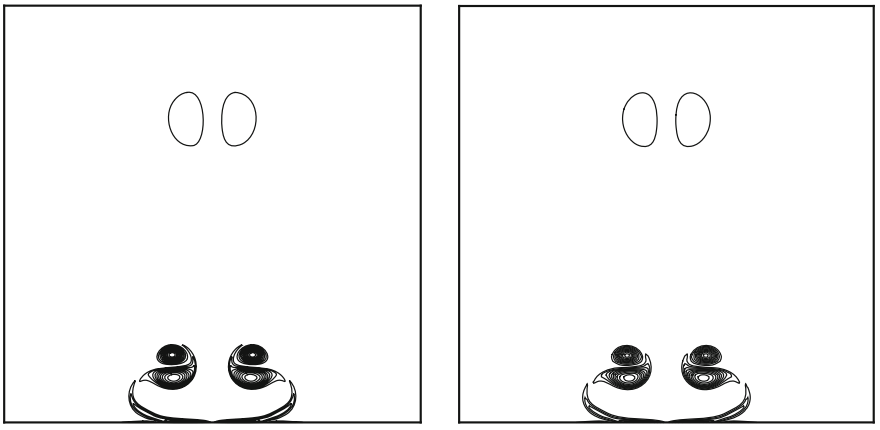

Fig. 2 Vorticity contours at $t = 0.5$ for the pseudo-spectra (*left*) and DG (*right*) computations

3.2 Turbulent Channel Flow

We consider in this section a DG computation of the turbulent channel flow, which is a more realistic configuration for the study of turbulence. The flow is developed between two walls separated by a distance $2h$, and the computational domain is $\Omega = [0, 4\pi h] \times [0, 2h] \times \left[0, \frac{4}{3}\pi h\right]$. We consider periodicity boundary conditions in the streamwise (x) and spanwise (z) directions. This flow is statistically homogeneous

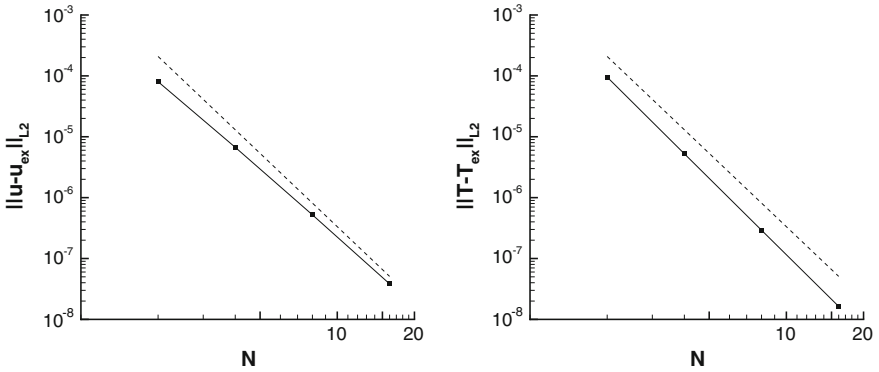

Fig. 3 L_2-error of velocity and temperature for different fourth-order DG discretizations, for the laminar channel flow. *Solid lines* fourth-order DG computations; *Dashed lines* theoretical error scaling

Table 2 Resolution details of the computations for the compressible channel flow

Computation	Degrees of freedom	Collocation / Quadrature points	Δy_1^+
DG $p = 3$	$104 \times 92 \times 64$	$130 \times 115 \times 80 \left(\approx 1.2 \times 10^6\right)$	5.7
Coleman et al	$110 \times 90 \times 60$	$144 \times 119 \times 80 \left(\approx 1.37 \times 10^6\right)$	–

in these two directions, allowing to plot the various profiles as a function of y only. We consider a body force as a source term in the x-momentum equation to account for the mean pressure gradient that drives the flow. In order to validate the isothermal boundary conditions, we first perform computations of the laminar channel flow. The evolution of the error in the L_2 norm is plotted for the velocity and the temperature, as a function of the number N of the elements of the discretization. As seen in Fig. 3, we verify the theoretical order of convergence $p + 1$, which validates the boundary conditions.

A DNS of the turbulent channel flow at Mach 1.5 is performed. We consider a bulk Reynolds number of 2,800, which corresponds to a friction Reynolds number of about 180. The reference spectral computation has been performed by Coleman et al. [9]. The details of the computations are shown in Table 2.

As seen in Fig. 4, the correlation is very good for the mean and fluctuating velocity profiles between the DG and the reference computation. There is also an excellent agreement between the mean and fluctuating density and temperature (see Fig. 5), showing that the DG method allows for an accurate representation of the compressibility effects in the channel. The friction Reynolds number, as seen in Table 3, is also in very good agreement with the reference computation.

This DG computation shows the suitability of high-order DG methods for the representation of near-wall turbulence submitted to compressibility effects.

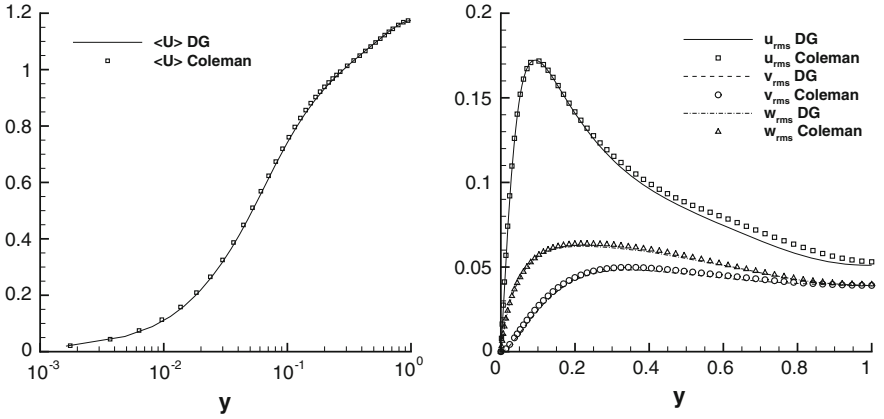

Fig. 4 Profiles of mean and fluctuating velocity for the compressible channel flow

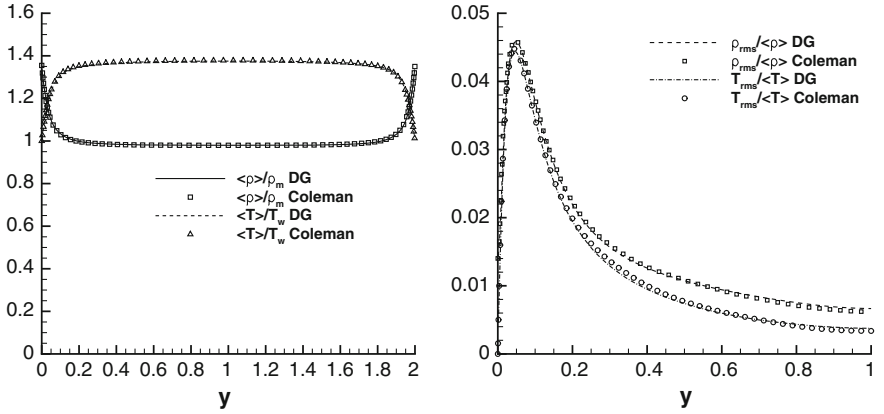

Fig. 5 Profiles of mean and fluctuating density and temperature for the compressible channel flow

Table 3 Physical parameters of the computations for the compressible channel flow

	Re_τ	u_τ	T_c	ρ_c	ρ_c/ρ_w
DG $p = 3$	221.4	0.0547	1.375	0.980	0.726
Coleman et al.	221.6	0.0545	1.378	0.980	0.723

4 Conclusion

The accuracy of the DG modal approach for the DNS of turbulent flows has been assessed by considering two different flow settings.

Firstly, a 2D configuration representing the normal collision of a dipole with a no-slip boundary has been investigated. It appears that the high-order DG approach

is able to provide good quality solutions on coarse meshes. In particular, we have shown that accurate solutions can be obtained with only 192^2 DOFs, with respect to the reference simulation which shows 2048×1024 DOFs.

Finally, a high-order DG computation has been performed for the turbulent channel flow configuration in the compressible regime. The DG solution turns out to be in good agreement with the reference computation both in terms of mean and fluctuating velocity profiles. We also found an excellent agreement with Coleman's reference DNS for the fluctuating thermodynamic quantities (density and temperature).

High-order DG discretizations are able to provide a level of accuracy equivalent to that offered by spectral methods for a comparable number of DOFs. Thanks to the flexibility provided by the DG method in terms of hp-refinement the size of the simulation can be further reduced through an appropriate choice of the discretization parameters h and p.

Acknowledgments This research is funded by ONERA's scientific board (DSG). We would like to thank Prof. G.N. Coleman for providing the reference data for the compressible channel flow, and Dr. Werner Kramer and Prof. Herman Clercx for the reference data for the dipole configuration. We are grateful to Dr. Emeric Martin for his valuable help regarding the parallel implementation issues.

References

1. Reed, W., Hill, T.: Triangular mesh methods for the neutron transport equation. Los Alamos Report LA-UR-73-479
2. Cockburn, B., Shu, C.: TVB Runge-Kutta local projection discontinuous Galerkin finite element method for conservation laws II: general framework. Math. Comp. **52**(186), 411–435 (1989)
3. Cockburn, B., Lin, S., Shu, C.: TVB Runge-Kutta local projection discontinuous Galerkin finite element method for conservation laws III: one-dimensional systems. J. Comput. Phys. **84**(1), 90–113 (1989)
4. Cockburn, B., Hou, S., Shu, C.: The Runge-Kutta local projection discontinuous Galerkin finite element method for conservation laws IV: the multidimensional case. Math. Compt. **54**(190), 545–581 (1990)
5. Bassi, F., Rebay, S.: A high-order accurate discontinuous finite element method for the numerical solution of the compressible Navier-Stokes equations. J. Comput. Phys. **131**(2), 267–279 (1997)
6. Bassi, F., Crivellini, A., Rebay, S., Savini, M.: Discontinuous Galerkin solution of the Reynolds-averaged Navier-Stokes and k-ω turbulence model equations. Comput. Fluids **34**(4–5), 507–540 (2005)
7. Clercx, H., Bruneau, C.: The normal and oblique collision of a dipole with a no-slip boundary. Comput. Fluids **35**(3), 245–279 (2006)
8. Keetels, G., D'Ortona, U., Kramer, W., Clercx, H., Schneider, K., Van Heijst, G.: Fourier spectral and wavelet solvers for the incompressible Navier-Stokes equations with volume-penalization: convergence of a dipole-wall collision. J. Comput. Phys. **227**(2), 919–945 (2007)
9. Coleman, G., Kim, J., Moser, R.: A numerical study of turbulent supersonic isothermal-wall channel flow. J. Fluid Mech. **305**, 159–184 (1995)

LES Using a Discontinuous Galerkin Method: Isotropic Turbulence, Channel Flow and Periodic Hill Flow

C. Carton de Wiart, K. Hillewaert, L. Bricteux and G. Winckelmans

1 Introduction

This paper presents the second step of the validation of a compressible discontinuous Galerkin method (DGM) for the Direct numerical simulation (DNS) and the large eddy simulation (LES) of turbomachinery flows. The method has already been successfully validated for the DNS of academic flows [1] as well as for the flow around complex geometries [2]. During these studies, the interesting dissipation properties of the method have been highlighted, showing a natural tendency to disspate only the under-resolved scales (i.e the smallest scales), leaving intact the larger scales. This phenomena is even emphasised when going to high order polynomials. Indeed, the dissipation increases on the largest wave numbers and its range of impact is reduced. These properties of DGM makes it an excellent candidate for efficient implicit LES (ILES). A validation of this DGM/ILES approach is here investigated on cannonical flows, allowing us to deeply study the impact of the discretisation for under-resolved computations. The first case studied is the homogeneous isotropic turbulence (HIT) at infinite Reynolds number, as studied by Cocle et al. [3]. This benchmark allows the assessment of the spectral behaviour of the method. The LES of the channel

C.C. de Wiart (✉) · K. Hillewaert
Cenaero, Rue des frères Wright 29, 6041 Gosselies, Belgium
e-mail: corentin.carton@cenaero.be

K. Hillewaert
e-mail: koen.hillewaert@cenaero.be

L. Bricteux
Fluids and Machines Department, Université de Mons, Mons, Belgium
e-mail: laurent.bricteux@umons.ac.be

G. Winckelmans
Institute of Mechanics, Materials and Civil Engineering (iMMC),
Université Catholique de Louvain (UCL), Louvain-La-Neuve, Belgium
e-mail: gregoire.winckelmans@uclouvain.be

J. Fröhlich et al. (eds.), *Direct and Large-Eddy Simulation IX*,
ERCOFTAC Series 20, DOI 10.1007/978-3-319-14448-1_13

flow [4, 5] at various high Reynolds numbers is then presented. Finally, the method is applied to the DNS of the two-dimensional periodic hill flow [6] at $Re_b = 2800$. This computation is the preliminary step to the LES at $Re_b = 10595$.

2 The Discontinuous Galerkin/Symmetric Interior Penalty Method

The discontinuous Galerkin method [7] is a Galerkin finite element method based on an interpolation space Φ, composed of functions v that are polynomials of order p on each of the elements e in the mesh $\mathscr{E}$, but not required to be continuous across any of the interfaces f between elements.

After choosing an appropriate set of basis functions ϕ_i for $\Phi = \texttt{span}\{\phi_0, \ldots, \phi_N\}$, with N the number of degrees of freedom per element, DGM then approximates the different components $\tilde{w}_m$ of $\tilde{w}$ by $w_m = \sum_i W_{im}\phi_i$.

As for any Galerkin method, the expansion weights W_{im} are found by requiring that the residual of the model equations, evaluated with w, is orthogonal to any function $v \in \Phi$. This principle is further complemented with consistent and penalty terms on the element interfaces, using, as Riemann solver $\mathscr{H}$, the Roe upwind flux for the convective terms whilst the diffusive terms are discretised according to the *Symmetric Interior Penalty* (*SIP*) method:

$$\forall \phi_i \in \Phi \ , \ \forall m : \sum_e \int_e \phi_i \frac{\partial w_m}{\partial t} dV - \sum_e \int_e \frac{\partial \phi_i}{\partial x^k} \left(\mathscr{F}_m^k + \mathscr{D}_m^k\right) dV$$
$$+ \underbrace{\sum_f \int_f [[\phi_i]]^k \, n^k \, \mathscr{H}_m\left(w^-, w^+, \mathbf{n}\right) dS}_{CI} + \underbrace{\sum_f \int_f [[\phi_i]]^k \left\{ D_{mn}^{kl} \, \frac{\partial w_n}{\partial x^l} \right\} dS}_{DI}$$
$$+ \underbrace{\sum_f \int_f [[w_n]]^k \left\{ D_{nm}^{kl} \cdot \frac{\partial \phi_i}{\partial x^l} \right\} dS}_{DS} + \underbrace{\sum_f \sigma \int_f [[w_m]]^k \, [[\phi_i]]^k \, dS}_{DP} = 0.$$

$\mathscr{F}$ and $\mathscr{D}$ respectively stand for the convective and diffusive fluxes, D_{mn}^{kl} for the Jacobian of the diffusive fluxes with respect to the solution gradients. {.} and [[.]] denote the interface average and jump operators. The penalty parameter σ must be chosen to be large enough to guarantee stability. Sharp bounds for the value of σ have been elaborated for simplices and recently for hybrid meshes [8].

3 HIT at Infinite Reynolds Number

The LES of incompressible decaying homogeneous isotropic turbulence (HIT) at very high number is considered. The molecular viscosity is negligible leading to an infinite Reynolds number. After a given transient phase, due to the sudden absence

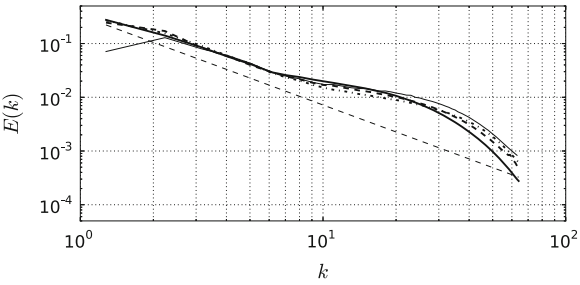

Fig. 1 Energy spectra (time averaged between $t = 5$ and $t = 20$). DGM/ILES results: $p = 2$ (*solid*), $p = 3$ (*dash*) and $p = 4$ (*dash-dot*); PS method: RVMs (*thin solid*). A $k^{-5/3}$ slope is also shown (*thin dash*)

of viscosity, the kinetic energy evolves following a power law $\frac{E(t)}{E_0} = \left(\frac{t}{t_0}\right)^{-a}$. In the spectral domain, the energy spectrum should give a semi-infinite range, with a true $k^{-5/3}$ behaviour according to Kolmogorov theory. Three orders of accuracy are investigated using DGM: third ($p = 2$), fourth ($p = 3$) and fifth ($p = 4$) order. The number of degrees of freedom (*dof*) is the same for all computations and is equal to 128^3. As the DGM solver is compressible, a Mach number of 0.1 is taken to simulate the incompressible flow.

Figure 1 presents the resulting energy spectra. The results are compared with those of Cocle et al. [3] obtained with a pseudospectral (PS) method on the same grid, using the "regularized variational multiscale" model, (RVMs, as applied on the small scales). DGM results present a behaviour very similar to the RVMs model, with a significant $k^{-5/3}$ inertial subrange, followed by a moderate bump. This one is even less pronounced for DGM/ILES than PS/RVMs. As expected, this bump moves towards the high wave numbers when increasing the order of accuracy of the computation, offering a slightly larger inertial range.

4 Channel Flow at $Re_\tau = 395$, 590 and 950

The wall-resolved LES of the fully developed two-dimensional turbulent flow between two parallel walls separated by a distance 2δ is investigated. The flow is assumed to be periodic in the streamwise and the spanwise directions. Three Reynolds numbers are considered: $Re_\tau = u_\tau \delta/\nu = 395$, 590 and 950, with u_τ the friction velocity based on the shear stress $u_\tau = \sqrt{\tau_w/\rho}$. The computational domain is the same for all computations: $2\pi\delta \times 2\delta \times \pi\delta$. The computational grids are summarized on Table 1. Here again, a Mach number of 0.1 (based on the bulk velocity) is chosen

Table 1 LES of the channel flow. Reynolds numbers, number of *dof* and order of accuracy considered

Re_τ	*dof* ($nx \times ny \times nz$)	Order (p)
395	$64 \times 48 \times 48$	4 ($p = 3$)
590	$96 \times 64 \times 96$	4 ($p = 3$)
950	$192 \times 96 \times 192$	4 ($p = 3$)

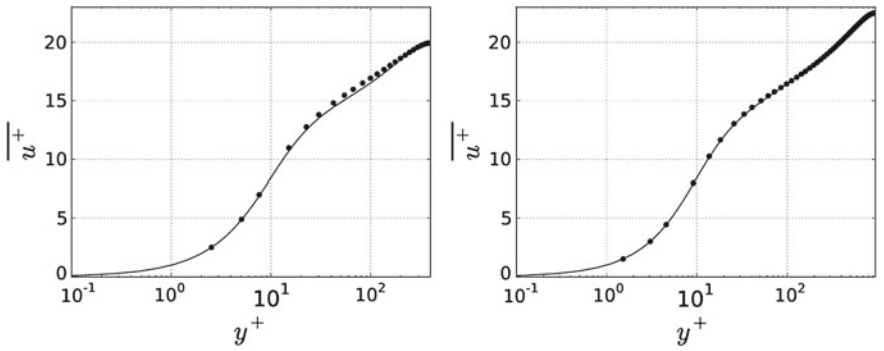

Fig. 2 LES of the channel flow at $Re_\tau = 395$ (*left*) and 950 (*right*). Mean velocity profiles. DGM/ILES (*dot*) compared to DNS (*solid line*) of Moser et al. [4] ($Re_\tau = 395$) and Hoyas et al. [5] ($Re_\tau = 950$)

to match the incompressible conditions of the reference DNS of Moser et al. [4] ($Re_\tau = 395,\ 590$) and Hoyas et al. [5] ($Re_\tau = 950$).

Figure 2 shows the averaged velocity profile obtained at $Re_\tau = 395$ and 950 with DGM/ILES. $Re_\tau = 590$ is not showed here for compacity but the behaviour at this Reynolds number is very similar to the $Re_\tau = 950$. The results are in very good agreement with the DNS references, especially for $Re_\tau = 950$. It is interesting to stress that this result is obtained on a very coarse mesh at the near wall. Indeed, for each computation, the first node is located at a wall distance $y^+ = 2.5$ when, typically, most methods need to stay below $y^+ = 1$ to obtain satisfactory results.

Figure 3 shows the three components of the turbulent intensity profile. Small oscillations can be seen. Those are due to the discontinuities in the solution and do not affect significantly the overall values. Globally, the profiles are well captured, even if some discrepancies can be found on u'^+_{RMS} at both Reynolds numbers. On the other hand, v'^+_{RMS} et w'^+_{RMS} are very well captured.

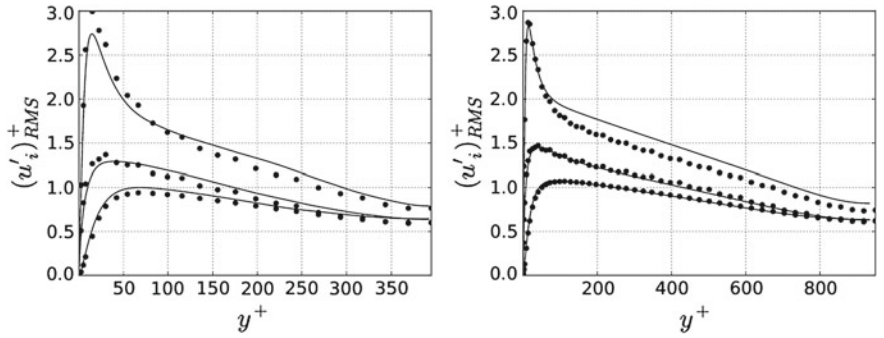

Fig. 3 LES of the channel flow at $Re_\tau = 395$ (*left*) and 950 (*right*). RMS turbulent velocities: u'^+_{RMS} (*top*), v'^+_{RMS} (*bottom*) and w'^+_{RMS} (*middle*). DGM/ILES (*dot*) compared to DNS (*solid line*) of Moser et al. ($Re_\tau = 395$) and Hoyas et al. ($Re_\tau = 950$)

5 DNS of the 2D Periodic Hill at $Re_b = 2800$

The 2D periodic hill is a generic case of a flow separating from a curved surface. As the channel flow, the computational domain is periodic in the streamwise and the spanwise directions. The flow separates at the hill crest and reattaches downstream, creating a large recirculation bubble. The Reynolds number of the flow is based on the bulk velocity at the hill crest $Re_b = u_b h/\nu$, with h the hill height and $u_b = \frac{1}{2.035h}\int_h^{3.035h} u(y)dy$. As preliminary study to the LES of the periodic hill at $Re_b = 10595$, a DNS is performed at $Re_b = 2800$.

As the previous cases, the Mach number is set to 0.1 to match incompressible conditions. The mesh is composed of $128 \times 64 \times 64$ elements (curved near the lower wall). Combined with a fourth order interpolant, this leads to $384 \times 192 \times 192$ *dof*. The results are compared to those obtained by Breuer et al. [6] on a 13M *dof* DNS using the LESOCC finite volume solver.

Figures 4 and 5 show the mean velocity profile and the x-component of the turbulent intensity profile at the hill crest ($x/h = 0$) and in the recirculation bubble

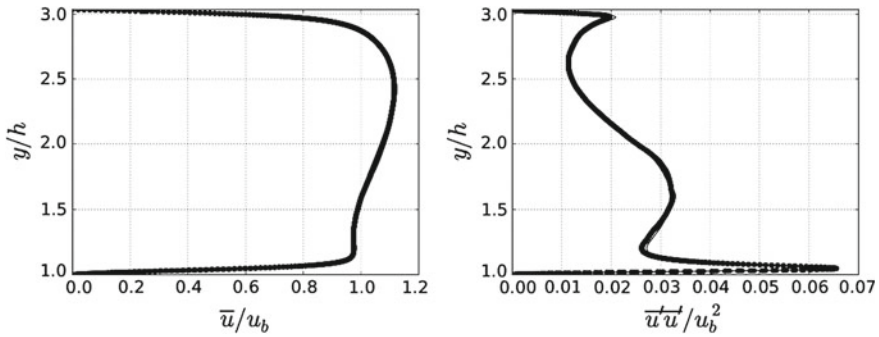

Fig. 4 DNS of the 2D periodic hill flow at $Re_b = 2800$. x-component of the turbulent velocity. DGM/DNS (*dot*) compared to DNS (*solid line*) of Breuer et al. at the hill crest ($x/h = 0$)

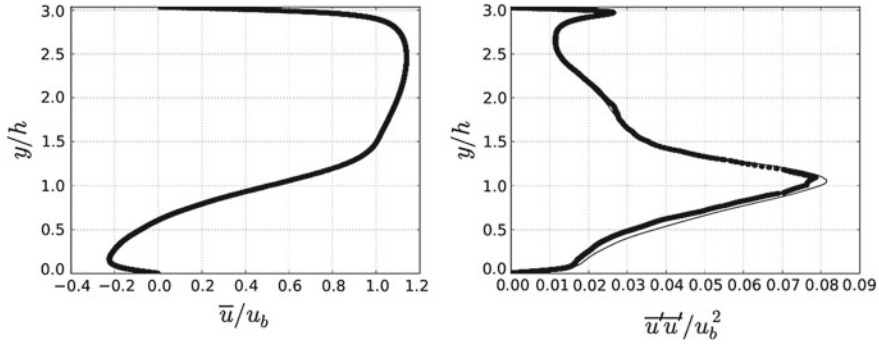

Fig. 5 DNS of the 2D periodic hill flow at $Re_b = 2800$. x-component of the turbulent velocity. DGM/DNS (*dot*) compared to DNS (*solid line*) of Breuer et al. [6] at $x/h = 2$

($x/h = 2$). The results are in excellent agreement with the reference. The curves are almost superimposed everywhere. Some discrepancies can be found on the mean velocity fluctuation and can be explained by the small number of convective times used to average the solution. Only a dozen of convective times have been computed so far.

6 Conclusion

A compressible DGM solver has been assessed for the LES of academic flows using an implicit LES strategy. This study pointed out the ability of DGM/ILES to perform accurate LES. The results on HIT at infinite Reynolds number showed the ability of the method to target the numerical dissipation only on the smallest scales, thus acting like a subgrid scale model. The behaviour of the method is very similar to a state of the art PS/RVMs method. The LES of the channel flow at $Re_\tau = 395$, 590 and 950 are also considered. The results match well those of the reference DNS, showing the ability of the method to capture wall-bounded turbulence on relatively coarse grid. Finally, a preliminary DNS has been successfully performed on the two-dimensional periodic hill flow at $Re_b = 2800$. This computation is a first validation for the LES of the case at $Re_b = 10959$ that will be performed shortly. Those results are very encouraging and studies are currently performed to validate the method on more complex cases.

References

1. Carton de Wiart, C., Hillewaert, K., Duponcheel, M., Winckelmans, G.: Assessment of a discontinuous galerkin method for the simulation of vortical flows at high Reynolds number (in preparation)
2. Carton de Wiart, C., Hillewaert, K., Geuzaine, P.: DNS of a low pressure turbine blade computed with the discontinuous Galerkin method. In: proceedings of ASME Turbo Expo 2012, Copenhagen, Danemark, June 2012
3. Cocle, R., Bricteux, L., Winckelmans, G.: Scale dependance and asymptotic very high Reynolds number spectral behaviour of multiscale subgrid models. Phys. Fluids **21**(8), 085101-1–085101-12. http://search.ebscohost.com/login.aspx?direct=true&db=a9h&AN=43975133&site=ehost-live (2009)
4. Moser, R.D., Kim, J., Mansour, N.N.: DNS of Turbulent channel flow up to $Re_\tau = 590$. Phys. Fluids **11**, 943–945 (1998)
5. Hoyas, S., Jimenez, J.: Reynolds number effects on the Reynolds-stress budgets in turbulent channels. Phys. Fluids **20**, 101511 (2008)
6. Breuer, M., Peller, N., Rapp, C., Manhart, M.: Flow over periodic hills–numerical and experimental study over a wide range of Reynolds numbers. Comput. Fluids **38**, 433–457 (2009)
7. Cockburn, B., Karniadakis, G.E., Shu, C.-W.: The development of discontinuous Galerkin methods. In: Cockburn, B., Karniadakis, G.E., Shu, C.-W. (eds.) Discontinuous Galerkin Methods. p. 350. Springer, New York (2000)
8. Hillewaert, K., Remacle, J.-F., Drosson, M.: Sharp constants in the hp-finite element trace inverse inequality for standard functional spaces on all element types in hybrid meshes. Accepted to the SIAM Journal of Numerical Analysis (2012)

Underresolved Turbulence Simulations with Stabilized High Order Discontinuous Galerkin Methods

Andrea D. Beck, Gregor J. Gassner, Thomas Bolemann, Hannes Frank, Florian Hindenlang and Claus-Dieter Munz

1 Motivation and Scope

Due to the broad range of spatial and temporal structures of turbulent flows, the resolution requirements for a fully resolved representation of all scales are prohibitively expensive and make Direct Numerical Simulations (DNS) impossible in all but a very limited number of cases. Thus, the simulation of turbulent flows becomes restricted to coarse grid solutions, combined with a suitable modeling approach for the subgrid physics. For the DNS simulations of turbulence, the superiority of high order schemes compared to their low order counterparts in terms of fidelity and efficiency is well-established. However, for coarse grid simulations which are by necessity underresolved, the term "order of convergence" of a formulation loses its meaningfulness, as its definition requires sufficient smoothness of the underlying flow field. Instead, other quality features of a discretization method have to be considered, such as e.g. dispersion and dissipation properties for a large range of scales.

In the case of the Discontinuous Galerkin (DG) method, it can be shown that its high order variants yield very favorable dispersion and dissipation behavior over a broad range of scales [17]. In addition, the DG method is particularly attractive for massively parallel simulations as it shows excellent strong scaling properties and it also allows geometry flexibility [1, 10]. Thus, the combination of these features make an interesting candidate for the simulation of underresolved turbulence. In this work, we will investigate the potential of DG methods for the simulation of turbulent flows and show applications to canonical test cases.

A.D. Beck (✉) · G.J. Gassner · T. Bolemann · H. Frank · F. Hindenlang · C.-D. Munz
Institute for Aerodynamics and Gasdynamics, University of Stuttgart, Stuttgart, Germany
e-mail: andrea.beck@uni-stuttgart.de

J. Fröhlich et al. (eds.), *Direct and Large-Eddy Simulation IX*, ERCOFTAC Series 20, DOI 10.1007/978-3-319-14448-1_14

2 Description of Numerical Method

Starting from a general system of hyperbolic conservation equations

$$U_t + \nabla \cdot \mathbf{F}(U) = 0 \tag{1}$$

with U being the vector of the conservative variables and $\mathbf{F} = (F, G, H)^T$ the flux vector, we obtain the weak form of the Discontinuous Galerkin method as

$$\frac{\partial}{\partial t} \int_Q U \, \phi d\mathbf{x} + \int_{\partial Q} (\mathbf{F} \cdot \mathbf{N})^* \phi \, dS \; - \int_Q \mathbf{F}(U) \cdot (\nabla_x \phi) \, d\mathbf{x} = 0 \tag{2}$$

where Q is an arbitrary grid cell, $\mathbf{N}$ denotes the surface normal vector, and the superscript * indicates the introduction of an approximate Riemann solver to remedy the double-valuedness at the grid cell interfaces. The solution U is approximated in each cell as

$$U(\mathbf{x}, t) = \sum_{i=0}^{P(N)} \hat{U}_i(t) \psi_i(\mathbf{x}) \tag{3}$$

with $\hat{U}_i(t)$ as the time-dependent degrees of freedom, $\psi_i(\mathbf{x})$ a suitable basis of the polynomial space with degree N and $P(N)$ the number of basis functions.

Many different choices of basis functions, element types, flux functions and integration methods exists, which all add their own flavor to the DG method (see e.g. [4, 8, 12]). In this work, we will focus on the Discontinuous Galerkin Spectral Element Method (DGSEM) proposed in [12], which employs tensor-product nodal Lagrange basis functions on Gauss points in hexahedral elements, together with the associated quadrature rules for volume and surface integrals. Full details can be found in [10]. The non-linearity of the flux function $\mathbf{F}(U)$ makes an exact evaluation of the inner products very expensive, and these integrals are thus often approximated by an inexact quadrature rule to keep the computations efficient. This numerical inaccuracy introduces an aliasing error into the solution, which can lead to positive eigenvalues in the operator spectrum and thus to an unstable computation (Fig. 1). There are a number of countermeasures to this unwanted build-up of aliased energy due to the inexact integration of the inner products, among them filtering and skew-symmetric formulations of the operator. We will focus herein on the application of the traditional spectral de-aliasing method for Fourier spectral methods by Orszag to a polynomial-based approximation: The so-called "polynomial de-aliasing" introduced by Kirby and Karniadakis [11]. It should be noted that this approach ensures an exact evaluation of the inner products and thus results in an "analytic" DG formulation, where the only remaining parameter in Eq. (2) is the choice of the numerical flux function. In this work, we use the local Lax-Friedrichs flux for the convective fluxes and the second method of Bassi and Rebay for the viscous contribution.

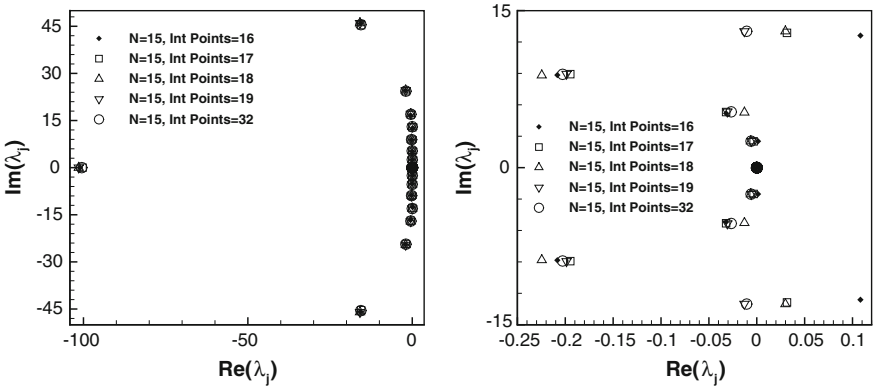

Fig. 1 *Left* DG operator spectrum with increasing quadrature precision, from [2]. *Right* Zoom

3 Results

As a first test case, we have investigated the results of very high order fully dealiased DG computations for the Taylor-Green Vortex test case [3]. To facilitate a fair comparison with results from literature, we have chosen the same total number of degrees of freedom (64^3) as previous authors. We have discretized the triple-periodic domain of this flow with only 4^3 elements, but chosen a polynomial ansatz of order 15 in each spatial direction, leading to the total of 64^3 degrees of freedom. While keeping the number of DOF fixed, three different Reynolds number were computed with this setup, ranging from 800 to 1,600 to 3,000. We have compared our results to those reported by Hickel [9], wherein he presented Finite-Volume based LES computations of this flow. It should be emphasized that our approach contains neither an explicitly added subgrid scale model for the unresolved terms, nor an adapted discretization in an implicit LES sense. Figure 2 presents the results of the underresolved computations of this turbulent flow for increasing Reynolds numbers and a comparison with an explicit LES with a dynamic Smagorinsky model and an implicit approach based on the Approximate Local Deconvolution implict LES method. The rate of kinetic energy dissipation of a DNS of this flow conducted by Brachet for the $Re = 1600$ case (from [3], using 256^3 pseudospectral DOF) and a DNS by Fauconnier for $Re = 3000$ (from [5], using 384^3 pseudospectral DOF) serve as a reference. As can be seen from Fig. 2, the results obtained with the $N = 15$ scheme are in very good agreement with the DNS results. The only deviation occurs at the maximum of the dissipation rate at $t \approx 9$ s. The slight general deterioration of the match with the DNS for increasing Reynolds number can be attributed to the increased ratio of physical to resolvable scales.

In a next step, we have extended our investigations to the flow over a circular cylinder at $Re_D = 3,900$, which has been studied extensively in literature as a benchmark for LES computations [6, 13, 15, 16]. Since most of the published results where obtained with incompressible codes, we select a Mach number for our

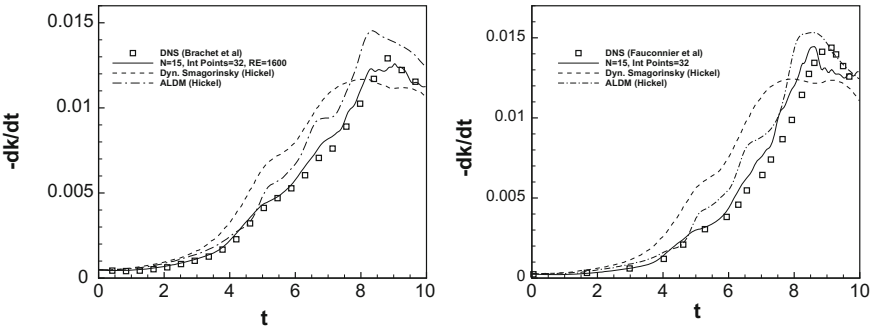

Fig. 2 Comparison of high order stabilized DG with LES computations for the Taylor-Green vortex for $Re = 1600$ (*left*) and $Re = 3000$ (*right*). More details can be found in [7]

computations of 0.1. For the spatial discretization, we choose two different setups: a coarse grid of $8 \times 6 \times 6$ grid cells and polynomial degree $N = 11$ resulting in about 500 k DOF and a medium grid of $16 \times 12 \times 12$ grid cells and polynomial degree $N = 7$ resulting in about 1.2 mio DOF. The full spatial domain is circular in the plane of the cylinder, with its center co-located with the geometry center and a radius of 40 cylinder radii. In the spanwise direction, the domain is extruded along the cylinder axis to a length of 8 radii. No-slip isothermal wall boundary conditions are applied on the geometry, periodicity is enforced in the spanwise direction and all other boundaries are set to the freestream values. Turbulent statistics are gathered over 144 shedding cycles after the initial transient phase from uniform flow conditions to the development of the steady vortex shedding.

As before for the Taylor-Green vortex test case, all computations are de-aliased with approximately $2\,N$ quadrature points to prevent a build-up of excess energy in the higher modes, i.e. the inner products are evaluated *exactly*. Figure 3 gives a

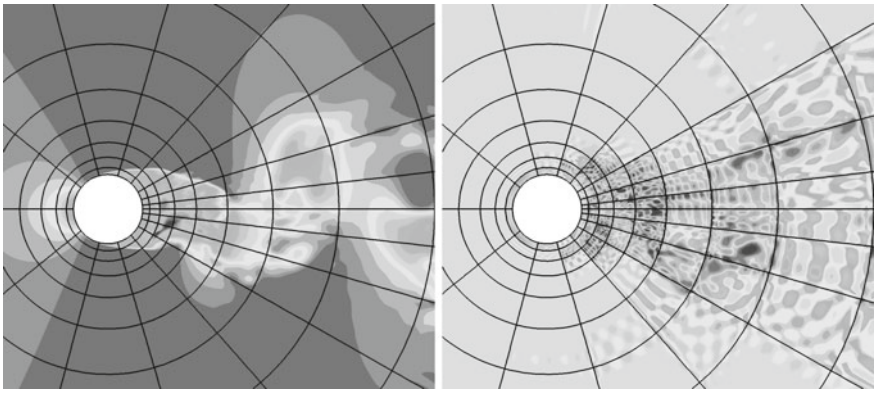

Fig. 3 Instantaneous flow around cylinder at $Re_D = 3900$, *Left* de-aliased streamwise momentum, *Right* aliasing error of streamwise momentum

Table 1 Integral quantities and simulation parameters for $Re_D = 3900$ cylinder flow

Author	$C_{p_{Base}}$	Str	C_D	L_r/D	Scheme	LES	DOF (M)
Kravchenko and Moin [13]	−0.94	0.210	1.04	1.35	B-Spline SEM	Smag	1–2
Meyer and Hickel [15]	−0.92	0.210	1.05	1.38	FV	ALDM	6.0
Fröhlich et al. [6]	−1.03	0.216	1.08	1.09	FV	Smag	1.4
Ouvrard et al. [16]	−0.85	0.218	0.99	1.54	FV/FE	Smag	1.5
Ouvrard et al. [16]	−0.81	0.226	0.93	1.68	FV/FE-VMS	Smag	1.5
Ma et al. (DNS) [14]	−0.96	0.203	0.96	1.12	h/p-FEM	–	30
Current: $\mathcal{O}(12)$	−1.00	0.212	1.09	1.26	DG	–	0.5
Current: $\mathcal{O}(8)$	−0.93	0.208	1.04	1.37	DG	–	1.2

visual impression of this instantaneous aliasing error introduced into the streamwise moment component by *inexact* integration and compares the error component with the fully de-aliased momentum. The error visualization was obtained by computing the instantaneous content of the higher polynomial modes that would be aliased onto the computational grid through inexact integration. It should be noted that the computation would become unstable immediately if the de-aliasing was turned off.

The shape and outline of the vortex street is clearly reflected in the aliasing error. This is to be expected, since it is the non-linear term in the momentum equation that causes the physical vortex cascade and through it the occurence of aliasing errors in underresolved regions. The excitation of the higher modes through aliasing is also evident in the high-frequency checkerboard pattern of the error.

Table 1 summarizes the integral quantities of interest for the cylinder flow and the simulation parameters, both for our computations and published results. A certain spread of the reported quantities exists, but our current results agree very well within this range while using no LES modelling approach and with equal or in most cases less DOF. In particular, the results obtained on the medium grid (Current: $\mathcal{O}(8)$ case) are for all integral quantities in very close agreement with the data published by Kravchenko and Moin.

4 Conclusion

In this work, we have investigated the potential of very high order Discontinuous Galerkin schemes with exact integration for the simulation of underresolved turbulence without explicitly added subgrid model (explicit LES) or adapted discretization (implicit LES). We have shown that for two canonical test cases of turbulent flows, our results are in very good agreement with DNS results and various LES approaches reported in literature, while using the same number or even less degrees of freedom. We attribute this favorable behavior to the very low approximation errors of high order DG schemes, resulting in a much wider range of well-resolved scales. Thus,

high order DG schemes are an attractive candidate as a baseline scheme for further LES studies of more complex, higher Reynolds number flows. In the future, we plan to extend our investigations by developing both explicit and implicit LES strategies for DG.

References

1. Altmann, C., Beck, A., Hindenlang, F., Staudenmaier, M., Gassner, G., Munz, C.-D.: An effcient high performance parallelization of a discontinuous Galerkin spectral element method. In: Keller, R., Kramer, D., Weiß, J.-P. (eds.) Facing the Multicore—Challenge III, pp. 37–47. Springer, Heidelberg (2013)
2. Beck, A., Gassner, G., Munz, C.-D.: High order and underresolution. In: Ansorge, R., Bijl, H., Meister, A., Sonar, T. (eds.) Recent Developments in the Numerics of Nonlinear Hyperbolic Conservation Laws. Springer, New York (2013)
3. Brachet, M.E., Meiron, D.I., Orszag, S.A., Nickel, B.G., Morf, R.H., Frisch, U.: Small-scale structure of the Taylor-Green vortex. J. Fluid Mech. **130**, 411–452 (1983)
4. Cockburn, B., Karniadakis, G. E., Shu, C.-W.: Discontinuous Galerkin Methods. In: Lecture Notes in Computational Science and Engineering. Springer, Heidelberg (2000)
5. Fauconnier, D., Dick, E., Bogey, C., Bailly, C.: Assessment of large eddy simulation based on relaxation filtering. In: Eaton, J., Friedrich, R. (eds.) Turbulence and Shear Flow Phenomena, 7th International symposium, Proceedings, 2011
6. Fröhlich, J., Rodi, W., Kessler, Ph, Parpais, S., Bertoglio, J.P., Laurence, D.: Large eddy simulation of flow around circular cylinders on structured and unstructured grids. In: Hirschel, E.H. (ed.) Numerical Flow Simulation I. Notes on Numerical Fluid Mechanics, Vieweg (1998)
7. Gassner, G.J., Beck, A.D.: On the accuracy of high-order discretizations for underresolved turbulence simulations. Theor. Comp. Fluid Dyn. (2012). doi:10.1007/s00162-011-0253-7
8. Hesthaven, J.S., Warburton, T.: Nodal Discontinuous Galerkin Methods: Algorithms, Analysis, and Applications. Springer, New York (2008)
9. Hickel, S.: Implicit turbulence modeling for large-eddy simulation, Ph.D. thesis, TU München (2007)
10. Hindenlang, F., Gassner, G., Altmann, C., Beck, A., Staudenmaier, M., Munz, C.-D.: Explicit discontinuous Galerkin methods for unsteady problems. Comput. Fluids. **61**, 86–93 (2012)
11. Kirby, R.M., Karniadakis, G.E.: De-aliasing on non-uniform grids: algorithms and application. J. Comput. Phys. **191**, 249–264 (2003)
12. Kopriva, D.A.: Implementing Spectral Methods for Partial Differential Equations. Springer, New York (2009)
13. Kravchenko, A.G., Moin, P.: Numerical studies of flow over a circular cylinder at ReD = 3900. Phys. Fluids **12**, 403 (2000)
14. Ma, X., Karamanos, G.-S., Karniadakis, E.: Dynamics and low-dimensionality of a turbulent near wake. J. Fluid Mech. **410**, 29–65 (2000)
15. Meyer, M., Hickel, S., Adams, N.A.: Assessment of implicit large-eddy simulation with a conservative immersed interface method for turbulent cylinder flow. Int. J. Heat Fluid Fl. **31**, (2010)
16. Ouvrard, H., Koobus, B., Dervieux, A., Salvetti, M.V.: Classical and variational multiscale LES of the flow around a circular cylinder on unstructured grids. Comput. Fluids. **39**, 1083–1094 (2010)
17. Stanescu, D., Kopriva, D.A., Hussaini, M.Y.: Dispersion analysis for discontinuous spectral element methods. J. Sci. Compt. **15**, 149–171 (2001)

A Characteristic-Based Volume Penalization Method for Arbitrary Mach Flows Around Solid Obstacles

Eric Brown-Dymkoski, Nurlybek Kasimov and Oleg V. Vasilyev

1 Introduction

Volume penalization is a subclass of immersed boundary methods for modeling complex geometry flows, which introduces the effects of obstacles by modifying the governing equations. The method presented in this paper encompasses general boundary conditions as an extension of the Brinkman Penalization Method (BPM) [1], which was originally developed for solid, isothermal obstacles in incompressible flows. A principal strength of Brinkman penalization is that error can be rigorously controlled a priori, with the solution converging to the exact in a predictable fashion [4, 5].

While much work has been done to refine BPM for various numerical techniques and flow regimes, boundary conditions have lacked generality, especially for compressible flows. They have been typically limited to slip and no-slip conditions for the inviscid and viscous flow around isothermal obstacles, though additional boundary conditions have been developed on a problem specific basis. In this way, BPM has been inapplicable and inflexible for many fluid problems, notably those demanding heat-flux and insulating boundary conditions on solid surfaces.

The novel Characteristic-Based Volume Penalization method (CBVP), discussed in this paper, employs hyperbolic forcing terms to impose general homogeneous and inhomogeneous Neumann and Robin boundary conditions. The method is flexible and can be applied to parabolic and hyperbolic evolutionary equations. In this paper

E. Brown-Dymkoski (✉) · N. Kasimov · O.V. Vasilyev
Department of Mechanical Engineering, University of Colorado Boulder,
427 UCB, Boulder, CO 80309, USA
e-mail: Eric.Browndymkoski@colorado.edu

N. Kasimov
e-mail: Nurlybek.Kasimov@colorado.edu

O.V. Vasilyev
e-mail: Oleg. Vasilyev@colorado.edu

J. Fröhlich et al. (eds.), *Direct and Large-Eddy Simulation IX*,
ERCOFTAC Series 20, DOI 10.1007/978-3-319-14448-1_15

it is demonstrated for viscous and inviscid flows of arbitrary Mach number. As with BPM, this method maintains rigorous control of the error through a priori chosen parameters for all boundary conditions.

2 Characteristic-Based Volume Penalization

The Characteristic-Based Volume Penalization method imposes Dirichlet, Neumann, and Robin type boundary conditions by introducing localized forcing terms into the constitutive equations. For a domain containing obstacles O_m, a masking function, $\chi(\mathbf{x}, t)$, is defined where

$$\chi(\mathbf{x}, t) = \begin{cases} 1 & \text{if } x \in O_m, \\ 0 & \text{otherwise,} \end{cases}$$

separates the domain into a physical region and a penalized region.

Dirichlet conditions are imposed in the same fashion as with the Brinkman penalization method [7, 9]. For the boundary condition $u = u_0(\mathbf{x}, t)$ on an obstacle surface $\partial O_m(\mathbf{x}, t)$, the constitutive equation is modified into the penalized equation

$$\frac{\partial u}{\partial t} = (1 - \chi) \times \text{RHS} - \frac{\chi}{\eta_b}(u - u_0(\mathbf{x}, t)) + \chi \nu_n \frac{\partial^2 u}{\partial x_i, \partial x_i}, \tag{1}$$

with summation implied over repeated indices and where RHS is simply the physical right hand side fluxes. Convergence of the penalization parameter, as $\eta_b \to 0$, controls the error on the solution by decreasing the timescale of the forcing term [1]. The Robin boundary condition, of which the Neumann condition is a special case, has the form $a(\mathbf{x}, t)u + b\partial u/\partial \mathbf{n} = g(\mathbf{x}, t)$ for inward-oriented surface normal $\mathbf{n} = n_k$. It is penalized through forcing applied to the appropriate derivatives of u. The result is a hyperbolic equation,

$$\frac{\partial u}{\partial t} = (1 - \chi) \times \text{RHS} - \frac{\chi}{\eta_c}\left(a(\mathbf{x}, t)u + bn_k \frac{\partial u}{\partial x_k} - g\right). \tag{2}$$

With the normal defined everywhere, (2) has inward-pointing characteristics that extend perpendicular to the surface into O_m. This propagates the solution at the surface inward with a spatial growth or decay, based on g and au, that enforces the desired BC. It can easily be seen that within O_m, Robin/Neumann penalized equation (2) converge to the desired boundary condition on the timescale η_c. With $\eta_c << 1$ on the normalized problem timescale, the disparity asymptotically controls the penalization error.

3 Compressible Viscous Flows

3.1 Penalized Navier-Stokes Equations

For viscous flows, the fluid is governed by the fully compressible Navier-Stokes equations. The nondimensionalized continuity, momentum and energy equations are

$$\frac{\partial \rho}{\partial t} = -\frac{\partial \rho u_j}{\partial x_j}, \tag{3}$$

$$\frac{\partial \rho u_i}{\partial t} = -\frac{\partial (\rho u_i u_j)}{\partial x_j} - \frac{\partial p}{\partial x_i} + \frac{1}{Re_a}\frac{\partial \tau_{ij}}{\partial x_j}, \tag{4}$$

$$\frac{\partial \rho e}{\partial t} = -\frac{\partial}{\partial x_j}\left[(\rho e + p)\, u_j\right] + \frac{1}{Re_a}\frac{\partial (u_i \tau_{ij})}{\partial x_j} + \frac{1}{(\gamma - 1)}\frac{1}{Re_a Pr}\frac{\partial}{\partial x_j}\left(\mu \frac{\partial T}{\partial x_j}\right). \tag{5}$$

The acoustic Reynolds number is Re_a and Pr is the Prandtl number, and the characteristic velocity is a reference speed of sound c_0.

For the viscous benchmark problems considered in this paper, no-slip and adiabatic/heat flux conditions are imposed on velocity and temperature through (1) and (2). In order to apply these penalized boundary conditions to the constitutive equations (3–5), the equations of state are used to determine consistent penalization of the integrated variables ρ, ρu, and ρe, from the native variables u, T, and an appropriate penalized equation for ρ.

For ρ to be a passive, evolutionary condition, a CBVP Neumann condition is applied within O_m, where the target is

$$\Phi = n_k \frac{\partial \rho}{\partial x_k}\bigg|_{\partial O_m}. \tag{6}$$

This closes the penalized equations for the desired conditions on u and T without over constraining the problem. The forcing terms for the compressible Navier-Stokes equations then become

$$\frac{\partial \rho}{\partial t} = (\chi - 1) \times \text{RHS} - \frac{\chi}{\eta_c}\left(n_k \frac{\partial \rho}{\partial x_k} - \Phi\right) \tag{7}$$

$$\frac{\partial \rho u_i}{\partial t} = (\chi - 1) \times \text{RHS} - \chi\left[\frac{1}{\eta_b}\rho\,(u_i - u_{0i}) + \rho \nu_n \frac{\partial^2 u_i}{\partial x_j \partial x_j} + \frac{1}{\eta_c} u_i \left(n_k \frac{\partial \rho}{\partial x_k} - \Phi\right)\right] \tag{8}$$

$$\frac{\partial \rho e}{\partial t} = (\chi - 1) \times \text{RHS} - \chi \left[\frac{1}{\eta_c} \left(n_k \frac{\partial \rho e}{\partial x_k} \right) + \frac{\rho (u_j - u_{0j}) u_j}{\eta_b} - \frac{\rho u_j}{\eta_c} n_k \frac{\partial u_j}{\partial x_k} - \rho u_j \nu_n \frac{\partial^2 u_j}{\partial x_i \partial x_i} - \frac{1}{\eta_c} e \Phi - \frac{1}{\eta_c} c_v \rho q \right], \tag{9}$$

where RHS denotes the corresponding right hand sides of Eqs. (3–5).

3.2 Benchmark: 2D Cylinder Flow

To verify the efficacy of CBVP for unsteady solutions, CBVP is applied for low Reynolds number vortex shedding around a two-dimensional cylinder. For $Ma = 0.2$ and $Re = 1000$, the flow past a cylinder remains laminar but experiences vortex shedding from the trailing edge. The domain discretization and penalization parameters remain as for the pseudo-incompressible case, namely $\Omega = [-5, 10] \times [-5, 5]$, $\eta_b = 5 \times 10^{-3}$ and $\eta_c = 10^{-2}$. Two temperature conditions are considered: an adiabatic cylinder and constant heat flux at $\partial T / \partial \mathbf{n} = 1.5$.

Periodic vortex shedding can be seen in the laminar wake behind the cylinder in Fig. 1. For laminar flows in the region of $Re \approx 1000$, the frequency is insensitive to the Reynolds number [3] and temperature driven viscosity fluctuations. The heating is therefore best seen only through the direct effect on the temperature of the fluid. Examination of the temperature profile along an arbitrary surface normal verifies that the desired heat-flux of $q = 1.5$ is properly enforced on the penalized boundary.

Time varient lift and drag coefficients C_L and C_D agree well with previous numerical results [3], though a slightly shorter shedding period can be seen. This higher frequency is reflected in a Strouhal number of $St = 0.245$, compared to $St = 0.238$ from published results [3].

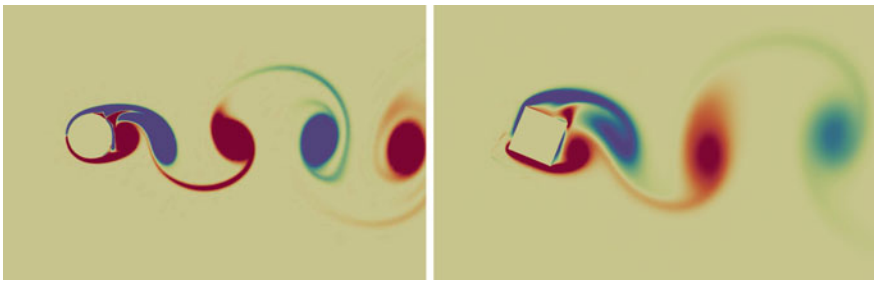

Fig. 1 The vorticity fields for flow past a *circular* ($Re = 1000$) and *square* ($Re = 150$) 2-D cylinders, demonstrating the flexibility of CBVP for arbitrary geometry

To demonstrate the applicability of the method to arbitrary geometry, flow past a square cylinder is shown in Fig. 1 for $Re = 150$. The masking function $\chi(x)$ and normal $\mathbf{n}(x)$ were assembled from piecewise smooth facets.

4 Compressible Inviscid Flows

4.1 Penalized Euler Equations

Inviscid flow is governed by the Euler equations, where the viscous terms are removed from (4) and (5). In this case, only the normal component of velocity will be penalized for a no-penetration condition and the curvature of the surface must be accounted for in the boundary conditions. For consistency, the energy and momentum equations are modified based upon the penalized native variables and the equations of state. The following terms are added to the Navier-Stokes equations (7–9) in the inviscid limit:

$$\frac{\partial \rho}{\partial t} = \cdots + \frac{\kappa}{\eta_c} \frac{\rho u_j^\tau \rho u_j^\tau}{p}, \tag{10}$$

$$\frac{\partial \rho u_j^\tau}{\partial t} = \cdots + \frac{\kappa}{\eta_c} \frac{\rho u_j^\tau \rho u_j^\tau u_i^\tau}{p}, \tag{11}$$

$$\frac{\partial \rho e}{\partial t} = \cdots + \frac{\kappa}{\eta_c} \frac{\rho u_j^\tau u_j^\tau}{\gamma - 1} + \frac{\kappa}{\eta_c} \frac{\rho u_j^\tau \rho u_j^\tau}{p} \frac{u_i^\tau u_i^\tau - u_i^n u_i^n}{2}, \tag{12}$$

where $u^n = (u \cdot n)n$, $u^\tau = u - u^n$, $\tau = u^\tau / \|u^\tau\|$, and $\kappa = \nabla_{n\tau} \cdot n$ is a curvature along the streamline based on τ. The operator $\nabla_{n\tau}$ is a projection of gradient operator to the n, τ plane, that is $\nabla_{n\tau} = n\,(n \cdot \nabla) + \tau\,(\tau \cdot \nabla)$.

4.2 Benchmark: 2D Shocks Around Obstacles

In order to evaluate efficacy of the method, several test problems were examined: supersonic flow around multiple cylinders, and supersonic flow around the wedges with sub- and supercritical apex angles. All results showed good qualitative correspondence with published experimental and numerical results [2, 8]. For the case with supersonic flow around a wedge at a subcritical angle, there is an oblique shock inclined with some angle β. The exact, steady-state oblique shock solution is well known [6]. As shown in Fig. 2, the numerical solution for a volume penalized wedge approaches the exact at steady-state. For the case with supercritical angle, a detached bow-shape shock was observed, in accordance with established results [6].

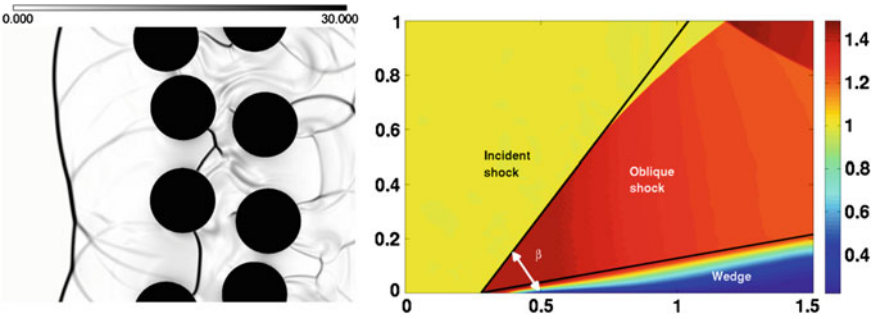

Fig. 2 Numerical Schlieren image of supersonic flow around randomly spaced multiple 2D cylinders (*left*) and density field of supersonic flow around the wedge with subcritical angle (*right*). The exact steady-state solution for the attached oblique shock wave at the wedge is drawn as the *solid black line*

5 Conclusions

A new volume penalization method has been developed and demonstrated to extend Brinkman penalization to generalized Neumann and Robin conditions. This is accomplished through hyperbolic penalization terms whose characteristics point inward along the surface-normal direction. The process of prescribing general boundary conditions is flexible and systematic, allowing for straightforward construction of penalization schemes for arbitrary Mach and Reynolds number flows.

Acknowledgments This work was supported by ONR MURI on Soil Blast Modeling and utilized the Janus supercomputer. Janus is supported by the National Science Foundation (award number CNS-0821794) and the University of Colorado Boulder. The Janus supercomputer is a joint effort of the University of Colorado Boulder, the University of Colorado Denver and the National Center for Atmospheric Research.

References

1. Angot, P., Bruneau, C.-H., Fabrie, P.: A penalization method to take into account obstacles in viscous flows. Numer. Math. **81**, 497–520 (1999)
2. Ben-Dor, G.: Shock Wave Reflection Phenomena. Springer, New York (2007)
3. Brentner, K.S., Cox, J.S., Rumsey, C.L., Younis, B.A.: Computation of sound generated by flow over a circular cylinder: an acoustic analogy approach. In: Tam, C.K.W., Hardin, J.C. (eds.) Second Computational Aeroacoustics (CAA) Workshop on Benchmark Problems, pp. 289–295. NASA (1997)
4. Feireisl, E., Neustupa, J., Stebel, S.: Convergence of a Brinkman-type penalization for compressible fluid flows. J. Diff. Equ. **250**, 596–606 (2011)
5. Kevlahan, N.K.-R., Ghidaglia, J.-M.: Computation of turbulent flow past an array of cylinders using a spectral method with Brinkman Penalization. Eur. J. Mech. B Fluids **20**, 333–350 (2001)
6. Liepmann, H.W., Roshko, A.: Elemenst of Gasdynamics. Dove Publications New York (2001)

7. Liu, Q., Vasilyev, O.V.: Brinkman Penalization method for compressible flows in complex geometries. J. Comput. Phys. **227**, 946–966 (2007)
8. Toro, E.: Riemann Solvers and Numerical Methods for Fluid Dynamics: A Practical Introduction. Springer, New York (2009)
9. Vasilyev, O.V., Kevlahan, N.K.-R.: Hybrid wavelet collocation-Brinkman Penalization method for complex geometry flows. Int. J. Numer. Meth. Fluids **40**, 531–538 (2002)
10. Wang, A.-B., Trávníček, Z., Chia, K.-C.: On the relationship of effective Reynolds number and Strouhal number for the laminar vortex shedding of a heated circular cylinder. Phys. Fluids **12**, 1401–1410 (2000)

DNS of Square-Cylinder Flow Using Hybrid Wavelet-Collocation/Volume-Penalization Method

G. De Stefano and O.V. Vasilyev

1 Introduction

The direct numerical simulation (DNS) of unsteady flow past a square-cylinder has a very high computational cost, even at moderately low Reynolds-numbers (Re), where the transition to a complex 3D wake occurs. In fact, the cylinder wake is unstable to two main spanwise disturbances that are referred to as "Mode A" and "Mode B" in the literature, similarly to what happens for circular cylinders. For the long-wavelength Mode A, the critical Re has been observed to be around 160, while the short-wavelength Mode B has been found to become unstable for Re $\approx$ 190. The spanwise wavelengths of the above two modes are about 5.2 and 1.2 times the side length of the cross section, respectively [1].

In order to numerically predict the essential features of the transitional shedding flow past the cylinder, the extent of the computational domain in the homogeneous spanwise direction, where periodic boundary conditions are applied, must be sufficiently high to capture the evolution of the 3D disturbances. Furthermore, the numerical grid must be properly refined close to the body surface, to resolve the boundary layer, as well as in the wake region. The degrees of freedom of the solution and, thus, the associated computational cost can be drastically reduced by using adaptive numerical methods, where the spatially non-uniform grid is not prescribed *a-priori* but dynamically adapted following the flow evolution.

In this study, the mesh adaptation is based on the wavelet decomposition of the velocity field, by automatically refining the grid where high gradients in the solution exist. The wavelet-based eddy-capturing approach [2] is extended to

G. De Stefano (✉)
DIII, Seconda Università di Napoli, 81031 Aversa, Italy
e-mail: giudeste@unina.it

O.V. Vasilyev
DME, University of Colorado, Boulder, CO 80309, USA
e-mail: oleg.vasilyev@colorado.edu

J. Fröhlich et al. (eds.), *Direct and Large-Eddy Simulation IX*,
ERCOFTAC Series 20, DOI 10.1007/978-3-319-14448-1_16

non-homogeneous bluff-body flow, where the presence of the obstacle is mimicked by using the Brinkman volume-penalization method [3].

2 Hybrid Method

The volume-penalization approach results in slightly modifying the governing equations with the addition of an appropriate forcing term, without altering the underlying numerical grid. Instead of solving the incompressible Navier-Stokes equations in the fluid domain Ω_f, with the associated no-slip BC on the body surface $\partial\Omega_\mathrm{s}$, the following (dimensionless) governing equations for the penalized velocity field $\tilde{u}_i$ are solved in the entire domain $\Omega = \Omega_\mathrm{f} \bigcup \Omega_\mathrm{s}$:

$$\frac{\partial \tilde{u}_i}{\partial x_i} = 0, \tag{1}$$

$$\frac{\partial \tilde{u}_i}{\partial t} + \left(\tilde{u}_j + U_j\right) \frac{\partial \tilde{u}_i}{\partial x_j} = -\frac{\partial \tilde{p}}{\partial x_i} + \frac{1}{\mathrm{Re}} \frac{\partial^2 \tilde{u}_i}{\partial x_j \partial x_j} - \frac{\chi_\mathrm{s}}{\eta} \left(\tilde{u}_i + U_i\right). \tag{2}$$

The imposed uniform velocity field U_j corresponds to the given freestream velocity. The additional term at the RHS of the penalized momentum equation (2) mimics the presence of a porous obstacle, where χ_s stands for the mask function associated with the obstacle domain Ω_s.

The positive constant η, which has the dimension of time and reflects the fictitious porousness of the obstacle, stands for the key-parameter in the volume-penalization approach. For vanishing η, the solution $\tilde{u}_i$ of the penalized equations (1) and (2) converges to the solution of the original equations with the global penalization error scaling as $\eta^{1/2}$ in Ω_f. Therefore, the no-slip BC can be enforced to any desired accuracy by appropriately reducing the penalization parameter. In addition, the Brinkman approach is particularly advantageous because the aerodynamic force acting on the obstacle can be simply evaluated as

$$F_i(t) = \frac{1}{\eta} \int\limits_{\Omega_s} (\tilde{u}_i + U_i) d\mathbf{x}, \tag{3}$$

i.e., by integrating the total velocity field over the volume occupied by the obstacle.

Generally, the continuity (1) and penalized Navier-Stokes (2) equations could be solved with any numerical technique. In this work, the efficient combination of the volume-penalization approach with the adaptive wavelet-collocation (AWC) solver is used [4]. The governing equations are evaluated at collocation points, which leads to a set of nonlinear ODEs for the collocated velocity unknowns. The method allows the numerical grid to be dynamically adapted in time, following the evolution of the dominant flow structures, which are unambiguously identified and tracked during

the simulation. Namely, the mesh adaptation is obtained through the use of nested wavelet grids, owing to the one-to-one correspondence between wavelets and grid points. The method is particularly effective in the simulation of shedding flow past bluff bodies, where the wavelet-based adaptation allows the grid to be continuously modified in time in order to follow the space-time evolution of the wake.

Formally, the perturbation velocity field, $\tilde{u}_i(\mathbf{x})$, is decomposed in terms of wavelet basis functions and approximated by retaining only significant wavelets:

$$\tilde{u}_i(\mathbf{x}) \cong \sum_{\mathbf{l}\in\mathscr{L}^0} c_{\mathbf{l}}^0 \phi_{\mathbf{l}}^0(\mathbf{x}) + \sum_{j=0}^{+\infty} \sum_{\mu=1}^{2^n-1} \sum_{\substack{\mathbf{k}\in\mathscr{K}^{\mu,j} \\ |d_{\mathbf{k}}^{\mu,j}|>\varepsilon|u_i|}} d_{\mathbf{k}}^{\mu,j} \psi_{\mathbf{k}}^{\mu,j}(\mathbf{x}). \tag{4}$$

Each level of resolution j consists of wavelets belonging to the same family, having the same scale but located at different grid positions. Collocation points are in fact omitted from the computational grid if the associated wavelets are omitted from representation (4), which occurs when the corresponding coefficients are below the given thresholding level. In a practical calculation, the level of resolution is bounded so that $j \leq j_{\max}$, where the choice of the maximum resolution, which corresponds to the finest allowable wavelet grid, is dictated by the physically required spatial resolution as well as the acceptable computational cost. Depending on the choice of the parameter ε, only a small fraction of the available wavelets is used in representing the velocity field $\tilde{u}_i$, which results in the characteristic compression property of the wavelet-based methods [5]. The thresholding level ε determines the relative energy level of the eddies that are resolved and, consequently, controls the importance of the residual field associated with the discarded wavelets. A very low but non-zero value for this parameter can be prescribed so that the effect of unresolved motions can be completely ignored and the wavelet-based DNS solution of the penalized equations (2) is carried out, like it happens for the present study.

When combining the AWC method with the volume-penalization technique, the presence of the cylinder is automatically taken into account by adapting the computational mesh on the penalized velocity field and, possibly, the mask function.

3 Square-Cylinder Flow

The hybrid method presented above is applied to the simulation of vortex shedding behind a stationary right prism with square cross-section, immersed in a uniform fluid stream. The flow around the cylinder is described in a Cartesian coordinate system (x, y, z), where the first axis corresponds to the inlet flow direction and the third one coincides with the spanwise direction. The computational domain is chosen to be $\Omega = [-6, 18] \times [-9, 9] \times [-3, 3]$, while the domain occupied by the cylinder is $\Omega_s = [-0.5, 0.5] \times [-0.5, 0.5] \times [-3, 3]$, the side length of the square-section being assumed as reference length. Zero-velocity conditions are imposed

at the inflow boundary ($x = -6$), while convective conditions are prescribed at the outflow boundary ($x = 18$). Free-slip conditions are imposed at the lateral boundaries ($y = \pm 9$), i.e. $\partial \tilde{u}_1/\partial y = \tilde{u}_2 = \partial \tilde{u}_3/\partial y = 0$, and periodicity is assumed in the homogeneous spanwise direction ($z = \pm 3$).

The DNS of square-cylinder transitional flow at Re = 200 is obtained starting from zero perturbation velocity. The incoming flow is undisturbed and the transition is naturally promoted by the numerical truncation errors. The penalization parameter is set to $\eta = 0.001$, while two different thresholding levels, namely, $\varepsilon = 0.005$ and $\varepsilon = 0.01$, and seven levels of resolution ($1 \leq j \leq 7$) are used for the AWC solver. Here, differently from similar studies, the non-uniform mesh spacing is not prescribed *a-priori*, but dynamically determined according to the flow evolution. In particular, close to the body surface, the local resolution is dictated by the high gradients of the mask function χ_s and, thus, the finest wavelet collocation grid is used. Due to the moderately low Re, the prescribed maximum resolution is adequate to resolve the kinematic boundary layer inside the fluid region.

After a transient period, during which the wake develops from initial free-stream conditions, the aerodynamic forces exhibit the classical oscillatory behavior of bluff-body flows, as illustrated in Fig. 1, where the time histories of the spanwise-averaged drag and lift coefficient are reported. In the higher accuracy case, the time-averaged drag-coefficient is $\overline{C}_D = 1.54$ and the associated RMS value is $C'_D = 0.027$ while, for the lift-coefficient, it holds $|\overline{C}_L| = 5.3 \times 10^{-3}$ and $C'_L = 0.31$. The fundamental frequency of vortex shedding corresponds to the Strouhal-number $\mathrm{St} = f_0 L/U = 0.15$. The present global results are in good agreement with solutions provided by different non-adaptive DNS solutions, e.g. [1], as well as experimental findings, e.g. [6].

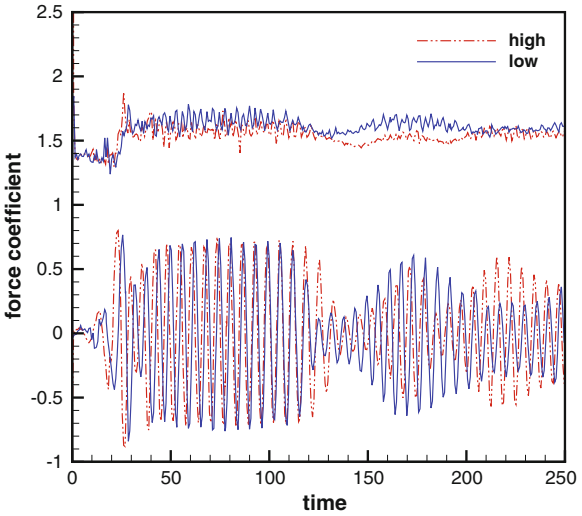

Fig. 1 Time-history of the drag (*top*) and lift (*down*) coefficient for two different wavelet thresholding levels that are $\varepsilon = 0.01$ (*lower*) and 0.005 (higher accuracy)

The flow dynamics is governed by the vortical structures that are shed from the cylinder and convected downstream, while secondary vortices are generated in the near wake. During a high-force phase, like for instance at $t \cong 175$, the wake is characterized by the presence of large spanwise vortices. Eventually, these structures are destroyed and, during a low-force phase, like for instance at $t \cong 190$, the wake shows a complex 3D shape due to symmetric two-sided dislocation. It appears that the time history of the retained wavelets number reflects the oscillations of the wake-induced forces, as demonstrated in Fig. 2.

In order to present a clear 3D view of the cylinder wake, the main vortical structures can be identified according to the *Q-criterion*, which simply defines a vortex as a connected region with a positive second invariant of the velocity-gradient tensor, e.g. [7]. The evolution of the wake is visualized on Fig. 3, by reporting three different pictures at three different time instants. The iso-surfaces of $Q = 0.1$ and 0.3 are drawn (on the left of the figure) along with the scatter plot (on the right) of the collocation points associated to the retained wavelets. Since all the wavelets belonging to the coarser levels of resolution with $j \leq 3$ are actually kept throughout the computational domain, for the sake of clarity, the scatter plot, which is colored by the variable grid level, is reported only for $4 \leq j \leq 7$.

In fact, the number and the spatial distribution of the retained wavelet collocation points follow the evolution of the wake. During a period of high force, the rather simple wake can be simulated by using a relatively low number of wavelets. On the contrary, during a period of low force, which corresponds to a very complex shape of the wake, much more grid-points are included in the computation as the wavelet collocation grid is automatically refined where smaller vortical structures are created.

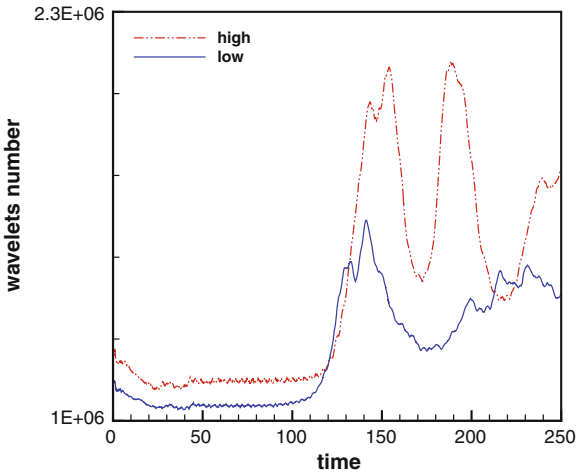

Fig. 2 Time-history of the number of retained wavelets for two different wavelet thresholding levels that are $\varepsilon = 0.01$ (*lower*) and 0.005 (higher accuracy)

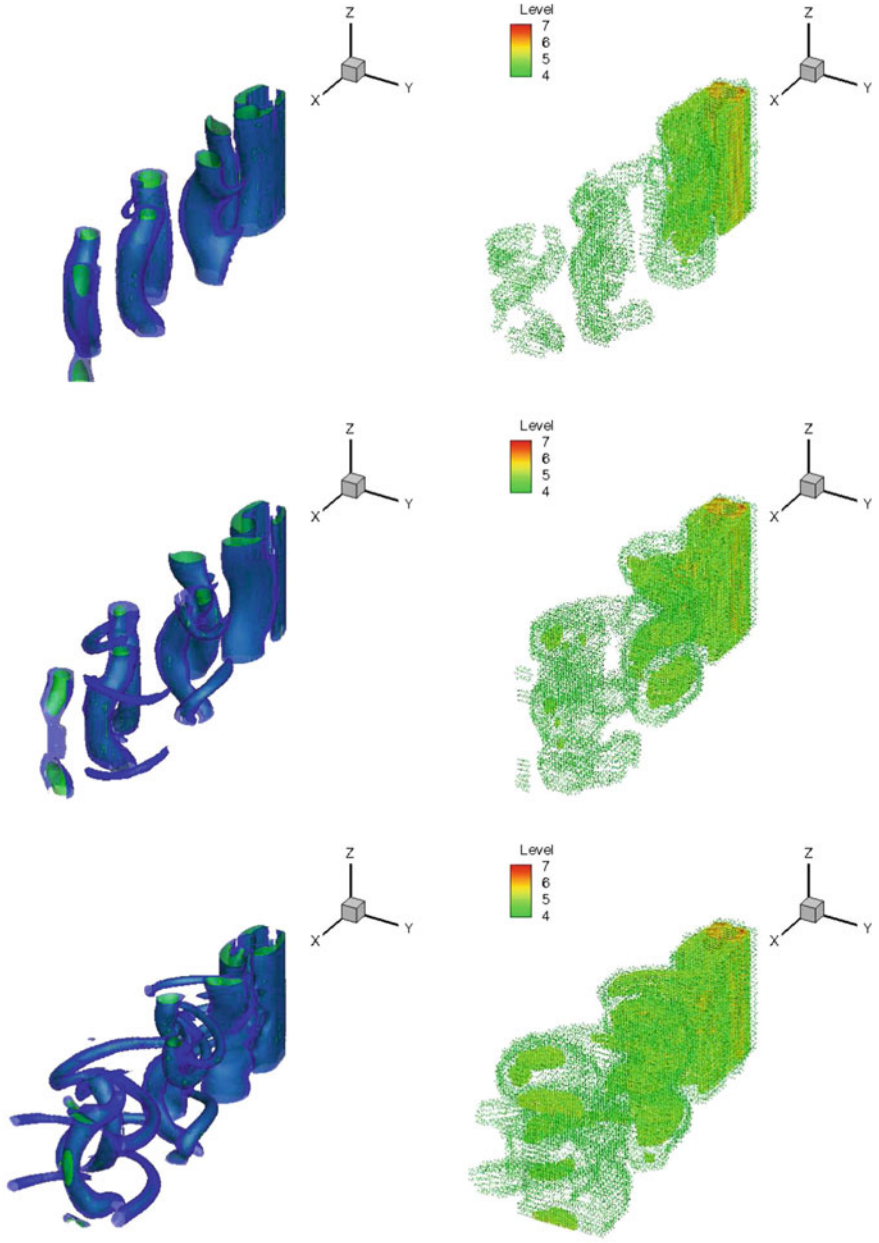

Fig. 3 Main vortical structures identified by the iso-surfaces of $Q = 0.1$ (*blue*) and 0.3 (*green*), on the*left*, and scatter plot of the wavelet collocation points at higher levels of resolution ($4 \leq j \leq 7$), on the *right*. Close-up view in the domain: $-2 < x < 17$, $-3 < y < 3$, $-3 < z < 3$, at three different time instants

4 Concluding Remarks

The application of the hybrid volume-penalization/wavelet-collocation method to the simulation of unsteady 3D incompressible square-cylinder transitional flow is presented. The method allows the adaptive DNS to be performed with a reasonable computational cost, while directly controlling the errors in the numerical approximation. Due to its flexibility and efficiency, the proposed combined method appears very promising for the simulation of more challenging flows. For instance, higher Re and/or more complex geometry bluff body flows could be considered, where the adaptive wavelet-based method are expected to become even more efficient.

Acknowledgments The support by the US NSF under grant No. CBET-1236505 is gratefully acknowledged. Authors are also thankful for the computing time on the Janus supercomputer, which is a joint effort of the University of Colorado and the National Center for Atmospheric Research.

References

1. Robichaux, J., Balachandar, S., Vanka, S.P.: Three-dimensional Floquet instability of the wake of square cylinder. Phys. Fluids **11**, 560–578 (1999)
2. De Stefano, G., Vasilyev, O.V.: A fully adaptive wavelet-based approach to homogeneous turbulence simulation. J. Fluid Mech. **695**, 149–172 (2012)
3. Angot, P., Bruneau, C.-H., Fabrie, P.: A penalization method to take into account obstacles in viscous flows. Numer. Mat. **81**, 497–520 (1999)
4. Kevlahan, N.K.-R., Vasilyev, O.V.: An adaptive wavelet collocation method for fluid-structure interaction at high Reynolds numbers. SIAM J. Sci. Comput. **26**, 1894–1915 (2005)
5. Schneider, K., Vasilyev, O.V.: Wavelet methods in computational fluid dynamics. Ann. Rev. Fluid Mech. **42**, 473–503 (2010)
6. Okajima, A.: Strouhal numbers of rectangular cylinders. J. Fluid Mech. **123**, 379–398 (1982)
7. De Stefano, G., Denaro, F.M., Riccardi, G.: High order filtering for control volume flow simulations. Int. J. Num. Methods Fluids **37**, 797–835 (2001)

Generation of Intermittent Turbulent Inflow and Initial Conditions Based on Wavelet Construction Method

L.Zhou, J.Grilliat and A.Delgado

1 Introduction

In the current context of steady computational power increase, high-resolved unsteady simulations such as Large Eddy Simulation (LES) or Direct Numerical Simulation (DNS) are no longer restricted to academic usage, and becoming tools of interest for the industry. Though, issues still remain, which prevent from getting a reliable picture of reality. Among them, initial boundary conditions techniques for DNS and LES are always the first barrier.

The current methods, the so-called stochastic methods, developed in the 1990s [4, 6] are now widely spread and intensively used for this purpose. These methods consist in generating velocity perturbations, assuming stationary stochastic distributions. They are able to successfully recover low-level statistical properties of the flow, such as energy spectra or spatial correlations, but unable to render high order statistics from turbulent flows. As the matter of fact, velocity fluctuations related to bursts of small eddies are typically non stationary processes. This phenomenon, often referred to as intermittency [3], is characterized with non zero statistical moments of third (skewness) and fourth (flatness) orders. Therefore, this accounts -at least partly- are not able achieved by current methods.

The present study shall address this problem. Based on the idea of random cascades on wavelet dyadic trees [1] and an energy cascade model, p-model, a series of velocity increments are constructed in different level of scales. Wavelet reconstruction method in multiresolution analysis (MRA) [7] is then performed on the generated velocity increments. As a results, a type of synthetic homogeneous velocities are created. The statistical properties are studied and compared with DNS results. It must be pointed out that although the current discussions are based on two-dimension, the method can be easily extended to three-dimension case.

L. Zhou (✉) · J. Grilliat · A. Delgado
Lehrstuhl Für Strömungsmechanik (LSTM), FAU, Erlangen-Nuremberg, Germany
e-mail: Long.Zhou@lstm.uni-erlangen.de

J. Fröhlich et al. (eds.), *Direct and Large-Eddy Simulation IX*,
ERCOFTAC Series 20, DOI 10.1007/978-3-319-14448-1_17

2 Description of the Numerical Method

The turbulence energy cascade is modeled with help of p-model [9, 10], which is a simplified case of Mandelbrot's multifractal theory. The basic idea is that the cascade can be cast into a successive breakdown of turbulent eddies. Each eddy with an energy p breaks into two eddies of same size, but different energy p_1 and p_2 such that $1 = p_1 + p_2$. Here p represents the percentage of total energy. The relative energy distribution p_1 and p_2 is evaluated by experimental results. Typically, p_1 and p_2 are set to 0.7 and 0.3 respectively. The p-model is able to successfully recover the multifractal properties of one-dimensional energy-cascading in the inertial range.

Juneja et al. [5] used a multiplicative method to construct one-dimensional intermittency signal. The statistical properties are close to turbulence. However, the method bears its limitation to one-dimension. The higher dimensional extension do not reproduce non-Gaussianity. Moreover, correlation and coherency will also be lost due to the superposition of signals in high dimensional extension.

The present method starts from this point. Mathematically, the method take advantage of the $\mathscr{W}$-cascade framework [1], which is a superclass of $\mathscr{M}$-cascade [8]. The $\mathscr{W}$-cascade is built using a wavelet orthogonal basis. The scaling function $\phi(x)$, and the wavelet function $\psi(x)$ are defined in $L^2([0, 1])$ space:

$$\phi_{j,k} = 2^{j/2}\phi(2^j x - k), \;\; \psi_{j,k} = 2^{j/2}\psi(2^j x - k). \tag{1}$$

Since $\phi(x)$ and $\psi(x)$ are orthonormal basis, the L^2 space can be constructed by two-dimensional MRA,

$$f(x, y) = c_{0,0,0}\phi_{0,0,0}(x, y) + \sum_{j=0}^{J-1}\sum_{i_x=0}^{2^j-1}\sum_{i_y=0}^{2^j-1}\sum_{\mu=1}^{3} c^{\mu}_{j,i_x,i_y}\psi_{j,i_x,i_y}(x, y). \tag{2}$$

The scaling coefficient c_0 and the wavelet detail coefficients c_j play an important role in capturing turbulent intermittency. The index j represents the level of scales, while i_x, i_y are spatial indexes in a specific level. The notation μ is a index of the three detail subbands. The construction method is shown in Fig. 1.

A recursive step to calculate the coefficients in HL ($\mu = 1$) suband can be defined as follows:

$$\begin{aligned}
c^1_{1,0,0} &= \tilde{E}_1, \\
c^1_{J+1,2i,2j} &= \tilde{E}_{J+1}G^l c_{J,i,j}, \\
c^1_{J+1,2i+1,2j} &= \tilde{E}_{J+1}G^r c_{J,i,j}, \\
c^1_{J+1,2i,2j+1} &= \tilde{E}_{J+1}\hat{G}^l c_{J,i,j}, \\
c^1_{J+1,2i,2j+1} &= \tilde{E}_{J+1}\hat{G}^r c_{J,i,j}.
\end{aligned} \tag{3}$$

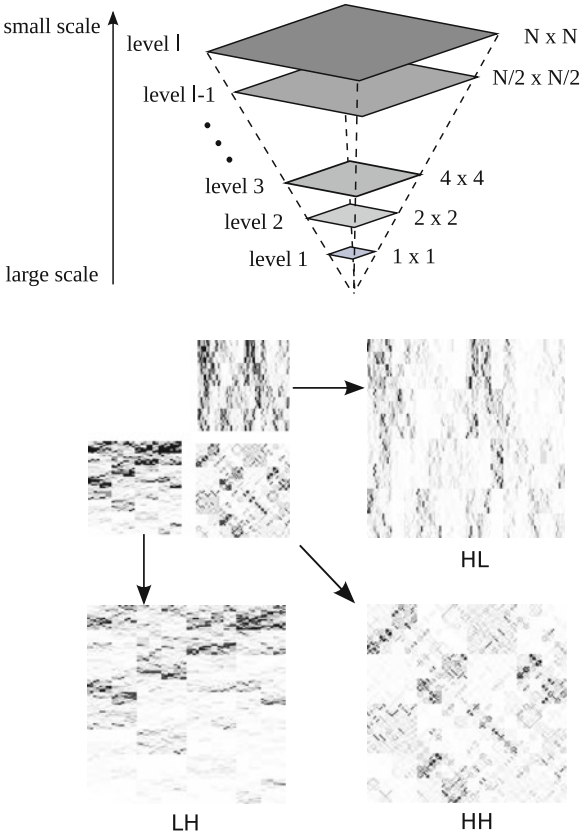

Fig. 1 In MRA, a two-dimensional data is divided into four subbands. Scaling coefficients which contain most informations from original data are stored in *LL* subband. Here *L* represents low frequency. The other three subbands *LH*, *HL* and *HH* containing detail informations correspond to the finer scale wavelet coefficients. The method starts to construct them from the coarsest level to the finest level. The coherent structures (*darker textures shown in bottom part*) are well preserved between different scales (levels)

Different as one-dimensional p-model, the two-dimensional wavelet p-model defined here, breaks energy into four pieces which represented as variables $G^l c$, $G^r c$, $\hat{G}^l c$ and $\hat{G}^r c$ in above equations. In order to consist with one-dimensional case, the summation of each two variables should be equal to 0.7 or 0.3 depending on which subbands they are located. For instance, in HL subband the four variables can be defined as $G^l c + \hat{G}^l c = 0.7$, $G^r c + \hat{G}^r c = 0.3$ while in LH subband, they are read as $G^l c + G^r c = 0.7$, $\hat{G}^l c + \hat{G}^r c = 0.3$.

The wavelet energy spectrum $\tilde{E}_J$ is explicitly given as a constrain in the corresponding level. Here wavelet energy spectrum $\tilde{E}$ is calculated from Fourier energy spectrum $E(k')$:

$$\tilde{E}(k) = \frac{1}{C_\psi k_\psi} \int_0^\infty E(k') \left| \hat{\psi}\left(\frac{k_\psi k'}{k} \right) \right|^2 \mathrm{d}k' \tag{4}$$

where k_ψ is the centroid wave-number of the analysing wavelet ψ and C_ψ is defined by the admissibility conditions given in [12].

In second step, the scheme outlined above is used to generate two independent scalar fields u' and v' which together define the vector field $\mathbf{u}$. A divergence-free velocity field ($\mathbf{u}^s$) can be obtained as follows:

$$\begin{aligned} \mathbf{u}^s &= \mathbf{u} - \nabla\psi, \\ \nabla \cdot \nabla\psi &= \nabla \cdot \mathbf{u}. \end{aligned} \tag{5}$$

The irrotational velocity potential ψ is computed by above Poisson equation which can be efficiently solved by multi-grid method.

3 Results and Discussions

The Daubechies wavelet are chosen here for reconstruction purpose. Velocities constructed by Daubechies wavelet with low moments (D2 or D4) are compared with velocities constructed by higher moments (D8 and D16). No surprise, higher moment filters which take advantage of less cut off loss, predict the velocities close to real turbulence. For this reason, The D8 are chosen for the rest of this section.

3.1 Some Statistical Properties

As similar with real turbulence, the flatness factor, an index of turbulent intermittency, grows slowly with construction levels. The PDF of vorticity in Fig. 2 shows a strong deviation from Gaussian with increasing of construction levels. Following with suggestion of Kolmogorov, the relation between construction levels and the Reynolds number can be predicted by

$$R_\lambda^{-3/2} = \eta/L \simeq \left(\frac{1}{2}\right)^n. \tag{6}$$

n represents current level. With five levels construction, the Reynolds number is $R_\lambda \simeq 10$. It must be pointed out that the construction level can be inconsistent with wavelet reconstruction level. For example, the coefficients can be constructed by level 1–5 whereas wavelet reconstruction can be performed on seven levels with the top two levels empty or nearly empty. This is specially useful when synthesizing fully developed turbulence, where the empty levels correspond to a dissipation region.

By using the framework of W-cascade and an explicit energy constrain, the energy spectrum shows a desired $-5/3$ slop in inertial range (see Fig. 3), typical for isotropic turbulence. Moreover, synthetic field which has banded shape of energy spectrum, absent from low frequencies for instance, could be interesting for LES simulation,

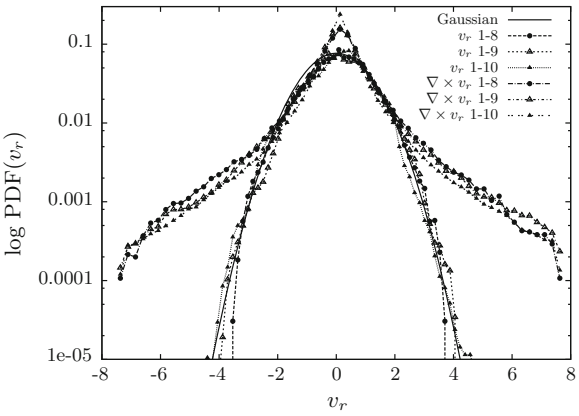

Fig. 2 PDF of velocity and vorticity in different construction levels. The PDFs of velocity remain basically Gaussian when construction level increasing, whereas the PDFs of vorticity depart from Gaussian strongly

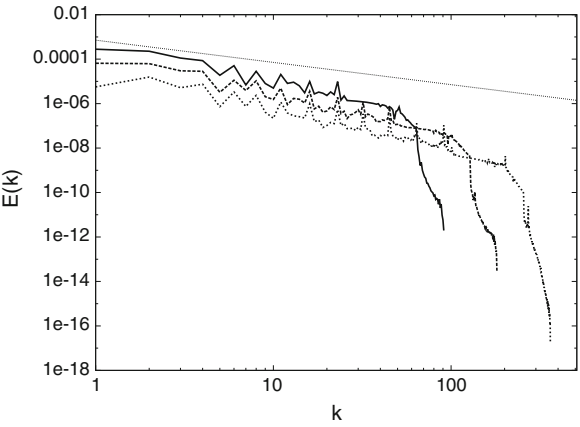

Fig. 3 Energy spectrum with 1–5, 1–6 and 1–7 construction levels correspond to seven, eight and nine levels of reconstruction. All levels of spectrum keep a $-5/3$ slop in inertial range

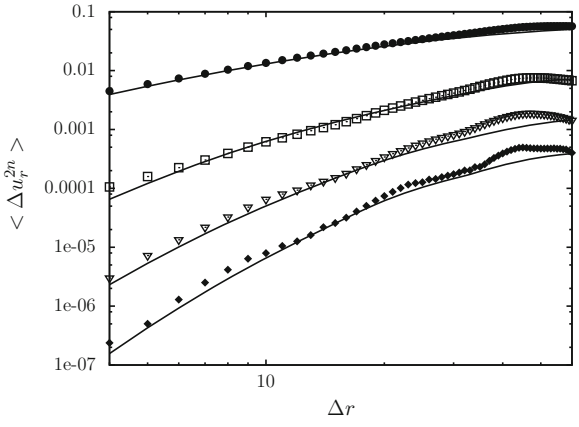

Fig. 4 From *top* to *bottom*, comparison between the second order to eighth order structure functions from synthetic turbulence with construction level 1–5 and seven levels of reconstruction (*dotted lines*) to DNS with $Re = 103$ (*solid lines*)

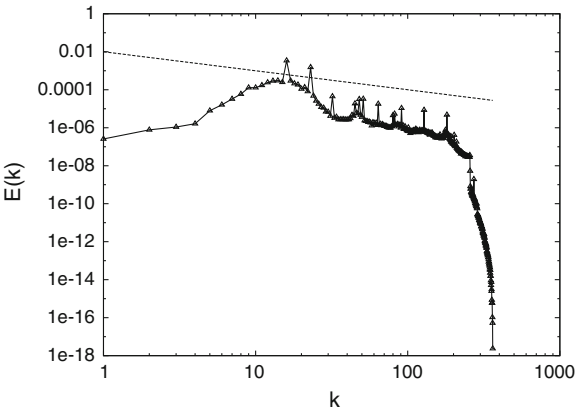

Fig. 5 Energy spectrum contains only high frequency constructed by level 5–8 with nine level reconstruction

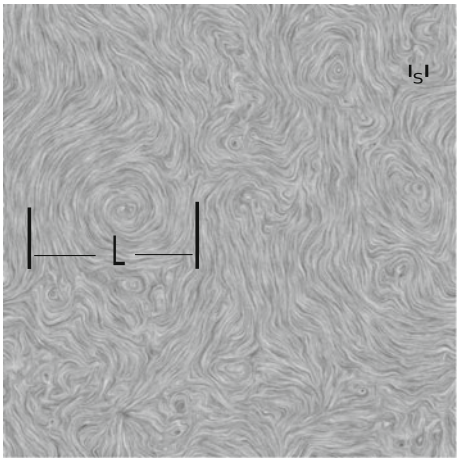

Fig. 6 Velocity field from DNS $Re = 103$

where the synthetic field can be served as sub-grid models. Those type of velocity fields can be constructed by simply jumping over the corresponding levels. Figure 5 shows an energy spectrum containing only high frequencies constructed by level 5–7 with nine levels reconstruction. Due to the constrain $\tilde{E}_J$, the spectrum still maintain a $-5/3$ slop though the low frequency information is absent. Furthermore, as the reconstruction proceeds in different level of scales in advantage of the multi-fractal structure of wavelet, a much better agreement is obtained between high order statistical moment from synthesized to measured velocity fluctuations. Figure 4 shows a series of even moment structure functions comparing with a DNS test case. The slops from synthetic turbulence which present exponent of structure functions agree well with corresponding DNS results. In the last two figures, the streamlines of DNS and synthetic velocity are plotted using linear integral convolution method (LIC). Figure 7 which depicts the integral scale L and a multiple of Kolmogorov scale η according to the construction levels resemble the ones in real turbulence (Fig. 6).

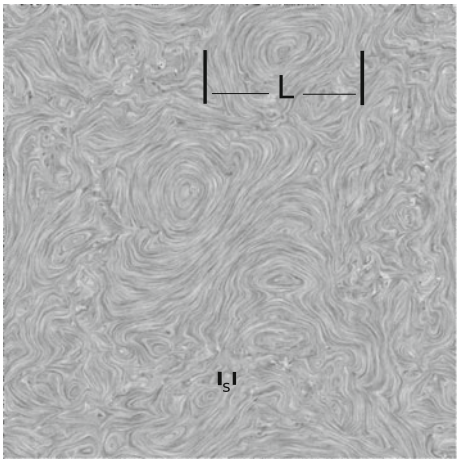

Fig. 7 Synthetic field with construction level 1–5 and seven levels of reconstruction

3.2 Conclusion

The features of wavelet based synthetic turbulence method have been presented. It can well predict the turbulence statistics based on scales as well as Reynolds numbers. Moreover, coherent structures are greatly preserved based on the modified wavelet 2-D p-model. Current ongoing work has as objective the extension of the method to three-dimension and inhomogeneous anisotropic turbulence.

References

1. Arneodo, A., Muzy, J.F., Roux., S.G.: Experimental analysis of self-similarity and random cascade processes: application to fully developed turbulence data. J. Phys. **2**, **7**(2), 363–370 (1997)
2. Arneodo, A., Bacry, E., Muzy, J.F.: Random cascades on wavelet dyadic trees. J. Math. Phys. **39**, 4142 (1998)
3. Farge, M.: Wavelet transforms and their applications to turbulence. Annu. Rev. Fluid Mech. **24**(1), 395–458 (1992)
4. Fung, J.C.H., Hunt, J.C.R., Malik, N.A., Perkins, R.J.: Kinematic simulation of homogeneous turbulence by unsteady random fourier modes. J. Fluid Mech. **236**(1), 281–318 (1992)
5. Juneja, A., Lathrop, D.P., Sreenivasan, K.R., Stolovitzky, G.: Synthetic turbulence. Phys. Rev. E **49**(6), 5179 (1994)
6. Lee, S., Lele, S.K., Moin, P.: Simulation of spatially evolving turbulence and the applicability of taylors hypothesis in compressible flow. Phys. Fluids A: Fluid Dyn. **4**, 1521 (1992)
7. Mallat. S.G.: A theory for multiresolution signal decomposition: the wavelet representation. Pattern Anal. Mach. Intell. IEEE Trans. **11**(7), 674–693 (1989)
8. Mandelbrot, B.B.: Intermittent turbulence in self-similar cascades- divergence of high moments and dimension of the carrier. J. Fluid Mech. **62**(2), 331–358 (1974)
9. Meneveau, C., Sreenivasan, K.R.: The multifractal spectrum of the dissipation field in turbulent flows. Nucl. Phys. B-Proc. Suppl. **2**, 49–76 (1987)

10. Meneveau, C., Sreenivasan, K.R.: Simple multifractal cascade model for fully developed turbulence. Phys. Rev. lett. **59**(13), 1424–1427 (1987)
11. Rogallo, R.S.: Numerical experiments in homogeneous turbulence. Natl. Aeronaut. Space Adm. **81315**, 94 (1981)
12. Schneider, K., Farge, M., Kevlahan, N.: Spatial intermittency in two-dimensional turbulence: a wavelet approach. Woods Hole Math. Perspect. Math. Phys. **34**, 302–328 (2004)
13. Yoshimatsu, K., Okamoto, N., Schneider, K., Kaneda, Y., Farge, M.: Intermittency and scale-dependent statistics in fully developed turbulence. Phys. Rev. E **79**(2), 026303 (2009)

A New High-Order Method for the Accurate Simulation of Incompressible Wall-Bounded Flows

Peter Lenaers, Phillip Schlatter, Geert Brethouwer and Arne V. Johansson

Abstract A new high-order method for the accurate simulation of incompressible wall-bounded flows is presented. In stream- and spanwise direction the discretisation is performed by standard Fourier series, while in wall-normal direction the method combines high-order collocated compact finite differences with the influence matrix method to calculate the pressure boundary conditions that render the velocity field divergence-free. The main advantage over Chebyshev collocation is that in wall-normal direction, the grid can be chosen freely and thus excessive clustering near the wall is avoided. Both explicit and implicit discretisations of the viscous terms are described, with the implicit method being more complex, but also having a wider range of applications. The method is validated by simulating fully turbulent channel flow at friction Reynolds number $Re_\tau = 395$, and comparing our data with existing numerical results. The results show excellent agreement proving that the method simulates all physical processes correctly.

1 Introduction

The last few decades, Direct Numerical Simulations (DNS) have proven very useful to investigate the features and properties of incompressible wall-bounded turbulent flows. A major issue when solving the governing three-dimensional incompressible

P. Lenaers (✉) · P. Schlatter · G. Brethouwer · A.V. Johansson
Linné FLOW Centre, KTH Mechanics, Osquars Backe 18, 100 44 Stockholm, Sweden
e-mail: Lenaers@mech.kth.se

P. Schlatter
e-mail: PSchlatt@mech.kth.se

G. Brethouwer
e-mail: Geert@mech.kth.se

A.V. Johansson
e-mail: Johansson@mech.kth.se

J. Fröhlich et al. (eds.), *Direct and Large-Eddy Simulation IX*,
ERCOFTAC Series 20, DOI 10.1007/978-3-319-14448-1_18

Navier–Stokes equations is the lack of an evolution equation for the pressure. Instead, the pressure is present in the momentum equations and instantaneously corrects the velocities such that the continuity equation is satisfied. Different methodologies have been developed to deal with this issue, one of them being the influence matrix method [1]. In this method, a Poisson equation for the pressure is derived that replaces the continuity equation in the interior of the flow domain. For problems with non-periodic boundaries in one dimension, this results in a sequence of one-dimensional scalar Helmholtz equations, which are solved to calculate the pressure boundary conditions that after applying a correction step, render the entire velocity field divergence-free. The advantage of this method is that continuity is fulfilled exactly in the discretised equations and that it can also be applied on a collocated grid, thus avoiding interpolation that can cause unwanted filtering effects. All of the previous implementations of the influence matrix method [5] use Chebyshev polynomials in wall-normal direction. Although the use of Chebyshev collocation is widespread in the simulation of wall-bounded flows, it also has its disadvantages. The prescribed grid when using Chebyshev collocation is the Gauss–Lobatto–Chebyshev grid which becomes extremely clustered near the wall at high resolution causing numerical errors. Because of the numerical issues caused by extreme clustering of gridpoints, there exists a desire to have more freedom in the location of the grid points in wall-normal direction. An alternative to Chebyshev collocations are compact finite difference schemes [2] which show good resolution characteristics over a large range of wavenumbers, while maintaining the freedom to choose the grid points and boundary conditions. We extend the influence matrix method to allow the use of compact finite differences, which gives the user the freedom to choose the location of the grid points and thus providing more flexibility.

The viscous terms can be treated both explicitly and implicitly. The equations are simpler when they are treated explicitly, but this does impose more severe restrictions on the maximum allowable time step in certain flow cases.

2 Problem Formulation

To illustrate our method we consider the case with one homogeneous and one inhomogeneous direction such as plane Poiseuille flow. It illustrates all of the features of the method while keeping the equations relatively simple. The theory is easily extended to three dimensions, or adapted when other boundary conditions are chosen.

In the periodic x-direction the velocity components and pressure are expanded in Fourier series while compact finite differences are used in y-direction. The compact finite difference scheme for the first derivative in wall-normal direction can be written in matrix form as:

$$A_1\mathbf{f}' = B_1\mathbf{f} \tag{1}$$

with $\mathbf{f} = [f_1, \ldots, f_{N_y}]$ where N_y is the number of points in y-direction, and A_1 and B_1 the coefficient matrices. It follows that:

$$\mathbf{f}' = A_1^{-1} B_1 \mathbf{f} := D_1 \mathbf{f}. \tag{2}$$

A analogous formulation holds for the second derivative matrix D_2.

The non-linear terms are discretised using a third-order Runga–Kutta method, while the viscous terms are split into an implicit and an explicit part using the theta-method. The discretised momentum equations are then:

$$L_{mom} u^{q+1} + ik_x \beta_q \Delta t p^{q+1} = r_x^q, \quad u^{q+1}(\pm 1) = 0 \tag{3}$$

$$L_{mom} v^{q+1} + \beta_q \Delta t D_1 p^{q+1} = r_y^q, \quad v^{q+1}(\pm 1) = 0 \tag{4}$$

with

$$L_{mom} := \left(1 + \beta_q \Delta t \frac{1}{\mathrm{Re}} \theta k_x^2\right) I - \beta_q \Delta t \frac{1}{\mathrm{Re}} \theta D_2, \tag{5}$$

$$\mathbf{r}^q = \left[1 + \beta_q \Delta t \frac{1}{\mathrm{Re}} (1-\theta) \left(D_2 - k_x^2 I\right)\right] \mathbf{u}^q - \gamma_q \Delta t \mathbf{N}^q - \zeta_q \Delta t \mathbf{N}^{q-1} \tag{6}$$

and $\mathbf{N}$ the non-linear term, the superscripts q the Runge–Kutta substeps, β_q, γ_q, and ζ_q the coefficients used in the Runge–Kutta method [6], k_x the wavenumber in streamwise direction, and θ the parameter used in the theta-method with $\theta = 0$ equal to the fully explicit method, and $\theta = 0.5$ corresponding to the Crank-Nicolson method. Taking the divergence of the momentum equations will give a Poisson equation for the pressure:

$$\beta_q \Delta t \left(D_1^2 - k_x^2 I\right) p^{q+1} = R^q + \beta_q \Delta t \frac{1}{\mathrm{Re}} \theta \left(D_1 D_2 - D_2 D_1\right) v^{q+1},$$
$$D_1 v^{q+1}(\pm 1) = 0 \tag{7}$$

with $R^q = ik_x r_x^q + D_1 r_y^q$. The term $\beta_q \Delta t \frac{1}{\mathrm{Re}} \theta \left(D_1 D_2 - D_2 D_1\right) v^{q+1}$ in the right-hand side of the Poisson equation stems from the fact that the matrices D_1 and D_2 do not commute and is not present when Chebyshev polynomials are used in wall-normal direction [1]. Usually, the system is solved by first calculating the new pressure p^{q+1} after which the velocities u^{q+1} and v^{q+1} are calculated. However, since v^{q+1} is unknown when solving for p^{q+1} an iterative scheme is required in this method to calculate the solutions. Note that in the fully explicit method $\theta = 0$, such that this term disappears and no iterations are required. A second problem when solving the Poisson equation is that the prescribed boundary conditions are a function of v^{q+1} and not of p^{q+1}. This problem is solved by applying the influence matrix method. The solution for p^{q+1} is written as a linear superposition as follows:

$$p^{q+1} = p_p + \delta_1 p_1 + \delta_2 p_2 \tag{8}$$

with p_p the solution of the Poisson Eq. (7) but with boundary conditions

$$p_p(\pm 1) = 0, \tag{9}$$

and p_1 and p_2 the solutions of the homogenous Poisson equation with boundary conditions

$$p_1(-1) = 1, \quad p_1(+1) = 0 \tag{10}$$
$$p_2(-1) = 0, \quad p_2(+1) = 1 \tag{11}$$

The parameters δ_1 and δ_2 follow from the boundary conditions $D_1 v^{q+1}(\pm 1) = 0$ and are thus solutions of:

$$\begin{pmatrix} D_1 v_1(-1) & D_1 v_2(-1) \\ D_1 v_1(+1) & D_1 v_2(+1) \end{pmatrix} \begin{pmatrix} \delta_1 \\ \delta_2 \end{pmatrix} = - \begin{pmatrix} D_1 v_p(-1) \\ D_1 v_p(+1) \end{pmatrix} \tag{12}$$

with v_p, v_1, and v_2 the solutions for the wall-normal velocity corresponding to p_p, p_1, and p_2 respectively. Note that all three solutions p_p, p_1, and p_2 contain a discretisation error that needs to be corrected for. This can be done by applying a superposition for each as described in detail by Kleiser and Schumann [1].

3 Results

To validate our method, we ran a simulation of a three-dimensional fully turbulent channel at friction Reynolds number $Re_\tau = 395$ where the third direction (the spanwise direction) is denoted by z. It is periodic and discretised using Fourier collocation just like the x-direction. To ensure that the grid spacing in the y-direction is clustered near both walls, we use a hyperbolic tangent spacing [4]:

$$y_i = \frac{\tanh\left(\alpha_s \left(\xi_i - 0.5\right)\right)}{\tanh(0.5\, \alpha_s)}, \quad \text{with} \tag{13}$$
$$\xi_i = \frac{i-1}{N_y - 1}, \quad \text{for } i = 1, \ldots, N_y. \tag{14}$$

For $\alpha_s \to 0$, the spacing becomes equidistant, while it becomes more stretched and thus more dense near the wall for higher values of α_s. Our simulation has been performed with $\alpha_s = 4$. The corresponding grid is sufficiently dense near the wall to resolve the viscous sublayer while avoiding excessive clustering which would severely lower the maximum allowable time step, in particular for the explicit method.

The bulk Reynolds number $Re := u_b h/\nu = 6{,}867$ with u_b the bulk velocity corresponds to a nominal friction Reynolds number of $Re_\tau := u_\tau h/\nu = 395$ with u_τ the friction velocity. We used the same parameters as Moser et al. [3], which means

the boxsize is $2\pi h \times 2h \times \pi h$, and the resolution $256 \times 193 \times 192$. This corresponds to a spacing of $\Delta x^+ = 9.6$, $\Delta z^+ = 6.4$, $\Delta y_w^+ = 0.6$, and $\Delta y_c^+ = 8.5$, with Δy_w^+ the spacing in y-direction near the wall, which is the minimum, and Δy_c^+ the spacing at the centre line, which is the maximum. The superscript $^+$ indicates wall units with $\Delta x^+ = u_\tau \Delta x/\nu$. The pressure gradient driving the flow is adjusted dynamically such that the mass flux is constant throughout. Statistics from the simulation were taken from $t = 500$ until $t = 1{,}500$, which corresponds to 38 eddy turnover periods $u_\tau T/h$, sufficient to ensure converged statistics. The actual calculated friction Reynolds number was $Re_\tau = 391.4$. Figure 1 compares the mean velocity and root mean square (rms) velocities as a function of the wall-normal distance y^+ of the new code with results by Moser et al. [3]. The results are virtually identical indicating that the new code performs well when simulating fully developed turbulent channel flow.

Figure 2 shows the bottom half of the flow field at $t = 750$. The structures are contours of negative $\lambda_2^+ = -0.003$ indicating vortical motion. They are coloured

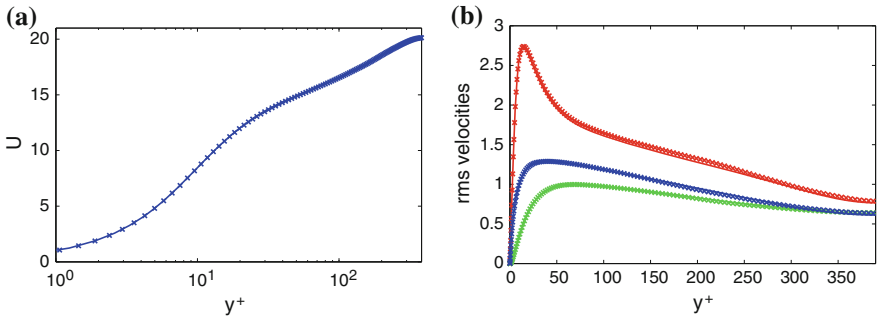

Fig. 1 The mean (**a**) and rms velocities (**b**) of the new code (*full lines*) and the code by Moser et al. [3] (× *symbols*). The *red line* and *symbols* in Fig. (**b**) represent u_{rms}, *green* v_{rms}, and *blue* w_{rms}

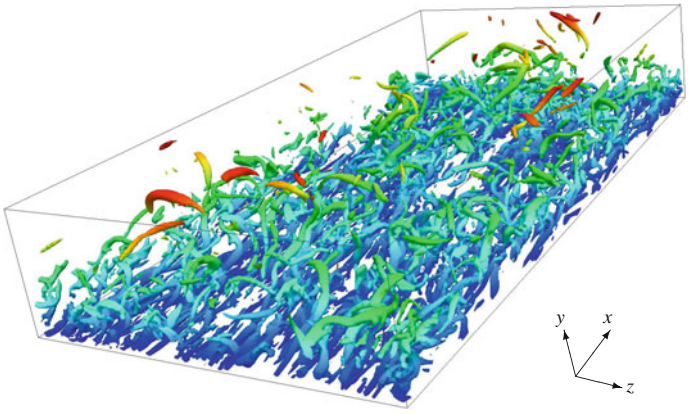

Fig. 2 A visualisation of the flow field at $t = 750$. Half of the flow field in y-direction is shown and the same colouring is used. The structures are isocontours of $\lambda_2^+ = -0.003$. Note that the mean flow is in positive x-direction

according to distance to the wall, from blue representing close to the wall through green and red for increasing wall-normal distance. The bulk of the vortices are clearly clustered near the wall, which is typical for turbulent wall-bounded flows.

4 Conclusions

In this paper we present a new high-order method to perform direct numerical simulations of wall-bounded flows. The novel feature is that it combines collocated compact finite differences in the wall-normal direction with the influence matrix method to calculate the boundary conditions that render the entire velocity field divergence-free. In stream- and spanwise direction, Fourier collocation is used, while any time discretisation can be used, but we illustrate the method by applying a third-order Runge–Kutta method. The fact that the grid is collocated means that it avoids interpolation, which is necessary on staggered grids and can cause unwanted filtering effects. A further advantage over other high-order methods such as Chebyshev collocation is that the grid is not predetermined and can thus be defined such that dense clustering of gridpoints near the wall is avoided. This becomes especially important when simulating high Reynolds number flows, which require a high wall-normal resolution. Note that the method is described with Dirichlet boundary conditions at the wall, but that this can easily be extended to Neumann or Robin boundary conditions by making minor alterations.

The method is validated by simulating fully developed turbulent channel flow. It shows excellent comparison with existing numerical results.

Acknowledgments Financial support from the Swedish Research Council and computer time provided by SNIC (Swedish National Infrastructure for Computing) is gratefully acknowledged.

References

1. Kleiser, L., Schumann, U.: Treatment of incompressibility and boundary conditions on 3-D numerical spectral simulations of plane channel flow. In: Proceedings of 3rd GAMM Conference on Numerical Methods in Fluid Mechanics, vol. 59, pp. 165–173 (1980)
2. Lele, S.K.: Compact finite difference schemes with spectral-like resolution. J. Comp. Phys. **103**, 16–42 (1992)
3. Moser, R.D., Kim, J., Mansour, N.N.: Direct numerical simulation of turbulent channel flow up to $Re_\tau = 590$. Phys. Fluids **11**, 943–945 (1999)
4. Orlandi, P.: Fluid flow phenomena, a numeric toolkit, pp. 12–17. Kluwer Academic Publishers, Antalya (2000)
5. Reuter, J., Rempfer, D.: Analysis of pipe flow transition. Part I. Direct numerical simulation. Theor. Comput. Fluid Dyn. **17**, 273–292 (2004)
6. Spalart, P.R., Moser, R.D., Rogers, M.M.: Spectral methods for the Navier-Stokes equations with one infinite and two periodic directions. J. Comp. Phys. **96**, 297–324 (1991)

Part III
Quality of LES Modelling

Investigations on the Effect of Different Subgrid Models on the Quality of LES Results

F. Proch, M.W.A. Pettit, T. Ma, M. Rieth and A.M. Kempf

1 Introduction

Subgrid stress modelling plays an important role in the quality of LES results, and a number of different closure methods exist. One of the most common is the eddy-viscosity approach, where subgrid stresses are treated as an additional contribution to the flow viscosity. Several models have been proposed to evaluate this 'turbulent' viscosity, with both static and dynamic variants. In this work, the classical Smagorinsky model and the relatively new and promising σ model are compared in their static and dynamic forms. To assess the performance of each model, simulation results for a simple channel flow, as well as for a more complex annular geometry, are compared against DNS and experimental data respectively.

2 Description of the Numerical Method

With the eddy-viscosity approach, the turbulent viscosity μ_t is modelled in a form that is similar to the mixing-length model in RANS:

$$\mu_t = \rho \left(C_m \Delta\right)^2 D_m \left(\tilde{u}\right) \tag{1}$$

where D_m is a differential operator depending on the resolved velocity field $\tilde{u}$, Δ is the LES filter width, ρ is the density, and C_m is a model constant.

F. Proch (✉) · M. Rieth · A.M. Kempf
Institute for Combustion and Gasdynamics (IVG), Chair for Fluid Dynamics,
University of Duisburg-Essen, 47048 Duisburg, Germany
e-mail: fabian.proch@uni-due.de

M.W.A. Pettit · T. Ma
Department of Mechanical Engineering, Imperial College London,
London SW7 2AZ, UK

J. Fröhlich et al. (eds.), *Direct and Large-Eddy Simulation IX*,
ERCOFTAC Series 20, DOI 10.1007/978-3-319-14448-1_19

The differential operator D_m for the classical Smagorinsky model [1] is

$$D_m = \sqrt{2 S_{ij} S_{ij}} \quad \text{where} \quad S_{ij} = \frac{1}{2}\left(\frac{\partial \tilde{u}_i}{\partial x_j} + \frac{\partial \tilde{u}_j}{\partial x_i}\right) \tag{2}$$

represents the strain rate of the resolved velocity field. For the static version of the model, the constant $C_m = C_s$ usually takes values between 0.05 and 0.2. Though the model is simple to implement, it tends to over-predict turbulent viscosity in regions with high strain rates, such as near walls or in shear layers. This behaviour can be overcome by adapting the modelling constant C_s in a dynamic procedure, as introduced by Germano et al. [2]. Within this work, a slightly modified version is used to adapt C_s in time and space [3] in a formulation for non-constant density.

The σ model [4] uses the singular values of the velocity gradient to build the differential operator:

$$D_m = \frac{\sigma_3 \left(\sigma_1 - \sigma_2\right)\left(\sigma_2 - \sigma_3\right)}{\sigma_1^2} \quad \text{with} \quad \sigma_1 \geq \sigma_2 \geq \sigma_3 \geq 0 \tag{3}$$

where the values σ_i are equal to the square root of the eigenvalues of the tensor

$$G_{ij} = \frac{\partial \tilde{u}_k}{\partial x_i}\frac{\partial \tilde{u}_k}{\partial x_j}. \tag{4}$$

This model yields $\mu_t \propto y^3$ near walls, where y is the wall-normal distance, and avoids the over-prediction of μ_t in shear layers. Furthermore it vanishes in purely two-dimensional or two-component flows, and for pure rotation or shear, as appropriate. The model constant usually takes values of $C_m = C_\sigma \approx 1.5$ [4], or is determined dynamically by the same procedure as used for the Smagorinsky model. Simulations are performed with the in-house 'PsiPhi' LES code [5–7].

3 Test Cases

To compare the influence of the different models on LES quality, the results of two different test cases are evaluated. To investigate any effect of filter width (cell size) on model performance, both cases are computed at two different grid resolutions.

3.1 Channel Flow

The primary purpose of the first test is to assess model behaviour in near-wall regions. The simulated geometry is chosen to be a cube that is periodic in the x- and z-directions, as this leads to maximum computational efficiency for the applied

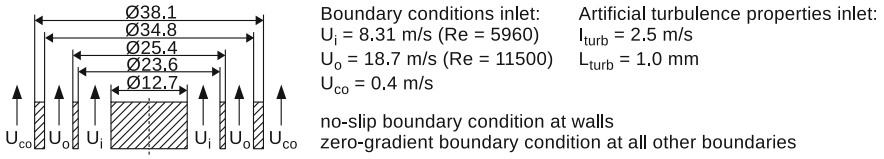

Fig. 1 Cross-section and boundary conditions of the Cambridge burner. Measurements are in mm

distributed memory parallelization. We found that the very shape of the computational domain has only minor influence on the results. The friction Reynolds number Re_τ is chosen as

$$Re_\tau = y^+|_\delta = 395 \quad \text{with} \quad y^+ = \frac{u_\tau \, y}{\nu} \tag{5}$$

where y^+ is the dimensionless wall co-ordinate, δ is the channel half-width, u_τ is the friction velocity and ν is the kinematic viscosity. The model constants are set to $C_s = 0.065$ [8] and $C_\sigma = 1.5$ for the static Smagorinsky and σ models, respectively. Coarse grids are usually more practically affordable; we therefore test the models at a relatively coarse resolution of $\Delta = 13.2\ y^+$, leading to 61 cells across the channel. The finer grid has $\Delta = 6.1\ y^+$, yielding 121 cells over the channel height. Using these grids we investigate the behaviour of the models within not perfectly resolved near-wall regions, which likely occur in meshes for engineering applications.

3.2 Cambridge Stratified Flame Series

A cross-section of the Cambridge stratified burner [9], consisting of a central bluff body and two annular jets, together with the corresponding boundary conditions is shown in Fig. 1. Fluid properties of air at standard temperature and pressure are assumed. Grid resolutions of 0.5 mm (coarse) and 0.25 mm (fine) are used, leading to domains of 13 and 105 million cells respectively. The static model constants are $C_s = 0.173$ [10] and $C_\sigma = 1.5$, where this (relatively high) Smagorinsky constant has previously delivered good results in simulations of the similar Darmstadt stratified flame series [7].

4 Results

This section compares simulation results from the two test cases, where the investigated models are as mentioned above: Smagorinsky static (SMA STA), Smagorinsky dynamic (SMA DYN), σ static (SIG STA) and σ dynamic (SIG DYN). As in all cases the discussed trends and conclusions are comparable for both investigated cell sizes, the coarse grid results have been omitted in the plots for clarity and brevity.

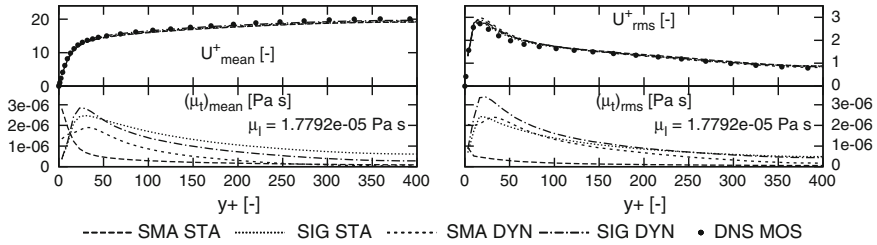

Fig. 2 Comparison of fine grid results to DNS data (DNS MOS), showing mean and rms profiles of dimensionless axial velocity and turbulent viscosity over dimensionless wall co-ordinates

4.1 Channel Flow

Profiles for mean and root mean square (rms) dimensionless axial velocity (normalised by u_τ) and turbulent viscosity over the wall co-ordinate y^+ are shown in Fig. 2. The velocity statistic is in agreement with the DNS data computed by Moser et al. [11], while an improvement with grid refinement is also observed. All models yield similar velocity, but differences become apparent in the predictions of turbulent viscosity. SIG STA and SIG DYN predict a decline of μ_t to zero at the wall; SMA DYN also yields declining values, but at a shallower gradient. In contrast, SMA STA predicts an inverse wall behaviour. Overall, SIG STA, SIG DYN and SMA DYN predict similar qualitative trends. The two versions of the σ model yield consistent values of μ_t in the free stream, but SIG DYN shows a larger peak near the wall. Values from SMA DYN are larger than for SMA STA, but generally less than for the σ models. The near-wall peak from SMA DYN is comparable to the peak of SIG STA.

4.2 Cambridge Stratified Flame Series

Mean and rms axial velocity profiles are compared to experimental measurements for a non-reactive case [9] at different heights above the burner nozzle exit in Fig. 3. Simulation results and experimental values are in good agreement. An improvement with grid refinement is observed, as before. Velocity predictions are not strongly dependent on the subgrid model; however, fluctuations near the burner exit show better agreement with SIG STA and SIG DYN. Instantaneous snapshots of μ_t are shown in Fig. 4. The predictions of SMA STA show the largest and least universal structures, where the influence of shear layers and walls can be clearly identified. In contrast, SIG STA predicts the smallest structures, while SMA DYN and SIG DYN yield intermediate structure sizes. Finally, turbulent viscosity statistics are shown in Fig. 5. Similar to the results of the channel flow, the differences in model predictions of μ_t are much larger than those observed for velocity predictions. The increased sensitivity of SMA STA to resolved strain rates results in over-prediction of μ_t in

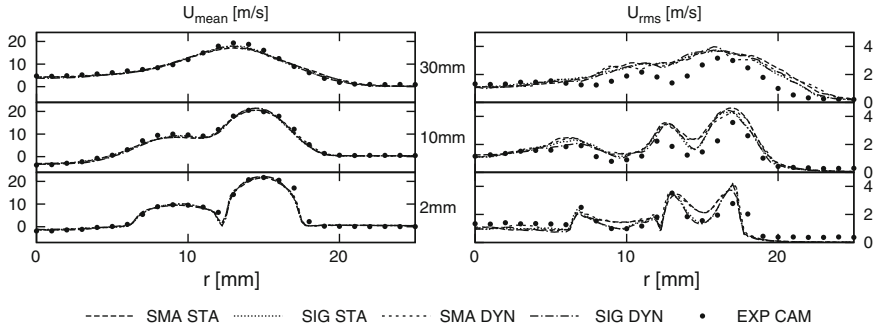

Fig. 3 Comparison of mean and rms axial velocity profiles from the fine grid to experimental data (EXP CAM) at different heights above the burner exit

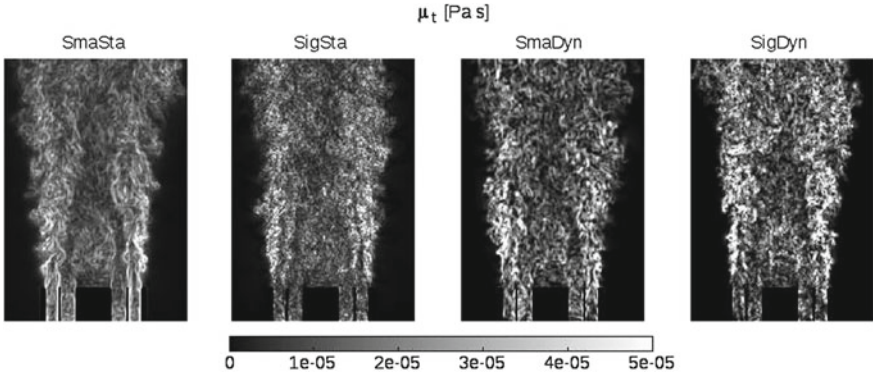

Fig. 4 Comparison of instantaneous snapshots of the turbulent viscosity field on the fine grid

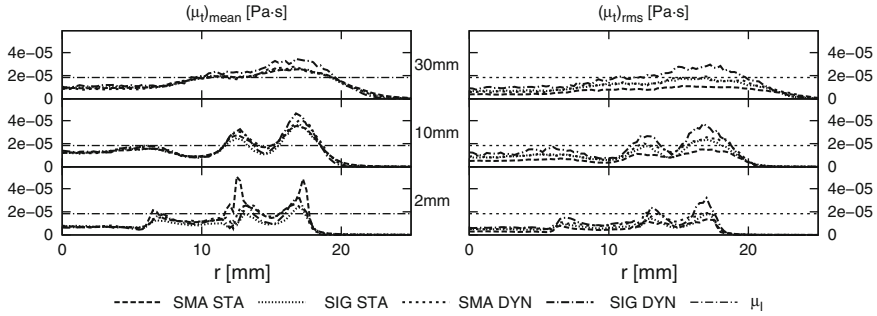

Fig. 5 Comparison of mean and rms turbulent viscosity profiles at different heights above the burner exit on the fine grid, *black horizontal lines* represent the laminar viscosity

the region near the burner exit, while SIG DYN generally yields the highest mean and rms values. The viscosity ratio $r_\mu = \mu_t/\mu_l$ has a maximum value of $r_\mu \approx 2$ for SMA STA and is less for the other models, indicating a sufficient grid resolution and a good LES quality [5].

5 Conclusions

Investigations have been carried out for two different subgrid models, in both static and dynamic forms. Two test cases of different complexity have been computed on coarse and fine grids. No major influence of the models on velocity predictions was observed. However, distinct differences were found in the predictions of turbulent viscosity. The subgrid model may therefore be more influential on velocity predictions for other cases, especially where Reynolds numbers are higher or the geometry plays a more significant role. The static σ model with $C_\sigma = 1.5$ produced good results for both cases, and avoids the shortcomings of the static Smagorinsky model at walls and within shear layers. The dynamic procedure for the σ model seems to have less influence on turbulent viscosity predictions than for the Smagorinsky model with these cases.

Acknowledgments The authors gratefully acknowledge funding provided from the state of Nordrhein-Westfalen, Germany. Research has been supported by the Center for Computational Sciences and Simulation (CCSS) of the University of Duisburg-Essen, Germany. The authors would like to thank Prof. Simone Hochgreb, Dr Robert S. Barlow and their group members for providing the experimental data.

References

1. Smagorinsky, J.: General circulation experiments with the primitive equations, 1. The basic experiment. Mon. Weath. Rev. **91**, 99–164 (1963)
2. Germano, M., Piomelli, U., Moin, P., Cabot, W.: A dynamic subgrid-scale eddy viscosity model. Phys. Fluids **3**, 1760–1765 (1991)
3. Piomelli, U., Liu, J.: Large-eddy simulation of rotating channel flows using a localized dynamic model. Phys. Fluids **7**, 839–848 (1995)
4. Nicoud, F.: Baya Toda, H., Cabrit, O., Bose, S., Lee, J.: Using singular values to build a subgrid-scale model for large eddy simulations. Phys. Fluids **23**, 085106 (2011)
5. Pettit, M.W., Coriton, B., Gomez, A., Kempf, A.M.: Large-Eddy Simulation and experiments on non-premixed highly turbulent opposed jet flows. Proc. Combust. Inst. **33**, 1391–1399 (2011)
6. Kempf, A.M., Geurts, B.J., Oefelein, J.: Error analysis of large-eddy simulation of the turbulent non-premixed sydney bluff-body flame. Combust. Flame **158**, 2408–2419 (2011)
7. Marincola Cavallo F., Ma, T., Kempf, A.M.: Large eddy simulations of the Darmstadt turbulent stratified flame series. Proc. Combust. Inst. 34, 1307–1315 (2013)
8. Moin, P., Kim, J.: Numerical investigation of turbulent channel flow. J. Fluid Mech. **118**, 341–377 (1982)
9. Sweeney, M.S., Hochgreb, S., Dunn, M.J., Barlow, R.S.: The structure of turbulent stratified and premixed methane/air flames I: Non-swirling flows. Combust. Flame **159**, 2896–2911 (2012)

10. Lilly, D.: Proc. IBM Sci. Comp. Symp. Environ. Sci. 1, 195–210 (1967)
11. Moser, R.D., Kim, J., Mansour, N.N.: Direct numerical simulation of turbulent channel flow up to $Re_\tau = 590$. Phys. Fluids **11**, 943–945 (1999)

Computational Complexity of Adaptive LES with Variable Fidelity Model Refinement

Alireza Nejadmalayeri, Oleg V. Vasilyev and Alexei Vezolainen

1 Introduction

Adaptive methods with both mesh and polynomial order refinements have been used extensively in computational fluid dynamics to achieve optimal accuracy with the minimal computational cost. However *hp*-refinement by itself is not sufficient for numerical simulation of turbulent flows of engineering interest. For instance, even for the extreme *hp*-refinement such as spectral DNS, the requirement to resolve Kolmogorov length-scale results in a daunting computational cost. LES is a much less expensive approach, but for high Reynolds number turbulent flows only large scales of the flow are captured and most of the dissipation is provided by the SGS model. The marginally resolved LES with small ratio of SGS and the total dissipations resolves more of the flow physics, but scales approximately the same as DNS in the limit of high Reynolds numbers, thus, making it impractical.

The quest for an appropriate criteria to identify the hierarchical change of scale for multi-scale simulations brought us to define the turbulence resolution in a broader perspective rather than the structure-size distinction as in classical LES, or the extreme case of resoling Kolmogorov length-scale as in DNS, or decomposing deterministic-coherent and stochastic-incoherent modes as in CVS, or even capturing more/less energetic structures as in SCALES. This new definition is based on the measure that is required in practical applications: "how much the flow-physics is modeled/resolved?" In essence, maintaining the percentage of modeled and resolved physically important

A. Nejadmalayeri (✉) · O.V. Vasilyev · A. Vezolainen
Department of Mechanical Engineering, University of Colorado,
Boulder, CO 80309, USA
e-mail: Alireza.Nejadmalayeri@Colorado.edu

O.V. Vasilyev
e-mail: Oleg.Vasilyev@Colorado.edu

A. Vezolainen
e-mail: Alexei.Vezolainen@Colorado.edu

J. Fröhlich et al. (eds.), *Direct and Large-Eddy Simulation IX*,
ERCOFTAC Series 20, DOI 10.1007/978-3-319-14448-1_20

quantity (e.g. turbulent kinetic energy, dissipation, or enstrophy) at a constant level implies that the methodology should exhibit synergistic transition between various levels of fidelity both in space and time as well as take advantage of spatial and temporal flow intermittency. This dynamically adaptive transition between different regimes necessitates the model adaptation.

Therefore, the missing component for turbulence simulation is not either *h*- or *p*-refinement but **coupling the model with the numerics**. That is to say, the selection and adjustments of the model fidelity, computational mesh, and/or the order of the numerical method need to be dynamically adaptive in order to take into account the intermittency of the turbulent flow filed. This new concept of *model*-refinement, which is named *m*-refinement [4], is utilized to perform Stochastic Coherent Adaptive Large Eddy Simulation (SCALES) of linearly-forced homogeneous turbulence at various fixed levels of turbulence resolution.

2 Computational Framework

The SCALES equations that govern evolution of coherent energetic structures are obtained by filtering the Navier-Stokes equations using wavelet-thresholding filter [2]. In this study, homogeneous turbulence with linear forcing [3] applied in the physical space over the whole range of wavenumbers [1] is investigated. The objective is to control the turbulence resolution, defined as the local fraction of SGS dissipation, $\mathscr{F} : \frac{\Pi}{\varepsilon_{\text{res}}+\Pi}$, where $\varepsilon_{\text{res}} = 2\nu \overline{S_{ij}}^{\varepsilon} \overline{S_{ij}}^{\varepsilon}$ is the resolved viscous dissipation and $\Pi = -\tau_{ij}^{*} \overline{S_{ij}}^{\varepsilon}$ is the local SGS dissipation. This ratio of the SGS dissipation to the total dissipation, can be viewed as turbulence resolution since it indicates how much the flow is modeled/resolved. Therefore, by controlling $\mathscr{F}$, one can explicitly control the percentage of the flow physics that is desired to be resolved. To maintain the turbulence resolution at a constant level, the spatially variable thresholding methodology [4, 5] is used. This approach automatically provides the required numerical resolution and the model-fidelity in a space/time adaptive fashion based on a two-way coupling of numeric and physics. This method dynamically tracks the regions of interest in spatial and time space and not only adapts the grid but adjusts the model as well (*hm*-refinement).

In the classical non-adaptive explicitly filtered LES, the filter-width is priori user-defined based on which the resolution is determined; therefore, both the CFD engine (through the resolution) and the filtering mechanism (via the filter-width) depend on priori defined filter-width, which is not fine-tuned based on the results (Fig. 1a). The original SCALES has improved this by its dynamically adaptive wavelet-filtering mechanisms via constantly adapting both the numerical grid and the filter-width based on the instantaneous flow field (Fig. 1b). However, the wavelet thresholding filter (WTF) uses a priori user-defined threshold-level and as a result of filtering the velocity-filed with this constant threshold, the WTF is indeed imposing a feedback based on a constant level of resolved kinetic energy. This limitation has been recently removed [4] by means of constructing a fully adaptive wavelet thresholding filter [5]. The new *m*-refined SCALES requires a priori user-defined level of resolution/fidelity

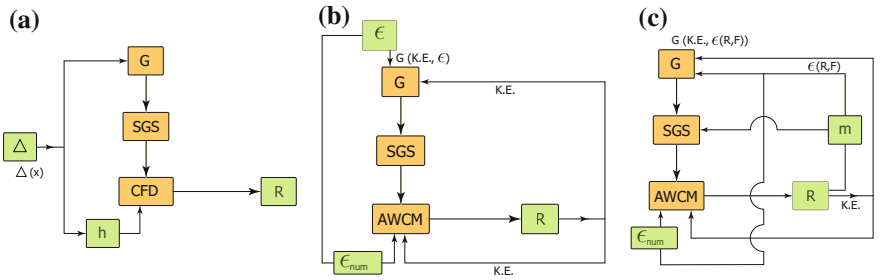

Fig. 1 Dependency diagram for **a** classical explicitly filtered LES, **b** original SCALES, and **c** the variable-fidelity SCALES. *Notation G* filter, *R* results, *m* model refinement, Δ user provided LES filter width, ε wavelet threshold for model adaptation, ε_{num} wavelet threshold controlling the accuracy of the solution, F an arbitrary dynamically important physical quantity to be controlled, e.g., $\mathscr{F}$

based on which the threshold is dynamically adapted in order to maintain the fidelity constant as user has requested. In original SCALES, the filtering mechanism is a function of the results (kinetic energy) and a constant threshold, while in the newly developed *m*-refined SCALES, threshold itself is a function of the results (any physical quantity and not limited to kinetic energy) and the user-defined fidelity. All in all, *m*-SCALES integrates all components of the computational methodology including numerics, models, and physics altogether to construct a fully dynamically adaptive computational framework (Fig. 1c).

3 Reynolds Number Scaling

To construct the Reynolds number scaling statistics, a series of simulations where the Reynolds number is progressively increased are performed. SCALES of linearly forced homogeneous turbulence [1] with linear forcing constant coefficient $Q = 20/3$ are performed in the computational domain of $[0, 2\pi]^3$ on a dynamically adaptive dyadic grid with effective nonadaptive resolutions of 256^3, 512^3, 1024^3, and 2048^3. These correspond to Taylor micro-scale Reynolds number of $Re_\lambda \cong 70, 120, 190, 320$ based on viscosities of $\nu = 0.09, 0.035, 0.015, 0.006$. These choices of viscosities are based on maintaining the ratio of Kolmogorov length-scale to the smallest grid-spacing constant, i.e., $\frac{\eta}{\Delta_{\min}} = 2$, to ensure the resolution required for a well-resolved DNS.

In order to study the influence of the fidelity of simulation on the Reynolds number scaling of SCALES, a series of simulations of different turbulence resolution is conducted. The different fidelity is achieved by using spatially variable thresholding approach [5] with different goal values of $\mathscr{F}$, namely $\mathscr{G} = 0.2, 0.25, 0.32, 0.4, 0.5$. It is observed that in the logarithmic scale the slope of Re_λ scaling of SCALES spatial modes at least up to 1024^3 remains approximately the same regardless of the level of turbulence resolution, Fig. 2. In other words, the scaling exponent of constant-fidelity *m*-SCALES is nearly insensitive to the level of fidelity.

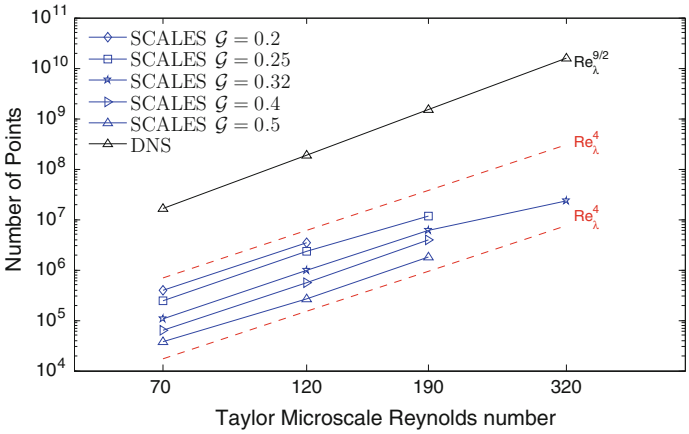

Fig. 2 Reynolds scaling of constant-dissipation SCALES at various goal values

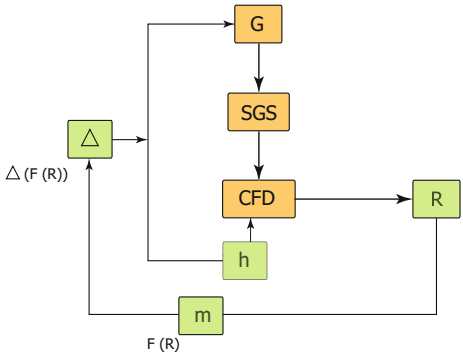

Fig. 3 Proposed dependency diagram for a possible variable-fidelity LES

The scaling statistics presented by this work proves that the developed model can resolves more flow-physics phenomena yet with profoundly smaller number of spatial modes compared with marginally resolved LES. It is demonstrated that depending on what flow physics is desired to be captured, the same model and the same numerical method result in different Reynolds scaling. Therefore, the broad message of this computational complexity work is not to advertise the wavelet-based methods but to promote the physics-based turbulence modeling as a marriage of model and numerics. This *m*-refinement concept can be easily implemented into the existing adaptive Large Eddy Simulation methodologies in order to construct continuously variable fidelity LES. The possible implementation can be illustrated as Fig. 3. Such an LES would include an additional feedback mechanism from the results (any physical quantity) in order to incorporate a filter-width/model adaptation preferably coupled with adaptation of the numerical resolution as well. Hence, both filtering-mechanism/model (via the filter-width) and CFD-engine/numerics (through the resolution) should be dynamically coupled based on any objective physics-based fidelity measure.

Acknowledgments This work was supported by the United States National Science Foundation (NSF) under grants No. CBET-0756046 and CBET-1236505. This support is gratefully acknowledged. Authors are also thankful for the computing time on the Janus supercomputer, which is supported by the National Science Foundation (award number CNS-0821794) and the University of Colorado Boulder. The Janus supercomputer is a joint effort of the University of Colorado Boulder, the University of Colorado Denver and the National Center for Atmospheric Research.

References

1. De Stefano, G., Vasilyev, O.V.: Stochastic coherent adaptive large eddy simulation of forced isotropic turbulence. J. Fluid. Mech. **646**, 453–470 (2010)
2. Goldstein, D.E., Vasilyev, O.V.: Stochastic coherent adaptive large eddy simulation method. Phys. Fluids **16**(7), 2497–2513 (2004)
3. Lundgren, T.S.: Linearly forced isotropic turbulence, pp. 461–473. Annual Research Briefs, Center for Turbulence Research, NASA Ames/Stanford University (2003)
4. Nejadmalayeri, A.: Hierarchical multiscale adaptive variable fidelity wavelet-based turbulence modeling with Lagrangian spatially variable thresholding. Ph.D. thesis, University of Colorado Boulder, Boulder (2012)
5. Nejadmalayeri, A., Vasilyev, O.V., Vezolainen, A., de Stefano, G.: Spatially variable thresholding for stochastic coherent adaptive LES. In: Kuerten, H., Geurts, B., Armenio, V., Fröhlich, J. (eds.) Proceedings of Direct and Large-Eddy Simulation Workshop 8: Eindhoven University of Technology, The Netherlands, July 7–9, 2010, pp. 95–100. Springer (2011)

Elimination of Curvature-Induced Grid Motion for *r*-Adaptation

C. Hertel, M. Joppa, B. Krull and J. Fröhlich

1 Introduction

Using an adaptive method in the context of a large eddy simulation (LES) is rarely seen in literature. A challenging aspect for this combination is the interplay between the resolution of the grid and the governing equations to be solved, since the grid spacing defines the scale separation between the resolved large-scale turbulent fluctuations and the unresolved subgrid-scale turbulence, so that whenever the grid changes in time this decomposition changes as well. The adaptive method employed here is a so-called *r*-adaptation, aiming at redistributing a given number of grid points in space to achieve a clustering in regions where a certain, preferably LES-specific, criterion indicates the need for a higher resolution. The movement of grid points can be realised by solving a moving mesh partial differential equation (MMPDE) in each time step or in selected time steps during an adaptation phase. The latter was applied to adapt the grid according to statistical quantities of interest [1–3], and substantial improvement of the results was demonstrated.

To carry the method over to unsteady adaptation by means of instantaneous quantities of interest, aiming to track vortices travelling through the domain for example, the flow around a circular cylinder was chosen as a test case. Using a low Reynolds number offers the opportunity to address unsteady grid movement in the well known context of the Kármán vortex street, while large Reynolds numbers offer the opportunity to use LES-specific criteria. First investigations for this test case, however, pointed to a serious problem concerning the adaptive method itself. Spurious clustering of points in radial direction was observed when using a body-fitted grid around the cylinder. This issue needs to be resolved before any adaptation can be performed.

C. Hertel (✉) · M. Joppa · B. Krull · J. Fröhlich
Institute of Fluid Mechanics, TU Dresden, Dresden, Germany
e-mail: claudia.hertel@tu-dresden.de

J. Fröhlich
e-mail: jochen.froehlich@tu-dresden.de

J. Fröhlich et al. (eds.), *Direct and Large-Eddy Simulation IX*,
ERCOFTAC Series 20, DOI 10.1007/978-3-319-14448-1_21

The present paper provides an analysis of this feature and proposes a versatile strategy for its remedy based on an appropriate modification of the monitor function.

All simulations below were conducted with the in-house code LESOCC2, a curvilinear block-structured finite volume solver [4] supplemented with the Arbitrary Eulerian Lagrangian (ALE) formulation to enable the solution of the governing equations on moving grids [3].

2 Curvature-Induced Grid Motion

2.1 Basic Method

To shift grid points in space the MMPDE proposed by Huang [5] is used

$$\tau \frac{\partial \mathbf{x}}{\partial t} = \frac{p}{\omega^2} \sum_{i,j} \left(\mathbf{a}^i \cdot \mathbf{a}^j \right) \frac{\partial}{\partial \xi_i} \left(\omega \frac{\partial \mathbf{x}}{\partial \xi_j} \right), \tag{1}$$

where $\mathbf{x}$ is a cell center point in physical space and ξ its coordinate in computational space. Furthermore, τ is a global time scaling parameter, $p(\xi, t)$ a local grid adjustment factor, and $\mathbf{a}^i$ the covariant basis vectors. The heart of this method is the monitor function ω, which is a scalar quantity here, governing the motion of the grid according to the quantity of interest ψ with [6]

$$\omega = \sqrt{1 + \alpha \left(\frac{\psi}{\psi_{max}} \right)^2}. \tag{2}$$

Here, ψ_{max} is the maximum of ψ in the domain, while the global parameter α is used to adjust the size of the monitor function.

A finite volume formulation is used to discretize (1) for the cell center coordinates. An interpolation algorithm is then employed to obtain the cell corners, in fact a non-trivial issue as discussed in [2]. The 'median-based interpolation' proposed in that reference is applied in the following.

2.2 Problem Description

The quasi two-dimensional test case, chosen for the results presented here, is the flow around a circular cylinder with R being its radius and D its diameter. For reasons of simplicity an O-grid is used in a circular computational domain of diameter 41 D. Simulations presented in the following sections were conducted at $Re = 100$ on a coarse grid consisting of $80 \times 80 \times 2$ cells in radial, azimuthal and axial direction.

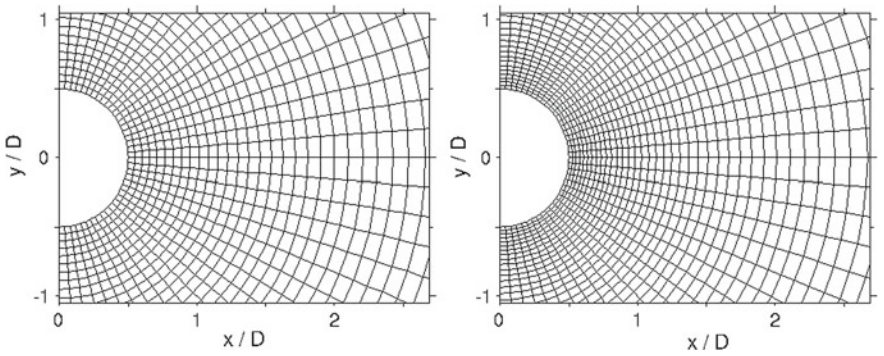

Fig. 1 Detail of the two dimensional grid. *Left* initial grid. *Right* obtained, stationary grid for a given constant monitor function ω

A detail of the initial grid is shown in Fig. 1 (left), displaying grid clustering near the cylinder.

The monitor function ω drives the adaptation such that the grid is refined in regions where ω or its gradient is large. It was then expected that an uniform value of ω leads to $\Delta r = const$ and $\Delta\theta = const$. Indeed, employing $\omega(\mathbf{x}, t) = \omega^* = const$ and running the adaptation according to (1) leads to a stationary grid. The resulting distribution of the grid points, shown in Fig. 1 (right), however, is not as expected. While in azimuthal direction a constant step $\Delta\theta$ is observed, the radial distribution of the grid points exhibits increasing step size Δr for increasing r.

2.3 Analysis of Grid Motion

To identify the origin of the grid finally obtained Eq. (1) is analysed. Motivated by the current grid topology, the MMPDE (1) is transferred to cylindrical coordinates and simplified using $r = r(\xi_1)$ and $\theta = \theta(\xi_2)$ motivated by the initial grid. A stationary grid has to fulfill (1) with the time derivative of the grid points set to zero. For radial and azimuthal direction, (1) then reads

$$\frac{1}{\omega}\frac{\partial\omega}{\partial r} = -\frac{\partial^2 r}{\partial\xi_1^2}\left(\frac{\partial r}{\partial\xi_1}\right)^{-2} + \frac{1}{r}, \tag{3}$$

$$\frac{1}{\omega}\frac{\partial\omega}{\partial\theta} = -\frac{\partial^2\theta}{\partial\xi_2^2}\left(\frac{\partial\theta}{\partial\xi_2}\right)^{-2}, \tag{4}$$

respectively. If the monitor function is constant, $\omega = \omega^*$, (4) requires the second derivative of θ to vanish. This is achieved with an equi-distributed grid ($\Delta\theta = const$)

in that direction. With $\omega = \omega^*$ the MMPDE for the radial direction (3) yields

$$\frac{\partial^2 r}{\partial \xi_1^2} = \frac{1}{r}\left(\frac{\partial r}{\partial \xi_1}\right)^2. \tag{5}$$

The term $\partial r/\partial \xi_1$ must be larger than zero to get non-vanishing Δr. Hence, the second derivative is $\partial^2 r/\partial \xi_1^2 > 0$ and $\Delta r \neq const$ for the steady-state solution of (3). Equation (3) was solved analytically for the present geometry, leading to a distribution where $\Delta r \sim r$, e.g. where the radial extent of a cell increases with increasing radius r, in agreement with the final grid shown in Fig. 1 (right).

2.4 Modification of the Monitor Function

A multiplicative factor, named ω_0, for the monitor function ω is introduced to compensate the geometry-induced grid motion. The combined monitor function then reads

$$\omega_{tot}(\mathbf{x}, t) \;=\; \omega(\mathbf{x}, t)\omega_0(\mathbf{x}). \tag{6}$$

Now, ω_0 is determined such that a desired reference grid $\mathbf{x}_{ref}$ is achieved for a given reference monitor function $\omega = \omega_{ref}$, e.g. $\omega_{ref} = const$. The combined monitor function ω_{tot} is then used in (1).

For the determination of ω_0 the MMPDE (1) must be solved once using the grid $\mathbf{x}_{ref}$ and the monitor function ω_{ref}. The time derivative on the left hand side of (1) is set to zero as the corresponding grid should be a steady state solution of (1), giving

$$0 \;\stackrel{!}{=}\; \tau\frac{\partial \mathbf{x}}{\partial t} \;=\; \frac{p}{(\omega_{ref}\omega_0)^2}\sum_{i,j}\left(\mathbf{a}^i \cdot \mathbf{a}^j\right)\frac{\partial}{\partial \xi_i}\left(\omega_{ref}\omega_0\frac{\partial \mathbf{x}_{ref}}{\partial \xi_j}\right) \tag{7}$$

which needs to be solved for ω_0. Equation (7) does not have a solution for arbitrary entries $\mathbf{x}_{ref}$, ω_{ref},an issue that will be considered elsewhere.

3 Results for the Modified Monitor Function

3.1 Reference Grid for Uniform Criterion

Here, we only report the result for $\omega_{ref} = \omega^* = const$ and the reference grid $\mathbf{x}_{ref}$ chosen to have constant step sizes in radial and azimuthal direction. Then (7) yields $\omega_0 = Cr$, with C being a constant. For obvious reasons, $\omega > 0$ in (1) and with (2) $\omega > 1$ for stability reasons. Hence we chose $C = 1/R$ here to yield $\omega_0 \geq 1$.

3.2 Physically Motivated Criterion

The modification of the monitor function described above is now used for unsteady adaptation of the flow around a circular cylinder at $Re = 100$. As a scalar quantity to capture the alternating separation of vortices the vorticity of the instantaneous fluid velocity $\mathbf{u}$ was used setting $\psi = |\nabla \times \mathbf{u}|$. The corresponding monitor function ω for a randomly chosen point in time during the simulation is displayed in Fig. 2 (left). A detail of the adapted grid obtained without correction of the monitor function is shown in Fig. 2 (right), revealing a strong clustering of grid points in the vicinity of the cylinder. The adaptation itself is dominated by the curvature-induced grid motion. This is visible due to the grid refinement behind the cylinder, although the criterion is vanishing there as illustrated by Fig. 2 (left). This strong and unwanted refinement leads to a limitation of the parameters for the MMPDE. For the results presented in Fig. 2 these are: $\tau = 0.001$, $\alpha = 10$. An increase of α or decrease of τ, both leading to a stronger refinement, resulted in the divergence of the simulation.

Employing the modification of the monitor function (6) successfully compensates the curvature-induced grid movement. The grid obtained for the previous values of τ and α, however, led to a non-physical velocity filed as the grid was too coarse near the cylinder.

Hence, α was adjusted to $\alpha = 10^2$ with the corresponding result reported in Fig. 3. The grid is now only refined in regions, where the criterion is large, as desired. The compensation of the curvature-induced grid motion now also allows even larger values for α leading to a stronger grid refinement (Fig. 4).

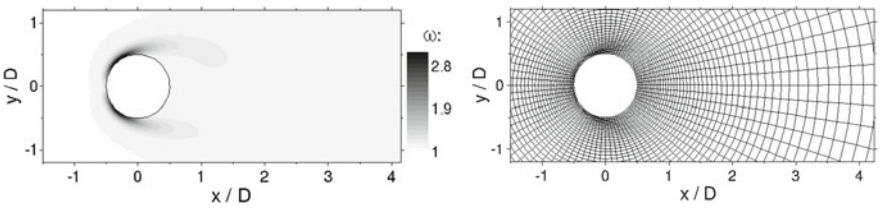

Fig. 2 Simulation result without correction of the monitor function for an randomly chosen point in time. *Left* monitor function, *right* corresponding grid

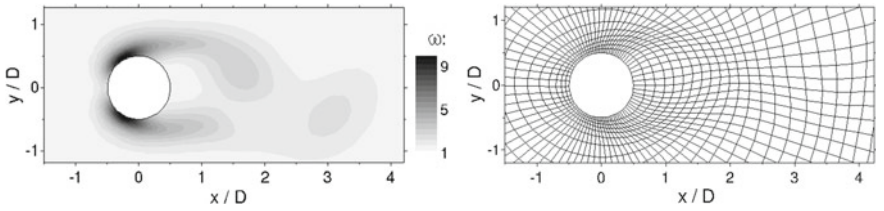

Fig. 3 Results at the same time as Fig. 2 for the monitor function ω (*left*) and the corresponding grid (*right*) for a simulation with correction of the monitor function and $\alpha = 10^2$

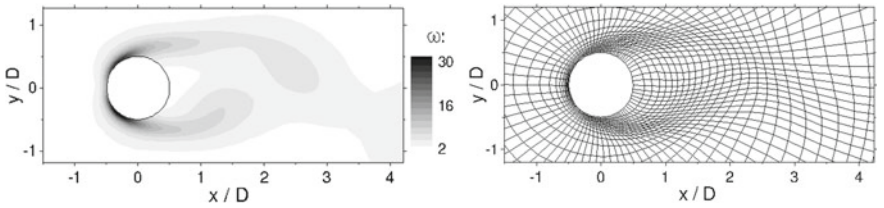

Fig. 4 Results at the same time as Fig. 2 for the monitor function ω (*left*) and the corresponding grid (*right*) for a simulation with correction of the monitor function and $\alpha = 10^3$

We conclude that the multiplicative factor $\omega_0(\mathbf{x})$ for the monitor function is an appropriate method to compensate unwanted curvature-induced grid motion.

Acknowledgments The present work is being funded by the German Research Foundation (DFG) via the Priority Programme SPP 1276 "MetStröm". The authors thank their colleagues in SPP1276 for fruitful exchange and stimulating discussions. Computation time was provided by ZIH at TU Dresden.

References

1. Hertel, C., Fröhlich, J.: Application of r-adaptation to LES of turbulent flow. In: Proceedings of the ETMM9, Thessaloniki, Greece, pp. 1–6 (2012)
2. Hertel, C., Schümichen, M., Lang, J., Fröhlich, J.: Using a moving mesh PDE for cell centers to adapt a finite volume grid. Flow Turbul. Combust. (2012). doi:10.1007/s10494-012-9442-8
3. Hertel, C., Schümichen, M., Löbig, S., Lang, J., Fröhlich, J.: Adaptive large eddy simulation with moving grids. Theor. Comput. Fluid Dyn. (2012). doi:10.1007/s00162-012-0280-z
4. Hinterberger, C., Fröhlich, J., Rodi, W.: Three-dimensional and depth-averaged large-eddy simulations of some shallow water flows. J. Hydraul. Eng. **133**, 857–872 (2007)
5. Huang, W.: Practical aspects of formulation and solution of moving mesh partial differential equations. J. Comput. Phys. **171**, 753–775 (2001)
6. Winslow, A.M.: Numerical solution of the quasilinear Poisson equation in a nonuniform triangle mesh. J. Comput. Phys. **2**, 149–172 (1967)

Reliability of LES Simulations in the Context of a Benchmark on the Aerodynamics of a Rectangular 5:1 Cylinder

M.V. Salvetti and L. Bruno

1 Introduction

The international Benchmark on the Aerodynamics of a Rectangular 5:1 Cylinder (BARC [2]) was launched in 2008 with the support of Italian and international associations. The flow setup is characterized by the high Reynolds number, low turbulence incoming flow around a stationary, sharp-edged rectangular cylinder of infinite spanwise length and of chord to depth ratio equal to 5. The considered flow configuration is of practical interest because many civil and industrial structures (e.g. tall buildings, towers and bridges) are characterized by rectangular cross sections. Moreover, the 5:1 aspect ratio was chosen because it is characterized by shear-layers detaching at the upstream cylinder corners and reattaching on the cylinder side rather close the downstream corners. This leads to a complex dynamics and topology of the flow on the cylinder side, which adds to the vortex shedding from the rear corners and to the complex unsteady dynamics of the wake (see e.g. [5]). Among the aims of the benchmark are the following: to assess the consistency of computational results obtained through different flow models and numerical approaches and of wind tunnel measurements carried out in different facilities, to compare experimental and computational results, to develop best practices for computations and to create a database to be made available to the scientific community for future reference. It is worth pointing out that BARC has not adopted a single set of measurements as a reference at its launching. Hence, statistics over a large enough number of realizations of the flow (obtained by means of both experimental and computational approaches) are preferred to validation against a single measure or simulation. In 2012 about

M.V. Salvetti (✉)
DICI, University of Pisa, Pisa, Italy
e-mail: mv.salvetti@ing.unipi.it

L. Bruno
DAD, Politecnico di Torino, Turin, Italy
e-mail: luca.bruno@polito.it

J. Fröhlich et al. (eds.), *Direct and Large-Eddy Simulation IX*,
ERCOFTAC Series 20, DOI 10.1007/978-3-319-14448-1_22

40 groups from 17 different countries were contributing to BARC and presently 70 realizations of this flow configuration obtained in both wind tunnel experiments [3, 4, 14, 15] and numerical simulations [1, 5–13, 16] have been collected. LES simulations [1, 5–9, 16] represent the 51 % of the collected numerical contributions, hybrid URANS/LES ones the 30 % [12, 16] and, finally, URANS computations the 29 % [10, 11, 13]. Therefore, this context gives also a good opportunity for the assessment and the validation of results obtained through LES codes. The aim of the present work is precisely to review the LES contributions to BARC currently available in order to quantify the result dispersion and to investigate the sensitivity to different simulation parameters, also in comparison with experiments and numerical simulations using different approaches to turbulence.

2 Description of the Test Case and of the Computational Studies

As previously mentioned, BARC addresses the flow around a stationary rectangular cylinder, and the associated aerodynamic actions [2]. The breadth (B) to depth (D) ratio is set equal to 5. The following common requirements are set for both wind tunnel tests and numerical simulations: (i) the Reynolds number based on the freestream velocity and the cylinder depth, Re_D, should be in the range of 2×10^4–6×10^4; (ii) the oncoming flow has to be set parallel to the breadth of the rectangle; (iii) the maximum intensity of the longitudinal component of the freestream turbulence is set to $I_x = 0.01$; (iv) the minimum spanwise length of the cylinder for wind tunnel tests and 3D numerical simulations is set to $L/D = 3$. Additional requirements are specified for wind tunnel tests [2], which are not listed herein for the sake of brevity. In addition to the main setup described above, sensitivity studies to some parameters, viz. the angle of attack, the Reynolds number and the freestream turbulence intensity are encouraged.

The various numerical contributions differ for modeling, numerical methods and simulation set-up. A brief overview is herein given of the main aspects of the studies based on the LES approach, while we refer to the original papers for hybrid and URANS simulations. As for modeling, both the classical and the Variational Multi Scale (VMS) LES formulations are used in conjunction with a number of subgrid models: standard and dynamic Smagorinsky model, kinetic-energy one-equation model, Wall-Adapting Local Eddy-viscosity (WALE) model. As for numerical discretization, commercial codes (Fluent in [1]), opensource codes (Openfoam in [5–7, 9]) and proprietary codes [8, 9] have been used. All codes are based on the finite-volume method, except for the one used in [8, 9], based on a mixed finite-element/finite-volume discretization. Only a single LES simulation in [1] adopts a 2D domain and it is aimed at comparing its accuracy with the 3D LES simulations in the same work. In most cases, the x- and y-wise domain dimensions ($\mathscr{D}_x$ and $\mathscr{D}_y$) are about 20–50 times the breadth B of the cylinder section, with the

exception of [16] ($\mathscr{D}_x/B = 8$, $\mathscr{D}_y/B = 3$). The ensemble-average value of the spanwise domain size $\mathscr{D}_z/B$ is close to unit, but higher values are adopted in studies addressed to the evaluation of spanwise correlation [7, 9], while shorter lengths are adopted in [16]. Most of the grids are hybrid in the $x - y$ plane (i.e. body-fitted, structured in the near wall region and unstructured elsewhere), and structured along the spanwise direction z. Remarkable exceptions are the fully unstructured grids adopted in [8, 9] and the fully structured ones used in [16]. The overall number of grid cells varies over 4 orders of magnitude among the studies, from 10^5 cells in the 2D simulation in [1] to more than 5×10^7 in [16]. All the LES simulations are wall resolved with a near wall grid resolution of $y^+ \simeq 1$ or lower. All the LES simulations consider a perfectly smooth incoming flow ($I_x = 0$), while Re_D ranges from 2×10^4 to 10^5.

2.1 Results and Discussion

As previously mentioned, the near wake flow is dominated by the vortex shedding from the rear corners of the cylinder. The mean flow is characterized by a recirculation region and by almost constant suctions on the cylinder base, which yield the largest contribution to the aerodynamic drag. An overall good agreement is found among the different numerical predictions of the near-wake dynamics and of its mean features; the comparison with the available experimental data is also generally good. As an example, let us analyze more in detail the mean drag coefficient, which is directly connected with the distribution of the mean pressure on the cylinder base. Only one measurement of this quantity is available [14] and it gives $\langle C_D \rangle = 1.029$; previous experimental works on similar configurations also indicate that the mean drag coefficient is very close to 1 (see, for instance, the data reported in [11]). The LES contributions to BARC give $\langle C_D \rangle \in [0.96, 1.39]$, while the URANS and hybrid simulations give $\langle C_D \rangle \in [0.965, 1.295]$. Therefore, rather surprisingly, the LES simulations are characterized by a larger dispersion than the URANS and hybrid ones, with a maximum discrepancy with the experimental value of 35 %. Nonetheless, it turns out that the largest values of $\langle C_D \rangle$ are obtained in the 2D simulation in [1] and in the LES carried out in [16] on a small computational domain. If these simulations are eliminated, the range of the LES predictions is reduced to $\langle C_D \rangle \in [0.96, 1.04]$, with an ensemble average of 0.99 and the largest discrepancy from the experimental value of -10 %. Similar considerations can be made for the vortex-shedding frequency (not shown here for the sake of brevity). Therefore, it appears that the choice of the computational domain may significantly affect also the prediction of quantities which are rather unsensitive to modeling and to the other simulation parameters.

Conversely, the flow features along the cylinder lateral surfaces and, hence, the lift are characterized by a significant dispersion of the numerical and experimental data. As an example, Fig. 1 summarizes the ensemble statistics of the mean pressure coefficient distributions on the lateral cylinder side; in particular, the range of the experimental and numerical mean C_p values is reported for different locations over

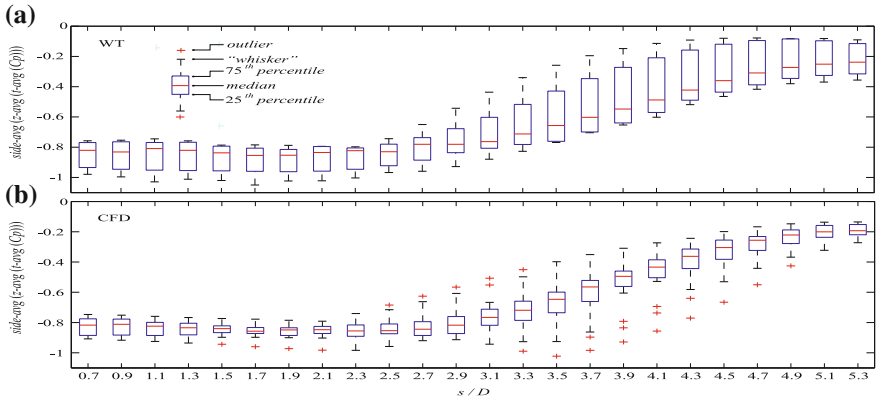

Fig. 1 Statistics of the mean Cp distributions: wind tunnel (**a**) and computational (**b**) results

the cylinder lateral side, together with the median, the 25-th and the 75-th percentile values computed among all the contributions. It is evident that a large dispersion is present both in experiments and in numerical simulations; surprisingly, most of the numerical results are contained in a narrower range than the experimental ones (note that Fig. 1b contains also URANS and hybrid URANS/LES results). Various sources of uncertainty are present in experiments, which are generally different from those affecting numerical simulations; experimental uncertainties may arise, for instance, from difficulties in controlling the characteristics of the oncoming flow (turbulence, homogeneity) or the quality of the model (e.g. sharpness of the corners) or from a possible misalignment between the oncoming flow and the model. As for the numerical simulations, the mean pressure coefficient distribution on the cylinder lateral side is strictly connected with the mean lateral flow topology, which is in turn highly sensitive to modeling and simulation parameters. The mean flow on the lateral cylinder side is characterized by a main recirculation region closing near the downstream corners, where the flow is reattaching to the surface. The numerical predictions of the position of the center of the main recirculation region range from 21.2 to 65 % of the cylinder breadth, while its reattachment point is found to vary between 63.2 and 95.8 %. Since the mean C_p behavior on the cylinder side is characterized by a low-pressure plateau extending from the upstream corners to the center of the main recirculation and then by a positive gradient roughly up to the reattachment point, the previous differences lead to a large dispersion of the mean C_p predictions, as observed in Fig. 1b.

The data obtained for the time fluctuations of the pressure coefficient are even more dispersed, as can be seen in Fig. 2, in which the same statistics as in Fig. 1 are reported now for the C_p standard deviation. In this case the variability is larger for the numerical results than for the wind tunnel measurements. In all cases there is a peak located slightly upstream of the reattachment of the main mean recirculation vortex, in the zone where the mean Cp increases. In average, the peak is located

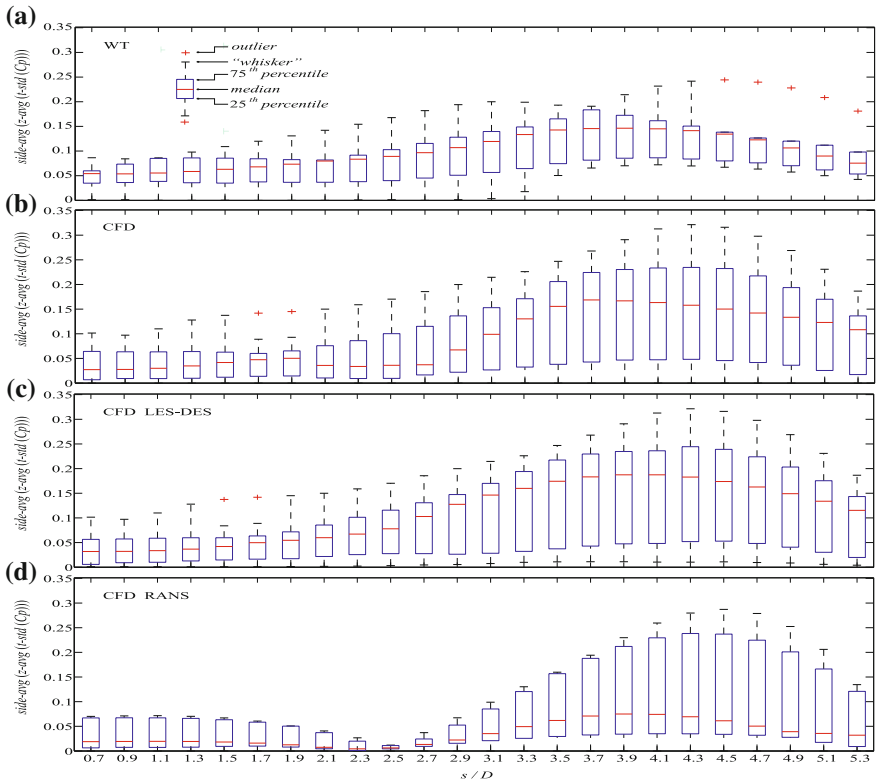

Fig. 2 Statistics of the lateral surface distribution of the Cp standard deviation: wind tunnel data (**a**), computational results (**b**), LES and hybrid URANS/LES results (**c**) and URANS results

more downstream and is more intense in numerical simulations than in experiments (compare Fig. 2a, b). Figure 2c, d compare the distributions of the standard deviation of C_p obtained on the cylinder lateral surface in hybrid and LES simulations to those given by URANS models. Quite surprisingly the differences in the intensity and location of the main peak are rather small; therefore, it seems that turbulence modeling has an effect on the dynamics of the flow over the lateral cylinder sides which is comparable to that of other sources of uncertainties present in simulations and experiments. The main difference is that in hybrid and LES simulations, consistently with the wind tunnel measurements, the value of the standard deviation of C_p has an unique peak along the cylinder side, while in the URANS ones a minimum is also found at a distance of approximately 2D from the upstream corner. The reasons of this behavior are not clear at this stage. The previously described variability in the values of pressure on the cylinder lateral sides leads to a large dispersion in the predictions/measurements of the amplitude of unsteady lift loads (not shown here for the sake of brevity).

As a general remark, the dispersion, which characterizes both the experimental and numerical results for some quantities in the considered flow configuration, suggests that the performance of a LES simulation (but also of an experiment) should be put and evaluated in a probabilistic context, possibly using tools developed in the context of uncertainty quantification. To this aim, the number of flow realizations in the ensemble should be increased. Collaborative and hybrid studies mixing wind tunnel tests and computational simulations are also encouraged.

Acknowledgments The authors acknowledge: the Italian National Association for Wind Engineering (ANIV), the International Association for Wind Engineering (IAWE), the European Research Community On Flow, Turbulence And Combustion(ERCOFTAC), the BARC organizing and scientific committees and the BARC participants for their contributions.

References

1. Arslan, T., Pettersen B., Andersson H.I.: Calculations of the flow around rectangular shaped floating structures. In: Proceedings of the Thirteenth International Conference on Wind Engineering, Amsterdam, The Netherlands (2011)
2. Bartoli, G., Bruno, L., Buresti, G., Ricciarelli, F., Salvetti, M.V., Zasso, A.: BARC overview document—requests for computational simulations—requests for wind tunnel tests. http://www.aniv-iawe.org/barc (2008)
3. Bartoli, G., Borsani, A., Mannini, C., Marra, A.M., Procino, L., Ricciardelli, F.: Wind tunnel study on the aerodynamics of a 5:1 rectangular cylinder in smooth flow. In: Proceedings of the Thirteenth International Conference on Wind Engineering, Amsterdam, The Netherlands (2011)
4. Bronkhorst, A.J., Geurts, C.P.W., van Bentum, C.A.: Unsteady pressure measurements on a 5:1 rectangular cylinder. In: Proceedings of the Thirteenth International Conference on Wind Engineering, Amsterdam, The Netherlands (2011)
5. Bruno, L., Fransos, D., Coste, N., Bosco, A.: 3D flow around a rectangular cylinder: a computational study. J. Wind Eng. Ind. Aerodyn. **98**, 263–276 (2010)
6. Bruno, L., Coste, N., Fransos, D.: Effect of the spanwise features of the computational domain on the simulated flow around a rectangular 5:1 cylinder. In: Proceedings of the Thirteenth International Conference on Wind Engineering, Amsterdam, The Netherlands (2011)
7. Bruno, L., Coste, N., Fransos, D.: Simulated flow around a rectangular 5:1 cylinder: spanwise discretisation effects and emerging flow features. J. Wind Eng. Ind. Aerodyn. **104–106**, 203–215 (2012)
8. Grozescu, A.N., Salvetti, M.V., Camarri, S., Buresti, G.: Variational multiscale large-eddy simulations of the BARC flow configuration. In: Proceedings of the Thirteenth International Conference on Wind Engineering, Amsterdam, The Netherlands (2011)
9. Grozescu, A.N., Bruno, L., Fransos, D., Salvetti, M.V.: Large-eddy simulations of a Benchmark on the Aerodynamics of a rectangular 5:1 cylinder. In: Proceedings of the 20th Italian Conference on Theoretical and Applied Mechanics, Bologna, Italy (2011)
10. Mannini, C., Šoda, A., Schewe, G.: Unsteady RANS modelling of flow past a rectangular cylinder: investigation of Reynolds number effects. Comput. Fluids **39**(9), 1609–1624 (2010)
11. Mannini, C., Šoda, A., Schewe, G.: Numerical investigation on the three-dimensional unsteady flow past a 5:1 rectangular cylinder. J. Wind Eng. Ind. Aerodyn. **99**, 469–482 (2011)
12. Mannini, C., Schewe, G.: Numerical study on the three-dimensional unsteady flow past a 5:1 rectangular cylinder using the DES approach. In: Proceedings of the Thirteenth International Conference on Wind Engineering, Amsterdam, The Netherlands (2011)

13. Ribeiro, A.F.P.: Unsteady RANS modelling of flow past a rectangular 5:1 cylinder: investigation of edge sharpness effects. In: Proceedings of the Thirteenth International Conference on Wind Engineering, Amsterdam, The Netherlands (2011)
14. Schewe, G.: Reynolds-number-effects in flow around a rectangular cylinder with aspectratio1:5. In: Proceedings of the Fifth European and African Conference on Wind Engineering, Florence, Italy (2009)
15. Shirato, H., Yuichi, S., Sasaki, O.: Surface pressure correlation and buffeting force evaluation. In: Proceedings of the Thirteenth International Conference on Wind Engineering, Amsterdam, The Netherlands (2011)
16. Wei, Z., Kareem, A.: A benchmark study of flow around a rectangular cylinder with aspect ratio 1:5 at Reynolds number 1.E5. In: Proceedings of the Thirteenth International Conference on Wind Engineering, Amsterdam, The Netherlands (2011)

Quantifying the Impact of Subgrid Scale Models in Actuator-Line Based LES of Wind Turbine Wakes in Laminar and Turbulent Inflow

H. Sarlak, C. Meneveau, J.N. Sørensen and R. Mikkelsen

1 Introduction

Large Eddy Simulations (LES) have in recent years been applied to studies of wind turbine wakes and their interactions with the atmospheric boundary layer [1–5]. While many subgrid-scale (SGS) models have, over the years, been proposed (see [6]), the effects of various SGS models in simulations of wind turbine wakes has not been documented in great detail yet. In this study, we explore such effects in simulations of single wind turbine under laminar and turbulent inflow conditions. LES of wind turbine wakes are carried out using the actuator line (ACL) model [7]. To examine the effect of using different turbulent closures, various SGS models including the Smagorinsky model and two variants of the mixed-scale model presented in [8], are tested. Simulations are performed on a single turbine placed in uniform and turbulent inflow. Four simulations are performed to identify the role of SGS modeling on the wake characteristics. It is shown that in the near wake region, the mean velocity profiles in the wake are rather insensitive to the SGS model while the different models predict a different far wake. Considerable effects can be observed in profiles of second-order statistics of resolved velocities, as well as in profiles of subgrid-scale eddy viscosity. From comparisons of laminar and turbulent flow it is confirmed that the wake region in laminar inflow case grows less rapidly and extends

H. Sarlak (✉) · J.N. Sørensen · R. Mikkelsen
Technical University of Denmark, Lyngby, Denmark
e-mail: hsar@dtu.dk

J.N. Sørensen
e-mail: jnso@dtu.dk

R. Mikkelsen
e-mail: rfmi@dtu.dk

C. Meneveau
The Johns Hopkins University, Baltimore, USA
e-mail: meneveau@jhu.edu

J. Fröhlich et al. (eds.), *Direct and Large-Eddy Simulation IX*,
ERCOFTAC Series 20, DOI 10.1007/978-3-319-14448-1_23

further downstream in a more concentrated fashion, as compared to the turbulent inflow case, in which the wake grows (i.e. the velocity recovers) much faster.

The Navier-Stokes equation for the problem reads

$$\frac{\partial \mathbf{v}}{\partial t} + \mathbf{v} \cdot \nabla \mathbf{v} = -\frac{\nabla p}{\rho} + \nabla \cdot [(\nu + \nu_{sgs}) \nabla \mathbf{v}] + \mathbf{f}, \tag{1}$$

where

$$\begin{aligned}
\nu_{sgs} &= 0 && \text{if No model (NO)} \\
\nu_{sgs} &= c_s \Delta^2 |\bar{S}| && \text{if Smagorinsky (SM)} \\
\nu_{sgs} &= c_{ms} \Delta^{1.5} q_c^{0.25} |\bar{S}|^{0.5} && \text{if Mix-S (MS)} \\
\nu_{sgs} &= c_{mo} \Delta^{1.5} q_c^{0.25} |\bar{\Omega}|^{0.5} && \text{if Mix-}\omega\text{ (MO)}
\end{aligned}$$

and ρ and ν are the fluid density and molecular viscosity, respectively. Also, $\mathbf{v}$ represents the filtered velocity vector, p is the modified pressure, and $\mathbf{f}$ is the external body force acting on the flow due to the presence of the wind turbine. ν_{sgs} is the eddy viscosity to be specified by the SGS model. Four different SGS models are used to evaluate ν_{sgs}, as described in Eq. 1. Here, *NO model* refers to the case in which there is no explicit representation for turbulent viscosity and the only effects of kinetic energy dissipation are those arising from numerical dissipation. This case is included here as a measure of the relative impact of the SGS models. *Smagorinsky* refers to the standard Smagorinsky model, and *Mix-S* and *Mix-*ω represent the two variants of the mixed-scale model [8]. $q_c = (\tilde{\bar{u}}_i - \tilde{u}_i)^2$ is the sub-filter scale kinetic energy obtained by an explicit filtering (shown by bar) of larger size than the grid size, δ being the grid size, $\tilde{S}_{ij}(\mathbf{x}, t)$ and $\Omega = \nabla \times \tilde{u}(\mathbf{x}, t)$ are the resolved strain rate and vorticity, respectively. $c_s = 0.01$, $c_{mo} = 0.01$ and $c_{ms} = 0.06$ are (fixed) model constants used in the present study. The mixed-scale model is chosen in the existing code (see below) because of its low computational cost and its performance. Formally, it depends on the small scales through the term q_c (as a result of scale similarity) and on the resolved large scales through the resolved velocity gradient tensor. As a result, the model is able to predict a laminar flow close to the solid wall without a damping function.

In the ACL approach [7], each turbine blade is represented by a line on which the forces are being applied according to the velocity field and the angle of attack:

$$\mathbf{f} = (L, D) = 0.5 \rho V_{rel}^2 c (C_L \mathbf{e}_L + C_D \mathbf{e}_D), \tag{2}$$

where V_{rel} is the relative velocity, C_L and C_D are lift and drag coefficients, $\mathbf{e}_L$ and $\mathbf{e_D}$ are unit vectors showing the direction of the (local) lift (L) and drag (D) forces and c is the airfoil section chord length. These forces are commonly smeared out by Gaussian regularization function which is applied to the flow field as shown in Fig. 1.

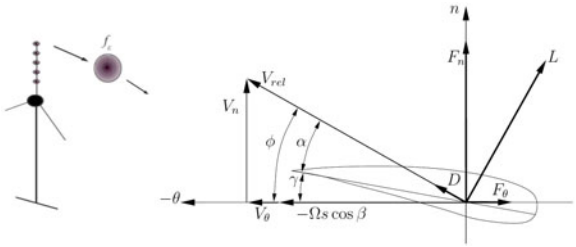

Fig. 1 Actuator line (ACL) concept and velocity triangle used to compute the angle of attack. V_{rel} is formed from the normal V_n and tangential V_θ velocity components, ϕ is the angle between V_{rel} and the rotor plane, Ω is the angular velocity of the rotor, and α is the angle of attack. The *circle* shows how the force is smeared out around the center point and applied to the flow field

2 Simulation Set Up

Simulations are performed using the in-house finite volume solver Ellipsys3D [9, 10]. The equations are discretized in time using a second order backward Euler method. The convective fluxes are discretized using a blend of fourth order central differencing (CDS4) (90 %) and QUICK (10 %) to maintain the required accuracy while avoiding numerical oscillations. The CFL number is kept around 0.1 using a non-dimensional time step of $dt^* = 0.005$ (time is non-dimensionalized with inflow velocity and the rotor radius). A structured grid with a total of $576 \times 144 \times 144$ points is employed in a domain of $50R \times 20R \times 20R$ (to avoid wall effects according to the criteria proposed in [11]) in the streamwise (x), spanwise (y) and vertical (z) directions, respectively. The turbine is resolved using 20 points per blade. R represents the blade length. Symmetry boundary condition is used for all surrounding walls while inflow and convective outflow BC are reserved for the inlet and outlet planes. Turbine is located at 7R downstream the inlet.

A uniform inlet velocity is applied to the flow, and the viscosity is set corresponding to a Reynolds number of $Re_r = 50{,}000$ where Re_r refers to the Reynolds number based on the inflow velocity and the rotor radius. For the turbulent case, (under) resolved turbulence [12], is generated with high mean turbulence intensity of 14 %. Based on the Taylor's frozen hypothesis, moving 2D snapshots are taken from the box and inserted upstream of the rotor using body forces (to maintain velocity profile) in the momentum equation, to input the turbulence.

3 Results

To have a clear comparison, both time averaged and instantaneous values are compared for different SGS models in laminar as well as turbulent inflow cases. The first step is to verify whether the different models predict different eddy viscosities. Figure 2 shows that in both laminar and turbulent inflow cases the different SGS models predict quite different values of eddy viscosity. The eddy viscosity predicted

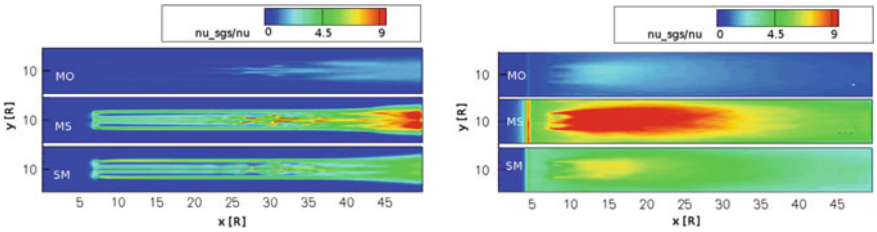

Fig. 2 Time averaged viscosity ratio in laminar (*left*) and turbulent (*right*) inflow. *Upper* MO, *middle* MS, *lower* SM

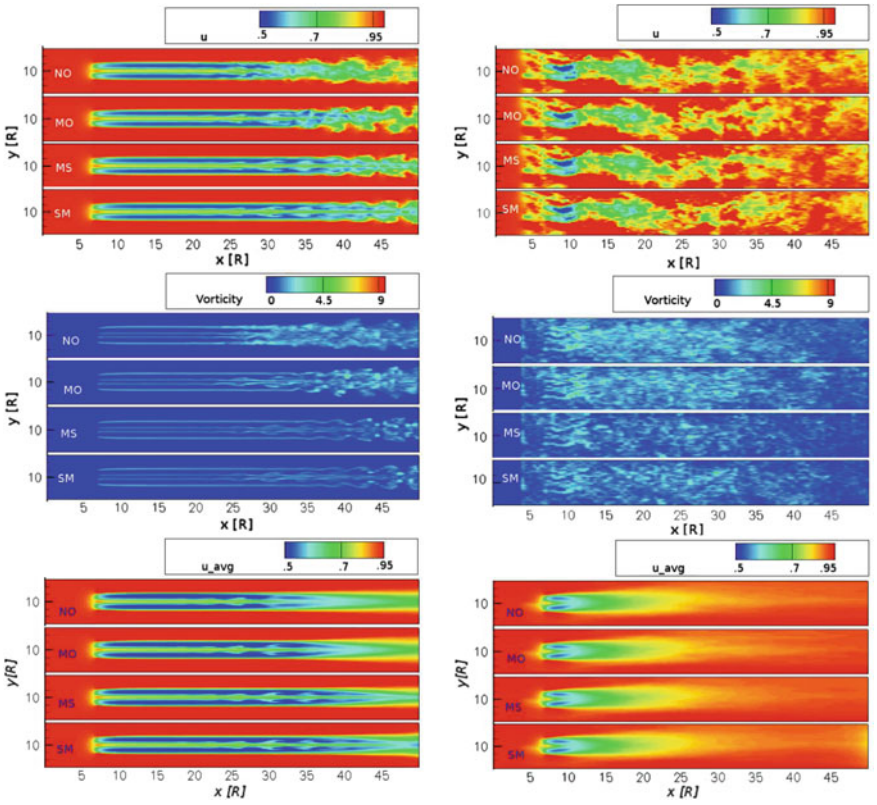

Fig. 3 (*Top* to *bottom*) Instantaneous streamwise velocity, vorticity field, and the mean streamwise velocity plots in laminar (*left*) and turbulent (*right*) inflow for (*top* to *bottom*) NO, MO, MS, and SM models respectively

by the NO model is obviously zero so it is excluded from the plots. As can be seen the Mix-ω model predicts the lowest eddy viscosity ratios, ranging around 2–3, while the Mix-S gives the highest ratios (Fig. 2).

Figure 3 shows the instantaneous streamwise velocity, vorticity and time averaged streamwise velocity plots in laminar inflow (left) as well as turbulent (right) inflow.

As can bee seen visually in the laminar inflow case, the velocity and vorticity are almost the same in the near wake region and the results are insensitive to the SGS model up to about 25R downstream. As one goes down to the far wake, differences begin to appear. The flow goes through a rapid transition and the vortices break down quickly when the NO model is used, and, correspondingly, the fastest wake recovery is obtained with the NO model. The wake recovery is slowest for the SM (Smagorinsky) model where the transition extends all the way to the outlet in 50R downstream. Both versions of the mixed model perform somewhere in between the NO model and the Smagorinsky model, with the Mix-ω closer to the NO model and the Mix-S closer to the Smagorinsky, the latter being reasonable due to the similarities of both models. Results of both mixed models are in agreement with the eddy viscosity behaviour plotted in Fig. 2.

For the turbulent inflow case, however, there is almost no difference in instantaneous and the time averaged velocities, neither in the near wake nor the far wake, although the eddy viscosities are still quite influenced by the SGS models. The instantaneous vorticity plots show however a small difference in the turbulent structures; notably, the flow downstream the ACL looks more homogeneous with stronger vorticity cores in the NO and Mix-ω models and, again, the Mix-S and Smagorinsky models are more similar.

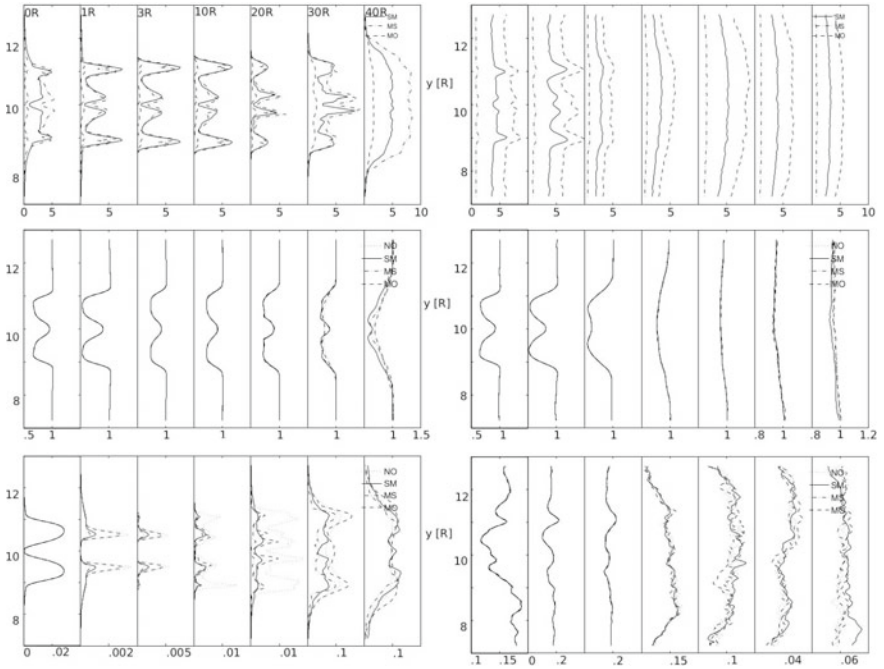

Fig. 4 (*Top* to *bottom*) Plots of the normalized eddy viscosity, streamwise mean velocity and $\overline{\langle u'u' \rangle}$ component of turbulent stress tensor downstream the rotor in laminar (*left*) and turbulent (*right*) inflow for (*top* to *bottom*) NO, MO, MS, and SM models respectively (the downstream location is indicated only in the *top left* figure)

Figure 4 compares the wake profile and turbulent (kinematic) normal stress obtained at different locations downstream of the turbine. As it was seen before, the eddy viscosities are predicted with very large variations for different models and also for laminar versus turbulent inflow. The velocity profiles are less sensitive to the SGS models and there is some difference in turbulent stresses predicted by different models, especially in the laminar near wake region, where the flow is more symmetric than is the far wake. It is also clear from the figures that the wake expansion is higher in turbulent inflow as compared to the laminar inflow, and hence it recovers much faster.

4 Conclusions and Future Work

Results from LES of a wind turbine using the ACL model with laminar and turbulent inflow are compared for four different SGS models. Results show that the SGS models have a strong impact for both laminar and turbulent inflow on the eddy viscosities and for the laminar inflow on the turbulent normal stresses in the near wake. There is however very little dependence of mean velocity profiles with respect to SGS models, for both laminar and turbulent inflows in the near wake region. From comparisons of laminar and turbulent inflow, it is shown that the wake region in the laminar inflow case grows less rapidly and extends further downstream in a more concentrate fashion, as compared to the turbulent inflow case in which the wake grows (recovers) much faster. Validation of the results with new experimental data is being performed and will be published in a later paper.

References

1. Jimenez, A., Crespo, A., Migoya, E., Garcia, J.: Advances in large-eddy simulation of a wind turbine wake. J. Phys. Conf. Ser. **75**, 012041 (2007)
2. Troldborg, N., Sørensen, J.N., Mikkelsen, R.F.: Numerical simulations of wake characteristics of a wind turbine in uniform inflow. J. Wind Energy **1**(13), 86–99 (2010)
3. Calaf, M., Meneveau, C., Meyers, J.: Large eddy simulation study of fully developed wind-turbine array boundary layers. Phy. Fluids **22**(015110), 116 (2010)
4. Calaf, M., Parlange, M.B., Meneveau, C.: Large eddy simulation study of scalar transport in fully developed wind-turbine array boundary layers. Phys. Fluids **23**(12), 126603 (2011)
5. Wu, Y., Porte-Agel, F.: Large-eddy simulation of wind-turbine wakes: evaluation of turbine parametrisations. Bound.-Layer Meteorol. **138**, 345366 (2011)
6. Sagaut, P.: Large-Eddy Simulation For Incompressible Flows—An Introduction, 3rd edn, 556 pp. Springer, New York (2005)
7. Sørensen, J.N., Shen, W.Z.: Numerical modeling of wind turbine wakes. J. Fluids Eng. **144**, 393–399 (2002)
8. Sagaut, P.: Simulations numeriques decoulements decolles avec des mod'eles de sous-maille. Ph.D. thesis, University of Paris VI, France (1995)
9. Michelsen, J.A.: Basis3D—a platform for development of multiblock PDE solvers. Technical report AFM 92–05, Technical University of Denmark (1992)

10. Sørensen, N.N.: General purpose flow solver applied to flow over hills. Risø-R-827-(EN), RisøNational Laboratory, Denmark (1995)
11. Baetke, F., Werner, H.: Numerical simulation of turbulent flow over surface-mounted obstacles with sharp edges and corners. J. Wind Eng. Ind. Aerod. **35**, 129–147 (1990)
12. Mann, J.: The spatial structure of neutral atmospheric surface-layer turbulence. J. Fluid Mech. **273**, 141–168 (1994)

Part IV
Hybrid Models

Elements and Applications of Scale-Resolving Simulation Methods in Industrial CFD

F. Menter

1 Introduction

Historically, industrial CFD simulations have been based on the Reynolds Averaged Navier-Stokes Equations (RANS). For many decades, the only alternative to RANS was Large-Eddy Simulation (LES), which has however failed to provide solutions for most flows of engineering relevance due to excessive computing power requirements for the simulation of wall-bounded flows. On the other hand, RANS models have shown their strength essentially for wall-bounded flows, where the calibration according to the law-of-the-wall provides a sound foundation for further refinement. For free shear flows, the performance of RANS models is much less uniform. For this reason, hybrid models are gaining acceptance, where large eddies are only resolved away from walls and where the wall boundary layers are entirely covered by a RANS model e.g. Detached Eddy Simulation DES [1] or Scale-Adaptive Simulation SAS [2].

Such simulations are possible today for industrial-scale applications on medium sized computing systems (100–1,000 cores) and make their way into the industrial environment. These models are typically applied to flows with strong flow instabilities which cover a wide range of applications. Examples are the simulation of heat-transfer phenomena [3], acoustic stimulations [4] or gas turbine simulations [5]. The grids used in such simulations are typically in the range of 10^7–10^8 and therefore not drastically larger than high quality RANS meshes. The increase in computing costs results mainly from a need to integrate the equations in the time domain. This requires sufficiently long running times for establishing a proper flow-field and for allowing sufficient time for statistical averaging.

F. Menter (✉)
ANSYS Germany GmbH, Otterfing, Germany
e-mail: florian.menter@ansys.com

J. Fröhlich et al. (eds.), *Direct and Large-Eddy Simulation IX*,
ERCOFTAC Series 20, DOI 10.1007/978-3-319-14448-1_24

While these methods can lead to a significant increase in accuracy, their application is still not a routine procedure in most companies, partly due to the intricacies in mesh generation and simulation setup and partly because of the long turn-around-time. Nevertheless, such methods are well on their way of gaining acceptance into the industrial design cycle within the next few years.

A further step in hybrid modeling involves the resolution of parts of the turbulence inside of wall boundary layers. Due the well-known resolution demands of classical wall-resolved LES, industrial methods aim at the application of a RANS model in the innermost part of the wall boundary layer and then to switch to an LES model for the main part of the boundary layer [6]. Such models are termed Wall Modelled LES (WMLES). It can be shown that this approach avoids/reduces the unfavorable Reynolds number scaling of classical LES, which results from ever decreasing scales (with increasing Reynolds number) close to the viscous sublayer. While such models are available in advanced industrial CFD codes, their exploration as industrial CFD tools is just starting. There are several reasons for that. The first being that RANS models are fairly strong in predicting attached and mildly separated boundary layers. The second is that the CPU power required for WMLES is still too high for most applications to be practical for complete configurations. However, such methods can be used for studying reduced parts of the flow domain, either in separation or in the framework of an embedded or zonal LES method.

Another essential element of Scale-Resolving Simulations (SRS) are methods for generating resolved turbulence structures at inlets to the LES domain. This is most conveniently achieved by synthetic turbulence generated from the information from the upstream RANS model. One of the methods favored by the authors group is the Vortex Method [7], which offers a fair compromise between complexity and accuracy.

Finally, for large domains, it is frequently only necessary/possible to cover a small portion with Scale-Resolving Simulation (SRS) models, while the majority of the flow can be computed in RANS mode. In such situations, zonal or embedded LES methods are attractive e.g. [8, 9]. Such methods are typically not new models in the strict sense, but allow the combination of existing models/technologies in a flexible way in different zones of the simulation domain. Important elements of zonal models are interface conditions, which convert turbulence from RANS mode to resolved mode at pre-defined locations. In most cases, this is achieved by introducing synthetic turbulence based on the length and time scales from the RANS model, however with direct coupling with the upstream RANS model.

The challenge for the engineer is to select the most appropriate model for the intended application. Unfortunately, none of the available SRS models is able to efficiently cover all industrial flows. A compromise has to be made between generality and CPU requirements. The paper will discuss the main modeling approaches available in todays industrial CFD codes and provide some guidelines as to their optimal usage. Numerous examples of validation cases will be shown and the pros and cons of the different methods will be highlighted.

2 Elements of Hybrid RANS-LES Turbulence Models

In this chapter, different elements and aspects of modeling industrial flows with hybrid RANS-LES methods will be discussed, focusing on formulations favored by the authors group.

2.1 Global RANS-LES Hybrid Model Formulation

The authors group focuses on two types of global hybrid RANS-LES models, namely, Detached Eddy Simulation (DES) and Scale-Adaptive Simulation (SAS). The first is an explicit blend of RANS and LES based on the ratio of the turbulence length scale and the grid spacing. The second is a so-called second generation URANS model, which does not involve the grid spacing explicitly in the RANS formulation. Both formulations have their advantages and disadvantages.

The main potential problem with DES is that the RANS solution can be affected by the grid spacing. If that happens inside boundary layers, the result is often "Grid-Induced Separation (GIS)" [10]. In order to protect the boundary layer from this effect, the use of shielding functions has been proposed [10] and later adopted by [11]. The resulting model is termed Delayed Detached Eddy Simulation (DDES). It should be noted that shielding can only reduce the problem, but not eliminate it. This means that GIS can still happen in case of strong mesh refinement. Without shielding, the problem appears approximately if $\Delta_{\max} < \delta$ and with shielding if $\Delta_{\max} < 0.2\delta$ ($\Delta_{\max}$ being the max. edge length of a local cell and δ the local boundary layer thickness) [12]. In addition, DDES can show "grey zones", where the model does operate neither in RANS nor in LES mode. This can happen either, because the grid resolution is not sufficient for LES (but already affects the RANS model) or when there is insufficient instability in the flow to generate turbulence structures quickly enough in the zone of interest.

The main potential problem with SAS is that it can remain in (U)RANS mode, even though the user is interested in a scale-resolved simulation. This situation occurs in flows, which do not show a strong enough flow instability to push the model into the LES regime [13].

2.2 Models for Large Eddy Simulation (LES)

There is a variety of model formulations for LES implemented in the ANSYS CFD codes.

- Smagorinsky (standard and dynamic [14, 15])
- k-equation based model (dynamic [16])
- WALE model [17]
- Wall Modelled LES (WMLES, [18])

In industrial CFD (and not only there) the LES models of choice are eddy-viscosity formulations. Their main purpose is to provide proper dissipation at the small scales. This is in principle not a very demanding task and can be achieved by all models listed. LES model selection is therefore much less demanding on the user than RANS model selection. However, the standard Smagorinsky model has the disadvantage that it does not provide zero eddy-viscosity for simple shear flows (laminar flows, viscous sublayer). This problem is avoided by the dynamic and the WALE model. Due to some of the conceptual problems of the dynamic modeling approach (need for averaging, potentially negative eddy-viscosities, large variation of dynamic coefficient), the more optimal choice in this authors opinion is the WALE model.

Wall Modelled LES (WMLES) models are a fairly new member of industrial LES formulations. Their main goal is to allow integration to the wall, even at high Reynolds numbers, without the excessive grid resolution requirements of classical wall-resolved LES. WMLES is based on the concept of covering the inner portion of the boundary layer by a RANS and the outer portion by a LES formulation. This avoids the very high resolution requirements of LES in the inner wall layer. A very simple and promising approach to WMLES has been proposed by Shur et al. [18]. It is based on a reformulation of the length scale used in the LES zone and by blending it with the mixing length (RANS) model in the inner part of the boundary layer. The formulation of Shur et al. is given by:

$$\nu_t = \min\left\{(\kappa d_W)^2\,,\,(C_{SMAG}\Delta)^2\right\}\left\{1-\exp\left[-\left(y^+/25\right)^3\right]\right\}S \qquad (1)$$

where d_W is the wall distance, S is the shear strain rate and Δ a measure of the cell size. This model was originally calibrated for a 4th order central difference scheme (Shur et al. [18]), and needs to be lightly adjusted for lower order schemes.

2.3 Periodic Channel Flow

Simulations were carried out for periodic channel flows on grids with the characteristics given in Table 1. The domain size was $LX = 16h$, $LY = 2h$, $LZ = 3h$ (h being half the channel height—this corresponds approximately to the boundary layer thickness for wall boundary layers). The main characteristics of WMLES is clearly visible from Table 1: the non-dimensional values for $\Delta X+$ and $\Delta Z+$ are far beyond the limits of standard LES methods (which are $\Delta X+ = 40$, $\Delta Z+ = 20$). For WMLES, one only has to ensure a minimum number of cells per boundary layer volume $\delta \times \delta \times \delta$. In the current formulation the minimum resolution per boundary layer volume is of the order of $10 \times 40 \times 20$ cells (streamwise, normal and spanwise).

Figure 1 shows the velocity profiles in logarithmic scale for these simulations using ANSYS-Fluent. It is well known that the use of hybrid models like DES can result in a strong log-layer mismatch and a corresponding error in the wall shear stress when applied as a WMLES model. Figure 1 shows that the log-layer miss-match

Table 1 Grids for periodic channel flow at different Reynolds number using WMLES

Re_τ	Cells	Nodes	$\Delta X+$	$\Delta Y+$	$\Delta Z+$
395	384,000	81 × 81 × 61	040.0	0.2 ÷ 30	20.0
395	1,764,000	141 × 141 × 91	026.6	0.2 ÷ 20	13.3
760	480,000	81 × 101 × 61	76.9	0.2 ÷ 30	38.5
1,100	480,000	81 × 101 × 61	111.4	0.2 ÷ 30	55.7
2,400	528,000	81 × 111 × 61	243.0	0.2 ÷ 30	121.5
18,000	6,240,000	81 × 131 × 61	1822.7	0.2 ÷ 30	911.4

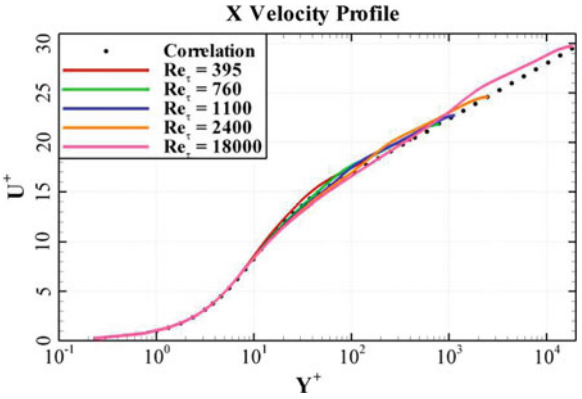

Fig. 1 Velocity profiles in logarithmic scale for periodic channel flow using WMLES for various Reynolds numbers

can be reduced to a relatively small shift at the RANS-LES interface, resulting in a high quality solution even at very high Re numbers for the above formulation (see also [18]).

2.4 Flat Plate Boundary Layer

A more challenging test case is the flow over a flat plate boundary layer, where the boundary layer grows and where synthetic turbulence needs to be provided at the inlet. The grid for the boundary layer test case has the parameters given in Table 2.

Table 2 Grids for boundary layer flow at different Reynolds number using WMLES

Re_Θ	Cells	Nodes
1,000/10,000	1,050,000	251 × 71 × 62

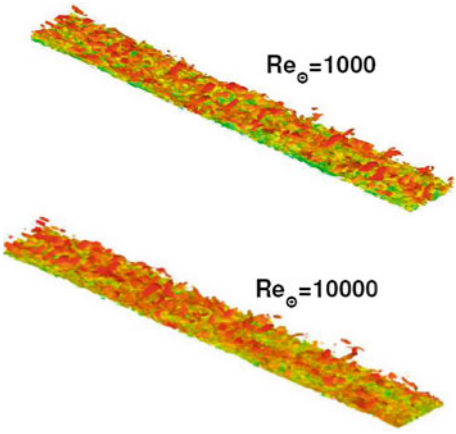

Fig. 2 Turbulence structures for wall boundary layer flow. *Top* $Re_\Theta = 1{,}000$, *Bottom* $Re_\Theta = 10{,}000$

Figure 2 shows the turbulent structures for a wall boundary layer flow using the WMLES option. Again the outer part is covered by LES and the near wall part by RANS. The flow was computed with ANSYS-Fluent and the turbulence at the inlet was generated by the Vortex Method (e.g. [19]). The turbulence was well maintained as can be seen from Fig. 2. In Fig. 3 the wall shear stress is displayed. The WMLES recovers quickly from the synthetic turbulence and maintains a proper wall shear stress downstream.

Figure 4 shows the velocity profile of a simulation for the boundary layer at $Re_\Theta = 10{,}000$. Such a Re number is typically out of reach for wall-resolved LES due to the large grid resolution required. In the present study a grid with only $\approx 1.3 \times 10^6$ cells was used ($\Delta x+ \approx 700$, $\Delta z+ \approx 350$). Synthetic inlet turbulence was generated using the Vortex Method. The logarithmic layer is captured very well as seen in Fig. 4.

It should be noted that WMLES is still substantially more computationally expensive than RANS. However, it avoids the excessive Re number scaling of classical wall-resolved LES and allows the simulation of limited parts of technical devices at high Reynolds numbers for which RANS model simulations are not of sufficient accuracy.

2.5 Zonal RANS-LES Models

As pointed out in the previous sections, hybrid models like DES and SAS rely on flow instabilities to generate turbulent structures in large separated regions without the explicit introduction of unsteadiness through the boundary conditions. However, there are situations, where such instabilities are not present or are not reliable to serve this purpose. In such cases, it is desirable to apply RANS and the LES models in predefined zones and provide clearly defined interfaces between them. At these interfaces, the modeled turbulent kinetic energy from the upstream RANS model is

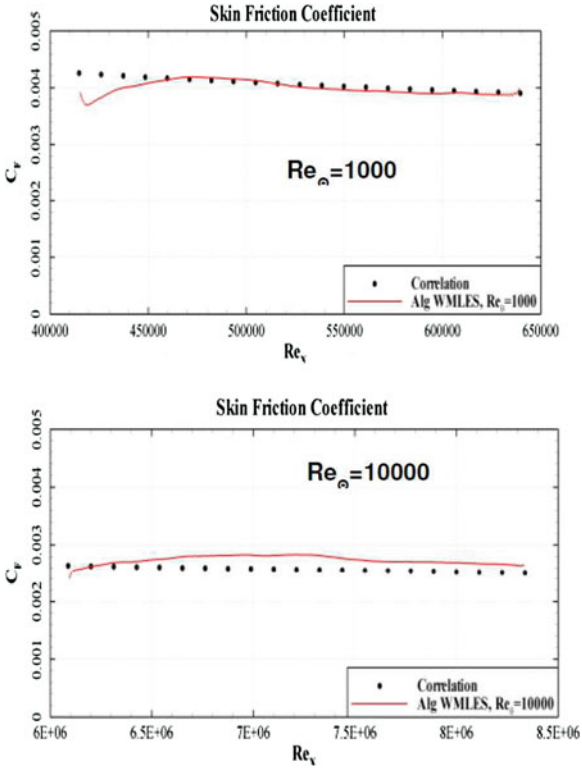

Fig. 3 Wall shear stress coefficient for wall boundary layer flow. *Top* $Re_\Theta = 1{,}000$, *Bottom* $Re_\Theta = 10{,}000$

converted explicitly to resolved scales at an internal boundary to the LES zone. The LES zone can then be limited to the region of interest where unsteady results are required. There are numerous zonal RANS-LES concepts, and it is not possible to cover all of them. The following results are therefore limited to the Embedded LES (ELES) method implemented in ANSYS-Fluent [8].

This approach has been selected as it is attractive from an industrial CFD perspective. It allows the user to pre-specify RANS and LES zones in a single CFD simulation. At the RANS-LES interface, the modeled turbulence from the RANS model is converted into resolved turbulence using the methods previously available for this purpose at inlets. ELES allows the selection of virtually all RANS models in the RANS domain and all algebraic LES models in the LES region. Figure 5 shows the application of ELES to a channel flow. The front portion of the channel is covered by the SST RANS model [20]. The RANS-LES interface uses the Vortex Method to convert modeled turbulence to resolved synthetic turbulence and the WALE LES [17] model to provide an LES eddy-viscosity. Downstream, the method switches back to RANS. The numerical method allows switching from Second Order Upwind to Central Difference between the RANS and the LES region.

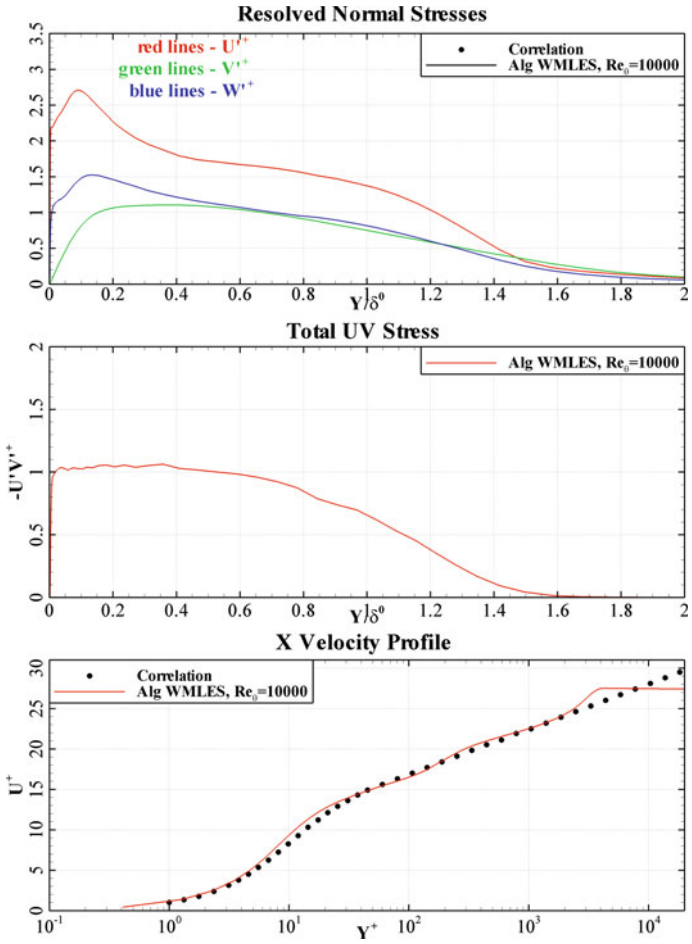

Fig. 4 Profile information for the flat plate boundary layer simulations. $Re_{\Theta} = 10{,}000$

Figure 6 shows a comparison of the LES results inside the embedded region with DNS data, both for the mean flow profile and the turbulence RMS values. The agreement is quite close, considering the limited length of the LES zone.

3 Application Examples

Numerous application examples will be shown. They typically originate from industry-specific validation projects/workshops in which the authors group has participated. Such test cases are characterized by reduced geometric complexity, but provide experimental data, typically not available for industrial applications.

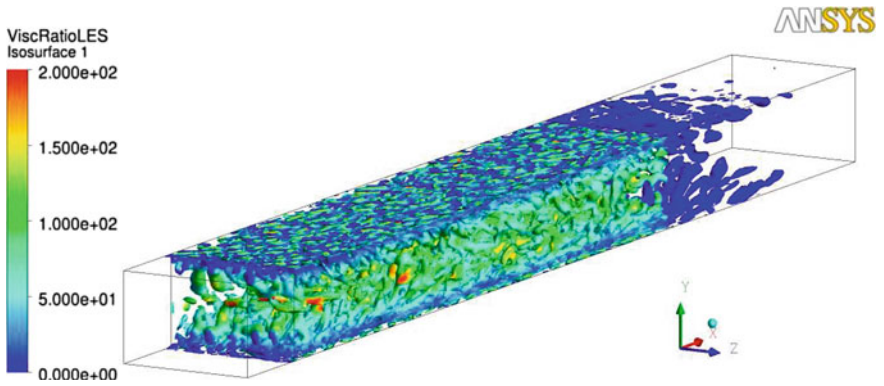

Fig. 5 Channel flow. Viscosity ratio on iso-surfaces of Q-criterion (−500)

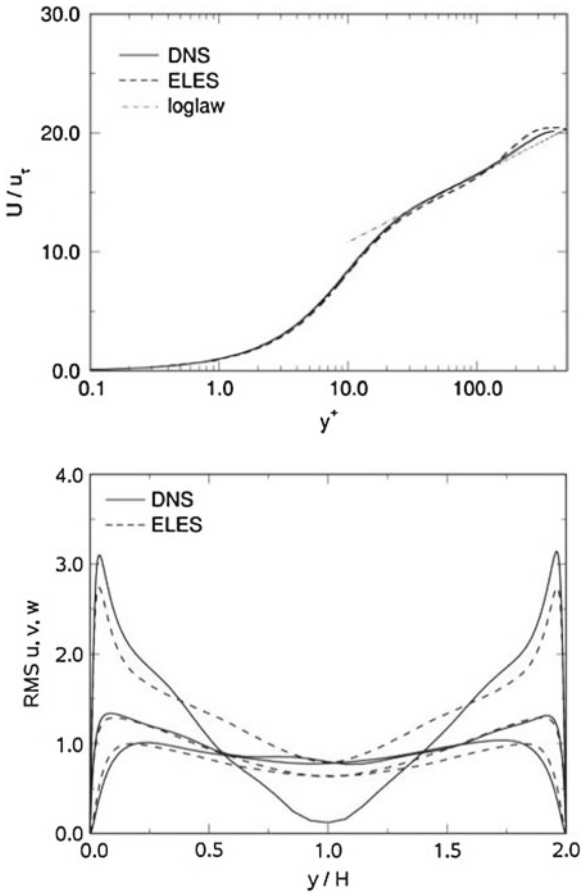

Fig. 6 Fully developed channel flow. Mean velocity values inside LES zone (*top*), rms values inside LES zone at $x = 1.5 + 1.5\pi$ (*bottom*)

3.1 Acoustic Cavity

Air flow past a 3-D rectangular shallow cavity was calculated in order to test the SAS models ability to predict correct spectral information for acoustics applications. The cavity geometry and flow conditions corresponding to the M219 experimental test case of Henshaw [21]. The experiment investigates the noise generation due to turbulent structures forming from the front lip of the cavity and interacting with the cavity walls.

Figure 7 shows the turbulent structures, produced by the SST-SAS model (iso-surface Q-criterion). The power spectral density (PSD) of the transient pressure signals calculated and measured by sensors on the cavity bottom near the leading and the downstream wall respectively is plotted in Fig. 8. These plots show that the PSD levels are captured in good agreement with the data. Similar agreement was achieved for the other experimental locations (not shown here) Kurbatskii et al. [22].

3.2 NACA 0021 Airfoil Beyond Stall

This low Mach number flow around a symmetric NACA 0021 airfoil was experimentally investigated by Swalwell et al. [23]. The flow is characterized by a massive separation zone behind the airfoil. The experiment was carried out at a high angle of attack of $\alpha = 60°$ and at a chord-based Reynolds number of $Re = 2.7 \times 10^5$.

The spanwise extension of the computational domain was selected to be four chord-lengths for this calculation, and an O-type hexahedral grid with $140 \times 101 \times 134$ nodes, provided for the DESider consortium, was used for the SST-SAS simulation with the ANSYS-CFX solver. A timestep equal to 3 % of the convective timescale (chord length over the inlet velocity magnitude) was used. This corresponds to a Courant number of about unity in the separated zone just downstream of the airfoil.

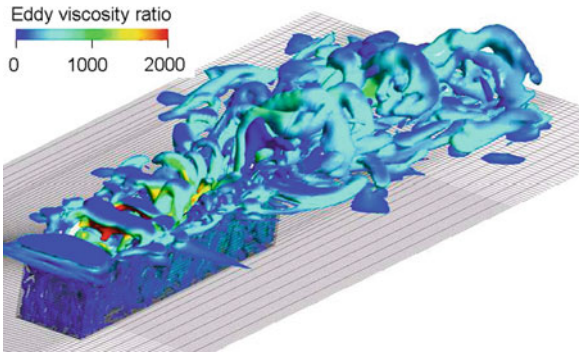

Fig. 7 Resolved turbulent structures for cavity flow: iso-surface $\Omega 2 - S2 = 5 \times 105\ s - 2$

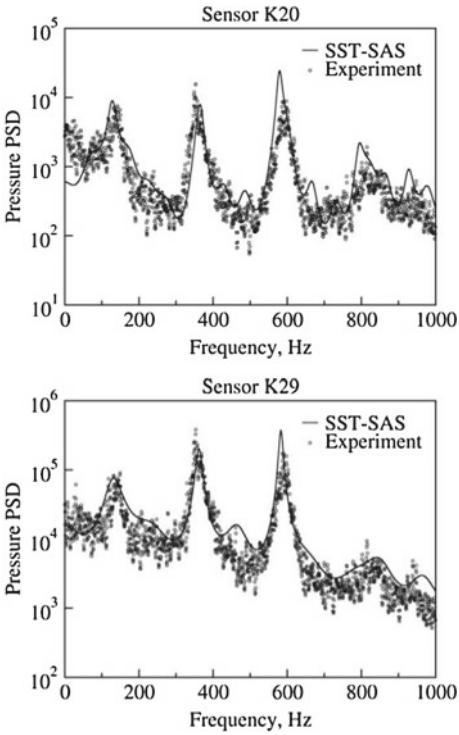

Fig. 8 Power spectral density of the transient wall pressure signals on the cavity *bottom left* sensor K20 located close the front wall, *right* sensor K29 located close to the rear wall

Figure 9 shows a comparison of the computed and the experimental pressure distributions. The agreement is good and within the range of other simulations in the DESider project. Figure 10 shows the turbulent structures (iso-surface Q-criterion) computed by the SST-SAS model behind the airfoil. The structures are essentially resolved down to the grid limit with the larger structures indicating the grid coarsening away from the airfoil. Unsteady SST simulations show the typical single-mode vortex separation expected from classical URANS models.

The experience gained during the simulation of this flow showed the importance of sufficiently long physical time integration for the correct prediction of the average surface pressure and for the low-frequency part of the spectra of forces. During the reported simulation, about 400 convective units based on chord length have been run for the transient statistics after first establishing the solution. In order to achieve better averaging, the spectra of forces have been calculated for each grid section separately and then averaged across the spanwise direction. Figure 11 shows the power spectral densities of the lift and drag coefficients, which are in good agreement with the data, demonstrating the correct temporal response of the model.

The integral lift and drag coefficients, presented in Table 3, are predicted with 2 % accuracy compared to the measurements. It should be noted that a slight dependency of these values on the spanwise size of the domain was observed by some partners in the DESIDER project. This ratio was not varied in the current simulations.

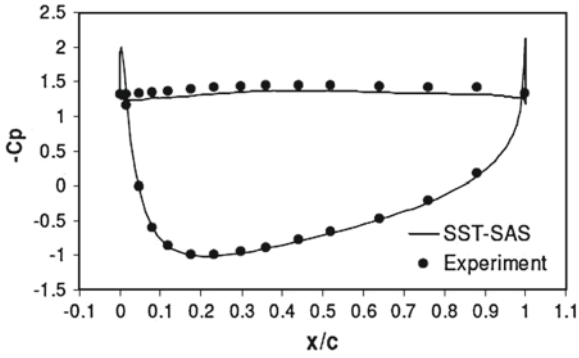

Fig. 9 Comparison of experimental and numerical wall pressure distribution

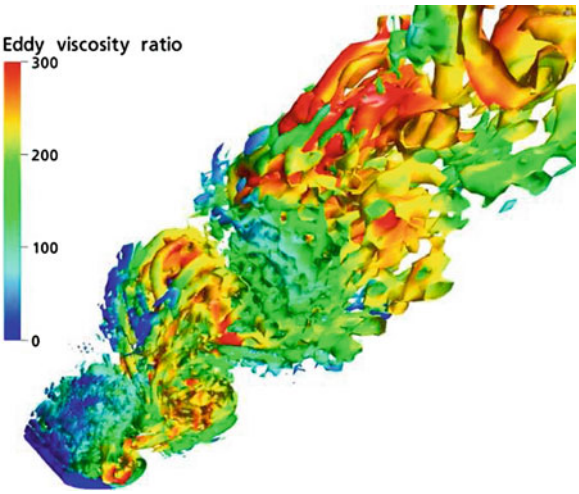

Fig. 10 SAS-resolved turbulent structures behind the airfoil

The good prediction of the power spectral densities for this test case using the SST-SAS model demonstrates the accuracy of the model in the time/frequency domain. In Refs. [2, 24] the SAS model is described in detail and is applied to a wide variety of generic and industrial-like flows.

3.3 Generic Fighter Aircraft

Figure 12 shows SAS simulations over a generic airplane geometry. The simulation ($Re = 2.8 \times 10^6$, $\alpha = 15°$) has been carried out on an unstructured mesh with 11×106 control volumes. The upper part shows the geometry and the turbulent structures produced by the simulation. The lower part shows a comparison between the experimental data and the time averaged simulation. The simulation is in good agreement with the exp. data [25].

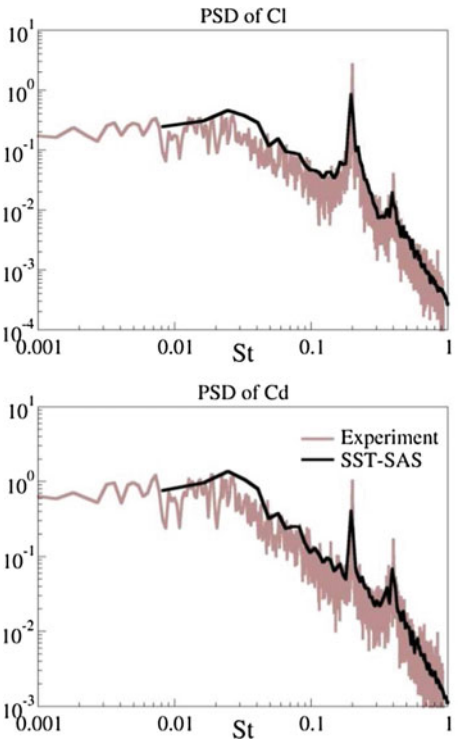

Fig. 11 Turbulent spectra of forces for NACA0021 airfoil: *top* power spectral density of the lift coefficient, *bottom* power spectral density of the drag coefficient

Table 3 Lift and drag coefficients for the NACA 0021 at 60° angle of attack

	Lift coefficient, CL	Drag coefficient, CD
SST-SAS	0.915	1.484
Experiment	0.931	1.517

3.4 Heat Transfer in T-Junction

The following example is a flow through a pipe T-junction with two streams at different temperatures. This testcase was a used as a benchmark of the OECD to evaluate CFD capabilities for reactor safety applications [26]. The geometry and grid are shown in Fig. 13a, b. The grid consists of ≈5 million hexahedral cells. This flow is not easily categorized. In principle it can be computed with SAS and DDES models in SRS mode (not shown). This means that the instability in the interaction zone between the two streams is sufficiently strong to generate unsteady resolved turbulence. However, it was also observed, that these simulations are extremely sensitive to the details of the numerical method employed or the shielding function used. The SAS model provided "proper" solutions only when a pure Central Difference scheme was selected, but remained in URANS mode in case of the Bounded Central Difference scheme. The DDES model provided correct solutions, when a non-conservative

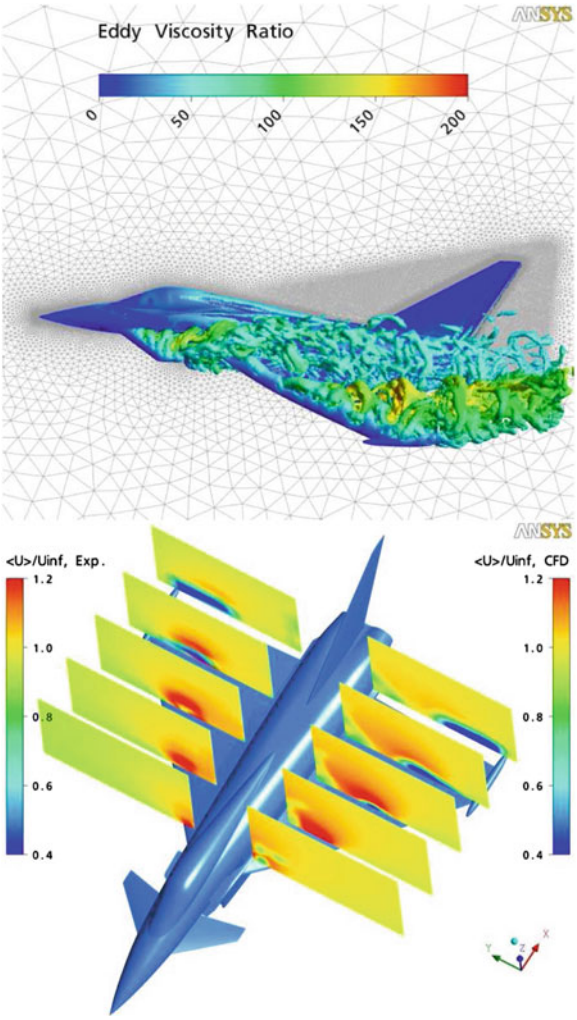

Fig. 12 Flow over generic airplane configuration FA-5. *Top* flow structures. *Bottom* comparison of exp. and SAS axial flow component (Geometry and data are Courtesy of EADS Deutschland)

shielding function was used but produced only weak unsteadiness in case of a conservative shielding function. It is therefore better to apply the ELES model, where modeled turbulence is converted into synthetic resolved turbulence in both pipes upstream of the interaction zone at pre-defined RANS-LES interfaces. In addition, the turbulence model was switched from SST to WMLES at these interfaces. This approach then avoids the need for the flow instability of the interacting streams to generate resolved scales.

Figure 13c shows that the resolved turbulence starts already upstream of the interaction zone due to the introduction of synthetic turbulence. Figure 13d shows a comparison of computed and experimental axial velocity profiles in the main pipe at

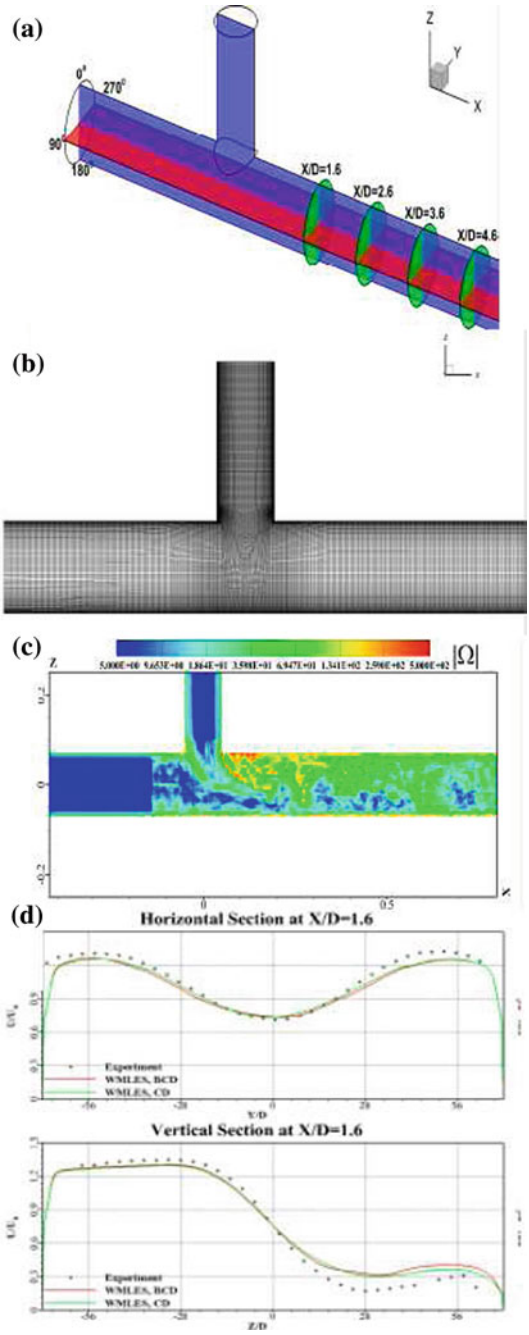

Fig. 13 T-Junction simulation. **a** Geometry. **b** Grid. **c** turbulence structures. **d** Axial velocity at station $X/D = 1.6$ for *horizontal* and *vertical lines*

$X/D = 1.6$. The method provides a good agreement between the simulations and the experimental data. It can also be seen that the switch from CD to BCD does not affect the solutions. This is different from the observation with the SAS model, which reacts sensitive to such changes in the current testcase.

4 Summary

An overview of Scale-Resolving Simulation (SRS) technologies developed for the ANSYS CFD codes was presented. The underlying principles, as well as some of the pros and cons of different modeling approaches haven been discussed. Numerous genetic and application-oriented examples have been shown.

References

1. Spalart, P.R.: Strategies for turbulence modelling and simulations. Int. J. Heat Fluid Flow **21**, 252 (2000)
2. Menter, F.R., Egorov, Y.: Scale-adaptive simulation method for unsteady flow predictions. Part 1: theory and model description. J. Flow Turbul. Combust. **85**(1), 113–138 (2010)
3. Duda, B.M., Menter, F.R., Deck, S., Bezard, H., Hansen, T., Esteve, M.-J.: Application of the scale-adaptive simulation to a hot jet in cross flow. AIAA. J. **51**(3), 674–685 (2013)
4. Langtry, R.B., Spalart, P.R.: Detached eddy simulation of a nose landing-gear cavity. In: IUTAM Bookseries, vol. 14 (2009)
5. Widenhorn, A., Noll, B., Aigner, M.: Numerical characterization of a gas turbine model combustor applying scale-adaptive simulation, GT2009-59038. In: Proceedings of ASME TURBO EXPO 2009
6. Shur, M.L., Spalart, P.R., Strelets, M.K., Travin, A.K.: A hybrid RANS-LES approach with delayed-DES and wall-modeled LES capabilities. Int. J. Heat Fluid Flow **29**, 1638–1649 (2008)
7. Mathey, F., Cokljat, D., Bertoglio, J.P., Sergent, E.: Specification of LES inlet boundary condition using vortex method. In: 94th International Symposium on Turbulence, Heat and Mass Transfer, Antalya (2003)
8. Cokljat D., Caradi, D., Link, G., Lechner, R., Menter, F.R.: Embedded LES methodology for general-purpose CFD solvers. In: Proceedings of Turbulent Shear Flow Phenomena, Proceedings of 6th International Symposium on Turbulence and Shear Flow Phenomena, Seoul, Korea, 22–24 June 2009, pp. 1191–1196 (2009)
9. Menter F.R., Garbaruk, A., Smirnov, P.: Scale adaptive simulation with artificial forcing. In: Proceedings of 3rd Symposium on Hybrid RANS-LES Methods (2009)
10. Menter, F.R., Kuntz, M.: Adaptation of eddy-viscosity turbulence models to unsteady separated flow behind vehicles. In: Proceedings of Conference the Aerodynamics of Heavy Vehicles, Trucks, Busses and Trains, Asilomar, CA, Springer (2003)
11. Spalart, P., Deck, S., Shur, M., Squires, K., Strelets, M., Travin, A.: A new version of detached eddy simulation. Resistant to ambiguous grid densities. J. Theor. Comput. Fluid Dyn. **20**, 181–195 (2006)
12. Gritskevich, M.S., Garbaruk, A.V., Schtze, J., Menter, F.R.: Development of DDES and IDDES formulations for the k-shear stress transport model. J. Flow Turbul. Combust. **88**(3), 431–449 (2012)

13. Menter, F.R., Gritskevich, M.S., Schtze, J.: Global vs. zonal approaches in hybrid RANS-LES turbulence modelling progress in hybrid RANS-LES modelling. Notes Numer. Fluid Mech. Multidiscip. Des. **117**(2012), 15–28 (2012)
14. Smagorinsky, J.: General circulation experiments with the primitive equations. Mont. Weather Rev. **91**, 99–165 (1963)
15. Lilly, D.K.: A proposed modification of the Germano subgrid-scale closure model. Phys. Fluids **4**, 633–635 (1992)
16. Schumann, U.: Subgrid scale model for finite-difference simulations of turbulent flows in plane channels and annuli. J. Comp. Phys. **18**, 376 (1975)
17. Nicoud, F., Ducros, F.: Subgrid-scale stress modelling based on the square of the velocity gradient tensor. Flow Turbul. Combust. **62**(3), 183–200 (1999)
18. Shur, M.L., Spalart, P.R., Strelets, M.K., Travin, A.K.: A hybrid RANS-LES approach with delayed-DES and wall-modeled LES capabilities. Int. J. Heat Fluid Flow **29**, 1638–1649 (2008)
19. Mathey, F., Cokljat, D., Bertoglio, J.P., Sergent, E.: Specification of LES inlet boundary condition using vortex method. In: 4th International Symposium on Turbulence, Heat and Mass Transfer, Antalya (2003)
20. Menter, F.R.: Two-equation eddy-viscosity turbulence models for engineering applications. AIAA J. **32**(8), 1598–1605 (1994)
21. Henshaw, M.J.: M219 cavity case, verification and validation data for computational unsteady aerodynamics. Technical report RTO-TR-26, AC/323(AVT)TP/19 (2000)
22. Kurbatskii, K.A., Menter, F., Schuetze, J., Fujii, A.: Numerical simulation of transonic cavity noise using scale-adaptive simulation (SAS) turbulence model. In: Inter-Noise 2011, September 2011
23. Swalwell, K.E., Sheridan, J., Melbourne, W.H.: Frequency analysis of surface pressures on an airfoil after stall. AIAA Paper 2003–3416 (2003)
24. Egorov Y., Menter F.R., Cokljat, D.: Scale-adaptive simulation method for unsteady flow predictions. Part 2: application to aerodynamic flows. J. Flow Turbul. Combus. **85**(1), 139–165 (2010)
25. Laschka, B., Ranke, H., Breitsamter, C.: Application of unsteady measurement techniques to vortical and separated flows. Z. Flugwiss. Weltraumforsch. **19**, 90–108 (1995)
26. Westin, J., Alavyoon F., Andersson, L., Veber, P., Henriksson, M., Andersson, C.: Experiments and unsteady CFD-calculations of thermal mixing in a T-junction. OECD/NEA/IAEA Workshop on the Benchmarking of CFD Codes for Application to Nuclear Reactor Safety (CFD4NRS), Munich Germany, pp. 1–15 (2006)

Hybrid LES–URANS Methodology for Wall–Bounded Flows

S. Schmidt and M. Breuer

1 Introduction

Since wall-resolved LES suffers from very fine near-wall grid resolutions required ($\Delta y^+_{1st} < 2$, $\Delta x^+ = \mathcal{O}(50–150)$, $\Delta z^+ = \mathcal{O}(15–40)$), the idea to embed a near-wall (U)RANS region within a LES represents both, a specific type of hybrid approach and an enhanced kind of wall model. A variety of hybrid LES-(U)RANS concepts were suggested during the last years [6] following different ideas to combine both methodologies. Nevertheless, the basic objective is always the same. By combining the advantages of the LES concept and the RANS approach a new simulation technique should emerge which consumes less CPU-time than pure LES and guarantees predictive capabilities much better than RANS and similar or even better than LES. Especially non-equilibrium turbulent flows for which the RANS approach evidently suffers from reliability, e.g., large-scale separation/reattachment or vortex shedding postulates the application of advanced simulation methodologies going beyond the capabilities of pure RANS. This is the main focus of interest of the present study.

2 Hybrid Methodology for Wall-Bounded Flows

According to the catalog of requirements mentioned above the strategy followed here is as follows: the URANS approach is used for the near-wall region, whereas LES is performed in regions, where large unsteady vortical structures such as flow

S. Schmidt · M. Breuer (✉)
Department of Fluid Mechanics, Helmut–Schmidt–Universität,
Hamburg, Germany
e-mail: breuer@hsu-hh.de

S. Schmidt
e-mail: schmidst@hsu-hh.de

J. Fröhlich et al. (eds.), *Direct and Large-Eddy Simulation IX*,
ERCOFTAC Series 20, DOI 10.1007/978-3-319-14448-1_25

separations are present, which should be resolved directly. Besides a definition of the interface between URANS and LES which is realized in the present study by a dynamic interface criterion automatically reacting on the flow field variations, appropriate models for both domains are decisive.

In the near-wall URANS region the strong anisotropy of the Reynolds stresses should be taken into account. Although a full Reynolds stress model (RSM) would be the optimal choice, an explicit algebraic Reynolds stress model (EARSM, Wallin and Johansson [13]) is applied instead owing to two reasons. First, it represents a compromise between the too expensive full RSMs and classical linear eddy-viscosity models not capable to account for the stress anisotropy. Second, for the implementation the EARSM can be formally expressed in terms of a non-linear eddy-viscosity model. Its extra computational effort is small, still requiring solely the solution of one transport equation for the modeled turbulent kinetic energy $k_{mod} = k_{URANS}$. This additional scale-determining part of EARSM provides the velocity scale. The transport equation for k_{mod} includes the production, diffusion and dissipation term which all presuppose reasonable modeling assumptions. Owing to EARSM the production term can be closed on the basis of the consistent Reynolds stress formulation including the anisotropy term [7] which improves the production term and subsequently k_{mod}. Instead of a classical gradient-diffusion approach as used for the LES zone, for EARSM (URANS only) the enhanced representation of the Reynolds stresses can be introduced into the diffusion term by applying the model of Daly and Harlow [5]. Finally, the dissipation rate was recently refined [2]. Originally, the near-wall model by Chen and Patel [4] relying on an algebraic relation for the length scale was applied. The drawback of this model is that it is based on the equilibrium assumption at solid walls ($P_k = \varepsilon$) not taking the anisotropy of the stresses into account. Recently, Jakirlić and Jovanović [8] showed that the total dissipation rate can be expressed as a sum of the homogeneous and the non-homogeneous dissipation. The latter is exactly equal to one half of the molecular diffusion of k_{mod}. Furthermore, in the direct vicinity of the wall the homogeneous part can be expressed by an exact formulation using the Taylor microscale. Both refinements were shown to further enhance the results [2]. In the following the Jakirlić and Jovanović formulation will be used for the dissipation term of the hybrid methodology. The modeling approach for the LES region is less sophisticated. In order to rely on a unique modeling concept also a one-equation subgrid-scale model is applied [11]. Here the transport equation describes the velocity scale based on the subgrid-scale turbulent kinetic energy $k_{mod} = k_{SGS}$. Furthermore, the length scale is naturally given by the filter width. In conclusion, the resulting modeling strategy consists of a single transport equation for k_{mod} with different meanings for the URANS (k_{URANS}) and LES (k_{SGS}) modes. Owing to the particular importance of the near-wall region, special emphasis is put on an adequate modeling in this critical region.

3 Applications and Results

The proposed hybrid LES-URANS approach for non-equilibrium turbulent flows was validated based on several well-known test cases, i.e., the plane channel flow, the periodic hill flow and two different 3-D diffuser flows [1, 2, 7]. Besides these internal flows the present application is concerned with the flow around a SD 7003 airfoil [12]. The airfoil possesses a relative thickness of 8.51 % and a relative camber of 1.46 %. The prediction of the flow around the airfoil was performed at a Reynolds number of 60,000 based on the chord length c and the free-stream velocity u_∞. An angle of attack $\alpha = 4°$ was chosen, where due to the adverse pressure gradient a stable laminar separation bubble (LSB) on the leeward side can be observed in the measurements [3] starting at about 0.25 c. Inside the LSB the transition to turbulence starts with the amplification of the two-dimensional instability mechanism known as Tollmien-Schlichting (TS) waves. In the separated shear layer Kelvin-Helmholtz (KH) instabilities are observed. Due to the onset of turbulence a rapid pressure drop leads to a highly instantaneous reattachment at about 0.7 c. The LSB is a major reason for the increase of the pressure drag and the decrease of the lift. To understand the fluid dynamic interactions represents a demanding benchmark. Earlier numerical investigations [10] based on the EARSM by Wallin and Johansson [13] in pure URANS mode showed at the same moderate angle of attack a too fast onset of turbulence, which leads to a too small bubble length. The inaccuracy of the pure URANS results and the CPU-time requirements of the LES predictions are the main motivations to promote the hybrid LES-URANS approach.

For comparison purposes a LES prediction was carried out on a fine grid allowing a detailed evaluation of the hybrid method. The grid for the pure LES consists of about 16.8 million control volumes (CVs) and satisfies the resolution requirements for a wall-resolved LES at the suction as well as the pressure side ($\Delta x^+ \leq 15, \Delta y^+ \leq 1.5, \Delta z^+ \leq 15$). Since an airfoil configuration is examined, the C-grid topology is suitable. The airfoil is placed inside a computational domain of the height $h/c = 14$ and the wake regime is prescribed with a length $l/c = 4$. At the inlet of the computational domain the constant velocity $U/U_\infty = 1$ is imposed, whereas at the outlet a convective boundary condition is used. For the lateral edges the symmetry boundary condition is applied. Furthermore, along the airfoil surface the no-slip boundary condition is employed. The flow past the airfoil is assumed to be homogeneous in spanwise direction allowing the application of periodic boundary conditions for a depth $z/c = 0.25$ of the domain. To ensure the correct prediction of the transition phenomenon, the dynamic SGS model of Germano/Lilly [9] was chosen as the reference case. In the present study, the hybrid LES-URANS method is performed on a coarser grid with 5.8 million CVs. In addition, to show the possible performance of the hybrid model a pure LES relying on a one-equation SGS model [11] was carried out on the same grid as the hybrid approach. Both grids offer the same wall-normal resolution for the wall-nearest grid point $y_{1st}/c = 5 \times 10^{-4}$ ($\Delta x^+ \leq 22, \Delta y^+ \leq 1.5, \Delta z^+ \leq 30$).

The dynamic interface criterion based on the modeled turbulent kinetic energy (C_{switch,y^*} criterion [1, 2, 7]) was developed and tested in the framework of internal flows. For the present external flow with a laminar boundary layer at the front of the airfoil an additional criterion is necessary to exclude that due to vanishing values of k_{mod} in this region the hybrid methodology switches into the URANS mode. For this purpose an additional criterion TR is introduced evaluating the ratio between two different meaningful length scales. The first length scale is prescribed owing to the filter width Δ of the mesh, whereas the flow setting is taken into account with the aid of the Kolmogorov length scale $L_K = (\nu^3/\varepsilon)^{1/4}$ with $\varepsilon = 2\,\nu \cdot s_{ij} \cdot s_{ij}$:

$$TR = \frac{\Delta}{L_K} \begin{cases} \leq 1 \rightarrow \text{laminar/DNS-like} \\ > 1 \rightarrow \text{turbulent/hybrid LES-URANS.} \end{cases}$$

This additional criterion TR is combined with the original one based on C_{switch,y^*} and thus dynamically reacts on the local flow structure. Since the transition onset is dominated by highly instantaneous processes, the calculation of the fluctuation strain rate s_{ij} for the determination of L_K ensures the right estimation of the transient flow phenomena. At the leading edge of the airfoil the values of TR are expected to be small. Thus it is possible to resolve all information of the flow field with the existing grid and the usage of the LES mode in this region guarantees the right flow description owing to the negligible influence of the subgrid-scale model. After the transition onset the values of TR rises and it can be expected to be larger than one. This region does not satisfy the well-known requirements of the LES grid resolution and furthermore the influence of the used SGS model is appreciable. Accordingly, the application of the hybrid LES-URANS is the natural choice. It is well known that the Kolmogorov length scale is derived for high Reynolds numbers to describe the universal smallest scales of turbulence. Despite the moderate Reynolds number of the present test case and the two-component anisotropy of the near-wall scales, the refined criterion produces meaningful results.

Figure 1 depicts the comparison of the mean streamwise velocity U/U_∞ and the total kinetic energy k_{tot}/U_∞^2 for the fine LES, the coarse LES and the hybrid LES-URANS approach at nine positions. First of all it is noteworthy that the hybrid method predicts the complete flow field well compared with the fine LES. The coarse LES shows inside the LSB area a high level of agreement with the reference LES, whereas the hybrid LES-URANS method slightly underestimates the reference LES. Further downstream in the trailing-edge region of the airfoil the hybrid model delivers superior results for the streamwise velocity compared to the coarse LES. As expected from the internal flow evaluations, the results for the total kinetic energy calculated by the hybrid methodology exhibit no visible kink in the profiles underlining the applicability of the LES-URANS approach for external flows. In the free shear layer the coarse LES strongly overpredicts the total kinetic energy in comparison to the fine LES. In contrast, the hybrid method exhibits smaller discrepancies regarding k_{tot}. Further downstream ($x/c \geq 0.6$) after the transition onset the hybrid model matches the results of the fine LES quite well.

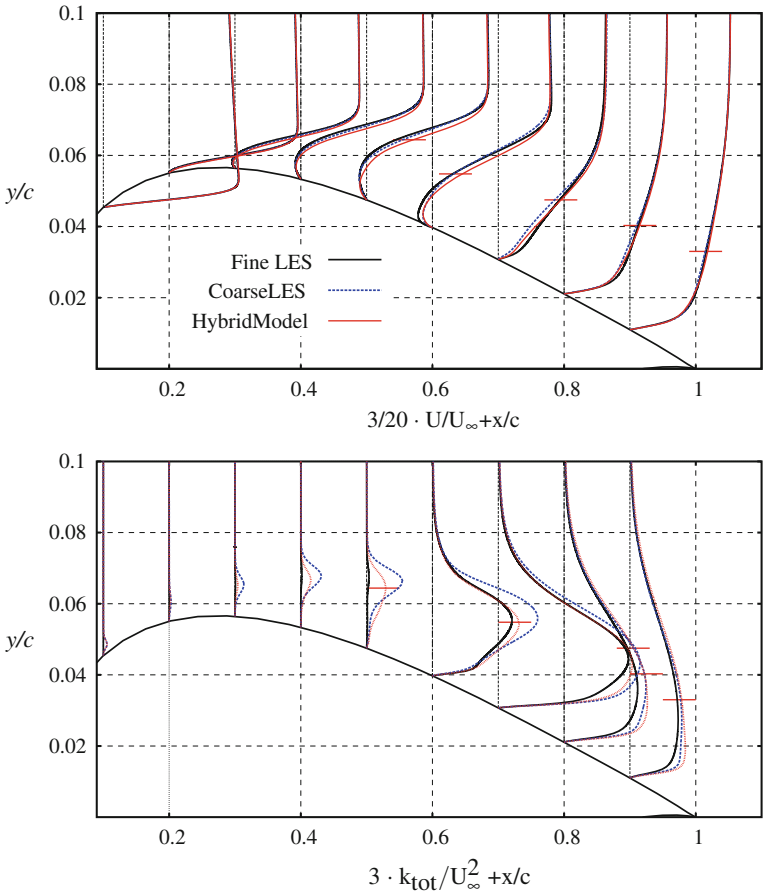

Fig. 1 Profiles of U/U_∞ (*upper*) and k_{tot}/U_∞^2 (*lower*) for the SD 7003 airfoil flow configuration at $\mathrm{Re}_c = 60{,}000$ and $\alpha = 4°$. *Short dashes* indicate the interface location in the averaged flow field

To assess the global performance of the simulations the pressure coefficient c_p and the friction coefficient c_f are plotted in Fig. 2a, b. The profile of c_p shows the typical distribution for a LSB. After the separation a plateau can be observed, which ends in a c_p drop in the area of the transition. The coarse LES as well as the hybrid method yields the right prediction of the LSB characteristics in agreement with the results of the fine LES. Based on Fig. 2b the exact location of the separation and reattachment points can be appointed. Due to the nearly steady location of the separation point it is not surprising that all three methods predict the same position. Owing to the highly instantaneous reattachment the estimation of the reattachment location seems to be more demanding. Compared with the fine LES the hybrid method exhibits a high level of agreement regarding the reattachment point. Contrarily, the coarse LES overestimates its position.

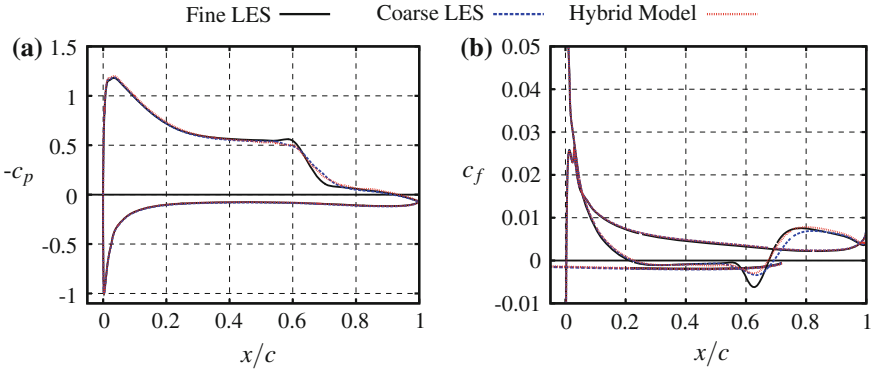

Fig. 2 **a** Distribution of the pressure coefficient $c_p = (p - p_\infty)/(0.5\,\rho_\infty\,U_\infty^2)$ of the time-averaged flow field. **b** Distribution of the friction coefficient $c_f = \tau_W/(0.5\,\rho_\infty\,U_\infty^2)$ of the time-averaged flow field

4 Conclusions

To validate the applicability of the hybrid LES-URANS methodology for external flows, the flow around the airfoil SD 7003 is considered comprising a LSB and transition. As shown the improvements by the hybrid LES-URANS approach are obvious compared to pure LES and justify the small additional CPU-time effort. To further increase the performance of the hybrid model, additional evaluations are needed including the application of even coarser grids, higher Re_c or other α.

References

1. Breuer, M., Jaffrézic, B., Arora, K.: Hybrid LES-RANS technique based on a one-equation near-wall model. J. Theoret. Comp. Fluid Dyn. **22**(3–4), 157–187 (2008)
2. Breuer, M., Schmidt, S.: Refinement of a hybrid LES-URANS approach for non-equilibrium turbulent flows. In: THMT-7, Palermo, Italy, 24–27 Sept 2012
3. Burgmann, S.: Investigation of transitional separation bubbles using three-dimensional measurement techniques. PhD thesis, RWTH Aachen, Germany (2009)
4. Chen, H.C., Patel, V.C.: Near-wall turbulence models for complex flows including separation. AIAA J. **26**(6), 641–648 (1988)
5. Daly, B.J., Harlow, F.H.: Transport equations in turbulence. Phys. Fluids **13**, 2634–2649 (1970)
6. Fröhlich, J., von Terzi, D.: Hybrid LES/RANS methods for the simulation of turbulent flows. Prog. Aerosp. Sci. **44**(5), 349–377 (2008)
7. Jaffrézic, B., Breuer, M.: Application of an explicit algebraic Reynolds stress model within an Hybrid LES-RANS method. J. Flow Turbul. Combust. **81**(3), 415–448 (2008)
8. Jakirlić, S., Jovanović, J.: On unified boundary conditions for improved predictions of near-wall turbulence. J. Fluid Mech. **656**, 530–539 (2010)
9. Lilly, D.K.: A proposed modification of the Germano subgrid scale closure model. Phys. Fluids A **43**, 633–635 (1992)

10. Radespiel, R., Windte, J., Scholz, U.: Numerical and experimental flow analysis of moving airfoils with laminar separation bubbles. AIAA J. **45**(6), 1346–1356 (2007)
11. Schumann, U.: Subgrid-scale model for finite-difference simulations of turbulent flows in plane channels and annuli. J. Comp. Phys. **18**, 376–404 (1975)
12. Selig, M., Guglielmo, J., Broeren, A., Giguére, P.: Summary of Low-speed Airfoil Data, vol. 1. SoarTech Publications, Virginia Beach (1995)
13. Wallin, S., Johansson, A.V.: An explicit algebraic Reynolds stress model for incompressible and compressible turbulent flows. J. Fluid Mech. **403**, 89–132 (2000)

Part V
Stability and Transition

Investigations of Stability and Transition of a Jet in Crossflow Using DNS

A. Peplinski, P. Schlatter and D.S. Henningson

1 Introduction

The so-called jet in cross-flow (JCF) refers to fluid that exits a nozzle and interacts with the surrounding boundary layer flowing across the nozzle. This case has been extensively studied both experimentally and theoretically over the past decades due to its high practical relevance. Smoke and pollutant plumes, fuel injection and mixing or film cooling are just a few applications. On the other hand, it is considered a canonical flow problem with complex, fully three-dimensional dynamics which makes the JCF a perfect tool for testing numerical methods and simulation capabilities. Recent reviews on this flow configuration are given in [7, 8].

The JCF is characterised by three independent non-dimensional parameters: free-stream and the jet Reynolds numbers ($Re_{\delta_0^\star}$, Re_{jet}) and jet to free-stream velocity ratio R, which is a key parameter in this work. The major flow features are (see e.g. Fig. 1 in [7]): the counter-rotating vortex pair (CVP) in the far field, the horseshoe vortex developing upstream of the jet orifice, and vortices shed from the shear layers that result from the interaction of the jet with the cross-flow both upstream and downstream of the jet trajectory. Some other features, such as wake vortices or upright vortices, are visible at higher values of the cross velocity ratio R only. As the ratio R increases, the flow evolves from a stable (and thus steady) configuration consisting of (steady) CVPs and horseshoe vortices, through simple periodic vortex shedding (a limit cycle) to more complicated quasi-periodic behaviour, before finally becoming turbulent. In Refs. [2, 6, 12] the stability of the JCF was studied by means of modal analysis. The first linear global stability analysis of this flow at $R = 3$ was presented by Bagheri et al. [2, 12]. For this jet to free-stream velocity ratio the JCF was found to be dominated by an interplay of three common instability mechanisms: a Kelvin–Helmholtz shear layer instability, a possible elliptic instability of the CVPs,

A. Peplinski · P. Schlatter · D.S. Henningson (✉)
Linné FLOW Centre and Swedish e-Science Research Centre (SeRC),
KTH Mechanics, Royal Institute of Technology, 100 44 Stockholm, Sweden
e-mail: henning@mech.kth.se

J. Fröhlich et al. (eds.), *Direct and Large-Eddy Simulation IX*,
ERCOFTAC Series 20, DOI 10.1007/978-3-319-14448-1_26

and a near-wall vortex shedding mechanism similar to a von Kármán vortex street. It was also shown that the flow acts as an oscillator, with high-frequency unstable global eigenmodes associated with shear-layer instabilities on the CVP and low-frequency modes resulting in vortex shedding in the jet wake. This work was later extended to the wider range of $R \in (0.55, 2.75)$ [6], focusing on transition from steady to unsteady flow as R is increased. The first bifurcation (first unstable eigenmode) was found to occur at $R \approx 0.675$, when shedding of hairpin vortices characteristic of a shear layer instability is observed, and the the source of this instability (*wavemaker*) was located in the shear layer just downstream of the orifice. Results of linear stability analysis were consistent with nonlinear direct numerical simulations (DNS) at the critical value of R predicting well the frequency and initial growth rate of the disturbance. It was also concluded that based on linear analysis good qualitative predictions about the flow dynamics can be made even for higher values of R, where multiple unstable eigenmodes are present. The authors pointed out, however, that the critical value of R cannot be determined exactly due to sensitivity of the results to changes in the domain length as well as to the presence of the fringe region enforcing periodic boundary condition (BC).

In the current study we follow Ref. [6] focusing on the transition from steady to unsteady flow and, using linear global stability analysis, searching for the value of R at which the first bifurcation occurs. The scope of this work is to test the numerical methods and techniques, and to identify the major difficulties related to linear stability of this type of complex flows. As modal analysis is known to fail in predicting the practical critical Reynolds number for transition to turbulence in a number of systems, we apply in our studies both modal and non-modal analyses. A classical example of such a flow is the convectively unstable flat-plate boundary layer [4], which behaves as broadband amplifier of incoming disturbances and is globally stable according to linear global analysis. However, a global stability analysis based on the asymptotic behaviour of single eigenmodes of the system does not capture relevant dynamics, and transition to turbulence at lower Re occurs due to transient effects. Following Refs. [9, 10] we investigate the linear growth of perturbations in the JCF for a limited time, before the exponential modal behaviour is most dominant, and determine an *optimal initial condition* (initial condition yielding largest possible growth in energy) adopting a time-stepper method.

2 Numerical Setup

We adopt the computational setup from Ref. [6], modelling the interaction of a boundary layer with a perpendicular jet exiting a circular pipe with diameter $D = 3 * \delta_0^\star$, where $\delta_0^\star$ is the displacement thickness at the inflow placed $9.375 * \delta_0^\star$ upstream the centre of the pipe orifice; $\delta_o^\star$ is adopted as length unit. Following Ref. [6] we use both laminar cross-flow and jet inflow profile and, as the jet pipe is absent in our simulations, an inhomogeneous (Dirichlet) BC prescribing the inflow jet profile is employed. This is an important limitation of the problem setup requiring

e.g. smoothing of the jet profile by a Gaussian function (Eq. 2.1 in [6]). We will list here only the key parameter of the setup referring the reader to [2, 6] for more details. The flow is fully described by pipe diameter D, cross-flow Reynolds number $Re_{\delta_0^\star} = U_\infty \delta_0^\star / \nu$ and jet to cross-flow velocity ratio $R = V/U_\infty$, where U_∞, V and ν are free-stream velocity, *peak* jet velocity and the kinematic viscosity, respectively. As before [6] we set $Re_{\delta_0^\star} = 165$, and choose R as 1.0, 1.4, 1.5 and 1.6.

The simulations are performed with two different massively parallel DNS solvers for the incompressible Navier–Stokes equations: `SIMSON` [3] and `Nek5000` [5]. `SIMSON` was used in Refs. [2, 6, 12] and is a fully-spectral code suitable for stability computations. However, a major constraint is the requirement for periodic BC in streamwise direction necessitating a fringe region (Sect. 4.2.2 in Ref. [3]) for damping disturbances. We use `SIMSON` to investigate the influence of the fringe length L_F on the stability results in nonlinear DNS. Fringe parameters are adopted from [6] with varying L_F set to 15 (like in [6]), 45 and 75 units. As the fringe region reduces the useful part of the computational domain we doubled the length of the box as compared to Ref. [6] setting its size to $L_x = 150$, $L_y = 20$, $L_z = 30$, with the resolution of $512 \times 201 \times 144$ modes in the streamwise (x), wall-normal (y), and spanwise (z) directions, respectively. `Nek5000` is a spectral-element code providing spectral accuracy while allowing for complex geometries. In this method the governing equations are cast into weak form and discretised in space by the Galerkin approximation, following the $P_N - P_{N-2}$ approach with the velocity space spanned by Nth-order Lagrange polynomial interpolants. In our studies we use `Nek5000` to investigate the influence of resolution ($N = 6$ and 9), box length ($L_x = 150$ and 250) and grid structure. Domain decomposition into hexahedral elements is used to reduce resolution where it is not needed. We keep uniform resolution in the pipe vicinity within 5 unit distance from the orifice, and reduce it at larger distance by smooth element stretching (mesh M1). In mesh M2 we double the vertical resolution next to the wall. There are no periodic BC in streamwise direction, however, we found our results to be dependent on the outflow BC unless we set a sponge layer at the outflow as well as making the computational domain longer to reduce reflections from the boundary. The forcing function for the sponge was adopted from the fringe in `SIMSON`, and the sponge length was set to 25 and 35 units for $L_x = 150$ and 250, respectively. `Nek5000` is also used as time-stepper for solving the linearised Navier–Stokes equations in modal and non-modal linear stability analyses. Detailed descriptions of the implementation and validation can be found in Refs. [5, 10].

3 Direct Numerical Simulations

We performed a number of nonlinear DNS to investigate the dependence of critical R value on different simulation parameters.

The studies of results sensitivity to damping in the fringe for $R = 1$ were performed with `SIMSON` and are presented in Fig. 1. The left plot shows the time dependent amplitude of a single Fourier component in the signal of the streamwise

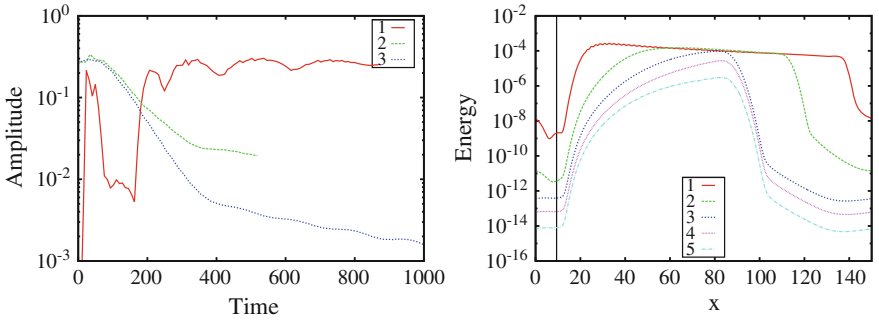

Fig. 1 Temporal amplitude evolution (*left*) and energy as function of streamwise position (*right*) of the single most unstable Fourier component for $R = 1$ and different fringe length L_F (1, 2, 3) and simulation time (4, 5). Simulation results of SIMSON

velocity component of a probe located 15 units downstream of the pipe centre for $L_F = 15$, 45 and 75 (curves 1, 2 and 3). The frequency of the chosen Fourier component is given by the period T_p of the signal, and the amplitude at time t is calculated by projection of the signal on sine and cosine functions within the window $(t - T_p/2, t + T_p/2)$ and finally smoothed by Bézier curves. The right plot presents the energy of the same Fourier component of the streamwise velocity component integrated over $y-z$ plane and plotted as a function of streamwise position x. Curves 1 and 2 correspond to $L_F = 15, t = 800$ and $L_F = 45, t = 500$ respectively, and curves 3, 4 and 5 give the time evolution of energy distribution for $L_F = 75$ and t equal 500, 1,000 and 1,500 (time is counted from the beginning of simulation). The pipe centre is marked by the vertical line, and the size of the fringe layer is clearly visible. The first simulation was performed with $L_F = 15$ and Blasius boundary layer as initial condition, and run up to $t = 880$, when the probe signal saturated. This state provided the initial conditions for the two other runs. Note that the final velocity field of the first run consists of more than one frequency component, and curve 1 in Fig. 1 give only an estimate of observed oscillations.

According to Ilak et al. [6] the JCF for $R = 1$ appears globally unstable, however, closer examination of Fig. 1 shows this flow to be convectively unstable, and the misinterpretation of the instability mechanism to stem from insufficient damping in the fringe. The temporal amplitude evolution of the simulation with the shortest fringe features a short phase of approximately exponential decay (after initial transient phase) ending at $t \approx 160$, when the signal from the fringe reaches the pipe after re-entering the domain and triggers instability. It is because the energy damping in the fringe (of the order of 10^5) is too small compared to the growth rate in the domain leading to nonlinear saturation of the signal. Similar conclusions can be drawn from the second run ($L_F = 45$), where the nonlinear saturation on the energy plot is still visible. To achieve sufficient damping the fringe with at least $L_F = 75$ (50 % of the computation domain) is required. In this case the signal amplitude decays exponentially and the saturation is no longer visible after 500 time units. However, even in this case the decay rate after $t = 400$ is relatively low leaving considerable

amount of energy in the strongest Fourier mode after $t = 1{,}500$. This proves that methods relying on periodic domains to be unsuited for flow cases with considerable spatial (and temporal) growth rates. To employ those methods one has to ensure the damping within the fringe region is sufficient to make perturbations re-entering the domain not relevant for the flow dynamics.

All subsequent runs are performed with `Nek5000`, which does not require periodicity in streamwise direction. Nevertheless, even in this case a correct treatment of outflow BC was found to be crucial. The time-dependent amplitudes of a single Fourier component in the signal of the streamwise velocity component of a probe located 15 units downstream of the pipe for $R = 1.4$ and 1.5 are shown in Fig. 2. Curves 1–3 correspond to lower resolution runs with $N = 6$, and curves 4, 5 show results with higher order $N = 9$ for $R = 1.5$. Two different domain lengths are studied: $L_x = 150$ (curves 1, 2 and 4) and 250 (curves 3 and 5). All DNS start with Blasius initial condition, and in runs 2, 3, 4 and 5 the instability is triggered by adding non-symmetric noise of amplitude 10^{-4} to the velocity field at $t = 500$ (marked by vertical line). All presented simulations were performed on the M1 mesh. For all cases, an initial transient phase (ending around $t = 220$) is followed by short phase of nearly exponential decay. Depending on the domain size and whether noise was added or not, this phase ends with a rapid amplitude increase followed by exponential decay/saturation, or with the slow growth of low amplitude oscillations. Strong dependency on grid resolution is clearly visible, as the $R = 1.5$ run is globally unstable for $N = 6$ and stable for $N = 9$. On the other hand, small amplitude ($10^{-4} - 10^{-3}$) oscillations visible at the end of all runs with shorter domain (independently whether noise was added or not) are manifestation of interaction between pipe vicinity and outflow BC. In the lower resolution simulations those oscillations are excited during the phase of exponential decay (at $t \approx 400$ and 370 for $R = 1.4$ and 1.5) and reach final amplitude of $10^{-4} - 10^{-3}$. In the unstable case $R = 1.5$ (curve 1 in right plot) they are later overtaken by growing unstable modes with similar frequency. Such oscillations are not visible in the simulations with longer domain,

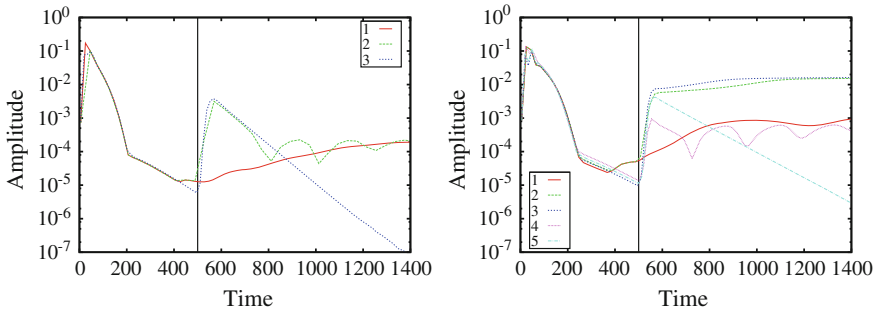

Fig. 2 Time dependent amplitude evolution of the single Fourier component of the velocity probe for $R = 1.4$ (*left*) and 1.5 (*right*) for different domain length and grid resolution. See text for description

where all the disturbances are damped exponentially. Increased resolution allows to delay excitation of those waves (no longer visible in the first decay phase), but it does not reduce significantly the final amplitude. Note that for the low resolution runs at $R = 1.5$ the final saturation is reached faster in the longer domain, and the maximum amplitude reached after the noise is added for $N = 9$ is higher in the longer domain as well. This illustrates the need for proper non-reflective BC.

4 Modal Analysis

Modal stability is the classical method hydrodynamics stability, where the critical value of given parameter, for which a single exponentially growing disturbance exist, is computed. In the linear theory for global analysis those disturbances, the so-called linear global modes, are associated with eigenmodes of the linearised Navier–Stokes operator. Their identification requires finding the base flow $\mathbf{U}_b$, i.e. stationary solution to the nonlinear Navier–Stokes equations, and next solving an eigenvalue problem of the linearised operator. As the considered flow configuration is usually unstable, to calculate $\mathbf{U}_b$ one has to adopt additional stabilisation mechanism to eliminate time dependency of the solution. In our calculations selective frequency damping (SFD) [1] was used. Furthermore, the dimension of the state space of the eigenvalue problem $\dim(\mathbf{U}) \sim 10^7$ makes explicit construction of the matrix impossible and requires projection on the low dimension subspace. To achieve this we adopt the Arnoldi algorithm using special matrix-free methods based on time-steppers. Detailed description of the problem with governing equations, implementation in `Nek5000`, validation and application to JCF can be found in Peplinski et al. [11]. An example of the base flow and spectra (growth rate ω_i vs frequency ω_r) is shown in Figs. 1 and 5 in Ref. [11]. Here we present results of the DNS performed on meshes M1 and M2 with domain length $L_x = 150$ for two resolutions $N = 6$ and 9, and two velocity ratios $R = 1.5$ and 1.6. As the plot of spectra is symmetric with respect to $\omega_r = 0$ we utilise the negative and positive ω_r parts to compare different cases, and we plot only those part of spectra matching for both direct and adjoint operator (compare positive ω_r part of the left plot in Fig. 5 in [11]).

Results are presented in Fig. 3. In all studied cases increasing resolution decreases the growth rates of all the modes except the ones with zero frequency. The upper left plot presents spectra for $R = 1.5$ and two meshes M1 and M2 (negative versus positive ω_r part of spectra) for two resolutions $N = 6$ (symbols 1 and 3) and 9 (symbols 2 and 4). The importance of high resolution close to the wall is shown, as the low resolution run on mesh M1 is globally unstable, and the run on mesh M2 is stable. On the other hand, most of the converged modes in the spectra of higher resolution runs match each other for both meshes suggesting the resolution necessary for numerical convergence was reached. Simulations with $R = 1.6$ and 1.5 performed on mesh M2 are presented in the upper right plot (negative versus positive ω_r). As before, symbols 1,3, and 4, 5 correspond to $N = 6$ and 9 respectively. The shift of ω_i is larger for higher ω_r, and it seems to be independent of value of R. For both resolutions

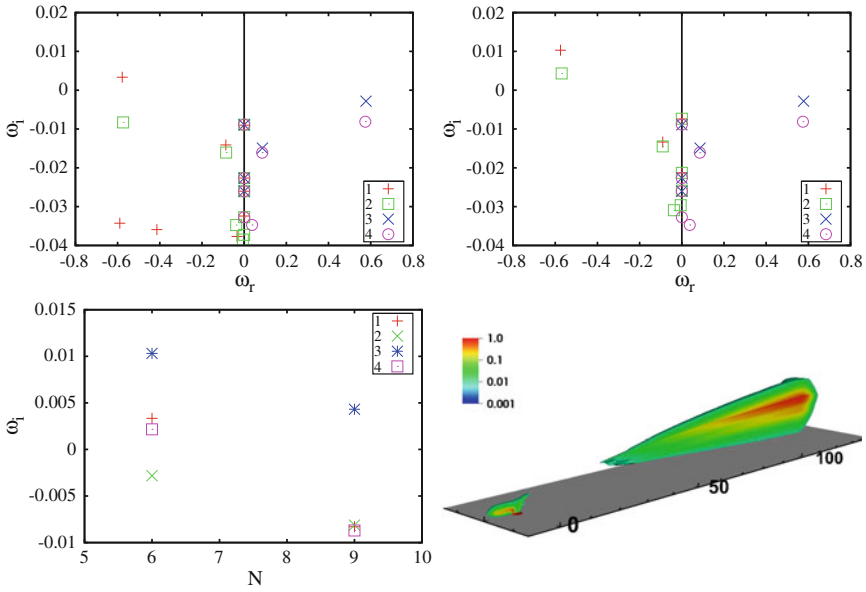

Fig. 3 *Upper row* sensitivity of the spectra to the mesh structure and resolution for different velocity ratios. *Left* spectra for $R = 1.5$ run on M1 (negative ω_r) and M2 (positive ω_r) meshes. *Right* spectra for $R = 1.6$ (negative ω_r) and $R = 1.5$ (positive ω_r) run on M2 mesh. *Lower left* growth rate of the strongest mode as the function of polynomial order N for the modal analysis and nonlinear DNS. *Lower right* Modulus of the direct (far field) and adjoint (pipe orifice) strongest eigenmode

the $R = 1.6$ case remains unstable. The results are summarised in the lower left plot presenting the growth rate of the strongest mode as a function of N for both linear modal analysis and nonlinear DNS. Symbols 1, 2, and 3 correspond to simulations at $R = 1.5$, mesh M1; $R = 1.5$, mesh M2; $R = 1.6$, mesh M2, respectively, while symbol 4 gives the growth rate of the strongest Fourier component in DNS for $R = 1.5$ (mesh M1). Higher resolution runs of the linear analysis and nonlinear DNS are consistent with each other giving similar frequency and growth rate.

The lower right plot shows the modulus of the strongest eigenmodes of the direct (far field) and adjoint (pipe vicinity) operators for $R = 1.5$ and $N = 9$. The pipe, marked by red circle, is located at $x = 0$ and the modes maxima are normalised to unity. The colour scale is logarithmic and the surface of the plotted region corresponds to 1 % of the maximum value illustrating fast decay of the eigenmodes. The total growth of the direct mode (ratio of the maximum to the value at the pipe orifice) is of the order of 10^9. The visible strong streamwise separation of the direct and adjoint global modes is induced by the basic flow advection and is a signature of non-normality of the linearised operator. This is important since a high degree of an operator non-normality leads to great sensitivity of the corresponding eigenvalues. It is also well-known that, as a result of non-normality, the perturbation energy may experience transient growth even though the flow is globally stable.

5 Non-Modal Analysis

In this section we discuss results of linear optimal disturbances, which is a well established technique to identify the initial condition leading to the largest growth of the disturbance at finite time. We look for the perturbation $\mathbf{u}(t = 0)$ which leads to maximum energy $\langle \mathbf{u}(T), \mathbf{u}(T) \rangle$ at time T. This problem is equivalent to solving the eigenvalue problem $\lambda \mathbf{u}(0) = \exp(\mathbf{A}^\dagger T) \exp(\mathbf{A}T)\mathbf{u}(0)$, where $\exp(\mathbf{A}^\dagger T) \exp(\mathbf{A}T)$ is the forward and adjoint composite propagator, and $\mathbf{A}$ is a linearised Navier–Stokes operator. The largest eigenvalue can be found iteratively by (matrix-free) power iterations, where the state is first marched forward in time with the standard numerical solver (direct propagator) and then backward with the corresponding adjoint solver (adjoint propagator). The initial condition is white noise and the procedure is repeated until the assumed convergence criterion for $|\mathbf{u}_n(0) - \mathbf{u}_{n-1}(0)|$ is reached, where n is the iteration number. For more detailed discussion, description of implementation in `Nek5000` and validation see Ref. [9, 10].

Our simulations were performed on the fine mesh M2 with domain length $L_x = 150$ and integration time $T = 77$ for $R = 1.5$ and 1.6. The initial state $\mathbf{u}(0)$ for each of step (direct and adjoint) was normalised $\langle \mathbf{u}(0), \mathbf{u}(0) \rangle = 1$, and the assumed convergence criteria was 5×10^{-5}, reached after 36 iterations. Note that the backward time marching in our simulations does not mean negative time step, so in the adjoint time stepper phase both time and energy are growing. To keep direct and adjoint problem consistent we apply sponge layers together with Dirichlet zero BC both at the inflow and outflow in the flow. The results are presented in Figs. 4 and 5.

The left plot in Fig. 4 presents the energy growth with time for direct (curves 1, 3) and adjoint (curves 2, 4) phases for stable ($R = 1.5$; curves 1, 2) and unstable ($R = 1.6$; curves 3, 4) cases. The energy evolution is similar in both cases and its final value differs only by factor of 2 ($E = 8 \times 10^{11}$ and 1.6×10^{12} for $R = 1.5$ and 1.6 respectively) showing the transient growth to be only weakly dependent on R. Similar conclusions can be drawn from the nonlinear DNS simulations, in which the optimal disturbance added on top of steady base flow is used as initial conditions. Evolution

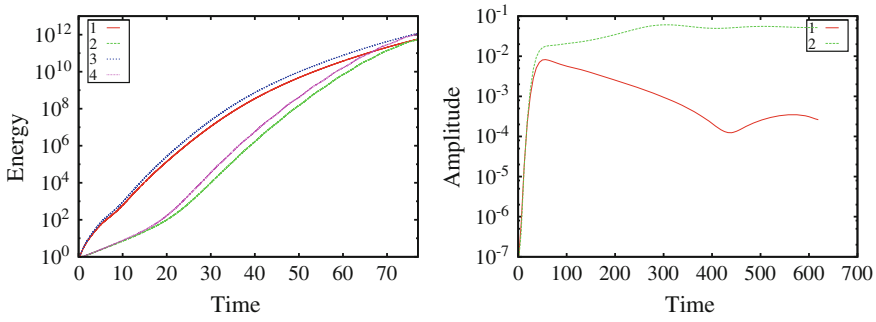

Fig. 4 Energy (*left*) and time dependent amplitude (*right*) evolution for the transient growth of the optimal disturbance. See text for description

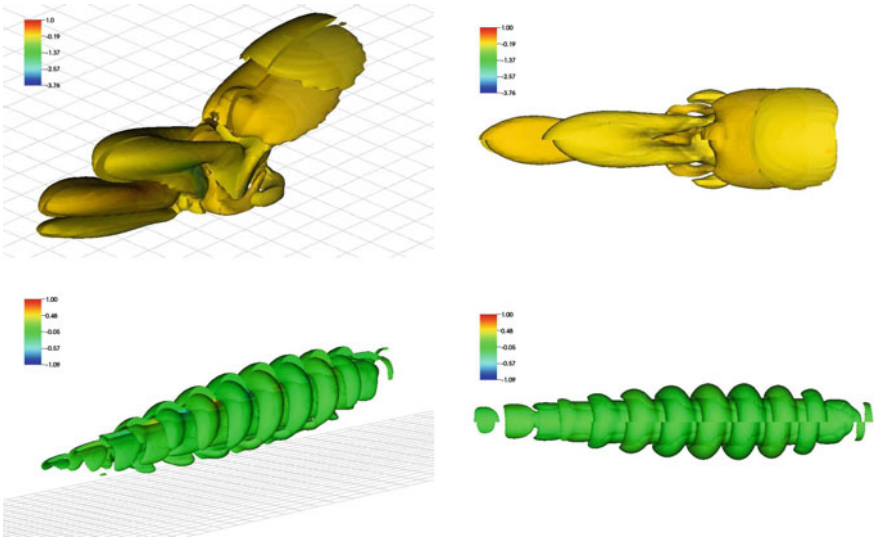

Fig. 5 Comparison of the optimal disturbance (*upper row*) and the resulting wave packet (*lower row*) for the stable (*front*, $R = 1.5$) and unstable (*back*, $R = 1.6$) case

of time dependent amplitude of a single Fourier component in the signal of the velocity probe (located 15 units downstream from the pipe) is presented in the right plot in Fig. 4 (curves 1 and 2 correspond to $R = 1.5$ and 1.6, respectively). The initial amplitude development is identical both for stable and unstable cases, however the final fate is consistent with modal analysis. The amplitude saturation at 10^{-4} for the stable case $R = 1.5$ (curve 1) is caused by interaction with outflow BC discussed in Sect. 3 above.

Figure 5 presents a comparison of optimal initial conditions for the streamwise velocity component $u_x(0)$ (upper row) and corresponding final wave packet $u_x(T)$ (lower row) for stable $R = 1.5$ and unstable $R = 1.6$ cases. Angled and top view are shown. As the optimal conditions and wave packets are symmetric with respect to the grid symmetry plane we plot results of both simulations on a single frame placing the stable case in front/lower part of the plot. The maximum value of all the functions is normalised to unity, and the plotted isosurface corresponds to 0.2. Both the optimal disturbances and wave packets for stable and unstable cases are almost identical, however they are slightly shifted with respect to each other due to different shape of the base flow. The wave packets differ also by the wavelength, which is minimally shorter for the stable case.

An important advantage of the non-modal analysis is its insensitivity to the outflow BC, as the travelling wave packet never reaches the outflow. However, in our simulations we could see the influence of the inflow BC on the adjoint stepper phase manifesting itself by small oscillations of the energy curve at the end of integration period (barely visible in Fig. 4).

6 Conclusions

In the current work we performed a stability analysis of the JCF testing the numerical methods and stability techniques. We focus on the calculation of the critical velocity ratio R, at which first bifurcation (transition from the steady to unsteady flow) occurs. We performed a number of simulations using different numerical methods and codes finding the JCF to be so sensitive to the simulation parameters and setup, that the critical velocity ratio can be found for a particular numerical setup only. In particular we found that spectral methods to be not well suited for simulation of the flow cases with considerable disturbance growth rate due to the periodic BC in streamwise direction, as the insufficient damping in the fringe region can significantly change the flow dynamics. Even for codes with inflow/outflow BC, we demonstrate the need for proper non-reflective BC for the spectral-element code, and the sensitivity of the modal stability analysis to the grid resolution. This great sensitivity of the eigenvalue at the bifurcation point indicates that it may not be a particularly interesting quantity to consider, as the flow itself is very sensitive to external disturbances and that transient effects are more relevant than the asymptotic growth rate associated with a particular global mode. We calculated the optimal disturbance finding its growth and shape robust and almost independent on R.

Acknowledgments Computer time was provided by Swedish National Infrastructure for Computing (SNIC).

References

1. Åkervik, E., Brandt, L., Henningson, D.S., Hœpffner, J., Marxen, O., Schlatter, P.: Steady solutions of the Navier-Stokes equations by selective frequency damping. Phys. Fluids **18**, 1–4 (2006)
2. Bagheri, S., Schlatter, P., Schmid, P.J., Henningson, D.S.: Global stability of a jet in crossflow. J. Fluid Mech. **624**, 33–43 (2009)
3. Chevalier, M., Schlatter, P., Lundbladh, A., Henningson, D.S.: SIMSON: a pseudo-spectral solver for incompressible boundary layer flows. Technical Report 2007:07, KTH mechanics (2007)
4. Ehrenstein, U., Gallaire, F.: On two-dimensional temporal modes in spatially evolving open flows: the flat-plate boundary layer. J. Fluid Mech. **536**, 209–218 (2005)
5. Fischer, P., Lottes, J., Kerkemeier, S.: Nek5000 web page. http://nek5000.mcs.anl.gov (2008)
6. Ilak, M., Schlatter, P., Bagheri, S., Henningson, D.S.: Bifurcation and stability analysis of a jet in cross-flow: onset of global instability at a low velocity ratio. J. Fluid Mech. **696**, 94–121 (2012)
7. Karagozian, A.R.: Transverse jets and their control. Prog. Energy Combust. Sci. **36**, 531–553 (2010)
8. Mahesh, K.: The interaction of jets with crossflow. Annu. Rev. Fluid Mech. **45**, 379–407 (2013)
9. Monokrousos, A., Åkervik, E., Brandt, L., Henningson, D.S.: Global three-dimensional optimal disturbances in the Blasius boundary-layer flow using time-steppers. J. Fluid Mech. **650**, 181–214 (2010)

10. Monokrousos, A., Brandt, L., Mavriplis, C., Henningson, D.S.: Optimal disturbances above and upstream a flat plate with elliptic leading edge. Technical Report, KTH mechanics (2011)
11. Peplinski, A., Schlatter, P., Henningson D. S.: Stability tools for the spectral-element code Nek5000; application to jet-in-crossflow. In: ICOSAHOM'12, Gammarth, Tunisia, to appear (2013)
12. Schlatter, P., Bagheri, S., Henningson, D.S.: Self-sustained global oscillations in a jet in cross-flow. Theor. Comput. Fluid Dyn. **25**, 129–146 (2011)

DNS of a Double Diffusive Instability

J.G. Wissink, H. Herlina, S.I. Voropayev and H.J.S. Fernando

1 Introduction

In the present numerical study we consider a body of water with a stable temperature-induced density gradient and an unstable salinity-induced density gradient resulting in an overall density gradient that is weakly stable. As a result of the difference in diffusivity between the temperature (with a Prandtl number of $Pr = 6$) and the salinity (with a Schmidt number of $Sc = 700$) any disturbance added to the temperature, salinity or velocity field will result in the development of a diffusive instability that eventually leads to the occurrence of so-called salt-fingers—consisting of fluid with a relatively high salinity contents—that penetrate the fluid immediately underneath.

This salt fingering phenomenon plays an important role in the oceanic vertical mixing. In regions where warm salty water lies over cool fresh water, such as in the Tyrrhenian Sea, researchers have recognized that the small scale salt fingers result in the generation of a salinity stratification with a distinct layering [1]. As it is important to oceanic mixing, double-diffusion processes also have a strong influence on the oceanic heat and gas fluxes [2]. In an experiment performed by Voropayev et al. [3] it was found that also in the case of a (single diffusive) unstable salinity-induced density gradient the developing instability led to the intermediate formation of a layered salinity distribution despite the initially smooth salinity gradient. To establish

J.G. Wissink (✉)
Brunel University, London, UK
e-mail: jan.wissink@brunel.ac.uk

H. Herlina
Karlsruhe Institute of Technology (KIT), Karlsruhe, Germany
e-mail: herlina.herlina@kit.edu

S.I. Voropayev · H.J.S. Fernando
University of Notre Dame, Indiana, USA
e-mail: s.voropayev@nd.edu

H.J.S. Fernando
e-mail: Harindra.J.Fernando.10@nd.edu

J. Fröhlich et al. (eds.), *Direct and Large-Eddy Simulation IX*,
ERCOFTAC Series 20, DOI 10.1007/978-3-319-14448-1_27

whether a similar layering in a double diffusive environment can be reproduced numerically and to obtain more insight in the physics that drives this phenomenon it was decided to perform a series of two-dimensional and three-dimensional direct numerical simulations (DNS-s).

2 Computational Details

The computational domain is shown in Fig. 1. Periodic boundary conditions for all variables were employed in the horizontal directions. At the top and bottom free-slip boundary conditions were used for the velocity. For the scalars in the two-dimensional simulations either constant flux or zero flux boundary conditions were employed. Two three-dimensional simulations are performed, one with a small height (as seen in Fig. 1) and one with a much larger height (to allow more space for the layer formation). In the three-dimensional simulations a zero flux boundary condition is used along the top and bottom of the computational domain. The Reynolds number, based on a characteristic length scale of $L = 1\,\text{cm}$ and a characteristic velocity scale of $U = 1\,\text{cm/s}$, is $Re = 100$. The simulations are initialised with constant salinity and temperature gradients. The salinity distribution induces an unstable constant density gradient $\frac{\partial \rho}{\partial z} = 5 \times 10^{-4} \frac{\text{g}}{\text{cm}^4}$, while the temperature distribution induces a stable density gradient $\frac{\partial \rho}{\partial z} = -6 \times 10^{-4} \frac{\text{g}}{\text{cm}^4}$. The resultant density gradient is stable (see Fig. 1). To seed possible instabilities a random disturbance of 1 % is added to the temperature field at $t = 0\,\text{s}$.

To accurately resolve the convection of low-diffusive scalars it is important to avoid any undershoot or overshoot at locations where the concentration gradient is steep without introducing an excessive amount of artificial diffusion. The problem of resolving steep gradients is very similar to the problem of shock-capturing in compressible fluid flow simulations. Because of this, it was decided to adopt the fourth-order accurate Weighted Essentially Non-Oscillatory (WENO) scheme—developed by Liu et al. [4]—to calculate the scalar convection. The scheme was adapted for usage on a staggered mesh and the coefficients of the third-order interpolation polynomials were determined using Lagrange interpolations so that the algorithm would also

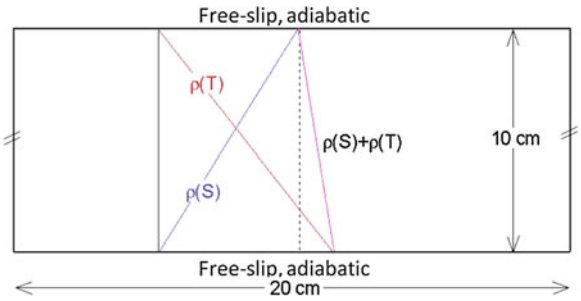

Fig. 1 Schematic of computational domain

work on stretched meshes. The scalar diffusion term was calculated using a fourth-order-accurate central discretisation and the time-integration of the scalar convection-diffusion equations was performed using a three stage Runge Kutta method.

The reason for using a staggered mesh was to avoid a decoupling of the flow and pressure field in the numerical approximation of the incompressible Navier-Stokes equations. A fourth-order-accurate kinetic energy conserving numerical method was used for the discretisation of the convective terms (a detailed description of this discretisation can be found in Wissink [5]). The diffusive terms were discretised by a fourth-order accurate central discretisation. Second-order central discretisations were used for the discretisation of the pressure gradients and the continuity equation. The Poisson equation for the pressure was iteratively solved using a conjugate gradient solver with a simple diagonal preconditioning. Time-stepping was performed using the second-order accurate Adams-Bashforth method.

Because the fluid viscosity can be more than two orders of magnitude larger than the scalar diffusivities it was decided to incorporate a dual mesh capability in the program in which the scalars are resolved on a mesh that can be up to eight times finer than the base mesh used to resolve the flow field. In the present calculations the base mesh (using sufficient mesh points to resolve the salt-fingering) was used for both flow and scalar fields.

A Boussinesq approximation was used to account for the small local differences in density of the fluid which is directly linked to the local temperature and salinity.

The numerical solver was parallellised by dividing the computational mesh in blocks that each contain the same number of grid points. Communications between blocks was performed by using the standard Message Passing Interface (MPI) protocol. More detailed information on the solver, including some grid refinement tests, can be found in [6].

3 Results

Figure 2 shows contours of the salinity distribution obtained for $t = 30, 40, 50, 60$ s after the start of the 2D simulation with a zero flux boundary condition for the scalars at the top and bottom of the computational domain. The sequence of snapshots illustrate the evolution of the diffusive instability driven by the difference in diffusivity between the temperature and the salinity. Salt fingers can already be clearly identified in the first snapshot at $t = 30$ s. In time a progressive mixing of fresh (blue) and salt (red) water can be seen. As a result, with increasing time the salinity-induced density gradient becomes less and less unstable.

The effect of the scalar boundary condition at the top and bottom of the computational domain only has a localised influence on the development of the instability. In the simulation with a zero scalar flux the overall density gradient (i.e. the sum of the temperature and salinity-induced density gradients) becomes unstable near the upper and lower boundary. Compared to the simulation with a constant scalar flux, a faster growth of the instability close to the upper and lower boundaries is obtained during

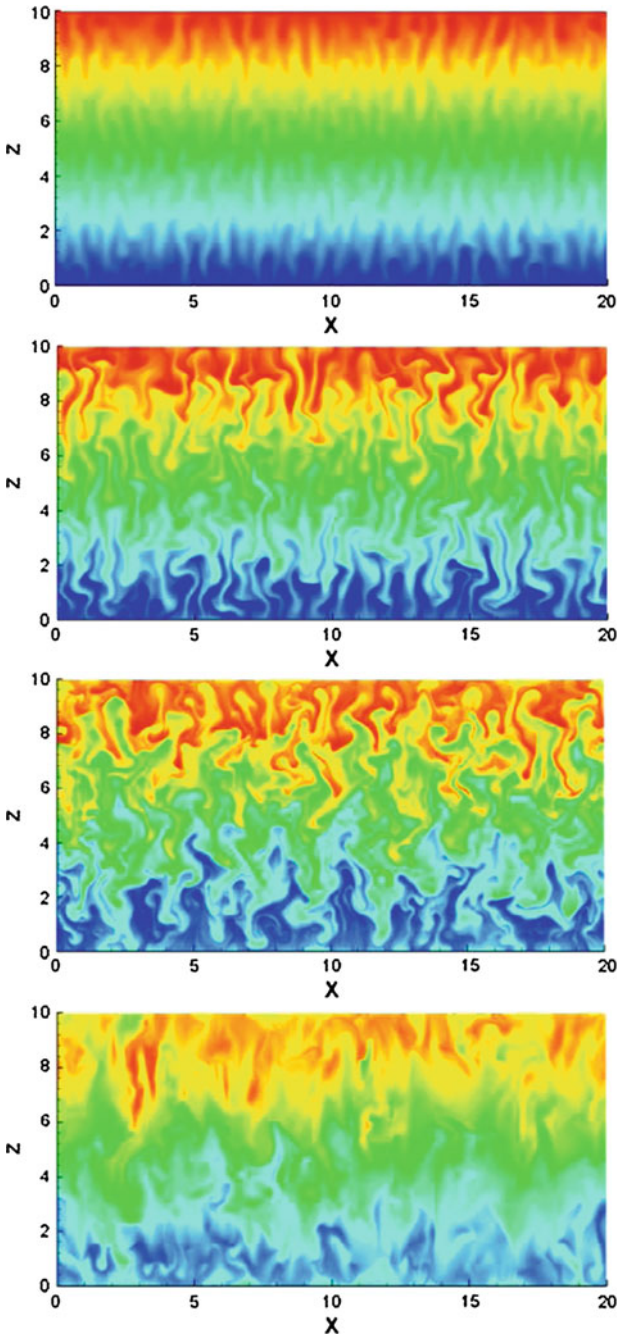

Fig. 2 Contours of the salinity distribution after $t = 30, 40, 50, 60\,\mathrm{s}$

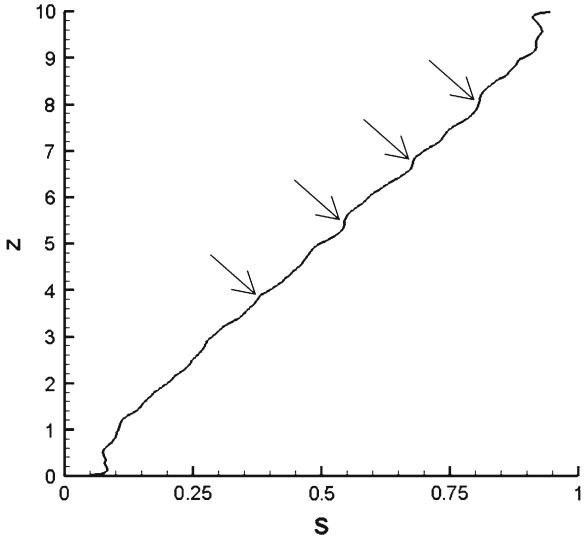

Fig. 3 Profile of the horizontally-averaged salinity concentration at $t = 40$ s. The *arrows* identify locations with weak evidence of intermediate layer formation

the early stages of the simulation. Figure 3 shows the non-dimensional horizontally-averaged salinity concentration. Weak evidence is found of layer formation (locations identified by the arrows).

The first results from the three-dimensional simulation with an increased vertical size can be seen in Fig. 4. The sequence of pictures shows contours of the salinity

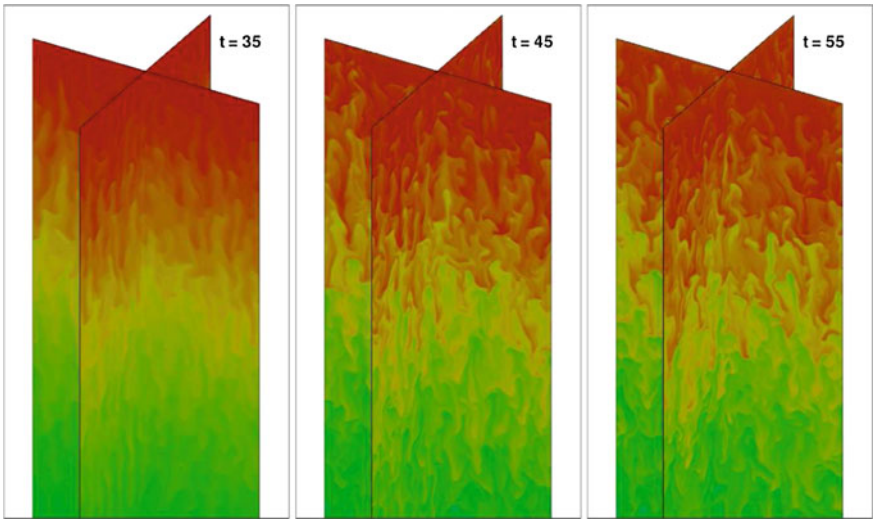

Fig. 4 Salinity contours in the *upper half* of the (x, z)- and (y, z)-planes through the centre of the computational domain. The three snapshots were taken at $t = 35, 45$ and 55 s. The *red* colour corresponds to the maximum salinity concentration

concentration in the (x, z)- and (y, z)-planes through the centre of the computational domain at $t = 35, 45, 55$ s. The initial development of the double diffusive instability through the formation of salt fingers is clearly visible. The boundary conditions applied at the top and bottom were found to lead to a gradual change in the horizontally-averaged density distributions related to both the salinity and the temperature. As a result, the salinity distribution becomes less and less unstable which affects the layer formation in the overall density gradient. To avoid this unwanted change in the mean salinity gradient, a new boundary condition at the top and bottom of the computational domain will be introduced. By assuming periodicity for the velocity and combining this with quasi-periodic boundary conditions for the scalar (which allows the scalar at the top to differ by a fixed constant from the scalar at the bottom thereby ensuring that the mean scalar gradient remains continuous) the mean temperature and salinity gradients will be forced to remain constant at all vertical locations of the computational domain. We are confident that in our further simulations, using this new boundary condition, we will be able to obtain a much clearer formation of layers in the overall density distribution. We also hope to further identify whether in three dimensions this layering—that should lead to a step-wise salinity distribution [1]—becomes more evident than in two dimensions, in which case we should be able to clarify/confirm the exact physical mechanisms that drive this phenomenon.

Acknowledgments This research was partially sponsored by the European Marie Curie project CLIMSEAS-PIRSES-GA-2009-247512.

References

1. Schmitt, R.W.: Double diffusion in oceanography. Annu. Rev. Fluid Mech. **26**, 255–285 (1994)
2. Polyakov, I.V., Pnyushkov, A.V., Rember, R., Ivanov, V.V., Lenn, Y.-D., Padman, L., Carmack, E.C.: Mooring-based observations of double-diffusive staircases over the Laptev sea slope. J. Phys. Oceanogr. **42**, 95–109 (2012)
3. Voropayev, S.I., Afanasyev, Y.D., van Heijst, G.J.F.: Experiments on the evolution of gravitational instability of an overturned, initially stably stratified fluid. Phys. Fluids A **5**(10), 2461 (1993)
4. Liu, X.D., Osher, S., Chan, T.: Weighted essentially nonoscillatory schemes. J. Comput. Phys. **115**(1), 200–212 (1994)
5. Wissink, J.G.: On unconditional conservation of kinetic energy by finite-difference discretisations of the linear and non-linear convection equation. Comput. Fluids **33**(2), 315–343 (2004)
6. Kubrak, B., Herlina, H., Greve, F., Wissink, J.G.: Low-diffusivity scalar transport using a WENO scheme and dual meshing. J. Comput. Phys. **240**, 158–173 (2013)

Flow Past a NACA0012 Airfoil: From Laminar Separation Bubbles to Fully Stalled Regime

I. Rodríguez, O. Lehmkuhl, R. Borrell and A. Oliva

1 Introduction

The flow around airfoils in full stall is a problem of great interest in aerodynamics and specifically for the design of turbo-machines (turbines, propellers, wind turbines, etc.). However, mechanisms of quasi-periodic oscillation observed near stall and stall behaviour, which affect airfoil efficiency, remain still not fully understood. Thus, the study of the separation mechanism and the correct prediction of boundary layer transition are both key aspects for improving engineering designs.

The advances in computational fluid dynamics together with the increasing capacity of parallel computers have made possible to tackle such complex turbulent problems by using high-performance numerical techniques such as direct numerical simulation (DNS) [1, 4]. DNS has a key role for improving the understanding of the turbulence phenomena and for the simulation of transitional flows in complex geometries. In the present work DNS of the flow past a NACA0012 airfoil at $Re = 5 \times 10^4$ and angles of attack (AOA) of 5°, 8°, 9.25° and 12° (the last one correspond to a full-stall situation) have been carried out. This work aims at investigating the mechanisms of separation and the prediction of the transition to turbulence in the separated shear-layer, while at the same time to gain insight into coherent structures formed in the separated zone at low-to-moderate Reynolds numbers.

I. Rodríguez (✉) · O. Lehmkuhl · A. Oliva
Technical University of Catalonia, Colom 11, 08222 Terrassa, Spain
e-mail: ivette@cttc.upc.edu

O. Lehmkuhl
e-mail: oriol@cttc.upc.edu

A. Oliva
e-mail: oliva@cttc.upc.edu

R. Borrell
Termo Fluids S.L., Avda. Jacquard 97 1-E, 08222 Terrassa, Spain
e-mail: ricardb@cttc.upc.edu

J. Fröhlich et al. (eds.), *Direct and Large-Eddy Simulation IX*,
ERCOFTAC Series 20, DOI 10.1007/978-3-319-14448-1_28

2 Numerical Method

The governing equations are discretised on a collocated unstructured grid arrangement, by means of second-order conservative schemes [9]. Such discretisation preserves the symmetry properties of the continuous differential operators, and ensure both stability and conservation of the global kinetic-energy balance on any grid. For the temporal discretisation the one-parameter second-order explicit scheme on a fractional-step method has been used for the convective and diffusive terms [8], while for the pressure gradient term an implicit first-order scheme has been implemented. This methodology has been previously used with accurate results for solving the flow over bluff bodies with massive separation (see for instance [7]).

3 Results

All computed flows are around a NACA-0012 airfoil extended to include sharp trailing edge. Solutions are obtained in a computational domain of dimensions $40\,C \times 40\,C \times 0.2\,C$ with the leading edge of the airfoil placed at $(0, 0, 0)$.The boundary conditions at the inflow consist of a uniform velocity profile (u, v, w) = $(U_{ref} \cos AOA,\ U_{ref} \sin AOA, 0)$. As for the outflow boundary, a pressure-based condition is imposed. No-slip conditions on the airfoil surface are prescribed. Periodic boundary conditions are used in the spanwise direction.

Flow around an airfoil is mostly laminar with the exception of a zone close to the surface of the airfoil (suction side) and in the wake of it. When performing DNS, it must be ensured that the grid size is enough to resolve the smallest flow scales well in the turbulent zones. Furthermore, within laminar zones boundary layer must be also well-resolved. Taking into account that the accuracy of the results is highly grid-dependent, specially in the region of the separated shear-layer where transition to turbulence occurs, care must be taken when the computational grid is constructed. Another critical region is the near wake of the airfoil, where a poor grid resolution may cause notable upstream flow distortions. With these criteria, more control volumes have been clustered in these zones. Although the grids used are unstructured, they have been constructed as uniform as possible in the regions of interest. Thus, simulations have been performed on different grids depending on the AoA: 263522×96 planes ($\sim$25.3 million CVs) for $AOA = 5°$; 280876×96 planes ($\sim$27 million CVs) for $AOA = 8°$ and 381762×128 planes ($\sim$48.9 million CVs) for $AOA = 9.25°$ and $12°$.

3.1 Instantaneous Flow Structures

In order to gain insight into the coherent structures developed in the separated zone, the Q-criterion proposed by Hunt et al. [3] has been used. Q iso-surface plots are

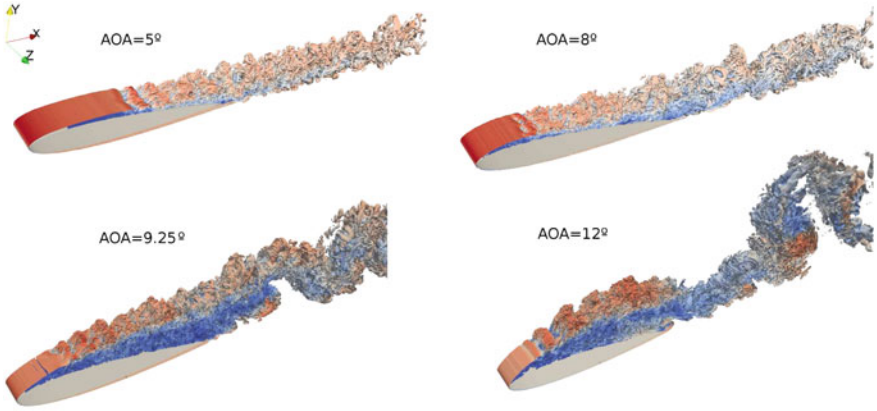

Fig. 1 Visualisation of the instantaneous vortical structures on the suction side of the airfoil by means of Q-iso-surfaces; $Q = 30$ coloured by the velocity magnitude

depicted in Fig. 1. A first inspection of the figure reveals the large quantity of small scales in the separated zone. In fact as the AOA increases one can note how this region is broadened due to the increase of the adverse pressure gradient. At all AOAs, the flow separates laminarly from the airfoil surface near the leading edge, as can be inferred from the two-dimensional shear-layer. Vortex breakdown occurs at the end of the laminar shear-layer as a consequence of the instabilities developed by the action of a Kelvin-Helmholtz mechanism (see Fig. 2). The velocity field which grow in magnitude as the distance from the leading edge increases and eventually causes shear layer to roll-up and undergo transition to turbulent flow. For instance, if the flow at $AOA = 12°$ is inspected, these instabilities can be seen at the end of the laminar shear-layer. Indeed, the increase in their amplitude until finally transition to turbulence occurs is also shown in the figure. This mechanism of transition is similar

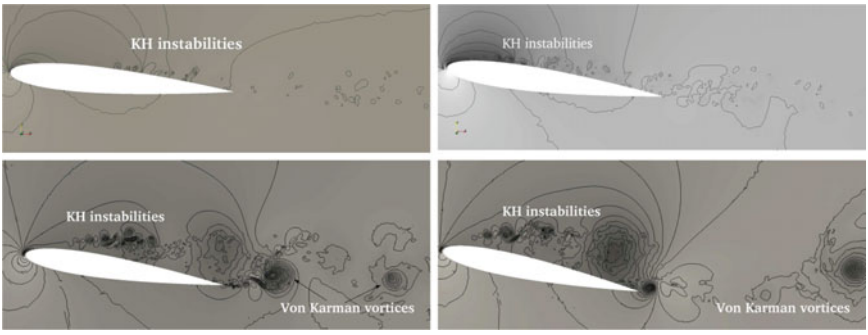

Fig. 2 Instantaneous pressure contours for *top left* $AOA = 5°$, *top right* $AOA = 8°$, *bottom left* $AOA = 9.25°$ and *bottom right* $AOA = 12°$

to that observed in shear-layers developed in other bluff bodies such as the flow past a circular cylinder (see for instance [5]) or the flow past a sphere [7].

A close-up of the developing flow structures in the separated shear-layer is shown in Fig. 2 by means of pressure and vorticity isocontours projected into a two-dimensional plane. The extension of the separated zone increases with the AOA. For the lower AOAs after transition to turbulence, the flow reattaches to the airfoil surface, while at the two largest AOAs, the flow fails to reattach and a large detached zone origins within the suction side. Kelvin-Helmholtz instabilities appear as small vortices in the pressure field at all AOAs. In fact, at $AOA = 12°$, trailing edge vortices enter the suction side and interact with those developed at the leading edge to form a pattern similar to a von Kármán like vortex street (not shown here), which resembles that of a circular cylinder.

According with Huang and Lin [2] observations of the flow past a NACA0012 airfoil at low-to-moderate Reynolds numbers, the way vortices are shed into the wake present four characteristics modes: laminar, subcritical, transitional and supercritical. In this characterisation, the subcritical mode corresponds with a vortex shedding process where turbulent fluctuations due to upstream instabilities are superimposed, in the transitional mode vortices shed are irregular and without coherence, forming a disorganised wake. They did not detect any vortex shedding in this regime. On the other hand, in the supercritical mode, the flow is coherent and turbulent vortex shedding is re-established. Following Huang and Lin classification, at $AOA = 5°$ the flow is in the subcritical mode, at $AOA = 8°$ and $9.25°$ the wake mode should correspond to the transitional one, whereas at $AOA = 12°$ the supercritical mode should be detected. In fact, from the inspection of time series at $x/C = 1.2$; $y/C = 0.04$ (see Fig. 3), stream-wise velocity exhibits an organised behaviour just disturbed by upstream fluctuations of the flow at $AOA = 5°$, while at $AOA = 8°$ and $9.25°$ the loss of coherence in the signal, typical of the transitional regime can be observed. At $AOA = 12°$, the stream-wise signal is highly coherent which agrees well with Huang and Lin's supercritical mode.

3.2 Mean Aerodynamic Coefficients

The pressure distribution on the airfoil surface obtained at all AOAs is plotted in Fig. 4 (left). In addition, the mean skin friction distribution is given in Fig. 4 (right). Near the leading edge, the pressure gradient causes separation of the boundary layer. This separation point moves towards the leading edge with the increase in the AOA (see also Fig. 4). When comparing the pressure distribution at the larger AOAs with that obtained at pre-stall angles of $AOA = 5°$ and $8°$, a strong decrease in the suction pressure peak near the leading edge, which is typical of stalled airfoils, can be observed. The pressure profile at $AOA = 9.25°$ exhibits a plateau after the suction peak and a further gradual pressure recovery until reaching the trailing edge. This behaviour is quite different of pre-stall angles in which there is a sudden recovery of the suction pressure. Indeed, at $AOA = 9.25°$ pressure behaviour is halfway

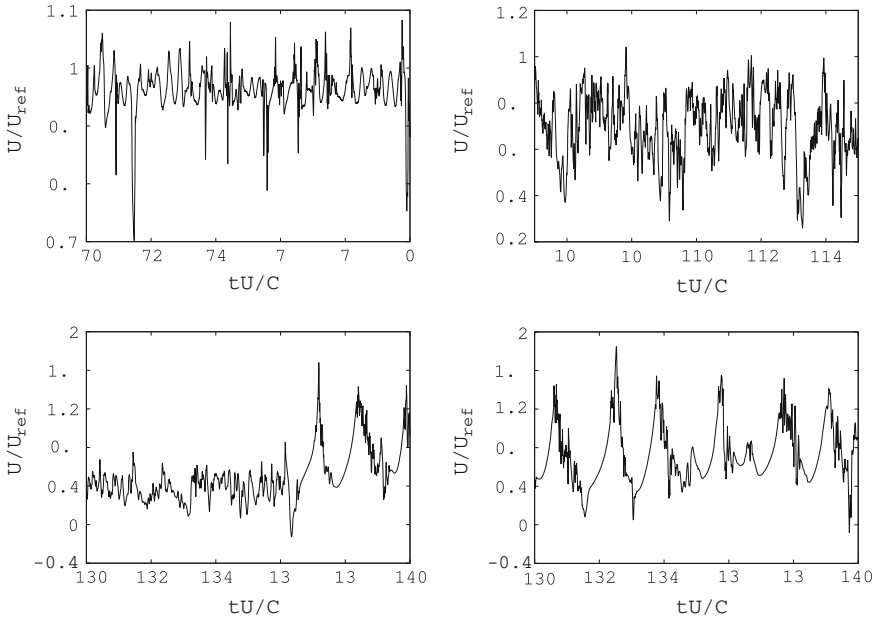

Fig. 3 Stream-wise velocity time series for *top left* $AOA = 5°$, *top right* $AOA = 8°$, *bottom left* $AOA = 9.25°$ and *bottom right* $AOA = 12°$

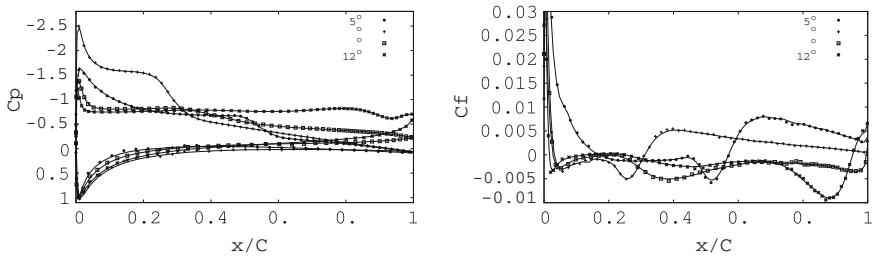

Fig. 4 *Left* Mean pressure coefficient distribution; *Right* Mean skin friction distribution

from the profile obtained in flows with laminar separation bubble and flows with full separation (e.g. $AOA = 12°$). A similar pressure distribution was obtained by Rinoie and Takemura [6] at $Re = 1.3 \times 10^5$ and $AOA = 11.5°$–$12°$, just after stall. At $AOA = 12°$ a much flatter profile is observed, which is typical of fully stalled airfoils. Near the trailing edge a slight depression is also observed. This is due to the vortex entrainment produced by the formation of a much wider wake in the detached zone and the shedding of vortices at the trailing edge (see Sect. 3.1). As for the mean skin friction distribution on the suction side of the airfoil, it is in correspondence with the pressure profile measured. For the larger AOAs, a large reversed flow forming a long bubble in the upper surface is observed. For $AOA = 12°$, there is a small

recirculation near the leading edge and underneath the large recirculation zone. It is between $x/C = 0.127$ and $x/C = 0.245$. The broad recirculation region at this AOA closes near the trailing edge at $x/C = 0.954$.

4 Conclusions

In the present work, the flow past a NACA0012 airfoil at a low-to-moderate Reynolds number of 50000 has been studied. Depending on the AOA, the flow separates forming a laminar separation bubble ($AOA = 5°, 8°$) with further reattachment to the airfoil surface or fails to reattach forming a large separated zone ($AOA = 9.25°, 12°$). It has been observed that the separated flow is slightly different depending on the AOA. Indeed, coherent structures identified have shown that, in agreement with the experimental observations, at $AOA = 5°$ the flow is in the subcritical mode, at $AOA = 8°$ and $9.25°$ the wake mode should correspond to the transitional one, whereas at $AOA = 12°$ the supercritical mode is detected. The pressure and skin friction distributions have also been evaluated. Pressure distribution at the larger AOAs exhibits a strong decrease in the suction pressure peak near the leading edge, if compared with that obtained at pre-stall angles of $AOA = 5°$ and $8°$. At $AOA = 9.25°$, the pressure exhibits a plateau after the suction peak and a further gradual recovery until reaching the trailing edge. This compares well to experimental observations measured just after stall.

Acknowledgments This work has been financially supported by the "Ministerio de Economía y Competitividad, Secretaría de Estado de Investigación, Desarrollo e Innovación", Spain (ref. ENE2009-07689 and ENE2010-17801) and by the Collaboration Project between Universidad Politècnica de Catalunya and Termo Fluids S.L. We acknowledge the technical expertise, assistance and access to MareNostrum II provided by the Red Española de Supercomputación.

References

1. Baez, A., Lehmkuhl, O., Rodríguez, I., Pérez-Segarra, C.D.: Direct numerical simulation of the turbulent flow around a NACA 0012 airfoil at different angles of attack. In: Proceedings of 24th Conference on Parallel CFD, Barcelona, Spain (2011)
2. Huang, R.F., Lin, C.H.: Vortex shedding and shear-layer instability of wing at low-Reynolds numbers. AIAA J. **33**(8), 1398–1403 (1995)
3. Hunt, J., Wray, A., Moin, P.: Eddies, stream and convergence zones in turbulent flows. Technical report CTR-S88, Center for Turbulent Research (1988)
4. Lehmkuhl, O., Baez, A., Rodríguez, I., Pérez-Segarra, C.D.: Direct numerical simulation and Large-Eddy simulations of the turbulent flow around a NACA-0012 airfoil. In: 7th International Conference on Computational Heat and Mass Transfer (2011)
5. Prasad, A., Williamson, C.: The instability of the shear layer separating from a bluff body. J. Fluid Mech. **133**, 375–492 (1997)
6. Rinoie, K., Takemura, N.: Oscillating behaviour of laminar separation bubble formed on an aerofoil near stall. Aeronaut. J. **1**, 2816 (2004)

7. Rodríguez, I., Borrell, R., Lehmkuhl, O., Pérez-Segarra, C.D., Oliva, A.: Direct numerical simulation of the flow over a sphere at Re = 3700. J. Fluid Mech. **679**, 263–287 (2011)
8. Trias, F., Lehmkuhl, O.: A self-adaptive strategy for the time integration of Navier-Stokes equations. Numer. Heat Transf. Part B **60**(2), 116–134 (2011)
9. Verstappen, R.W.C.P., Veldman, A.E.P.: Symmetry-preserving discretization of turbulent flow. J. Comput. Phys. **187**, 343–368 (2003)

Large-Eddy Simulation of a Shallow Turbulent Jet

R. Mullyadzhanov, B. Ilyushin, M. Hadžiabdić and K. Hanjalić

1 Introduction

Turbulent shallow jets discharged into ambient fluid of much larger spanwise and streamwise dimensions can be considered as a paradigm of effluent discharges into shallow lakes, rivers, and coastal waters as well as large-scale geophysical flows in the atmosphere and oceans. It is also a generic configuration for a number of cooling devices encountered in various industries. However, because of a large disparity between the small fluid thickness and much larger width and length of the receiving fluid, the flow contains interesting physics as the unsteady large-scale structures tend to remain basically two-dimensional. The small lateral dimension inhibits the natural vortex stretching, thus far blocking the natural down-scale energy cascade making room for small scales to exert feedback on the large-scale quasi-two-dimensional motion. If the flow is bounded by narrowly-spaced solid walls on both sides, the wall impermeability and viscous damping exert additional effects that influence the vortex and turbulence dynamics. The characteristic feature of the far-field in such flows reported by several researchers is the dominant two-dimensional large-amplitude

R. Mullyadzhanov (✉) · B. Ilyushin
Institute of Thermophysics SB RAS, Novosibirsk, Russia
e-mail: rustammul@gmail.com

B. Ilyushin
e-mail: ilyushin@itp.nsc.ru

B. Ilyushin · K. Hanjalić
Novosibirsk State University, Novosibirsk, Russia

M. Hadžiabdić
International University of Sarajevo, Sarajevo, Bosnia and Herzegovina
e-mail: mhadziabdic@ius.edu.ba

K. Hanjalić
Delft University of Technology, Delft, Netherlands
e-mail: khanjalic@gmail.com

J. Fröhlich et al. (eds.), *Direct and Large-Eddy Simulation IX*,
ERCOFTAC Series 20, DOI 10.1007/978-3-319-14448-1_29

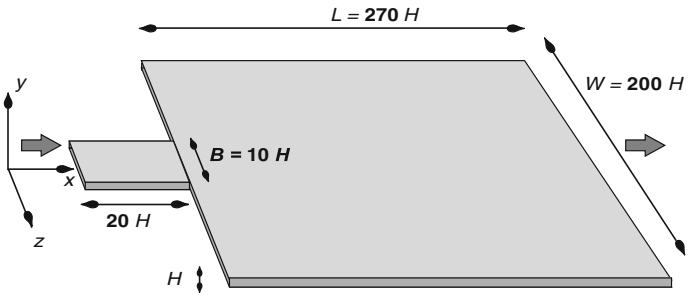

Fig. 1 Flow geometry and solution domain (streamwise and spanwise dimensions of receiving tank are not in scale)

quasi-periodic motion, which gives it the appearance of a meandering jet (e.g. [3]). Experiments (e.g. [3, 6, 10, 12]) indeed showed that the flow is strongly unsteady despite the steady inflow and strong wall damping, but the effects depend on the ratio of the jet slot height H and its spanwise width B.

We report on large-eddy-simulation (LES) of a turbulent plane jet discharged from a rectangular slot $H \times B$ into an open-ended wall-bounded container having the same flow depth H as the jet, but much larger width W and length L, Fig. 1. This configuration with $H \ll B$ was selected because it mimics more closely the typical real-life situations of environmental effluent discharge ($B/H > 4$) in contrast to the cases with $H > B$ or $H \gg B$ considered in most of the earlier studies reported in the literature. The aim of the work is to gather information from LES about the flow and turbulence dynamics in general, and especially on the interaction and energy transfer between different scales of turbulence.

2 Computational Details and Flow Characteristics

The LES is performed using the finite-volume computational code T-FlowS, with the cell-centred collocation grid structure. We solve the equations for the filtered incompressible velocity field $\overline{u}_i$, where the overbar denotes the low-pass filter:

$$\partial_t \overline{u}_i + \partial_j(\overline{u}_i \overline{u}_j) = -\partial_i \overline{p} + \nu \partial_j^2 \overline{u}_i - \partial_j \tau_{ij}, \tag{1}$$

$$\partial_j \overline{u}_j = 0, \tag{2}$$

where $\overline{p}$ is the (modified) pressure, ν is the kinematic viscosity. The subgrid-scale stress tensor $\tau_{ij} = \overline{u_i u_j} - \overline{u}_i \overline{u}_j$ is modelled using the dynamic Smagorinsky model. A fully implicit three-level time scheme is used for time-marching, while the diffusion and convection terms in the momentum equations are discretized by the second-order central-differencing scheme. The velocity and pressure fields are coupled by the iterative pressure correction algorithm SIMPLE. The computations have been

performed for the Reynolds number $Re = U_b H/\nu = 10^4$, where U_b is the bulk velocity in the slot (duct) flow. The convective outflow condition is used at the end of the domain, while the no-slip condition is applied for all walls. The inflow channel ($20H \times 10H \times H$) is meshed with $N_x \times N_y \times N_z = 220 \times 72 \times 190$ hexahedral cells in streamwise (x), wall-normal (y), and spanwise (z) directions respectively. The mesh of the receiving volume consists of about 15 mln cells ($336 \times 72 \times 622$). A velocity profile is extracted every time step from the precursor simulation of a duct flow ($10H \times 10H \times H$, $N_x \times N_y \times N_z = 200 \times 72 \times 190$) with periodic streamwise conditions and imposed as the inflow condition. The mesh is clustered towards the walls and within the mixing layers with an increment $\leq 5\,\%$. In the duct cell sizes in wall units near the wall are $\Delta x^+ = 23.1$, $y_1^+ = 1.49$, $\Delta z^+ = 91$, thus satisfying the recommended criteria, apart from Δz^+, which was expected to be of little importance for our analysis. The value for ν_t/ν in the mixing layer is less than 4, where ν_t is the turbulent viscosity defined by the dynamic Smagorinsky model.

The computated results were compared with the PIV data of [1] (not shown here because of space limitation) obtained in a configuration of the same geometry and flow parameters. Admittedly the inflow into the experimental duct was generated by a matrix of small jets issuing through holes in a pipe wall placed across the flow at a distance of about $7B$ upstream from the inlet, which produces much higher inflow turbulence than generated numerically by imposing periodic conditions. This led to a slower decay of the computed axial velocity downstream compared to the experiments. However, both sets of data exhibit linear decay.

Following [7], we consider a time correlation function $R(\tau)$ between two points of the fixed x coordinate at opposite sides of the jet to detect the meandering motion. Figure 2 suggests that the Strouhal number $St_H = fH/U_b$ is around 10^{-2}, where $f = \tau^{-1}$ is the frequency of the meandering. However, using $B = 10H$ for the

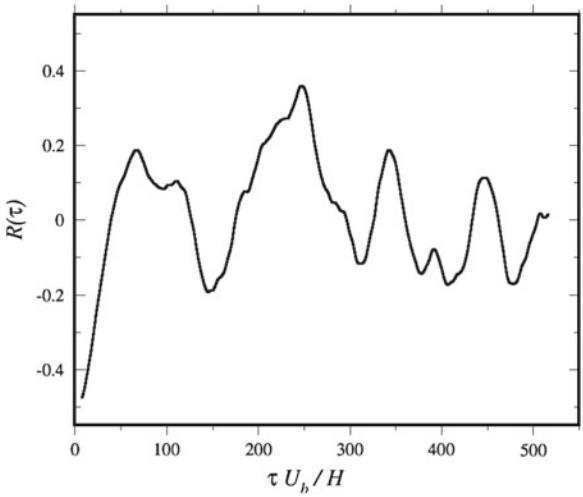

Fig. 2 Correlation function $R(\tau)$ at $x = 92H$ downstream from the inflow at $z = \pm 5H$

scaling of St we obtain $St_B = 10^{-1}$, which agrees well with $St = 0.07$ measured in [3, 10], thus supporting the earlier findings that B (or the half-width of the jet) is the proper scaling length.

3 Energy Transfer Analysis

A strictly two-dimensional turbulence may exhibit two inertial ranges, with the isotropic energy spectrum $E(\kappa) \propto \varepsilon^{2/3}\kappa^{-5/3}$ at small wavenumbers and $E(\kappa) \propto \eta^{2/3}\kappa^{-3}$ at larger wavenumbers κ, where ε and η denote the constant energy and enstrophy flux respectively [9]. The same spectral distributions have been detected in atmospheric wind [2], but also in some quasi-two-dimensional laboratory flows such as shallow meandering jets [1, 3, 10], but with interchanged wavenumber ranges, i.e. the "−3" distribution at low and "−5/3" at higher wavenumbers. The consequence of the constant enstrophy flux in the "−3" range is the upscale (inverse) energy transfer which feeds into the large-scale meandering vortices, as manifested in their continuous growth as they move downstream. The probable source of energy is the instability of the meandering jet.

In this section we attempt to identify this inverse energy transfer from the LES results. Despite 15 mln cells, the mesh resolution in the central zone seems just sufficient to capture only the "−3" range, but not the "−5/3" one, Fig. 3. Nevertheless, the obtained spectra permit still to detect the inverse transfer, as shown below.

The technique described in [5] is usually used to study the energy transfer among scales in spectral space via the Fourier transforms. However, it is limited to the flows with homogeneous directions. The averaged equations relating the second-order to

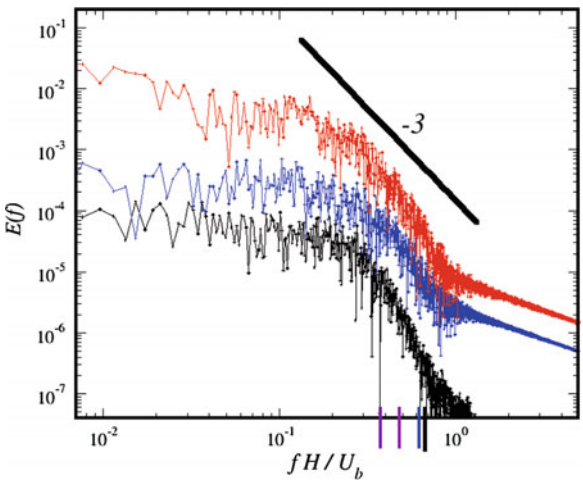

Fig. 3 Normalised energy spectra of axial velocity at $x = 49H$; $92H$; and $110H$ (*bottom* to *up*). For clarity, the two *bottom curves* are shifted downwards by one decade each

the third-order structure function derived in [8] represent a generalization of the Kolmogorov equation. In [8, 13] the authors studied a channel flow using DNS and showed that the buffer layer provides the inverse energy transfer. This methodology requires time-averaging and, as a consequence, abundant reliable statistics.

In the present geometry no periodic directions are available, which poses a problem of detecting the energy transfer via correct averaging. Instead of working with averaged quantities we analyze the flow using instantaneous fields. We introduce an additional filtering following the ideas described in [4]. Providing $\overline{\Delta}$ is the characteristic value of the grid, we introduce a new scale $\tilde{\Delta} > \overline{\Delta}$. Filtering equation (1) on this new scale and multiplying it by $\tilde{\overline{u}}_i$, we obtain an equation for kinetic energy of motion $\tilde{K} = \tilde{\overline{u}}_j \tilde{\overline{u}}_j/2$ for scales larger than $\tilde{\Delta}$:

$$\partial_t \tilde{K} + \partial_j \left(\tilde{K} \tilde{\overline{u}}_j + \tilde{\overline{p}}\, \tilde{\overline{u}}_j - \tilde{\overline{u}}_i \tilde{S}_{ij} - \tilde{\overline{u}}_i (\tilde{\tau}_{ij} + \tilde{T}_{ij}) \right) = (\tilde{\tau}_{ij} + \tilde{T}_{ij}) \tilde{S}_{ij} - 2\nu \tilde{S}_{ij} \tilde{S}_{ij}, \quad (3)$$

where S_{ij} is the strain-rate tensor and $\tilde{T}_{ij} = \widetilde{\overline{u}_i \overline{u}_j} - \tilde{\overline{u}}_i \tilde{\overline{u}}_j$ is introduced for convenience. The first term on the right-hand side of the equation

$$(\tilde{\tau}_{ij} + \tilde{T}_{ij}) \tilde{S}_{ij} = -\tilde{\Pi} \quad (4)$$

corresponds to the energy transfer between scales smaller and larger than $\tilde{\Delta}$. Note that this representation of source terms is Galilean invariant. If $\tilde{\Pi} < 0$, the energy moves from scales less than $\tilde{\Delta}$ to larger ones, and vice versa if $\tilde{\Pi} > 0$. In this work additional filtering on various $\tilde{\Delta}$ scales is made in the finite-volume sense. The averaging over neighboring cells is performed where only neighbors in y and z are taken into account. Figure 3 show $\overline{\Delta}$ (black line) and $\tilde{\Delta}$ (a set of colour lines) at $x = 92H$ as vertical dashes. These frequencies $f_{\overline{\Delta}} < f_{\tilde{\Delta}}$ are computed as follows: $f_\Delta = U_x/\Delta$, where U_x is the mean axial velocity at that point, $\Delta = (\Delta_x^2 + \Delta_y^2 + \Delta_z^2)^{1/2}$ and Δ_x, Δ_x, and Δ_x are the cell size in the corresponding direction.

Figure 4 shows instantaneous vector and pressure fields together with $\tilde{\Pi}$ contours characterizing local energy transfer between turbulent scales. Pressure minima identify large-scale growing vortices due to the meandering of the jet. At some distance downstream several areas with $\tilde{\Pi} < 0$ are revealed. These areas happen to be inside (and around) quasi-two-dimensional vortices. Note that varying $\tilde{\Delta}$ blue areas do not change their positions downstream, while upstream they move corresponding to the common backscatter. $\tilde{\Pi}$ represents the transfer of energy through the particular scale defined by $\tilde{\Delta}$. According to the spectral cascade ideas, the presented analysis suggests that the energy goes from smaller to larger scales once the "−3"-slope appears in this particular situation.

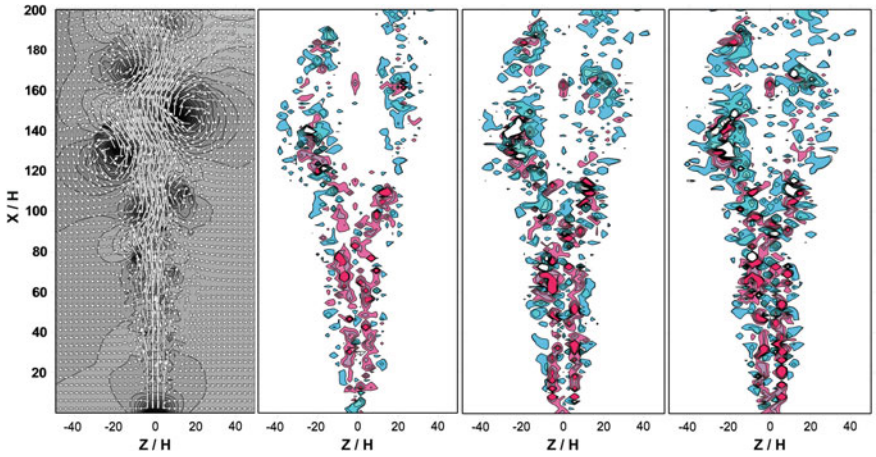

Fig. 4 Snapshot of instantaneous velocity vectors and pressure field at $y = H/2$ (*dark* low pressure) together with contours of $\tilde{\Pi}$ for $\tilde{\Delta} = 1.08\overline{\Delta}$, $1.4\overline{\Delta}$, and $1.84\overline{\Delta}$. *Red* $\tilde{\Pi} > 0$, *blue* $\tilde{\Pi} < 0$

4 Conclusions

Large-eddy simulation of a turbulent shallow jet issuing from a plane channel into a much larger wall-bounded receiver of the same depth reveals meandering large-scale quasi-two-dimensional vortices growing on both sides of the jet. The axial velocity decreases linearly downstream in accordance with the experiment, though at a slower rate due to less turbulent inflow fluid. The time correlations confirms the meandering motion, with a Strouhal number $St_B = 10^{-1}$, in agreement with the experimental data in the literature.

The energy spectra of the axial velocity showed a consistent "-3" slope at lower wavenumbers in the flow region where meandering motion appears indicating at an inverse energy transfer. This has been confirmed by the analysis of energy transfer of the LES data using several test filters larger than the computational cell size. The approach reveals that the inverse energy transfer takes place inside (or around) these quasi-two-dimensional vortices. We do not discuss any analogies with two-dimensional turbulence on purpose since the nature of "-3" cascade in this case is not yet clear.

It is interesting that the main physics of the flow is captured together with its right meandering frequency using a relatively coarse mesh. A better resolution with much finer mesh (10 times finer in the jet core) is required to identify the "$-5/3$"-slope spectrum at large wavenumbers to study the interaction between broad range of turbulent scales of the flow. These simulations are currently in progress together with the application of some other energy transfer detection methods such as the local scale-by-scale analysis [11] and interactions between the ensemble-averaged and stochastic fields.

Acknowledgments The authors acknowledge Dr. D.Ph. Sikovsky for fruitful discussions. This work was supported by Siberian Supercomputer Centre SB RAS. This work was performed with funding from the Government of Russian Federation (Lead Scientists Grant No. 11.G34.31.0046 for K. Hanjalic) and from the Ministry of Education and Science of the Russian Federation (Grant No. 14.518.11.7075).

References

1. Bilsky, A.V., Lozhkin, V.A., Markovich, D.M., Shestakov, M.V., Tokarev, M.P.: Tomographic PIV and planar time-resolved PIV measurements in a turbulent slot jet. In: Proceedings of 16th International Symposium on Applications of Laser Techniques to Fluid Mechanics, Lisbon, Portugal, 09–12 July 2012
2. Danilov, S.D., Gurarie, D.: Quasi-two-dimensional turbulence. Phys. Uspekhi. **43**(9), 863–900 (2000)
3. Dracos, T., Giger, M., Jirka, G.H.: Plane turbulent jets in a bounded fluid layer. J. Fluid Mech. **241**, 587–614 (1992)
4. Eyink, G.L., Aluie, H.: Localness of energy cascade in hydrodynamic turbulence. I. Smooth coarse-graining. Phys. Fluids **21**, 115108 (2009)
5. Frisch, U.: Turbulence: The Legacy of A.N. Kolmogorov. Cambridge University Press, Cambridge (1995)
6. Giger, M., Dracos, T., Jirka, G.H.: Entrainment and mixing in plane turbulent jets in shallow water. J. Hydraul. Res. **29**, 615–642 (1991)
7. Goldschmidt, V.W., Bradshaw, P.: Flapping of a plane jet. Phys. Fluids **16**, 354 (1973)
8. Hill, R.J.: Exact second-order structure-function relationships. J. Fluid Mech. **468**, 317–326 (2002)
9. Kraichnan, R.H.: Inertial ranges in two-dimensional turbulence. Phys. Fluids **10**(7), 1417–1422 (1967)
10. Landel, J.R., Caulfield, C.P., Woods, A.W.: Meandering due to large eddies and the statisticcaly sef-similar dynamics of quasi-two-dimensional jets. J. Fluid Mech. **692**, 347–368 (2012)
11. Marati, N., Casciola, C.M., Piva, R.: Energy cascade and spatial fluxes in wall turbulence. J. Fluid Mech. **521**, 191–215 (2004)
12. Rowland, J.C., Stacey, M.T., Dietrich, W.E.: Turbulent characteristics of a shallow wall-bounded plane jet: experimental implications for river mouth hydrodynamics. J. Fluid Mech. **627**, 423–449 (2009)
13. Saikrishnan, N., De Angelis, E., Longmire, E.K., Marusic, I., Casciola, C.M., Piva, R.: Reynolds number effects on scale energy balance in wall turbulence. Phys. Fluids **24**, 015101 (2012)

Part VI
Turbulence

Large Scale Motions in the Direct Numerical Simulation of Turbulent Pipe Flow

B.J. Boersma

1 Introduction

From an engineering point of view turbulent pipe flow is a very important flow geometry, because of its wide range of technical applications. Although most engineering problems involving pipe flows can be solved by simple engineering correlations, there is still considerable fundamental interest in turbulent pipe flow. One of the open questions is the scaling of turbulent statistics in pipe flows. For instance, in the past it has been argued that the peak of the axial root mean square (rms) value of the turbulent fluctuations is nearly constant and thus independent of the Reynolds number, see for instance [10]. However, the Princeton super pipe experiments indicate that there is a strong dependence of the peak value of the axial rms on the Reynolds number, see for instance [9, 12]. In a recent paper [5] by the Princeton group a new calibration procedure has been used for the probe which is more accurate for low values of the velocity, hence it should be more reliable near the curved pipe wall. The new calibration gives results which are more or less in line with the observation of [10]. Other issue in pipe flow are for instance, the scaling of the mean velocity profile and the existence of very long meandering structures. Large scale meandering structures have been observed in turbulent boundary layers [6] and channel flow [7]. They are also experimentally observed in pipe flows [11] however two point correlations indicate that these structures are considerably longer in pipes than in channels. Hutchins and Marusic [6] argue that these large scale structures can penetrate into the near wall layer and can make a significant contribution to the kinetic energy in this layer, even down to $D/2-r = 15\,\nu/u_*$, (where u_* is the friction velocity, D the pipe diameter and ν the kinematic viscosity). This is the location where in general the peak of the turbulent kinetic energy is observed. Given the points above, and the lack of accurate simulation data for pipe flow, it is in our view useful to perform well resolved direct numerical simulations of pipe flow at high Reynolds numbers. These

B.J. Boersma (✉)
Department of Process & Energy, Delft University of Technology, Delft, The Netherlands
e-mail: b.j.boersma@tudelft.nl

J. Fröhlich et al. (eds.), *Direct and Large-Eddy Simulation IX*,
ERCOFTAC Series 20, DOI 10.1007/978-3-319-14448-1_30

simulations will be especially useful for the study of near-wall quantities which are very difficult to measure experimentally, especially at high Reynolds numbers where distances to the wall become extremely small.

2 Numerical Method

In we will shortly describe the numerical method which has been used to solve these equations.

It is assumed that the flow in the pipe is governed by the incompressible equations for conservation of mass and momentum. The governing equations are normalized with the friction velocity u_* and the pipe diameter D. The friction velocity is by definition equal to the square root of the wall friction divided by the fluids density, i.e. $u_* = \sqrt{\tau_w/\rho}$. The frictional Reynolds number can now be defined as $Re_* = u_* D/\nu$ and the bulk Reynolds number $Re_b = (U_b/u_*)Re_*$, where U_b is the bulk velocity.

In the present study we have chosen, for a pseudo spectral method in the streamwize and circumferential direction combined with a highly accurate 6th order staggered compact finite difference method in the radial direction. This solution strategy has been employed by us before [1, 2]. The non-linear terms in equation momentum equation are reformulated in the skew symmetric form, with an additional term involving the divergence $\partial u_j/\partial x_j$:

$$\frac{\partial u_i u_j}{\partial x_j} = \frac{1}{2}\left(\frac{\partial u_i u_j}{\partial x_j} + u_j\frac{\partial u_i}{\partial x_j} + u_i\frac{\partial u_j}{\partial x_j}\right)$$

This formulation is sometimes referred to as the Arakawa form [4].

The time integration of the momentum equation is split into two steps. In the first step the velocity vector $\mathbf{u}^n$ is integrated from t to $t + \Delta t$ with help of 3rd order Adams-Bashforth method

$$\mathbf{u}^* - \mathbf{u}^n = \Delta t\left[\frac{23}{12}g^n - \frac{16}{12}g^{n-1} + \frac{5}{12}g^{n-2})\right] + O(\Delta t)^3 \tag{1}$$

where $\mathbf{u}^*$ is the predicted value of the velocity vector at time level $t + \Delta t$, with Δt as the time step and g^{n-j} denotes the spatial discretization of the terms in the momentum equation at time $t = (n - j)\Delta t$. Subsequently the pressure at time level $n + 1/2$ can be used to calculate the velocity at time level $n + 1$:

$$\mathbf{u}^{n+1} = \mathbf{u}^* - \Delta t\frac{1}{\rho}\nabla p^{n+1/2} \tag{2}$$

So far the pressure at the time level $n + 1/2$ is unknown but it can be be computed from a Poisson equation which can be derived by taking the divergence of Eq. (2), and enforcing the divergence to zero at time level $n + 1$, this gives:

$$\nabla \cdot \mathbf{u}^* = \frac{\Delta t}{\rho}\nabla \cdot \left(\nabla p^{n+1/2}\right) \tag{3}$$

After the solution of the pressure $p^{n+1/2}$ from the Poisson equation, Eq. (3), the final velocity $\mathbf{u}^{n+1}$ can be computed with help of Eq. (2). It should be noted that for a consistent formulation it is essential to use the form given by Eq. (3) and not to replace the term on the right hand side of Eq. (3) by the Laplacian of $p^{n+1/2}$. The algorithm above is well known and has with an explicit advection and diffusion step in principle third order time accuracy for the velocity and second order time accuracy for the pressure. The Poisson equation for the pressure is solved with help of Fourier Transforms in the axial and circumferential direction. The compact discretization in the radial directions results in matrix vector system with a full coefficient matrix. This system is solved with an LU decomposition (routines **dgetrf/dgetrs** from the LAPACK library). The L and U matrices are only calculated during the first time step and stored in memory, for subsequent time steps the L and U are retrieved from the memory and not recomputed to save computational time.

For an explicit method in a cylindrical system the time step is in general limited by the gridspacing in the circumferential direction ($r\Delta\theta$) close to the centerline where $r \approx 0$. In previous studies this limitation is overcome by using in an implicit time integration method for the circumferential direction, see for instance [3] and [14]. Here we have followed a different approach. At $r = 0$ there is only a single Fourier mode in the θ direction, i.e. the velocity is single valued at the centerline. For larger values of r there are multiple Fourier modes.To mimic this effect we have assumed that the number of Fourier modes in the circumferential direction depends on the radial position r. For $r > r_c$ we use the full Fourier expansion. In the region $0 < r < r_c$ we gradually reduce the number of modes from N at r_c to 8 at $r = \Delta r/2$. A typical value of $r_c = 0.02D$. It turned out that the results are insensitive to the value of r_c.The value of the time step Δt is estimated from a Courant criterion and eventually set to a fixed value of $\approx 0.2 \ldots 1.0 \times 10^{-4} D/u_*$ depending on the Reynolds number and on the grid size.

3 Results

In this section we will present results obtained from three DNS of pipe flow, details of the simulations are given in Table 1. The Reynolds number of the first simulations corresponds with the Reynolds number of the experiments reported by [13]. In Fig. 1 we have compared the root mean square profiles from our DNS with the experimental data reported by [13], furthermore we have also included the result of the DNS carried

Table 1 A list of the simulations, with some details

Re_*	$N_r \times N_\theta \times N_z$	N_{proc}	L_z	Re_{bulk}	Δr_w
1,383	206 × 896 × 2,560	512	18D	24,688	0.52 r^+
1,840	320 × 1200 × 3,360	3,840	18D	34,351	0.54 r^+
3,685	440 × 2400 × 7,200	12,009	18D	76,191	0.54 r^+

Re_* denotes the frictional Reynolds number, N_i the number of grid point in the i-direction, N_{proc} the number of CPUS used for the calculation, L_z the domain length, Re_{bulk} the bulk Reynolds number and Δr_w the radial distance between the first grid point and the wall

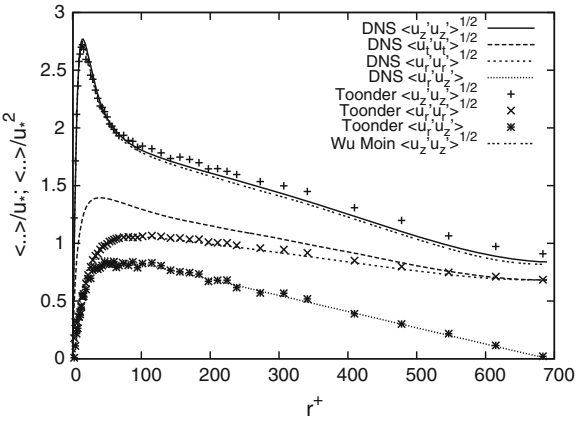

Fig. 1 The root mean square profiles obtained from the DNS with a Reynolds number of 24,600. The symbols are the experimental results reported by [13] for the same Reynolds number. As a further validation we have also included the DNS results of [14]

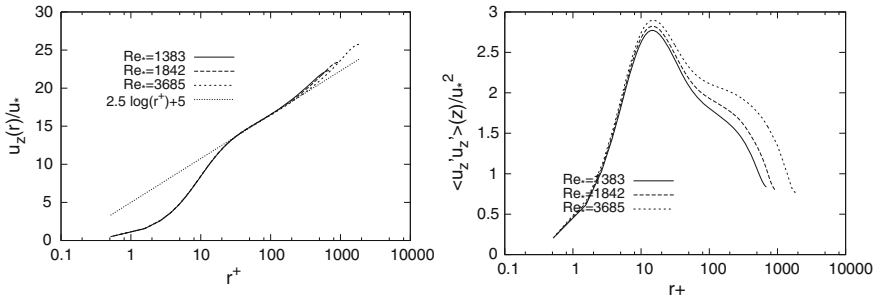

Fig. 2 *Left figure* The mean velocity profiles for the three Reynolds numbers reported in Table 1. *Right figure* The axial rms profiles for the Reynolds numbers reported in Table 1

out by [14]. Overall the agreement between DNS and experiment is very good. In Fig. 2 we present the mean axial velocity and rms profiles of the three simulations reported in Table 1. The peak of the axial rms presented in Fig. 2 shows a slight, but noticeable, dependence on the Reynolds number. In Fig. 3 the Reynolds shear stress and the flatness of the radial velocity component are reported. All profiles show a slight dependence on the frictional Reynolds number.

In Fig. 4 a snapshot of the instantaneous axial velocity component as a function of θ and z at a radial location $r = D/4$ is shown for two different Reynolds numbers. It can clearly be observed that there is an increased small scale activity but also that there are structures present with have an extend comparable or longer than the pipe diameter. (The vertical extend of the picture is equal to $2D/4\pi \approx 1.5D$).

In Fig. 5 we show the autocorrelations of the axial velocity in the streamwize direction as a function of r and z. For increasing Reynolds numbers we observe a

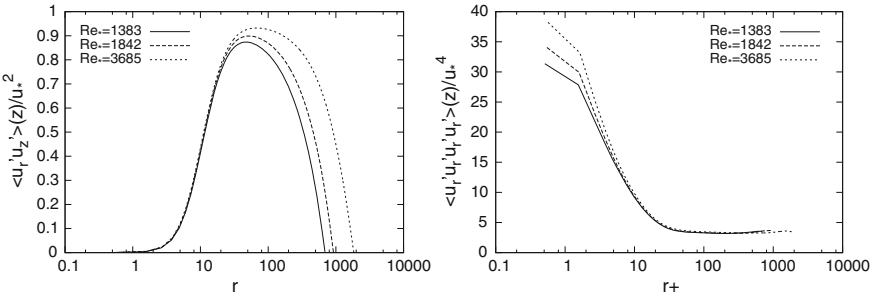

Fig. 3 *Left figure* The profiles of the Reynolds shear stress for the three Reynolds numbers reported in Table 1. *Right figure* The flatness of the radial velocity for the Reynolds numbers reported in Table 1.

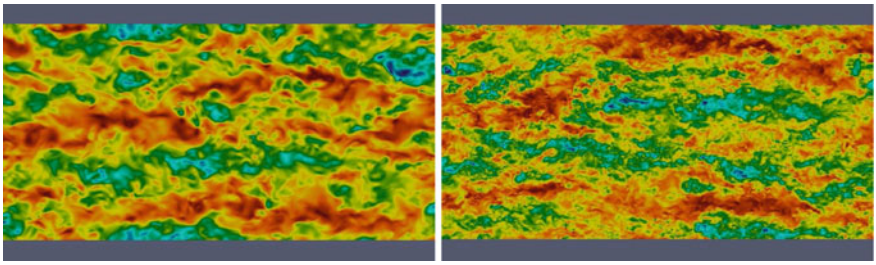

Fig. 4 The instantaneous axial velocity component as a function of θ and z at a radial location $r = D/4$; *top* Re = 24,600, *bottom* Re = 75,009

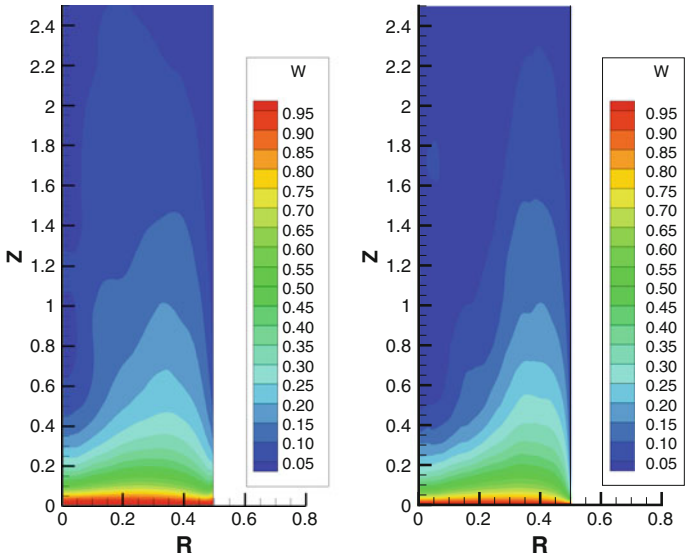

Fig. 5 The autocorrelation of the streamwize velocity in the downstream direction versus the radial coordinate; *left* Re = 24,600, *right* Re = 75,009

longer area in the downstream direction were a noticeable non-zero correlation exits. This is an indication that turbulent structures tend to become longer with increasing Reynolds number. These long structures we observe for higher Reynolds numbers is in agreement with experimental observations by [8, 11].

4 Conclusion

In this paper we have presented results of the DNS of turbulent pipe flow at bulk Reynolds numbers of 24600, 35009 and 76009. The numerical model uses a combination of spectral and high order compact finite difference methods. The results agree very well with existing experimental and numerical data. It is shown that the peak of the axial root mean square profile is a weak function of the Reynolds number. It is shown that large scale streamwize structures with a spatial extend of the order of the pipe diameter exist for all studied Reynolds numbers. For the highest Reynolds number there is some indication that structures with a streamwize dimension exceeding the pipe flow diameter exist.

Acknowledgments The CPU time for the work has been provided by the Netherlands computer facilities NCF and the European PRACE supercomputing initiative.

References

1. Boersma, B.J.: A staggered compact finite difference formulation for the compressible Navier-Stokes equations. J. Comp. Phys. **208**, 675–690 (2005)
2. Boersma, B.J.: A 6th order staggered compact finite difference method for the incompressible Navier-Stokes and scalar transport equations. J. Comp. Phys. **230**, 4940–4954 (2011)
3. Eggels, J.G.M., Unger, F., Weiss, M., Westerweel, J., Adrian, R.J., Friedrich, R., Nieuwstadt, F.T.M.: Fully developed turbulent pipe flow: a comparison between direct numerical simulation and experiment. J. Fluid Mech. **268**, 175–209 (1993)
4. Horiuit, K.: Comparison of conservative and rotational forms in large eddy simulation of turbulent channel flow. J. Comp. Phys. **71**, 343–370 (1987)
5. Hultmark, M., Bailey, S.C.C., Smits, A.J.: Scaling of near-wall turbulence in pipe flow. J. Fluid Mech. **649**, 103–113 (2010)
6. Hutchins, N., Marusic, I.: Evidence of very long meandering features in the logarithmic region of a turbulent boundary layer. J. Fluid Mech. **579**, 1–28 (2007)
7. Jimenez, J., Hoyas, S.: Turbulent fluctuations above the buffer layer of wall-bounded flows. J. Fluid Mech. **611**, 215–236 (2008)
8. Kim, K.C., Adrian, R.J.: Very large-scale motion in the outer layer. Phys. Fluids **11**, 417–422 (1999)
9. McKeon, B.J., Li, J., Jiang, W., Morrison, J.F., Smits, A.J.: Further observations on the mean velocity distribution in fully developed pipe flow. J. Fluid Mech. **501**, 135–147 (2004)
10. Mochizuki, S., Nieuwstadt, F.T.M.: Reynolds-number-dependence of the maximum in the streamwise velocity fluctuations in wall turbulence. Exp. Fluids **21**, 218–226 (1996)
11. Monty, J.P., Stewart, J.A., Williams, R.C., Chong, M.S.: Large-scale features in turbulent pipe and channel flows. J. Fluid Mech. **589**, 147–156 (2007)

12. Morrison, J.F., McKeon, B.J., Jiang, W., Smits, A.J.: Scaling of the streamwise velocity component in turbulent pipe flow. J. Fluid Mech. **508**, 99–131 (2004)
13. Den Toonder, J.M.J., Nieuwstadt, F.T.M.: Reynolds number effects in a turbulent pipe flow for low to moderate Re. Phys. Fluids **9**, 3398 (1997)
14. Wu, X., Moin, P.: A direct numerical simulation study on the mean velocity characteristics in turbulent pipe flow. J. Fluid Mech. **608**, 81–112 (2008)

Turbulent Kinetic Energy Transport in Oscillatory Pipe Flow

Claus Wagner and Daniel Feldmann

1 Introduction

Laminar as well as turbulent oscillatory pipe flows occur in many fields of biomedical science and engineering. Pulmonary air flow and vascular blood flow are usually laminar, because shear forces acting on the physiological system ought to be small. However, frictional losses and shear stresses vary considerably with transition to turbulence. This plays an important role in cases of e.g. artificial respiration or stenosis. On the other hand, in piston engines and reciprocating thermal/chemical process devices, turbulent or transitional oscillatory flows affect mixing properties, and also mass and heat transfer. In contrast to the extensively investigated statistically steady wall bounded shear flows, rather little work has been devoted to the onset, amplification and decay of turbulence in pipe flows driven by an unsteady external force. Experiments [1–3] indicate that transition to turbulence depends on only one parameter, i.e. $Re_\delta \sim Re/Wo$ with a critical value of about 550, at least for Womersley numbers $Wo > 7$. We perform direct numerical simulations (DNS) of oscillatory pipe flows at several combinations of Re and Wo to extend the validity of this critical value to higher Wo. To better understand the physical mechanisms involved during decay and amplification of the turbulent flow, we further analyse the turbulent kinetic energy distribution and its budgets terms.

2 Numerical Approach

We consider a Newtonian fluid confined by a straight pipe of diameter D and length L. The fluid is driven in axial direction (z) by the time dependent pressure gradient

C. Wagner (✉) · D. Feldmann
German Aerospace Center (DLR), Institute of Aerodynamics
and Flow Technology, SCART, Bunsenstr. 10, Gottingen, Germany
e-mail: claus.wagner@dlr.de

J. Fröhlich et al. (eds.), *Direct and Large-Eddy Simulation IX*,
ERCOFTAC Series 20, DOI 10.1007/978-3-319-14448-1_31

$$\mathbf{P}(t) \equiv \left[0,\, 0,\, \partial_z \langle p \rangle_\phi\right]^\mathsf{T} = \left[0,\, 0,\, -4\cos\left(\frac{4Wo^2}{Re_\tau} t\right)\right]^\mathsf{T}, \text{ where } \quad p = p' + \langle p \rangle_\phi \quad (1)$$

according to Reynolds' decomposition. Prime denotes the fluctuating part and angle brackets the mean quantity averaged over equal oscillation phases. Normalisation and the set of non-dimensional control parameters is given by the Womersley number $Wo = D/2\sqrt{\omega/\nu}$ and the friction Reynolds number $Re_\tau = u_\tau D/\nu$. Here, $\omega = 2\pi/T$ is the forcing frequency, ν the kinematic viscosity, and u_τ the friction velocity of a fully developed statistically steady turbulent pipe flow. Thus, the governing equations read

$$\nabla \cdot \mathbf{u} = 0 \qquad \text{and} \qquad \partial_t \mathbf{u} + (\mathbf{u} \cdot \nabla)\,\mathbf{u} + \nabla p' - \tfrac{1}{Re_\tau} \Delta \mathbf{u} = \mathbf{P(t)} \qquad (2)$$

with $\mathbf{u}$ denoting the velocity vector, ∂_t being the partial derivative with respect to time t and ∇ and Δ being the Nabla operator and the Laplacian, respectively. Equations (1) and (2) are supplemented by periodic boundary conditions (BC) for $\mathbf{u}$ and p in the homogeneous directions z and φ and no-slip and impermeability BC at $r = D/2$ in the radial direction. They are directly solved by means of a fourth order accurate finite volume method and advanced in time using a second order accurate leapfrog–Euler time integration scheme. Further details on the numerical method are given in Feldmann Wagner [5] and references therein. The initial flow field was taken from a well correlated statistically steady turbulent pipe flow at $Re_\tau = 1{,}440$ discussed in [5]. The criterion $\overline{h}^* < \pi(Re_\delta/\langle k_\varepsilon^* \rangle_{z,\varphi,\phi})^{1/4}$ for the mean grid size leads to $\overline{h}^* = \{6.2; 7.1; 5.7\}$ for cases I to III based on the maximum turbulent dissipation rates plotted in Fig. 3. Since the mean grid spacing varies from the wall to the axis between $0.6 < \overline{h}^* < 1.0$, $1.3 < \overline{h}^* < 2.2$, and $0.6 < \overline{h}^* < 1.1$, respectively, we conclude, that the used grids are sufficiently fine to resolve all relevant length scales.

3 Computational Parameters and Flow Regimes

We focus on DNS results obtained for three combinations of $Wo = \{13, 26, 52\}$ and $Re_\tau = \{1440, 5760, 11520\}$, resulting in different peak Reynolds numbers $Re = \hat{u} D/\nu$ based on the maximum value of the respective bulk velocity $\langle \bar{u}(t) \rangle_\phi$ within $0 < t \leq T$. Here, ϕ symbolises averaging over $N = 14$ equal phases with $t + nT/2$ for $n = \{n \in \mathbb{N} : n \leqslant N\}$. The resulting parameter space in terms of Re and Wo is shown in Fig. 1, where $Re_\delta = \delta\hat{u}/\nu = Re/Wo\sqrt{1/2}$ is the Reynolds number based on the Stokes layer thickness $\delta = \sqrt{2\nu/\omega}$. All flows denoted by circles laminarise despite of high Re up to ~12,000. The stabilising effect of the oscillatory forcing increases with Wo, at least beyond a certain value of about seven, in agreement with findings from stability analysis [4] and experimental investigations [1–3].

Figure 2 presents time series of the applied forcing $\mathbf{P}(t)$, the predicted mean shear stress at the wall $\langle \tau_w^* \rangle_{z,\varphi}$, and the axial velocity component $u_z(r, t)$ close to the wall ($r/D = 0.49$) and near the center line ($r/D = 0.01$). The time series of u_z

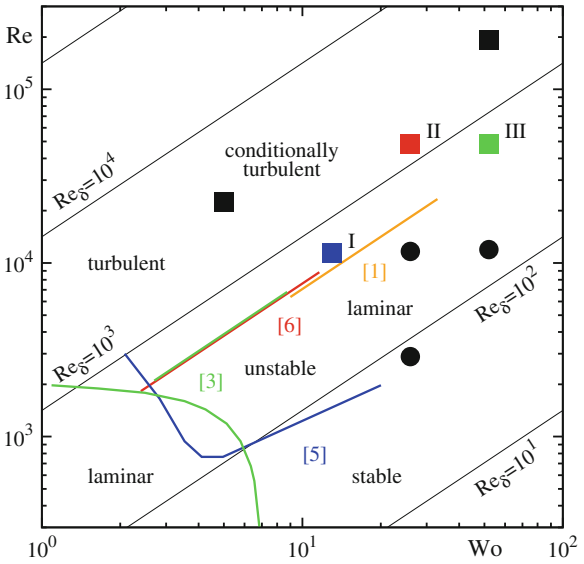

Fig. 1 Non-dimensional parameter space and flow regimes in terms of *Re* and *Wo*. *Circles* denote laminarised flows and *squares* turbulent flows. Here, we focus on the turbulent cases I, II, and III. Transition from laminar to the turbulent flow regime is indicated by the *green* [2], *red* [3], and *orange* [1] *lines* as obtained experimentally. The *blue line* [4] separates regions of stability according to a quasi-steady stability analysis

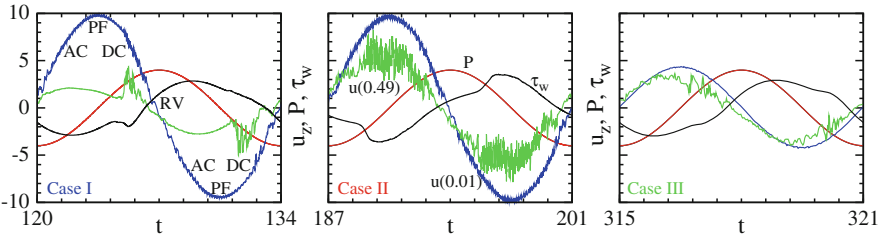

Fig. 2 Time series of the axial velocity component $u_z(r, t)$ close to the wall at $r/D = 0.49$ and close to the *centre line* at $r/D = 0.01$, the forcing $\mathbf{P}(t)$, and the mean wall shear stress $\langle \tau_w^* \rangle_{z,\varphi}$

reveal conditionally turbulent flows for all three parameter combinations, i.e. case I at $Wo = 13$ and $Re = 11{,}460$, case II at $Wo = 26$ and $Re = 48{,}175$, and case III at $Wo = 52$ and $Re = 48{,}250$, respectively. For I and III, i.e. the two slightly supercritical cases both at $Re_\delta \sim 600$, the near wall velocity characteristics are similar. Fluctuations suddenly grow only at deceleration (DC), while they are damped again during flow reversal (RV) and the following acceleration (AC) phase. These turbulent bursts during DC are also reflected in the τ_w^* history. However, the most conspicuous difference between I (lower *Wo*) and III (higher *Wo*) in this respect

is that the AC phase is more stable for $Wo = 13$ despite of the similar Re_δ, while fluctuations in the near wall flow do not completely decay for higher Wo. Contrarily, the u_z history at the centre line is completely smooth for case III, while for case I the core region is characterised by substantial velocity fluctuations throughout the whole oscillation cycle.

For higher values of Re_δ, i.e. case II, the velocity time series reveal a completely different behaviour without distinct bursts and strong velocity fluctuations at the centre line. The turbulence intensity close to the wall and in the core region rather increases during AC and decreases during DC analogously to the bulk flow with laminarisation only during RV.

4 Turbulent Kinetic Energy

To shed light on the mechanisms leading to the different behaviour in decay and amplification of turbulence in the oscillatory pipe flows discussed above, we analyse the turbulent kinetic energy k^* as well as the production and dissipation terms of its transport equation, see e.g. [5]. During all oscillation phases, both flows at $Re_\delta \sim 600$ develop a boundary layer with one major characteristic, which is typical for wall-bounded shear flows. The turbulent kinetic energy profiles exhibit an obvious maximum very close to the wall with a very steep decrease towards the wall ($r^* = 0$) and a moderate drop towards the pipe centre line. This can be seen from the radial k^* distribution for I and III, shown in Fig. 3. They reach the same maximum value for similar Re_δ and thus the ratio of Re to Wo is the governing parameter defining equally turbulent oscillatory pipe flows. However, due to the shorter oscillation phase in case III, i.e. a four times higher Wo, the same amount of energy is produced in a shorter period of time, as reflected by the four times higher production rate k_π presented in Fig. 3. For I and III, the turbulent kinetic energy monotonically decays from DC via RV even until AC. The production term k_π^* further confirms, that turbulence is mostly generated when turbulent near-wall bursts occur during DC, cf. Fig. 2. During RV, more energy is dissipated than produced at a dissipation rate k_π^* even higher as during AC. Furthermore, for $Re_\delta \sim 600$ the k_π^* profile becomes negative in a small annular region, where turbulent kinetic energy is transferred back to the mean flow, see also [5]. Both phenomena in combination account for the rigorous laminarisation during RV.

In contrast, for $Re_\delta = 1{,}310$ the turbulent kinetic energy decreases to the half during RV and increases again during AC to about the same value as in DC, due to the highest production rate k_π^* during AC. Case II is also different in such a way that the turbulent kinetic energy is also rather high in most of the core region during DC, characterised by a flat broad k^* profile only showing a vague near-wall maximum. While during AC the k^* distribution clearly exhibits the above described typical shear flow profile. The same typical shear flow behaviour is reflected by the k_ε^* distribution with a maximum dissipation at the wall and a distinct plateau during all oscillation phases for $Re_\delta = 1{,}310$. The slightly supercritical cases I and III at $Re_\delta \sim 600$, on

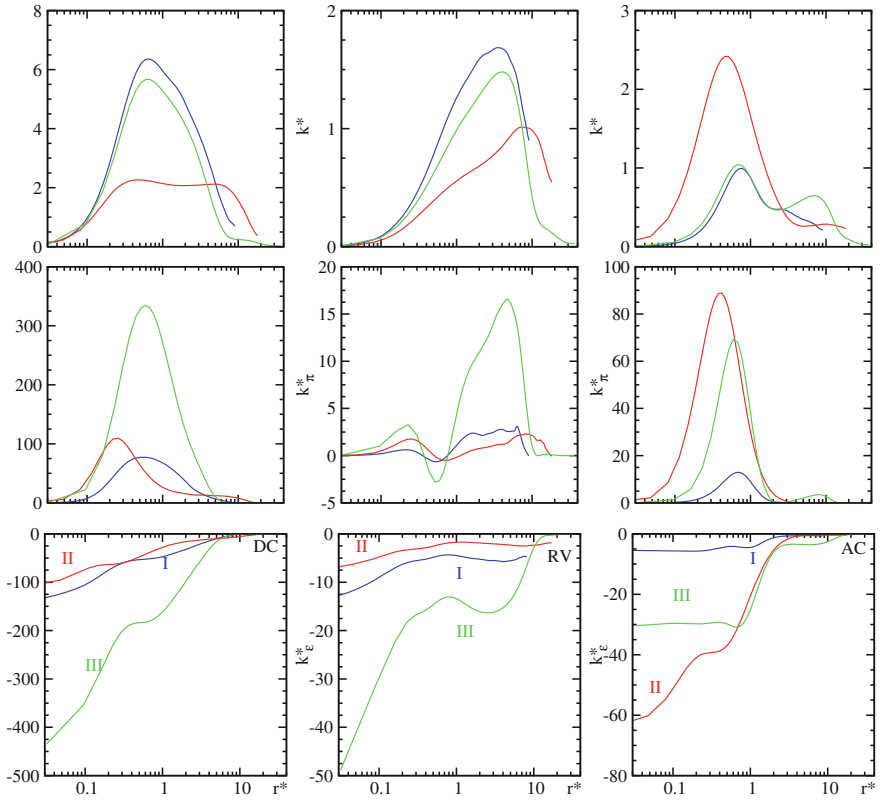

Fig. 3 Radial distribution of turbulent kinetic energy k^*, its production term k^*_π, and its turbulent dissipation term k^*_ε scaled in Stokes layer thicknesses during DC, RV, and AC for I: $Wo = 13$, $Re_\delta = 623$; II: $Wo = 26$, $Re_\delta = 1310$; and III: $Wo = 52$, $Re_\delta = 656$

the other hand, develop a second local dissipation maximum, which becomes more pronounced in the k^*_ε profiles with ongoing laminarisation during RV and AC.

The wall distance $r^* = (1/2 - r)\, D/\delta$ of the k^* maxima are also the same for similar Re_δ, when the length is scaled in Stokes layer thicknesses δ. During DC and AC, when the bulk flow is high, the k^* maximum occurs closer to the wall for higher Re_δ. Vice versa, the energy maximum occurs closer to the wall for lower Re_δ during RV, when viscous effects dominate. Thus, the ratio of Re to Wo defines the thickness of the annular region in terms of δ, in which the oscillatory pipe flow exhibits turbulent features, even though the thickness of this turbulent boundary layer is strongly phase dependent. Also the budget terms shown in Fig. 3, reveal that the wall distance of all the characteristics in the profiles, i.e. maxima, inflection points, plateaus and so on, scale with Re_δ. However, for decreasing Wo per definition the Stokes layer becomes large compared to the pipe radius and thus the geometrical constraint of the pipe wall gains importance. In case I turbulent near-wall structures

evolve during DC and RV, penetrate farther towards the centre line, and thus span almost the whole core region, cf. Fig. 2. As a result, the turbulent kinetic energy is rather high over most parts of the pipe radius and, more important, does not vanish at the pipe axis for lower Wo. Whereas, in case III at higher Wo but equal Re_δ the k^* distribution reflect a high turbulent kinetic energy for $r^* < 9$ and an almost laminar flow over the second half of the pipe radius. As indicated before by the velocity time series shown in Fig. 2, the turbulence is confined to a smaller (in terms of r) annular region close to the wall, while the flow remains very smooth in the whole core region for the highest Wo. The contribution of all other transport terms, i.e. the viscous, turbulent, and pressure diffusion as well as the pressure strain, to the overall budget is much lower. In principle, these terms reflect the typical shear flow mechanisms, which are simply damped and amplified by the oscillatory forcing, and thus for the sake of brevity not further discussed here.

5 Conclusions

Decay, amplification, and redistribution of turbulent kinetic energy in oscillatory pipe flow were studied by means of DNS for various combinations of Re and Wo. We found, that oscillatory flows at $Re_\delta < 550$ relaminarise when started from a fully developed turbulent flow field despite of high Re. In very good agreement with experiments [1–3], we confirm oscillatory flows at $Re_\delta > 550$ to be conditionally turbulent.

However, we contradict [1] who stated that core flow remains stable for $Re_\delta < 1{,}310$. Our DNS results extend the validity of this experimentally determined critical value up to $Wo = 52$ in the Re-Wo-space. Nevertheless, from the analysed turbulent kinetic energy distributions we conclude that decay and amplification of turbulence in oscillatory pipe flows rather depend on the combination of Re and Wo then on its ratio (Re_δ) alone. This is a significant difference to the case for the oscillating boundary layer over a flat plate, which has been extensively studied by Spalart and Baldwin [6] using DNS. Even if experiments have shown that, the transition to turbulence can be characterised by only using Re_δ, at least for $Wo > 7$, our study revealed that for oscillatory pipe flow the additional geometrical constraint considerably affects the decay and amplification of turbulence in the core flow.

References

1. Eckmann, D.M., Grotberg, J.B.: Experiments on transition to turbulence in oscillatory pipe flow. J. Fluid Mech. **222**, 329–350 (1991)
2. Hino, M., Sawamoto, M., Takasu, S.: Experiments on transition to turbulence in an oscillatory pipe flow. J. Fluid Mech. **75**, 193–207 (1976)
3. Zhao, T.S., Cheng, P.: Experimental studies on the onset of turbulence and frictional losses in an oscillatory turbulent pipe flow. Int. J. Heat Fluid Fl. **17**, 356–362 (1996)

4. Trukenmüller, K.E.: Stabilitätstheorie für die oszillierende Rohrströmung. Ph.D. thesis, Helmut-Schmidt-Universität, Hamburg (2006)
5. Feldmann, D., Wagner, C.: Direct numerical simulation of fully-developed turbulent and oscillatory pipe flows at $_\tau = 1440$. J. Turb. **13**, 1–28 (2012)
6. Spalart, P.R., Baldwin, B.S.: Direct simulation of a turbulent oscillating boundary layer. In: Andre, J.C. et al. (eds.) Turbulent Shear Flows, vol. 6, pp. 417–440. Springer, Berlin (1989)

Large-Eddy Simulation of the Interaction of Wall Jets with External Stream

I.Z. Naqavi and P.G. Tucker

1 Introduction

The jets issuing tangentially to a solid surface are called wall jets. Plane two dimensional wall jets are the simplest and have been studied extensively [5]. The wall jets are used in heat, mass and momentum transfer along the walls. A large part of wall jet study is concerned with the search for the existence of self-similar parameters [3, 13].

Bradshaw and Gee [1] made early fundamental studies on the wall jets with an external stream. It was shown that for thin incoming boundary layer with no wake, the jet shear layer can absorb the boundary layer in a short distance. However, the presence of external stream results in the involvement of several parameters, determining the evolution of the wall jet. These external parameters can be controlled to produce the desired effects in the wall jets, depending on their application. The two major applications of wall jets with external streams are cutback trailing edge (TE) film cooling in gas turbines and the control of the boundary layers over high lift bodies e.g. Coanda jets [9]. In both of these cases wall jets are interacting with the external stream, however, the desired outcome of the interactions are completely opposite. In case of TE thin film cooling a cold stream is introduced as a wall jet along the trailing edge. The objective is to keep the external hot stream (combustion gases) away from the wall and to avoid the mixing of the two streams as far downstream as possible. For the Coanda jet a strong mixing of two streams is required to prevent the boundary layer separation.

In case of TE film cooling major focus is the measurement and prediction of film-cooling effectiveness of this flow. Martini and Schulz [7] performed measurements

I.Z. Naqavi (✉) · P.G. Tucker
Whittle Laboratory, Cambridge University, Cambridge, Uk
e-mail: izn20@eng.cam.ac.uk

P.G. Tucker
e-mail: pgt23@eng.cam.ac.uk

J. Fröhlich et al. (eds.), *Direct and Large-Eddy Simulation IX*,
ERCOFTAC Series 20, DOI 10.1007/978-3-319-14448-1_32

on scaled-up trailing edge model with internal structures for coolant slot. These structures determine the turbulence character of incoming jet and have strong influence on the film cooling effectiveness. Recent LES of TE film cooling [10, 11] for a series of blowing ratios (i.e. jet to free stream velocity ratio), in the rage of 0.35–1.4, showed large coherent structures shed from the plate separating the two streams. These have dominant role in the heat transfer. The jet velocity ratio is usually around 1.5 or less for TE film cooling. Whereas for Coanda jets based flow control it is higher than 2.0 [9]. In previous studies the wake plate thickness separating the two streams is also of the order of the slot height for wall jets. In this work a high resolution LES is performed to study a geometrically simple model for wall jet with external stream and a thin wake plate. Two different velocity ratios are considered. The objective is to study the effect of the velocity ratios on the development of the coherent structures in the near field and the development of the mean flow properties downstream.

2 Problem Formulation and Validation

The interaction of wall jet with external stream is simulated with filtered conservation of mass and momentum equations for incompressible flow. A finite volume code with second order collocated descretization and semi-implicit time advancement scheme is used. The subgrid-scale (SGS) stresses are modeled with Lagrangian-averaged dynamic eddy-viscosity model [8].

In this study the blowing ratios U_j/U_∞ of 0.75 and 2.30 are considered. The U_∞ is free stream velocity of external incoming boundary layer and U_j is the wall jet bulk velocity. The domain is shown in the schematic Fig. 1. This case has been studied experimentally by [4]. At the inlet plane of the computational domain, mean streamwise velocity profiles for the wall-jet and boundary layer from the experiment are used. A channel and a boundary layer flow simulation based on [6] are used to generate time dependent turbulence fluctuations for inlet profiles. The slot height of wall jet is $h = 2.767\delta_0^*$ and the thickness of the plate separating the two streams (wake plate) is $w = 0.126$, $h = 0.349\delta_0^*$. The inlet Reynolds number based on the displacement thickness δ_0^* of external boundary layer is $Re_{\delta_0^*} = 2,776$. The Reynolds numbers for slot jet based on slot height are $Re_h = 5,760$ and 17,700, for

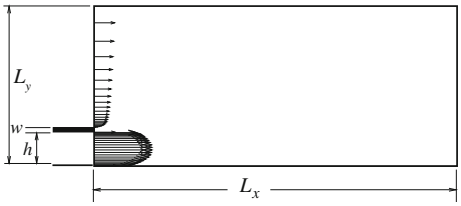

Fig. 1 Schematic of the domain for wall jet and external stream

Table 1 Summary of the domain and grid

Grid	L_x/h	L_y/h	L_z/h	N_x	N_y	N_z
Coarse	80.0	16.0	5.5	512	147	66
Fine	45.0	16.0	5.5	1,026	220	130

$U_j/U_\infty = 0.75$ and 2.30, respectively. Two different grids are used in this simulation and their details are summarised in Table 1.

The maximum grid size for the fine grid is $\Delta x < 47.0$ and $\Delta z < 38.0$ in wall units. In the wall normal direction first grid point is $y^+ < 1.0$. The mean flow profiles and Reynolds stresses are compared with the experiments [4] at $x = 10h$ in Fig. 2. The simulations give same trends as in the experimental data for mean flow and Reynolds stress. The mean velocity profiles for both jets are in good agreement with the experimental data numerically. The higher velocity ratio jet simulation give better agreement for Reynolds stresses $\langle v'v'\rangle/U_\infty^2$ and $\langle w'w'\rangle/U_\infty^2$. However, the peak $\langle u'u'\rangle/U_\infty^2$ and $\langle u'v'\rangle/U_\infty^2$ are higher than the experimental values. This over-prediction may be the outcome of the uncertainty at the inlet in the simulation and in the hot-wire measurements. The Reynolds normal and shear stresses for $U_j/U_\infty = 0.75$ jet are an order of magnitude smaller than $U_j/U_\infty = 2.3$ jet.

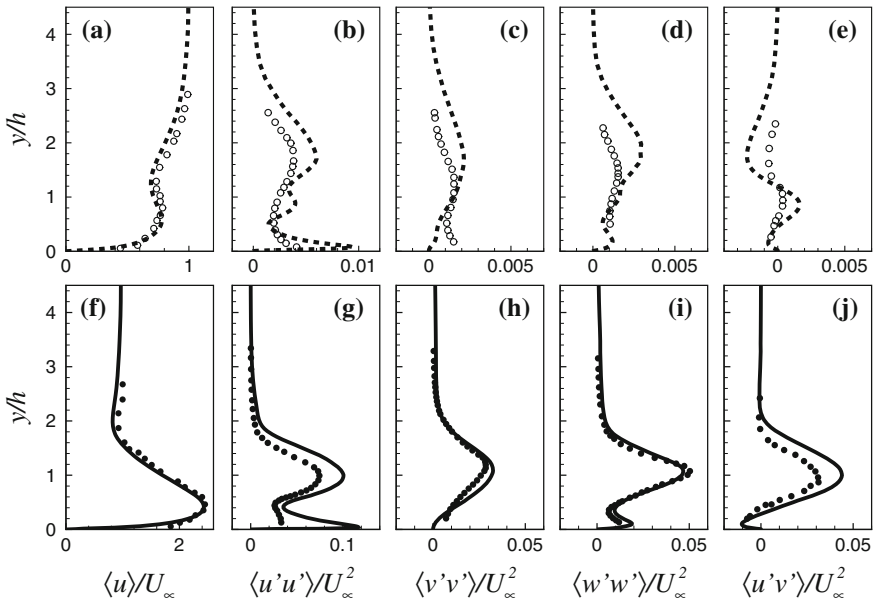

Fig. 2 Comparison of $\langle u\rangle/U_\infty$, $\langle u'u'\rangle/U_\infty^2$, $\langle v'v'\rangle/U_\infty^2$, $\langle w'w'\rangle/U_\infty^2$ and $\langle u'v'\rangle/U_\infty^2$ profiles at $x = 10\,h$ with the experimental data [4]. *Top* $U_j/U_\infty = 0.75$, *bottom* $U_j/U_\infty = 2.3$: *line* simulation, *symbols* experiment

3 Results

In this work the interaction of a wall jet with the outer boundary layer is studied when the separation between the two streams i.e. w is small. Previous studies, with larger separation [9, 10], have shown the existence of large scale coherent structures in the near wake region. Those determine the mixing of momentum and heat between the wall jet and outer stream.

In current simulation various kind of vortical structures are involved. There are streamwise near wall structures coming in from the incoming boundary layers and the slot jet. Apart from these structures, the interaction of the boundary layer with a wall jet generates further dynamic complexity, instability and more large scale structures. The coherent structures are visualised through the isosurfaces of the second-invarient of the velocity gradient tensor $Q = -(\partial\langle u_i\rangle/\partial x_j)(\partial\langle u_j\rangle/\partial x_i)$. Figure 3 shows the coherent structures in the near wake region up to $x = 4.0\,h$. The right frames in the figure show the span wise vorticity at the plane $z = 0.0\,h$, which give the foot prints of the structures presented through the Q isosurfaces. The span wise structures generated for the low velocity ratio jet lose the coherence very quickly. However, the foot prints in the span wise vorticity contours show that structures are similar to von-Karman type shed vortices in the wake region. The high velocity ratio jet presents a very different picture. The structures appear like roll structures, resulting from the jet shear layer Kelvin-Helmholtz instability. At higher wall jet velocity, shear layer on the jet side is strong and it drags the shear layer from the boundary layer side of the wake. The roll structures interact and merge with each other downstream.

This vortical structure evolution in the near field is also confirmed by the mean flow in the wake as shown in Fig. 4. The streamlines for low velocity ratio jet gives a counter rotating vortex pair in the wake, which is the average outcome of von-Karman type structures. The high velocity ratio jet gives a single recirculation lobe in the wake. This single lobe results from the drag of the boundary layer flow along with the high velocity jet shear layer.

Figure 5 plots the streamwise velocity profiles for the two jets at various streamwise locations. To show the development of the flow in the farfield region, wall co-ordinates are used. Standard log-law profile $2.5\log(y^+) + 5.0$ and linear profile $\langle u\rangle^+ = y^+$ in the near wall viscous sub-layer region are also added for the comparison. The profile for the high velocity ratio jet, close to the inlet, at $x = 10.0\,h$, shows a sharp peak in velocity. Away from the wall, this reduces to outer stream velocity. Around $y^+ = 1000.0$ there is a narrow wake region. As flow moves downstream the sharp peak in the velocity profile reduces. The profile becomes flatter with jet spreading. The profiles generally resemble those for a plane wall jet, but are altered by the presence of the external stream. The low velocity ratio jet $\langle u\rangle^+$ profile at $x = 10.0\,h$ is quite different to the high velocity ratio. The peak in the jet region is lower and the wake is wider extending in the range of $y^+ = 200.0 - 1000.0$. The wake persist up to $x = 20h$. A comparison with log-law profile suggests that the velocity profiles for low velocity ratio jet are shifting towards the log-law in the farfield region i.e. developing towards a boundary layer. However there is an offset

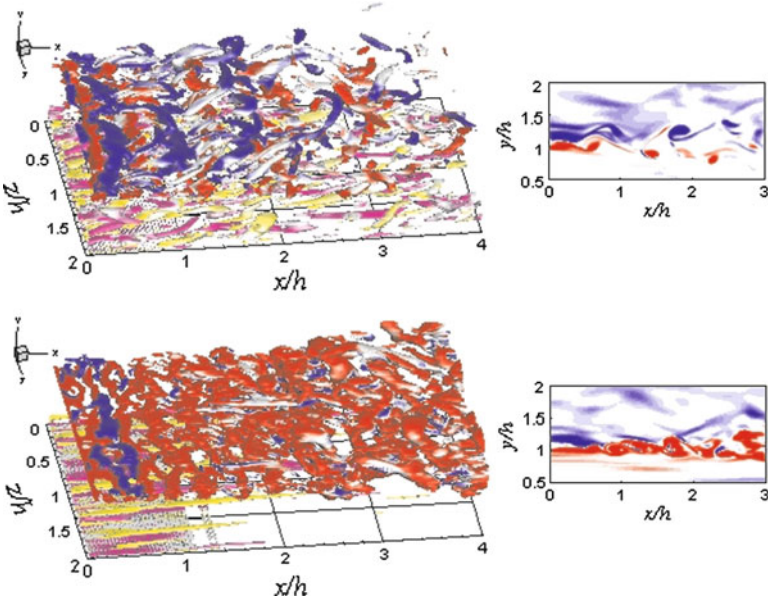

Fig. 3 Coherent structures in the near field region of wall jet and boundary layer interaction, using Q criteria. *Top* $U_j/U_\infty = 0.75$ and *bottom* $U_j/U_\infty = 2.30$. Isosurfaces are coloured with span wise vorticity Ω_z

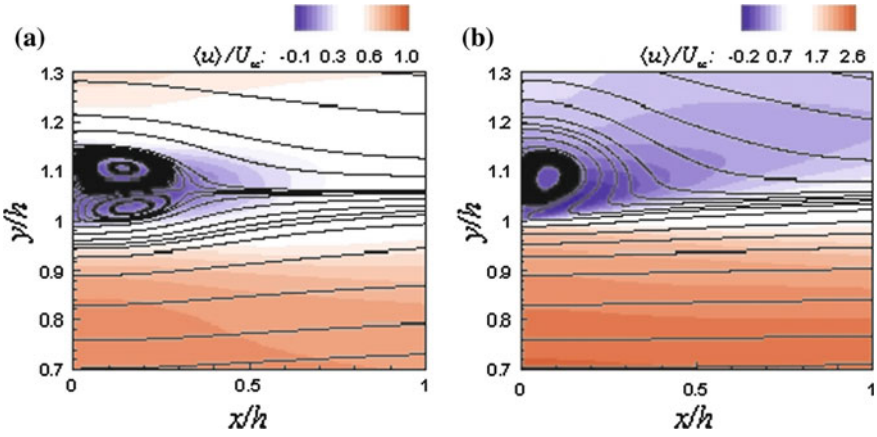

Fig. 4 Mean stream wise velocity contours and streamlines in the wake region near *inlet* plane. **a** $U_j/U_\infty = 0.75$ and **b** $U_j/U_\infty = 2.30$

due to the low value of wall friction coefficient. The mean velocity profiles for both jets in the near wall region are in agreement with the $\langle u \rangle^+ = y^+$ up to $y^+ = 8.0$. Hence, in this region the behaviour is identical to that for a classical boundary layer.

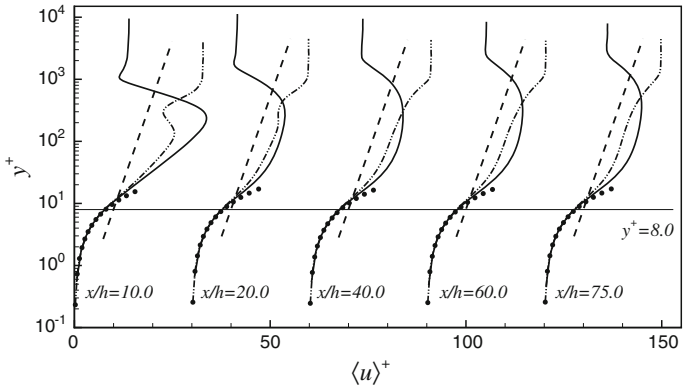

Fig. 5 Mean $\langle u \rangle^+$ profiles at various stream wise location, $U_j/U_\infty = 0.75$ (*dashdotdot*), $U_j/U_\infty = 2.30$ (*solid*), log-law (*dash*) and $y^+ = \langle u \rangle^+$ (*solid circle*)

The $U_j/U_\infty = 2.3$ jet has similarities with the plane wall jet. At large distance downstream $U_j/U_\infty = 0.75$ jet develops towards a turbulent boundary layer. The Reynolds stress profiles are compared with the plane wall jet measurements [2] and also with turbulent boundary layer data of [12] in Fig. 6. The Reynolds and shear stress profiles for low velocity ratio jet in the farfield attains the boundary layer behaviour. The stresses for high velocity ratio jet in the shear layer region are close to wall jet measured values. The u^+_{rms} for high velocity ratio jet has two peaks one in shear layer region and one near the wall. The low velocity ratio jet has near wall u^+_{rms} much higher than shear layer region. The shear stress profiles for high velocity ratio jet follow wall jet behaviour. For low velocity ratio jet $\langle u'v' \rangle^+$ peak in shear layer region is in opposite direction from high velocity ratio jet. It is the consequence of shedding type structures.

4 Conclusions and Future Work

The near field coherent structures for wall jet and external boundary layer interaction with a thin wake plate are different from previous studies [9–11]. The low velocity ratio jet results in shedding type von-Karman structures, whereas high velocity ratio jet give rise to Kelvin-Helmholtz instability and roll structures. The low velocity ratio jet develops towards a zero-pressure gradient boundary layer in the farfield. High velocity ratio jet behaves like plane wall jet. The velocity and Reynolds stress profiles in the near wall region scaled with inner or wall variables. In future a comprehensive study with a wider range of velocity ratios will be performed and detailed scaling behaviour and heat transfer properties near wall will be discussed.

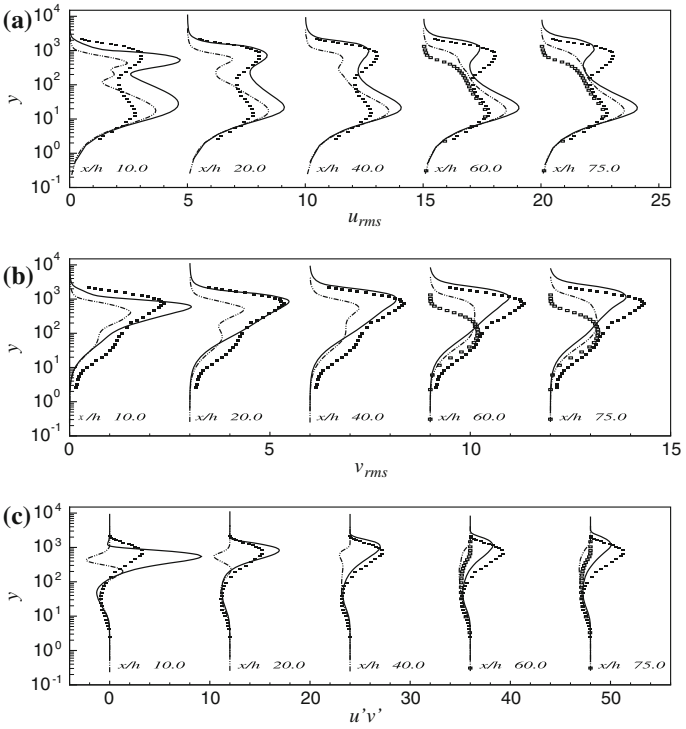

Fig. 6 Reynolds stresses at various streamwise locations. **a** u^+_{rms}, **b** v^+_{rms} and **c** $\langle u'v' \rangle^+$. [12] DNS boundary layer (*open squares*), wall jet measurements at $x = 20\,\mathrm{h}$ [2] (*fill square*)

References

1. Bradshaw, P., Gee, M.T.: Turbulent wall jets with and without an external stream. *British Aeronautical Research Council*, R&M 3252 (1962)
2. Eriksson, J.G., Karlsson, R.I., Persson, J.: An experimental study of a two-dimensional plane turbulent wall jet. Exp. Fluids **25**, 50–60 (1998)
3. Glauert, M.B.: The wall jet. J. Fluid Mech. **1**, 625–643 (1956)
4. Kacker, S.C., Whitelaw, J.H.: The turbulence characteristics of two-dimensional wall-jet and wall-wake flows. J. Appl. Mech. **38**, 239–251 (1971)
5. Launder, B.E., Rodi, W.: The turbulent wall jet measurements and modeling. Annu. Rev. Fluid Mech. **15**, 429–459 (1983)
6. Lund, T.S., Wu, X., Squires, K.D.: Generation of inflow data for spatially-developing boundary layer simulations. J. Comput. Phys. **140**, 233–258 (1998)
7. Martini, P., Schulz, A.: Experimental and numerical investigation of trailing edge film cooling by circular coolant wall jets ejected from a slot with internal rib arrays. ASME J. Turbomach. **126**, 229–236 (2004)
8. Meneveau, C., Lund, T.S., Cabot, W.H.: A Lagrangian dynamic subgrid-scale model of turbulence. J. Fluid Mech. **319**, 353–385 (1996)
9. Nishino, T., Hahn, S., Shariff, K.: Large-eddy simulations of a turbulent Coanda jet on a circulation control airfoil. Phys. Fluids **22**, 125105 (2010)

10. Schneider, H., von Terzi, D., Bauer, H.J.: Large-eddy simulations of trailing-edge cutback film cooling at low blowing ratio. Int. J. Heat Fluid Flow **31**, 767–775 (2010)
11. Schneider, H., von Terzi, D., Bauer, H.J.: Turbulent heat transfer and large coherent structures in trailing-edge cutback film coolin. Flow Turbul. Combust. **88**, 101–120 (2012)
12. Spalart, P.R.: Direct simulation of a turbulent boundary layer up to $R_\theta = 1410$. J. Fluid Mech. **187**, 61–98 (1988)
13. Wygnanski, I., Katz, Y., Horev, E.: On the applicability of various scaling laws to the turbulent wall jet. J. Fluid Mech. **234**, 669–690 (1992)

Turbulent Boundary Layers in Long Computational Domains

G. Eitel-Amor, R. Örlü and P. Schlatter

1 Introduction and Numerical Setup

Wall-bounded turbulence emerges e.g. along the surface of moving ships and airplanes or in pipelines. The prediction of skin friction and drag is directly related to fuel consumption or the power needed to transport gases through pipelines, thereby emphasizing the practical relevance of wall turbulence. Canonical wall-bounded flows are the flat-plate boundary layer, pipe and channel flows. While these flows are in essence theoretical abstractions and do not appear as such in reality it is necessary to study them separately by means of experiments, simulations or theory, since they constitute basic building blocks of more complete, i.e. real, flows.

Simulations of turbulent flows are particularly helpful in identifying physical processes occurring in near-wall turbulence, as the whole velocity field is available for analysis. In particular, higher Reynolds numbers (Re) are necessary to obtain a clear separation of scales related to the near-wall turbulence cycle (i.e. scaling in wall units) and the mechanisms and structures related to the outer region of the boundary layer, i.e. living in the logarithmic region and beyond. However, it remains crucial to properly validate simulation data with corresponding experimental results to ascertain that the turbulence at high Re has reached its developed state.

In order to contribute to the available simulation data, a new numerical simulation of a spatially evolving turbulent boundary layers is discussed, reaching up to a high Re for wall-resolved simulations. To be more precise, we present recent numerical results obtained from highly resolved large-eddy simulations (LES) of an incompressible, zero-pressure gradient, turbulent boundary layer flow up to $Re_\theta = 8{,}300$. The obtained statistics are compared with numerical and experimental data from the literature, in particular with former direct numerical simulations (DNS) for $Re_\theta \leq 4{,}300$ [9] and with experimental data from hot-wire measurements [7]. Fur-

G. Eitel-Amor · R. Örlü · P. Schlatter (✉)
Linné FLOW Centre, KTH Mechanics, Stockholm, Sweden
e-mail: pschlatt@mech.kth.se

J. Fröhlich et al. (eds.), *Direct and Large-Eddy Simulation IX*,
ERCOFTAC Series 20, DOI 10.1007/978-3-319-14448-1_33

thermore, the extended Re range allows for an examination of predicted asymptotic behaviour and provides insight to scale separation and amplitude modulation effects.

Similar as in experiments, the flow enters the domain as an unperturbed laminar Blasius flow, which is then tripped to transition and turbulence via a trip forcing [9], thereby avoiding the use of a recycling/rescaling technique to generate turbulent unsteady inflow conditions. The flow response to tripping is most efficient when performed at lower Re, i.e. close to the leading edge of the plate. Therefore, our simulation technique requires very long computational domains, essentially reproducing a wind-tunnel setup. In the present case, the domain starts at a low (laminar) $Re_\theta = 180$, directly followed by the tripping location. Transition to turbulence is assumed to be complete by $Re_\theta \approx 700$, and a state independent of initial conditions is reached at $Re_\theta \approx 1{,}500$. The outflow of our domain is located at the (computationally) very high $Re_\theta = 8{,}500$. In this single long domain, the boundary layer is allowed to develop naturally from the tripping location to the higher Re.

However, such domains require a large number of grid points: We employ a grid with a total of $13,824 \times 513 \times 1,152$ collocation points in physical space in the streamwise, wall-normal and spanwise directions. As in our previous studies [9], the spectral code SIMSON is employed, giving very high accuracy and dispersion properties, coupled with efficient massive parallelisation. The grid resolution in viscous units is $\Delta x^+ = 18$ and $\Delta z^+ = 8$ which is good, but not quite as high as for proper DNS. Therefore, the ADM-RT subgrid-scale model is employed, adding some limited dissipation only at the smallest scales improving the accuracy of our results. Note that the chosen resolution in this study corresponds to highly resolved LES, and there are simulations in the literature with poorer resolution that are denoted DNS. The simulation was run for sufficiently long time to ascertain statistical convergence of statistics, including one- and two-dimensional spectra. Efficient parallelisation was employed, allowing to use 4,096 cores on an Infiniband cluster.

2 Results

In the following analysis, the free-stream velocity U_∞^+ and the local boundary layer thickness $Re_\tau = \delta_{99}^+$ are re-evaluated using a composite-profile fit proposed by Nickels [5]. Based on these parameters, integral values like the shape factor H_{12} are computed by evaluating the integrals from the wall up to δ_{99}^+. This procedure eases comparability with other numerical and experimental studies, where varying boundary conditions or box heights may aggravate a consistent definition of measured quantities [9]. The relation between the consistently determined, i.e. box-compensated, Reynolds numbers Re_θ and Re_τ is shown in Fig. 1. For comparison, the same quantities were determined using U^+ at the upper domain boundary as free-stream velocity, illustrating the effect of the employed compensation. The values agree very well with the DNS of Schlatter and Örlü [9], and from a power-law fit ($Re_\tau = a\, Re_\theta^b$) the constants $a = 0.596$ and $b = 0.923$ are obtained.

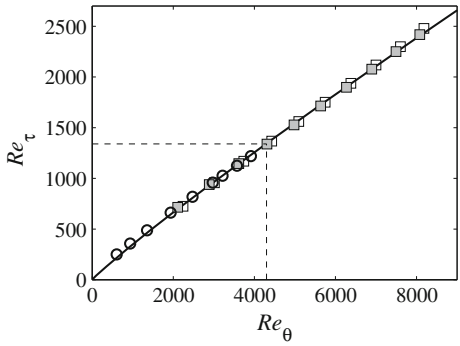

Fig. 1 Relation between Reynolds numbers Re_θ and $Re_\tau = \delta_{99}^+$. *Filled squares* box-compensated LES data; *open squares* uncompensated LES data; *circles* box-compensated DNS data from Schlatter and Örlü [9]; *dashed lines* range of the DNS domain

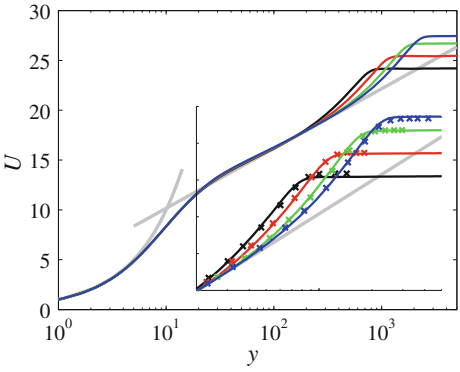

Fig. 2 Mean streamwise velocity profiles for Re_θ=2500, 3600, 5600, and 7500. *Color lines* present LES; *gray line* log-law. *Inset* magnifies wake region and includes experimental data from Örlü [7] (*symbols*)

The present results show good agreement with experiments for the mean velocity profile as apparent from Fig. 2. The data follows the expected linear and logarithmic behaviour in the viscous sublayer and overlap region, respectively. Especially in the wake region, where discrepancies usually show up due to incomplete development of the flow, the agreement is convincing. The log-law indicator function Ξ closely follows the correlation proposed by Monkewitz et al. [4] as shown in Fig. 3. A plateau in Ξ indicating a definite value of κ is though not yet reached.

The aforementioned agreement also extends to the variance profile $\langle uu \rangle$ shown for $Re_\theta = 2{,}500$ in Fig. 4. The profile matches the experimental data in the outer region and the DNS data is reproduced accurately with a slight attenuation in the buffer layer. This underestimation can be traced back to spanwise filtering effects as exemplified in Fig. 4 by z-filtered DNS data ($\Delta z^+ = 8$) which collapses almost with the LES result. It appears feasible to use a correction for under-resolved measurements or simulations as proposed by Segalini et al. [10]. The near-wall peak exhibits the expected logarithmic increase with increasing Re due to outer layer influences. In Fig. 5 the peak values are compared with data from several numerical studies. A fit to the present data yields $\langle uu \rangle_{\max}^+ = 2.307 + 0.799 \ln(Re_\tau)$.

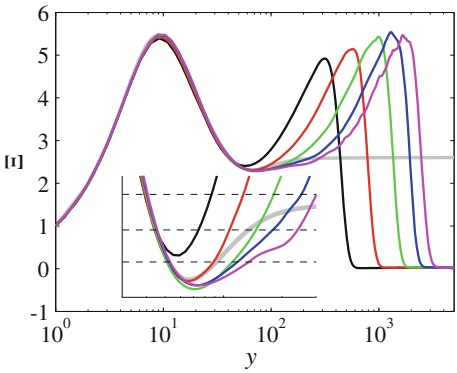

Fig. 3 Log-law indicator function $\Xi = y^+ \frac{dU^+}{dy^+}$. *Color lines* present LES for $Re_\theta = 1400$, 2500, 4400, 6400, and 8200; *gray line* Monkewitz et al. [4]. *Dashed lines* in *inset* indicate $\kappa = 0.38$, 0.4, and 0.42

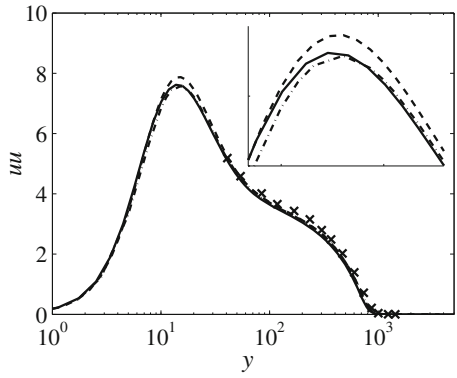

Fig. 4 Comparison of streamwise velocity fluctuations at $Re_\theta = 2{,}500$. *Dashed line* DNS [9]; *solid line* present LES; *dot-dashed line* z-filtered DNS data; *symbols* experimental data [7]

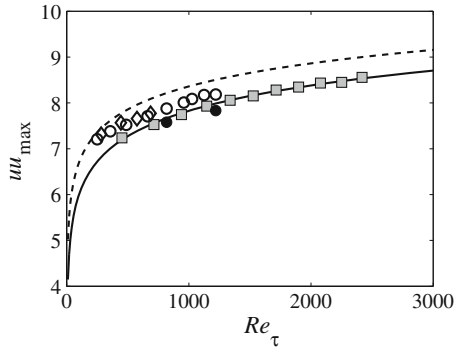

Fig. 5 Growth of $\langle uu \rangle_{\max}$. *Squares* present LES and fit (*solid line*); *open circles* DNS [9]; *filled circles* z-filtered DNS; *diamonds* DNS from Ref. [3]; *dashed line* fit to DNS from Ref. [8]

The skin-friction coefficient c_f and shape factor H_{12} are compared with literature data in Figs. 6 and 7, respectively, showing a very good agreement. Interestingly, the power-law behaviour for c_f at $Re_\theta \leq 2{,}500$ is superseded by the logarithmic Coles-Fernholz relation at higher Re [1], while H_{12} follows the correlation by Chauhan et al. [1]. Considering the fluctuations of the wall-pressure p_w and the

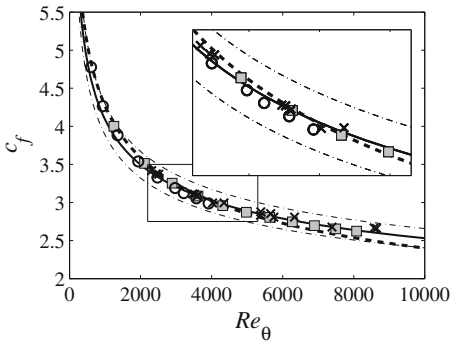

Fig. 6 Skin friction coefficient c_f. *Squares* present LES; *circles* DNS [9]; × experiments [7]; *solid/dot-dashed line* Coles-Fernholz relation [1] with ±5 % tolerances; *dashed line* low-Re power-law relation

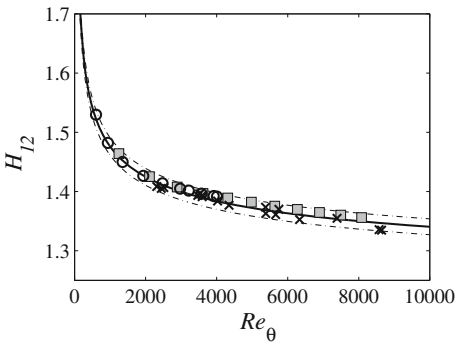

Fig. 7 Shape factor $H_{12} = \delta^*/\delta_\theta$. *Squares* present LES; *circles* DNS [9]; × experiments [7]; *solid line* correlation by Chauhan et al.[1] with ±1 % tolerances (*dot-dashed lines*)

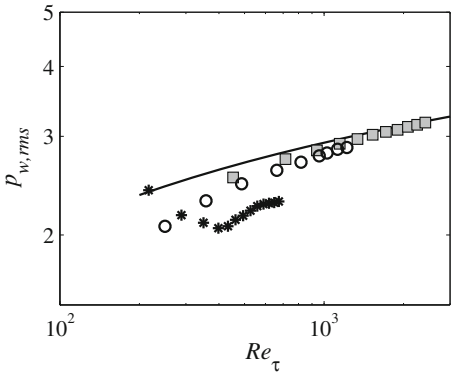

Fig. 8 RMS value of the wall-pressure p_w. *Squares* present LES; *circles* DNS [9]; *asterisks* DNS by Wu and Moin [11]; *line* correlation by Farabee and Casarella [2]: $(p^+_{w,\mathrm{rms}})^2 = 6.5 + 1.86\ln(Re_\tau/333)$

wall-shear stress τ_w, it is found that the LES follows closely the trends predicted by DNS studies (*cf.* Figs. 8 and 9). A slight systematic over-prediction is, however, observed, which is contradictory to the mentioned filtering effect; the source remains to be clarified.

The downstream development of characteristic spanwise scales is illustrated in Fig. 10 through the spanwise two-point correlation of the wall-shear stress τ_w. For

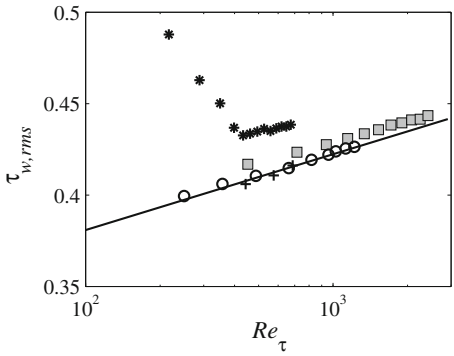

Fig. 9 RMS value of wall-shear stress τ_w. *Squares* present LES; *circles* DNS [9]; *asterisks* DNS by Wu and Moin [11]; *plus signs* DNS by Jimenez et al. [3]; *line* correlation by Schlatter and Örlü [9]: $\tau_w = 0.298 + 0.018\, Re_\tau$

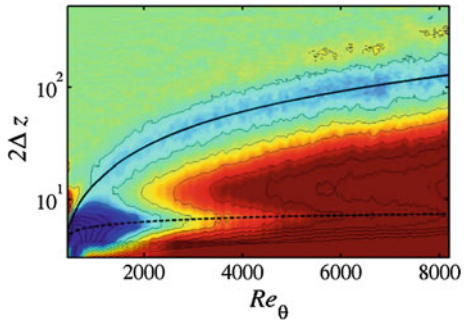

Fig. 10 Spanwise two-point correlation $R_{\tau\tau}$ of wall-shear stress τ_w from the present LES. Spanwise axis is scaled by $2\Delta z$ to show the spanwise pattern spacing. *Solid line* $2\Delta z = 0.85\delta_{99}$, *dashed line* $2\Delta z^+ = 120$

$Re_\theta > 2{,}000$, two distinct minima can be observed. The first appears at a spacing of about 120 wall units and is related to the near-wall streak spacing, while the second scales with $0.85\delta_{99}$, thereby evincing the influence of outer-layer structures on τ_w.

Pre-multiplied spanwise energy spectra for the streamwise velocity are shown in Fig. 11 for $Re_\theta = 2{,}500$ and $Re_\theta = 8{,}200$. Comparing both Re, an invariant maximum of the spectral energy distribution is evidenced at the wavelength $\lambda_z^+ \approx 120$ corresponding to the near-wall streaks. A second peak at $\lambda_z \approx \delta_{99}$ becomes more prominent with increasing Re and is the source for the amplitude modulation of the small-scales near the wall, which is responsible for the aforementioned increase of $\langle uu \rangle_{\max}$. Furthermore, the pre-multiplied spectrum at $y^+ = 15$ shows a plateau for the higher Re; equivalent to a k_z^{-1} dependence. This proves the existence of an overlap region where both inner and outer scaling are valid. A clear observation of a k_z^{-1} region has so far only been reported in an experiment by Nickels et al. [6] and very recently by Pirozzoli and Bernardini in a DNS of a supersonic boundary layer [8].

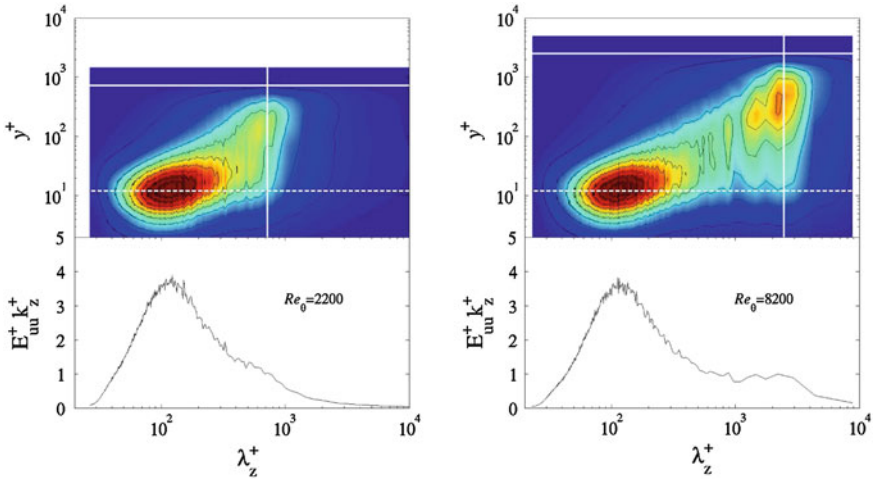

Fig. 11 Spanwise power-spectral density of streamwise velocity at $Re_\theta = 2{,}200$ and 8,200; boundary layer thickness δ_{99} (*solid lines*) and $y^+ = 15$ (*dashed line*)

3 Conclusions

A new highly resolved large-eddy simulation was presented for a spatially developing turbulent boundary layer, covering in a single domain the range $Re_\theta = 180$–8,300. Turbulence statistics and integral values are in close agreement with experiments and other simulations. The evolution of the large outer-layer structures was examined using spectra and a k_z^{-1} range was observed for the streamwise velocity.

References

1. Chauhan, K.A., Monkewitz, P.A., Nagib, H.M.: Criteria for assessing experiments in zero pressure gradient boundary layers. Fluid Dyn. Res. **41**, 021404 (2009)
2. Farabee, T.M., Casarella, M.J.: Spectral features of wall pressure fluctuations beneath turbulent boundary layers. Phys. Fluids **3**, 2410–2420 (1991)
3. Jiménez, J., Hoyas, S., Simens, M.P., Mizuno, Y.: Turbulent boundary layers and channels at moderate Reynolds numbers. J. Fluid Mech. **657**, 335–360 (2010)
4. Monkewitz, P.A., Chauhan, K.A., Nagib, H.M.: Self-consistent high-Reynolds-number asymptotics for zero-pressure-gradient turbulent boundary layers. Phys. Fluids **19**, 115101 (2007)
5. Nickels, T.B.: Inner scaling for wall-bounded flows subject to large pressure gradients. J. Fluid Mech. **521**, 217–239 (2004)
6. Nickels, T.B., Marusic, I., Hafez, S., Chong, M.S.: Evidence of the k_1^{-1} law in a high-Reynolds-number turbulent boundary layer. Phys. Rev. Lett. **95**, 074501 (2005)
7. Örlü, R.: Experimental studies in jet flows and zero pressure-gradient turbulent boundary layers. Ph.D. thesis, Department of Mechanics, KTH Stockholm, Sweden (2009)
8. Pirozzoli, S., Bernardini, M.: Probing high-Reynolds-number effects in numerical boundary layers. Phys. Fluids **25**, 021704 (2013)

9. Schlatter, P., Örlü, R.: Assessment of direct numerical simulation data of turbulent boundary layers. J. Fluid Mech. **659**, 116–126 (2010)
10. Segalini, A., Örlü, R., Schlatter, P., Alfredsson, P.H., Rüedi, J.-D., Talamelli, A.: A method to estimate turbulence intensity and transverse taylor microscale in turbulent flows from spatially averaged hot-wire data. Exp. Fluids **51**, 693–700 (2011)
11. Wu, X., Moin, P.: Transitional and turbulent boundary layer with heat transfer. Phys. Fluids **22**, 085105 (2010)

Investigation of Dual-Source Plume Interaction in a Turbulent Wall-Bounded Shear Layer

Shahin N. Oskouie, Bing-Chen Wang and Eugene Yee

1 Introduction

An understanding of mixing and dispersion rates and the characterization of concentration fluctuations of a passive scalar in a turbulent flow is relevant for a broad range of scientific and engineering applications of both practical and fundamental interest. In consequence, a number of theoretical, numerical and experimental studies of concentration fluctuations in plumes dispersing in turbulent flows have been undertaken in recent years. Most of these studies have focussed on the plume concentration statistics from a single source release. Unfortunately, the interaction of passive scalars emitted from two (or more) sources and the nature of the concomitant joint concentration statistics arising from this interaction has received considerably less attention.

In this regard, Warhaft [1] extended his previous work on scalar mixing in grid turbulence to investigate the interference of passive thermal wakes generated by two thermal cross-stream line sources. He determined the correlation coefficient between the two thermal wakes at eight downstream positions for ten different line source separations. Tong and Warhaft [2] investigated the mixing characteristics of temperature fluctuations produced by two fine annular sources placed axisymmetrically at a given downstream position in a turbulent jet. Vrieling and Nieuwstadt [3] applied direct numerical simulation (DNS) to study the turbulent dispersion from two line sources in a plane channel flow. Costa-Patry and Mydlarski [4] conducted laboratory studies of the interaction of two passive scalars generated by line sources in a fully-developed high-aspect-ratio turbulent channel flow.

S.N. Oskouie (✉) · B.-C. Wang
University of Manitoba, Winnipeg, MB, Canada
e-mail: nasseris@cc.umanitoba.ca

B.-C. Wang
e-mail: wang44@cc.umanitoba.ca

E. Yee
Defence R&D Canada – Suffield, Medicine Hat, AB, Canada
e-mail: Eugene.Yee@drdc-rddc.gc.ca

J. Fröhlich et al. (eds.), *Direct and Large-Eddy Simulation IX*,
ERCOFTAC Series 20, DOI 10.1007/978-3-319-14448-1_34

In spite of these experimental and numerical investigations, high-quality data sets of concentration fluctuation statistics arising from the interaction of two passive scalars dispersing in a turbulent flow are still rather limited (and, in particular, there is a paucity of data concerning higher-order concentration moments and higher-order correlation functions resulting from the interaction of two passive scalars). In this paper, we use DNS (in which the entire range of spatial and temporal scales of the turbulent flow and dispersion are fully resolved) to study the statistical characteristics of dual-plume interaction generated by two (concentrated) point sources emitting passive scalars into a neutrally-stratified wall-bounded shear flow.

2 Numerical Methodology

The DNS was performed using an in-house code developed using the FORTRAN 90/95 programming language, and fully parallelized using the message passing interface (MPI) paradigm. The code is based on a fully conservative and fully implicit second-order finite difference scheme and utilizes a staggered grid arrangement. For our simulations, we solved the momentum equations for an incompressible flow in an open channel, together with an advection-diffusion equation for a passive scalar. For the velocity field, we applied periodic conditions in the streamwise (x) and spanwise (z) directions and a no-slip condition at the bottom wall (at $y = 0$, where y is the vertical direction) of the open channel. For the concentration field, we imposed a zero concentration at the inlet boundary, and zero Neumann conditions were applied in the spanwise direction, at the bottom wall and top of the open channel and at the outlet. The simulations were executed until statistically stationary conditions were attained for the velocity and concentration fields, after which various statistics of the instantaneous concentration field were obtained by averaging over a temporal interval of $5T$ where $T \equiv \delta/u_\tau$, $\delta = 0.04$ m is the height of the open channel and u_τ is the friction velocity.

The computational domain has dimensions $2\pi\delta \times \delta \times \pi\delta$ and has been discretized using $256 \times 128 \times 192$ grid nodes in the x-, y-, and z-directions, respectively. A Reynolds number was set to $Re_\tau \equiv u_\tau \delta/\nu = 395$. The two sources were located in the log-law region of the wall shear layer at a normalized vertical height of $y^+ \equiv yu_\tau/\nu = 40$. The size (radius) of each source is $\sigma_0 = 0.008\,\delta$ and the Schmidt number $Sc \equiv \nu/\kappa$ (κ is the molecular diffusivity) of the scalar is 1.0. In our simulations, we considered four different spanwise separations d between the two point sources; namely, $d = 0.049\,\delta$, $0.115\,\delta$, $0.279\,\delta$ and $0.541\,\delta$.

3 Results and Discussion

Owing to space limitations, we will focus primarily on the scalar correlation coefficients of order two and three relevant for the study of the interference of the second- and third-order concentration moment, respectively, arising from the interaction of plumes from two point sources.

3.1 Scalar Correlation Coefficient

If we let c_1 and c_2 denote the instantaneous concentration from (point) sources 1 and 2, respectively, then the linearity of the advection-diffusion equation implies that the total instantaneous concentration c_T from both sources is linearly superposable and given by $c_T = c_1 + c_2$. Concentration moments higher than first order (mean concentration) are not linearly superposable, with the result that higher moments of the total concentration cannot be obtained from the concentration moments of the individual instantaneous concentration. The total concentration moments higher than first order can be obtained only from a knowledge also of the joint statistics of the individual instantaneous concentration in the form of certain higher-order correlation functions. To this purpose, we can define the second- and third-order correlations functions, respectively, as follows:

$$\rho^{[1|1]} = \frac{\overline{c_T'^2} - \overline{c_1'^2} - \overline{c_2'^2}}{2\left(\overline{c_1'^2}\right)^{1/2}\left(\overline{c_2'^2}\right)^{1/2}}, \tag{1}$$

and

$$\rho^{[1|2]} = \frac{\overline{c_T'^3} - \overline{c_1'^3} - \overline{c_2'^3}}{3\left(\left(\overline{c_1'^4}\right)^{1/2}\left(\overline{c_2'^2}\right)^{1/2} + \left(\overline{c_1'^2}\right)^{1/2}\left(\overline{c_2'^4}\right)^{1/2}\right)}, \tag{2}$$

where the overbar denotes an ensemble average and $c_i' \equiv c_i - \overline{c_i}$ ($i \equiv 1, 2, T$) is the instantaneous concentration fluctuation about the mean concentration. As discussed in Yee et al. [5], the correlation coefficients $\rho^{[1|1]}$ and $\rho^{[1|2]}$ either enhance or reduce the second- and third-order total concentration moments, respectively, from those obtained from the simple linear superposition of the individual concentration moments.

Figure 1 displays crosswind (spanwise) profiles of the second-order correlation function $\rho^{[1|1]}$ obtained from our numerical simulations. The results are shown at four different downwind locations x/δ for the four source separations d mentioned previously. Generally, the minimum value of $\rho^{[1|1]}$ is found midway between the two sources (owing to the symmetry in the positioning of the sources in the

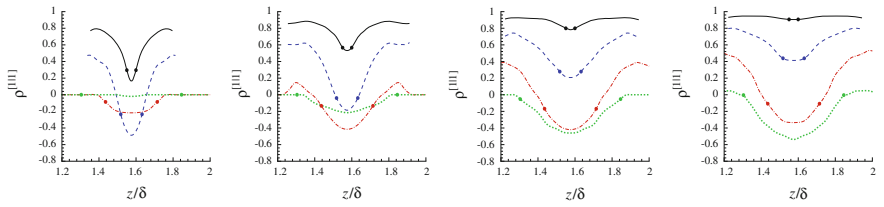

Fig. 1 Spanwise profiles of $\rho^{[1|1]}$ at four downstream distances from the source corresponding to (panels from *left* to *right*) $x/\delta = 1$, 2, 4, and 6. The *dots* on each line are drawn at the locations of the sources, and correspond to source separations of $d/\delta = 0.049$ (*solid line*); 0.115 (*dashed line*); 0.279 (*dash-dot line*); and, 0.541 (*dotted line*).

inhomogeneous flow) and the maximum $\rho^{[1|1]}$ values are found at the plume fringes. For sources that are close enough together, the maximum values in $\rho^{[1|1]}$ far from the centerline where the plume intermittency is large arise from the fact that at these locations a large eddy can occasionally transport both plumes together causing the two concentrations to either increase or decrease simultaneously. The minimum in $\rho^{[1|1]}$ at the midpoint between the two sources is due to the fact a large eddy at this location can move one of the plumes over the location, while simultaneously moving the other off this location (causing the concentration contributed by one plume to increase and that contributed by the other plume to decrease).

Figure 2 shows spanwise profiles of the third-order correlation function $\rho^{[1|2]}$ at four downstream distances. Note that the behavior of $\rho^{[1|2]}$ is very similar to that of $\rho^{[1|1]}$ (cf. Fig. 1). However, $\rho^{[1|2]}$ contains fine-scale variations (modulations) in z that are not exhibited in $\rho^{[1|1]}$. Finally, in comparison to $\rho^{[1|1]}$, it is seen that $\rho^{[1|2]}$ (especially for the larger source separations) tend to exhibit smaller variations in the spanwise direction at a fixed x and with increasing x at a fixed spanwise location.

Figure 3 exhibits the streamwise (x) development of $\rho^{[1|1]}$ and $\rho^{[1|2]}$ along the midpoint between the two sources. At downstream fetches where the mean plume width σ_a is much less than the source separation d, a location at the midpoint between

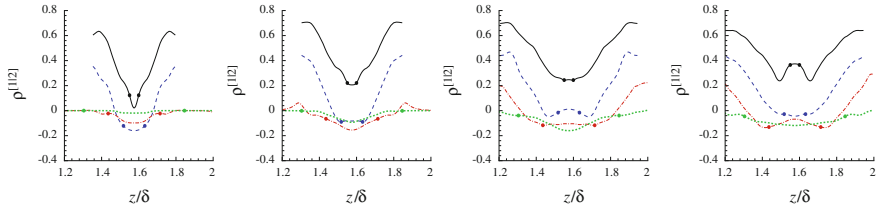

Fig. 2 Spanwise profiles of $\rho^{[1|2]}$ at four downstream distances from the source corresponding to (panels from *left* to *right*) $x/\delta = 1$, 2, 4, and 6. The dots on each line are drawn at the locations of the sources, and correspond to source separations of $d/\delta = 0.049$ (*solid line*); 0.115 (*dashed line*); 0.279 (*dash-dot line*); and, 0.541 (*dotted line*).

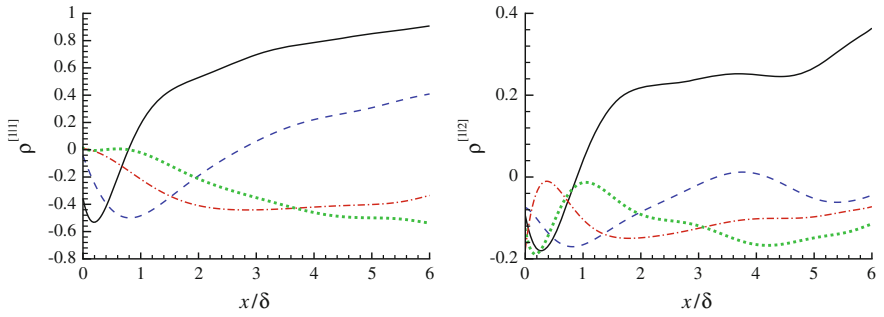

Fig. 3 Streamwise evolution of *left panel* $\rho^{[1|1]}$ and *right panel* $\rho^{[1|2]}$ at the *centerline* between two sources for source separations of $d/\delta = 0.049$ (*solid line*); 0.115 (*dashed line*); 0.279 (*dash-dot line*); and, 0.541 (*dotted line*)

the two sources is rarely exposed to either plume and never to both simultaneously, so the correlation is effectively zero in this regime of development. At downstream fetches where σ_a greatly exceeds d but the instantaneous plume width σ_r is much less than d, the meandering of the two plumes by the large eddies causes the concentration from one plume to decrease at a location at the midpoint between the two sources, whilst simultaneously causing the concentration from the other plume to increase (and vice-versa, as the flapping occurs in the opposite direction). This physical process leads to negative correlations, corresponding as such to the anti-correlated fluctuations in the two plumes. Finally, at downwind fetches where σ_r is much greater than d, the plumes overlap and mix significantly. At this stage in the plume development, the two plumes meander together (although the importance of meandering decreases with increasing downstream distance) and also undergo internal turbulent mixing with each other (with the importance of the internal turbulent mixing increasing with increasing downstream distance), leading to increasing positive correlations with increasing downstream fetch. It is noted that both $\rho^{[1|1]}$ and $\rho^{[1|2]}$ exhibit similar behavior and can be seen to transition between these three regimes of plume development. The similar behaviour of the second- and third-order correlation functions would seem to suggest that there might be some relationship between the various higher-order moments of the total concentration.

3.2 Relationships Between Higher-Order Concentration Statistics

Figure 4 shows the normalized concentration moment scatterplots of $\overline{c^n}/\bar{c}^n$ ($n = 3, 4$) plotted against $\overline{c^2}/\bar{c}^2$ on a double logarithmic scale for a large number of points in the plume. The scatterplots are plotted for the total concentration as well as for the individual concentrations. Remarkably, each of these scatterplots is seen to collapse

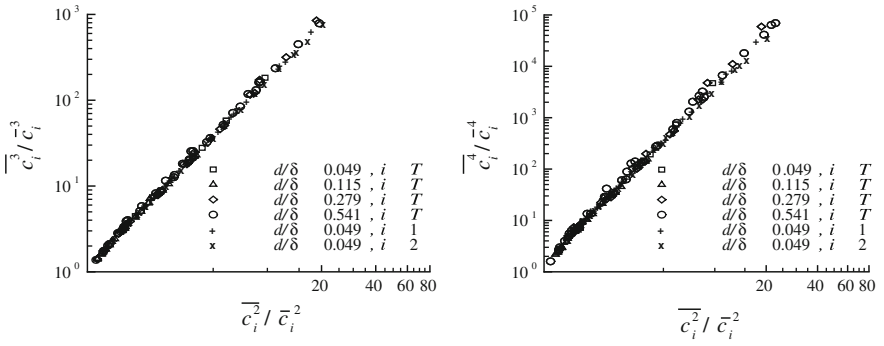

Fig. 4 Scatterplots of normalized higher-order concentration moments for a large number of locations in the plume: *left panel* third-order moment $\overline{c^3}/\bar{c}^3$ and *right panel* fourth-order moment $\overline{c^4}/\bar{c}^4$ plotted against the second-order moment $\overline{c^2}/\bar{c}^2$.

onto a curve which implies that the higher-order moments (for both the individual and total concentrations) are determined effectively by knowledge of only the two lowest order moments of the concentration. The observed universal relationships between the various higher-order concentration moments are the same for the concentration from a single source or the total concentration from two sources. This observation has important implications for the modeling of concentration fluctuations. Firstly, the collapse of the normalized third- and fourth-order concentration moments on the normalized second-order concentration moment implies that the concentration probability density function (PDF) can be described adequately by at most two parameters. Secondly, this two-parameter concentration PDF appears to be universal in the sense that it applies to the concentration from a single source or from two (or more) sources. Thirdly, a knowledge of the first- and second-order concentration moments for each source along with the second-order correlation function, required for the prediction of the total concentration variance, is sufficient for the prediction of all the higher-order moments of the total concentration.

4 Conclusion

Direct numerical simulation has been applied to the study of the interference of the fluctuating concentration fields from a dual-source release. The interference of two scalars as manifested in the second and third moment of the total concentration is investigated through a determination of the second- and third-order correlation function. The evolution of these two correlation functions as a function of downstream distance and the variation of the correlation functions in the spanwise direction for particular downstream distances (from the source) have been extracted from the numerical simulations of the instantaneous concentration fields for various values of the transverse source separation. A remarkably robust feature of both the individual and total concentrations was the observed collapse of the normalized third- and fourth-order concentration moments on the normalized second-order concentration moment, with significant implications for the simplification of the modeling of the interference of two passive scalars in a turbulent flow.

Future work will investigate interference of the concentration statistics for passive scalars dispersing in turbulent flows at higher Reynolds numbers. Furthermore, we will consider also source separations in the streamwise and vertical directions, as well as ground-level source releases.

References

1. Warhaft, Z.: The interference of thermal fields from line sources in grid turbulence. J. Fluid Mech. **144**, 363–387 (1984)
2. Tong, C., Warhaft, Z.: Passive scalar dispersion and mixing in a turbulent jet. J. Fluid Mech. **292**, 1–38 (1995)

3. Vrieling, A.J., Nieuwstadt, F.T.M.: Turbulent dispersion from nearby point sources-interference of the concentration statistics. Atmos. Environ. **37**, 4493–4506 (2003)
4. Costa-Patry, E., Mydlarski, L.: Mixing of two thermal fields emitted from line sources in turbulent channel flow. J. Fluid Mech. **609**, 349–375 (2008)
5. Yee, E., Gailis, R.M., Wilson, D.J.: The interference of higher-order statistics of the concentration field produced by two point sources according to a generalized fluctuating plume model. Bound.-Layer Meteorol. **116**, 297–348 (2003)

LES of the Flow in a Rotating Rib-Roughened Duct

D. Borello, A. Salvagni, F. Rispoli and K. Hanjalic

1 Introduction

Interior channels of gas-turbine blades are often lined with ribs, which act as turbulence promoters to enhance heat transfer between the hot blade surface and the cooling air. The rib orientation to the mainstream flow strongly influences the ensuing phenomena such as unsteadiness, boundary layer separation, reattachment and recirculation. To improve the cooling design and especially to detect and prevent possible development of critical hot spots that may lead to material failure, it is essential to predict accurately the flow field and heat transfer under various operating conditions. Whilst the flow features inside stationary ribbed channels have been well researched, the effects of rotation encountered in rotor blades are less known. Rotation introduces a background vorticity that stabilizes the fluid flow on the suction side, while destabilizing it on the pressure side. The effect is commonly defined by the nondimensional Rotation number, $\mathrm{Ro} = \Omega D/U$, where U is the bulk velocity, D the hydraulic diameter of the duct and Ω is the angular velocity. Recently, Coletti and co-workers carried out extensive PIV analysis of flow in a rib-roughened

D. Borello (✉) · A. Salvagni · F. Rispoli
Dipartimento di Ingegneria Meccanica E Aerospaziale,
'Sapienza' Universit di Roma, Rome, Italy
e-mail: domenico.borello@uniroma1.it

A. Salvagni
e-mail: alessandro.salvagni@uniroma1.it

F. Rispoli
e-mail: franco.rispoli@uniroma1.it

K. Hanjalic
Delft University of Technology, Delft, The Netherlands
e-mail: khanjalic@gmail.com

K. Hanjalic
Novosibirsk State University, Novosibirsk, Russia

J. Fröhlich et al. (eds.), *Direct and Large-Eddy Simulation IX*,
ERCOFTAC Series 20, DOI 10.1007/978-3-319-14448-1_35

channel subjected to rotation [1]. They investigated the influence of rotation in a rib-roughened channel containing 10 equally spaced ribs. The rotational axis is parallel to the rib-roughened surface, aligned with the ribs and placed far upstream of the first rib. The test section and instrumentation were mounted on a disk rotating in a direction perpendicular to the main flow. Flow measurement were carried out while the disk was rotating. Under these conditions the wall-normal pressure gradient is modified to balance the centrifugal and Coriolis forces. For the configuration considered, rotation stabilizes the flow adjacent to the ribbed wall in the case of clockwise rotation and destabilizes it in counter-clockwise rotation. We report here some results of a well-resolved dynamic Smagorinsky LES of the configuration of Coletti et al. [1] for the anti-clockwise rotation.

2 Flow Specification and Computational Details

The rectangular channel with ribs placed on the bottom wall has a width-to-hight aspect ratio of 0.9. The flow blockage due to ribs is $h/D = 0.1$, h being the rib height. The Navier-Stokes equations system was solved in dimensionless form using as reference the duct hydraulic diameter, bulk flow velocity and air properties at 20 °C. The ensuing Reynolds number, based on D and bulk velocity is 15,000. According to Coletti et al. [1], after the 6th rib the flow can be considered as periodic. Thus we considered only one section between two successive ribs subjected to anti-clockwise rotation with $\mathrm{Ro} = 0.3$. For comparison, we also provide solutions for the non-rotating configuration. The LES was performed using the unstructured FV code T-FlowS, used successfully in a number of earlier LES studies, e.g. [2]. The computational domain was meshed using a block-structured hexahedral orthogonal grid with about 6.5 M cells. All the wall neighbouring cells have a y^+ value lower than 0.5. A coarser grid with 3 M cells was also considered for comparisons.

A Crank-Nicolson/CDS scheme was used to guarantee a second-order accuracy. The coupling of the velocity and pressure field was ensured by using the SIMPLE scheme, while the Preconditioned BiCG solver was applied for solving the linearized algebraic equation system. Periodic boundary conditions were imposed at the inlet and outlet surface, while no-slip conditions were set at solid boundaries. The nondimensional time step was set to 5e-4 ensuring the maximum CFL number to be smaller than 0.3 over the whole domain. The computations were performed on the CRESCO SP5 cluster at Casaccia (ENEA) using 32 processors. On such a computer 25 s are required for performing one time step for computations on the fine grid. Computations were performed for 2 flow through times (FTT) before starting to collect statistics. Table 1 summarizes the time averaging periods.

Table 1 Time averaging period

Case	Coarse grid	Refined grid
No rotation	11 FTT	13 FTT
Anti-clockwise rotation	22 FTT	15 FTT

3 Results

The streamlines obtained by the LES for the rotating and stationary case are shown in Fig. 1.

Both subfigures show the expected flow pattern with a large recirculation bubble behind the ribs. However, the anti-clockwise rotation enhances the entrainment into the separated bubble, leading to a pressure reduction inside the recirculation region. This stronger pressure gradient causes a streamlines deflection and a reduction in the length of the separation bubble, as also found by Coletti et al. [1]. The analysis of the pressure gradient plots (not shown here) confirms these findings. It is noted that, when using the coarse grid the quality of the predictions deteriorated (Table 2).

The Coriolis force also affects the vortical structures in front, around and on the top of the rib. The downstream corner vortex generated by the large recirculation bubble is shrank and the upstream corner vortex is enlarged. Furthermore, the recirculation bubble generated on the top of the rib is affected by the curvature of the streamlines passing above the rib. Due to the Coriolis effects, the recirculation bubble is thicker and the streamlines have a lower curvature when passing above the rib. The rib recirculation bubble becomes thicker than in the non-rotating case and extends over the whole rib (Fig. 2).

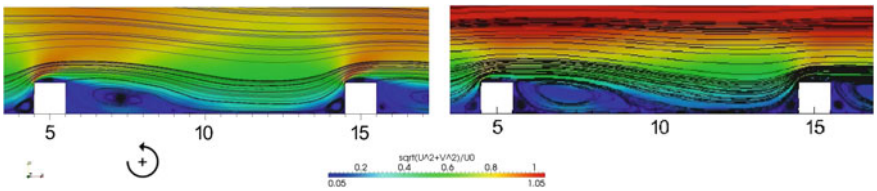

Fig. 1 Streamlines for the LES—*left* rotating case; *right* non rotating case

Table 2 Length of recirculation bubble

Case	Coarse grid (h)	Refined grid (h)	Exp (h)
No rotation	3.90	3.90	3.85
Anti-clockwise rotation	3.85	3.50	3.45

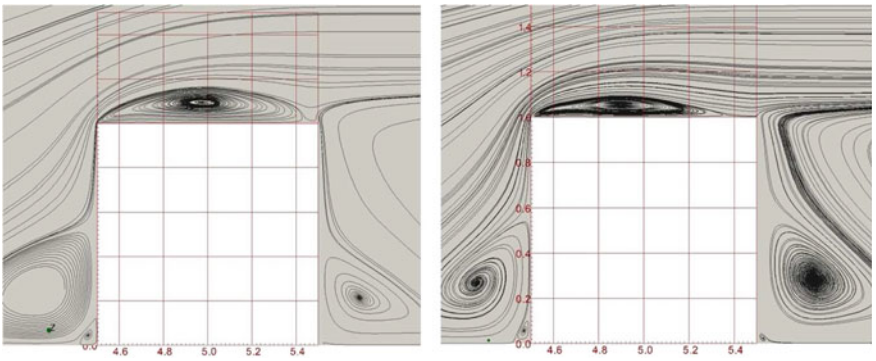

Fig. 2 Vortical structures around the rib—*left* anti-clockwise rotation; *right* non-rotating

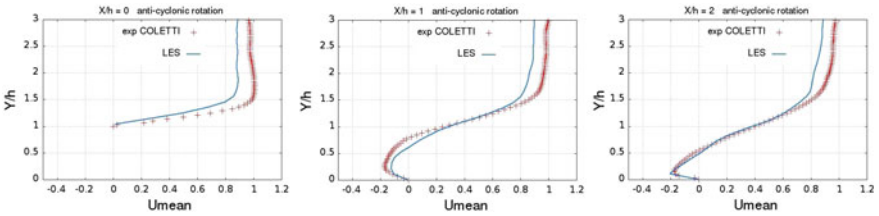

Fig. 3 Streamwise velocity downstream from the rib—*left* x/h = 0; *center* x/h = 1; *right* x/h = 2 (anti-clockwise rotation case)

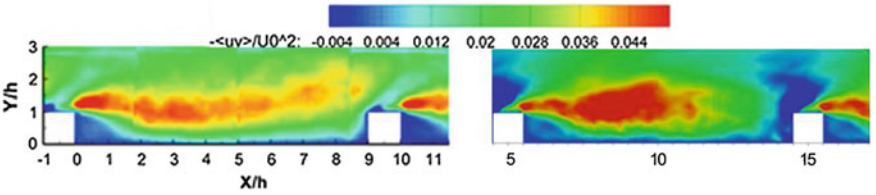

Fig. 4 Shear stress -uv (anti-clockwise rotation case): *left* exp, *right* LES

The plots of the axial velocity downstream from the rib demonstrate that a fair agreement is obtained between the experiments and LES, especially when considering the thickness of the recirculation bubble (see Fig. 3).

Figure 4 shows that the rib is the main source of the shear stress and the rotation enhances the production of the uv component. Over the rib the shear stress is suppressed due to the low turbulence level in the slow recirculation bubble.

The influence of the lateral walls on the flow field was out of the scope of the PIV analysis (performed only in the mid-plane). As such information is available from LES, we discuss briefly the effect of rotation by considering flow patterns in planes parallel to the rib-roughened wall. The results are compared qualitatively with

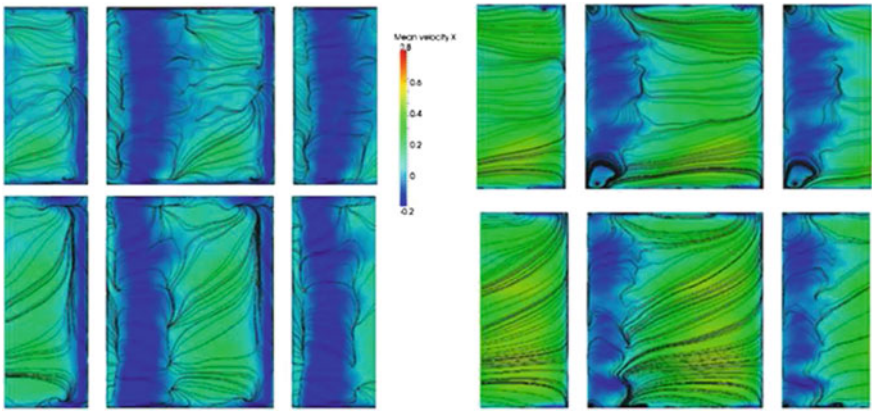

Fig. 5 Streamlines on the rib-roughened wall parallel plane; *left* 0.05 h; *right* 0.5 h; *up* non rotating; *down* anti-clockwise rotating

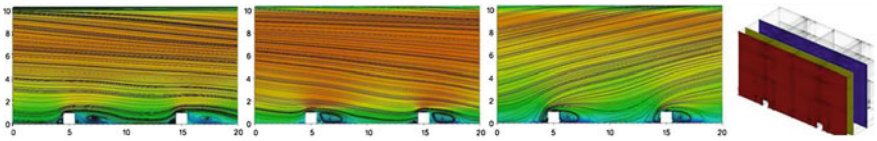

Fig. 6 Streamlines along pitchwise planes; *left* mid-pitch; *center* 0.15 pitch; *right* 0.05 pitch

those of Casarsa and Arts [3] for a non-rotating rib-roughened channel with a high blockage ratio. The streamlines plots in two planes: at 0.05 and 0.5 h from the wall are shown in Fig. 5. In the first plane (0.05 h) one can see the vortical structures discussed above: an upstream corner vortex (clockwise rotation), a downstream corner vortex (anti-clockwise) and the recirculation bubble extending for about 0.3 of the space between two consecutive ribs. In the nonrotating case, when moving towards the lateral walls, the recirculation bubble length is strongly reduced with its footprint on this plane having a bow shape. Notably, this effect is less evident in the rotating case due to the mentioned shrinking of the recirculation bubble that is particularly visible in the mid-plane. The section at y/h = 0.5 shows some differences: first, the two small vortices close to the rib disappeared at this distance from the wall (see also Fig. 2). Furthermore, two vortical structures are present close to the lateral walls immediately downstream from the rib. Again, the bow shape of the recirculation bubble is suppressed in the rotating case.

Two Coriolis induced secondary flows extending over the whole section are present in the rotating case. Such structures push the fluid from the central part of the duct towards the lateral walls. Therefore the streamlines are swept towards the rib-roughened wall in the mid-plane and in the opposite direction when moving close to the lateral walls (see Fig. 6).

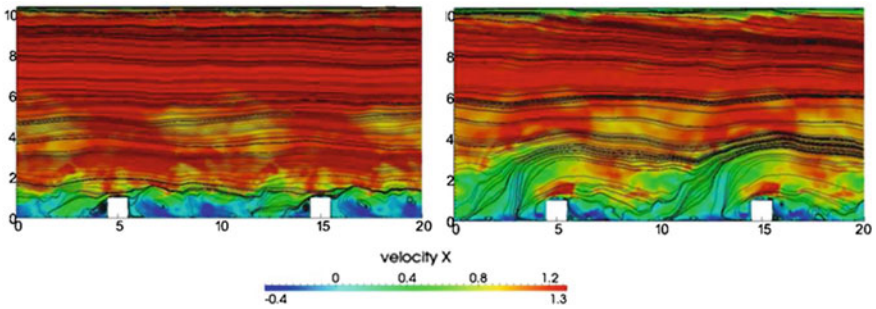

Fig. 7 Unsteady streamlines along the mid-pitch plane; *left* non-rotating; *right* anti-clockwise rotation

Finally, in Fig. 7 the instantaneous velocity plots are presented. In the non-rotating case the velocity is not perturbed by the rib presence for y greater than 2.5. In contrast, in the rotating case the vortical structures extend for about half of the channel height, suggesting that a more vigorous heat removal is expected in the rotating case.

4 Conclusions

LES of the flow in a rib-roughened channel subjected to anti-clockwise rotation was carried out. The turbulent flow structures induced by the geometry and the rotation were identified and discussed. In particular, we noticed the presence of large Coriolis-induced secondary flows and the change in the bow shape of the recirculation bubble when considering an anti-clockwise rotation. The presence of rotation induced a destabilizing effect increasing the turbulence and flow unsteadiness, which should enhance heat transfer.

References

1. Coletti, F., Maurer, T., Arts, T., Di Sante, A.: Flow field investigation in a rotating rib-roughened channel by means of particle image velocimetry. Exp. Fluids **52**, 1043–1061 (2012)
2. Delibra, G., Borello, D., Hanjalic, K., Rispoli, F.: LES of flow and heat transfer in a channel with a staggered cylindrical pin matrix. In: Armenio, V., Geurts, B., Froelich, J. (eds.) Direct and Large-Eddy Simulation VII, Proceedings of 7th International ERCOFTAC Workshop, Trieste. Springer Science and Media B.V., 9–10 Sept 2008
3. Casarsa, L., Arts, T.: Experimental investigation of the aerothermal performance of a high blockage rib-roughened cooling channel. J. Turbomach. **127**, 580–588 (2005)

On the Large-Eddy Simulations of the Flow Past a Cylinder at Critical Reynolds Numbers

O. Lehmkuhl, I. Rodríguez, J. Chiva and R. Borrell

1 Introduction

The flow past a circular cylinder is associated with different types of instabilities which involve the wake, the separated shear layers and the boundary layer. A comprehensive description of the flow phenomena at different Reynolds numbers (Re) can be found in [15]. It is well known that when the Reynolds number approaches 2×10^5 the boundary layer undergoes a transition from laminar to turbulent regime. The range of Reynolds numbers up to $\sim 3.5 \times 10^5$ is characterised by a rapid decrease of the drag coefficient with the Reynolds number. Another feature which characterises this regime is the presence of asymmetric forces during the transition regime as reported experimentally [2]. During this transition, the separation point moves towards the rear end of the cylinder until it reaches a stationary point with a stable drag coefficient. This marks the transition from the critical to the supercritical regime [11].

This work aims at shed some light into the complex physics present at these critical Reynolds numbers. To do this, large-eddy simulations of the flow at Reynolds numbers in the range of $Re = 1.4 \times 10^5$–5.3×10^5 are carried out. Solutions are compared to experimental measurements available in the literature. One of the

O. Lehmkuhl (✉) · I. Rodríguez · J. Chiva
Universitat Politècnica de Catalunya - BarcelonaTech, Colom 11,
08222 Terrassa, Spain
e-mail: oriol@cttc.upc.edu

I. Rodríguez
e-mail: ivette@cttc.upc.edu

J. Chiva
e-mail: jordic@cttc.upc.edu

R. Borrell
Termo Fluids S.L., Avda. Jacquard 97 1-E, 08222 Terrassa, Spain
e-mail: ricardb@cttc.upc.edu

J. Fröhlich et al. (eds.), *Direct and Large-Eddy Simulation IX*,
ERCOFTAC Series 20, DOI 10.1007/978-3-319-14448-1_36

major outcomes is to understand the physics that characterises the critical regime and the role of the turbulent transition in the boundary layer on the drag crisis phenomena.

2 Numerical Method

Large-eddy simulations (LES) of the flow are here performed. The methodology for solving the filtered Navier-Stokes equations is detailed in [8, 10]. As for the turbulence model, large-eddy simulations are carried out using the Wall-Adapting Local Eddy diffusivity model [9] within a Variational Multi-Scale framework (VMS-WALE subgrid-scale model) [6].

2.1 Definition of the Case: Geometry and Mesh Resolution

The flow past a circular cylinder at critical Reynolds numbers in the range of $Re = U_{ref}\ D/\nu = 1.4 \times 10^5$–$5.3 \times 10^5$ is considered. The Reynolds number is defined in terms of the free-stream velocity U_{ref} and the cylinder diameter D. The cases are solved in a computational domain of dimensions $x \equiv [-16D, 16D]$; $y \equiv [-10D, 10D]$; $z \equiv [0, 0.5\pi D]$ in the stream-, cross- and span-wise directions respectively, with a circular cylinder at (0, 0, 0). The boundary conditions at the inflow consist of uniform velocity (u,v,w) = (1, 0, 0), slip conditions at the top and bottom boundaries of the domain, while at the outlet a pressure-based condition is used. At the cylinder surface, no-slip conditions are prescribed. As for the span-wise direction, periodic boundary conditions are imposed.

The governing equations are discretised on an unstructured mesh generated by the constant-step extrusion of a two-dimensional unstructured grid. Different grids up to ∼64 million CVs are used, depending on the Reynolds number (see Table 1). The boundary layer at the cylinder surface is well resolved, i.e. no wall function is used. Thus, the meshes are designed so as to keep the non-dimensional wall distance $y^+ \leq 2$. To do this, a prism layer is constructed around the cylinder surface. In the problem here considered, transition to turbulence occurs in the boundary layer. Thus,

Table 1 Main parameters for the different computations

Re	NCV_t [MCVs]	$N_{CV\ plane}$	N_{planes}
1.44×10^5	38.4	299,683	128
2.6×10^5	38.4	299,683	128
3.8×10^5	48.6	379,950	128
5.3×10^5	64	500,516	128

NCV_t total number of CVs; $N_{CV\ plane}$ number of CVs in the plane; N_{planes} number of planes in the span-wise direction

it should be stressed that in the present formulation transition to turbulence is well captured by the model, i.e. no artificial mechanism is imposed for triggering this phenomenon to occur.

3 Results

For obtaining the numerical results presented, the simulations are started from an initially homogeneous flow field. Then, simulation is advanced in time until statistical stationary flow conditions are achieved and the initial transient is completely washed out. Average statistics are then computed for a sufficient long time span of about $\sim 100\, tU/D$, in order to assure that the flow is statistically converged.

In order to gain insight into the coherent structures developed in the separated zone, the Q-criterion is used [7]. Figure 1 shows the isocontours of second invariant of the velocity gradient tensor (Q) coloured by the velocity magnitude at Reynolds numbers of 2.5×10^5, 3.8×10^5 and 5.3×10^5. While the lower Reynolds number exhibits a flow topology more similar to that observed in the sub-critical regime, i.e. laminar flow

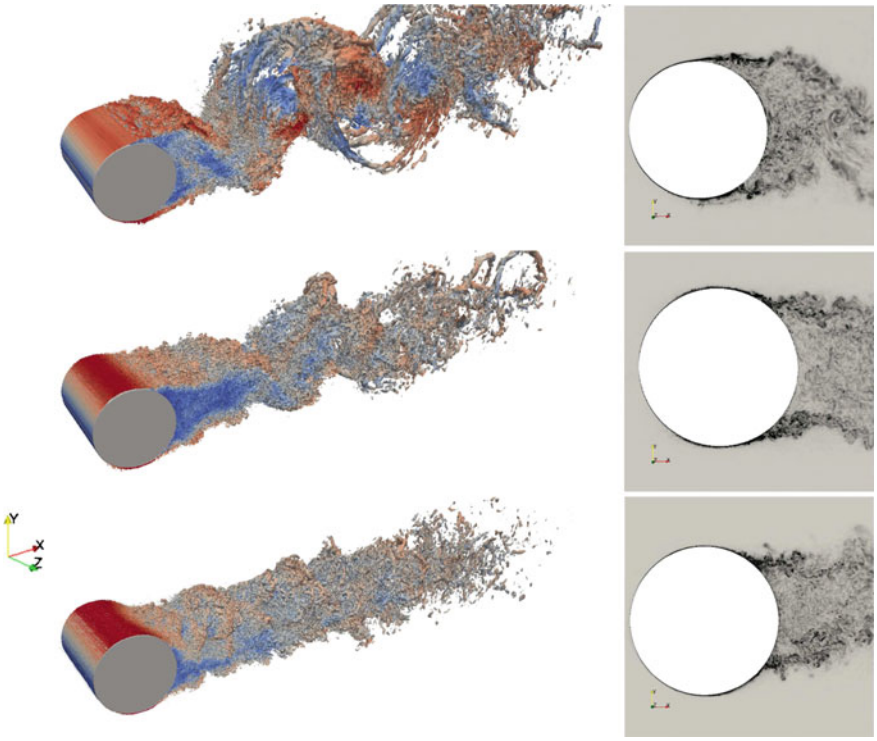

Fig. 1 Wake configuration. *Left* Q iso-countours coloured by the velocity magnitude; *right* instantaneous vorticity magnitude. From *top* to *bottom*: $Re = 2.6\times10^5$; $Re = 3.8\times10^5$; $Re = 5.3\times10^5$

separation at about ($\phi_s \sim 90°$) from the stagnation point and transition to turbulence in the separated shear layers, at the higher Reynolds numbers the flow shows a narrow wake with the separation point moving towards the rear end of the cylinder ($\phi_s \geq 90°$). The wake topology obtained at these critical Reynolds number can also be observed by means of the vorticity contours depicted at the half span-width plane.

Time-averaged statistical features resulting from the simulation are summarized in Table 2. In the table, the drag coefficient (C_D), the base pressure ($-Cp_b$), the separation angle measured from the stagnation point (φ_{sep}), and the angular position where the pressure reaches a minimum (φ_{Pmin}), are given. Experimental data from the literature are also given. As can be seen, in the range of Reynolds numbers considered, there is a pronounced decrease in the magnitude of the drag coefficient accompanied with an increase in the base pressure coefficient. As observed from the instantaneous flow, separation in the boundary layer is delayed, with increasing separation angle. The location of the pressure minimum also increases with the Reynolds number, moving towards the rear end of the cylinder, while its absolute value decreases (see also Fig. 2).

The variation of the drag coefficient with the Reynolds number is plotted in Fig. 2 together with reference data from the literature. At these Reynolds numbers, the measured data of the drag coefficient present a large scattering, due to the difficulties

Table 2 Statistical flow features at different Reynolds numbers

Re	C_D	$-Cp_b$	$\varphi_{sep}[°]$	$\varphi_{Pmin}[°]$
1.4×10^5	1.215	1.3	95.5	68.5
2.6×10^5	0.83	0.984	95/252	70/280
3.8×10^5	0.328	0.347	102	83.8
5.3×10^5	0.247	0.15	121	86
Cantwell and Coles Re = 1.4e5	1.237	1.21	–	–
Achenbach Re = 2.6e5	–	–	94	–

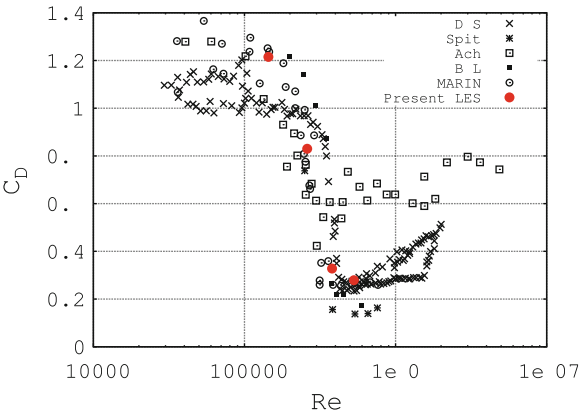

Fig. 2 Variation of the drag coefficient with the Reynolds number. Comparison with the literature. *Red circles* present results, *squares* Achenbach [1], *solid squares* Bursnall and Loftin [3], *stars* Spitzer [13], *crosses* Delany and Sorensen [5]., *circles* Vaz et al. [14]

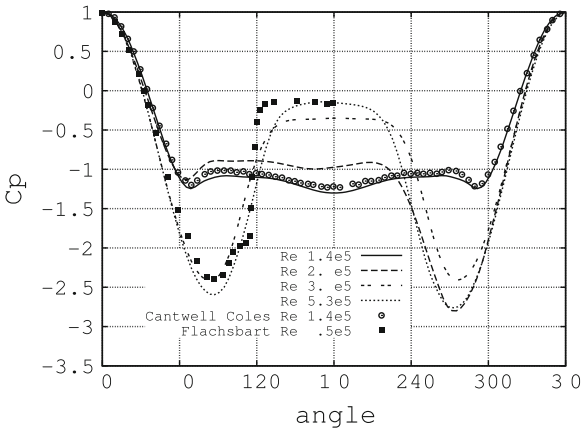

Fig. 3 Pressure distribution for the different Reynolds numbers

associated with the measurements; i.e. sensitiveness to turbulence intensity, cylinder end conditions, surface roughness, blockage ratio, etc. In spite of the large scattering in the reference data, results obtained with the present simulations show a fair agreement, being in the same range of the measured data.

In addition to the total drag coefficient, the pressure distribution at the cylinder surface at different Reynolds numbers is depicted in Fig. 3. As can be seen, at $Re = 1.44 \times 10^5$ it compares very well with that measured by Cantwell and Coles [4] at the same Reynolds number. As the Reynolds number increases, the pressure distribution changes with a pronounced decrease in the magnitude of the minimum pressure, and the position of this minimum moving towards the rear end of the cylinder. At the same time, the cylinder base pressure rises as was also shown by Achenbach [1] in his study. This behaviour is characteristic of the critical regime.

One interesting feature observed in the present computations is the presence of asymmetric forces at the cylinder surface in the regime transition (in the present computations at $Re = 2.5 \times 10^5$). Transition to turbulence occurs earlier at one side of the cylinder boundary layer. Thus, separation in the turbulent side is delayed. This behaviour, which causes large fluctuations in the cylinder forces and yields average lift $C_l > 0$, was also observed experimentally by Bearman [2] and Schewe [12]. As can be observed, at the $Re = 3.8 \times 10^5$ the forces at the cylinder recover their symmetry (see Fig. 3), whereas at $Re = 5.3 \times 10^5$ the drag coefficient reaches its minimum value (see also Fig. 2), but the pressure distribution is again slightly asymmetric.

4 Concluding Remarks

The flow past a circular cylinder at critical Reynolds numbers in the range of $Re = 1.4 \times 10^5$–5.3×10^5 is computed by means of large-eddy simulations. In the present computations, the mesh used is highly refined in the near-wall, as no wall

function is used for solving the turbulent boundary layers. Furthermore, it should also be stressed the capabilities of the current formulation for capturing quite well the transition to turbulence in the boundary layer without the use of any artificial mechanism which triggers this phenomenon to occur. Results shown are very promising as they correctly predict the steep drop in the drag coefficient in this range of Reynolds numbers and the delayed turbulent separation from the cylinder surface, being consistent with the experimental measurements. The presence of asymmetric forces on the cylinder surface occurring during the critical regime in agreement with previous experiments is also detected. It should be pointed out that in the present computations, these asymmetric forces are detected at the Reynolds number of 2.5×10^5, which is slightly earlier than in experimental measurements. The asymmetries in the pressure distribution should be interpreted as the starting point of the drag crisis, with the transition to turbulence occurring earlier at one side of the cylinder boundary layer, whereas the other side is still laminar. Thus, separation in the turbulent side is delayed. Last but not the least, mean pressure distributions on the cylinder surface are computed showing a reasonable agreement with previous experimental results.

Acknowledgments This work has been financially supported by the Ministerio de Economía y Competitividad, Secretaría de Estado de Investigación, Desarrollo e Innovación, Spain (Ref. ENE2010-17801) and, by the Collaboration Project between Universitat Politècnica de Catalunya and Termo Fluids S.L. We acknowledge PRACE for awarding us access to resource MareNostrum III based in Barcelona, Spain. We also acknowledge the technical expertise, assistance and access to MareNostrum II provided by the Red Española de Supercomputación.

References

1. Achenbach, E.: Distribution of local pressure and skin friction around a circular cylinder in cross-flow up to Re=5e6. J. Fluid Mech. **34**, 625–639 (1968)
2. Bearman, P.: On vortex shedding from a circular cylinder in the critical Reynolds number regime. J. Fluid Mech. **37**, 577–585 (1969)
3. Bursnall, W., Loftin L.J.: Experimental investigation of the pressure distribution about a yawed circular cylinder in the critical Reynolds number range. Technical report NACA TN2463, NACA (1951)
4. Cantwell, B., Coles, D.: An experimental study of entrainment and transport in the turbulent near wake of a circular cylinder. J. Fluid Mech. **136**, 321–374 (1983)
5. Delany, N., Sorensen, N.: Low-speed drag of cylinders of various shapes. Technical report NACA TN3038, NACA (1953)
6. Hughes, T., Mazzei, L., Jansen, K.: Large eddy simulation and the variational multiscale method. Comput. Vis. Sci. **3**, 47–59 (2000)
7. Hunt, J., Wray, A., Moin, P.: Eddies, stream and convergence zones in turbulent flows. Technical report CTR-S88, Center for Turbulent Research (1988)
8. Lehmkuhl, O., Rodríguez, I., Baez, A., Oliva, A., Pérez-Segarra, C.: On the large-eddy simulations for the flow around aerodynamic profiles using unstructured grids. Comput. Fluids **84**, 176–189 (2013)
9. Nicoud, F., Ducros, F.: Subgrid-scale stress modelling based on the square of the velocity gradient tensor. Flow Turbul. Combust. **62**, 183–200 (1999)
10. Rodríguez, I., Borrell, R., Lehmkuhl, O., Pérez-Segarra, C., Oliva, A.: Direct numerical simulation of the flow over a sphere at Re = 3700. J. Fluid Mech. **679**, 263–287 (2011)

11. Roshko, A.: Experiments on the flow past a circular cylinder at very high Reynolds number. J. Fluid Mech. **10**(03), 345–356 (1961)
12. Schewe, G.: On the force fluctuations acting on a circular cylinder in crossflow from subcritical up to transcritical Reynolds numbers. J. Fluid Mech. **133**, 265–285 (1983)
13. Spitzer, R.: Measurements of unsteady pressures and wake fluctuations for flow over a cylinder at supercritical Reynolds number. Ph.D. thesis, California Institute of Technology (1964)
14. Vaz, G., Mabilat, C., van der Wal, R., Gallagher, P.: Viscous flow computations on a smooth cylinders: a detailed numerical study with validation. In: Proceedings of 26th International Conference on Offshore Mechanics and Arctic Engineering. OMAE2007, San Diego, California (2007)
15. Williamson, C.H.K.: Vortex dynamics in the cylinder wake. Annu. Rev. Fluid Mech. **28**(1), 477–539 (1996)

Large Eddy Simulation of Fluidic Injection into a Supersonic Convergent-Divergent Duct

B. Semlitsch, M. Mihăescu and L. Fuchs

1 Introduction

Convergent-divergent (C-D) ducts operating in supersonic flow-regimes provoke choked flow conditions in the region of the narrowest cross-section. The developed internal shocks can be unwanted for various reasons, e.g. the associate pressure losses [1]. Fluidic injection onto the exhaust of a gas turbine engine or internal fluidic injection in ducts or nozzles have been performed for various reasons, e.g. improvement of mixing, noise reduction, performance improvement, cooling, or thrust vectoring. The effect of injection was observed to depend highly on the location of injection, injection pressure, duct pressure, and inclination angle [2].

The present study investigates the behaviour of the shock-pattern inside a C-D duct, without and with fluidics. The effect of circumferential injection into the divergent part of the C-D duct is analysed. The main focus is on the transformability and the control of the shock-pattern in the duct and the disruption of the quasi-static shock-structure, with the purpose of decreasing the occurring losses in the duct.

2 Case Setup

Injection into the C-D duct is performed by using twelve cylindrical tubes of diameter D_i, equidistant spaced on the circumference of the duct. The geometry can be seen in Fig. 1. The injectors are assumed to be fed by a compressed airstream. The total

B. Semlitsch (✉) · M. Mihăescu · L. Fuchs
Linné Flow Center, KTH Mechanics, Osquars Backe 18, 10044 Stockholm, Sweden
e-mail: bernhard@mech.kth.se

M. Mihăescu
e-mail: mihai@mech.kth.se

L. Fuchs
e-mail: lf@mech.kth.se

J. Fröhlich et al. (eds.), *Direct and Large-Eddy Simulation IX*,
ERCOFTAC Series 20, DOI 10.1007/978-3-319-14448-1_37

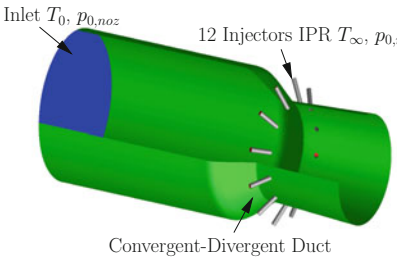

parameter	symbol	value	unit
duct exit diameter	D_e	57.5	mm
injectors diameter	D_i	2.67	mm
area ratio	$A_e/A^\star$	1.23	(-)
duct design Mach-number	M_e	1.56	(-)
ambient pressure	p_∞	101,325	Pa
ambient temperature	T_∞	288.15	K

Fig. 1 The investigated geometry and the initial parameters. The injectors are located −0.857 duct exit diameters (D_e) upstream from the duct exit, i.e. in the divergent part of the duct. The tubes are inclined 60° to the duct mid-axis, and the tubes are orientated into flow direction

temperature at the injector inlet $T_{0,i}$ was chosen to be the ambient temperature T_∞. Different tubing systems could potentially be used, but for simplicity a short injection-tube is considered. The injected flow is imposed in the direction of the injector-tubes axis, towards the centreline of the C-D duct. The tube is pressurised to a certain injection pressure ratio (IPR), defined as the injection total pressure divided by the ambient pressure.

The C-D duct is driven by a total pressure source acting at the inlet, which is four times larger than the ambient pressure p_∞ outside of the duct. At the duct inlet, the flow is assumed only in the axial direction and the total temperature $T_{0,n}$ is imposed at 367 K. The flowing media is air, where the isentropic exponent was assumed to be 1.4. Viscosity was modelled to be temperature dependent according to Sutherland's formula, where the standard coefficients where used.

3 Description of the Numerical Method

The simulations were performed with a finite volume code, solving the three-dimensional compressible Navier-Stokes equations. For the time integration, a four-stage Runge-Kutta scheme was applied. For the spatial discretisation a central difference scheme was used. A blend of second and fourth order differences are chosen to provide artificial dissipation to avoiding separation of solutions and numerical oscillations near sharp discontinuities like shocks.

Turbulence was handled by the Large Eddy Simulation (LES) approach. The turbulent small-grid scales were not modelled by any sub-grid scale (SGS) model in explicit form. The numerical dissipation acted implicitly as a SGS model.

The computational domain contains an inlet region, the investigation section, and the outer jet development region. The mesh is stretched by a factor of 1.06 to smooth out waves traveling against the flow direction. The inlet boundary is treated via a characteristic total pressure condition, where the flow is directed in the axial direction. The investigation section was designed as a fine equally cell-spaced section. The entire inner duct region (including injectors), incorporates a boundary-layer refined

mesh, since the walls were treated as adiabatic, no-slip surfaces. The wall region resulted in being very important to the flow solution. Hence, a solution without modelling of the compressible boundary-layer via wall-functions was preferred.

The further jet development after the duct exit is essentially a buffer layer for modelling outlet conditions at the duct exit plane. This region stretches fifteen duct exit diameters downstream, three duct exit diameters upstream, and five duct exit diameters to the side, measured from the duct exit. The mesh is designed in such a manner that the growth factors do not exceed a value of 1.06.

4 Results and Discussions

The investigated interval of injection pressure ratios is between 1 and 5.6. The losses in the duct section are assessed by exerting the thrust equation over the duct. The thrust was monitored within the simulations and is quantified in Fig. 2. The generated thrust can be increased by a few percent using fluidic injection.

Neither the thrust nor the variation of the thrust follow a straightforward pattern. However, the change of thrust or a change in thrust variance is an indication that the flow and shock structure are significantly changed in this range of IPRs. Hence, the individual flow-field needs to be analysed, to discover the reason for this behaviour.

Without injection, one general shock pattern occurs in the duct. For the IPR of 5.6, local stocks evolve in the vicinity of injection. However, only one general shock-pattern spans over the entire duct length. In the intermediate range two intersecting shock-pattern occur.

The *baseline* case, is defined as running the duct at the duct pressure ratio of 4 without injection. Hence, IPR is one. This case can be seen in Fig. 3, where the upper half shows the instantaneous Mach-numbers, while the lower half illustrates

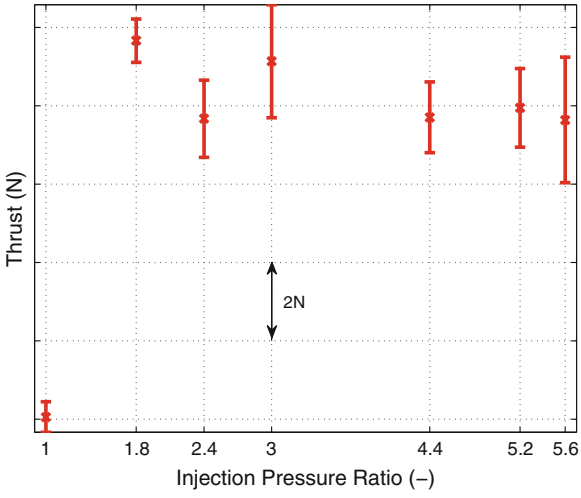

Fig. 2 The mean and the variance of the resulting thrust performance of the C-D duct is illustrated as a function of IPR. The thrust was computed including the pressure term and respecting the total demanded momentum in the injection tubes. Values were sampled at cut planes with a distance to the inlet boundaries. The fluctuations imposed by the fluidic injections lead to a variance in the generated thrust

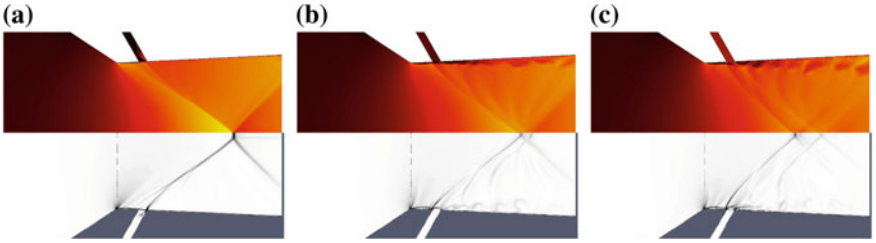

Fig. 3 **a** IPR 1.0, **b** IPR 1.8, **c** IPR 2.4

the density gradient. Inside of the duct, nearly inviscid conditions are present due to the large Reynolds number flow. Due to the damping effects of the compressible flow and the absence of turbulence, the variance in the generated thrust is low. However, a small separation bubble can be observed after the sharp transition passage and an expansion-fan establishes in the front of it at the smallest cross-section. Slightly downstream, at the middle of the separation bubble, a lambda shock forms one of its roots. Due to the sharp transition from the convergent section of the duct to the divergent section a shock pattern arises from this root.

The separation bubble stretches to the downstream located intersection of injection tube and the duct wall. The other lambda shock-root forms from this location, stronger than the one sitting on the separation bubble the branches of the shock-structure merge in the middle into a Mach-disk. From the Mach-disk a slip-line forms and the incident shock is reflected.

The shock-pattern occurring for the baseline case can be considered as static in the investigated section of the duct. Not any unsteady shock motion could be observed during the unsteady simulation.

By considering fluidics, at high injection pressure ratios IPR $\geq$ 2.4, the shock-pattern can be significantly altered compared to the baseline. The separation bubble occurring at the narrowest cross-section increases in its height with increasing IPR. For very low injection pressures, the injected flow creeps along the duct walls in the cross-stream, as it can be seen in Fig. 3b for an injection pressure ratio of 1.8. The vortical structures created due to injection are creeping along the nozzle walls, and do not cause turbulent fluctuations in this section. Even low injection pressure ratios cause a bow-shock in front of the injection, which replaces the lambda-shock roots observed at baseline. Several curved expansion-waves can be seen in the region between the first shock and its reflection. The shock-structure is not influenced drastically compared to the baseline case. The Mach-disk disappeared and a second weak shock-pattern becomes visible. The increase of IPR from 1.8 to 2.4 leads to a separation of the two shock-patterns (Fig. 3b, c). The reflection of the first shock-pattern becomes weaker and weaker with increased IPR. Also remarkable is that after a certain injection pressure ratio, the first reflected shock branch seams to disappear and does not cause any further shock-reflections.

The second downstream shock-pattern has the roots on the injected stream and the shock angles are, in the first occurring instances, almost equal with those from the first

upstream located shock. With increasing injection pressure the second downstream located shock becomes stronger and the upstream located shock-pattern gets weaker. The transition of the downstream shock-pattern becoming stronger than the upstream shock-pattern, occurs between an IPR of 2.5 and 2.7.

The static pressure distribution at the duct exit is increased with injection. Hence, due to the additional injected mass, the expansion rate is lower for the jet in the divergent section. As a result of that, the first shock changes its angle and becomes almost normal with increased IPR and finally reduces to a bow-shock in front of the injection, as illustrated in Fig. 4 showing the instantaneous Mach-number (above) and density gradient (below). It was also observed that, the second shock-pattern at high injection pressure ratios is quite static, although the shock feeding expansion waves show remarkable transient motion. The second shock-pattern provokes initially a regular reflection, while a Mach-reflection starts to occur at higher injection pressure ratios.

Between an IPR of 3.0 and 4.4 the injected flow chokes as leaving the injection tubes. Once the injected flow is choked, the generated vortical structures duet injection become less coherent and their shedding frequency increases in accordance with the fact that the structures are smaller in size. Figure 5a, b show a λ_2 visualisation of the flow structures occurring at an IPR of 3.0 and 4.4, respectively. The hairpin vortices persisting undisturbed for a longer time for the not-choked case of IPR 3.0, while for an IPR of 4.4 the structures evolve more chaotic. For the case of IPR 3.0, the larger structures and the lower shedding frequency most probably cause the increased thrust variation displayed in Fig. 2.

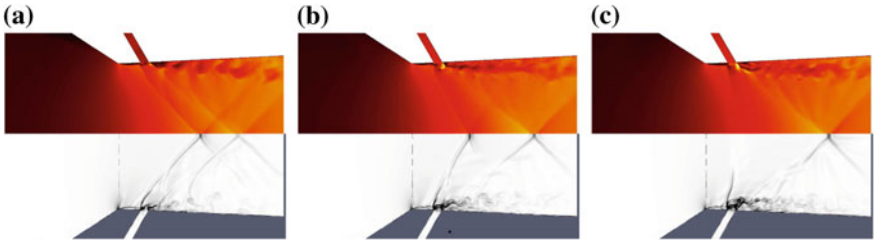

Fig. 4 **a** IPR 3.0, **b** IPR 4.4, **c** IPR 5.6

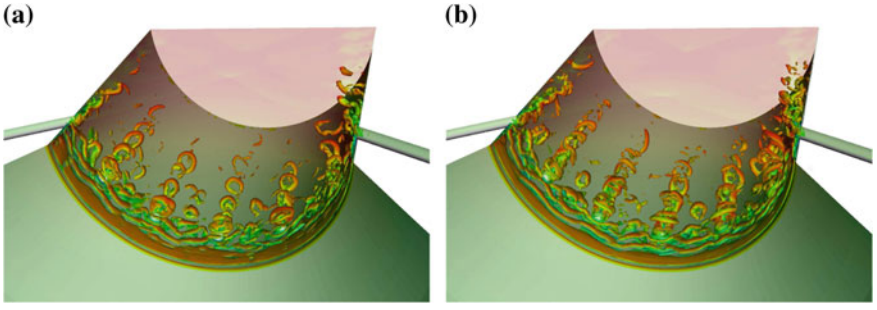

Fig. 5 **a** λ_2 visualisation at IPR 3.0, **b** λ_2 visualisation at IPR 4.4

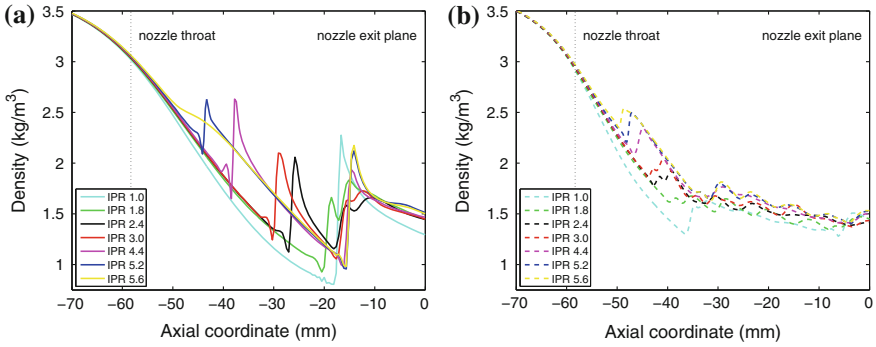

Fig. 6 **a** *Midline* Time-averaged density. **b** Time-averaged density at half radius

Supporting the observation for the thrust estimations, the losses provoked due to the shocks can be illustrated by the density plots along the centreline of the duct and along an axial and an axial line at half radius, (Fig. 6a, b). It can be observed that the shock strength is a minimum for the case of using injection at an IPR of 1.8.

5 Conclusions

LES simulations of fluidic injection, using twelve cylindric circumferential disposed tubes, into the divergent section of a supersonic C-D duct have been performed. The improvement of performance control by transforming the occurring shock-pattern has been assessed. A range of cases have been simulated, investigating the optimisation parameter injection pressure ratio.

The reduction of losses using fluidic injection have been exhibited by the means of density gradient and thrust penalty. The thrust generation could be increased by a few percent compared to the baseline. The occurring increased variance in several cases of the thrust estimations could be explained by the generated vortical structures in the flow and the shifting of the shock-systems.

Acknowledgments This work was supported by the Swedish National Infrastructure for Computing (SNIC 002-12-11) via PDC.

References

1. Munday, D., Gutmark, E., Liu, J., Kailasanath, K.: Flow structure and acoustics of supersonic jets from conical convergent-divergent nozzles. Phys. Fluids **23**, 116102 (2011)
2. Semlitsch, B., Mihăescu, M., Fuchs, L., Gutmark, E.: Numerical investigation of fluidic control on supersonic jet of a gas turbine engine. In: Proceedings of 20th International Shock Interaction Symposium, pp. 161–164 (2012)

Part VII
Compressible Flows

Simulation and Modeling of Turbulent Jet Noise

T. Colonius, A. Sinha, D. Rodríguez, A. Towne, J. Liu, G.A. Brès, D. Appelö and T. Hagstrom

1 Introduction

Jet noise reduction remains an important long-range goal in commercial and military aviation. Compared with their early counterparts, modern, ultrahigh-bypass-ratio turbofans on commercial aircraft are very quiet, but ever more stringent noise regulations dictate further reductions. In addition, hearing loss by personnel and community noise issues are prompting the military to seek noise reduction on future tactical aircraft. Further increase in bypass ratio not being a practical option, military applications in particular call for nuanced approaches to noise reduction including mixing devices like chevrons or even active noise control approaches using unsteady air injection. In this paper, we briefly review some recent developments in theoretical, experimental and computational approaches to understanding the sound radiated by large-scale, coherent structures in jet turbulence that might guide these noise reduction efforts.

T. Colonius (✉) · A. Sinha · D. Rodríguez · A. Towne · J. Liu
Mechanical Engineering, California Institute of Technology, Pasadena, CA, USA
e-mail: colonius@caltech.edu

G.A. Brès
Cascade Technologies Inc., Palo Alto, CA, USA
e-mail: gbres@cascadetechnologies.com

D. Appelö
Applied Mathematics, University of New Mexico, Albuquerque, NM, USA
e-mail: appelo@math.unm.edu

T. Hagstrom
Mathematics, Southern Methodist University, Dallas, TX, USA
e-mail: thagstrom@smu.edu

J. Fröhlich et al. (eds.), *Direct and Large-Eddy Simulation IX*,
ERCOFTAC Series 20, DOI 10.1007/978-3-319-14448-1_38

2 Wavepacket Models

We begin by discussing wavepackets–coherent but intermittent advecting disturbances that are correlated over distances far exceeding the integral scales of turbulence and that are, on one hand, related to fundamental low frequency instabilities (or more precisely amplified modes) of the turbulent mean flow field, and, on the other hand, directly correlated with the most intense (aft-angle), peak frequency sound radiation [1].

In particular, large eddy simulations (LES) and advanced experimental diagnostics are providing richer and higher fidelity data sets from which acoustically important motions can be educed and used to validate theories of noise emission from large-scale structures. In previous studies, we have shown in particular how the combined data from microphone arrays, time-resolved PIV data, and LES data sets have been used to validate reduced-order models for wavepackets in both subsonic [2, 3] and supersonic [4, 5] regimes. Figure 1 provides an example comparing supersonic wavepackets computed via the Parabolized Stability Equations (PSE) with those educed using proper orthogonal decomposition of LES data. Further details are presented in Ref. [6].

3 PSE and Beyond

In constructing reduced-order models to describe the evolution of wavepackets in turbulent jets, we have up to now relied on the linearized Parabolized Stability Equations (PSE) [7] to solve for disturbances to the (assumed known) mean turbulent flow. PSE is an *ad hoc* generalization of linear stability theory (LST) that captures the downstream evolution of wavepackets using a spatial marching technique in which initial perturbations are specified at the jet inlet and propagated downstream by integration of the PSE equations.

Despite their name, the PSE equations are not parabolic in the downstream direction due to the existence of upstream acoustic modes in the PSE operator [8]. These elliptic modes must be eliminated to prevent instability in the downstream march. PSE uses implicit Euler integration along with a *minimum* step size restriction to numerically damp these modes. This parabolization strategy allows a stable march, but has the unintended consequence of damping all of the Euler modes, not just the unstable upstream acoustic ones. In particular, the downstream acoustic modes are heavily damped, limiting PSEs ability to properly capture downstream acoustic radiation.

A new spatial parabolization technique has recently been developed [9] that explicitly removes the unstable upstream modes without damaging the downstream modes, resulting in a fully parabolic one-way Euler equation that can be stably marched without numerical damping. The upstream modes are removed using a recursive

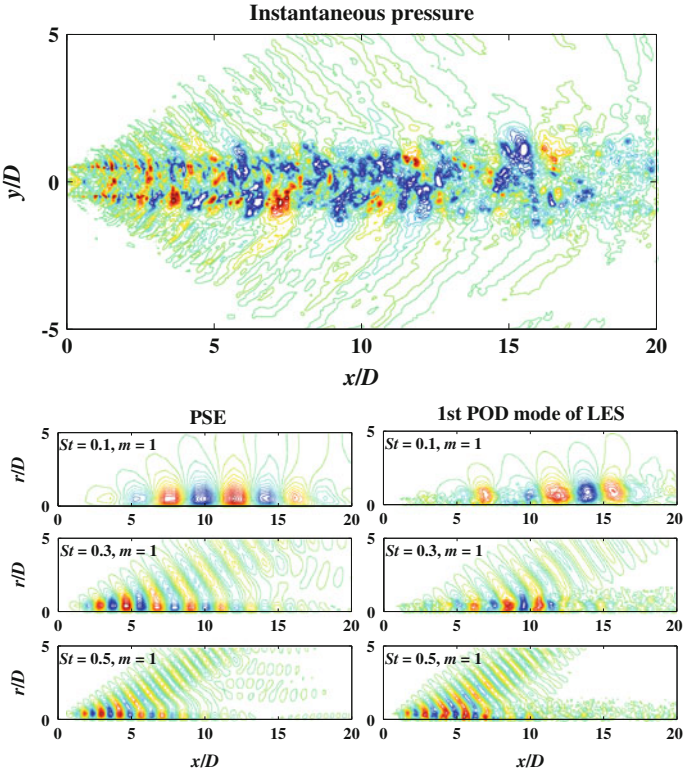

Fig. 1 *Top* instantaneous pressure contours in a plane through the nozzle exit from LES of a heated ($T_j/T_\infty = 1.74$), Mach 1.5 jet simulated with the unstructured grid compressible finite-volume solver "Charles" (see [4]). *Bottom* comparison of linear disturbances about the mean turbulent flow field computed with the PSE Ansatz to wavepackets educed from the LES data using the temporal and azimuthal Fourier transform and proper orthogonal decomposition (most energetic mode shown)

filtering technique that was originally developed for generating nonreflecting boundary conditions [10, 11]. Since the downstream acoustic modes are accurately retained, the one-way Euler equations are capable of accurately capturing downstream acoustic radiation.

This improvement over PSE is demonstrated by the results shown in Fig. 2. An LST Kelvin-Helmholtz eigenfunction is specified at the inlet of a mixing layer and propagated downstream by both PSE and the one-way Euler equations. Reasonable agreement is observed in the near-field, but the PSE solution contains little-to-no acoustic radiation while the one-way Euler solution includes a strong, directive acoustic field generated by the growth and decay of the near-field wavepacket. This method is currently being extended to turbulent jets and has the potential to provide significantly improved noise predictions, particularly for subsonic jets.

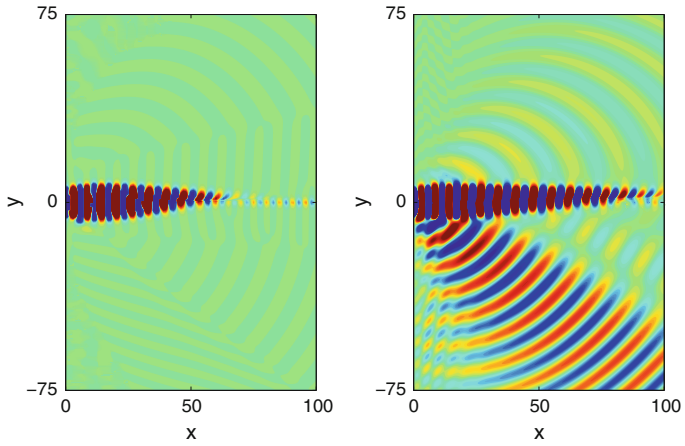

Fig. 2 Pressure field generated by a subsonic Kelvin-Helmholtz instability in a linearly spreading mixing layer with fast and slow stream Mach numbers of 0.8 and 0.2, respectively. Solution computed using **a** PSE and **b** the one-way Euler equation

4 Faster Computation

While reduced-order models are needed in the near term as surrogates for large, time-consuming simulations, in future LES will likely be used directly to provide function evaluations to formal optimization techniques. LES is being increasingly used to study jet noise in both academic and industrial settings. A range of technical issues such as numerical dispersion and dissipation, boundary conditions, extrapolation of acoustics to the far field, the inclusion of nozzle geometry and inlet disturbances, and the development of hybrid shock capturing schemes are but a few of the many technical challenges that must be resolved in obtaining high-fidelity predictions for the far acoustic field. The unstructured, locally adaptive, compressible flow solver "Charles" developed at Cascade Technologies, and used in the aforementioned wavepacket studies, leverages advances in these component algorithms to provide a unified approach towards best practices in jet noise simulation [4]. Like most modern CFD methods, Charles is designed and implemented using domain decomposition and Message Passing Interface (MPI) to exploit massively parallel, distributed memory environments.

For very large grids with $O(10^8)$ degrees of freedom, these algorithms can still achieve nearly perfect parallel scaling to $O(10^5)$ cores, but the Amdahl limit is a serious impediment to the efficiency of future jet noise computations on peta- and exa-flop machines, especially in the context of moderate-scale computations of about $O(10^7)$ grid points. Likewise, the so-called von Neumann bottleneck associated with widening speed gap between floating-point operations and memory fetches is driving research into methods that maximize the amount of operations conducted on the same data. We close this review by briefly highlighting progress on a class of methods

known as Hermite methods (see [12] and references therein), which can be designed to have very high computation-to-communication ratio.

Hermite methods are arbitrary-order polynomial-based general-purpose methods for solving time dependent PDE. In one dimension the degrees of freedom at a single grid point in a Hermite method can be thought of as the $m+1$ coefficients in a degree m polynomial centered at the grid point or, equivalently, the solution and the m first spatial derivatives at that grid point. In d-dimensions this generalizes to the $(m+1)^d$ coefficients in a centered tensor product polynomial or the solution and (mixed) derivatives in the d directions up to degree m.

Advancing the solution in time is a two stage procedure. First the unique degree $(2m+1)$ tensor product polynomial that interpolates the polynomials at the 2^d corners of a d-dimensional cuboid is constructed. This polynomial is centered at the midpoint of the cuboid and it also interpolates the solution and its derivatives at the corners of the cell, hence the name Hermite (interpolation) method. In the second stage the $(2m+2)^d$ coefficients of the Hermite interpolation polynomial are expanded in a temporal Taylor series. The coefficients in this Taylor series are found by applying a recursion relation derived by a Cauchy-Kowalewski procedure applied to the PDE at hand and the solution is advanced by evaluation the series at a later time. The procedure is repeated on the cell centered data to complete a full time step. For problems with smooth solutions this yields a method of order $2m+1$ in space and time.

For a linear PDE the main computational cost, $\mathcal{O}(m^d)$ per degree of freedom, is forming the Hermite interpolating polynomial while for a non-linear PDE with product non-linearities the main cost is computing the multiplication of degree $(2m+1)$ tensor product polynomials needed for the coefficients in the temporal Taylor series. This cost scales as $\mathcal{O}(m^{d+1})$ if a direct polynomial multiplication algorithm is used or $\mathcal{O}(m^d \log(m))$ if a FFT based algorithm is used.

One of the best features of the Hermite method, and central to our claim to have high computation to communication ratio, is that for a wave dominated problem (high Reynolds number) the time step is limited only by the wave speeds of the problem and not by the order of the method (as is the case for discontinuous Galerkin or classic spectral elements which have to take at least m times smaller time steps.) Thus, using a Hermite method for high Reynolds number flows yields an algorithm whose error scales like $\mathcal{O}(h^{(2m+1)})$ with a cost $\mathcal{O}(m^d \log(m))$ per degree of freedom to advance the solution one time step and with a need to communicate at least m times less frequently than other polynomial spectral methods. The locality of the method is highly useful for efficient parallel implementation as well as tackling the von Neumann bottleneck.

References

1. Jordan, P., Colonius, T.: Wave packets and turbulent jet noise. Annu. Rev. Fluid Mech. **45**, 173–195 (2013)
2. Cavalieri, A.V.G., Jordan, P., Colonius, T., Gervais, Y.: Wavepackets in the velocity field of turbulent jets. AIAA Paper 2012–2115 (2012)

3. Gudmundsson, K., Colonius, T.: Instability wave models for the near field fluctuations of turbulent jets. J. Fluid Mech. **689**, 97–128 (2011)
4. Brès, G.A., Nichols, J.W., Lele, S.K., Ham, F.E.: Towards best practices for jet noise predictions with unstructured large eddy simulations. AIAA Paper 2012–2965 (2012)
5. Rodríguez, D., Sinha, A., Brès, G.A., Colonius, T.: Parabolized stability equation models in turbulent supersonic jets. AIAA Paper 2012–2117 (2012)
6. Rodríguez, D., Sinha, A., Brès, G.A., Colonius, T.: Acoustic field associated with parabolized stability equation models in turbulent jets. AIAA Paper 2013–2279 (2013)
7. Herbert, T.: Parabolized stability equations. Annu. Rev. Fluid Mech. **29**, 245–283 (1997)
8. Li, F., Malik, M.R.: On the nature of pse approximation. Theor. Comput. Fluid Dyn. **8**, 253–273 (1996)
9. Towne, A., Colonius, T.: Improved parabolization of the euler equations. AIAA Paper 2013–2171 (2013)
10. Givoli, D., Neta, B.: High-order nonreflecting boundary scheme for time- dependent waves. J. Comput. Phys. **186**, 24–46 (2003)
11. Hagstrom, T., Warburton, T.: A new auxiliary variable formulation of high-order local radiation boundary conditions: corner compatibility conditions and extensions to first-order systems. Wave Motion **39**, 890–901 (2004)
12. Appelö, D., Inkman, M., Hagstrom, T., Colonius, T.: Hermite methods for aeroacoustics: Recent progress. AIAA Paper 2011–2757 (2011)

Mach Number Influence on Vortex Breakdown in Compressible, Subsonic Swirling Nozzle-Jet Flows

Tobias Luginsland and Leonhard Kleiser

1 Introduction

The phenomenon of vortex breakdown is observed in a variety of technical (vortex burners, delta wing aircraft) and environmental flows (tornadoes, hurricanes). A field of ongoing research is vortex breakdown in swirling jet flows. For a sufficiently high ratio of the circumferential to the stream wise velocity vortex breakdown occurs. Its flow field is characterised by a strong recirculation in the centreline region of the swirling jet. Helical instabilities of co-rotating, counter-winding type dominate the flow field. A conical vortex breakdown configuration develops with a high radial spreading rate and enhanced mixing and entrainment.

In the present contribution, we study the effects of a Mach number variation on vortex breakdown of swirling nozzle-jet flows in the compressible, subsonic regime.

2 Numerical Framework

We numerically investigate vortex breakdown by means of Large-Eddy Simulations (LES) utilising the simulation code PARACONCYL, which solves the Navier-Stokes equations on a cylindrical grid using high-order schemes in space [1] and time [2], see [3] for details. The governing equations are non-dimensionalized by the nozzle inner radius R and centreline quantities at inflow, indicated by the subscript $()_c$. For modelling the subgrid scales, we use the approximate deconvolution model in the simplified relaxation-term formulation (ADM-RT) with the model parameter set to

T. Luginsland (✉) · L. Kleiser
Institute of Fluid Dynamics, ETH Zurich, 8092 Zurich, Switzerland
e-mail: luginsland@ifd.mavt.ethz.ch

L. Kleiser
e-mail: kleiser@ifd.mavt.ethz.ch

J. Fröhlich et al. (eds.), *Direct and Large-Eddy Simulation IX*,
ERCOFTAC Series 20, DOI 10.1007/978-3-319-14448-1_39

$\chi = 1/\Delta t$ [4]. A rotating nozzle is included in our computational domain, modelled as an isothermal wall, to account for a more realistic setup [5]. The nozzle length is $L/R = 5$ and the nozzle wall thickness $d = (R_o - R)/R = 0.1$, where R_o denotes the outer nozzle radius. The simulation code has been used in previous jet flow investigations and has been validated extensively (cf. [5, 6] and references therein). At the inflow and outflow, the three velocities as well as pressure and density are set using non-reflecting boundary conditions supplemented with sponge-layers. In the far-field, only pressure and density are prescribed.

The Reynolds number is set to $Re = \rho_c w_c R/\mu_c = 5,000$, the Mach number is varied in the range $0.4 \leq Ma = w_c/\sqrt{\gamma R_{air} T_c} \leq 0.8$, where w denotes the streamwise velocity, ρ the density, μ the dynamic viscosity, $\gamma = 1.4$ the ratio of specific heats, $R_{air} = 287.15\,\text{J/kg/K}$ the gas constant of air and T denotes the temperature, as in [6]. r, θ and z denote the radial, azimuthal and streamwise coordinate directions, respectively. We define the integral swirl number S_{int} according to [7], which leads to an initial swirl number of $S_{int} = 0.75$ at $Ma = 0.6$ (reference case), which is above the threshold for vortex breakdown [5]. The streamwise velocity component at the inflow plane ($z/R = -5$) is defined as $w = 1 - r^7$ for $r \leq R$ and $w = 0$ elsewhere, the azimuthal velocity component is $v = r$ for $r \leq R_o$ (solid-body rotation) and vanishes outside the nozzle. The radial velocity component u is identically zero initially. The pressure p and density ρ are derived following [6] using the equation of state, $\gamma Ma^2 p = \rho T$.

The simulations were run with a grid resolution of $N_r \times N_\theta \times N_z = 288 \times 128 \times 288$ on a domain of size $L_r \times L_\theta \times L_z = 10R \times 2\pi \times 20R$. The time-step was set to $\Delta t = 0.004$. The simulations were performed on 256 cores in parallel on a CRAY XE6.

3 Results and Discussion

Figure 1 displays the three $\langle t, \theta \rangle$-averaged velocity components at subsequent downstream locations. For a small Mach number $Ma = 0.4$, vortex breakdown is suppressed, while for increasing Mach numbers the intensity of the vortex breakdown is enhanced. The streamwise as well as the azimuthal velocity components deviate from their initial distribution in the downstream part of the nozzle due to the vortex breakdown downstream of the nozzle end and its upstream effect on the nozzle flow. The larger the Mach number, the stronger the deviation. The nozzle flow is laminar, which is indicated by the solid-body rotation profile of the azimuthal velocity component. Downstream of the nozzle end, the velocity maxima are shifted radially outwards due to the vortex breakdown configuration and the developing conical shear-layers. The radial velocity component increases in the nozzle end section indicating high spreading rates of the swirling jets. It increases with Mach number for $Ma \leq 0.6$ and decreases again for higher Mach numbers. Further downstream at $z/R = 3$, the radial velocity component is negative as fluid is entrained into the swirling jet.

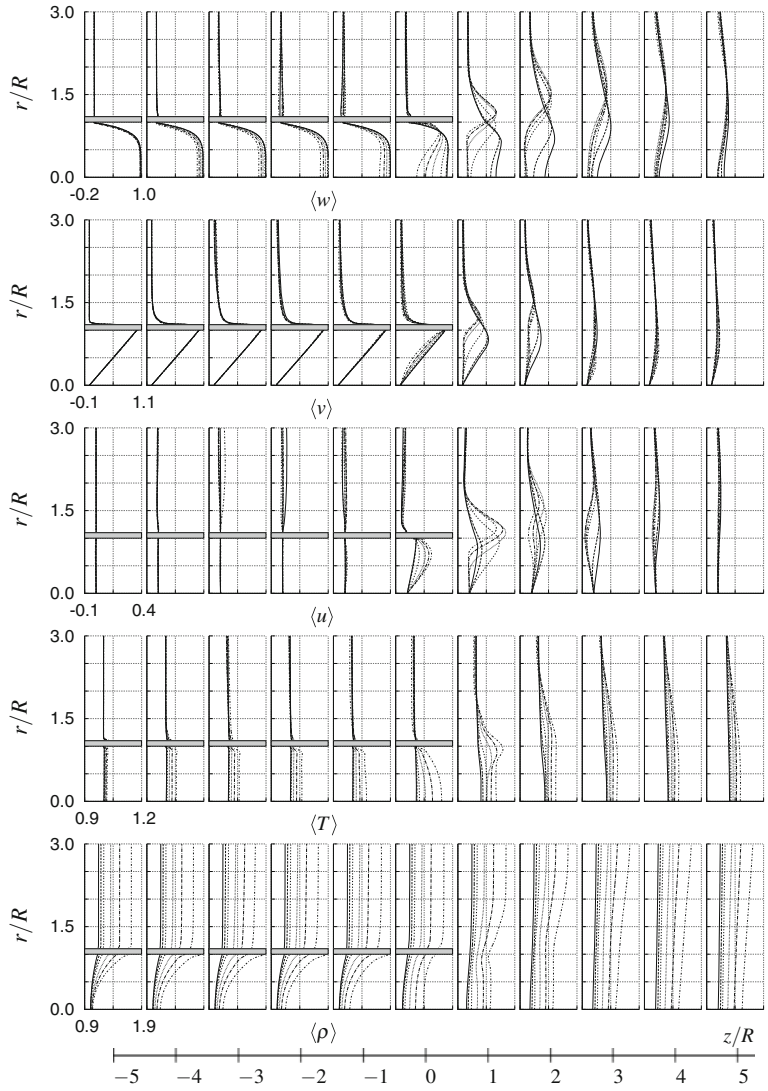

Fig. 1 Development of $\langle t, \theta \rangle$-averaged streamwise, azimuthal and radial velocity, temperature and density (*top* to *bottom*) at axial positions $z/R = -5, \ldots, 5$. The *grey bar* indicates the position of the nozzle wall. $Ma = 0.4$ (*solid*), $Ma = 0.45$ (*dashed*), $Ma = 0.5$ (*dotted*), $Ma = 0.6$ (*fine-dotted*), $Ma = 0.7$ (*dash-dotted*), $Ma = 0.8$ (*fine-dash-dotted*)

The $\langle t, \theta \rangle$-averaged temperature and density are also shown in Fig. 1. For high Mach numbers, the temperature within the nozzle increases in the downstream direction with a maximum in the end section of the nozzle. The ratio of the far-field temperature to the centreline temperature T_∞ / T_c decreases for increasing Mach number.

The temperature increase is mainly due to the growth of the recirculation region (see Fig. 4) and the induced deceleration of the flow. Behind the nozzle lip, the radial maximum is located within the inner shear-layer of the conical vortex breakdown (if observed). Further downstream, the temperature slowly converges to a uniform profile.

For all values of the Mach number, the density at the centreline is identically 1 initially.It increases by definition more strongly in the radial direction for increasing Mach number leading to a higher ratio of the far-field to centreline density ρ_∞/ρ_c in the nozzle flow regime. Downstream of the nozzle, the density converges towards the far-field value in the downstream direction.

Lesshafft and Huerre [8] showed theoretically that for heated round jets an increased jet-to-ambient temperature ratio promotes absolute instability. Additionally, the authors showed that an increase of Mach number prevents absolute instability. Results by [9] revealed that hot jets are generically more unstable than light jets (positive radial density gradient) and that a low jet density compared to the far-field density may promote absolute instability. Since it is believed that the existence of a sufficiently large pocket of absolute instability in the wake of the recirculation region is a requirement for vortex breakdown to occur [10] and for the onset of global instabilities, we draw the following conclusion from the observations made here: the stabilizing effect due to an increased Mach number (as also reported in [11]) is counter-acted by the increase in jet-to-ambient temperature ratio. This leads to a destabilisation of the swirling jet, a promotion of absolute instability and therefore to a promotion of vortex breakdown. For increasing Mach number the jet-to-ambient density ratio decreases leading additionally to a destabilising effect and a promotion of absolute instability.

The $\langle t, \theta \rangle$-averaged centreline streamwise velocity is depicted in Fig. 2. The larger the Mach number the stronger the velocity decrease in the downstream direction along the centreline. The deceleration in the nozzle end section is more pronounced for increasing Mach numbers. Vortex breakdown is observed for $Ma \geq 0.45$. The overall strongest backflow is found for $Ma = 0.5$.

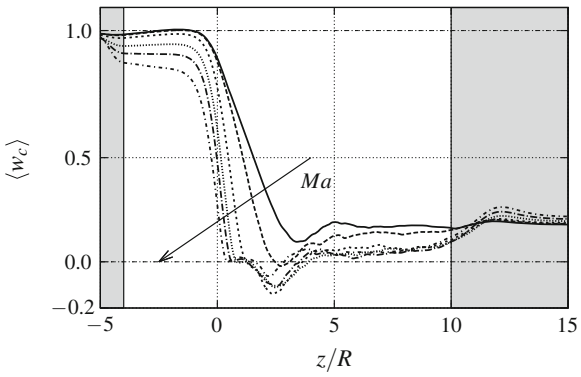

Fig. 2 $\langle t, \theta \rangle$-averaged streamwise velocity at centreline. Regions where sponges act on the flow field are shaded in *grey*. For colour code see Fig. 1

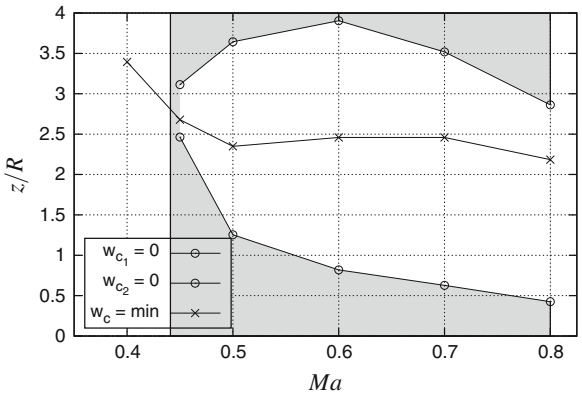

Fig. 3 Length of the $\langle t, \theta \rangle$-averaged recirculation region between first and second stagnation point on the jet centreline. The *grey-shaded* area indicates the parameter regime of stable vortex breakdown ($Ma \geq 0.44$). The enclosed white area indicates the zone of recirculation ($\langle w_c \rangle \leq 0$), and $\langle w_c \rangle =$ min the location at which $\langle w_c(z) \rangle$ is a minimum

No recirculation along the centreline is observed at all for Mach number Ma=0.4, see Fig. 3. For increasing Mach number, the first mean flow stagnation point at the centreline of the swirling jet moves upstream. The recirculation zone grows in radial and streamwise extent for $0.45 \leq Ma \leq 0.6$ and becomes smaller again for higher Mach number due to the upstream-moving second stagnation point which marks the end of the recirculation zone. Its upstream motion can be explained by the growth of the secondary vortical structure within the recirculation region (Fig. 4), which grows for increasing Mach number, thereby intensifying the positive streamwise centreline velocity induced. The described trend is visible in the results discussed above, leading to a decreasing radial velocity component behind the nozzle lip, a larger minimum centreline streamwise velocity and a smaller recirculation zone. The position of minimum centreline streamwise velocity $\langle w_c(z) \rangle =$ min is shifted in the downstream direction to the leeward part of the breakdown zone for increasing Mach number.

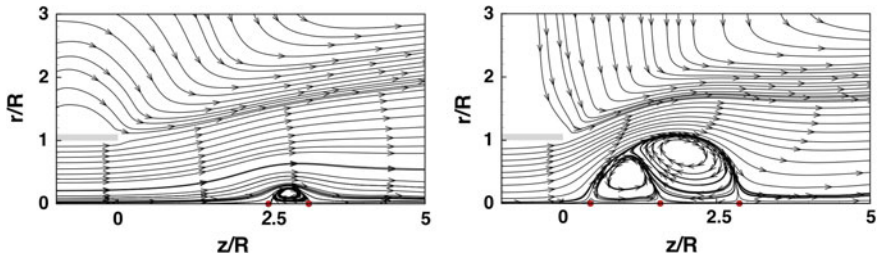

Fig. 4 Streamlines of the $\langle t, \theta \rangle$-averaged flow field for $Ma = 0.45$ (*left*) and $Ma = 0.8$ (*right*). The *grey bar* indicates the nozzle wall and the *circles* the stagnation points at the jet centreline

4 Summary and Conclusions

We investigated the influence of the Mach number on vortex breakdown in swirling nozzle-jet flows in the range $0.4 \leq Ma \leq 0.8$. We observe that vortex breakdown is enhanced for high subsonic Mach numbers, while below $Ma = 0.44$ (linearly interpolated) it is completely suppressed. The critical amount of swirl sufficient for vortex breakdown to occur increases with decreasing Mach number, a finding in contradiction to [11] and in accordance with [12]. As pointed out in [12], an increased Mach number promotes vortex breakdown when the expansion rate $p_c/p_\infty = \text{const.}$ of the swirling jet is held fixed (as it is the case here). An increased jet core temperature comes along with an increasing Mach number in our investigation leading to the promotion of absolute instability [8] and therefore to an intensification of vortex breakdown.

Overall, the results of our study of Mach number effects on the vortex breakdown behaviour of compressible, subsonic swirling jets are largely in agreement with results reported in literature. The modulation of density and temperature is the main reason for the observed changes for increasing Mach number in the vortex breakdown behaviour of the swirling jets.

Acknowledgments The present work was funded by an ETH research grant ETH-18 08-1 and supported by a grant from the Swiss National Supercomputing Centre (CSCS), Lugano, under project ID s52. We thank M. Gloor for comments on a draft of this paper.

References

1. Lele, S.K.: Compact finite difference schemes with spectral-like resolution. J. Comp. Phys. **103**(1), 16–42 (1992)
2. Berland, J., Bogey, C., Bailly, C.: Low-dissipation and low-dispersion fourth-order runge-kutta algorithm. Comput. Fluids **35**, 1459–1463 (2006)
3. Müller, S. B.: Numerical investigations of compressible turbulent swirling jet flows. Doctoral Thesis, ETH Zurich (2007)
4. Schlatter, P., Stolz, S., Kleiser, L.: Analysis of the SGS energy budget for deconvolution-and relaxation-based models in channel flow. In: Lamballais, E., Friedrich, R., Geurts, B.J., Métais, O. (eds.) Direct and Large-Eddy Simulation VI, pp. 135–142. Springer, Heidelberg (2006)
5. Luginsland, T.: Numerical investigation of compressible, turbulent vortex breakdown in swirling jet flows, Doctoral Thesis, ETH Zurich (2013), in preparation.
6. Müller, S.B., Kleiser, L.: Large-eddy simulation of vortex breakdown in compressible swirling jet flow. Comput. Fluids **37**(7), 844–856 (2008)
7. Chervinsky, A., Chigier, N.: Experimental and theoretical study of turbulent swirling jets issuing from a round orifice. Isr. J. Technol. **4**, 44–54 (1965)
8. Lesshafft, L., Huerre, P.: Linear impulse response in hot round jets. Phys. Fluids **19**, 024102 (2007)
9. Coenen, W., Sevilla, A.: The structure of the absolutely unstable regions in the near field of low-density jets. J. Fluid Mech. **713**, 123–149 (2012)

10. Liang, H., Maxworthy, T.: An experimental investigation of swirling jets. J. Fluid Mech. **525**, 115–159 (2005)
11. Rusak, Z., Lee, J.H.: On the stability of a compressible axisymmetric rotating flow in a pipe. J. Fluid Mech. **501**, 25–42 (2004)
12. Melville, R.: The role of compressibility in free vortex breakdown. AIAA Paper **96–2075**, 1–16 (1996)

A Symmetry-Preserving Discretization and Regularization Subgrid Model for Compressible Turbulent Flow

W. Rozema, R.W.C.P. Verstappen, J.C. Kok and A.E.P. Veldman

1 Introduction

The Navier-Stokes equations for compressible flow can be expressed in different forms. Although the forms are mathematically equivalent, each form emphasizes different properties of compressible flow, and each form yields a different numerical discretization.

This paper introduces a new form of the compressible Navier-Stokes equations. This form expresses conservation properties in terms of inner products and differential operator symmetries. This allows for the straightforward derivation of a symmetry-preserving discretization [1] and a symmetry-preserving regularization [2] for compressible flow. These methods preserve conservation properties on the discrete level, and are stable without artificial dissipation. The proposed symmetry-preserving methods are validated in a simulation of compressible channel flow.

W. Rozema (✉) · J.C. Kok
National Aerospace Laboratory (NLR), Anthony Fokkerweg 2,
1059 CM Amsterdam, The Netherlands
e-mail: wybe.rozema@nlr.nl

J.C. Kok
e-mail: johan.kok@nlr.nl

R.W.C.P. Verstappen · A.E.P. Veldman
Johann Bernoulli Institute for Mathematics and Computer Science,
University of Groningen, 407, 9700 AKGroningen, The Netherlands
e-mail: r.w.c.p.verstappen@rug.nl

A.E.P. Veldman
e-mail: a.e.p.veldman@rug.nl

J. Fröhlich et al. (eds.), *Direct and Large-Eddy Simulation IX*,
ERCOFTAC Series 20, DOI 10.1007/978-3-319-14448-1_40

2 A New Form of the Compressible Navier-Stokes Equations

In this section a new form of the compressible Navier-Stokes equations is proposed. It is shown that this form naturally expresses conservation properties in the language of functional analysis. Also an energy bound for compressible flow is identified.

The compressible fluid is assumed to occupy a periodic domain Ω. In this paper, the state of the compressible fluid is given by the real-valued vector function

$$\mathbf{h}(\mathbf{x}) = (\sqrt{\rho}, \sqrt{\rho}\mathbf{u}/\sqrt{2}, \sqrt{\rho e})(\mathbf{x})$$

where ρ is the mass density, $\mathbf{u} = (u, v, w)$ the flow velocity, and e the internal energy per unit mass. A new form of the compressible Navier-Stokes equations is obtained by deriving the evolution equation for $\mathbf{h}$

$$\partial_t \mathbf{h} = A(\mathbf{h})\mathbf{h} = (C(\mathbf{h}) + P(\mathbf{h}) + V(\mathbf{h}) + H(\mathbf{h}))\,\mathbf{h} \tag{1}$$

where the non-linear differential operators $C(\mathbf{h})$, $P(\mathbf{h})$, $V(\mathbf{h})$, and $H(\mathbf{h})$ are terms related to respectively convection, pressure forces, viscous friction, and heat diffusion.

Consider the Hilbert spaces $L^2(\Omega)$ and $L^2(\Omega)^5$ of real-valued square-integrable scalar and state vector functions on Ω. The standard inner products are

$$(f, g) = \int_\Omega fg \,\mathrm{d}x \quad \text{and} \quad \langle \mathbf{f}, \mathbf{g} \rangle = \int_\Omega \mathbf{f} \cdot \mathbf{g} \,\mathrm{d}x \;,$$

and the induced norms are denoted $|h|$ and $||\mathbf{h}||$. The mass, momentum, kinetic energy, and internal energy inside Ω can be expressed as $L^2(\Omega)$ inner products of the components of $\mathbf{h}$; for example $(\sqrt{\rho}, \sqrt{\rho})$ is the mass inside Ω, and $\sqrt{2}(\sqrt{\rho}, \sqrt{\rho}w/\sqrt{2})$ is the momentum in the z-direction inside Ω.

Desired solutions of the compressible Navier-Stokes equations conserve the mass, momentum, and total energy inside Ω. Conservation of mass and energy induces the bound $||\mathbf{h}||^2 = \text{constant}$, because

$$\partial_t ||\mathbf{h}||^2 = \partial_t \langle \mathbf{h}, \mathbf{h} \rangle = \partial_t \int_\Omega \rho \,\mathrm{d}x + \partial_t \int_\Omega \rho \left(\frac{1}{2}\mathbf{u} \cdot \mathbf{u} + e \right) \mathrm{d}x = 0 \tag{2}$$

and therefore $\mathbf{h}$ is in $L^2(\Omega)^5$. The bound induces a property of the right-hand-side of the evolution Eq. (1)

$$\langle \mathbf{h}, A(\mathbf{h})\mathbf{h} \rangle = \langle \mathbf{h}, \partial_t \mathbf{h} \rangle = \frac{1}{2} \partial_t \langle \mathbf{h}, \mathbf{h} \rangle = \frac{1}{2} \partial_t ||\mathbf{h}||^2 = 0 \,. \tag{3}$$

In the sequel, the bound (2) and the induced equality (3) will provide numerical stability to the symmetry-preserving discretization and regularization.

The mass, momentum, kinetic energy, and internal energy inside Ω can be expressed as inner products of the components of $\mathbf{h}$. Therefore, the conservation properties of a differential operator depend on its interaction with inner products. To see this, consider the convection operator $C(\mathbf{h})$. Each component of the convection operator can be expressed as the scalar convection operator

$$c(\mathbf{u})\phi = -\frac{1}{2}\mathbf{u}\cdot\nabla\phi - \frac{1}{2}\nabla\cdot(\mathbf{u}\phi) = \frac{1}{2}(\nabla\cdot\mathbf{u})\phi - \nabla\cdot(\mathbf{u}\phi)\,. \tag{4}$$

An important property of the scalar convection operator is its skew-symmetry with respect to the $L^2(\Omega)$ inner product: $(\psi, c(\mathbf{u})\phi) = -(c(\mathbf{u})\psi, \phi)$. Because the i-th component of the evolution equation (1) is $\partial_t h_i = c(\mathbf{u})h_i + \cdots$, for each h_i and h_j

$$\partial_t(h_i, h_j) = (c(\mathbf{u})h_i, h_j) + (h_i, c(\mathbf{u})h_j) + \cdots = 0 + \cdots \quad .$$

Thus because $c(\mathbf{u})$ is skew-symmetric, convection conserves inner products of the components of $\mathbf{h}$. Therefore convection conserves the mass, momentum, kinetic energy, and internal energy inside Ω. In the sequel, the symmetry-preserving discretization will preserve the skew-symmetric nature of convection, so that convection also conserves mass, momentum, internal energy, and kinetic energy on the discrete level.

3 Symmetry-Preserving Discretization

In the previous section, it was shown that conservation properties can be expressed in terms of inner products and differential operator symmetries. In order to express discrete conservation properties in a similar notation, the numerical solution is stored as a collocated grid function $\mathbf{h}$, and discrete inner products are defined as

$$(f, g) = \sum_j \Omega_j f_j g_j \quad \text{and} \quad \langle \mathbf{f}, \mathbf{g}\rangle = \sum_j \Omega_j \mathbf{f}_j \cdot \mathbf{g}_j \ ,$$

where Ω_j is the volume the of grid cell j. The induced discrete norms are denoted $|h|$ and $||\mathbf{h}||$. A real-valued numerical solution $\mathbf{h}$ is locally bounded if its norm $||\mathbf{h}||$ is bounded from above. The aim of a symmetry-preserving discretization is to apply the continuous bound (2) to numerical solutions by preserving conservation laws on the discrete level, so that numerical stability is attained for a physical reason.

More specifically, here a spatial discretization of the compressible Navier-Stokes equations is called symmetry-preserving if equality (3) holds on the discrete level, and if the conservation properties of mass, momentum, kinetic energy, and internal energy of each differential operator from (1) are preserved on the discrete

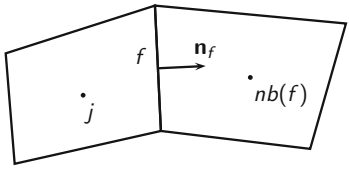

Fig. 1 The grid cell j. The outward-pointing unit normal at face f is denoted $\mathbf{n}_f$ and the neighbour at face f is denoted $nb(f)$

level. Discretizations with these conservation properties already exist [3, 4]. These discretizations are not derived from the form (1), and do not derive all the conservation properties of convection from a skew-symmetry.

The scalar convection operator (4) is discretized on a curvilinear collocated grid (see Fig. 1) as a skew-symmetric discrete operator

$$(c(\mathbf{u})\phi)_j = \frac{1}{2}\phi_j \frac{1}{\Omega_j} \sum_{f \in F_j} A_f \mathbf{n}_f \cdot \mathbf{u}_f - \frac{1}{\Omega_j} \sum_{f \in F_j} A_f \mathbf{n}_f \cdot \mathbf{u}_f \frac{1}{2} \left(\phi_j + \phi_{nb(f)}\right) \quad (5)$$

where F_j are the faces of cell j, Ω_j the volume of cell j, A_f the area of face f, and $\mathbf{u}_f$ some interpolation of $\mathbf{u}$ to face f. Because this discretization is skew-symmetric with respect to the discrete $L^2(\Omega)$ inner product, mass, momentum, kinetic energy, and internal energy are conserved by discrete convection. Therefore, unlike a general finite-volume discretization, the discrete scalar convection operator does not unphysically exchange kinetic and internal energy. The velocity interpolation used in this paper is $\mathbf{u}_f = \frac{1}{2}(\mathbf{u}_j + \mathbf{u}_{nb(f)})$.

The pressure force operator is discretized as in [3], and the discretization of the terms related to the viscous friction and heat diffusion is derived from a finite-volume discretization. The resulting second-order accurate discretization is used as the starting point for a Richardson extrapolation procedure [3]. The result is a fourth-order accurate, optimized, symmetry-preserving spatial discretization.

A Runge-Kutta method is used to integrate the semi-discrete system $\partial_t \mathbf{h}_j = (A(\mathbf{h})\mathbf{h})_j$. The total mass, momentum, kinetic energy, and internal energy inside Ω, and the stability bound (2) can be expressed as inner products of the components of $\mathbf{h}$. Therefore, a Runge-Kutta method that preserves these inner products is symmetry-preserving. Such a Runge-Kutta methods is called symplectic [5].

The use of symplectic methods is outside the scope of this paper. Instead, an explicit, four-stage, low-storage Runge-Kutta method is used for time integration.

4 Symmetry-Preserving Regularization

A promising subgrid-scale model for incompressible flow is the symmetry-preserving regularization [2]. This regularization applies explicit filtering to the convection operator in order to suppress the creation of subgrid scales, but preserves the skew-symmetric nature of convection. The symmetry-preserving regularization does not dissipate kinetic energy, contrary to most subgrid-scale models.

A symmetry-preserving regularization of the skew-symmetric compressible convection operator can be obtained by replacing the scalar convection operator (4) by one of

$$c_2(\mathbf{u})\phi = \overline{c(\overline{\mathbf{u}})\overline{\phi}} \tag{6}$$

$$c_4(\mathbf{u})\phi = c(\overline{\mathbf{u}})\overline{\phi} + \overline{c(\overline{\mathbf{u}})\phi'} + \overline{c(\mathbf{u}')\overline{\phi}} \tag{7}$$

where $\phi' = \phi - \overline{\phi}$ and the filter is self-adjoint $(\overline{\phi}, \psi) = (\phi, \overline{\psi})$. These filtered approximations of the convection operator are skew-symmetric by the self-adjointness of the filter, and are respectively second-order and fourth-order accurate with respect to the filter length [2].

In this paper a self-adjoint differential filter $\overline{\phi} = \phi + \sum_{i=1}^{3} \partial_i (\frac{\Delta_i^2}{24} \partial_i \phi)$ is used. As a first try, the filter length is set proportional to the local mesh spacing; $\Delta_i = r\Delta x_i$. In this paper r is set equal to 1, so that $\Delta_i = \Delta x_i$. The filter is discretized as a self-adjoint discrete operator

$$\overline{\phi}_j = \phi_j + \frac{1}{\Omega_j} \sum_f \frac{r^2}{24} A_f \mathbf{n}_f \cdot (\mathbf{x}_{nb(f)} - \mathbf{x}_j)(\phi_{nb(f)} - \phi_j)$$

where $\mathbf{x}_j$ is the location of the center of cell j. By the self-adjointness of this discretization, the skew-symmetry of the regularizations of the convection operator is preserved on the discrete level.

5 Results and Discussion

To validate the proposed symmetry-preserving discretization and regularization, simulations of a compressible channel flow at Mach 0.2 are performed. The dimensions of the channel are $4\pi H \times 2H \times 2\pi H$. The flow is driven by a uniform body force per unit mass. The bulk Reynolds number is fixed at 2,800, corresponding to a wall Reynolds number of approximately 178 [6].

The computational grid is rectangular. The grid is stretched in the wall-normal direction with a stretching parameter γ, as in [1]. Table 1 lists the computational grids used in this paper. For each grid, the time-step size is chosen so that the Courant number based on the speed of sound is approximately 1.

Table 1 The computational grids and the wall Reynolds numbers obtained without regularization

Grid	Dimensions	γ	$\Delta y^+_{\min}$	Δt	Re_τ
A	$256 \times 128 \times 128$	7.0	0.6	6.6×10^{-4}	178.7
B	$128 \times 64 \times 64$	7.0	1.2	1.3×10^{-3}	179.3
C	$32 \times 32 \times 32$	6.0	3.4	2.5×10^{-3}	182.3

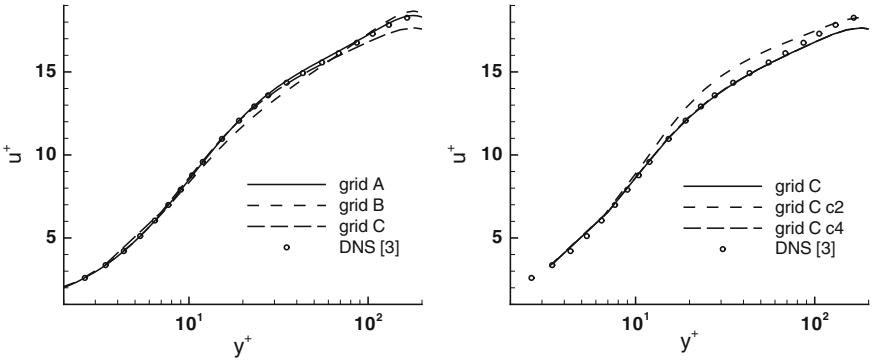

Fig. 2 Mean streamwise flow velocity obtained without (*left*) and with (*right*) regularization. The c_4 regularization results collapse on the results obtained without regularization

The simulations are stable without artificial dissipation. Figure 2 shows the obtained mean streamwise velocity profiles. The results obtained on grid A accurately coincide with an incompressible DNS [6]. The high accuracy and the absence of artificial dissipation make the symmetry-preserving discretization a very suitable method for direct numerical simulation of compressible flow.

The symmetry-preserving discretization for incompressible flow accurately captures channel flow without a subgrid-scale model already on very coarse grids [1]. The results obtained on the coarse grids B and C indicate that this property is not inherited by the symmetry-preserving discretization for compressible flow. The wall Reynolds numbers obtained on the grids B and C are satisfactory (see Table 1), but the slope in the log layer is not captured correctly. This suggests that on the grids B and C an explicit subgrid-scale model should be used.

The results obtained with the regularization subgrid-scale models on grid C are not satisfactory. The c_2 regularization (6) yields a wall Reynolds number of 175.2, but does not capture the slope in the log layer correctly. The results of c_4 regularization (7) collapse on the no model results, which suggests that these regularization results are mainly due to the numerical discretization.

6 Conclusion

This paper introduces a new form of the compressible Navier-Stokes equations, an energy bound for compressible flow, and a skew-symmetric form of the compressible convection operator. A symmetry-preserving discretization and regularization for compressible flow are proposed. Channel flow simulations indicate that the discretization is stable without artificial dissipation and yields accurate results on sufficiently fine grids. This makes the symmetry-preserving discretization a very suitable method for direct numerical simulation of compressible flow. On coarse grids

the proposed regularization subgrid-scale models yield satisfactory wall Reynolds numbers, but do not capture the law of the wall as accurate as the regularizations for incompressible flow.

References

1. Verstappen, R.W.C.P., Veldman, A.E.P.: Symmetry-preserving discretization of turbulent flow. J. Comput. Phys. **187**, 343–368 (2003)
2. Verstappen, R.W.C.P.: On restraining the production of small scales of motion in a turbulent channel flow. Comput. Fluids **37**, 887–897 (2008)
3. Kok, J.C.: A high-order low-dispersion symmetry-preserving finite-volume method for compressible flow on curvilinear grids. J. Comput. Phys. **228**, 6811–6832 (2009)
4. Morinishi, Y.: Skew-symmetric form of convective terms and fully conservative finite difference schemes for variable density low-mach number flows. J. Comput. Phys. **229**, 276–300 (2010)
5. Sanderse, B.: Energy-conserving Runge-Kutta methods for the incompressible Navier-Stokes equations. J. Comput. Phys. **233**, 100–131 (2013)
6. Moser, R.D., Kim, J., Mansour, N.N.: Direct numerical simulation of turbulent channel flow up to $\mathrm{Re}_\tau = 590$. Phys. Fluids **11**, 943–945 (1999)

Implicit LES of Noise Reduction for a Compressible Deep Cavity Using Pulsed Nanosecond Plasma Actuator

Z.L. Chen, B.Q. Zhang, S. Hickel and N.A. Adams

1 Introduction

High-subsonic cavity flows have been intensively studied due to their practical importance in aeronautical applications, such as, weapon bays, measurement windows and wheel wells [1]. These flows are characterized by a rich variety of flow phenomena including resonant tones, acoustic instabilities, and complex wave interactions, which is a challenging test case for the numerical simulation methods. Large-eddy simulation (LES) is the most promising tool to study the complex turbulent flows over cavities. Detailed numerical simulation of a compressible deep cavity were carried out by Larchevêque et al. [2] and Forestier et al. [3] using traditional and implicit LES methods. Besides the numerical benchmarking, the main motivations for studying cavity flows are noise reduction and flow control [1]. Many passive and active control methods have been investigated to reduce cavity noise.

In order to study the cavity flow and to apply an active flow control method, two objectives are promoted. First, an implicit LES based on the Adaptive-Local Deconvolution Method (ALDM) [4] is adopted to predict the high-subsonic flow

Z.L. Chen (✉) · B.Q. Zhang
School of Aeronautics, Northwestern Polytechnical University, Xi'an, People's Republic of China
e-mail: zhenlichen@nwpu.edu.cn

B.Q. Zhang
e-mail: bqzhang@nwpu.edu.cn

S. Hickel · N.A. Adams
Institute of Aerodynamics and Fluid Mechanics, Technische Universität München, Munich, Germany
e-mail: sh@tum.de

N.A. Adams
e-mail: nikolaus.adams@tum.de

J. Fröhlich et al. (eds.), *Direct and Large-Eddy Simulation IX*, ERCOFTAC Series 20, DOI 10.1007/978-3-319-14448-1_41

over the same deep cavity as in the experiment of Forestier et al. [3]. Second, a pulsed nanosecond plasma actuator is adopted to control the acoustic noise of this cavity, and the control mechanisms are analyzed.

2 Numerical Method

The unsteady compressible Navier-Stokes equations in conservative form are used to describe the gas dynamics, which are written as:

$$\partial_t \mathbf{U} + \nabla \cdot \mathbf{F}(\mathbf{U}) + \nabla \cdot \mathbf{D}(\mathbf{U}) = \mathbf{S}, \tag{1}$$

with the solution vector $\mathbf{U} = [\rho, \rho u_1, \rho u_2, \rho u_3, E]^T$. The conserved variables are density ρ, momentum ρu_i and total energy $E = \rho e + 0.5\rho u_i u_i$. The convective flux is

$$\mathbf{F}_i(\mathbf{U}) = [u_i\rho, u_i\rho u_1 + \delta_{i1}p, u_i\rho u_2 + \delta_{i2}p, u_i\rho u_3 + \delta_{i3}p, u_i(E+p)]^T,$$

and the diffusive flux is

$$\mathbf{D}_i(\mathbf{U}) = [0, -\tau_{i1}, -\tau_{i2}, -\tau_{i3}, -u_k\tau_{ik} + q_i]^T, \tag{2}$$

where u_i is the velocity vector, τ_{ij} are the components of the viscous stress tensor

$$\tau_{ij} = \mu(\partial_j u_i + \partial_i u_j - 2/3\delta_{ij}\partial_k u_k), \tag{3}$$

and the heat flux is

$$q_i = -\kappa\partial_i T. \tag{4}$$

The transport properties, dynamic viscosity μ and thermal conductivity κ depend on temperature T. They are calculated as

$$\mu = \mu_\infty(\frac{T}{T_\infty})^{2/3},\ \kappa = \frac{\mu c_p}{Pr}, \tag{5}$$

where μ_∞ and T_∞ are the freestream dynamic viscosity and temperature. $c_p = \gamma R/(\gamma - 1)$ is the heat capacity at constant pressure with $\gamma = 1.4$ and gas constant $R = 287.15(\mathrm{J/kg\,K})$. A constant Prandtl number $Pr = 0.72$ for air is used. To close the system of equations the pressure p and temperature T are related to density ρ and internal energy ρe by the equation of state

$$p = \rho RT = (\gamma - 1)\rho e. \tag{6}$$

A simplified version of ALDM is used to reconstruct the flow variables from the cell-averaged values at the cell interfaces for the convective flux calculation [4]. The second-order central scheme is used to discretize the diffusive terms. An explicit third order TVD Range-Kutta method is used for time advancement. The cavity is the same as in the experiment of Forestier [3] with $L/D = 0.42$. The computational domain $x/L \times z/L$ is 8×1 in streamwise and spanwise directions. There are 12 grid blocks and each has resolution $64 \times 161 \times 48$ in streamwise, vertical and spanwise directions, respectively. There are totally 2, 248, 704 cells. A recycling inflow technique and non-reflective outflow boundaries are adopted in the streamwise direction. Slip condition is used on the upper wall and the periodic condition is applied in the spanwise direction. All other boundaries are no-slip adiabatic walls. The Reynolds number is $Re_L = 860,000$ and the free stream Mach number is $Ma = 0.8$. To couple the effect of plasma actuator to the governing equations of gas, the source term is taken as $\mathbf{S} = [0, 0, 0, 0, q_v]^T$, where q_v is calculated by an validated inhomogeneous phenomenological plasma model of nanosecond pulsed plasma actuators [5].

3 Results and Discussion

3.1 Results Without Control

The sampling of statistics started after the flow had well established and lasted for approximately 30 shear-layer shedding periods. The mean velocities and Reynolds stresses are compared with those of experiment [3] and computational results of Larchevêque et al. [2] and Forestier et al. [3] in Figs. 1, 2 and 3. We observe an excellent agreement with the results from literature, which indicates that present implicit LES can capture the mean flow and Reynolds stresses well.

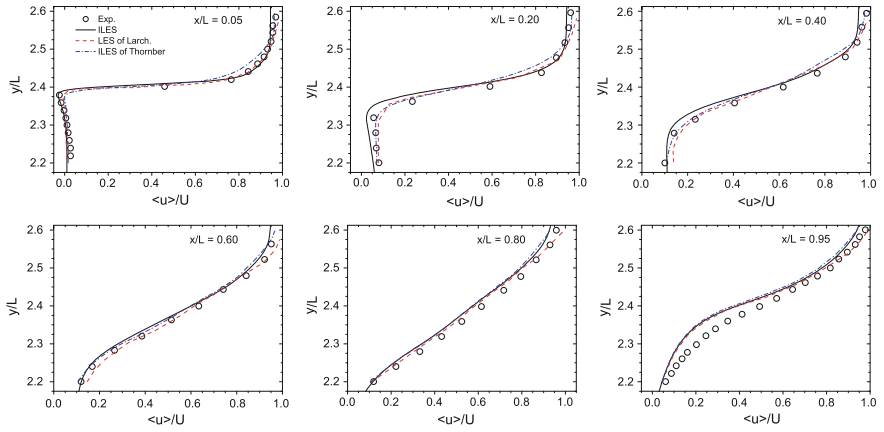

Fig. 1 Comparisons of mean streamwise velocity at different streamwise positions

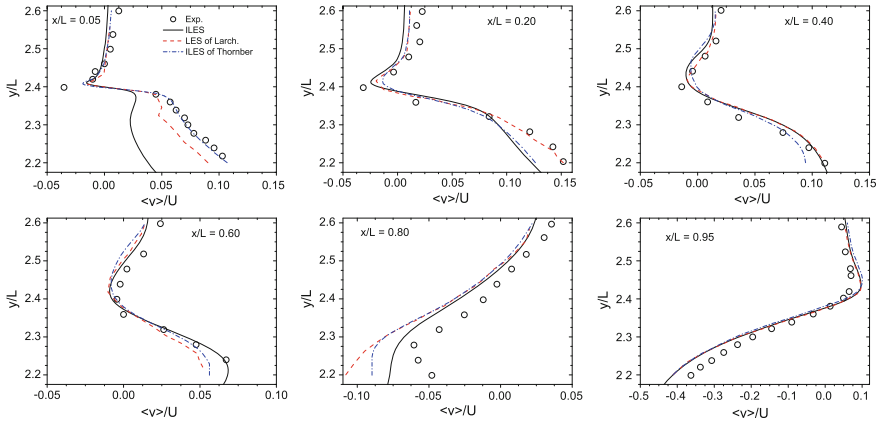

Fig. 2 Comparisons of mean vertical velocity at different streamwise positions

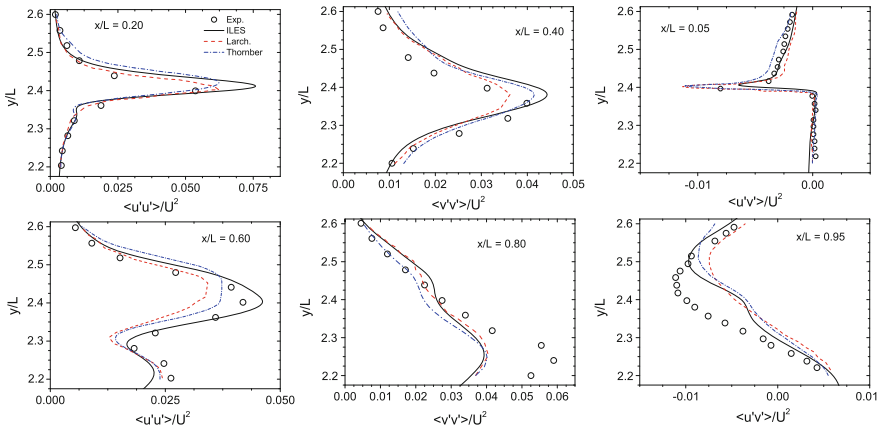

Fig. 3 Comparisons of Reynolds stresses at different streamwise positions

To quantify the spreading rate of the shear layer, the incompressible momentum thickness δ_m and the vorticity thickness δ_ω are evaluated. The incompressible momentum thickness and vorticity thickness are compared with experimental result [2] in Figs. 4 and 5. It can be seen that δ_m is underpredicted near the leading edge of the cavity but it is predicted well after the middle streamwise position. It is found that the value of δ_m is very sensitive to the integration range. The vorticity thickness is underpredicted along most of the shear layer compared to the experimental data. This indicates that the maximum gradient of streamwise velocity is not resolved by the relative coarse spatial resolution in the experiment.

The computational Sound Pressure Level (SPL) vs. frequency is compared with experimental results in Fig. 6. The instantaneous pressure is probed at the same point as in the experiment. The SPL is in units of decibels (dB) and is calculated

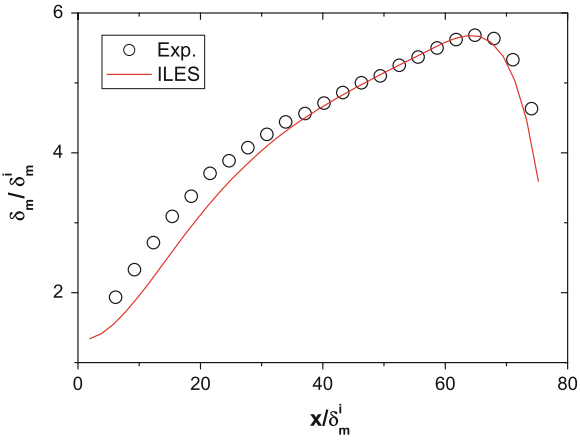

Fig. 4 Comparison of the incompressible momentum thickness

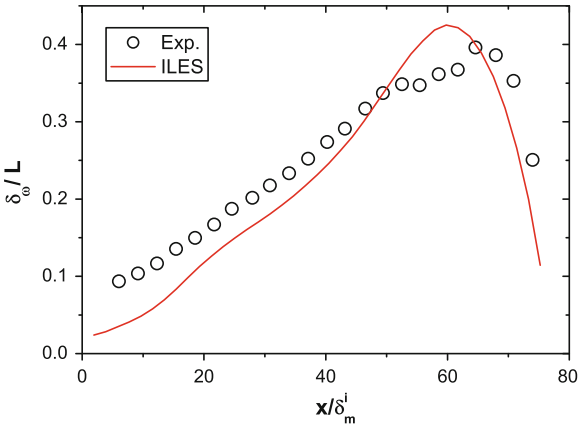

Fig. 5 Comparison of the vorticity thickness

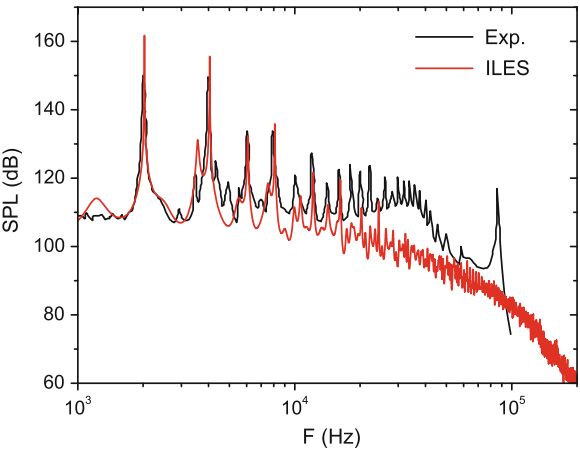

Fig. 6 Comparison of the SPL between experimental data and computational results

as in Ref. [6]. The minimum entropy method is employed to extract sharp peaks of the pressure power spectra from short data samples. The experimental data is also shown in Fig. 6. The first several modes of frequencies up to 12,152 Hz are predicted very well.

3.2 Results with Control

Based on the well predicted flowfield of the baseline configuration, a plasma actuator is mounted at $x/L = 1.0$ upstream of the cavity leading edge. The length and thickness of the plasma layer are 0.1 L and 0.008 L, respectively. The input energy density is 0.55 mJ/cm in spanwise direction. The repetitive frequency is 2,025 Hz, which is near the frequency of the fundamental mode 1,975 Hz [3]. In each actuation period, the energy releasing duration is 100 ns in each pulse. The sound pressure levels with and without control are compared in Fig. 7. The frequencies of the resonant modes do not change, but the magnitudes of the peak sound pressure level decrease. The maximum reduction of noise is 12.3 dB at 8,100 Hz. At high frequencies, the sound pressure levels almost does not change.

In order to investigate the effect of the plasma actuator on the development of the shear layer, the incompressible momentum thicknesses with and without control are compared in Fig. 8. The initial momentum thickness of the shear layer with the control is larger than that without control. However, the spreading rate of the shear layer with control is much smaller than that without control. The shear layer with control remains much thinner than that without control when it approaches the trailing edge of the cavity. The computational schlieren images with and without control at the same phase are compared in Fig. 9a, b. The spanwise vortices are

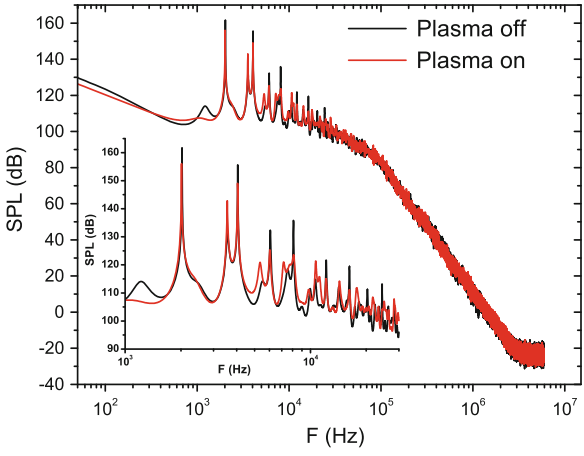

Fig. 7 Comparison of SPL with and without control

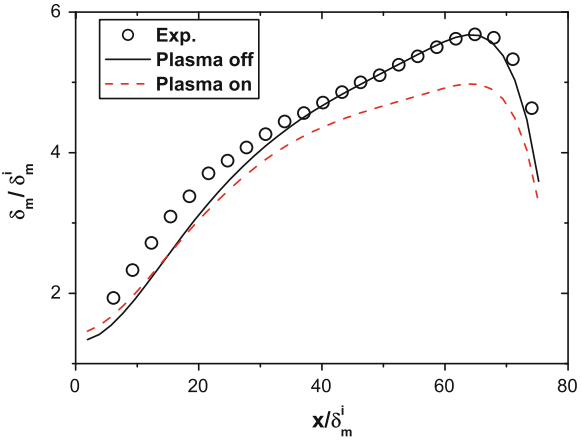

Fig. 8 Comparison of incompressible momentum thickness with and without control

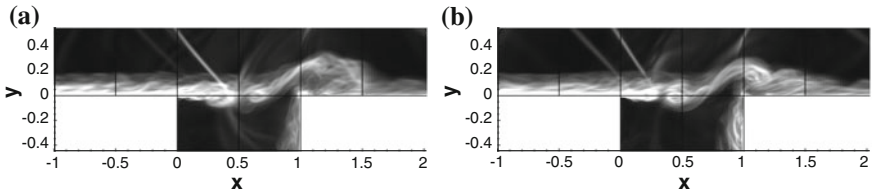

Fig. 9 **a** Computational schlieren image without control. **b** Computational schlieren image with control

much more concentrated with control than those without control. The vortices with control can pass over the trailing edge without breaking up, which is responsible for the observed noise reduction.

4 Conclusions

We performed implicit LES using the adaptive-local deconvolution method (ALDM) a Mach 0.8 cavity flow. Through flow control with a nanosecond pulsed plasma actuator the cavity noise is reduced at several low frequency resonant modes up to 12.3 dB. The control mechanisms can be deduced from the comparisons of the shear layer thickness and schlieren images. First, the flow control reduces the spreading rate of the shear layer, which results in thinner shear layer approaching the cavity trailing edge. Second, when the plasma actuator is applied, the spanwise vortices are much more concentrated and can pass over the cavity trailing edge.

References

1. Cattafesta, L.N., Song, Q., Williams, D.R., Rowley, C.W., Alvi, F.S.: Active control of flow-induced cavity oscillations. Prog. Aerosp. Sci. **44**, 479–502 (2008)
2. Larcheveque, L., Sagaut, P., Mary, I., Labbe, O.: Large-eddy simulation of a compressible flow past a deep cavity. Phys. Fluids **15**(1), 193–209 (2003)
3. Forestier, N., Jacquin, L., Geffroy, P.: The mixing layer over a deep cavity at high-subsonic speed. J. Fluid Mech. **475**, 101–144 (2003)
4. Hickel, S., Larsson, J.: An adaptive local deconvolution model for compressible turbulence. In: CTR Proceedings of Summer Program, pp. 85–96 (2008).
5. Chen, Z.L., Hao, L.Z., Zhang, B.Q., Liang, H., Li, Y.H.: A model for nanosecond pulsed dielectric barrier discharge (NSDBD) actuator and its investigation on the mechanisms of separation control over an airfoil. Sci. China Tech. Sci. (2013). doi:10.1007/s11431-013-5179-4
6. Thornber, B., Drikakis, D.: Implicit large eddy simulation of a deep cavity using high-resolution methods. AIAA J. **46**(10), 2634–2645 (2008)

Part VIII
Heat Transfer and Natural Convection

DNS of Thermal Convection in Rectangular Domains with Different Depth

S. Wagner and O. Shishkina

1 Introduction

As a simplified model of a large class of convective processes, Rayleigh-Bénard convection (RBC) enables fundamental and numerical studies of convection including Direct Numerical Simulations (DNS). Although it has been investigated for more than hundred years there are still many open questions including the influence of the geometrical characteristics of the convection cell on the flow dynamics.

Usually in experiments and simulations cylindrical convection cells are used in which time-dependent three-dimensional (3D) global flow structures develop. Investigation of these structures in 3D requires much more complicated analysis of the fluid motion than for example in the two-dimensional (2D) case. To circumvent these difficulties, in some experiments a different geometry was used, namely a rectangular convection cell with equal height and length but rather small depth. This leads to a large-scale flow which is fixed orthogonal to the short extension of the cell [1]. The dimensionless temperature gradient between the heated bottom plate and the cooled top plate, called Rayleigh number *Ra*, was about 10^{10} in these experiments, i.e. rather high. Consequently the influence of the side-walls was negligible and the flow was bulk-dominated. Since for DNS lower *Ra* are preferable due to the smaller computational effort [2], the question about the influence of the walls on global flow characteristics for lower *Ra* arises.

The aim of the present work is to find a proper geometry for studying the influence of surface roughness and obstacles in 3D flows with a global structure similar to 2D ones [3]. Three-dimensional DNS are required for this study, since not only the global dynamics but even integral quantities might differ in 2D and 3D DNS, especially for

S. Wagner (✉) · O. Shishkina
German Aerospace Center (DLR), Institute of Aerodynamics and Flow Technology, Göttingen, Germany
e-mail: Sebastian.Wagner@dlr.de

O. Shishkina
e-mail: Olga.Shishkina@dlr.de

J. Fröhlich et al. (eds.), *Direct and Large-Eddy Simulation IX*,
ERCOFTAC Series 20, DOI 10.1007/978-3-319-14448-1_42

small Prandtl numbers Pr [4]. The influence of the shape of the domain on those integral quantities is thus investigated together with the state of the equilibrium flow (stationary/unsteady).

2 Methodology

DNS of thermal convection have been performed in a rectangular domain with equal height and length for different ratios Γ = depth/height between 0.1 and 1. Apart from the geometry of the container the convective flow is determined by fixing the Rayleigh number $Ra = \alpha g \Delta H^3/(\nu\kappa) \in [10^5, 10^7]$ and the Prandtl number $Pr = \nu/\kappa = 0.786$. A fourth-order accurate finite volume code in Cartesian coordinates [5] has been used to solve the equations representing the conservation laws for mass, momentum and energy in Oberbeck-Boussinesq approximation. As usual for confined Rayleigh-Bénard cells the boundary conditions have been chosen as follows: top and bottom plates are isothermal with $T_{\text{bottom}} > T_{\text{top}}$, while all four rigid vertical walls are adiabatic. Further, no-slip and impermeability conditions are prescribed on all walls. The spatial grid resolution has been chosen according to [2]. To characterise the flow, besides time-averaged fields, also a large amount of instantaneous flow fields has been collected with a sampling frequency of $4\sqrt{\alpha g \Delta/H}$, which is large enough to resolve the global dynamics of the flow [6]. Note that for the time-averaging a far higher sampling frequency was used.

3 Results

For the considered parameter range we investigate certain properties of the flow and their dependence on Ra and Γ. First of all the state of the equilibrium is discussed. Further the mean heat flux and the mean kinetic energy are investigated and finally a comparison with the 2D case is given.

3.1 Equilibrium State

We investigate whether the equilibrium state of the flow is stationary or unsteady in dependence of Ra and Γ. Based on our previous DNS in a cylindrical domain with equal diameter and height [6] one might expect that in rectangular domains for $Pr = 0.786$ and Γ about one a stationary equilibrium can be obtained only for Ra up to 10^5, while already for $Ra \approx 3 \times 10^5$ a (chaotic) time-dependent equilibrium takes place. For Ra about 10^7 the coherence-length apart from the walls becomes so small, that the bulk flow might be called turbulent [7].

To determine the state of the equilibrium, we consider time series of the normalised area averaged vertical heat flux $q_z = -(H/\Delta)\langle \partial_z T \rangle_{x,y}$ at the bottom and and the top

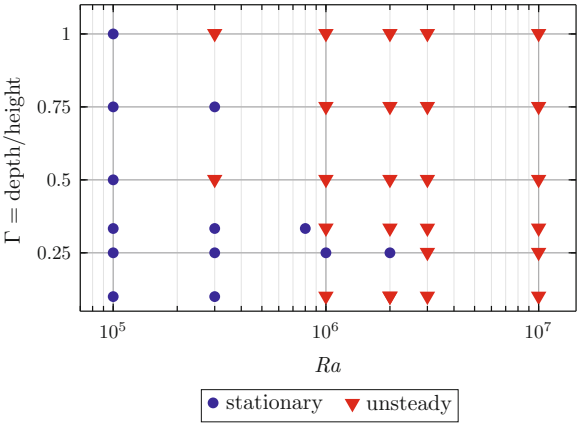

Fig. 1 State of the equilibrium (stationary/unsteady) in dependence of Ra and Γ, $Pr = 0.786$

plate separately. (Here $\langle\cdot\rangle_{x,y}$ denotes averaging over a horizontal cross-section.) If these quantities do not change in time for several turnovers we call this a stationary equilibrium.

In Fig. 1 the state of the equilibrium is depicted for the considered parameter range. It turns out that eventhough the flow is stationary for a certain $Ra-\Gamma-$combination, a decrease of Γ can lead to an unsteady flow again (e.g. $Ra = 10^6$ and $\Gamma = 1/4$ and $\Gamma = 1/10$). One might expect that for a smaller Γ the influence of the viscous boundary layers becomes stronger and leads to a further supression of unsteady motion. But of course the general tendency is that larger Γ and large Ra lead to an unsteady motion.

3.2 Mean System Responses

The two mean responses of a fluid to a temperature gradient is an (increased) heat flux and motion. They are expressed by the Nusselt number $Nu = \langle (u_z T - \kappa \partial_z T)/(\kappa \Delta/H)\rangle_{x,y,t}$, and the Reynolds number $Re = \sqrt{\langle \mathbf{u}^2\rangle_{x,y,z,t}}\, H/\nu$. There exist several numerical, experimental and theoretical studies about their scaling with Ra and Pr [7], but the influence of the aspect ratio especially in quasi two-dimensional domains is unknown. In Fig. 2 the Ra-dependences of Nu and Re for different aspect ratios Γ are depicted. To clarify the differences for varying Γ, Nu and Re have been reduced by a certain power of Ra which is generally obtained.

Several things can be observed. First, there is no monotonic Γ dependence and in particular no well-pronounced power law scaling. (The latter becomes more obvious from double logarithmic plots of Nu versus Γ and Re versus Γ, which are not shown here). Further, the differences in Nu for different Γ decreases for larger Ra. So there is almost no difference in Nu for $Ra = 10^7$ except of $\Gamma = 1/10$. One might expect that this difference will disappear for even higher Ra. Analogously, the Ra-dependence of

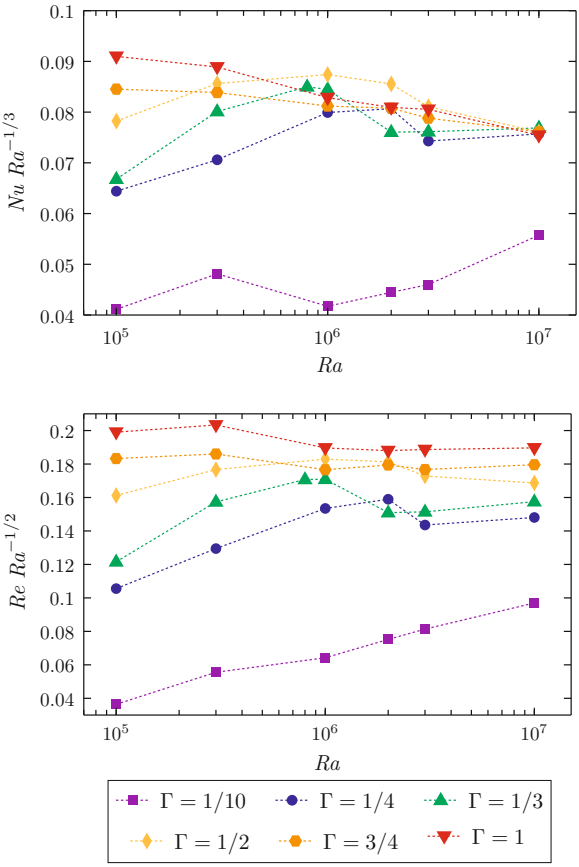

Fig. 2 Rayleigh number dependence of mean heat flux (*Nu*) and mean kinetic energy (*Re*) for different aspect ratios and $Pr = 0.786$

Re becomes similar for larger *Ra*. Since *Re* is a function of the mean kinetic energy, the differences in the value of *Re* are expected as long as the influence of the viscous boundary layers attached to all walls is not negligible.

Further it can be recognised, that for $Ra \approx 10^6$ drops in the reduced *Nu* and *Re* are obtained for $\Gamma = 1/4$ and $\Gamma = 1/3$. This drop is present also for $\Gamma = 1/10$ but only in case of *Nu*. All these drops appear at the transition to an unsteady flow.

3.3 Differences to 2D Flow

We are interested at most in quasi 2D convection, i.e. a three-dimensional flow which shows a comparable flow structure as it is found in 2D simulations [3]. It has the advantage of three-dimensionality while analysis is simpler than in the case of e.g. a cylinder [6]. Thus we concentrate on $\Gamma = 1/10$ and $\Gamma = 1/4$. In Fig. 3 (instantaneous) temperature fields for $Ra = 10^6$ with superimposed velocity vectors are

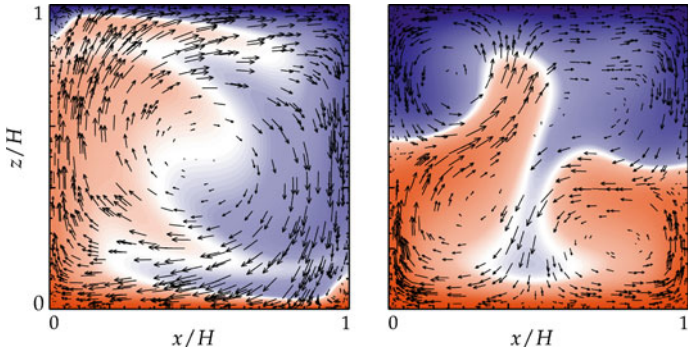

Fig. 3 Vertical slice at half depth of the instantaneous temperature distribution (red = warm, blue = cold) with superimposed velocity vectors. On the left the stationary flow for $\Gamma = 1/4$ and on the right the instationary flow for $\Gamma = 1/10$ is depicted for $Ra = 10^6$, $Pr = 0.786$

displayed. They show that the unsteady flow for $\Gamma = 1/10$ has a different global structure compared to that obtained for $\Gamma = 1/4$. It consists of alternating large warm and cold plumes rising/falling in the center of the domain, which leads to a global four roll structure. Expected from a previous study in a cylinder and the literature on 2D RBC (e.g. [8]) is a single roll with thermal plumes rising/falling close to the vertical walls. To understand the global structure also for $Ra - \Gamma$-combinations apart from that extreme cases, we decompose instantaneous velocity fields at half depths into four two-dimensional modes (as described by in [9]). In Fig. 4 for $\Gamma = 1/10,\ 1/4$ the contributions of four different modes depending on Ra are displayed together with sketches of the particular modes. It gets obvious that during the onset of unsteady motion (marked with a vertical black line) the modes mix up. For both Γ the four-roll

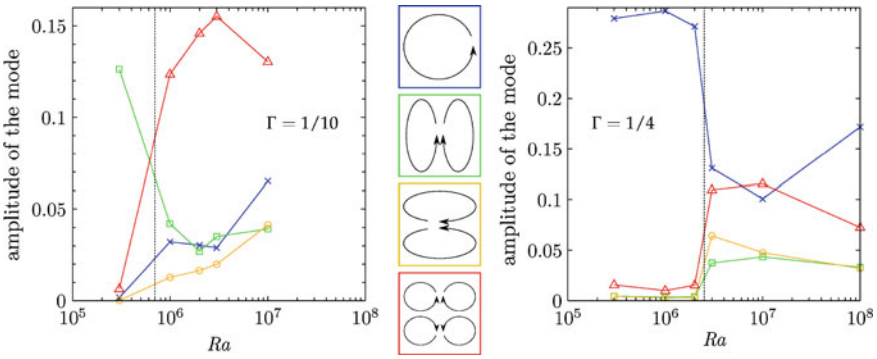

Fig. 4 Contributions of four modes (shown as sketches) for varying Ra and $\Gamma = 1/10$ (*left*) and $\Gamma = 1/4$ (*right*) and $Pr = 0.786$. The colour of the graphs corresponds to the colours of the particular modes: a single roll (*blue crosses*), two horizontally aligned rolls (*green squares*), two vertical aligned rolls *yellow circles*, four-roll mode (*red triangles*). The transition to an unsteady flow is marked with a vertical black line

mode becomes stronger while the dominating mode of the steady flow (single roll and two horizontally aligned rolls, respectively) becomes weaker. With further increased Ra the single-roll mode gets stronger. In case of $Ra = 1/4$ it becomes dominant at much lower Ra than for $\Gamma = 1/10$. In particular in an additional simulation for $Ra = 10^8$ the single-roll mode is already the strongest one for $\Gamma = 1/4$. Thus for intermediate Ra (feasible for DNS) $\Gamma = 1/4$ is preferable, since the expected single-roll mode is much more present as in case of $\Gamma = 1/10$. This is in good agreement to what we have found for the integral quantities.

4 Conclusions

DNS of RBC in rectangular domains with equal length and height but variable depth have been performed for $Pr = 0.786$ and Ra between 10^5 and 10^7. The equilibrium state, the mean heat flux and the mean kinetic energy have been evaluated and their Ra and Γ dependencies were studied. Main result is that already for $Ra = 10^7$ and $\Gamma = 1/4$ the mean heat flux is Γ-independent. The global flow structure is only weakly influenced by thermal plumes moving through the cell center for large Ra and Γ, i.e. a single large scale circulation generally develops. For $\Gamma = 1/10$ as soon as the flow has an unsteady equilibrium, a global flow structure consisting of single plumes moving just vertically takes place. Consequently we obtain a mixture of a large scale circulation and those plumes in the center of the domain for intermediate Ra and very small Γ.

Acknowledgments The authors would like to thank Matthias Kaczorowski and Tomasz Czarnota for updating the computational code in Cartesian coordinates and acknowledge support by the Deutsche Forschungsgemeinschaft (DFG) under grant SH405/3-1.

References

1. Xia, K.-Q., Sun, C., Zhou, S.: Particle image velocimetry measurement of the velocity eld in turbulent thermal convection. Phys. Rev. E. **68**, 066303 (2003)
2. Shishkina, O., Stevens, R.J.A.M., Grossmann, S., Lohse, D.: Boundary layer structure in turbulent thermal convection and its consequences for the required numerical resolution. New J. Phys. **12**, 075022 (2010)
3. Shishkina, O., Wagner, C.: Modelling the influence of wall roughness on heat transfer in thermal convection. J. Fluid Mech. **686**, 568–582 (2011)
4. Schmalzl, J., Breuer, M., Hansen, U.: On the validity of two-dimensional numerical approaches to time-dependent thermal convection. Europhys. Lett. **67**, 390–396 (2004)
5. Shishkina, O., Shishkin, A., Wagner, C.: Simulation of turbulent thermal convection in complicated domains. J. Comput. Appl. Mech. **226**, 336–344 (2009)
6. Wagner, S., Shishkina, O., Wagner, C.: Boundary layers and wind in cylindrical Rayleigh-Bénard cells. J. Fluid Mech. **697**, 336–366 (2012)
7. Ahlers, G., Grossmann, S., Lohse, D.: Heat transfer and large scale dynamics in turbulent rayleigh-bénard convection. Rev. Mod. Phys **82**, 503–537 (2009)

8. van der Poel, E.P., Stevens, R.J.A.M., Lohse, D.: Connecting flow structures and heat flux in turbulent rayleigh-bénard convection. Phys. Rev. E **84**, 045303(R) (2011)
9. Chandra, M., Verma, M.K.: Flow reversals in turbulent convection via vortex reconnections. Phys. Rev. Lett. **110**, 114503 (2013)

Direct Numerical Simulation of Low-Mach Turbulent Natural Convection Flow in an Open Cavity of Aspect Ratio 4

J. Chiva, O. Lehmkuhl, J. Ventosa and A. Oliva

1 Introduction

Natural convection heat transfer in cavities has been studied extensively in the literature due to its relevance to many engineering areas such as low temperature solar collectors, design of buildings, cooling of nuclear reactors, etc. However, the majority of the studies are devoted to the behavior of closed cavities. To mention a few: de Vahl Davis [1] provided a well known set of benchmark solutions for steady natural convection of air in a horizontally heated square cavity for Rayleigh numbers up to $Ra = 10^6$, Le Quéré [2] extended the analysis up to $Ra = 10^8$, Trias et al. [3, 4] computed direct numerical simulations (DNS) of two- and three-dimensional turbulent natural convection flows in a differentially heated cavity of aspect ratio 4 for Rayleigh numbers up to $Ra = 10^{10}$.

The situation under consideration in this work is 3D turbulent natural convection in an *open cavity* with high temperature differences. In this case, the boundary conditions are more complex and the domain has to be extended to include part of the external environment in order to avoid any interaction between the boundary conditions and the flow inside the cavity (Juárez et al. [5]). The low-Mach Number approximation proposed by Chiva et al. [6] has been used because the high temperature differences cast doubt upon the validity of the Boussinesq approximation. The main focus of the work is to assess on the validity of the Boussinesq approximation on

J. Chiva (✉) · J. Ventosa · A. Oliva
Technical University of Catalonia, Colom 11, 08222 Terrassa, Spain
e-mail: jordic@cttc.upc.edu

J. Ventosa
e-mail: jordivm@cttc.upc.edu

A. Oliva
e-mail: oliva@cttc.upc.edu

O. Lehmkuhl
Termo Fluids S.L., Avda. Jacquard 97 1-E, 08222 Terrassa, Spain
e-mail: oriol@cttc.upc.edu

J. Fröhlich et al. (eds.), *Direct and Large-Eddy Simulation IX*,
ERCOFTAC Series 20, DOI 10.1007/978-3-319-14448-1_43

open cavities with high temperature differences, hence, the effects of the radiation have been negleted. The simulations for this work have been obtained using a general CFD&HT code called Termofluids [7].

2 Mathematical Formulation

The governing equations used in TermoFluids have been discretised on a collocated unstructured grid arrangement by means of second-order spectro-consistent schemes. Such schemes are conservative, i.e. they preserve the kinetic energy equation. These properties ensure both stability and conservation of the kinetic-energy balance even at high Reynolds numbers and with coarse grids (Verstappen and Van Der Velde [8]). For the temporal discretisation a Runge-Kutta semi-explicit scheme has been used because of the instabilities introduced by the density time derivative in fully-explicit temporal schemes [6].

3 Problem Definition and Numerical Domain

The situation under consideration in this work is natural convection of air ($Pr = \nu/\alpha = 0.71$) in an *open cavity* (see Fig. 1) with a Rayleigh number, based on the height of the cavity ($H2$), of $Ra = g\beta(T_h - T_c)(H2)^3 Pr/\nu^2 = 10^{12}$, a non-dimensional temperature value of $\varepsilon = (T_h - T_c)/(T_h + T_c) = 0.4$ and height aspect ratio $H2/L1 = 4$.

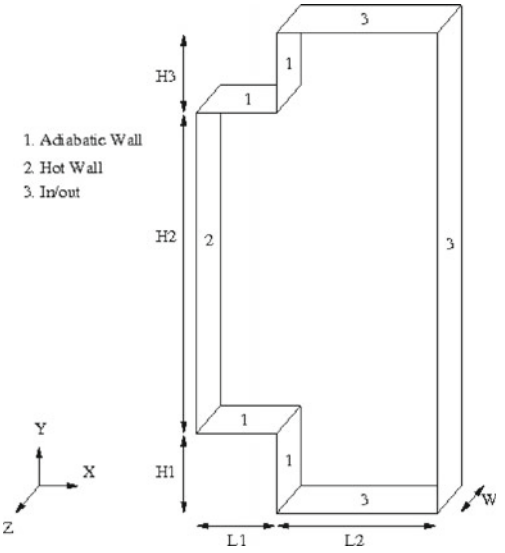

Aspect ratio	Value
H2/L1	4
H1/L1	1
H3/L1	1
L2/L1	2
W/L1	0.5

Fig. 1 Scheme of the open cavity

The vertical hot wall (identified with 2 in Fig. 1) is considered isothermal with temperature $T_h = 686.35$ K. The top, bottom and surfaces attached to them (corresponding with boundary 1 in Fig. 1) are considered adiabatic. No slip conditions are set at the solid walls. The flow has been considered periodic in the z axis. Pressure boundary conditions are imposed at the top, bottom and left boundaries of the domain (boundary 3 in Fig. 1), with Neumann condition for temperature if the air goes out of the system and temperature $T_c = 294.15$ K if it goes in.

Considering the reference scales for length, time, velocity, temperature and dynamic pressure as $H2, ((H2)^2/\alpha)Ra^{-0.5}, (\alpha/H2)Ra^{0.5}, T_h - T_c, \rho(\alpha/(H2)^2)Ra$, respectively, thermal convection in the cavity is governed by the Rayleigh number, Prandtl number, non-dimensional temperature difference and height aspect ratio.

The meshes used for solving the domain considered have been generated by a constant step extrusion of a two-dimensional (2D) structured grid. Under these conditions, the spanwise coupling of the discrete Poisson equation, which results from the incompressibility constrain, yields circulant sub-matrices that are diagonalizable in a Fourier space. This allows to solve the Poisson equation by means of a Fast Fourier Transform (FFT) method. The algorithm used is based on the explicit calculation and direct solution of a Schur Complement system for the independent 2D systems. For more details the reader is referred to [9].

The number of control volumes of the final mesh has been 145,506 by 64 planes (about 9.3 million control volumes). In order to properly evaluate the boundary layer near the hot wall, a stretching has been applied to concentrate the maximum number of control volumes inside the boundary layer. The mesh size has been designed using knowledge from previous works [3, 6].

4 Results

In the present work, direct numerical simulations assuming the Boussinesq hypothesis and variable thermo-physical properties have been carried out. The simulation has been started with the air temperature set to T_c. Then, the simulation has been advanced in time until statistical stationary flow conditions have been achieved. After the initial transient has been completely washed out, averaged statistics have been computed.

4.1 Instantaneous Flow

A comparison of the instantaneous magnitude of the velocity at the symmetry plane (Fig. 2) show clear differences between the two approaches. The values close to the hot wall and at the top of the cavity are higher with variable properties than with the Boussinesq approximation. Yet, in both cases, a small recirculation can be observed at the top corner of the cavity, caused by the ascension of thermal plumes next to the hot wall. There is also an entrainment of cold fluid from the bottom of the cavity

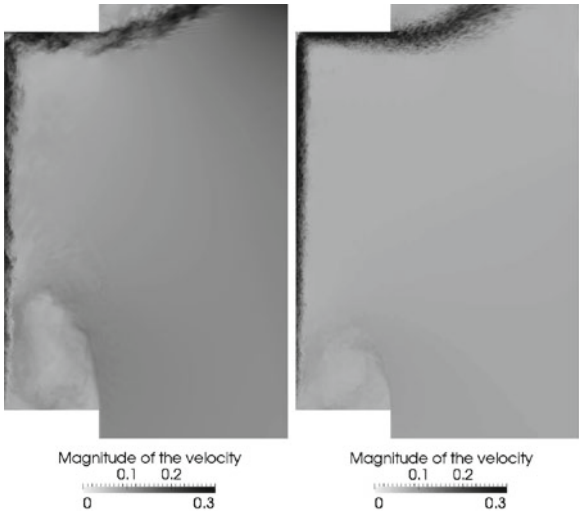

Fig. 2 2D view at the symmetry plane of the instantaneous magnitude of the velocity: (*left*) Boussinesq approximation and (*right*) variable properties

which produces a recirculation which seems to be close to a quarter of the total height of the cavity ($H2$). The interaction between the recirculation in this zone with the hot wall produces fluid instabilities at the bottom of the boundary layer, promoting the generation of turbulence.

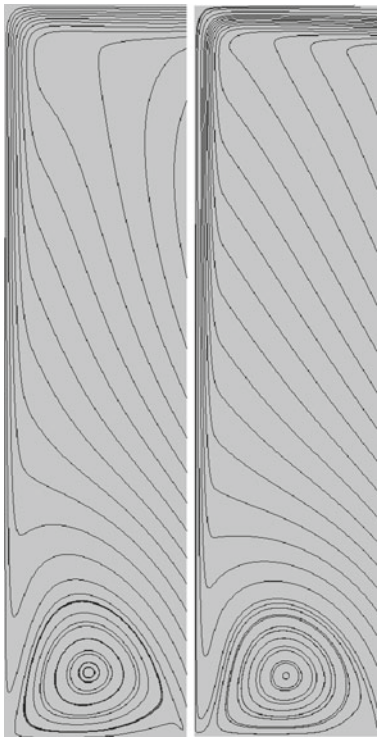

Fig. 3 Stream lines: (*left*) Boussinesq approximation and (*right*) variable properties

4.2 Time-Averaged Statistics

Time-averaged statistics presented in this paper have been obtained by averaging the computed variables in time and homogeneous direction. The recirculation between the hot wall and the bottom of the cavity observed from the analysis of the instantaneous flow is clearly represented by the stream lines in Fig. 3. The center is situated at $x/L1 = 0.465$ and $y/L1 = 0.353$ with Boussinesq approximation and $x/L1 = 0.502$ and $y/L1 = 0.334$ with variable properties. Temperature contours are depicted in Fig. 4. Temperature gradients can be seen over the whole cavity with Boussinesq approximation while it is not the case for variable properties.

The distributions of temperature variance in Fig. 5 show that there is some influence of the recirculation at the bottom with Boussinesq approximation, while with variable properties it is mainly concentrated close to the hot wall and at the top. The turbulent kinetic energy distributions depicted in Fig. 6 show higher values close to the hot wall and at the top of the cavity with variable properties, and clear differences in the central region of the cavity between both approaches.

In Fig. 7 profiles of the averaged Nusselt number along the hot wall are shown. There is no transition point between laminar and turbulent regime as the flow is fully turbulent from the beginning due to the influence of the fluid entrainment from the bottom of the cavity. Near the top the Nusselt number manifests the behavior of an

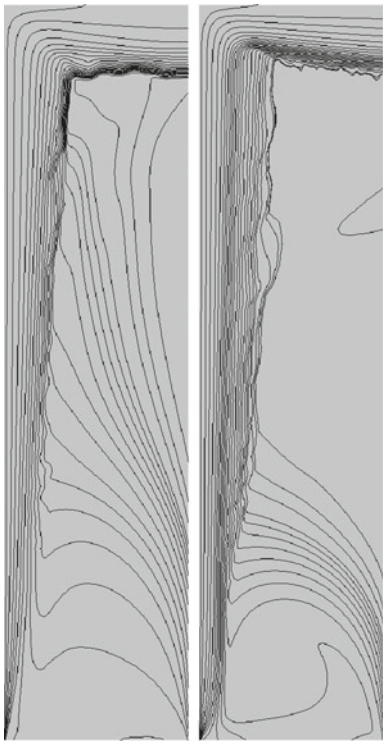

Fig. 4 Temperature distribution: (*left*) Boussinesq approximation and (*right*) variable properties

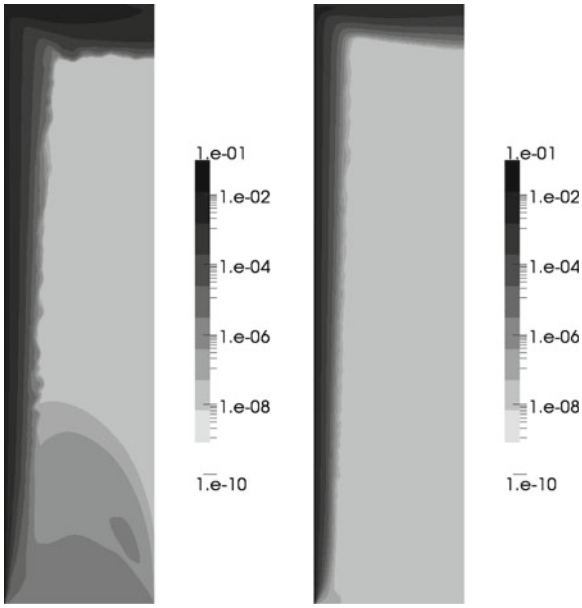

Fig. 5 Temperature variance: (*left*) Boussinesq and (*right*) variable properties

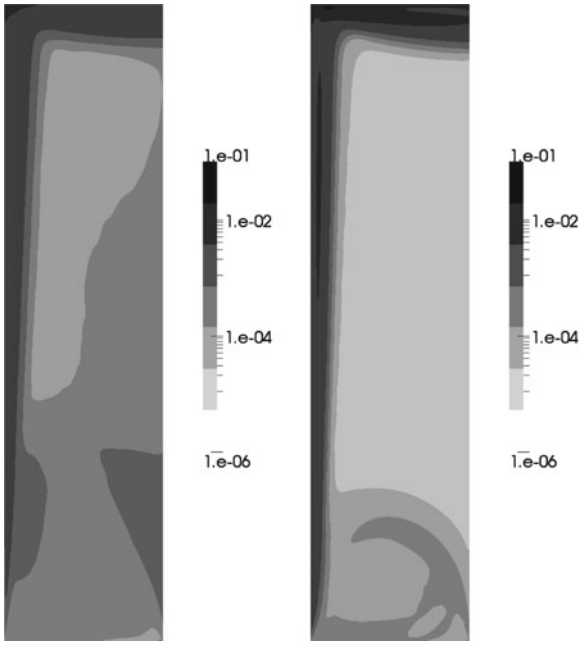

Fig. 6 Turbulent kinetic energy: (*left*) Boussinesq and (*right*) variable properties

impinging phenomena, where the temperature of the air gets closer to the temperature of the wall due to the collision of the vertical flow against the top of the cavity. The overall averaged Nusselt number is 978 with Boussinesq approximation and 1110 with variable properties.

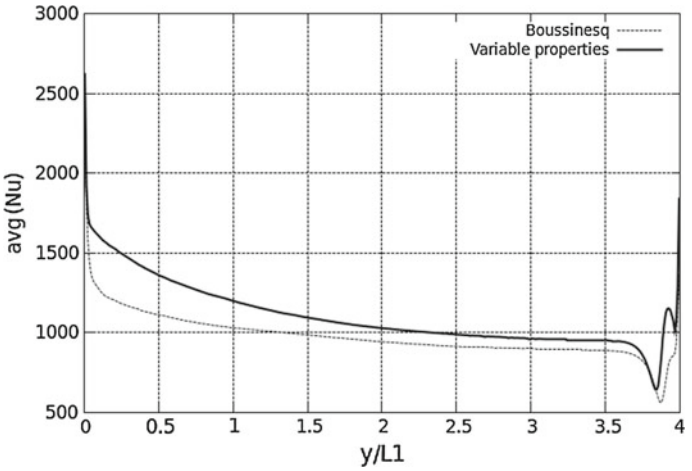

Fig. 7 Profile of the averaged Nusselt number along the hot wall

5 Conclusions

The turbulent natural convection of air in an *open cavity* of aspect ratio 4, $Ra = 10^{12}$ and $\varepsilon = 0.4$ has been studied by means of DNS. The validity of the Boussinesq approximation has been tested comparing the results of simulations with this hypothesis against simulations with variable thermo-physical properties. Instantaneous flow and the time averaged statistics have been presented and analyzed. The conclusion obtained from the comparison of the averaged Nusselt number at the hot wall is that the convective heat transfer is understimated when the Boussinesq approximation is used at high temperature differences.

Acknowledgments This work has been financially supported by the Ministerio de Educación y Ciencia, Secretaría de Estado de Universidades e Investigación, Spain (ref. ENE2010-17801) and by the Collaboration Project between Universidad Politècnica de Catalunya and Termo Fluids S.L.

References

1. de Vahl Davis, G.: Natural convection of air in a square cavity: a bench mark numerical solution. Int. J. Numer. Methods Fluids **3**, 227–248 (1983)
2. Le Quéré, P.: Accurate solutions to the square thermally driven cavity at high Rayleigh number. Comput. Fluids **20**, 29–42 (1991)
3. Trias, F.X., Soria, M., Pérez-Segarra, C.D., Oliva, A.: Direct numerical simulation of a three-dimensional natural convection flow in a differentially heated cavity of aspect ratio 4. Numer. Heat Transfer Part A-Appl. **45**, 649–673 (2004)
4. Trias, F.X., Soria, M., Pérez-Segarra, C.D., Oliva, A.: Direct numerical simulations of two and three dimensional turbulent natural convection flows in a differentially heated cavity of aspect ratio 4. J. Fluid Mech. **586**, 259–293 (2007)

5. Juárez, J.O., Hinojosa, J.F., Xamán, J.P., Pérez-Tello, M.: Numerical study of natural convection in an open cavity considering temperature-dependent fluid properties. Int. J. Thermal Sci. **50**(11), 2184–2197 (2011)
6. Chiva, J., Ventosa, J., Lehmkuhl, O., Pérez-Segarra, C.D.: Modelization of the low-Mach Navier Stokes equations in unstructured meshes. In: Proceedings of the 7th International Conference on Computational Heat and Mass Transfer (2011)
7. Lehmkuhl, O., Pérez Segarra, C.D., Borrell, R., Soria, M., Oliva, A.: Termofluids: a new parallel unstructured CFD code for the simulation of turbulent industrial problems on low cost PC cluster. In: Proceedings of the Parallel CFD 2007 Conference, pp. 1–8 (2007)
8. Verstappen, R.W.C.P., Van Der Velde, R.M.: Symmetry-preserving discretization of heat transfer in a complex turbulent flow. J. Eng. Math. **54**(4), 299–318 (2006)
9. Borrell, R., Lehmkuhl, O., Trias, F., Oliva, A.: Parallel direct Poisson solver for discretisations with one Fourier diagonalisable direction. Comput. Phys. **230**(12), 4723–4741 (2011)

Rotating Rayleigh–Bénard Convection of SF_6 in a Slender Cylinder

S. Horn and C. Wagner

1 Introduction

The large structures occurring in the fluid flow on the Sun's outer layer, in the atmosphere and oceans of planets, including our Earth, are primarily driven by convection. The flow structure but also the efficiency of the heat transport are, however, significantly influenced by the Coriolis force due to rotation. Understanding these fundamental processes is thus utterly important for geo- and astrophysics. In an idealised way, these systems can be represented as a fluid heated from below and cooled from above, the so-called Rayleigh–Bénard convection.

The most important control parameters of this system are the Prandtl number $Pr = \nu/\kappa$ and the Rayleigh number $Ra = g\alpha H^3 \Delta/(\kappa\nu)$, where g is the gravitational acceleration, α the isobaric expansion coefficient, κ the heat diffusivity, ν the kinematic viscosity, H the height of the system, and Δ the imposed temperature difference between top and bottom. The Rayleigh numbers occurring in an astrophysical context are usually very high, for example, in the Sun it is $Ra \approx 10^{23}$. On the other hand, the Rayleigh numbers that can be achieved by experiments and Direct Numerical Simulations (DNS) are magnitudes lower. Present experiments are limited to $Ra \approx 10^{15}$ [2] and DNS to $Ra \approx 10^{12}$ [9]. In rotating Rayleigh–Bénard an additional control parameter is needed, which characterises the importance of rotation. Commonly, the convective Rossby number is used, defined as $Ro = \sqrt{\alpha g \Delta H}/(2\Omega H)$, where Ω is the rotation rate.

The objective of this work is, to study the influence of rotation on a low-Pr fluid within a slender cylindrical cell, especially at higher Ra, by means of DNS and large

S. Horn (✉) · C. Wagner
Institute for Aerodynamics and Flow Technology, German Aerospace Center (DLR), Göttingen, Germany
e-mail: susanne.horn@dlr.de

C. Wagner
e-mail: claus.wagner@dlr.de

J. Fröhlich et al. (eds.), *Direct and Large-Eddy Simulation IX*,
ERCOFTAC Series 20, DOI 10.1007/978-3-319-14448-1_44

eddy simulations (LES). The numerical parameters are chosen in such a way that they will allow for a comparison to an experiment, that has recently been built.

2 Numerical Methodology

We conduct DNS for $10^5 \leq Ra \leq 10^9$ and LES for $10^6 \leq Ra \leq 10^{10}$ in a cylindrical domain with an diameter-to-height aspect ratio of $\Gamma = D/H = 1/2$. The working fluid has a Prandtl number of $Pr = 0.8$, as is for air or SF_6. The rotation rates span a range of $10.0 \leq Ro \leq 0.05$, and $Ro = \infty$, corresponding to the non-rotating case. For our DNS, we use a fourth order finite volume code for cylindrical domains [6], solving the three-dimensional Navier-Stokes equations under Oberbeck–Boussinesq conditions. To study the influence of rotation, we included the Coriolis force, $f_c = -2\boldsymbol{\omega} \times \mathbf{u}$, with $\boldsymbol{\omega} = (0, 0, \Omega)$; the centrifugal acceleration is incorporated in the reduced pressure. For our LES we use an approximation by the first term of the exact series expansions for filtered products for the subgrid scale stress tensors, according to the model by Leonard [5]. It was adapted to our finite-volume method by Shishkina and Wagner [7].

3 Results

3.1 Temperature Distribution

Figure 1 presents instantaneous temperature isosurfaces, that are equidistantly distributed between the top and bottom temperature for $10^5 \leq Ra \leq 10^{10}$. They visualise the dramatic change of the flow structures and the flow behaviour with

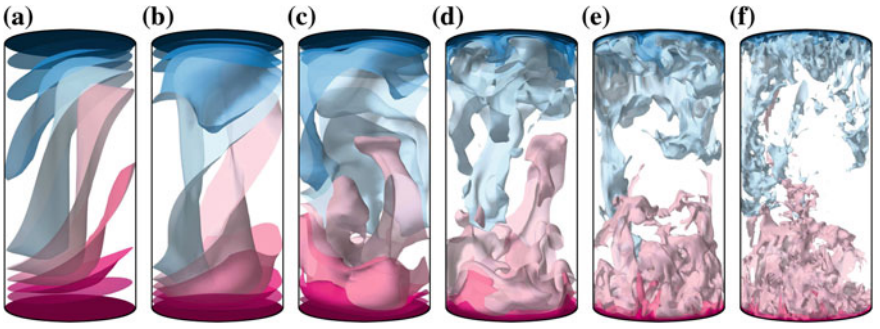

Fig. 1 Temperature isosurfaces, equidistantly distributed between the *top* and *bottom* temperature in the non-rotating case, i.e. $Ro = \infty$, obtained by DNS for $Ra \in [10^5, 10^9]$ and LES for $Ra = 10^{10}$, respectively. (**a**) $Ra = 10^5$, (**b**) $Ra = 10^6$, (**c**) $Ra = 10^7$, (**d**) $Ra = 10^8$, (e) $Ra = 10^9$, (**f**) $Ra = 10^{10}$

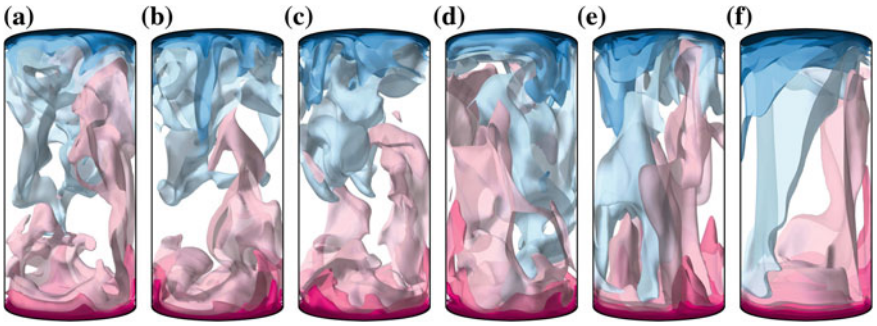

Fig. 2 Temperature isosurfaces, equidistantly distributed between the *top* and *bottom* temperature, for different Rossby numbers and constant $Ra = 10^8$, obtained by DNS. (**a**) $Ro = 10.0$, (**b**) $Ro = 1.0$, (**c**), $Ro = 0.1$, (**d**) $Ro = 0.05$, (**e**) $Ro = 5.0$, (**f**) $Ro = 0.5$

increasing Ra. For the smallest Ra the flow is steady and one large convection roll fills the whole cylinder. With increasing Ra the single structures become gradually smaller, and while for moderate Ra the LSC is clearly recognisable in the instantaneous flow fields, this becomes hardly possible for higher Ra. But the LSC can be recovered in the sufficiently long temporal averaged flow fields; its break-down is not expected until $Ra \geq 10^{13}$ [2]. However, it is noteworthy, that due to the small aspect ratio of $\Gamma = 1/2$, we do not only have a single-roll state, but also a frequent switching to a double-roll state [11], which in our considered cases appears most often for $Ra = 10^6$. Rotation is able to change the picture completely. Exemplarily, this is shown for $Ra = 10^8$ and $10.0 \geq Ro \geq 0.05$ in Fig. 2. For $Ro \geq 1.0$, i.e. low rotation rates, there is no obvious change in the instantaneous flow fields, but we will elaborate below, that a weak background rotation will nonetheless stabilise the flow and make the LSC longer-lived. For $Ro = 0.5$ and $Ro = 0.1$ the plumes become more elongated and they do no longer solely ascend and descend close to the wall, but also in the bulk. Despite that, we never obtain the distinctive columnar vortex structures, extending from the bottom to the top, as is the case for higher Pr [8]. For very fast rotation, $Ro = 0.05$, all turbulent features are suppressed and the flow resembles again an LSC, but now being twisted [10]. This alteration of the flow with Ro has significant influence on the heat transport, as we will show in the following.

3.2 Heat Transport

The Nusselt number Nu, characterising the dimensionless heat transport, is one of the most important quantities in turbulent Rayleigh–Bénard convection, and definitely the one, which received most attention in recent years. Of special interest here is the dependence on Ra, and in the rotating case on Ro. The most striking feature is actually the lack of the well-known heat transfer enhancement, found in experiments and

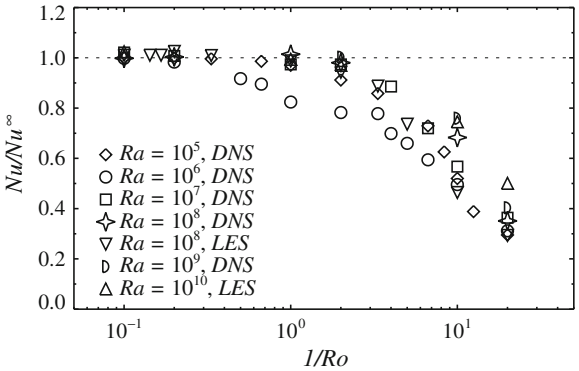

Fig. 3 The Nusselt number Nu for rotating Rayleigh–Bénard convection normalised by the Nusselt number in the non-rotating case Nu^{∞} as function of the inverse Rossby number $1/Ro$ for different Ra. Shown are DNS results for $10^5 \leq Ra \leq 10^9$ and LES results for $Ra = 10^8$ and 10^{10}

numerical simulations of water [3, 10, 12]. The reason for this lies in the less effective Ekman pumping for lower Prandtl numbers, as in our case $Pr = 0.8$. Since the diffusivity of the fluid is higher, the columnar vortices are short, as discussed above, thus heat is not transported efficiently but spreads out in the bulk. The dominating effect of rotation for $Pr = 0.8$ is, thus, the suppression of turbulent motion and the stabilisation, as predicted by the Taylor–Proudman theorem. This implies, that the Nusselt number decreases for $Ro < 1.0$, and the switching between single-roll and double-roll states is suppressed, leading to an at least slight increase of Nu for $Ro > 1.0$. Overall, the general behaviour of Nu with Ra presented in Fig. 3 is very similar for all Ra, only for $Ra = 10^6$ some larger deviation can be seen, probably because the switching between single-roll and double-roll states happens most frequently in that case. Furthermore, however, the employed LES model is less reliable for $Ro \approx 0.1$, i.e. the point, when short columnar vortex structures occur, thus more sophisticated approaches might be necessary in that case.

3.3 Strength and Precession of the Large Scale Circulation

To further investigate the persistency of the LSC, and also with regard to a planned comparison with the experiment, we perform an analysis of the temperature distribution at the sidewalls. For this purpose, we place n numerical probes at $r = R$ and at half height, $z = H/2$, similar as with thermistors in conventional experiments [1]. Every half time unit, the following function is fitted, $T_f(r = R, z, \phi) = T_w - \delta_0 \cos\left(\frac{2i\pi}{n} - \phi_0\right)$, where T_w is the mean temperature at the wall at this instant in time; the amplitude δ_0 and the orientation ϕ_0 of the LSC are fit parameters. In experiments, the number of thermistors is typically 8, while in numerical simulations we can choose n to be up to the full azimuthal resolution. However, our study has

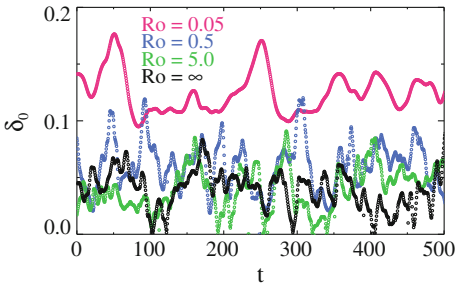

Fig. 4 Amplitude δ_0 for $Ra = 10^8$ and three different Ro and the non-rotating case $Ro = \infty$

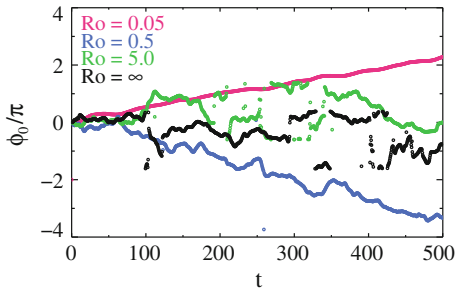

Fig. 5 Orientation ϕ_0 of the LSC, belonging to the amplitudes δ_0 in Fig. 4

shown, that at least up to $Ra = 10^9$, eight sensors are indeed sufficient to capture the general trend of the orientation and the strength of the LSC.

Figure 4 shows that the amplitude δ_0 and hence, the strength of LSC increases with decreasing Ro, which further confirms the stabilising effect of rotation. This also agrees well with the qualitative observation in Fig. 2, that the flow becomes more organised with faster rotation. The corresponding orientation angels ϕ_0 of the LSC are shown in Fig. 5. They reveal certain salient features. For $Ro = \infty$ several discontinuities exist, which indicate state changes, i.e. reversals or a switch from a single-roll to a double-roll state. For $Ro = 5.0$ fewer discontinuities show up, and for $Ro = 0.5$ they are completely gone. Furthermore, for $Ro = 0.5$ it becomes clear, that the LSC rotates in opposite direction to the applied outer rotation, i.e. it is slower. This precession motion of the LSC is caused by the confinement due to the cylinder sidewall [4]. However, a suprising observation is, that for $Ro = 0.05$ apparently the LSC rotates faster than the outer rotation.

To study this unexpected behaviour in more detail, we compare the temperature T and azimuthal velocity u_ϕ distribution for $Ro = 0.5$ (Fig. 6a, b) with the ones for $Ro = 0.05$ (Fig. 6c, d). The T fields show the already discussed twisting of the LSC, but more interestingly, the u_ϕ fields for $Ro = 0.05$ show a thin layer at the sidewalls with u_ϕ directed in opposite way than in the interior. Noteworthy is, that this characteristic is absent in the case of $Ro = 0.5$. This might have serious consequences for experimental sidewall measurements. First, they might give wrong results concerning the actual LSC orientation, and secondly, the measured orientation

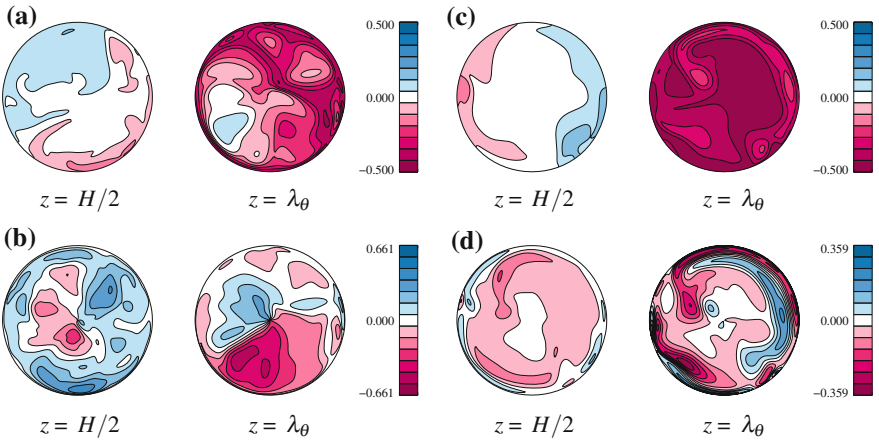

Fig. 6 Cross-sections of the temperature T and the azimuthal velocity u_ϕ at half height of the cylinder, $z = H/2$, and at the edge of the lower thermal boundary layer, $z = \lambda_\theta$, for $Ra = 10^8$ and $Ro = 0.5$ and $Ro = 0.05$, respectively. (**a**) Temperature T for $Ro = 0.5$, (**b**) Azimuthal velocity u_ϕ for $Ro = 0.5$, (**c**) Temperature T for $Ro = 0.05$, (**d**) Azimuthal velocity u_ϕ for $Ro = 0.05$

would also depend on the size of the thermistors, whether they are nested within the layer, or whether they reach far enough into the bulk.

4 Summary

A series of DNS and LES has been conducted to study the effect of rotation ($10.0 \leq Ro \leq 0.05$) on turbulent Rayleigh–Bénard convection in a slender cylinder with $\Gamma = 1/2$ filled with a fluid with $Pr = 0.8$, for a Ra-range of $10^5 \leq Ra \leq 10^{10}$. Rotation stabilises the flow, thus the switching between single and double roll states, induced by the small aspect ratio, is suppressed. As a result Nu is slightly higher for high Ro. For lower Ro, the LSC persists for all times, but because of the small Prandtl number, no heat flux enhancement due to Ekman pumping is found. Furthermore, sidewall measurements have been performed to mimic experiments, showing apparent different precession directions of the LSC depending on Ro. However, for $Ro = 0.05$ this is caused by a thin layer at the sidewalls with an azimuthal velocity component pointing in opposite direction as in the bulk.

Acknowledgments The authors acknowledge support by the German Research Foundation within the CRC 963 *Astrophysical Flow Instabilities and Turbulence*.

References

1. Brown, E., Ahlers, G.: Temperature gradients, and search for non-Boussinesq effects, in the interior of turbulent Rayleigh-Bénard convection. EPL **80**, 14001 (2007)
2. He, X., Funfschilling, D., Nobach, H., Bodenschatz, E., Ahlers, G.: Transition to the ultimate state of turbulent Rayleigh-Bénard convection. Phys. Rev. Lett. **108**, 024502 (2012)
3. Horn, S., Shishkina, O., Wagner, S.: The influence of non-Oberbeck-Boussinesq effects on rotating turbulent Rayleigh-Bénard convection. J. Phys. Conf. Ser. **318**, 082005 (2011)
4. Kunnen, R.P.J., Clercx, H.J.H., Geurts, B.J.: Breakdown of large-scale circulation in turbulent rotating convection. EPL **84**, 24001 (2008)
5. Leonard, A.: Energy cascade in large eddy simulations of turbulent fluid flows. Adv. Geophys. **18A**, 237–248 (1974)
6. Shishkina, O., Wagner, C.: A fourth order accurate finite volume scheme for numerical simulations of turbulent Rayleigh-Bénard convection in cylindrical containers. C. R. Mec. **333**, 17–28 (2005)
7. Shishkina, O., Wagner, C.: Local heat fluxes in turbulent Rayleigh-Bénard convection. Phys. Fluids **19**, 085107 (2007)
8. Stevens, R.J.A.M., Clercx, H.J.H., Lohse, D.: Optimal Prandtl number for heat transfer in rotating Rayleigh-Bénard convection. New J. Phys. **12**, 075005 (2010)
9. Stevens, R.J.A.M., Lohse, D., Verzicco, R.: Prandtl and Rayleigh number dependence of heat transport in high Rayleigh number thermal convection. J. Fluid Mech. **688**, 31–43 (2011)
10. Weiss, S., Ahlers, G.: The large-scale flow structure in turbulent rotating Rayleigh-Bénard convection. J. Fluid Mech. **688**, 461–492 (2011)
11. Xi, H.-D.: X. K.-Q.: Flow mode transitions in turbulent thermal convection. Phys. Fluids **20**, 055104 (2008)
12. Zhong, J.-Q., Stevens, R.J.A.M., Clercx, H.J.H., Verzicco, R., Lohse, D., Ahlers, G.: Prandtl-, Rayleigh-, and Rossby-number dependence of heat transport in turbulent rotating Rayleigh-Bénard convection. Phys. Rev. Lett. **102**, 044502 (2009)

Large-Eddy Simulation of Flow and Heat Transfer Around a Low-Mach Number Turbine Blade

N. Maheu, V. Moureau and P. Domingo

1 Introduction

In the last decades, the compression ratio in aeronautical gas turbines has been in constant increase. In the ideal Brayton cycle, an increase of the pressure ratio directly leads to an increase of the thermodynamic efficiency and subsequently to a decrease of the specific fuel consumption. Unfortunately, this pressure ratio growth causes a direct increase of the temperature ratio through the turbine stages, which may impact the design of turbine blades. Large-Eddy Simulation (LES) is a promising tool for the prediction of heat transfer on turbine blades. However, wall treatment in LES is a well-known issue mainly related to the high resolution required to capture near-wall phenomena. Several strategies have been proposed to tackle this issue. In the thin-boundary layer (TBL) model [1] or in detached-eddy simulations (DES) [8], a different set of equations is solved in the near-wall region. Another solution is to impose the viscous and thermal fluxes at the wall assuming that the velocity and the temperature in the near-wall region follow the law-of-the-wall. However, the model choice may have a dramatic influence on local pressure losses and heat transfer and as a consequence improvements are still needed to achieve a better reliability of the closures. The present study relies on the creation of a highly refined LES database, in order to gain insight into the flow physics of heat transfer in turbine blades.

N. Maheu (✉) · V. Moureau · P. Domingo
CORIA, CNRS UMR-6614, 76801 Saint Etienne du Rouvray, France
e-mail: nicolas.maheu@coria.fr

V. Moureau
e-mail: vincent.moureau@coria.fr

P. Domingo
e-mail: pascale.domingo@coria.fr

J. Fröhlich et al. (eds.), *Direct and Large-Eddy Simulation IX*,
ERCOFTAC Series 20, DOI 10.1007/978-3-319-14448-1_45

2 Construction of the Database

In the present work, highly-refined simulations of a low-Mach number turbine blade, namely the T7.2 blade designed by MTU Aero Engines, are performed. A detailed experimental investigation of this blade was conducted by Ladisch et al. [4]. Measurements were performed in an atmospheric linear cascade facility, which allowed for a variation of the free-stream Reynolds number and turbulence intensity. The Reynolds number based on the chord is 150,000 with a turbulence injection rate of 6 %. The blade, which is immersed in a hot turbulent flow at $T_{in} = 350\,\mathrm{K}$, is internally liquid-cooled in order to maintain a nearly constant wall temperature of $T_w = 290\,\mathrm{K}$. The chosen turbine blade design is typical of a cooled low-pressure turbine blade with moderate to nearly high loading. The intent of the design was to generate a large flow separation zone on the blade pressure side.

The computations are carried out with the YALES2 solver [5] with a variable-density low-Mach number formulation of the Navier-Stokes equations. The dynamic Smagorinsky model [6] has been used to close the subgrid transport for the velocity, and a constant turbulent Prandtl number is assumed ($\mathrm{Pr}_t = 0.7$). A fourth-order finite-volume spatial scheme for unstructured meshes has been used. The temporal advancement is fourth-order in time, implicit for diffusion and explicit for advection. The simulation database consists of LES with increasing resolutions that are summarized in Table 1. All the meshes are tetrahedron-based. Figure 1 presents the topology followed by all the meshes. One node of thirty-five of the first mesh is shown.

Table 1 Description of the computational database

Mesh	Cell count	Min. cell size (μm)	Max. y^+ (−)	Number of flow-through times
M1	35M	30	24	19.5
M2	280M	15	20	33
M3	2.2B	7.5	14	11.1
M4	18B	3.75	4	1.0

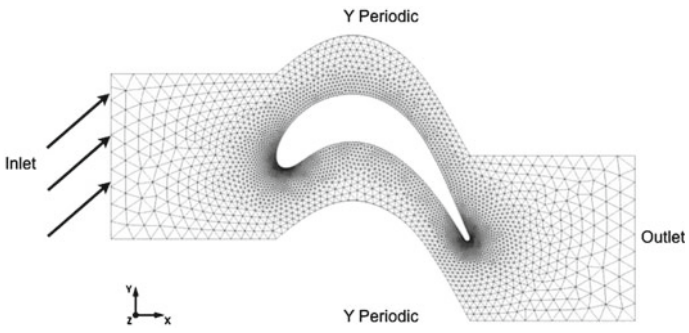

Fig. 1 Side view of the mesh topology of the T7.2 blade

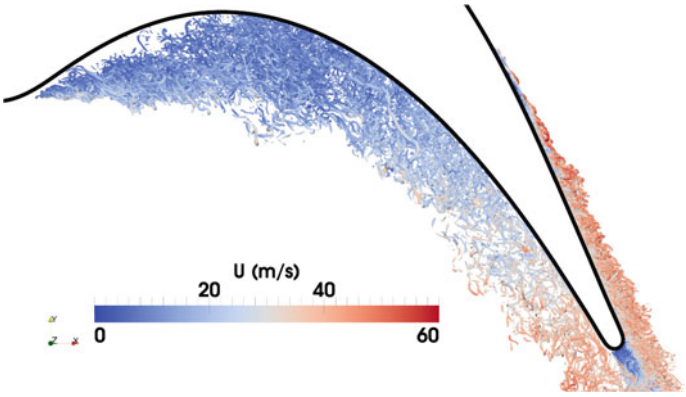

Fig. 2 Turbulent structures around the blade with the M4 mesh. iso-Q criterion $1.5625 \times 10^9\ \mathrm{s}^{-2}$

y^+ is the nondimensional distance from the wall defined as

$$y^+ = \frac{y_n u_\tau}{\nu} = \frac{y_n}{\sqrt{\nu}} \sqrt{\left.\frac{\partial u}{\partial y_n}\right|_w} \tag{1}$$

with y_n the distance from the wall in the wall normal direction, u_τ the friction velocity, ν the kinematic viscosity and u the streamwise velocity in the local blade coordinates.

As illustrated in Fig. 2, where coherent structures are represented by an iso-contour of Q-criterion on the M4 mesh, the flow around the blade features a transition of the boundary layer from laminar to turbulent on the suction side, due to the adverse pressure gradient met in this area of the blade. The large separation zone on the pressure side is also clearly visible.

3 Comparison Between Computations and Experimental Results

In order to assess the mesh resolution of the computations for heat transfer prediction, a Nusselt number based on the resolved fields is investigated and compared to the experimental values. This Nusselt number plotted in Fig. 3 is computed using the resolved temperature gradient, i.e. the value of the temperature $\widetilde{T}$ provided by the resolution of the LES equations at the first node in the fluid from the wall,

$$Nu = \frac{(\nabla \widetilde{T})C}{T_{in} - T_w} \tag{2}$$

where T_{in} and T_w are the inlet and wall temperatures, respectively. This Nusselt number is used here as a resolution indicator, as it is computed without taking into

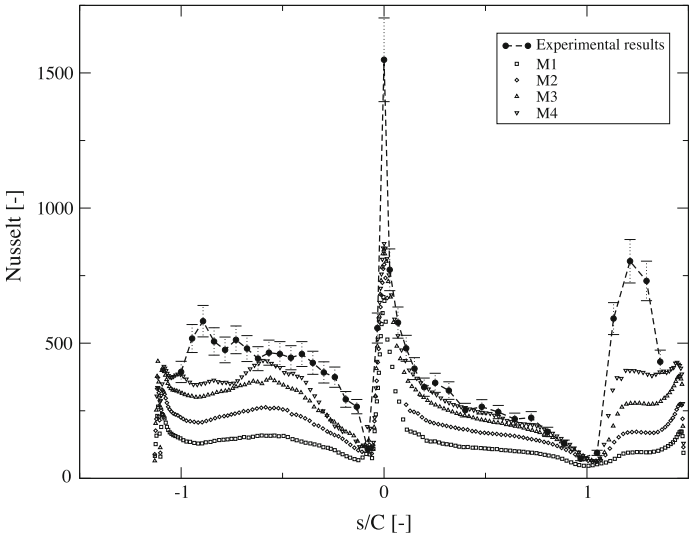

Fig. 3 Evolution of the Nusselt number based on the resolved gradient with the level of refinement of the meshes

account the sub-grid scale contribution of the temperature flux. The evolution of the Nusselt number for the four levels of mesh refinement is depicted in Fig. 3.

The Nusselt number is plotted as a function of s/C, s being the curvilinear abscissa and C the chord length equal to 7.39 cm for this blade. $s/C = 0$, $s/C < 0$, $s/C > 0$ correspond to the stagnation point, the pressure side and the suction side, respectively. For the two finest meshes that have been converged, i.e. M3 and M4, the resolution of the temperature gradient is good enough to capture the heat transfer in most areas: in the laminar and turbulent layers on the suction side with the correct position of the transition at $s/C = 1.1$ and in the recirculation zone on the pressure side. However, at the stagnation point where the strongest gradient is met, even if the y^+ is small the experimental value of the Nusselt number is not recovered.

4 Focus on the Turbulent Boundary Layer of the Suction Side

The transition from laminar to turbulent boundary layer flow on the suction side follows features of a by-pass transition scenario. Figure 4 presents an isosurface of the nondimensional temperature $Z = 0.5$, with $Z = (T - T_w)/(T_{in} - T_w)$ that can be used as a turbulence marker. This flow visualization allows to understand that the free stream turbulence disturbs the laminar shear layer and, in combination with the streamwise pressure gradient, induces transition.

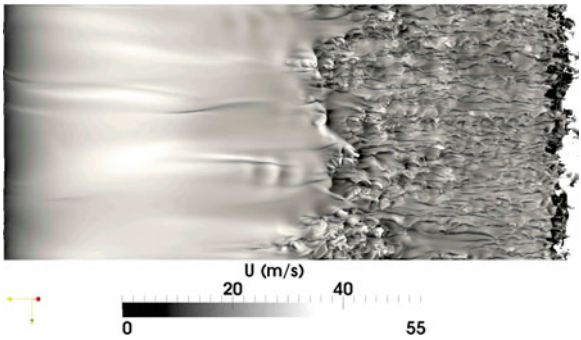

Fig. 4 Isosurfaces of temperature Z = 0.5 at the suction side of the M4 colored using the magnitude of the instantaneous velocity

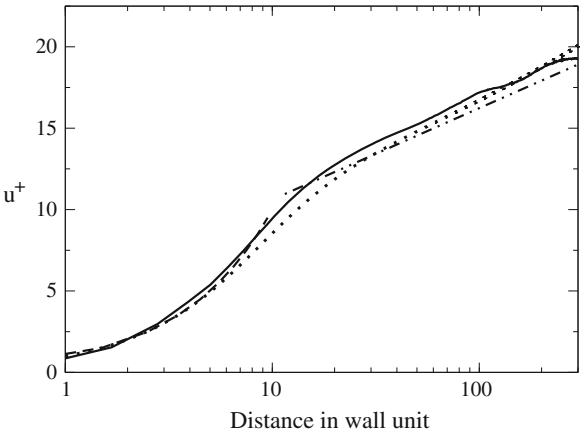

Fig. 5 Mean velocity profiles at 98 % of the curvilinear abscissa of the suction side. Mesh M4. *Line* present LES; *dashed* $u^+ = y^+$; *dashed-dotted-dotted* $u^+ = ln(y^+)/\kappa + C$; *dotted* Duprat law

The mean streamwise velocity profile in the blade coordinates is plotted in Fig. 5 for the M4 grid. It is compared with the classical analytical laws, namely the linear law for $y^+ < 10$ and the log-law for $y^+ > 14$. The values of the constants come from [6]. The velocity profile from our computation is in very good agreement with these laws. We also present a comparison with the law derived by Duprat et al. [2] which takes into account the streamwise pressure gradient via a pressure velocity proposed by Simpson [7]: $u_p = \left|\frac{\nu}{\rho}\frac{\partial p}{\partial x}\right|^{1/3}$. In Fig. 5, the mean velocity is non-dimensionalized by u_τ. The results are in very good agreement with this law, highlighting the fact that on such a configuration the streamwise pressure gradient has a noticeable effect on the dynamics of the boundary layer. Figure 6 presents the temperature profile which shows very good agreement with the classical log-law adapted to temperature via the laminar Prandtl number for the viscous sub-layer, and using a different set of constants, namely $\kappa_\theta = 0.47$ and $C_\theta = 3.3$ for the log-layer.

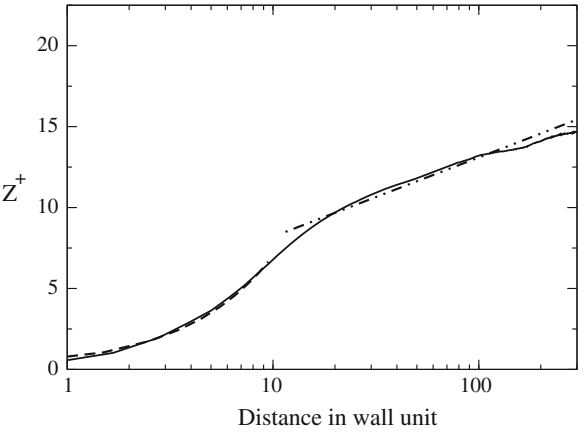

Fig. 6 Mean temperature profiles at 98 % of the curvilinear abscissa of the suction side. Mesh M4. *Line* present LES; *dashed* $u^+ = Pr\ y^+$; *dashed-dotted-dotted* $u^+ = ln(y^+)/\kappa_\theta + C_\theta$

Acknowledgments Computational time was provided by GENCI (Grand Equipement National de Calcul Intensif) under the allocation x2012026880 at IDRIS (CNRS) and by PRACE in the MS-COMB project at TGCC (CEA).

References

1. Balaras, E., Benocci, C., Piomelli, U.: Two-layer boundary conditions for large-eddy simulations. AIAA J. **34**, 1111–1119 (1996)
2. Duprat, C., Balarac, G., Métais, O., Congedo, P.M., Brugière, O.: A wall-layer model for large-eddy simulations of turbulent flows with/out pressure gradient. Phys. Fluids **22**, 1–12 (2010)
3. Germano, M., Piomelli, U., Moin, P., Cabot, W.: A dynamic subgrid scale eddy viscosity model. Phys. Fluids **3**, 1760–1765 (1991)
4. Ladisch, H., Schultz, A., Bauer H.-J.: Heat transfer measurement on a turbine airfoil with pressure side separation. In: ASME Turbo Expo, Orlando, Florida, USA (2009)
5. Moureau, V., Domingo, P., Vervisch, L.: Design of a massively parallel CFD code for complex geometries. Comptes rendus de Mécanique **339**, 141–148 (2011)
6. Schlichting, H.: Boundary Layer Theory, 8th edn. Springer, Berlin (2000)
7. Simpson, R.L.: A model for the backflow mean velocity profile. AIAA J. **21**, 142 (1983)
8. Spalart P.R., Jou W.H., Strelets M., Allmaras S.R.: Comment on the feasibility of LES for wings and on the hybrid RANS/LES approach. In: Advances in DNS/LES, 1st AFOSR International Conference on DNS/LES. Greyden Press, Columbus, pp. 4–8 (1997)

Part IX
Aerodynamics and Fluid-Structure Interaction

Large-Eddy Simulations for Wind Turbine Blade: Dynamic Stall and Rotational Augmentation

Y. Kim, I.P. Castro and Z.T. Xie

1 Introduction

Wind turbines operate in the atmospheric boundary layer and their rotating mechanisms provide complicated aerodynamic phenomena within their operating environments. When the upstream wind is uniform and normal to the plane of a rotating blade, rotational effects (i.e. rotational augmentation) emerge. Rotational augmentation means that stall occurs at a higher angle of attack on the rotating blade section than it does on an analogous stationary airfoil. It is conjectured that the rotational augmentation is a main reason for the deviations between the predicted and measured performance of wind turbines [9]. Understanding the mechanism for rotational augmentation is important to design prediction models. At yaw, the blades operate in periodically oscillating condition and dynamic stall is dominant on the flow around the blade. The generated force accumulates fatigue loads reducing the life cycle of wind turbines. In this study, dynamic stall and rotational augmentation are investigated using large-eddy simulations (LES). In particular, the effect of freestream turbulence on the dynamic stall hysteresis is studied by using the recently developed divergence-free turbulence inflow generation method [6]. Up to our knowledge, this is the first numerical study on the effect of freestream turbulence on dynamic stall.

Y. Kim (✉) · I.P. Castro · Z.T. Xie
Faculty of Engineering and the Environment, University of Southampton, Southampton, UK
e-mail: yusik.kim@soton.ac.uk

I.P. Castro
e-mail: i.castro@soton.ac.uk

Z.T. Xie
e-mail: Z.Xie@soton.ac.uk

J. Fröhlich et al. (eds.), *Direct and Large-Eddy Simulation IX*,
ERCOFTAC Series 20, DOI 10.1007/978-3-319-14448-1_46

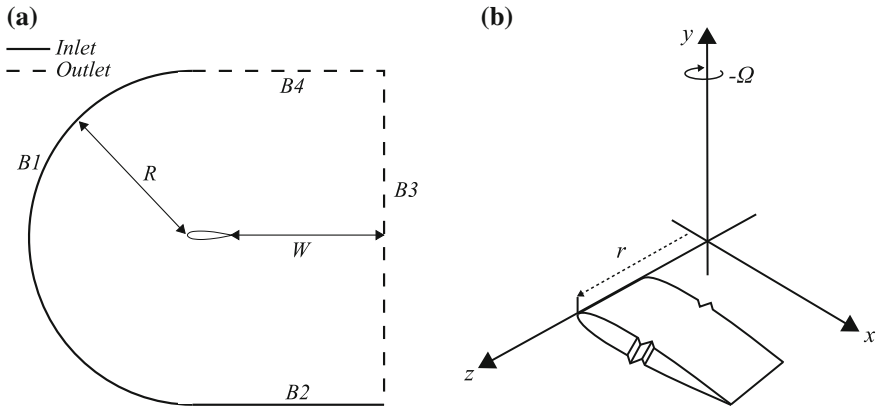

Fig. 1 Schematics of **a** the domain and boundary conditions (not to scale) and **b** coordinate system on the rotating blade

2 Methodology

A NACA 0012 airfoil was used for both the dynamic stall and rotational augmentation studies. A dynamic mesh was used for the former and a rotating reference frame was applied for the latter to model the motions. A common methodology for both studies is described first, then details will be explained in the following sections. A Reynolds number $Re = U_\infty c/\nu = 135{,}000$ was used where U_∞ is the freestream velocity and c is the chord length. The domain size was $R = 22c$, $W = 33c$ (see Fig. 1a). The mixed-time-scale (MTS) SGS model [3] was used and a simple top-hat filter was applied for the explicit filter in the MTS model.

A second order, implicit scheme was used for the time derivative and the second order bounded scheme was used for the convection term. The finite volume based, transient incompressible flow solver from OpenFOAM was used and the PIMPLE (SIMPLE + PISO) algorithm was used for the velocity-pressure coupling. Constant velocity components and zero pressure gradients were imposed on the inlet boundary and zero velocity gradients and a constant pressure were imposed on the outlet boundary. Note that the x and y coordinates (with the origin at the leading edge of the airfoil) used throughout all simulations represented the streamwise and cross-flow directions respectively.

3 Dynamic Stall

Dynamic stall is a phenomenon associated with an unsteady airfoil (or lifting surface) motion that presents large hysteresis on lift, drag and pitching moment while the incidence is beyond its static stall angle. For the dynamic stall study, a pitching airfoil was simulated by using a dynamic mesh [4]. The pitching motion was described by

$\alpha(t) = 10° + 15°\sin(\omega t)$. The reduced frequency, $k_{red}(= \frac{\omega c}{2U_\infty})$, was 0.05 where ω was the pitching frequency. This frequency is typical operating conditions for wind turbines.

Prior to the current study, the effect of freestream turbulence on flow over a static NACA 0006 airfoil was investigated [5]. It showed that the separation bubble near the leading edge was diminished by upstream turbulence; the reattachment point changed from $x/c = 0.445$ to $x/c = 0.089$ for laminar and turbulent ($TI = 10\,\%$) inflows respectively. The effect of freestream turbulence on the flow over a pitching airfoil is reported here. The divergence-free turbulence inflow model [6] was applied on a 2-D transverse plane placed at $7c$ upstream from the leading edge. Having solved momentum equation by using the pressure and flux at previous time level, the divergence-free condition was achieved by inserting synthetic turbulence before the continuity (Poisson) equation was solved. Then the final turbulence field was divergence free. The turbulence intensity (TI) was set to 10 % and it decayed along the streamwise direction as freestream turbulence contained no shear forcing. The turbulence intensity at the leading edge location was $TI = 6.3\,\%$, and kept nearly constant down to the trailing edge location when the airfoil was not placed in the domain.

A strong shear layer is developed near the leading edge. It is important that the mesh is fine enough to capture the shear layer. Thus the effects of the resolution in the cross-flow and chordwise directions were tested, then the optimal mesh was chosen. The number of grid points was $738 \times 205 \times 20$ in the circumferential, cross-flow and spanwise directions respectively. The first wall-off grid points were located at $y_1 \approx 2 \times 10^{-4}c$, which corresponded to $y^+_{1,\max} \approx 1.5$ near the maximum lift angle, $\alpha = 19.2° \uparrow$ (pitch-up). The domain width was set to $L_z = 0.5c$ and a symmetric boundary condition was applied in this direction as the periodic boundary condition could not be used due to the dynamic mesh. Note that adopting $L_z = 1c$ showed no noticeable difference in the force hysteresis compared with $L_z = 0.5c$.

Lift and drag coefficients for pitching airfoil cases are shown in Fig. 2. The numerical results are taken from the second cycle and two cycles were used for the phase average. The calculated lift and drag hysteresis for $TI_0 = 0\,\%$ generally show good agreement with the experimental data. The maximum lift occurs at slightly

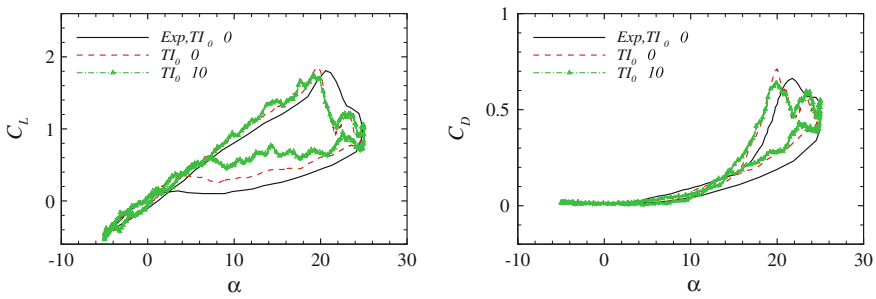

Fig. 2 The effect of freestream turbulence on the lift and drag coefficients. Note that the suffix '$_0$' indicates the input variables. Exp is taken from [7]

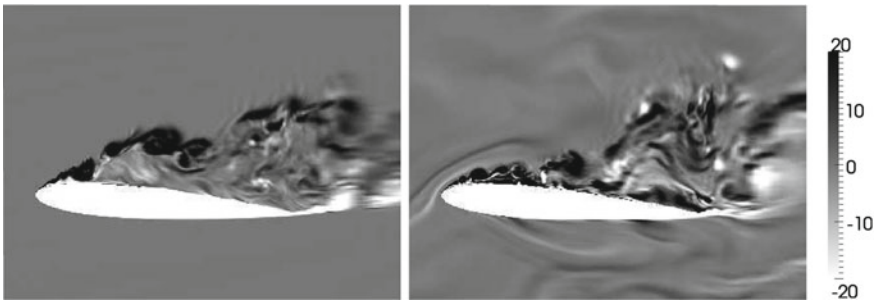

Fig. 3 Instantaneous spanwise (z) vorticity component at the mid-span at $\alpha = 14.2° \downarrow$ (pitch-down) with $TI_0 = 0\,\%$ (*left*) and with $TI_0 = 10\,\%$ (*right*). The vorticity fields are normalized by U_∞ and c

lower incidence and the hysteresis loop is smaller for the calculation than that in the experiment.

Generally freestream turbulence does not significantly change the drag and moment (not shown) hysteresis at the given conditions as shown in Fig. 2. It only slightly reduces the maximum drag coefficient, which might because the freestream turbulence suppresses the separated flows. The angles for the maximum lift and drag are nearly the same as those for case $TI_0 = 0\,\%$. However, it is evident that freestream turbulence does have an impact on the lift during the downstroke. The lift increases for the turbulence inflow case compared with that for the laminar inflow case and the increment is $\Delta C_L \approx 0.2$. This is again because the separated flow is suppressed by freestream turbulence. Similarities can be found in [1] although the setting parameters are not the same.

Figure 3 shows snapshots of the effect of freestream turbulence on the pitching airfoil during the downstroke. The separated flows are significantly suppressed by the freestream turbulence. The interactions are also found evidently in other incidence during the downstroke. These interactions lead a decrease of the separated region and an increase of the lift during the downstroke.

4 Rotational Augmentation

A sectional blade flow was simulated in rotating reference frame for the rotational augmentation study, i.e. a static mesh was used. This was because a full 3D blade simulation would be excessively expensive. Gross et al. [2] derived the governing equations in a rotating reference frame by using an order-of-magnitude analysis for the blade sectional simulation with a periodic boundary condition in the spanwise direction. The y-axis was the rotating axis with a constant angular velocity, $-\Omega$, as shown in Fig. 1b where $\mathbf{r}$ was the radial vector from the rotating axis. With $\mathbf{r} = [0, 0, r]^T$, it is assumed that r is constant for the whole domain so that the source term on the right-hand side of the Navier-Stokes equations in Cartesian coordinates is $\mathbf{f_s} = \left[2w\Omega - \frac{wu}{r}, 0, r\Omega^2 - 2u\Omega + \frac{uu}{r}\right]^T$.

The mesh convergence tests showed that a much finer mesh was required for the static airfoil case than the pitching airfoil case in Sect. 3, especially in the spanwise direction. This was because the transition point was very sensitive to the resolution for the static airfoil case. The total number of cells was about 21×10^6 with 942 grid points along the airfoil surface and 128 points were used in the spanwise direction around the airfoil. The domain width was $L_z = 0.25c$. The corresponding resolutions in wall-unit were $\Delta x^+ < 25$, $\Delta y^+ < 1$ and $\Delta z^+ < 32$ on the upper airfoil surface at $\alpha = 10°$. Averaging started once the lift coefficient reached a statistically converged state and the averaging was done over $8T$, where $T = c/U_\infty$; the time step was $t/T = 1.5 \times 10^{-4}$.

Two different flow conditions, pre- (i.e. $\alpha = 10°$) and post- (i.e. $\alpha = 14°$) stall, were simulated as baseline cases and compared with experimental data [7, 8]. Pressure coefficients are shown in Fig. 4. The peak pressure plateau, size of the bubble and separation points for the pre- and post-stall cases are predicted well compared with the reference data. Based on these stationary cases, the Rotation numbers were set to $Ro = \Omega c/U_\infty$ are 2.27 and 1.60 for pre- and post-stall cases respectively. When the flow is attached (e.g. at $\alpha = 10°$ in Fig. 4), there is little difference between the flows over the stationary and rotating airfoils. This is because the spanwise flow due to the centrifugal force is weak which leads little Coriolis acceleration. When the flow is detached (i.e. at $\alpha = 14°$), however, the spanwise flow increases, leading to a strong and favourable pressure gradient in the chord-wise direction, generated by the Coriolis force.

The mechanism for rotational augmentation has been explained mainly in two ways. Firstly, the centrifugal force pushes the air to the tip and the mass depletion due to the radial flow, thins the boundary layer thickness leading a low pressure on the suction side. Secondly, the radial flow to the blade tip provides Coriolis acceleration toward the trailing edge. This acceleration acts as favourable pressure gradient thus increases the lift. Gross et al. [2] further scrutinized that the spanwise flow provides cross-flow instability which triggers early transition thus it delays separation and the lift increases. They excluded the mass depletion effect by adopting

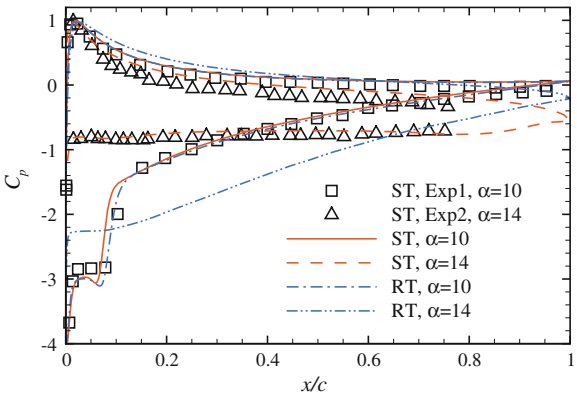

Fig. 4 Pressure coefficients from experiments (Exp1: [8], Exp2: [7]), stationary (ST) and rotating (RT) airfoil cases

the periodic boundary condition in the spanwise direction but did not discriminate the contributions between the Coriolis acceleration and cross-flow instability. In order to further specifically identify the problem, we excluded the mass depletion effect as in [2] and used a NACA 0012 airfoil rather than a S833 airfoil. The former is a leading edge separation type and the transition point is very close to the leading edge. Thus it is expected that the effect of the early transition by the cross-flow instability would be minor for this airfoil. Therefore, it is exclusively demonstrated that the Coriolis acceleration is a primary mechanism for rotational augmentation.

5 Conclusion

This paper addresses three challenging points in LES/DNS approaches for wind turbine flows, namely using dynamic mesh, inflow generation and modelling rotation augmentation. The required massive computational resources (i.e. simulations of a few cycles of pitching motion) make these tasks even more difficult in practice. Our numerical work is novel in terms of identifying the mechanism which is crucial in understanding these flows. The effect of freestream turbulence on dynamic stall is investigated using our recently developed efficient inflow generator, and is found not small which confirms the experiments in literature. In addition, the LES capability has been demonstrated for highly separated and strong 3-D flows, e.g. the dynamic stall. We exclusively identify that the effect of the Coriolis acceleration is a primary mechanism for rotational augmentation.

Acknowledgments YK acknowledges provision of a Ph.D studentship from FEE, University of Southampton. All the computations were performed on supercomputers IRIDIS3 and HECToR.

References

1. Amandolèse, X., Széchényl, E.: Experimental study of the effect of turbulence on a section model blade oscillating in stall. Wind Energy **7**, 267–282 (2004)
2. Gross, A., Fasel, H.F., Friederich, T., Kloker, M.J.: Numerical investigation of rotational augmentation for S822 wind turbine airfoil. Wind Energy **15**, 983–1007 (2012)
3. Inagaki, M., Kondoh, T., Nagano, Y.: A mixed-time-scale SGS model with fixed model-parameters for practical LES. J. Fluids Eng. **127**, 1–13 (2005)
4. Jasak, H., Tuković, Ž.: Automatic mesh motion for the unstructured finite volume method. Trans. FAMENA **30**, 1–18 (2004)
5. Kim, Y.: Wind turbine aerodynamics in freestream turbulence. Ph.D. thesis, University of Southampton (2013)
6. Kim, Y., Castro, I.P., Xie, Z.T.: Divergence-free turbulence inflow conditions for large-eddy simulations with incompressible flow solvers. Comput. Fluids **84**, 56–68 (2013)
7. Lee, T., Gerontakos, P.: Investigation of flow over an oscillating airfoil. J. Fluid Mech. **512**, 313–341 (2004)

8. Rinoie, K., Takemura, N.: Oscillating behaviour of laminar separation bubble formed on an aerofoil near stall. Aeronaut. J. **108**, 153–163 (2004)
9. Simms, D., Schreck, S., Hand, M., Fingersh, L.J.: NREL unsteady aerodynamics experiment in the NASA-Ames wind tunnel: a comparison of prediction to measurements. NREL/TP-500-29494, NREL (2001)

Unsteady Characteristic of Stall Around an Airfoil by Means of High Fidelity LES

N. Alferez, I. Mary and E. Lamballais

1 Introduction

Dynamic stall refers to the stall process of an airfoil which is moved around the critical stall angle of attack. It is a complex phenomenon and a well known constraining parameter for designers.

The most complex phenomena occur at the suction side of the airfoil. The laminar boundary layer which spreads from the stagnation point usually undergoes separation under the strong adverse pressure gradient near the point of maximum suction. This separation leads to the formation of a highly unstable local free shear layer. Therefore the transition to turbulence occurs shortly after separation leading to the reattachment of the boundary layer. A Laminar Separation Bubble (LSB) is formed. McCroskey et al. [3] spend years of experiments with static and oscillating airfoil. They reported that in the case of dynamic stall a hysteresis behaviour occurs when moving through the critical stall angle of attack. Doligalski et al. [1] reviewed vortex interaction involved during dynamic stall. They show that this hysteresis is related to the formation and advection of a large Leading Edge Vortex (LEV), and that for moderate Reynolds numbers, the origin of the LEV is linked with the LSB.

Numerous investigations focus on the LEV formation process (Visbal [5], Mulleners et al. [4]). In all these studies the influence of the dynamical effects on the LEV formation stage is explored by moving the airfoil around a wide range of angle

N. Alferez (✉) · I. Mary
ONERA - The French Aerospace Lab, Châtillon, France
e-mail: nicolas.alferez@onera.fr

I. Mary
e-mail: ivan.mary@onera.fr

E. Lamballais
PPRIME Insititute, Université de Poitiers, 11 Boulevard Marie et Pierre Curie,
86962 Futuruscope Chasseneuil, France
e-mail: eric.lamballais@univ-poitiers.fr

J. Fröhlich et al. (eds.), *Direct and Large-Eddy Simulation IX*,
ERCOFTAC Series 20, DOI 10.1007/978-3-319-14448-1_47

of attack including the critical static stall value. It is found that the unsteadiness of the motion speeds up the massive separation process.

The aim of the study described in this article is to investigate the unsteady mechanisms responsible for the growth and burst of the LSBs generated at the leading edge of an airfoil at a high angle of attack. High fidelity large eddy simulations of a NACA-0012 airfoil at moderate chord Reynolds number 10^5 are performed. The Mach number in the farfield is $M_\infty = 0.16$. The methodology is different from what we found in previous dynamic stall studies. Indeed in all these studies the airfoil is moved around a wide range of angle of attack. In consequence, the airfoil is pitch-up well above the critical static stall angle and the surrounding potential flow is still changing during the LEV formation process. In this study, the airfoil is moved in a narrow range of angle of attack around the critical stall value to avoid this issue and clearly isolate the effect of motion dynamic when passing through the critical angle. The influence of the motion dynamics on the evolution of stall is presented.

2 Numerical Methods

The conservative compressible Navier-Stokes equations are solved directly, without employing an explicit subgrid scale model. A second-order accurate centred scheme is used to approximate the viscous fluxes whereas the Euler flux discretization uses a hybrid centred/upwind version of the AUSM+(P) scheme, in which the numerical dissipation is proportional to the local fluid velocity (this slight amount of dissipation ensure the small-scale regularization) and without shock capture properties. Time integration is performed by a second order implicit Gear scheme. Newton sub-iterations are used to solve the non-linear problem, whereas the LU-SGS algorithm provides a solution of the linear system. The calculations are performed with the FUNk solver developed at ONERA. A C-type mesh with 160 million cells is employed (with adaptation in spanwise direction, see Fig. 1). The farfield is located 20 chords away from the airfoil surface and non-reflective boundary condition are imposed. The span is one chord length and periodic conditions are used in this direction. In terms of spatial resolution, the most critical conditions are expected in the turbulent boundary layer region where the friction velocity is maximum (below critical stall angle). At this location, the near-wall mesh size is $\Delta x^+ = 6$, $\Delta y^+ = 0.8$, $\Delta z^+ = 7$ where the superscript + refers to wall units. With this resolution Laurent et al. [2] have been able to provide DNS results of a laminar separation bubble using the same code.

The non-dimensional time step is $\Delta t^* = 2.75 \times 10^{-4}$ (using the farfield velocity U_∞ and the chord length c). The Newton procedure ensures a decrease of one order of magnitude of the residuals of the implicit method in all turbulent regions. The maximum CFL number is 48 whereas the convective CFL number is less than 1 everywhere in the flow. All quantities are normalized using the farfield velocity U_∞ and the chord length c.

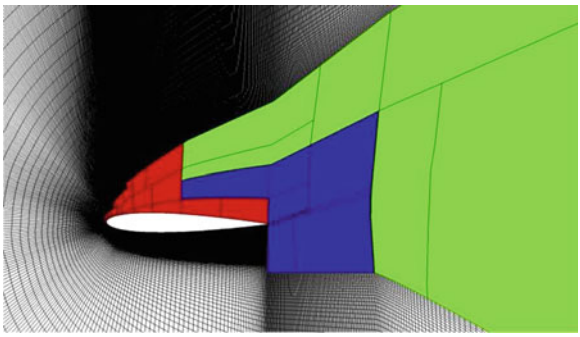

Fig. 1 View of the spanwise mesh resolution adaptation. From the wall to the farfield, 900, 300, 150 and 1 cells (2D domain) are used in the different blocks

3 Motion Parameters

LES of an airfoil undergoing a single pitch-up motion described by the Eq. (1) are performed. Zero angular acceleration $\partial^2\alpha/\partial t^2$ and velocity $\partial\alpha/\partial t$ at both the beginning and ending of the motion is imposed. The airfoil pitch axis is located a quarter chord downstream of the leading edge. In Eq. 1, α_0 and $\Delta\alpha$ stands for the initial angle of attack and the angle range of the motion, respectively. As previously mentioned, a particular attention has been paid to choose an optimal value of the angle range $\Delta\alpha$. In this study $\Delta\alpha = 0.25°$ and $\alpha_0 = 10.55°$. With this set of parameters the airfoil is moved from an attached high lift state to a fully separated stalled state within a narrow angle range. T_0 is the initial time of the motion and T_{mv} is the motion duration. In the following we investigate the influence of T_{mv} on the LSB bursting process. To achieve this, 3 different motion speeds are investigated: a base case for which $T_{mv} = 2.24$, a faster motion with $T_{mv} = 0.224$ and a slower motion velocity with $T_{mv} = 4.48$ (see Fig. 2).

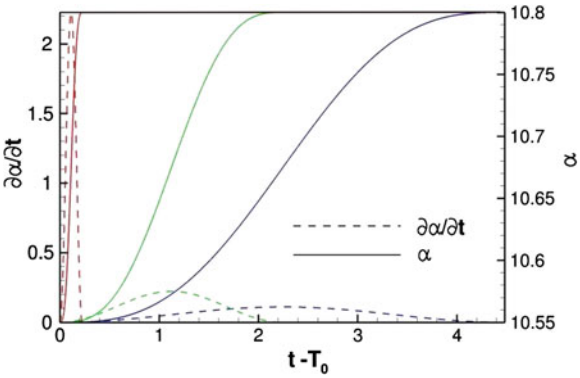

Fig. 2 Time-motion history (*plain line*) with velocity (*dash line*) for the three motion speed investigated (fast, base and slowest case)

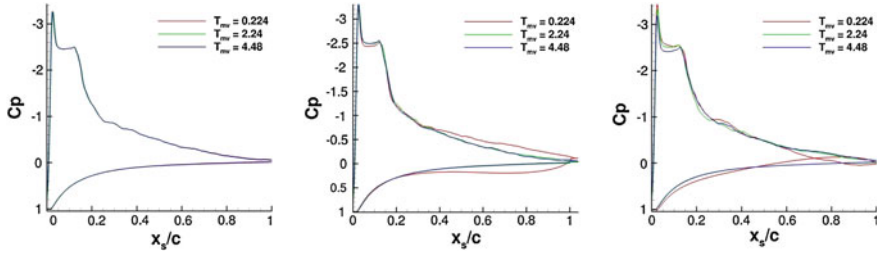

Fig. 3 Spanwise averaged pressure coefficient, at $t = T_0$, $t = T_0 + T_{mv}/2$ and $t = T_0 + T_{mv}$ (from *left* to *right*)

$$\begin{aligned} \alpha(t) &= \alpha_0 && \forall t \leq T_0 \\ \alpha(t) &= \alpha_0 + \Delta\alpha \left(\frac{t - T_0}{T_{mv}} - \frac{sin(2\pi/T_{mv}(t - T_0))}{2\pi} \right) && \forall t \in [T_0, T_0 + T_{mv}] \\ \alpha(t) &= \alpha_0 + \Delta\alpha && \forall t \geq T_0 + T_{mv} \end{aligned} \tag{1}$$

Figure 3 show the spanwise averaged pressure coefficient for the three cases at different instants during the pitch-up motion (x_s/c is the normalized curvilinear coordinate with $x_s/c = 0$ at the stagnation point). At $t = T_0$, the variation of pressure along the suction side ($Cp < 0$) reveals the presence of a short LSB (whose length is about 15 %c) characterised by the constant pressure plateau right after the leading edge suction peak. At $t = T_0 + T_{mv}/2$, no difference is seen between the base case and the slowest case in the pressure signal whereas for $T_{mv} = 0.224$ the high rotation speed enhances the suction and the pressure effect behind the point of rotation on the suction side and the pressure side, respectively. At $t = T_0 + T_{mv}$, it can be observed no significant variantions on the shape of the pressure signal for the base and the slowest case. However, for $T_{mv} = 0.224$, the vorticity generated by the high rotation speed is released into the wake leading to a crossing of the suction and pressure side pressure level. Moreover, the pressure in the LSB is no longer constant, suggesting a strong deformation of the mean velocity streamlines in this region.

4 Effects on Lift and Drag

Figure 4 shows the time evolution of the lift and drag coefficients for the three different motion velocities. The three realizations possess common features. For all the three motion speed, both lift and drag increase sharply to a large value (for $t - T_0 \approx 10$) and decrease to a stable value when the flow reaches the stall state. This behaviour is the signature of the low pressure region that is spreading along the suction side of the airfoil with the growing LSB and his subsequent evacuation into the wake. Two distinct regimes can be observed for the three realizations. A first one during which the lift coefficient stays constant and the drag grows linearly, and a second one corresponding to the fast LSB bursting process (with the previously mentioned sharp

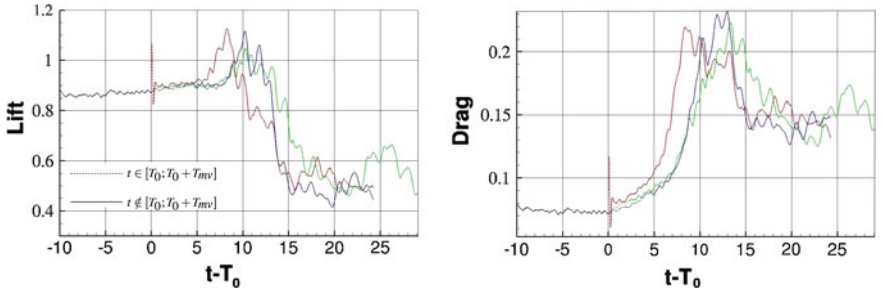

Fig. 4 Time history of lift and drag coefficient obtained for three different motion laws (*red*, *green* and *blue lines* correspond to $T_{mv} = 0.224$, $T_{mv} = 2.24$ and $T_{mv} = 4.48$)

increase of global efforts). Notable differences are observable during the motion, in particular there is a large overshoot of efforts during the fastest motion with respect to the two other motion velocities. It is a confirmation that strong dynamical effect are creating during the motion in this particular case. In spite of these strong motion differences, the two regime previously observed are quite similar in every case. Indeed the characteristic times corresponding to these two regimes are the same (around $5c/U_\infty s$ for the slow regime and $3c/U_\infty s$ for the LSB bursting) and the delay of stall observed is a more likely to be a consequence of differences between times the effective angle exceeds the critical stall angle than pure dynamical effect.

5 Effects on the LSB Bursting

Figure 5 is a space/time diagram of spanwise averaged skin friction coefficient along the suction side. Grey zones stands for reverse flow. A short LSB can be observed at the beginning of the motion for the three different motion speeds. The transition point in the LSB can be estimated near the zone of first appearance of highly time-dependent fluctuations at the wall (in the secondary recirculation zone inside the LSB). The LSB topology is kept during the whole stall process for all the three

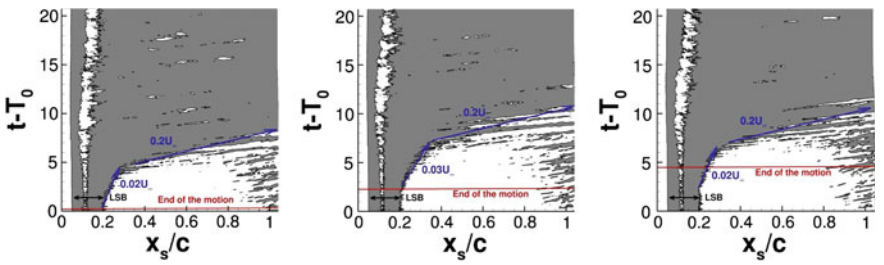

Fig. 5 Space time diagram of spanwise averaged skin friction coefficient, for $T_{mv} = 0.24$ (*left*), $T_{mv} = 2.24$ (*center*) and $T_{mv} = 4.48$ (*right*)

motion velocities investigated in this paper which confirms the idea that the stall originates from the LSB bursting. The space/time diagram gives more details about the two transient regimes previously mentioned. Blue arrows are drawn in the Fig. 5 to figure out the evolution of the LSB during these two characteristic regimes. It is found that the slow drift of the drag coefficient corresponds to a slow growth of the LSB and that the fast increase of global efforts matches the LSB bursting regime. The corresponding phase velocities of the reattachment point during each regimes is mentioned. These velocities are the same for all the motion speed investigated, confirming that the unsteadiness introduced during the motion does not affect the downstream development of the LSB. The same two regimes are observed for the three different motion speeds, the only difference is seen in the initial time of these process. As previously noted, this dependency is linked with the position of the critical angle in the range $[\alpha_0; \alpha_0 + \Delta\alpha]$, so that it is hard to quantify any possible effect of motion unsteadiness in the triggering of stall without knowing this value.

6 Conclusions

High fidelity LES of a NACA-0012 airfoil ($Re_c = 10^5$) undergoing slight pitching motion around the static stall angle of attack have been performed. It is found that the stall is originated from the abrupt leading-edge LSB bursting. Three different rotation speed have been used to examine the influence of motion unsteadiness on stall. It has been shown that, in spite of the great differences between the rotation velocities investigated, no significant distinctions on the characteristic time involved in the LSB bursting phenomenon have been observed.

Acknowledgments This work was granted access to the HPC resources of CINES under the allocation 2012/2013-c20132a7086 made by GENCI (Grand Equipement National de Calcul Intensif) and have been supported by the Direction Générale de l'Armement (DGA).

References

1. Doligalski, T., Smith, C., Walker, J.: Vortex interactions with walls. Ann. Rev. Fluid Mech. **26**, 573–616 (1994)
2. Laurent, C., Mary, I., Gleize, V., Lerat, A., Arnal, D.: DNS database of a transitional separation bubble on a flat plate and application to RANS modeling validation. Comput. Fluids **61**, 21–30 (2012)
3. McCroskey, W.J., Carr, L.W., McAlister, K.W.: Dynamic stall experiments on oscillating airfoils. AIAA J. **14**, 57–63 (1976)
4. Mulleners, K., Henning, A., Mai, A., Raffel, M., Le Pape, A., Costes, M.: Investigation of the unsteady flow development over a pitching airfoil by means of TR-PIV. AIAA Paper 2009–3504 (2011)
5. Visbal, M.R.: Numerical investigation of deep dynamic stall of a plunging airfoil. AIAA J. **49**(10), 2152–2170 (2011)

Compressible DNS of a Low Pressure Turbine Subjected to Inlet Disturbances

L.W. Chen, R. Pichler and R.D. Sandberg

1 Introduction

In modern low pressure turbines (LPT), reducing the number of airfoils in a turbine leads to an increase in the blade loading, which inevitably increases the possibility of laminar separation. Moreover, both separation bubbles and the type/location of laminar-turbulent transition are known to be sensitive to inlet disturbances. The influence of inlet disturbances has been studied experimentally with background turbulence generated by a grid and wakes by upstream moving bars in the pitchwise direction [1–3]. The first incompressible direct numerical simulation (DNS) for a turbine cascade flow was performed by Wu and Durbin [4] using prescribed wake disturbances and it was found that incoming wakes are responsible for longitudinal structures forming on the pressure side. The same inlet conditions were later applied to additional studies using incompressible DNS and large-eddy simulations (LES) [5], which have contributed further to the understanding of the effect of incoming wakes on boundary layer characteristics. More recently, Sarkar [6] performed incompressible LES using wakes generated by a precursor simulation of a cylinder flow and showed that the structure of the incoming wakes strongly affects blade performance and wake losses.

In the current paper, we are going to look into the effect of incoming bar wakes at different reduced frequencies and its combination of inflow background turbulence, and study their influences on the blade performance and loss generation.

L.W. Chen (✉) · R. Pichler · R.D. Sandberg
Aerodynamics and Flight Mechanics Research Group,
University of Southampton, Southampton SO17 1BJ, UK
e-mail: l.chen@soton.ac.uk

R. Pichler
e-mail: r.pichler@soton.ac.uk

R.D. Sandberg
e-mail: R.D.Sandberg@soton.ac.uk

J. Fröhlich et al. (eds.), *Direct and Large-Eddy Simulation IX*,
ERCOFTAC Series 20, DOI 10.1007/978-3-319-14448-1_48

2 Methodology and Computational Details

The compressible Navier-Stokes equations for the conservative variables are solved using a DNS code. The numerical method comprises a five-step, fourth-order accurate low-storage Runge-Kutta method for the time integration, state-of-the-art parallelizable wavenumber optimized compact finite differences for the spatial discretization in the streamwise and pitchwise directions and a Fourier method using the FFTW3 library for discretization of the spanwise direction. Additionally, a skew-symmetric splitting is used to stabilize the convective terms. The inflow turbulence is generated using a synthetic turbulence generation method [7, 8]. More details about the numerical method can be found in [8].

The linear turbine cascade geometry in the present work is the T106 profile experimentally investigated by Stadtmüller [9]. 9 blocks are connected using characteristic interface conditions [8], and 864 grid points are distributed along the blade surface. In the spanwise direction, the width of the computational domain was chosen as 0.2 chord lengths and 32 Fourier modes were employed with 100 % de-aliasing (using 66 collocation points in physical space), resulting in a total of 25×10^6 grid points for each simulation. The mesh resolution has been tested sufficient for DNS [8].

The isentropic Reynolds number $Re_{2is} = 60{,}000$ and the isentropic Mach number $M_{2is} = 0.405$ are kept the same for all cases. At the outlet boundary non-reflective characteristic boundary condition was applied. At the inlet boundary, a fixed inflow condition with an inflow angle of $\alpha = 46.1°$ was specified and a sponge layer, forcing the flow solution to a target state, was employed in the inlet region to remove unphysical acoustic waves [8]. To generate periodically incoming bar wakes, an immersed boundary method is implemented using feedback forcing terms proposed by Goldstein et al. [10]. In all the simulations, each cylinder bar at $x/C = -0.7$ contains 90 time-varying immersed boundary points with the diameter of $0.02C$ and the velocity in $y-$direction is $V_{bar} = -0.41$. Here, C is the blade chord length. Through changing the bar spacing, various reduced frequencies $F_{red} = f \cdot C / V_{2is}$ can be achieved, where f and V_{2is} are bar passing frequency and isentropic exit velocity, respectively. The cascade inlet measurement plane is at 30 % chord upstream the blade leading edge and outlet measurement plane at 40 % chord downstream of the trailing edge.

3 Results

The present study is aimed to investigate the effect of incoming bar wakes at different reduced frequencies and its combination of inflow background turbulence. Several typical cases are discussed, i.e. $F_{red} = 0$ cases with $Tu = 0$ and 4 % (no moving bar), $F_{red} = 0.31$ case with $Tu = 0\,\%$, and $F_{red} = 0.61$ cases with $Tu = 0$ and 4 %. For each case, the simulation was run for 5 pass through time in 2D, then 3D simulation was restarted from the fully developed 2D result. After about 10 pass through time,

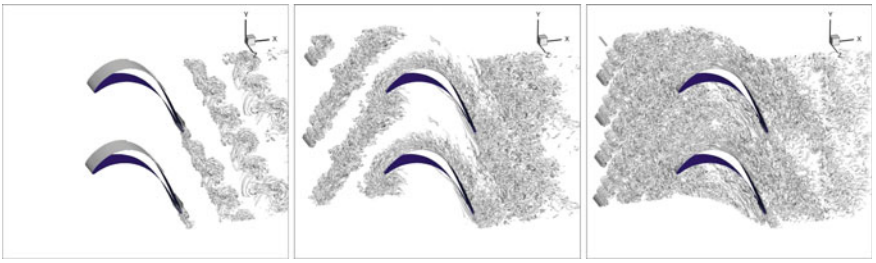

Fig. 1 Instantaneous iso-surfaces of the second invariant of the velocity-gradient tensor ($Q = 100$) for $F_{red} = 0$ (*left*), $F_{red} = 0.31$ (*middle*) and $F_{red} = 0.61$ (*right*)

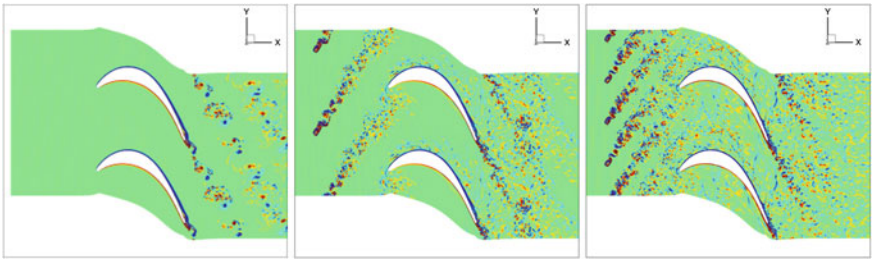

Fig. 2 Instantaneous contours of the spanwise component of vorticity (−50 to 50) for $F_{red} = 0$ (*left*), $F_{red} = 0.31$ (*middle*) and $F_{red} = 0.61$ (*right*)

to avoid the transient period, samples were then collected for 20 bar passing periods to obtain statistically meaningful turbulence properties.

To assess the existence of coherent structures, Fig. 1 shows the instantaneous snapshots of $F_{red} = 0$, 0.31 and 0.61 cases (without inflow turbulence) depicted by iso-surface of the Q criterion. In the case of $F_{red} = 0$ (or clean case), laminar flow separation in the aft section of the suction side can be observed with highly spanwise coherent vortex shedding. In the $F_{red} = 0.31$ and $F_{red} = 0.61$ cases, the bar wakes generated by moving cylinders develop downstream into highly 3D structures and interact with the blade boundary layers. Compared to the clean case, the wake downstream of the blade trailing edge look less spanwise coherence, which can also be seen when looking at instantaneous contours of the spanwise vorticity component in Fig. 2.

For more quantitative assessment of the effect of reduced frequency on the blade performance, the pressure coefficient C_p, is compared to experimental data in Fig. 3. A zoom-in view near the trailing edge also shows the differences. The result of the $F_{red} = 0$ case with $Tu = 0\,\%$ (clean case) compares well with the experimental data and the plateau near the trailing edge indicates a laminar separation bubble. For $F_{red} = 0$ with $Tu = 4\,\%$, the separation bubble shrinks and reattachment appears to occur further upstream with pressure rising to a larger value. Due to the movement of bars, the cascade inlet angles measured at $x/C = -0.3$ became 43.76° for $F_{red} = 0.31$ and 41.72° for $F_{red} = 0.61$, which lead to the differences from the clean case

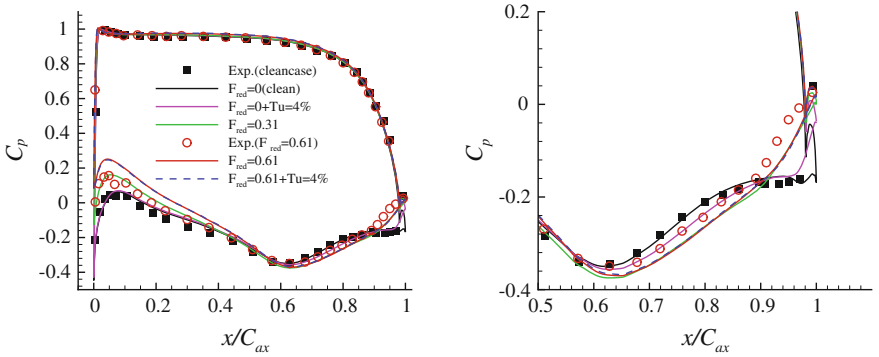

Fig. 3 Pressure coefficient distribution on the blade surface and a zoom-in view near the trailing edge. Here, C_{ax} is the axial chord length

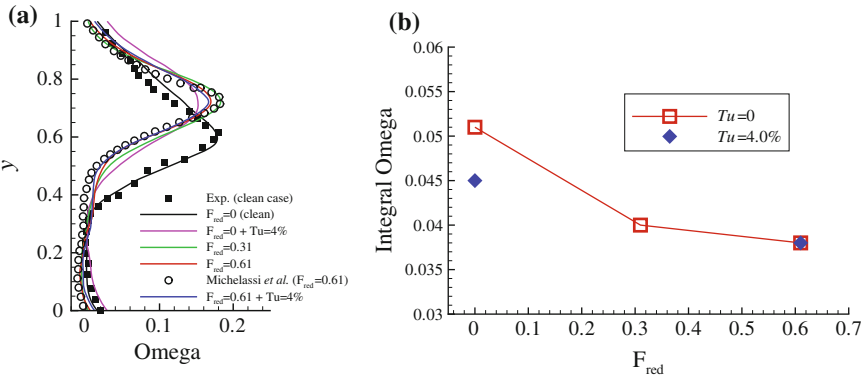

Fig. 4 Comparison of the wake stagnation pressure loss profiles with reference data (**a**) and the scalar integral of wake losses (**b**)

at the suction side. There is no noticeable difference between $F_{red} = 0.61$ with $Tu = 0\,\%$ and $Tu = 4\,\%$, and reasonable agreement with the experimental data is obtained. Aft the suction peak, it is clear that in the mean sense the incoming wakes suppressed the separation bubble. This finding was also confirmed in some incompressible DNS studies [5].

The stagnation pressure losses Ω are of the obvious importance in the engineering and also very challenging for DNS studies [8]. In Fig. 4a, the wake losses from all the cases are compared to the reference data. The coordinate y^* is a normalized scale in the pitchwise direction from the suction to the pressure side, defined as $y^* = \frac{(y-y_{max})}{(y_{max}-y_{min})}$. The result of $F_{red} = 0$ case with $Tu = 0\,\%$ matches the experimental data very well, while the $Tu = 4\,\%$ case shows a lower peak value and also the location of the peak moves closer to the pressure side. This can be explained by the change of the suction side separation bubble for the turbulent cases which leads to a different

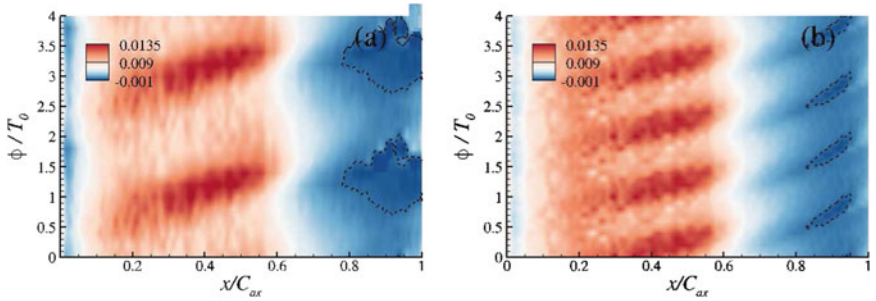

Fig. 5 Space-time diagrams of wall shear stress: **a** $F_{red} = 0.31$, $Tu = 0\,\%$; and **b** $F_{red} = 0.61$, $Tu = 0\,\%$

defect of the wake. Similar phenomena can be found for $F_{red} = 0.31$ and 0.61 cases, but the profiles of wake loss are sharper. The $F_{red} = 0.61$ case result agrees well with the incompressible one by Michelassi et al. [5] and $Tu = 4\,\%$ does not show significant difference except a broader profile at the pressure side and slightly smaller value at the suction side.

A scalar integral over pitchwise direction has been done for each wake loss profile in order to study the overall losses at different reduced frequencies. Figure 4b shows the scalar integral wake losses versus three reduced frequencies. With the increment of reduced frequency, the wake loss is dramatically reduced. Also, the influence of the inflow turbulence level is less significant in $F_{red} = 0.61$ case.

To better understand the physical process in the moving bar cases, the phase-averaged statistics have been collected during 30 bar passing periods for $F_{red} = 0.31$ and 0.61 ($Tu = 0\,\%$). Each period is divided into 10 equal phases. The phase ϕ is defined by $\phi = t/T_0 - n$, where n is an integer such that $0 \leq \phi < 1$, where T_0 is the bar passing period for $F_{red} = 0.61$. The space-time diagrams of wall shear stress τ_w on the suction side are shown in Fig. 5. In Fig. 5a, b, the 'red' regions of high wall shear from leading edge to 0.6 are the response of the laminar boundary layers to the passage of the incoming wakes. The negative value marked in dashed lines indicate the evolution of the separation bubbles. At $F_{red} = 0.31$ the separation region is larger than that of $F_{red} = 0.61$ case, corresponding to a larger wake loss generation discussed above.

4 Conclusions

Direct numerical simulations of the compressible flow pass through a low pressure turbine have been conducted to study the effect of incoming wakes generated by moving bars at different reduced frequencies as well as the combined effect with 4 % inflow turbulence level. The results compare favorably with the reference data in terms of the pressure distributions and wake losses. It is evident that with the increment of reduced frequency, the wake loss is dramatically reduced and the influence

of the inflow turbulence level is less significant in $F_{red} = 0.61$ case. The space-time diagrams of wall shear stress also show that the separation bubble can be suppressed effectively by the incoming wakes, especially at higher reduced frequency case.

References

1. Coull, J.D., Hodson, H.P.: Unsteady boundary-layer transition in low-pressure turbines. J. Fluid Mech. **681**, 370–410 (2011)
2. Engber, M., Fottner, L.: The effect of incoming wakes on boundary layer transition of a highly loaded turbine cascade. In: AGARD-CP-571 (1996)
3. Stieger, R.D., Hodson, H.P.: The unsteady development of a turbulent wake through a downstream low-pressure turbine blade passage. J. Turbomach. **127**(2), 388–394 (2005)
4. Wu, X., Durbin, P.A.: Evidence of longitudinal vortices evolved from distorted wakes in a turbine passage. J. Fluid Mech. **446**, 199–228 (2001)
5. Michelassi, V., Wissink, J., Rodi, W.: Analysis of DNS and LES of flow in a low pressure turbine cascade with incoming wakes and comparison with experiments. Flow Turb. Comb. **69**, 295–330 (2002)
6. Sarkar, S.: Influence of wake structure on unsteady flow in a low pressure turbine blade passage. J. Turbomach. **131**(4), 041016 (2009)
7. Touber, E., Sandham, N.D.: Large-eddy simulation of low-frequency unsteadiness in a turbulent shock-induced separation bubble. Theor. Comput. Fluid Dyn. **23**(2), 79–107 (2009)
8. Sandberg, R.D., Pichler, R., Chen, L.W.: Assessing the sensitivity of turbine cascade flow to inflow disturbances using direct numerical simulation. In: ISUAAAT 13, Tokyo, Japan, 11–14 Sept 2012
9. Stadtmüller, P.: Investigation of wake induced transition on the LP turbine cascade T106A-EIZ. DFG-Verbundprojekt Fo, 136/11, Version 1.0, University of the Armed Forces Munich, Germany (2001)
10. Goldstein, D., Handler, R., Sirovich, L.: Modeling a no-slip flow boundary with an external force field. J. Comput. Phys. **105**, 354–366 (1993)

Large Eddy Simulation of a NACA-0012 Airfoil Near Stall

J. AlMutairi, I. AlQadi and E. ElJack

1 Introduction

Laminar separation bubble (LSB) is a phenomenon that can greatly affect the performance of wings at a low Reynolds number. Beside the increase in drag, the dynamics of LSB can lead to undesirable effects such as flow oscillations due to bubble flapping, and abrupt airfoil stall due to bubble bursting. LSB forms when laminar flow over an airfoil is subjected to a strong adverse pressure gradient causing the boundary layer to separate from the airfoil surface. The highly receptive shear layer is prone to disturbances and goes through a transition to a turbulent flow through Kelvin-Helmholtz instability [17]. The energized flow, due to a transition to turbulence, reattaches to the airfoil surface forming the separation bubble. The length of the separation bubble is a function of Reynolds number as well as the angle of attack [6, 12]. As the angle of attack approaches the stall angle, the laminar separation bubble exhibits a quasi-periodic switching between long bubble and short bubble. The phenomenon is known as low-frequency flow oscillations. Although low-frequency flow oscillation phenomenon has been extensively studied, the underlying mechanism is still elusive. Low-frequency flow oscillations were initially reported by Zaman et al. [18]. The phenomenon was observed to cause 50 % fluctuations in lift with a Strouhal number in the order of 10^{-3} [3, 4]. Rinoie and Takemura [14] performed an experimental study of a $NACA-0012$ airfoil at a Reynolds number of 1.3×10^5 and angle of attack $\alpha = 11.5°$. They observed a low-frequency flow oscillation

J. AlMutairi (✉)
Department of Mechanical Engineering, College of Technological Studies,
70654 Shuwaikh, Kuwait
e-mail: jh.almutairi@paaet.edu.kw

I. AlQadi · E. ElJack
King Abdulaziz University, Jeddah P.O. Box 80204, 21589, Saudi Arabia
e-mail: ialqadi@kau.edu.sa

E. ElJack
e-mail: eljack@kau.edu.sa

J. Fröhlich et al. (eds.), *Direct and Large-Eddy Simulation IX*,
ERCOFTAC Series 20, DOI 10.1007/978-3-319-14448-1_49

phenomenon in which the laminar separation bubble grows and shrinks between a short bubble of about 10 % chord length near the leading edge and a long bubble resulting in fully separated flow. The availability of supercomputing capability has facilitated the investigation of laminar separation bubbles. Many studies have been performed to investigate the behavior of LSB [3–5, 9, 14, 16, 18]. However, only few simulations have been performed to capture low-frequency flow oscillations and have met with limited success [13]. The first successful simulation of low-frequency oscillations was done by Almutairi and AlQadi [1]. They investigated natural low-frequency flow oscillation phenomenon using a large eddy simulation in which they performed four simulations of flow around a $NACA-0012$ airfoil at a Reynolds number of 50, 000 and Mach number $M_\infty = 0.4$ at four angles of attack $\alpha = 9.25°$, 9.29°, 9.40°, and 9.60°. Natural low-frequency flow oscillation was detected with a quasi-periodic behaviour at $\alpha = 9.29°$ and 9.40°. They also observed an intermittent bursting of the laminar separation bubble at $\alpha = 9.25°$. At $\alpha = 9.60°$ the flow was stalled for most of the time with occasional reattachment. Averaged, as well as instantaneous turbulent flow fields, revealed that the location of transition moves downstream and away from the surface during bubble bursting and upstream and close to the surface during short bubble reformation. Pressure power spectra in the surrounding potential flow field illustrated the global effect of low-frequency flow oscillations on the flow field as a whole. The physics of bubble bursting is yet to be understood. Marxan and Henningson [10] studied bubble bursting and how it is related to airfoil stall. They argued that changes in the transition process play a major role in bubble bursting along with the viscous-inviscid interaction. They performed a systematic study of bubble response to incoming disturbances and concluded that bubble bursting occurs when incoming disturbances are switched off. Their hypothesis is that bursting takes place when saturated disturbances can't reattach the flow right after transition. Marxan et al. [11] illustrated that leading edge stall and bubble bursting can be eliminated using high-frequency zero net mass flux (ZNMF) actuators. For the current study, a large eddy simulation was performed to investigate low-frequency flow oscillation phenomenon for flow around a $NACA-0012$ airfoil at an incidence of $\alpha = 11.5°$ and a Reynolds number of 1.3×10^5 at Mach number $M_\infty = 0.4$. The simulation was validated through quantitative comparison with the experiment of Rinoie and Takemura [14]. The study's main objective is to better understand the underlying mechanism of low-frequency flow oscillation phenomenon near stall conditions.

2 Mathematical Model and Computational Setup

In Large Eddy Simulation turbulent fluctuations are decomposed into resolved large scales and unresolved small scales. The decomposition process is carried out by low-pass special-filtering. For compressible flows Favre-filtering is implemented to simplify the non-dimensional Navier-Stokes equations and retain terms corresponding to the original equations. The LES of the present study incorporates the

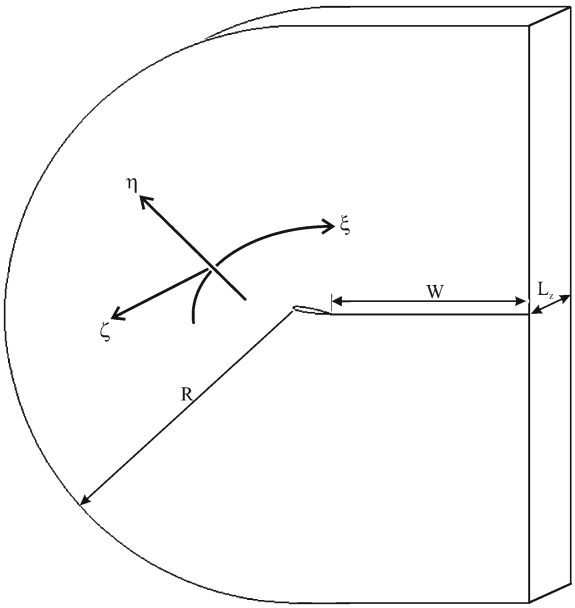

Fig. 1 Computational domain

Mixed-Time-Scale (MTS) model developed and validated by Inagaki et al. [7]. It was shown that this model can overcome the drawbacks of other SGS models by turning off in the laminar flow region and thus not requiring a wall-damping function. Subgrid terms in the energy equation were neglected for this relatively low Mach number. The LES code used in the present study has been validated extensively by Jones et al. [8] and Almutairi [2]. Details of the numerical approach can be found in Almutairi and AlQadi [1]. A grid of size $1,485 \times 500 \times 86$ was constructed around $NACA-0012$ airfoil oriented at an angle of $11.5°$. The computational domain, Fig. 1, width is set to 50 % of the chord length which was found to be necessary to obtain accurate results [1]. The grid parameters are as follows: Wake length $W/c = 5$, radius $R/c = 7.3$, and the domain length in the spanwise direction $L_z/c = 0.5$. The numbers of grid points along the curvilinear directions ξ is $N_\xi = 1{,}485$, along η is $N_\eta = 500$, and along ζ is $N_\zeta = 86$.

3 Results and Discussion

In the current study, a large eddy simulation of flow around a $NACA-0012$ airfoil was conducted at an angle of attack of $\alpha = 11.5°$ and Reynolds number of 1.3×10^5 at Mach number $M_\infty = 0.4$. The LES was performed with a time step of 1.0×10^{-4}. Figure 2 shows an isosurface of Q over the upper surface of the airfoil. From this figure, it is clear that the process of breakdown to turbulence is captured in the LES. Starting from the leading edge, the shear layer is detached from the wall with

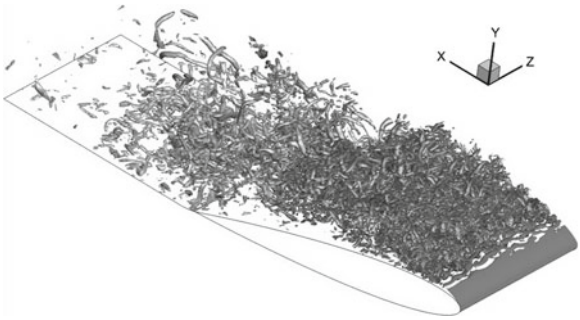

Fig. 2 Iso-surface of Q-criterion

a laminar two-dimensional behavior. The transition becomes visible where small distortions of the shear layer takes place and the three-dimensionality of the flow starts to grow. Large-scale structures form and then break down into small-scale structures followed by fully three-dimensional turbulent flow. Data was collected from the fully developed flow obtained after initializing the entire computational domain with free-stream conditions with no artificial forcing. The time history of lift, pressure drag and skin-friction coefficients are clearly oscillating in a quasi-periodic manner as shown in Fig. 3 which is an indication of the occurrence of the low-frequency flow oscillation phenomenon. The lift coefficient oscillates between 0.964 and 0.445 with an oscillation amplitude of about 73 % of the mean value, which is larger than the amplitude of the low-frequency flow oscillation for a lower Reynolds number reported by Almutairi and AlQadi [1]. This is in agreement with the observation of Almutairi [2] who found that as the Reynolds number and incidence increase, the peak-to-peak amplitude tend to increase. It is interesting to mention that the oscillation behavior of the lift coefficient obtained in the current study is more regular than that observed in the study of Almutairi and AlQadi [1]. It is observed from Fig. 3 that the lift and drag coefficients reached the maximum value at nearly the same time, with a small phase shift. The maximum value of the skin friction coefficient coincides with the minimum value of the pressure drag coefficient at which the flow is fully attached except for the laminar separation bubble near the leading edge. The spectrum of the lift coefficient as a function of Strouhal number ($St = fc\sin(\alpha)$) is computed using FFT. The dominant Strouhal number is found to be 0.00826 which is comparable to the Strouhal number of 0.008 measured by Rinoie and Takemura [14]. This implies that the current LES has successfully captured the low-frequency flow oscillations. Dynamic Mode Decomposition (DMD) [15] analysis was performed on a sample of 12,438 snapshots spanning over one low-frequency cycle. Instantaneous Pressure is recorded along the middle plane in the spanwise direction. The snapshots are taken every time step. The growth rate of the computed modes are shown in Fig. 4 as a function of Strouhal number. The modes are represented by a circle with a radius proportional to the norm of its eigenvector. We will consider only the first four dominant modes. The growth rate of the first two modes is negative which indicate decaying stable modes. However, mode 3 and 4

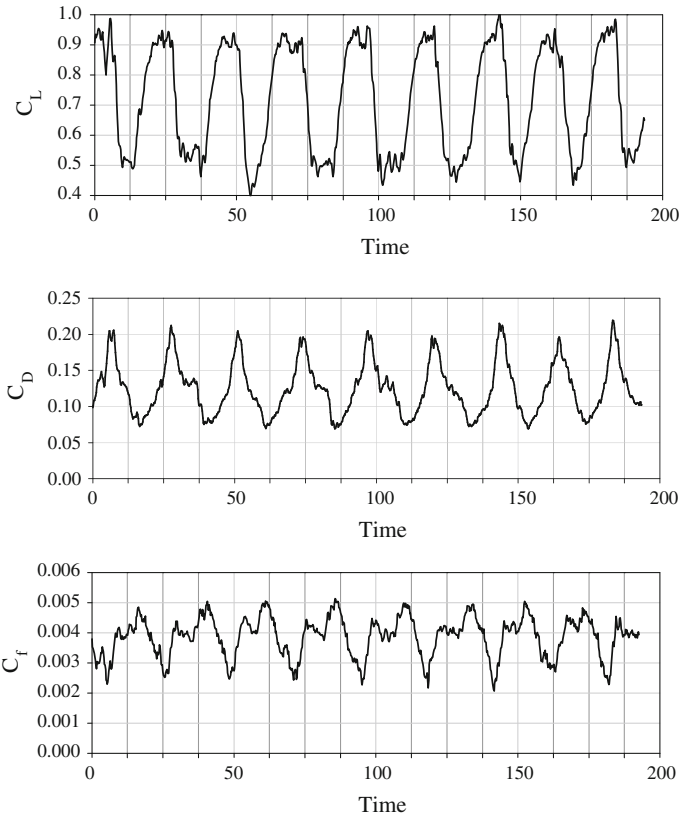

Fig. 3 Time history of C_L, C_D, and C_f

Fig. 4 DMD−spectrum of the pressure field

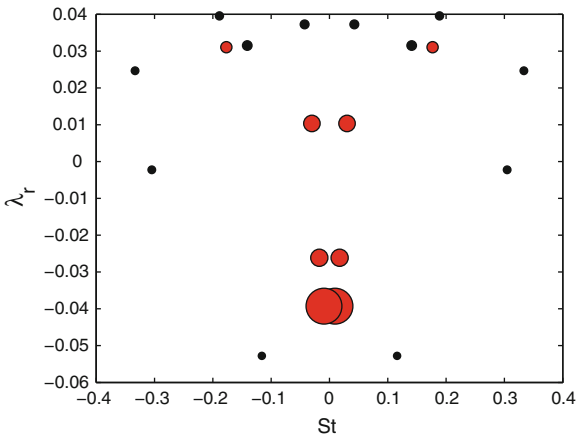

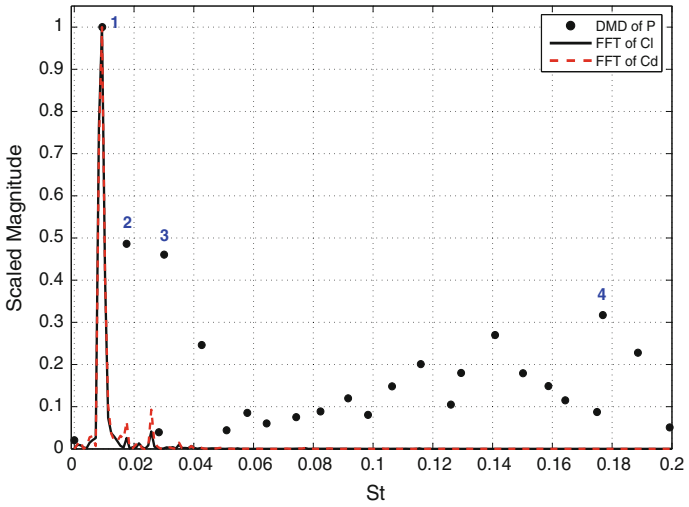

Fig. 5 Scaled amplitude of pressure's dynamic modes, FFT of C_L, and FFT of C_D Versus St

have positive growth rate hence indicating growing unstable modes. Figure 5 plots the spectrum of C_L and C_D history along with the frequencies of the DMD modes. The frequencies of the first four modes are labeled by their number in the plot. It can be easily seen that the first three modes correspond with the first three peaks in the spectrum of C_L and C_D. However, the fourth modes does not show up in the C_L and C_D spectrum. The first mode is the low-frequency oscillation mode. The 2nd and 3rd modes can be thought of as the second and third harmonic of the low frequency oscillation mode. The fourth mode is at much higher frequency. Reconstruction of the flow field corresponding to the 4th dynamic mode shows that this high frequency is due to vortex shedding at the trailing edge. In general there is good agreement between measured and computed low frequency mode (Table 1).

Animation of streamlines and turbulent kinetic energy (not shown here) reemphasize the mechanism for low-frequency oscillation which was suggested by Almutairi and AlQadi [1]. The mechanism is as follows: For an airfoil near stall conditions the flow over the upper surface undergoes a strong adverse pressure gradient causing the separation bubble to burst and leading to complete stall. During stall, vortex shedding

Table 1 Dominant modes frequencies

DMD (pressure)	FFT (C_L)	FFT (experiment)[a]
0.00839	0.00826	0.0080
0.01650	0.01650	–
0.02910	0.02470	–
0.01669	–	–

[a] Rinoie and Takemura [14]

over the upper surface creates a low pressure wake region pulling the separated shear layer at the trailing edge and accelerating the flow on the airfoil lower surface. The resulting strong vortex shedding at the trailing edge entrain the separated flow leading to reattachment and the reformation of the leading-edge separation bubble again. As the flow reattaches, the vortex shedding from the trailing edge dies down and a strong adverse pressure gradient starts to build up behind the separation bubble causing the process to repeat itself. It is therefore argued that control of trailing edge shedding can be used to prevent low-frequency flow oscillations near stall.

References

1. Almutairi, J.H.: Large-eddy simulation of flow around an airfoil at low Reynolds number near stall. Ph.D. thesis, School of Engineering Sciences, Southampton University, Southampton, UK (2010)
2. Almutairi, J.H., AlQadi, I.M.: Large-eddy simulation of natural low-frequency oscillations of separating-reattaching flow near stall conditions. AIAA J. **51**, 981–991 (2013)
3. Bragg, M.B., Heinrich, D.C., Khodadoust, A.: Low-frequency flow oscillation over airfoils near stall. AIAA J. **31**(7), 1341–1343 (1993)
4. Bragg, M.B., Heinrich, D.C., Balow, F.A., Zaman, K.B.M.Q.: Flow oscillation over an airfoil near stall. AIAA J. **34**(1), 199–201 (1996)
5. Broeren, A.P., Bragg, M.B.: Flowfield measurements over an airfoil during natural low-frequency oscillations near stall. AIAA J. **37**(1), 130–132 (1998)
6. Gault, D.: A correlation of low-speed airfoil-section stalling characteristics with Reynolds number and airfoil geometry. NACA TN 3963, 1957
7. Inagaki, M., Kondoh, T., Nagano, Y.: A mixed-time-scale SGS model with fixed model-parameters for practical LES. J. Fluid Eng. **127**(1), 1–13 (2005)
8. Jones, L.E., Sandberg, R.D., Sandham, N.D.: Direct numerical simulation of forced and unforced separation bubbles on an airfoil at incidence. J. Fluid Mech. **602**, 175–207 (2008)
9. Jones, L., Sandberg, R., Sandham, N.: Stability and receptivity characteristics of a laminar separation bubble on an airfoil. J. Fluid Mech. **648**, 257–296 (2010)
10. Marxen, O., Henningson, D.: Numerical simulation of the bursting of a laminar separation bubble. High Perform. Comput. Sci. Eng. **06**, 253–267 (2007)
11. Marxen, O., You, D., Moin, P.: Numerical simulations of the bursting of a laminar separation bubble and its relation to airfoil stall. Adv. Turbul. XI **117**, 712–714 (2007)
12. McCullough, G.B., Gault, D.E.: Examples of three representative types of airfoil-section stall at low speed. NACA TN 2502, 1951
13. Mukai, J., Enomotom, S., Aoyama, T.: Large-eddy simulation of natural low-frequency flow oscillations on an airfoil near stall. AIAA paper 2006–1417, 44th AIAA aerospace sciences meeting, Reno, Nevada, 2006
14. Rinoie, K., Takemura, N.: Oscillation behavior of laminar separation bubble on an aerofoil near stall. Aeronaut. J. **108**, 153–163 (2004)
15. Schmid, P.: Dynamic mode decomposition of numerical and experimental data. J. Fluid Mech. **656**, 5–28 (2010)
16. Tanaka, H.: Flow visualization and PIV measurements of laminar separation bubble oscillating at low frequency on an airfoil near stall. In: 24th International Congress of the Aeronautical Sciences, ICAS2004. Yokohama, Japan, 2004
17. Wissink, J.G.: Separating, transitional flow affected by various inflow oscillation regimes. ANZIAM J. **46**, 117–132 (2005)
18. Zaman, K.B.M.Q., Mckinzie, D.J., Rumsey, C.L.: A natural low-frequency oscillation of the flow over an airfoil near stalling conditions. J. Fluid Mech. **202**, 403–442 (1988)

Large-Eddy Simulation of a FSI-Induced Oscillation Test Case in Turbulent Flow

M. Münsch, A. Delgado and M. Breuer

1 Introduction

Within many technical fields like aerospace and naval engineering, civil engineering and biomedical applications, fluid-structure interactions (FSI) can be observed. Moreover, most of the flows in these fields are dominated by turbulence, which can be predicted in a reasonable manner by Large-Eddy Simulation (LES). In LES subgrid-scale models (SGS) are used to account for the effect of the small unresolved scales on the larger scales. Within a pure flow simulation SGS models and the corresponding model parameters are known to have an impact on the results obtained such as the separation and recirculation length. Thus, an impact of SGS models on the results of FSI computations in terms of amplitudes and oscillation frequencies can be expected. In this contribution the results of still ongoing investigations on the impact of SGS models and their corresponding parameters on FSI computations are presented. Based on an experimental FSI benchmark developed by Gomes and Lienhart [4], the turbulent flow at a Reynolds number of 23,423 around a swiveling cylinder with an attached splitter plate is considered. The SGS model of Smagorinsky [9] with van Driest damping, the WALE model [2] and the dynamic model of Germano et al. [3] with modifications by Lilly [5] are applied. In addition, the effect of the boundary conditions and the extension of the domain in spanwise direction is investigated.

M. Münsch (✉) · A. Delgado
Institute of Fluid Mechanics, Technical Faculty, FAU Erlangen-Nuremberg, Germany
e-mail: manuel.muensch@lstm.uni-erlangen.de

A. Delgado
e-mail: antonio.delgado@lstm.uni-erlangen.de

M. Breuer
Department of Fluid Mechanics, Helmut-Schmidt-University Hamburg,
Hamburg, Germany
e-mail: breuer@hsu-hh.de

J. Fröhlich et al. (eds.), *Direct and Large-Eddy Simulation IX*,
ERCOFTAC Series 20, DOI 10.1007/978-3-319-14448-1_50

2 Description of the Numerical Method

The present investigations are conducted with the in-house code FASTEST-3D to compute the flow field. The code was extended for the purpose of FSI in combination with LES and makes use of a finite-volume scheme to discretize the mass conservation and the Navier-Stokes equations by standard schemes on a curvilinear, block-structured and body-fitted mesh. The variables are arranged in a colocated manner in the cell-centers of the control volume (CV). A midpoint rule approximation of second-order accuracy for the integrals is applied and a linear interpolation of the flow variables to the cell faces is used. Thus, a second-order accurate central scheme is obtained. Besides a fine spatial resolution also a proper temporal resolution of the turbulent flow field is required in the framework of LES. Since explicit time-marching schemes are favored, the fluid solver is based on a predictor-corrector scheme, whereas in the predictor step a five substeps low-storage Runge-Kutta scheme of second-order accuracy advances the momentum equation in time. The pressure-velocity coupling is assured by the Rhie-Chow interpolation [8]. The moving mesh is considered via the ALE formulation of the filtered conservation equations:

$$\frac{d}{dt}\int\limits_{V(t)} \rho^f \, dV + \int\limits_{S(t)} \rho^f (\overline{u}_j - u_{g,j})\, n_j \, dS = 0 \,, \tag{1}$$

$$\begin{aligned}\frac{d}{dt}\int\limits_{V(t)} \rho^f \overline{u}_i \, dV + \int\limits_{S(t)} \rho^f \overline{u}_i (\overline{u}_j - u_{g,j})\, n_j \, dS \\ = -\int\limits_{S(t)} (\overline{\tau}_{ij} + \tau_{ij}^{SGS})\, n_j \, dS - \int\limits_{S(t)} \overline{p}\, n_i \, dS \,.\end{aligned} \tag{2}$$

The Space-Conservation Law (SCL):

$$\frac{d}{dt}\int\limits_{V(t)} dV - \int\limits_{S(t)} u_{g,j}\, n_j \, dS = 0 \tag{3}$$

is considered to determine the grid velocities $u_{g,j}$. Here, the SGS tensor τ_{ij}^{SGS} is modeled with the help of the SGS models mentioned above. Regarding the structure domain, the investigated structure shown in Fig. 1 is considered to be inflexible with a single rotational degree of freedom around the center of the cylindrical front end. The movement of the structure is specified via an ordinary equation of motion:

$$I\ \ddot{\varphi}(t) \ + \ D(\varphi)\ \dot{\varphi}(t) \ + \ C\ \sin(\varphi(t)) \ = \ M(t), \tag{4}$$

where I is the moment of inertia, D the damping coefficient and C the stiffness of the system. The angular displacement, the angular velocity and the angular acceleration are represented by φ, $\dot{\varphi}$ and $\ddot{\varphi}$. Here, the system is driven by the moment $M(t)$ around

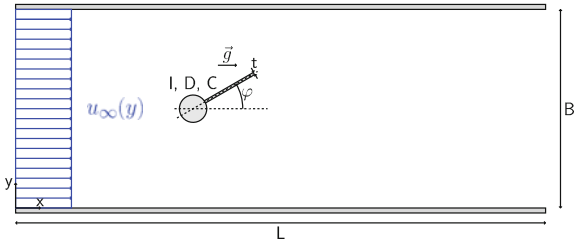

Fig. 1 Illustration of the computational domain

the rotational axis arising from pressure and shear stresses acting on the structure. The equation of motion is solved via the Newmark method and an equal (small) time-step size for both domains. The coupling between the fluid and structure was done with a new semi-implicit coupling approach which was specially designed for LES-FSI applications. Further details regarding the performance of this algorithm can be found in [1, 6] where satisfying results of a numerical FSI benchmark [10] have been presented.

3 Test Case: FSI4

A cylinder (d = 22 mm) with an attached rectangular splitter plate (l = 42 mm, t = 2 mm) is mounted on the centerline of an rectangular three-dimensional channel (L = 405 mm, B = 240 mm) with a spanwise extension of 177 mm. The cylinder center is located at the position (5.5 d, 0.5 B) whereas gravitation **g** works in the direction of the x-axis. The cylinder and the plate have a density of 2,828 and 1,475 kg/m^3, respectively. The surrounding fluid is water at 20 °C and a density of 997 kg/m^3. At the inflow a block-profile with zero velocity at the walls is considered and a convective outflow boundary condition is set on the outflow plane. Initially, all four channel walls and the surface of the structure are considered to be no-slip walls. The fluid domain is resolved with in total 11,548,800 CVs and a spanwise resolution of 81 CVs delivering a y^+-value of 2.3 at the trailing edge of the plate. In a first stage, pure flow computations have been conducted, i.e., the structure was fixed at an angle of $\varphi = 0\,°$, by applying the Smagorinsky model with $C_s = 0.1$, the WALE model with $C_w = 0.32$ and the dynamic model with a filtering parameter of $\varepsilon = 10^{-3}$ for the recursive low-pass filter. Based on the obtained flow fields, fully coupled FSI simulations have been started in a next step. A sensitivity study was carried out in which the model parameters of the Smagorinsky and the WALE model have been varied from $C_s = 0.065$ to more realistic 0.2 and $C_w = 0.32$ to 0.65, respectively. In addition, the impact of replacing the no-slip boundary condition by artificial periodic boundary conditions in spanwise direction was investigated. Here, the extension of the computational domain was reduced to 42 mm, whereas the number of CVs in spanwise direction was kept constant. Consequently, the momentum $M(t)$ was scaled up by a factor of 177/42 for the usage of Eq. (4). For this case, the Smagorinsky model with $C_s = 0.1$ was applied.

4 Results

For the pure flow simulations, time averaging has been performed for a duration of 4.7 seconds physical time, which covers about 45 shedding cycles considering a classical Strouhal number of a pure cylinder flow of about 0.2. Exemplarily, the absolute value of the time-averaged mean velocity at the centerplane for the case $C_s = 0.1$ are shown in Fig. 2, whereas the streamlines are based on the time-averaged velocities. Here, two major vortical structures are visible in the wake of the cylinder: a large recirculation zone (RC1) and a smaller counter-rotating second vortical structure (VS2). The normalized length of these vortical structures, the angle of separation θ and the mean drag coefficient $\overline{C}_d$ are specified in Table 1 for each of the cases. As expected, the results shown vary for each particular SGS model, which is in accordance with the literature. After releasing the structure, a strong influence of the SGS models and parameters on the oscillation frequencies and amplitudes of the structure was found, which is summarized in Table 2. Here, the frequencies, the global peak values of the amplitudes $\varphi_{min/max}$ and the phase-averaged amplitudes $\overline{\varphi}_{min/max}$ are based on an evaluation time of 3.28 seconds. For the Smagorinsky model the amplitudes are increasing with increasing C_s, whereas the frequencies are slightly reducing. The same behavior can be observed for the WALE model up to a C_w-value of 0.55. For $C_w = 0.65$ the amplitudes decrease and the frequency increases. In [7] it was demonstrated for the Germano model that unfavorable initial conditions might lead to strange results for the coupled case. Thus in the present study the FSI prediction based on the Germano model was redone starting from a running FSI simulation based on the Smagorinsky model with $C_s = 0.1$ which results in a proper oscillation at a frequency of 5.8 Hz. For detailed investigations a phase-angle dependent averaging of the flow field over fifteen oscillation cycles was performed. Exemplarily, the

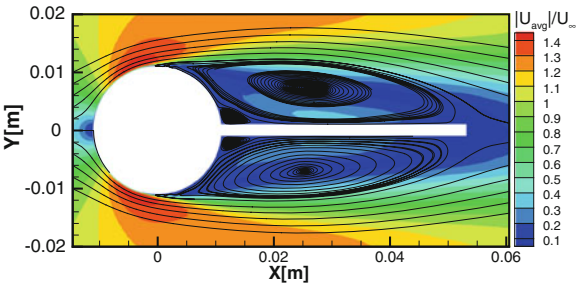

Fig. 2 Normalized time-averaged mean velocity

Table 1 Results obtained for pure flow computations

SGS Model	RC1 [(X − 0.5d)/l]	VS2 [(X − 0.5d)/l]	θ (°)	$\overline{C}_d$
Smag, $C_s = 0.1$	0.96	0.19	81.3	0.730
WALE, $C_w = 0.32$	0.81	0.09	82.8	0.728
Germ, $\varepsilon = 10^{-3}$	>1.0	0.18	83.1	0.700

Table 2 Results obtained for fully coupled FSI simulations

SGS Model	Frequency (Hz)	φ_{min}	φ_{max}	$\overline{\varphi}_{min}$	$\overline{\varphi}_{max}$
Smag, $C_s = 0.065$	5.19	−0.155	0.153	−0.132	0.131
Smag, $C_s = 0.1$	5.19	−0.206	0.194	−0.178	0.181
Smag, $C_s = 0.1$[a]	5.80	−0.146	0.143	−0.097	0.107
Smag, $C_s = 0.17$	4.89	−0.230	0.232	−0.211	0.207
Smag, $C_s = 0.2$	4.89	−0.243	0.255	−0.213	0.206
WALE, $C_w = 0.32$	5.50	−0.052	0.051	−0.029	0.027
WALE, $C_w = 0.45$	5.19	−0.178	0.175	−0.150	0.147
WALE, $C_w = 0.55$	5.19	−0.205	0.212	−0.191	0.191
WALE, $C_w = 0.65$	6.41	−0.130	0.128	−0.113	0.109
Germ, $\varepsilon = 10^{-3}$	5.80	−0.171	0.188	−0.144	0.149
Ref. experiment	≈5.5	–	–	−0.262	0.262

[a] with periodic b.c., else no-slip

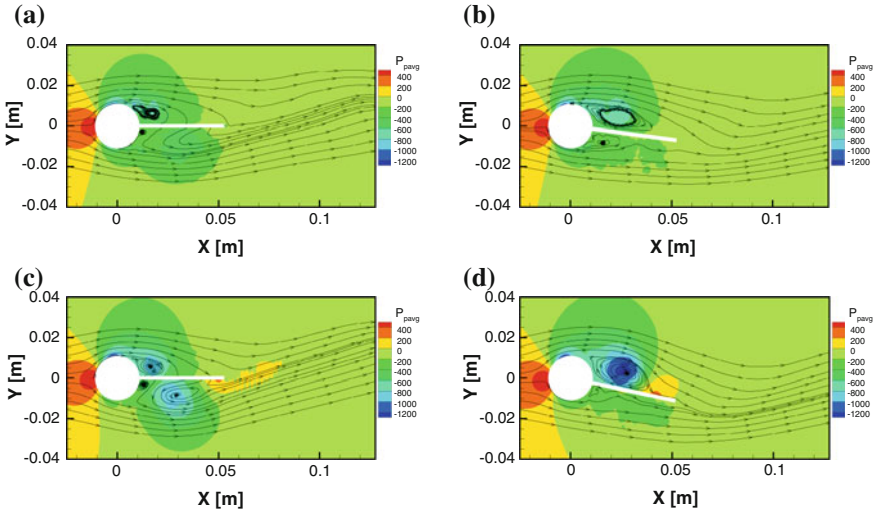

Fig. 3 **a** P_{pavg} for $C_s = 0.065$ and $\theta = 180°$. **b** P_{pavg} for $C_s = 0.065$ and $\theta = 270°$. **c** P_{pavg} for $C_s = 0.2$ and $\theta = 180°$. **d** P_{pavg} for $C_s = 0.2$ and $\theta = 270°$

contour plot of the phase-averaged pressure P_{pavg} and the streamlines based on the phase-averaged velocities $u_{x,pavg}$ and $u_{y,pavg}$ at the centerplane for the Smagorinsky cases $C_s = 0.065$ and 0.2 at phase angles of 180° and 270° are shown in Fig. 3a–d. Here, the development and propagation of vortical structures associated with induced low pressure zones which cause the movement of the structure are clearly visible. Comparing the pressure fields, the strength of the low pressure zones in the core region of the vortical structures on the suction side is higher for the case $C_s = 0.2$ than for $C_s = 0.065$. At the same time the pressure maximum on the pressure side of the structure is of the same order. Thus, the increase of the strength of the shed vortical structures

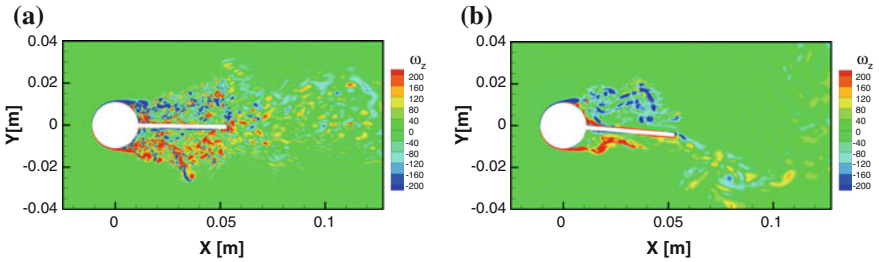

Fig. 4 **a** Vorticity ω_z for $C_s = 0.065$, **b** vorticity ω_z for $C_s = 0.2$

and their corresponding low pressure zones with increasing C_s is identified as the main reason for the variation of the oscillation amplitudes. These observations are caused by a reduction of the vorticity transfer from the main component ω_z normal to the x-y-plane to the other directions (vortex tilting) which is found for an increasing Smagorinsky constant C_s depicted in Fig. 4a, b as instantaneous snapshots. Here, the ω_z-structures are more coherent for $C_s = 0.2$ than for 0.065. Similar observations have been found for the WALE model. For the simulation with periodic boundary conditions and $C_s = 0.1$ a frequency of 5.8 Hz was obtained, which is a slight increase compared to the no-slip case. At the same time the phase-averaged peak-to-peak amplitude is strongly reduced (see Table 2). This finding can also be attributed to the relation between the strength of the low pressure zones and the vorticity transfer, which is intensified by an increased relative grid resolution in spanwise direction in the periodic case. Thus reduced amplitudes are observed.

5 Conclusions and Outlook

The impact of different SGS models and parameters on the results of a fully coupled FSI test case were investigated. The FSI results in terms of oscillation frequencies and amplitudes turned out to be strongly dependent on the SGS model and its parameters which is due to a relation between the strength of low pressure zones in vortical structures, the vorticity transfer and the applied SGS model or model parameter. In a next step, the investigations regarding the grid resolution, periodic boundary conditions and the spanwise extension of the fluid domain will be continued.

References

1. Breuer, M., De Nayer, G., Münsch, M., Gallinger, T., Wüchner, R.: Fluid-structure interaction using a partitioned semi-implicit predictor-corrector coupling scheme for the application of large-eddy simulation. J. Fluids Struct. **29**, 107–130 (2012)
2. Ducros, F., Nicoud, F., Poinsot, T.: Wall-adapting local eddy-viscosity models for simulations in complex geometries. In: Baines, M. (ed.) Numerical Methods for Fluid Dynamics VI, pp. 293–299 (1998)

3. Germano, M., Piomelli, U., Moin, P., Cabot, W.H.: A dynamic subgrid-scale eddy viscosity model. Phys. Fluids A **3**, 1760–1765 (1991)
4. Gomes, J. P., Lienhart, H.: Combined flow and deformation measurements of FSI-induced oscillation of a bluff flexible structure in uniform flows. ERCOFTAC Class. Coll. Database **87** (2011)
5. Lilly, D.K.: A proposed modification of the Germano subgrid-scale closure method. Phys. Fluids A **4**, 633–635 (1992)
6. Münsch, M., Breuer, M.: Numerical simulation of fluid-structure interaction using eddy-resolving schemes. In: Bungartz, H.-J., Mehl, M., Schäfer, M. (eds.) Fluid Structure Interaction II, pp. 221–253. Springer, New York (2010)
7. Münsch, M., Delgado, A., Breuer, M.: Fluid-structure interaction in turbulent flows and the influence of LES subgrid-scale models. In: ECCOMAS 2012—European Congress on Computational Methods in Applied Sciences and Engineering, pp. 3944–3963. www.scopus.com (2013)
8. Rhie, C.M., Chow, W.L.: Numerical study of the turbulent flow past an airfoil with trailing edge separation. AIAA J. **21**, 1525–1532 (1983)
9. Smagorinsky, J.: General circulation experiments with the primitive equations. Mon. Weather Rev. **91**, 99–164 (1963)
10. Turek, S., Hron, J., Razzaq, M., Wobker, H., Schäfer, M.: Numerical benchmarking of fluid-structure interaction: a comparison of different discretization and solution approaches. In: Bungartz, H.-J., et al. (eds.) Fluid Structure Interaction II, pp. 413–424. Springer, New York (2010)

Shape Optimization and Active Flow Control of Truck-Trailers for Improved Aerodynamics Using Large-Eddy Simulation and Response Surfaces

M. El-Alti, P. Kjellgren and L. Davidson

1 Introduction

Most of the drag on a truck is caused by the wake behind the trailer. It is caused by the sharp edges on the rear end. This effect gives rise to a large low pressure region that increases the pressure difference between the front and back. An effective way to increase the pressure on the back is to use angled flaps and active flow control. Previous research shows possibilities to decrease the drag by re-attaching the flow on a straight flap [1]. The present objective is to investigate the shape of the flap.

2 Optimization Approach

Surrogate models are adopted as the optimization approach. The specific model is the polynomial response surface methodology (RSM). The idea of RSM is to build an empirical model of the true response surface of the system. A second-order polynomial model has been adopted to capture non-linearities. Follow the procedure in [2], if the true response is denoted y and the design parameters are $x_1, x_2, x_3, \ldots, x_n$, we have the following statement: $y = f(x_1, x_2, x_3, \ldots, x_n) + \varepsilon$ where ε is all sources of errors. By using second-order RSM the regression model is written as

$$y = \beta_0 + \sum_{i=1}^{k} \beta_i x_i + \sum_{i=1}^{k} \beta_{ii} x_i^2 + \sum_{i<j} \sum_{j=2}^{k} \beta_{ij} x_i x_j + \varepsilon \tag{1}$$

M. El-Alti (✉) · P. Kjellgren · L. Davidson
Division of Fluid Dynamics, Department of Applied Mechanics,
Chalmers University of Technology, 412 96 Gothenburg, Sweden
e-mail: mohammad.el-alti@chalmers.se

J. Fröhlich et al. (eds.), *Direct and Large-Eddy Simulation IX*,
ERCOFTAC Series 20, DOI 10.1007/978-3-319-14448-1_51

where βs are the regression coefficients, x_i is the ith design parameter and k is the total number of design parameters. By minimizing the error using least-square fit of the regression coefficients, the approximation of the true response, $\hat{y}$, is

$$\hat{y} = b_0 + \sum_{i=1}^{k} b_i x_i + \sum_{i=1}^{k} b_{ii} x_i^2 + \sum_{i<j} \sum_{j=2}^{k} b_{ij} x_i x_j \tag{2}$$

The bs are now the least-square estimators of the regression coefficients. It is important to choose appropriate values of the parameters for each design candidate. The method of the statistically appropriate choice for best fit is called "Design of Experiment" (DOE). The design chosen is the face-centered central composite design.

3 Numerical Method

The flow behind the truck is unsteady and the pulsating (i.e. oscillating) jets are used as forcing. The modeled actuator is very narrow, and the excitation velocity is about 110 % of the free stream velocity. Thus a fine resolution in both space and time is needed. In order to make an accurate prediction of the turbulent flow, large-eddy simulation is therefore used. This provides both instantaneous field data and high accuracy. The Reynolds number is 200,000 based on the width (w) of the truck, which is in the range of manageable LES. The inlet velocity is $U_\infty = 25\,\text{m/s}$ and the truck width is $w = 2.6\,\text{m}$, see Fig. 1. The commercial CFD code FlowPhys ver. 2.0 is used for the computations in this work. The Smagorinsky model for the sub-grid scales is used with the Smagorinsky constant $C_S = 0.25$. FlowPhys has a semi-implicit, fractional step finite element solver. The temporal discretization is the explicit four-step Runge-Kutta scheme for the convection terms and the Crank-Nicholson method for the diffusion terms. The spatial discretization scheme is the pure central difference (CD). The forcing is modeled as a transient velocity inlet, and the governing variables are the slot width, Δh, the velocity (both magnitude and

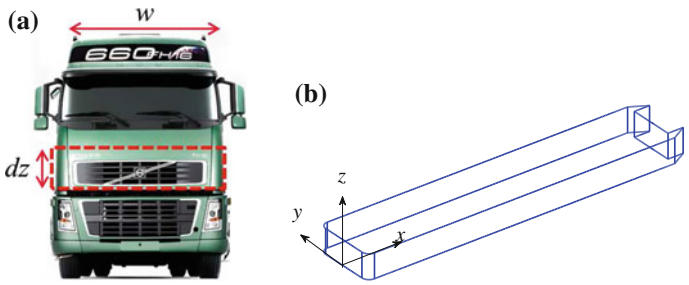

Fig. 1 The spanwise slice and the simplified truck model. **a** The spanwise slice of the truck. **b** Simplified truck model. Inlet at $x = -12$ w; outlet at $x = 30$ w; side walls at $y = -8.5$ w and $y = 8.5$ w

direction) and the frequency. The RMS momentum and coefficient from the slot are defined as

$$J_{RMS} = \int \rho u_{RMS}^2 \, dh = \rho u_{RMS}^2 \Delta h, \quad C_{\mu\ RMS} = \frac{J_{RMS}}{w\frac{1}{2}\rho u_\infty^2} = \frac{u_{RMS}^2 \Delta h}{w\frac{1}{2}u_\infty^2} \tag{3}$$

Δh is the effective slot width. From Eq. 3 the velocity (assuming purely sinusoidal) in the slot and the non-dimensional forcing frequency are given by

$$u_{RMS} = \sqrt{\frac{C_{\mu\ RMS}\, w\, u_\infty^2}{2\Delta h}}, \quad u(t) = \sqrt{2} u_{RMS} \sin(2\pi F t), \quad F^+ = \frac{F \cdot X_{TE}}{U_\infty} \tag{4}$$

where X_{TE} is the distance from the slot to the trailing edge of the flap.

We use a simplified truck model in our simulations. The truck is simplified as a rectangular bluff body with a typical width ($w = 2.6\,\text{m}$, y direction) and length ($l = 13.0\,\text{m}$) relevant for a real truck. The height (the z direction) is $H = 0.2\,\text{m}$, i.e. the domain is three-dimensional (Fig. 1). The truck is mounted with angled flaps on the rear end in which the oscillating synthetic jet actuators are placed (Fig. 2).

3.1 Procedure and Parameters Investigated

Several parameters have to be considered during optimization. There are at least nine parameters that govern AFC: flap angle, flap length, slot position, slot angle, slot width, actuation frequency, actuation amplitude, first and second shape coordinates, y_1 and y_2 (see Fig. 2). Previous simulations [1] proposed optimal values of the actuation frequency and amplitude. The optimal actuation frequency is $F^+ = 0.5$ and the optimal amplitude (Eq. 3) is $C_\mu = 1.0$. The flap length has to be as short as possible for practical purposes, and is limited to $0.3\,w$. The slot width is set to a relatively large value of $0.02\,w$ in order to avoid too small cells and make the computations more robust. The remaining five parameters are included in the optimization. The

AFC parameter	Min value	Max value	index
Flapangle α	10 *deg*	40 *deg*	1
1^{st} flap coord y_1	$-0.1\ m$	$0.1\ m$	2
2^{nd} flap coord y_2	$-0.1\ m$	$0.1\ m$	3
Slot angle β	15 *deg*	45 *deg*	4
Slot position X_f	10%	30%	5

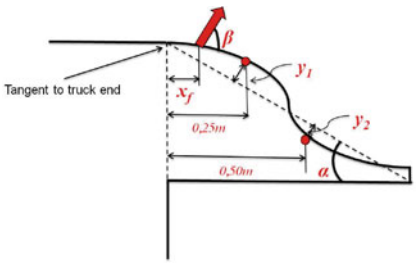

Fig. 2 Specifications of the parameters and a drawing of the flap with defined optimization parameters

number of simulations (designs) that must be carried out is $2^k + 2k + 1$, where k is the number of optimization parameters, thus we have $2^5 + 2 \cdot 5 + 1 = 43$ different cases to be simulated. There is no sharp edge between the rear end and the flap. For each design, the flap starts as a tangent to the edge and then reshapes according to the flap angle and y-coordinates. This is why the slot starts at $X_f = 0.03\,w$ (10 %). In the previous simulations in [1], there was a sharp edge between the truck rear end and the flap. The separation point was hence known. In this design, the separation location is unknown and is dependent on the shape of the flap chosen during the optimization.

4 Results

This section presents the final response surface after statistical treatments and improvements. The final response surface is analyzed to find the regions of feasible optimal designs. We start with the full model (Eq. 2) and increase the model fit using test statistics and rejecting terms in Eq. 2 until the model fit is optimal. The final model has 12 terms and is given in Eq. 5

$$C_{D,model} = \beta_0 + \beta_1 X_1 + \beta_5 X_5 + \beta_6 X_1 X_2 + \beta_7 X_1 X_3 + \beta_8 X_1 X_4 + \beta_9 X_1 X_5 + \beta_{10} X_2 X_3 + \beta_{12} X_2 X_5 + \beta_{13} X_3 X_4 + \beta_{16} X_1^2 + \beta_{18} X_3^2 \tag{5}$$

Indices 1–5 in parameter X are given in the table in Fig. 2.

4.1 Results and Analysis of the Response Surface

The response surface obtained in the previous section gives a minimum in drag of $C_D = 0.52$. Figure 3 gives the parameter values that correspond to this minimum and shows the geometry and mesh. Figure 4 shows variations of the different parameters in the contour plots. Figure 4a–c plot the response surfaces for β versus α at three different slot positions, X_f. The minimum on this surface occurs at the lowest slot

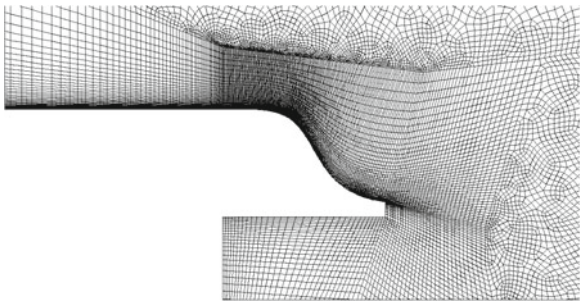

Fig. 3 The geometry of the proposed optimized case by RSM for drag. $\alpha = 30°$, $y_1 = 0.10$ m, $y_2 = 0.015$ m, $\beta = 15°$ and $X_f = 30\,\%$

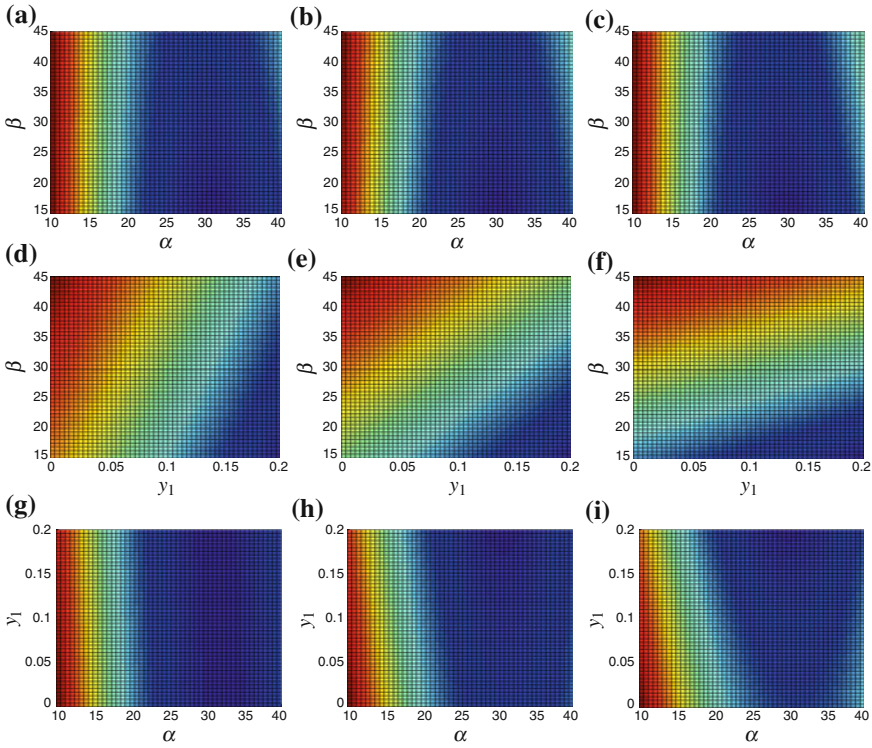

Fig. 4 Analysis plots of the response surface. **a** Optimized case, $Min\ C_D = 0.59$, $X_f = 0.1$. **b** Optimized case, $Min\ C_D = 0.56$, $X_f = 0.2$. **c** Optimized case, $Min\ C_D = 0.52$, $X_f = 0.3$. **d** $a = 20°$, $Min\ C_D = 0.64$, const $y_2 = 0.0857 Xf = 0.2$. **e** $a = 30°$, $Min\ C_D = 0.66$, const $y_2 = 0.0857\ X - f = 0.2$. **f** $a = 40°$, $Min\ C_D = 0.65$, const $y_2 = 0.0857 X_f = 0.2$. **g** $X_f = 0.1$, $Min\ C_D = 0.59$, const $y2 = 0.0857$, $b = 15°$. **h** $X_f = 0.2$, $Min\ C_D = 0.56$, const $y_2 = 0.0857$, $b = 15°$. **i** $X_f = 0.3$, $Min\ C_D = 0.52$, const $y_2 = 0.0857$, $b = 15°$

angle $\beta = 15°$ but drag is almost independent of β. The flap angle, α, is around $\alpha = 30°$. The shape of the response surface suggests an even lower slot angle. Figure 4d–f plot C_D versus β and y_1 for different flap angles. The minimum occurs in the end points of the parameters, suggesting an increase in y_1 and a further decrease in β. Figure 4g–i plot C_D versus y_1 and α at different X_f. It is shown that, for low values of X_f, y_1 is drag invariant but $\alpha = 30$ is optimum. As X_f increases, the y_1 dependency increases and shows an optimum for large values of y_1.

In Fig. 5 the pressure contours for a case with straight flap without AFC compared with the optimal case with AFC are plotted. The pressure recovery due to AFC in the wake is evident. To check the proposed optimal design by the response surface, a LES of this is carried out which gives $C_{D,LES} = 0.59$. This is in poor agreement with the value from the RSM. One reason may be that the design space is too wide, other reasons may that LES in general produces highly unsteady turbulent flow fields, which are sensitive to averaging times, mesh quality and fluctuations in the CD-scheme.

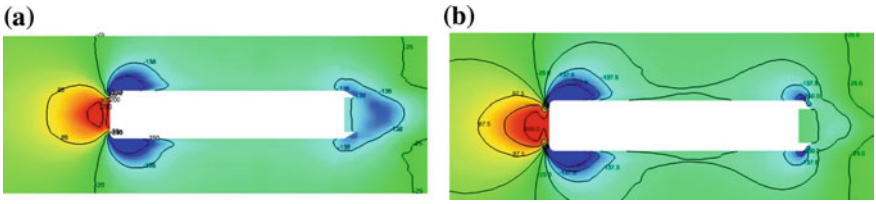

Fig. 5 Time-averaged pressure contours comparing the optimal and the case without AFC

5 Conclusions and Discussion

The present results indicate a region of feasible designs. The flap angle, α, has an optimum at 30° and a slot angle as low as possible. The slot position is very dependent on the proposed flap shape. An LES was carried out for the optimal design point. Poor agreement was found with the C_D obtained with the RSM. possible reasons for the discrepancy are given at the end of the previous section.

Acknowledgments This work is supported by the **Swedish Agency of Innovation Systems (VINNOVA)**, **Volvo 3P**, **SKAB** and **CD-ADAPCO**. Financial support by SNIC (the Swedish National Infrastructure for Computing) for computer time at C3SE (Chalmers Centre for Computational Science and Engineering) is gratefully acknowledged.

References

1. El-Alti, M., Kjellgren, P., Davidson, L.: Drag reduction of trucks by active flow control of the wake behind the trailer. In: 6th International Symposium on THMT, Rome, Italy (2009)
2. Myers, R.H., Montgomery, D.C.: Responce Surface Methodology: Process and Product Optimization Using Designed Experiments. A Wiley-Interscience Publication, USA (2002)

Part X
Environmental Flows

Numerical Simulation of Breaking Gravity Waves

S. Remmler, M.D. Fruman, U. Achatz and S. Hickel

Abstract Geophysical flows including stable stratification and system rotation are a special challenge for turbulence subgrid-sclae models for large-eddy simulation (LES) and hence require validation with suitable test cases. We validate different subgrid-scale models for this kind of flows using a breaking monochromatic inertia-gravity wave that has been studied before. We find that the standard Smagorinsky model cannot be recommended while the dynamic Smagorinsky model and the implicit turbulence model ALDM are suitable to simulate this complex flow with high accuracy.

1 Introduction

Gravity waves (GWs) play an important role for the global circulation in the atmosphere, especially above the tropopause, where the transport of momentum from the troposphere to the mesosphere cannot be neglected in global circulation modelling. Despite this importance of GWs, their treatment in present general circulation models remains unsatisfactory. Improvements in the physical understanding and the parameterization of the breaking process of GWs in global circulation models require high resolution benchmark simulations.

In a previous study [1], we have performed a fully resolved three-dimensional direct numerical simulation (DNS) of a statically unstable monochromatic inertia-gravity wave (IGW), i.e. a gravity wave with a very long oscillation period so that Coriolis forces strongly influence the associated velocity field. The chosen parameters were characteristic for a GW with almost vertical direction of propagation breaking in the middle atmosphere. The initial condition for our simulations was a

S. Remmler (✉) · S. Hickel
Institute of Aerodynamics and Fluid Mechanics, Technische Universität München, Munich, Germany
e-mail: remmler@tum.de

M.D. Fruman · U. Achatz
Institute of Atmosphere and Environment, Goethe-Universität Frankfurt, Frankfurt, Germany

J. Fröhlich et al. (eds.), *Direct and Large-Eddy Simulation IX*,
ERCOFTAC Series 20, DOI 10.1007/978-3-319-14448-1_52

perturbed monochromatic wave. The chosen perturbations were the most unstable transverse normal mode of the wave and the leading secondary instability modes of the time-dependent wave breaking in a two-dimensional space [2]. In the present paper we use this DNS database to validate different turbulence subgrid-scale (SGS) models for LES. Among other SGS models, we analyse the Adaptive Local Deconvolution Method (ALDM) [3] with regards to its suitability for the efficient numerical simulation of gravity wave breaking events, where stable stratification and rotation affect the SGS turbulence.

2 Numerical Method

We use the finite-volume solver INCA for explicit time integration of the Boussinesq equations on staggered Cartesian grids. For time advancement the explicit third-order Runge-Kutta scheme of Shu [4] is used. The time-step is dynamically adapted to satisfy a Courant-Friedrichs-Lewy condition with $CFL \leq 1.0$. The flow solver offers different spatial discretization schemes depending on the application. For DNS and LES with explicit SGS model, we used a non-dissipative central difference scheme with 4th order accuracy for the convective terms and 2nd order central differences for the diffusive terms and the continuity equation (Poisson equation for pressure).

Alternatively, the central difference scheme for the convective terms can be replaced by the implicit turbulence model ALDM, which integrates numerical discretization scheme and physical SGS model into a holistic approach (implicit LES). The method is based on a reconstruction of the unfiltered solution on the represented scales by combining Harten-type deconvolution polynomials. The different polynomials are dynamically weighted based on the smoothness of the filtered solution. A tailored numerical flux function operates on the reconstructed solution. Both, the solution-adaptive polynomial weighting and the numerical flux function involve free model parameters, that were calibrated in such a way that the truncation error of the discretized equations correctly represents the SGS stresses of turbulence [3]. This set of parameters was not changed for any subsequent applications of ALDM. For the presented computations, we used an implementation of ALDM with improved computational efficiency [5]. The validity of this method has been proved for a number of different applications [6]. Recently, we could also successfully apply ALDM to stably stratified turbulent flows [7, 8], which is a key prerequisite of the breaking wave problem.

For comparison we can replace the implicit turbulence SGS model ALDM by an explicit SGS model. Within the present study we used the standard Smagorinsky model [9] (SSM) with a constant prescribed model coefficient C_S and the dynamic Smagorinsky model [10] (DSM). In the DSM the model coefficient is variable in time and space. It is automatically computed by explicitly filtering the resolved flow field and assuming similarity of energy transport between the test filter scale and the grid scale compared to the transport from the grid scale to the subgrid scale.

Table 1 Physical parameters of the investigated inertia-gravity wave

Wavelength	$\lambda = 3\,\mathrm{km}$
Wave vector orientation	$\Theta = 89.5°$
Dimensional wave amplitudes	$\hat{u} = 8.97\,\mathrm{m/s}$; $\hat{v} = 14.56\,\mathrm{m/s}$; $\hat{b} = 0.0234$
Non-dimensional wave amplitude	$a = 1.2$
Kinematic viscosity	$\nu = 1\,\mathrm{m^2/s}$
f-plane latitude	$\phi = 70°$
Brunt-Väisälä frequency	$N = 0.02\,\mathrm{s^{-1}}$
Gravitational acceleration	$g = 9.81\,\mathrm{m/s^2}$
Thermal diffusivity	$\alpha = 1\,\mathrm{m^2/s}$
Phase velocity	$c_p = 0.106\,\mathrm{m/s}$
Wave oscillation period	$T = 7.87\,\mathrm{h}$

3 Computational Set-Up

We initialize our simulation with a monochromatic gravity wave perturbed by its leading primary and secondary instability modes. The computational domain is aligned with the direction of wave propagation ($L_z = 3\,\mathrm{km}$) and with the directions of the perturbations ($L_x = 4\,\mathrm{km}$, $L_y = 0.4\,\mathrm{km}$). The domain is moving in the negative z-direction at the phase speed of the wave, so that the most unstable part of the wave remains in the upper half of the domain. The wave parameters are chosen such that velocities in the x and y-direction have comparable magnitudes. A list of the physical parameters of the IGW can be found in Table 1. We provide a more detailed description of the set-up in the DNS paper [1].

4 Results

Selected results of the DNS [1], i.e. the evolution of the base wave amplitude and the energy dissipation rate, are shown in Fig. 1. A non-dimensional wave amplitude a larger than unity means that the flow is statically unstable in the least stable region of the wave. The primary breaking event is initiated by the optimal perturbations superposed to the base wave. The perturbations are strong enough to result in overturning and turbulence generation not only in the unstable part of the wave but also in the stable half. Turbulence in the stable region is damped strongly, but some turbulence energy remains for a sufficiently long time to trigger the secondary breaking events (after 3 and 5 h, respectively), as soon as the unstable part of the wave has propagated into the region where initially the stable part had been situated. The secondary breaking events, which appear after the non-dimensional wave amplitude has decreased below unity, are hence a result of the similar time scales of breaking, turbulence decay and wave propagation.

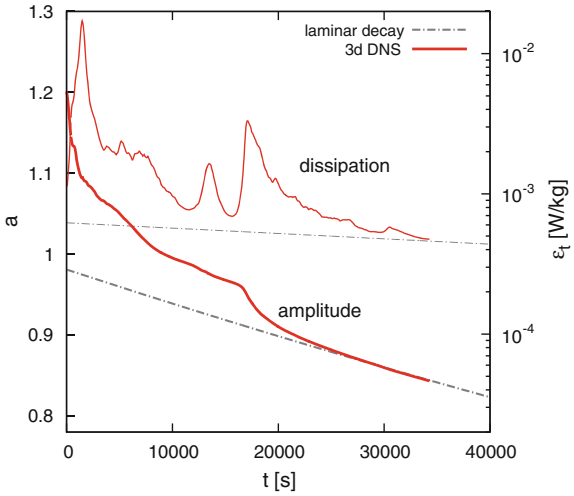

Fig. 1 Results of the fully resolved DNS [1]. Time series of non-dimensional amplitude a of the primary wave and total energy dissipation ε_t

We performed a number of large-eddy simulations of the described wave breaking problem at a numerical resolution of $100 \times 24 \times 80 = 192,000$ cells. Note that this means a ten times coarser resolution in all three directions compared to the fully resolved DNS with 173 million cells. In Fig. 2 we compare the results with different turbulence SGS models. The standard Smagorinsky model (Fig. 2a) has the disadvantage that it requires prescribing a model coefficient C_S which depends on the type of flow to be simulated. We selected three different values for C_S finding

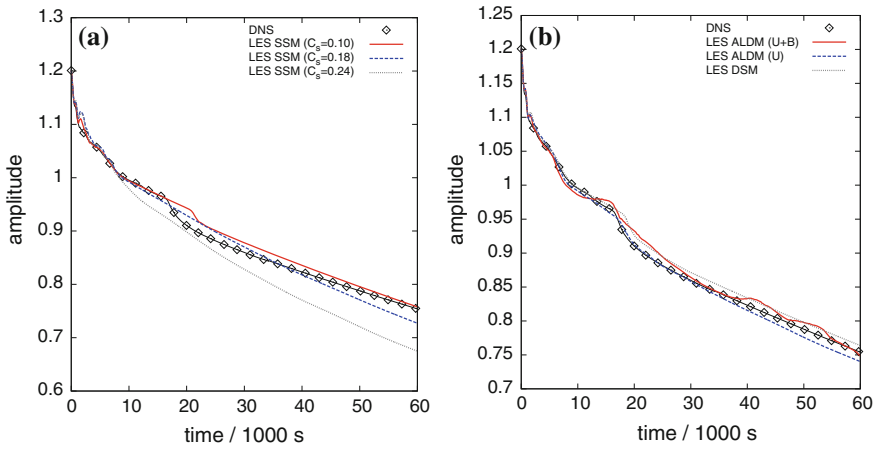

Fig. 2 **a** Non-dimensional wave amplitude computed with the standard Smagorinsky model with different values for the model coefficient. **b** Non-dimensional wave amplitude computed with the dynamic Smagorinsky model and ALDM, respectively

that the choice of C_S strongly affects the result of the simulation. All values of C_S lead to too strong energy dissipation and hence the wave amplitude decay rate is overpredicted, especially during the second half of the simulated time span where the wave has almost completely relaminarized. Only for $C_S = 0.10$ a secondary breaking event can be observed. However, the laminar decay rate is also overpredicted in this case. We conclude that the standard Smagorinsky model is not suitable to simulate the present problem given the uncertainty in choosing the coefficient C_S and the fact that the prediction is never satisfactory.

In Fig. 2b we compare the results with three more advanced turbulence SGS models. The first one is ALDM applied to the non-linear terms in both the momentum and buoyancy equations. The agreement with the DNS reference data is good, although the amplitude decay is less smooth with ALDM. This is due to spurious oscillations in the buoyancy field. We are currently investigating the origin of those, but have no final conclusion on that topic. A better result is obtained if ALDM is applied only to the momentum equations and the buoyancy equation is discretized with the 4th order central scheme using no SGS model for the buoyancy at all. The oscillations in the buoyancy field do not appear in this case and the amplitude decay matches the reference DNS almost perfectly, especially during the first half of the simulated time span, where breaking generates turbulence. A result with similar quality was obtained using the dynamic Smagorinsky model. Though the intensity of the secondary breaking events is a little bit underpredicted, the overall agreement with the reference DNS is good. The model is able to deactivate itself when the wave has relaminarized and there are hardly any small scale turbulent motions left.

The velocity fluctuations (i.e. the root-mean-square deviations from the spatial average in the y-direction) are displayed in Fig. 3 for the DNS and the LES with

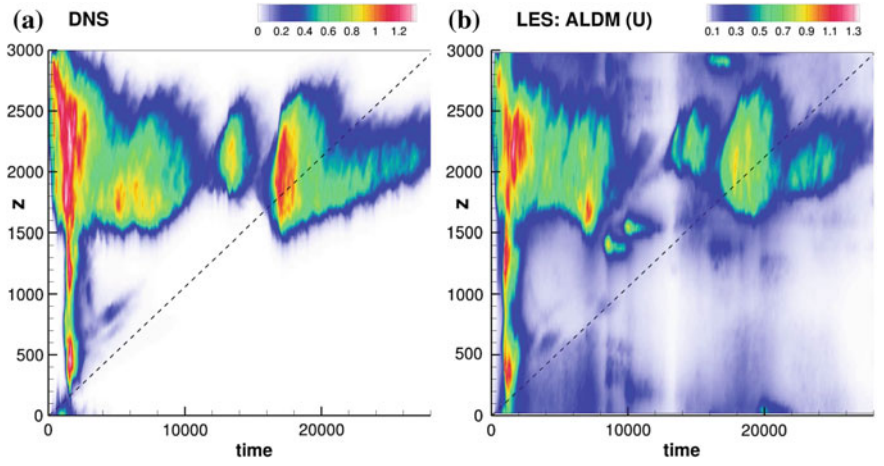

Fig. 3 **a** Hovmöller plot of velocity fluctuations (in the y-direction) in the DNS (the *dashed lines* indicates a fixed position in space). **b** Hovmöller plot of velocity fluctuations in the LES with ALDM (applied to the momentum equation only)

ALDM applied only to the momentum equation. Obviously, the LES is able to predict the spatial and temporal structure of the breaking events correctly. Although the LES seems to be slightly more noisy, this is an excellent agreement given the much coarser resolution. Even the secondary breaking events are predicted well.

5 Conclusion

We presented results of large-eddy simulations of a breaking monochromatic inertia-gravity wave. The same case has been studied by direct numerical simulation before [1]. The present LES use a ten times coarser resolution in all spatial directions and hence do not resolve all scales of turbulence generated during the breaking event.

We found that the standard Smagorinsky model is not suitable for this kind of simulations. The predicted decay rate was too high for all tested model coefficients C_S. On the other hand the two tested advanced turbulence SGS models revealed good agreement with the reference DNS. The implicit turbulence model ALDM works well if it is applied only to the momentum equations and not to the buoyancy equation. The dynamic Smagorinsky model in combination with a non-dissipative 4th order central discretization scheme is also capable to predict the primary and secondary breaking events correctly and switches itself off when the turbulence has decayed.

References

1. Remmler, S., Fruman, M.D., Hickel, S.: Direct numerical simulation of a breaking inertiagravity wave. J. Fluid Mech. **722**, 424–436 (2013)
2. Fruman, M.D., Achatz, U.: Secondary instabilities in breaking inertia-gravity waves. J. Atmos. Sci. **69**, 303–322 (2012)
3. Hickel, S., Adams, N.A., Domaradzki, J.A.: An adaptive local deconvolution method for implicit LES. J. Comput. Phys. **213**, 413–436 (2006)
4. Shu, C.-W.: Total-variation-diminishing time discretizations. SIAM J. Sci. Stat. Comput. **9**(6), 1073–1084 (1988)
5. Hickel, S., Adams, N.A.: A proposed simplification of the adaptive local deconvolution method. ESAIM **16**, 66–76 (2007)
6. Hickel, S., Kempe, T., Adams, N.A.: Implicit large-eddy simulation applied to turbulent channel flow with periodic constrictions. Theor. Comput. Fluid Dyn. **22**, 227–242 (2008)
7. Remmler, S., Hickel, S.: Spectral structure of stratified turbulence: direct numerical simulations and predictions by large eddy simulation. Theor. Comput. Fluid Dyn. 2012. doi:10.1007/s00162-012-0259-9
8. Remmler, S., Hickel, S.: Direct and large eddy simulation of stratified turbulence. Int. J. Heat Fluid Flow **35**, 13–24 (2012)
9. Smagorinsky, J.: General circulation experiments with the primitive equations. I: The basic experiment. Mon. Wea. Rev. **91**, 99–164 (1963)
10. Germano, M., Piomelli, U., Moin, P., Cabot, W.H.: A dynamic subgrid-scale eddy viscosity model. Phys. Fluids A **3**(7), 1760–1765 (1991)

DNS of a Radiatively Driven Cloud-Top Mixing Layer as a Model for Stratocumulus Clouds

A. de Lózar and J.P. Mellado

1 Introduction

The marine planetary boundary layer topped by stratocumulus clouds (STBL) is key for the planetary radiation balance [5]. In its simplest configuration the STBL consists of a lower moist boundary layer which is topped by a dry and warm free atmosphere. The top of the STBL is populated by stratocumulus clouds that emit long wave radiation, cooling the moist boundary layer. Radiative cooling is thought to be the main source of turbulent energy for the STBL.

Despite its apparent simplicity, there is still a great degree of uncertainty in current models of the STBL. One of the main problems arises when modeling the exchange of heat and moisture between the free atmosphere and the moist boundary layer, the so-called entrainment [4]. Climate models rely on accurate predictions of the entrainment because it determines how much energy and water is available for the STBL. Most attempts to solve the entrainment problem rely on LES but to date entrainment values measured in LES strongly depend on the subgrid-scale parameterization and on the advection scheme.

From the fluid dynamics point of view, the study of the entrainment combines two fundamental problems. First, the entrainment in the cloud top is a case of turbulent mixing across an stratified interface, a classical problem in the fluid dynamics literature. However, many aspects of this classical problem are still unknown, as to the question on how do large eddies participate in the mixing. This question is particularly interesting for the stratocumuli dynamics because the scales representing the STBL (typically one kilometer) are usually much larger than the scales representing the stratification jump (of the order of several meters). Second, the main driving force for turbulence in stratocumuli is radiation. In this case we encounter with a relatively new problem because there are still very few studies that focus on the interaction of

A. de Lózar (✉) · J. P. Mellado
Max Planck Institute for Meteorology, Hamburg, Germany
e-mail: adelozar@gmail.com

J. Fröhlich et al. (eds.), *Direct and Large-Eddy Simulation IX*,
ERCOFTAC Series 20, DOI 10.1007/978-3-319-14448-1_53

radiation with turbulence. This interaction is relevant not only for geophysical flows but also for some applications in engineering [2]. In stratocumuli the radiative forcing and the flow are strongly coupled, because the forcing is determined by the shape of the cloud interface, and this shape is given by the flow-stratification interplay. This strong radiation-flow interaction promises to reveal new interesting dynamics.

2 Problem Description

We have investigated a mixing-layer stably-stratified configuration that is driven by radiative cooling, using Direct Numerical Simulations in the Boussinesq approximation. This simplified configuration mimics relevant aspects of the cloud top in the STBL, in particular the mixing across an inversion that bounds a radiatively driven turbulent flow. We apply three main simplifications with respect to the real clouds: flow scales much larger than the optical length (defined below) are neglected, the radiation is calculated in a one-dimensional approximation and there is no evaporative cooling. These simplifications allow us to reduce the problem to only two parameters: a Reynolds number and the stratification strength, which can be described by a reference Richardson number.

The problem is non-dimensionalized using the scales that define the radiative forcing: the optical length λ and a reference buoyancy flux B_0. The optical length provides the region where radiation cools the cloud and the buoyancy flux indicates the strength of this cooling. For this study we choose a reference stratification that corresponds to a temperature jump $\Delta T \sim 10\,\mathrm{K}$, an optical length $\lambda = 15\,\mathrm{m}$ and a reference buoyancy flux $B_0 = 1.9 \times 10^{-3}\,\mathrm{m^2\,s^{-3}}$, as measured in the flight RF-01 in the DYCOMS-II field campaign. The molecular Prandtl number was fixed to one which is reasonably close to the atmospheric value. Our numerical algorithm uses compact schemes for the calculation of the derivatives which are characterized by small numerical diffusion.

The initial condition is set so that the bottom layer (the cloud) is at constant temperature with very weak turbulence. As radiation cools the top of the cloud, a convective boundary layer (CBL) grows downwards into the cloud bulk (see Fig. 1). The main advantage of our configuration is that the integral scale grows continuously. This allows us to investigate the effect of diverse scales on the entrainment.

3 Results

It is useful to divide the problem in two regions attending to the dominating flow dynamics. On the top of the domain, the cloud mixes with the free atmosphere across a stratification jump. This region is usually called inversion due to the temperature inversion that characterizes the cloud top interface. Below the inversion, the radiative forcing cools cloud parcels that fall into the interior of the cloud. The flow there

shows the typical structure of a CBL, as in Fig. 1. We refer to this region as the cloud bulk. The point that separates the inversion from the cloud bulk is usually called the inversion point, z_i.

In [1] we propose a definition of the inversion point with the mean buoyancy, $\langle b \rangle(z_i) = 0$. At this inversion point an exact energy balance equation divides the total radiative cooling into two components: the buoyancy flux into the cloud bulk and the cooling of the inversion layer, responsible for the entrainment. We find that the Deardorff's convective scalings in the CBL are consistent with this energy balance, justifying our election for the inversion point.

In Fig. 2 we show the contributions to the turbulent kinetic energy (TKE) from the TKE conservation equation [3]: the source of TKE by buoyancy $\langle w'b' \rangle$, the dissipation rate and the total transport (the sum of pressure transport, viscous transport and turbulent convection). The TKE grows with the CBL during the simulation period, so that the presented terms of the TKE budget do not compensate. In the TKE budget we clearly differentiate the inversion dynamics from the cloud bulk dynamics. In the inversion ($(z_i - z) < 0$) the buoyancy production of TKE is negative due to the entrainment of warm air from above. This negative tendency of TKE adds to the TKE dissipation, and it is compensated by a strong transport of TKE from the CBL to the inversion. In the cloud bulk ($(z_i - z) > 0$) there is a strong buoyancy production of TKE. Radiation cools air that lies close to the inversion over a thickness $\sim \lambda$,

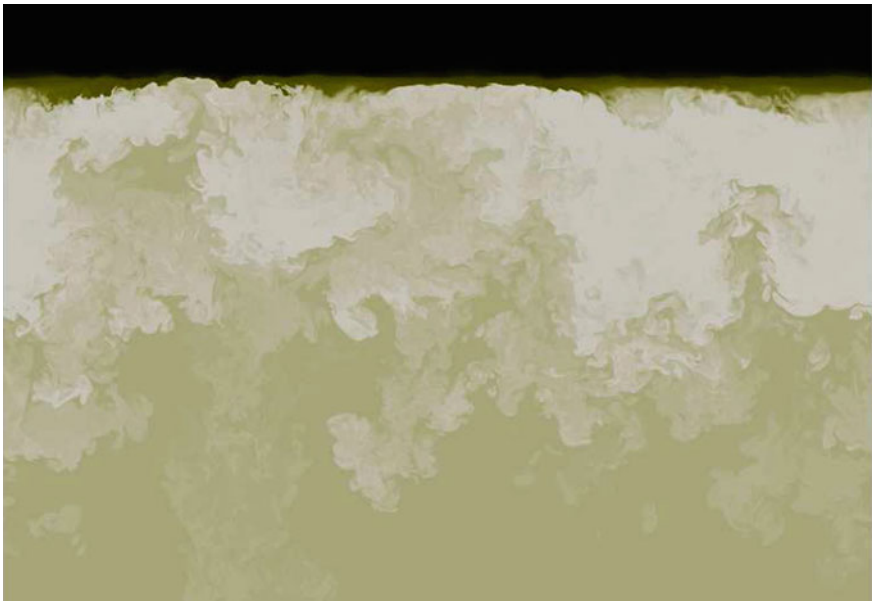

Fig. 1 Buoyancy field. The air is cooled by radiation closely below the temperature inversion. The horizontal domain is $18\,\lambda$, meaning that the extension where the radiative cooling is active covers approximately 1/18 of the horizontal domain size. The cooled air falls into the cloud bulk generating a CBL. This turbulent motion also induces the entrainment of hot air from the *top*, heating the cloud

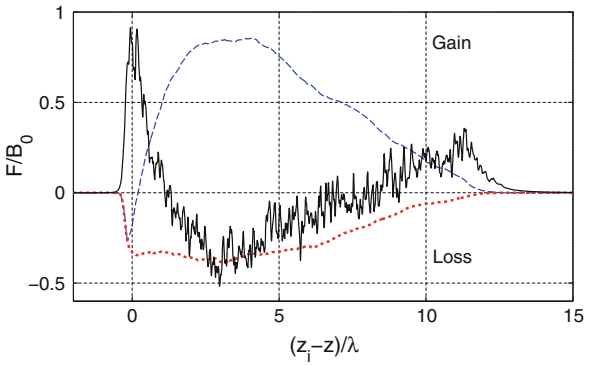

Fig. 2 Horizontally averaged contributions to the turbulent kinetic energy balance equation at the end of the simulations. Positive values represent a source of TKE while negative values represent a sink. The *dashed line* stands for the buoyancy production, the *dotted line* for the dissipation and the *continuous line* for the transport

and these air parcels fall into the cloud bulk generating the turbulent motion. This production clearly overcomes the dissipation of TKE along the whole domain. The TKE transport term distributes the TKE from the middle of the CBL to the inversion, where this TKE is used for the entrainment, and to the bottom of the CBL, where the TKE is employed to grow the CBL.

References

1. De Lozar, A., Mellado, J.P.: Direct numerical simulations of a smoke cloud-top mixing layer as a model for stratocumuli. J. Atmos. Sci. **70**, 2356–2375 (2013)
2. Ghosh, S., Friedrich, R., Pfitzner, M., Stemmer, C., Cuenot, B., Hafi, M.E.: Effects of radiative heat transfer on the structure of turbulent supersonic channel flow. J. Fluid Mech. **677**, 417–444 (2011)
3. Pope, S.B.: Turbulent Flows. Cambridge University Press, Cambridge (2000)
4. Stevens, B.: Entrainment in stratocumulus-topped mixed layers. Q. J. R. Meteorol. Soc. **128**, 2663–2690 (2002)
5. Wood, R.: Stratocumulus clouds. Mon. Wea. Rev. **140**, 2373–2423 (2012)

Effect of Ekman Layer on Windfarm Roughness and Displacement Height

J.P. Goit and J. Meyers

1 Introduction

With increasing sizes of wind farms, the influence of large scale wind farms on the Atmospheric Boundary Layer (ABL) has become an area of interest recently. While for a lone-standing turbine, power extraction equals to the difference between upstream and downstream kinetic energy fluxes, for a turbine in a large wind farm the kinetic energy must be entrained from the faster moving flow above [4]. In that case, the vertical transport of kinetic energy by turbulence is of the same order of magnitude as the power extracted by the wind turbines. Therefore, the understanding of the interaction between wind farm and the ABL becomes crucial, e.g., to maximize the extracted energy, etc.

In large wind farms, the effect of wakes, and their interaction leads to a reduction in farm efficiency. Based on extensive measurement campaigns, Barthelmie et al. [1, 2, 5] have presented detailed quantitative analysis of power losses, and the increases in turbulence intensity, observed in a medium size wind farm. Although such measurements provide precious information on farm behavior, they cannot present in full detail the three-dimensional flow field that is at the root of this reduced farm performance. To that end, detailed wind tunnel investigation and large-eddy simulations are used. For instance, Cal et al. [3] reproduced atmospheric turbulence prevalent in neutral conditions in a wind tunnel, and performed experiments on an array of 3×3 miniature turbines. Their main conclusion is that in an array interacting with a turbulent boundary layer, the vertical fluxes of kinetic energy that are due to the Reynolds stresses, are of the same order of magnitude as the power extracted by wind turbines. Calaf et.al. [4] performed large-eddy simulations of a complete wind farm, reaching similar conclusions. Later, these studies were followed by several

J.P. Goit (✉) · J. Meyers
Department of Mechanical Engineering, KU Leuven, Leuven, Belgium
e-mail: jay.goit@mech.kuleuven.be

J. Meyers
e-mail: johan.meyers@mech.kuleuven.be

J. Fröhlich et al. (eds.), *Direct and Large-Eddy Simulation IX*,
ERCOFTAC Series 20, DOI 10.1007/978-3-319-14448-1_54

others, aiming at a better understanding of the physics involved in wind-farm power extraction [7, 8].

In recent years, most wind-farm LESs have focused on the interaction of a farm with a pressure-driven boundary layer, ignoring outer-layer effects and Coriolis forces in the Atmospheric boundary layer (ABL). The main working hypothesis for this, is that turbines are situated in the inner layer of the boundary layer, and further using the classical notion that inner layer dynamics display 'universal' behavior, independent of outer-layer effects. However, if a wind farm is very large, or the boundary layer is shallow, the interaction with the outer layer may not be negligible. Therefore, in the current work we use Large Eddy Simulations (LES) to investigate the influence of an outer-layer Ekman spiral (caused by Coriolis forces) on the mean flow solution in wind farms. Furthermore, effects on the global wind-farm induced roughness $z_{0,hi}$, are also investigated. In our simulations, we focus on truly neutral ABLs. While these are rare in nature, various relevant physics such as roughness length, variation in boundary layer height etc., may still be investigated in such a simulation environment. We show that $z_{0,hi}$ changes with ABL height (H_G), when the boundary layer becomes shallow. We also compare wind farm simulation with an ABL simulation in which the farm is replaced by an increased equivalent surface roughness. Finally, we also investigate the displacement height d induced by farms. This is a parameter that is usually used for forest canopies.

Section 2 describes the governing equations and the LES code along with the implementation of coriolis force and a controller for the wind farm orientation. This is followed by results and discussions in Sect. 3, where we present the influence of wind farm to the ABL. Finally a summary of the current work is presented in Sect. 4.

2 Numerical Method

The KU Leuven LES code used in this study is an in-house code developed in earlier studies [4, 10]. The code solves filtered Navier–Stokes (NS), and continuity equations,

$$\frac{\partial \tilde{\mathbf{u}}}{\partial t} + \tilde{\mathbf{u}} \cdot \nabla \tilde{\mathbf{u}} = -\frac{1}{\rho}\nabla \tilde{p} - \nabla \cdot \tau_{sgs} + f_{turb} - f_c\ \tilde{\mathbf{u}} \times \mathbf{e}_z - \frac{1}{\rho}\nabla p_\infty, \tag{1}$$

$$\nabla \cdot \tilde{\mathbf{u}} = 0, \tag{2}$$

where $\tilde{\mathbf{u}}$ is the filtered velocity field, $\tilde{p}$ the pressure, and τ_{sgs} the subgrid-scale tensor.

f_{turb} is the forcing term due to turbines. This turbine induced force is based on the classical actuator-disk method which models the total thrust force acting on fluid due to the turbine and is written as

$$f_{\text{turb}} = -\rho \frac{1}{2} C_T' \langle \bar{u}^T \rangle_d^2, \tag{3}$$

where $\langle \bar{u}^T \rangle_d$ is the average turbine-disk velocity obtained during the simulation. C_T' is the thrust coefficient defined using the velocity at the turbine-disk and its value is set to 1.33 in the current study [4].

The term $f_c \tilde{\mathbf{u}} \times \mathbf{e}_z$ is a Coriolis force with f_c being a Coriolis parameter. The last term in Eq. (1) i.e., $(1/\rho)\nabla p_\infty$is a pressure-gradient force which drives the ABL. This driving force should balance the Coriolis force in the outer atmosphere and therefore depends upon the geostrophic velocity above the ABL.

$$- f_c V_G = -\frac{\partial p_\infty}{\partial x}, \quad f_c U_G = -\frac{\partial p_\infty}{\partial y}. \tag{4}$$

The code uses pseudo-spectral discretization techniques and periodic boundary conditions in the horizontal directions, whereas in the vertical direction a fourth-order energy-conservative finite difference discretization is used. The boundary condition imposed at the bottom surface comes from relating the wall stress to the velocity at the first grid-point using Monin-Obukhov similarity theory [11]. At the top of the domain a symmetry condition is used. Time advancement is performed using a four-stage fourth-order Runge-Kutta scheme. The subgrid scale model is a standard Smagorinsky model with a constant coefficient $C_s = 0.14$, and Mason and Thomson's damping function is used near the wall [9].

Because of the Coriolis force, the velocity vector rotates with height above the surface. Thus an angle exists between the geostrophic wind direction, and the wind direction at turbine hub height. This angle is not known a priori, as it depends on the total drag exerted on the boundary layer by the turbines and the ground surface. Hence, it is necessary to reorient wind turbines so that they are always perpendicular to the incoming velocity. However, doing so, would alter the inter-turbine spacing, such that the geometrical arrangement pattern is not fixed a priori. To avoid this, instead we artificially control the pressure gradient angle during the simulations such that we obtain a desired wind direction at turbine hub height (i.e. in the positive x-direction). To that end, a PID controller is implemented: the equation for the controller corresponds to

$$\alpha_{\text{out}} = K_p e(t) + K_i \int_0^t e(\tau)\, d\tau + K_d \frac{d}{dt} e(t), \tag{5}$$

where α_{out} is an output angle, K_p, K_i, K_d are proportional, integral and derivative gain parameters respectively, and e stands for the error on the angle. In the current work, we set $K_p = 0.008$, $K_i = 2 \times 10^{-8}\ \text{s}^{-1}$, and $K_d = 0\ \text{s}$. Proportional constant K_p does not have a unit. This controller maintains the incoming flow direction perpendicular to the rotor (as is the case in a real wind farm), additionally it also fix the inter-turbine spacing so that simulation results give a correct roughness length value.

3 Results and Discussions

The parameter that affects the height of the boundary layer in an Ekman spiral, is the Rossby number

$$Ro_h = \frac{G}{f_c z_h}, \tag{6}$$

defined here based on the hub height of the wind turbines. G is the magnitude of geostrophic velocity. We perform a set of simulations in which we keep the wind-farm arrangement fixed, but use 9 different Rossby numbers between 400 and 1,200. In addition, simulations with different geometrical arrangement are used, keeping $Ro_h = 1{,}000$. Since the height of the boundary layer depends on Ro_h, domain heights are adapted such they are at least 1.5 times the expected boundary layer height. Domain sizes in streamwise and spanwise directions are kept constant. In an additional LES case, a classical pressure-driven wind-farm boundary layer is considered (i.e. a half-channel flow). Full details are provided in Table 1.

3.1 Velocity Profiles

In Fig. 1, a typical instantaneous u velocity field is shown for case 1d. In the horizonal plane, we observe significant meandering of the turbine wakes. At the same time patches of high speed fluid can also be seen passing through the spaces between

Table 1 Simulation cases based on the Rossby number and other parameters

Cases	Ro_h	$L_x \times L_y \times H\ (\mathrm{m}^3)$	$N_x \times N_y \times N_z$	N_t	$s_x \times s_y$	$z_{0,lo}/z_h$
1a	400	6,280 × 3,140 × 4,000	128 × 192 × 241	8 × 6	7.85 × 5.23	10^{-3}
1b	500	6,280 × 3,140 × 4,000	128 × 192 × 241	8 × 6	7.85 × 5.23	10^{-3}
1c	600	6,280 × 3,140 × 4,000	128 × 192 × 241	8 × 6	7.85 × 5.23	10^{-3}
1d	700	6,280 × 3,140 × 4,000	128 × 192 × 241	8 × 6	7.85 × 5.23	10^{-3}
1e	800	6,280 × 3,140 × 4,000	128 × 192 × 241	8 × 6	7.85 × 5.23	10^{-3}
1f	900	6,280 × 3,140 × 4,500	128 × 192 × 281	8 × 6	7.85 × 5.23	10^{-3}
1g	1,000	6,280 × 3,140 × 5,000	128 × 192 × 311	8 × 6	7.85 × 5.23	10^{-3}
1h	1,100	6,280 × 3,140 × 5,000	128 × 192 × 311	8 × 6	7.85 × 5.23	10^{-3}
1i	1,200	6,280 × 3,140 × 5,200	128 × 192 × 321	8 × 6	7.85 × 5.23	10^{-3}
2	1,000	6,280 × 3,140 × 5,000	128 × 192 × 311	6 × 4	10.47 × 7.85	10^{-3}
3	1,000	6,280 × 3,140 × 5,000	128 × 192 × 311	11 × 6	5.71 × 5.23	10^{-3}
4	Half-channel	6,280 × 3,140 × 4,000	128 × 192 × 241	8 × 6	7.85 × 5.23	10^{-3}
5	1,200	6,280 × 3,140 × 5,200	128 × 192 × 321	No wind	Farm	0.0372

$L_x \times L_y \times H$ Domain size, $N_x \times N_y \times N_z$ Grid-resolution, N_t Number of turbines, $s_x \times s_y$ turbine spacing normalized by rotor diameter $D = 100$ m, $z_{0,lo}/z_h$ surface roughness

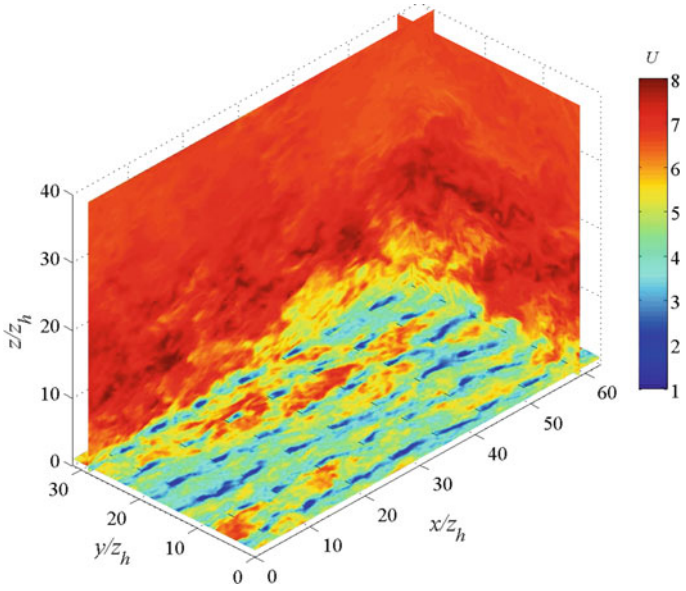

Fig. 1 Contours of instantaneous streamwise velocity. *Horizontal plane* in the figure is taken at the hub height

turbine columns. In the vertical planes, a higher u-velocity is observed around $z/z_h = 20$ than above the boundary layer. This is the characteristic of the Ekman layer; remember that the direction of the geostrophic wind is not parallel to the wind direction at turbine hub height, which is parallel to the x-direction.

Figure 2 shows x- and y-components of the mean velocity profiles for cases 1a–1i. In these different simulations, the geostrophic wind speed ranges from $G = 4$ to

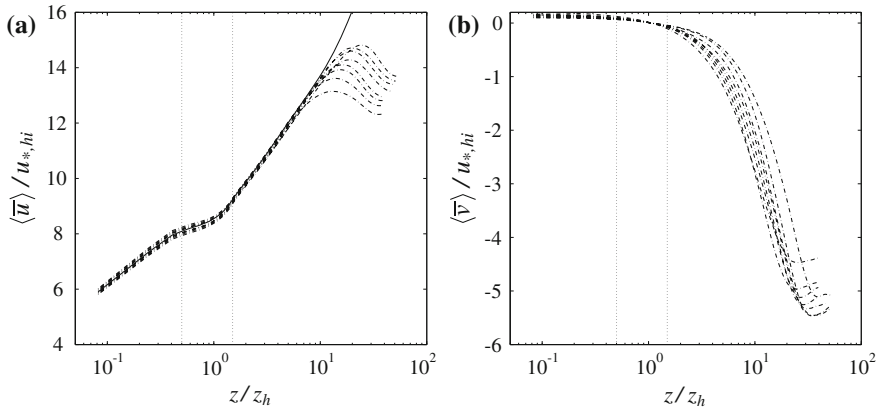

Fig. 2 Mean velocity profiles. **a** Stream wise component, **b** spanwise component. *Dot-dashed line* Ekman layer(cases 1a–1i), *full line* half-channel flow (case 4)

$G = 12$ (cf. Table 1). We normalize velocities with the total friction velocity above the farm. Similar to the observations by Calaf et al. [4], the streamwise velocity profile displays three regions around the turbines: (i) below the turbine disk, (ii) at the disc and (iii) above the turbine. Next to results obtained using Coriolis forcing of the simulations, the result of a pressure-driven channel flow (case 4) is also shown in Fig. 2a. It is appreciated that below $z/z_h = 10$, this pressure-driven velocity profile collapses remarkably well with the results using Coriolis forcing.

3.2 Roughness Length

Following Calaf et al. [4], we estimate the roughness length induced by the wind farm for our different simulations. To that end, we simply identify the surface roughness $z_{0,hi}$ associated with the logarithmic velocity profile above the turbines. This logarithmic profile is given by

$$\langle \bar{u} \rangle (z) = \frac{u_{*,hi}}{\kappa} \ln \left(\frac{z}{z_{0,hi}} \right), \tag{7}$$

$$u_{*,hi}^2 = \int_0^{H_G} f_c (V - V_G) dz, \tag{8}$$

and where the second relation is simply a result of an integrated x-momentum balance over the height of the boundary layer H_G. In Eq. (8), $u_{*,hi}$ is the friction velocity, which is the sum of the total friction imposed by the ground and the wind farm and the term on the right hand side is the difference between the driving pressure gradient and the Coriolis force. To obtain the surface roughness, we choose a point $z = 2z_h$, and substitute the velocity value into these equations to estimate $z_{0,hi}$.

In Fig. 3, results are shown for cases 1a–1i, i.e. all cases with the same turbine arrangement pattern, but different geostrophic wind speeds, and corresponding Rossby numbers. As point of reference, the value obtained by Calaf et al.'s analytical model for the wind-farm induced surface roughness is also displayed. This model corresponds with

$$\frac{z_{0,hi}}{z_h} = \left(1 + \frac{D}{2z_h}\right)^{\frac{\nu_w^*}{(1+\nu_w^*)}} \exp\left(- \left[\frac{c_{ft}}{2\kappa^2} + \left(\ln \left[\frac{z_h}{z_{0,lo}} \left(1 - \frac{D}{2z_h}\right)^{\frac{\nu_w^*}{(1+\nu_w^*)}} \right] \right)^{-2} \right]^{-1/2} \right), \tag{9}$$

where $\nu_w^* \approx 28\sqrt{1/2c_{ft}}$ and $c_{ft} = \pi C_T / 4 s_x s_y$. For further details regarding the parameters and the derivation of Eq. (9) reader is refered to Ref. [4]. It is appreciated that this model does not display any Rossby-number dependence, as it is developed under the assumption that the outer-layer dynamics of the boundary layer are not

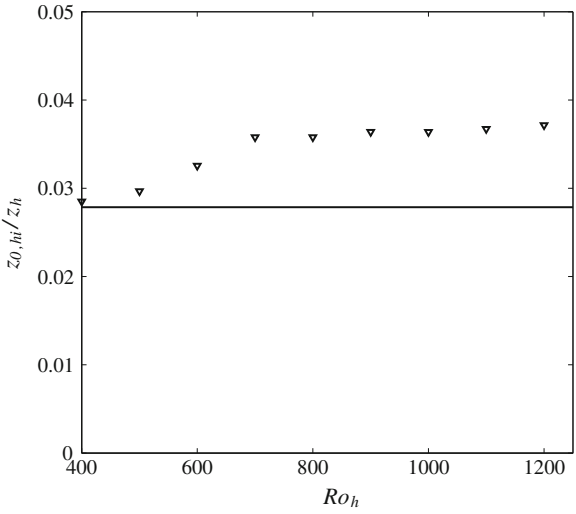

Fig. 3 Comparison between the roughness height from the LES results and the model predicted value. ∇ from simulations, *line* model of Calaf et al.

affecting the inner-layer behavior characterized by the induced surface roughness. Thus in Fig. 3, Eq. (9) corresponds to a constant value.

We observe (cf. Fig. 3) for high Rossby numbers (i.e., when the ABL height is large), that the surface roughness $z_{0,hi}$ is almost constant, with a value $z_{0,hi}/z_h \approx 0.037$ for the current wind-farm lay-out. In this case, the turbines are situated well inside the inner layer of the boundary layer ($<0.1\,H_G$), and thus, the classical hypothesis that inner-layer dynamics are separated in scale from outer-layer effects may be justified, such that the global effect of the wind-farm on the outer layer can be lumped into one parameter, i.e. the surface roughness $z_{0,hi}$, that is further independent of Rossby number or ABL height.

For lower Rossby numbers ($Ro_h < 700$), we observe that $z_{0,hi}$ is not anymore constant, but gradually decreases with Ro_h. However, even at the lowest value $Ro_h = 400$, the truly neutral boundary layer is still rather thick, with $H_G/z_h = 18$. In reality, neutral atmospheric boundary layers are so-called 'conventionally neutral', i.e. in these ABLs stable atmospheric stratification damps the maximum thickness that the boundary layer can attain. Hence, in these cases, the dependence of $z_{0,hi}$ on boundary layer height may be even more prominent.

In Fig. 4, results are shown for cases 1g, 2, and 3 (cf. Table 1), i.e. all with geostrophic wind $G = 10$, and $Ro_h = 1{,}000$, but with different turbine spacings. The model of Calaf, Meneveau and Meyers is also displayed, and it is appreciated that trends are well followed by this model, though it underpredicts the induced surface roughness at smaller turbine spacings.

Finally, we perform an additional numerical experiment, in which we evaluate how well the surface roughness $z_{0,hi}$ characterizes the wind-farm boundary layer flow. Therefore, we remove the wind turbine forces from the domain, and instead replace the boundary condition with a stress-boundary condition with surface roughness

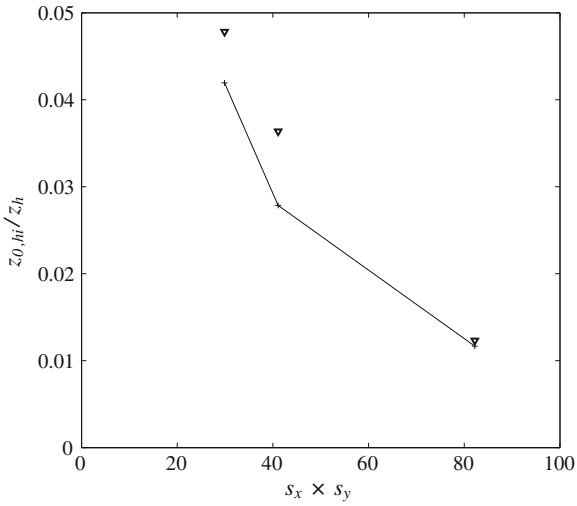

Fig. 4 Roughness length for different turbine spacings.∇ from simulations, + model of Calaf et al.

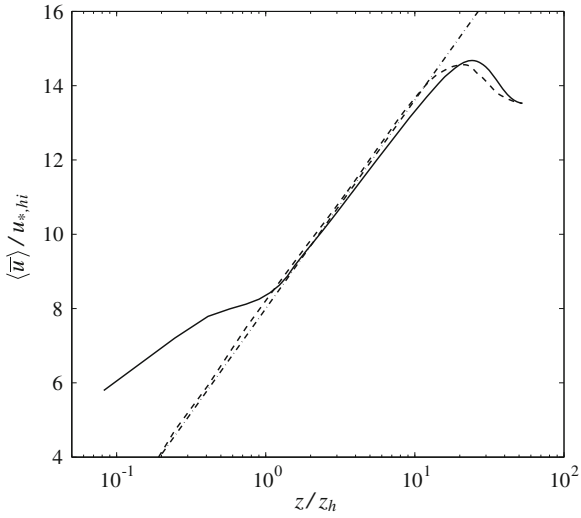

Fig. 5 Comparison of profile for Winfarm simulation with the simulation in which farm is replaced by equivalent roughness length. *Full line* Windfarm ABL, *dashed line* with equivalent roughness, *dot-dashed line* log law approximation

$z_{0,hi}$ (case 5). In Fig. 5, we compare this simulation to a case with wind farm. It is appreciated from this figure that the profile with surface roughness agrees well with the wind-farm simulation case and especially with its logarithmic fit. This agreement justifies the replacement of wind-farm by its characteristic roughness length as a surface stress in a large scale simulations such as regional climate model. In such simulation it is not feasible to simulate whole wind-farm canopies. Furthermore we compare the resolved part of normal and shear stresses profiles in Fig. 6a, b, and we found also for these properties that the comparison between both cases is reasonable.

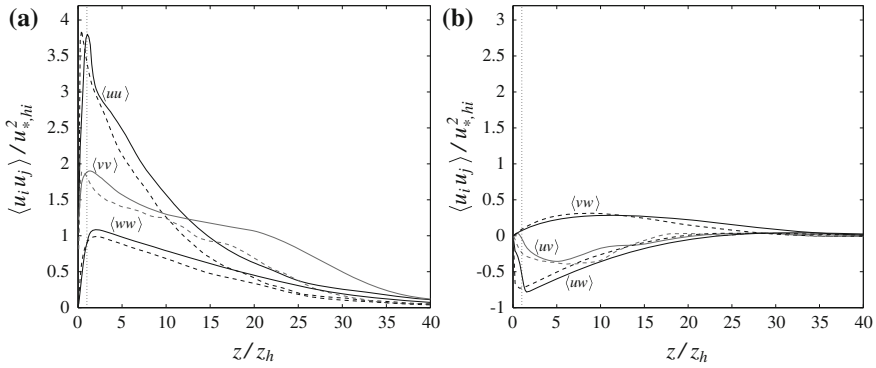

Fig. 6 Comparison of profiles of Reynolds stresses. **a** Normal stresses, **b** shear stresses. *Full line* windfarm simulation, *dashed line* farm replaced by equivalent roughness

3.3 Displacement Height

In this section we discuss the relevance of the displacement height (d) for a logarithmic fit of the velocity region above the turbines. The displacement height is typically used to set the zero level of logarithmic velocity profiles above rough surfaces such as tree canopies. It corresponds to the vertical elevation at which a substitute stress, representing all drag forces on the roughness elements, should be inserted, and is defined as the height around which the total moment of all these drag forces equals to zero [6]. Following a similar approach, we can thus define the displacement height d for a wind farm using

$$\frac{F_{turb}}{s_x s_y D^2}\,(z_h - d) - \tau_w d = 0, \tag{10}$$

with τ_w the wall stress at the ground surface.

Figure 7 displays values of d obtained for cases 1a–1i as a function of Rossby number. We observe that d is roughly independent of Rossby number for the range considered, with a value that is approximately 66% of the hub height. When looking at cases 1g, 2, and 3, i.e. for different turbine spacings in Fig. 8, we find that d increases with decreasing turbine spacing.

Above canopies, the logarithmic velocity profile is usually fitted such that the velocity at height $z = d + z_0$ equals to zero, using $\langle\bar{u}\rangle(z) = (u_{*,hi}/\kappa)\ln[(z-d)/z_0]$. However, for wind farms, this is not relevant, since the total wind-farm stress $u^2_{*,hi}$ is partially due to turbine forces that extract energy from the flow, so that velocity at these forces cannot be zero. Equaling total power P extracted by the wind farm to the power extracted by the lumped stress $u^2_{*,hi}$ times the velocity at the height d yields

$$\frac{P}{s_x s_y D^2} = \rho\langle\bar{u}\rangle_{z=d} \cdot u^2_{*,hi} \tag{11}$$

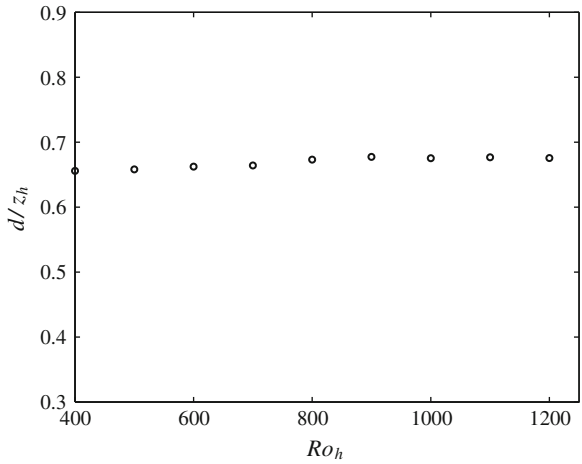

Fig. 7 Displacement height d as a function of Rossby number for cases 1a–1i

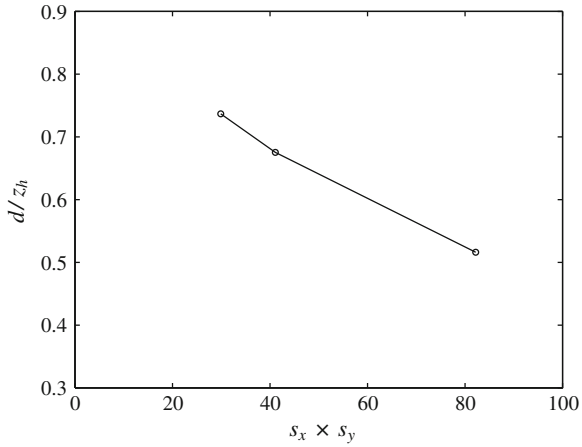

Fig. 8 Displacement height d for different turbine spacings

Using a slightly more general form of the logarithmic profile, i.e.

$$\langle \bar{u} \rangle (z) = \frac{u_{*,hi}}{\kappa} \ln \left(\frac{z + ad}{z_0} \right), \tag{12}$$

we find

$$a = \frac{z_0}{d} \exp \left(\frac{\kappa P}{\rho u_{*,hi}^3 s_x s_y D^2} \right) - 1. \tag{13}$$

In Fig. 9 we compare a conventional logarithmic profile (without displacement height), and the modified profile proposed above with the velocity profile obtained from large eddy simulations. We observe that the conventional logarithmic profile

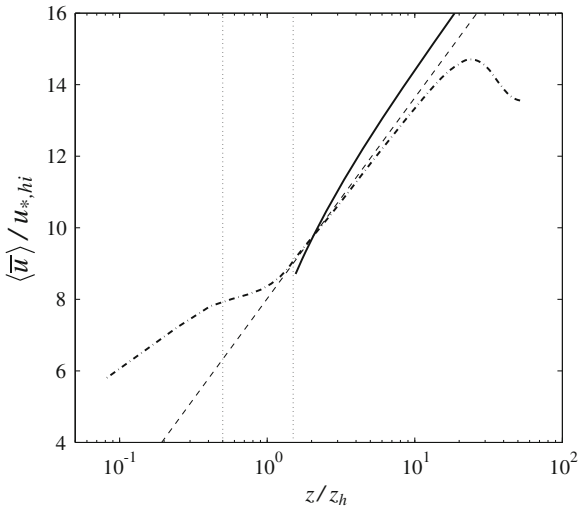

Fig. 9 Fit for the proposed profile with simulation result. *dot-dashed line* LES result, *dashed line* log law, full line: proposed profile

gives a much better fit of the logarithmic velocity profile above the turbines than the fit including the displacement height. Thus the inclusion of a displacement height, as commonly used for fitting logarithmic profiles above rough canopies, and other types of complex terrain, appears not to be beneficial for the case of wind farms. The main difference is that the total lumped shear force is partially extracting power in the case of wind farms (i.e. the portion from the wind-turbine trust forces), while this is not the case for drag forces in conventional rough terrain.

4 Summary

In the current study, we investigated wind-farm boundary layers, and the mean velocity solution in wind farms under different forcing condition. Apart from a classical pressure-driven boundary layer, that has been often used in previous studies, we also included systems driven by a geostrophic balance and Coriolis forces, such that an Ekman layer emerges. Different cases were included with a range of Rossby numbers between 400 and 1,200, each leading to a different boundary layer height. In particular when the boundary layer is shallow, outer-layer effects may become important at the level of the wind farm. To investigate this, we determined the dependency of the wind-farm induced surface roughness $z_{0,hi}$ on the Rossby number and boundary-layer depth. For the particular turbine arrangement pattern used in our current simulation, we found that $z_{0,hi}$ is constant for $Ro_h \geq 700$. At lower values, $z_{0,hi}$ starts to slightly decreases with Rossby numbers.

The simulations in the current study correspond to what is often called a 'truly' neutral boundary layer. In reality, atmospheric stratification above the boundary layer inhibits boundary-layer growth, such that the depth of such a 'conventionally' neutral

boundary layer is significantly lower (typically <1,000 m). Current results suggest that for such situations, outer-layer dynamics may have an important effect on the mean-flow distribution at wind-turbine level. This is subject of further research.

Acknowledgments J.M. acknowledges the European Research Council (FP7 Ideas—grant no 306471) and the Flemish Science Foundation (grant number G.0376.12) for support.

References

1. Barthelmie, R.J., Framdsen, S.T., Nielsen, M.N.: Modelling and measurements of power losses and turbulence intensity in wind turbine wakes at middelgrunden offshore wind farm. Wind Energy **10**, 517–528 (2007)
2. Barthelmie, R.J., Jensen, L.E.: Evaluation of wind farm efficiency and wind turbine wakes at the nysted offshore wind farm. Wind Energy **13**, 573–586 (2010)
3. Cal, R.B., Lebron, J.L., Castillo, L., Kang, H.S., Meneveau, C.: Experimental study of the horizontally averaged flow structure in a model wind-turbine array boundary layer. J. Ren. Sust. Energy **2**, 013106 (2010)
4. Calaf, M., Meneveau, C., Meyers, J.: Large eddy simulation study of fully developed wind-turbine array boundary layers. Phys. Fluid **22**, 015110 (2010)
5. Hansen, K.S., Barthelmie, R.J., Jensen, L.E., Sommer, A.: The impact of turbulence intensity and atmospheric stability on power deficits due to wind trubine wakes at horns rev wind farm. Wind Energy **15**, 183–196 (2011)
6. Jackson, P.S.: On the displacement height in the logarithmic velocity profile. J. Fluid Mech. **111**, 15–25 (1994)
7. Johnstone, R., Coleman, G.N.: The turbulent ekman boundary layer over an infinite wind-turbine array. J. Wind Eng. Ind. Aerodyn. **100**, 46–57 (2012)
8. Lu, H., Porte-Agel, F.: Large-eddy simulation of a very large wind farm in a stable atmospheric boundary layer. Phys. Fluid. **23**, 065101 (2011)
9. Mason, P.J., Thomson, D.J.: Stochastic backscatter in large-eddy simulations of boundary layers. J. Fluid. Mech. **242**, 51 (1992)
10. Meyers, J., Meneveau, C.: Large eddy simulations of large wind-turbine arrays in the atmospheric boundary layer. In: 48th AIAA Aerospace Sciences Meeting Including the New Horizons Forum and Aerospace Exposition, Orlando, Florida. AIAA 2010–827, pp. 1–10 (2010)
11. Moeng, C.-H.: A large-eddy simulation model for the study of planetary boundary-layer turbulence. J. Atmos. Sci. **6**, 2311 (1984)

Pollutant Dispersion in the Urban Boundary Layer

J.M. Tomas, M.J.B.M. Pourquie, H.E. Eisma, G.E. Elsinga, H.J.J. Jonker and J. Westerweel

1 Introduction

Traffic is known to be a significant pollutant emission source in urban environments. To gain insight into dispersion of pollutants in the urban boundary layer at the 'neighbourhood scale' (10–1,000 m) the Dutch Atmospheric Large-Eddy Simulation (DALES) model [1] has been extended with an Immersed Boundary Method (IBM) [4] in order to take into account obstacles like buildings, fences or banks. As a first application the flow over a sound barrier—an obstacle often found along urban roadways—is considered. The results are compared with results from experiments in the water tunnel facility of the Aero and Hydrodynamics Laboratory at the TU Delft. In addition, the passive dispersion of a pollutant released from a line source (representing a straight section of a roadway) is investigated in the simulation.

2 Numerical Method

Details about the DALES code can be found in a paper by Heus et al. [1]. The model is based on the spatially filtered equations of motion under the assumption of the Boussinesq approximation. The subgrid-scale momentum and scalar fluxes are modeled through an eddy viscosity and eddy diffusivity, respectively. These are modeled by relating them to the subgrid-scale turbulence kinetic energy using a one-equation model. All spatial derivatives in the governing equations are discretized

J.M. Tomas (✉) · M.J.B.M. Pourquie · H.E. Eisma · G.E. Elsinga · J. Westerweel
Laboratory for Aero- and Hydrodynamics, TU Delft,
Leeghwaterstraat 21, 2628 CA Delft, The Netherlands
e-mail: j.m.tomas@tudelft.nl

H.J.J. Jonker
Department of Geoscience & Remote Sensing, TU Delft,
Stevinweg 1, 2628 CA Delft, The Netherlands

J. Fröhlich et al. (eds.), *Direct and Large-Eddy Simulation IX*,
ERCOFTAC Series 20, DOI 10.1007/978-3-319-14448-1_55

with second-order central-differencing on a staggered grid. To account for obstacles in the domain an immersed boundary method is applied to impose a no-slip condition to cell faces [4]. By this method boundaries that are aligned with grid faces can be considered. When a cell face contains a wall, the velocity normal to the wall is simply set to zero. Moreover, the computed shear stress at that face (corresponding to the situation without a wall) is replaced by the stress as computed when a wall is present. In case of scalar quantities (temperature, subgrid energy, or passive pollutant) a flux boundary condition is imposed by replacing the computed flux at that face with the desired flux (which is zero in this work). Finally, the near-wall length scale λ is decreased using a damping function, $D = \sqrt{1 - \exp\left(-r^+/A^+\right)^3}$, thereby decreasing the near-wall subgrid energy computed by the subgrid model. Here, r^+ is the distance to the closest wall in viscous units and $A^+ = 25$. Because the pressure correction may introduce velocities penetrating the boundaries the correction is kept as small as possible by applying a slightly different pressure correction method than in the DALES version described by Heus et al. [1]. The modified pressure at the new time step is decomposed into the result from the previous time step and an unknown increment: $\pi' = \pi_{n+1} - \pi_n$. The result from the previous time step is used to predict the pressure-gradient term. An efficient Poisson solver is used to solve for π'. Subsequently, the time derivatives of the velocity components (predicted by using the modified pressure as computed in the previous time step, π_n) can be corrected. Next, the solution is integrated in time one substep of the applied third-order Runge-Kutta method.

Since it is computationally unfavorable to fully simulate the spatial development of the flate plate boundary layer corresponding to the experiments in the water tunnel, a proper representation needs to be constructed in a more efficient but still accurate way. The method by Lund et al. [3] was applied in a separate simulation in which the average inlet profile is controlled through a rescaling procedure of the velocity at a chosen downstream location. The free parameters are the free stream velocity, U_∞ and the average boundary layer height, δ_{99}. These are set to the values found in the experiment. Figure 1a, b show the time-averaged results for the case of a

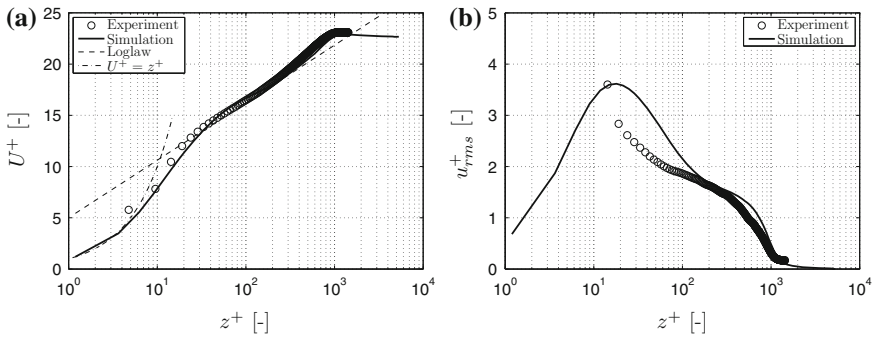

Fig. 1 **a** Time-averaged streamwise velocity (*inner* scaling); $Re_\theta = 1860$. **b** Root mean square of streamwise velocity fluctuations

zero-pressure-gradient boundary layer at a Reynolds number of 1860 based on the momentum thickness, together with results from planar PIV measurements in a water tunnel experiment. The simulated domain has a length of $11.1\delta_{99}$, a width of $2.8\delta_{99}$ and a height of $6.1\delta_{99}$, using 96 by 48 by 104 cells, respectively. The center of the first cell adjacent to the wall has a wall-distance of one viscous unit. In the wall-normal direction cells grow exponentially in height. At the beginning of the simulation a time-average with a weight that decreases exponentially backwards in time was used to remove start-up effects. The averaging interval was increased from $10T$ ($T = \delta_{99}/U_\infty$) to $100T$ and eventually a running average was used. This process took $1{,}800T$ of the simulation. Then, the simulation was continued for another $5{,}000T$ during which the inlet plane was saved. The mean velocity shows good agreement with the experimental data. The profile of u_{rms} differs quantitatively, most likely due to the coarseness of the mesh.

3 Surface-Mounted Fence in a Turbulent Boundary Layer

In a water tunnel experiment turbulent flow over a surface-mounted fence is measured by planar PIV. A neutrally stratified turbulent boundary layer over a flate plate is created by tripping the laminar flow with a threaded rod mounted at the inlet of the test section just above the flate plate. Downstream, where the boundary layer has developed, the fence is mounted perpendicular to the approaching flow. The fence height, h, is 2.5×10^{-2} m and its thickness 1.5×10^{-3} m. In the simulation the generated boundary layer explained in Sect. 2 is used as inlet condition. At the top an average outflow velocity is specified corresponding to the inlet simulation. On all walls no-slip and zero-flux conditions (for the scalar pollutant) are applied. The convective outflow condition $\frac{\partial \psi}{\partial t} + C\frac{\partial \psi}{\partial x} = 0$ is imposed at the outlet, where ψ represents all prognostic variables and C is the bulk velocity. The domain has a length of $38h$, a width of $10h$ and a height of $22h$ using 272 by 48 by 104 cells, respectively. The fence is located $8h$ downstream of the inlet. In the streamwise and wall-normal directions the grid is stretched with the smallest cell dimension being equal to the height of the first wall-normal cell at the inlet, which corresponds to $z^+ = 1$. Averaging is done over 1,800 time scales T, where $T = h/U_\infty$. The sample interval of the simulation was $0.5T$. For the experiment the Reynolds number based on the fence height is 5,240. For the simulation this is 5,650. The ratio of the boundary layer height and the fence height, δ_{99}/h, is 3.64 for the simulation. Because in the experimental setup the field of view was not large enough to capture the full height of the boundary layer, δ_{99}/h is estimated to be 3. Figure 2 shows the first-order statistics at several downstream locations. Figure 3 shows the second-order statistics at these locations. Upstream of the fence a clockwise rotating recirculation zone with a length of $1h$ exists (not shown). In this region a comparison with the experiment cannot

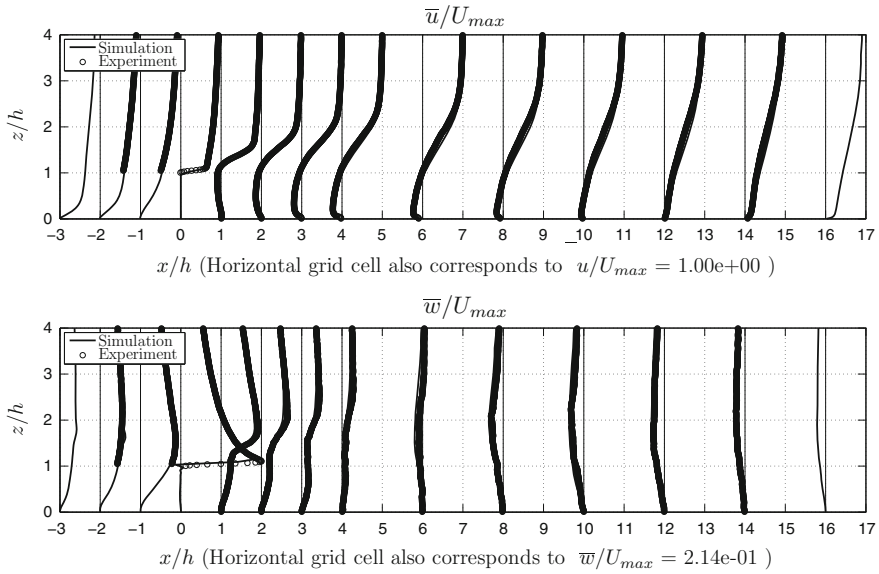

Fig. 2 Time-averaged velocity field around a surface-mounted fence

be made, since the flow field has not been measured there due to blockage of the laser sheet by the fence. Both the results from the experiment and the simulation show a large clockwise rotating recirculation zone at the downstream side, which has a length of $11.6h$ in the experiment and $10.7h$ in the simulation. Liu et al. [2] showed that for the flow over a square riblet the size of the recirculation zone depends on the ratio of the boundary layer height to fence height, which might explain the difference, since this ratio is different in the experiment and the simulation. In both results in the downstream region near the fence a second recirculation appears (not shown), rotating counter-clockwise in this case. It extends less than $1h$ downstream and about $2/3h$ from the ground. Clearly visible in both results is the acceleration of the flow just above the fence resulting in a strong shear layer. The time-averaged Reynolds-stress and variances of u and w seem to be slightly overpredicted near the fence, while further downstream they are underpredicted. The coarseness of the applied grid can be the cause of this discrepancy, which is to be checked by a grid refinement study. Note, however, that close to the wall and at the top of the fence the accuracy of the PIV method deteriorates due to reflections making it difficult to accurately determine for example the peak values of $\overline{u'u'}$ and $\overline{w'w'}$.

In the simulation a line source of passive pollutant was added to the domain to resemble the emission of exhaust gases from traffic. The release location is $7.9h$ downstream of the fence at a height of $h/4$. Results are shown in Fig. 4. Because the source location is in the recirculation zone, the pollutant is advected in the direction

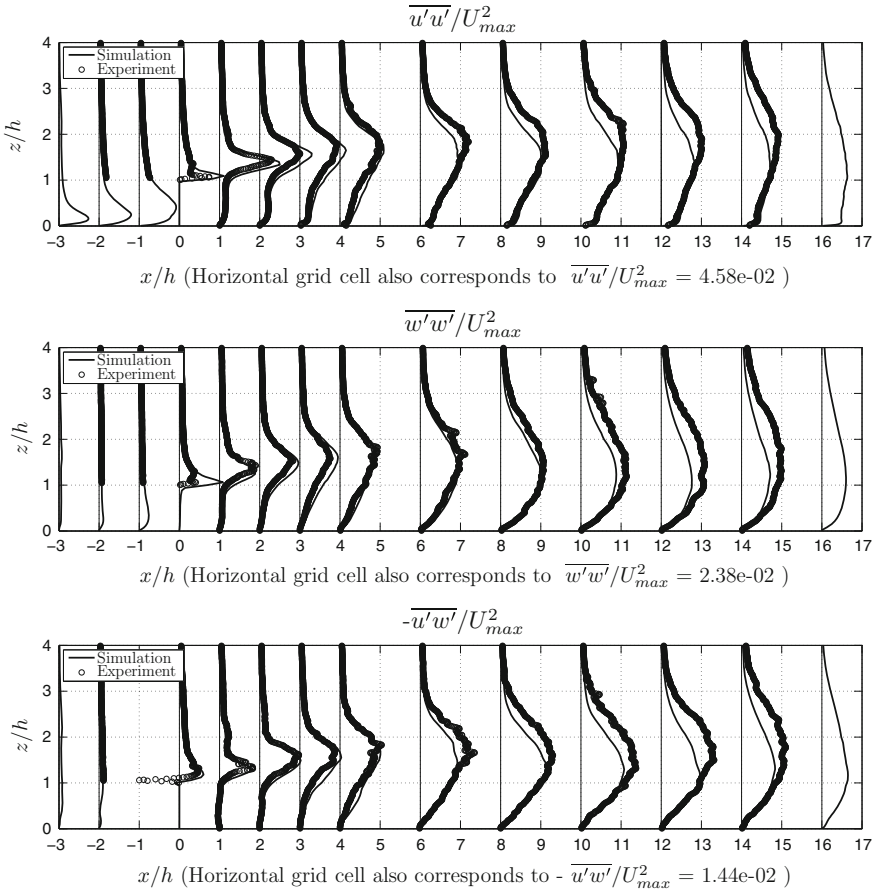

Fig. 3 Second-order statistics of the velocity field around a surface-mounted fence. Simulation results are the sum of resolved solution and subgrid-scale contribution

opposite to the free stream. Close to the fence pollutant concentration builds up, while at the top of the fence it is released and entrained by the shear layer. The positive and negative contributions to the mean concentration fluxes are plotted together with the total mean in the middle and bottom graphs of Fig. 4. In the region $z/h = 1$–3 downstream of the source the streamwise flux $\overline{u'c'}$ has a negative sign, while the mean streamwise gradient is also negative, i.e. counter-gradient transport occurs. Therefore, models based on mean gradient transport will not be able to predict this behaviour correctly.

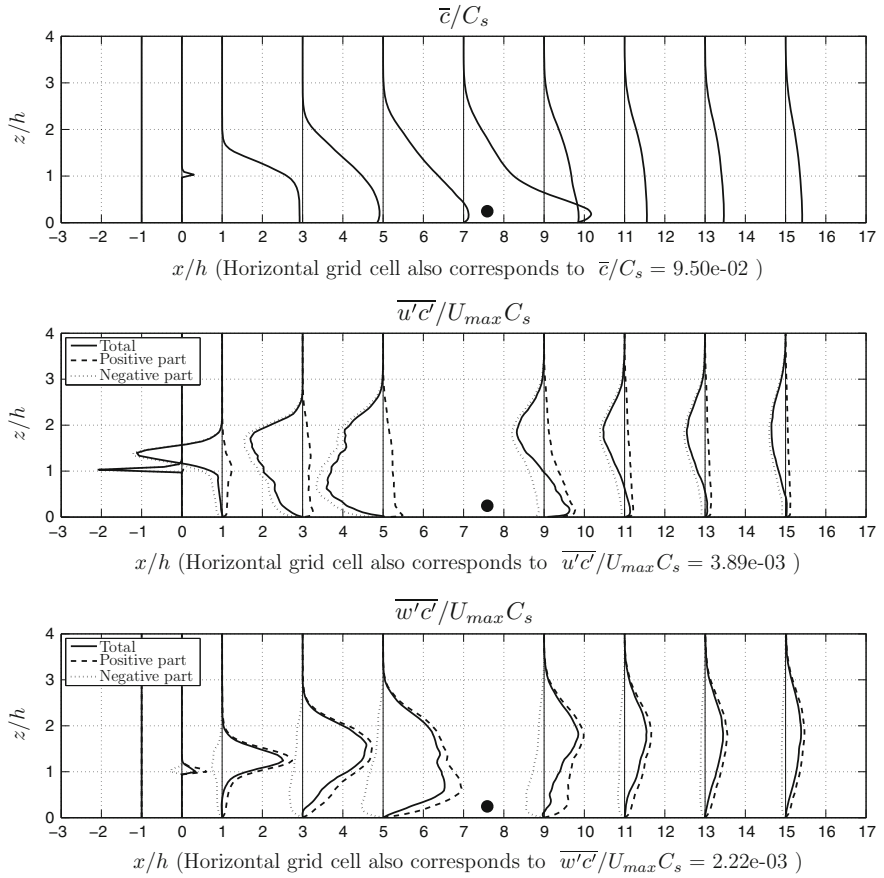

Fig. 4 *Top figure* time-averaged concentration. *Middle figure* time-averaged streamwise concentration flux. *Bottom figure* time-averaged vertical concentration flux. The concentration fluxes are the sum of the resolved solution and subgrid-scale contribution. The • resembles the location of the line source

4 Conclusions

The DALES code is extended with an IBM enabling the simulation of flow over obstacles. By rescaling a spatially-developing boundary layer the turbulent profile measured in a water tunnel experiment is successfully reproduced. Simulating the flow over a surface-mounted fence using this boundary layer as inflow condition results in a velocity field that is in good agreement with experimental data. A line source was added to the domain that resembles passive pollutant emission from traffic. Based on a comparison between the direction of the local mean concentration fluxes and the direction of the mean concentration gradient it is shown that locally countergradient behaviour occurs.

To progress from a single obstacle case study to the investigation of urban boundary layers the following activities are in preparation; firstly, the ratio of the boundary layer height and the obstacle height as well as the Reynolds number need to approximate real-life values. In addition, thermal stratification effects will be included and situations with greater geometric complexity will be investigated.

References

1. Heus, T., van Heerwaarden, C.C., Jonker, H.J.J., Siebesma, A.P., Axelsen, S., van den Dries, K., Geoffroy, O., Moene, A.F., Pino, D., de Roode, S.R., Vila-Guerau de Arrellano, J.: Formulation of the Dutch atmospheric large-eddy simulation DALES and overview of its applications. Geosci. Model Dev. **3**, 415–444 (2009)
2. Liu, Y.Z., Ke, F., Sung, H.J.: Unsteady separated and reattaching turbulent flow over a two-dimensional square rib. J. Fluids Struct. **24**, 366–381 (2008)
3. Lund, T.S., Wu, X., Squires, K.D.: Generation of turbulent inflow data for spatially-developing boundary layer simulations. Int. J. Comput. Phys. **140**, 233–258 (1998)
4. Pourquie, M., Breugem, W.P., Boersma, B.J.: Some issues related to the use of immersed boundary methods to represent square obstacles. Int. J. Multiscale Comput. Eng. **7**(6), 509–522 (2009)

Large-Eddy Simulation Model for Urban Areas with Thermal and Humid Stratification Effects

A. Petronio, F. Roman, V. Armenio, F. Stel and D. Giaiotti

1 Introduction and Governing Equations

The problem of pollutant dispersion is a crucial issue for life quality in urban areas. Accurate prediction of the phenomenon is required in highly complex domains: at urban scale, local effects are ruled by the buildings canopy along with stratification due to the presence of humidity and heat sources within the canopy. Moreover the flow in the canopy is strongly dependent on atmospheric conditions and circulations ongoing on the specific area. Therefore suitable nesting methods are required in the framework of LES simulations of urban areas in order to provide suitable and realistic boundary conditions, BCs, to the solver. LES-AIR has proven to be well suited to predict air quality at urban scale, and it has been already developed and validated for reliable high spatial and temporal resolution simulations.

LES-AIR solves the Boussinesq form of the 3-dimensional, non-hydrostatic Navier-Stokes equations together with the equations for energy, in terms of the potential temperature θ, and for humidity, in terms of the specific humidity Q. Both θ

A. Petronio (✉) · F. Roman · V. Armenio
Dipartimento di Ingegneria e Architettura, Università di Trieste,
Piazzale Europa 1, 34127 Trieste, Italy
e-mail: petronioa@units.it

F. Roman
e-mail: froman@units.it

V. Armenio
e-mail: armenio@dica.units.it

F. Stel · D. Giaiotti
ARPA FVG - CRMA, Regional Center for Environmental Modeling,
Via Cairoli 14, 33057 Palmanova (UD), Italy
e-mail: fulvio.stel@arpa.fvg.it

D. Giaiotti
e-mail: dario.giaiotti@arpa.fvg.it

J. Fröhlich et al. (eds.), *Direct and Large-Eddy Simulation IX*,
ERCOFTAC Series 20, DOI 10.1007/978-3-319-14448-1_56

and Q are treated as active scalars and the buoyancy force is taken into account by the Boussinesq approximation. Transport of pollutants (treated as passive scalars) is also implemented in the model.

The sub-grid scale stress is parameterized by Smagorinsky model, and for the active scalars the Reynolds analogy is assumed with $Pr_{sgs} = 1$, $Sc_{sgs} = 1$. A body fitted curvilinear grid is adopted to follow the macro geometry such as the terrain slopes, while smaller complexities, such as buildings, are represented by using the Immersed Boundary methodology (IBM). In the present paper we present: (1) the model implemented to deal with stratification effect due to humidity and validation against experimental field data; (2) the implementation of a nesting procedure that takes advantage of the larger scale flow data from WRF model [6].

2 Surface Fluxes Definition and Validation

At the solid boundaries, i.e. terrain and buildings, specific conditions must be applied in order to properly account for the interaction between the ABL and the ground. A standard approach is to define the fluxes of momentum, heat and humidity at the surface taking advantage of the well known Monin-Obukhov similarity theory (MOS). More details about the theory itself can be found in [1, 2]. The present study validates the numerical model, and in particular the numerical implementation of the Monin-Obukhov fluxes, with respect to field measurements. Different literature approaches are considered to compute the fluxes from experimental data providing significant differences in the results, i.e. the *bulk, gradient*, and the *integral relation*, IR, methodology. The latter that takes advantage of the integral relations of the similarity functions is found to be the best method, in agreement with other related works, as for example [4]. The IR method requires only one measure of velocity in the atmospheric surface layer. Temperature, pressure and humidity require one more sample at ground level. The characteristic surface roughness, z_0 is the only parameter to be set in the formulas.

The experimental field data are recorded from 1:00 a.m 22/06/2010 until 0:00 23/06/2010 (UTC), by the ARPA meteorological stations 6 in Udine San Osvaldo. In that period a light diurnal breeze is present along with unstable atmospheric condition enhancing the mixing of both scalars along the air column. The measured data are the horizontal hourly mean wind speed, probed at heights of 2 and 10 m, the temperature at 0 and 2 m, pressure and relative humidity at 2 m. The numerical domain is a box of $600 \times 600 \times 600$ m discretized by $64 \times 128 \times 64$ cells, stretched in the vertical direction. On the lateral boundaries periodic conditions are applied, at the top layer a rigid-lid condition for the velocity is imposed, for the scalars a zero vertical flux is applied.

The validation is performed developing the flow under the surface conditions present at 11:00 a.m. of June 23-th 2010, until the statistical steady state is reached. The results are then compared to radio-sounding data along the air column, recorded

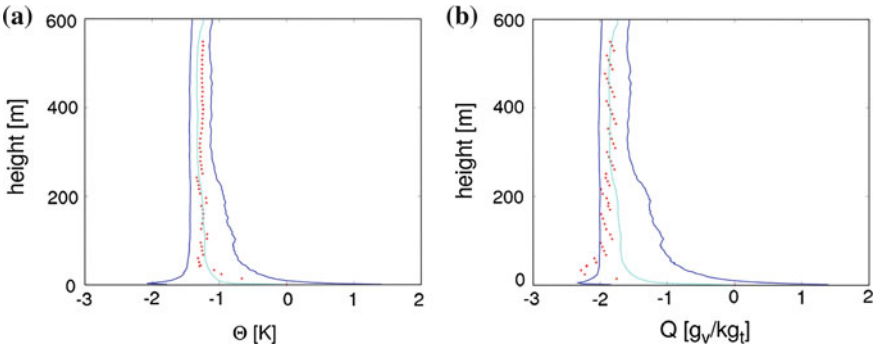

Fig. 1 **a** Comparison between LES-AIR results and experimental data for θ. **b** Comparison between LES-AIR results and experimental data for Q

nearby the meteorological station at the same time. The comparisons are shown in Fig. 1a, b for θ and Q, in which red dots represent the radio-sounding samples, the light blue lines are the horizontally space-average quantities while the blue lines represent the 5-th and 95-th percentile of the numerical sample. An overall good agreement between numerical results and experimental data is found.

2.1 Pollutant Dispersion Test

Another simulation for the same case considers the presence of an idealized source of pollutant concentration C, in order to enlighten the release effects in convective or stable atmospheric conditions. The pollutant source is modelled imposing $\frac{\partial C}{\partial y} = 1$ on 4 cell faces at the middle of the bottom surface and $\frac{\partial C}{\partial y} = 0$ elsewhere. The run covers the period from the 11:00 a.m to 11:00 p.m. of June 23-th 2010, considering surface conditions computed from experimental data. The numerical domain consists of a box of $2 \times 1 \times 2$ km discretized by $64 \times 64 \times 64$ cells, stretched in the vertical direction. The same BCs as for the validation case are used except for those for the scalar fluxes now obtained from the radio-sounding data. A linear interpolation between the hourly available data is required for both the top layer and the MOS fluxes at the solid surface.

In Fig. 2a the evolution of the pollutant concentration C during 12 h is shown through horizontally plane-average profiles. During unstable atmospheric conditions turbulence enhances mixing in the air column diffusing the active scalars and C, as shown by blue, green, and red lines for conditions at 11:00 a.m., 2:00 p.m. and 6:00 p.m. respectively. As the heat and humidity fluxes diminish, the flow enters a stable stratification regime, in which the scalars accumulate in the lower part of the ABL (see light blue, magenta and yellow lines).

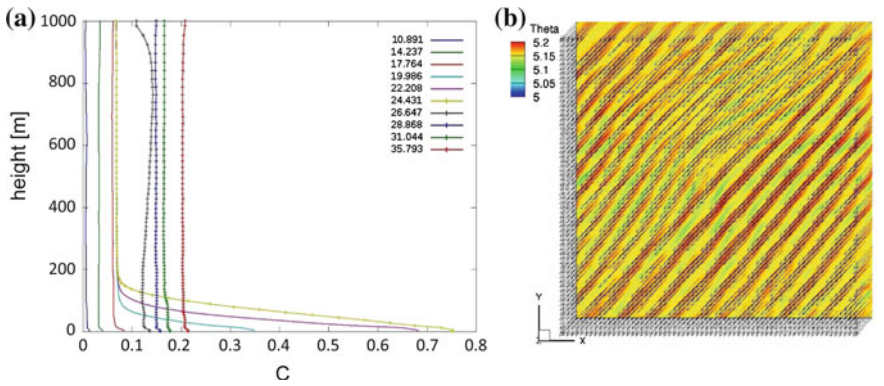

Fig. 2 **a** Evolution of the pollutant dispersion during the convective and stable regime. **b** An instantaneous contour plot of θ and velocity vectors, revealing the internal waves

It must be noted that zero flux condition for C at the top layer allows its accumulation in the volume, as can it be seen in Fig. 2a. The present simulation is able also to reproduce the developing of internal waves in stable stratified conditions with the consequent horizontal transport of C in the lower layers. The Fig. 2b shows at the first computational plane close to the ground the contour plot of temperature field and velocity vectors: the phase velocity of the temperature waves is orthogonal to velocity vector.

3 Nesting Procedure

In real-scale applications the flow field at neighbour scale is usually strongly affected by meteorological conditions at the mesoscale. Thus BCs must be supplied through nesting the microscale model within a general circulation model. The nesting methodology herein discussed provides suitable and realistic BCs to the LES-AIR model, taking advantage of large scale model (WRF) output. It consists mainly of two steps. (1) WRF data (velocity components, turbulent kinetic energy, TKE, and active and passive scalars) are interpolated at the boundaries of the LES-AIR domain; (2) A buffer region within the LES domain is used to trigger a fluctuating turbulent field starting from the information given by WRF. This is accomplished using a divergence-free *synthetic body force*, b_i', added to the right hand side of the momentum equation of the LES-AIR. The intensity of the body force is automatically adjusted based on the mean velocity profile and the TKE content coming from WRF through the interpolation procedure. In the buffer region the TKE equation reads:

$$\frac{\partial TKE}{\partial t} = transport - \overline{u_i' u_j'} \frac{\partial U_i}{\partial x_j} + \overline{b_i' u_i'} - dissipation \tag{1}$$

where $\overline{b_i' u_i'}$ acts as the turbulence source term in the bulk flow. In high Reynolds number flows, most of TKE dissipation and production takes place in the near wall region, which is not solved directly but modelled by means of wall-function approach. As a consequence b_i' can be formulated in a discretized form as

$$b_i' = \frac{TKE_{RANS}}{u_i'/\Delta t} \tag{2}$$

where TKE_{RANS} denotes the TKE supplied by WRF at the LES-AIR boundaries.

A preliminary validation test is performed simulating a turbulent plane-channel flow, at $Re_\tau = u_\tau \delta/\nu = 20{,}000$, using wall-layer model approach. We simulate this flow using periodic conditions as reference case, and successively using inflow-outflow conditions. The inflow conditions is given by a time-varying instantaneous velocity field obtained in the periodic-conditions case. The inflow-outflow simulations are run respectively without and with synthetic generation of turbulence. Different channel lengths and mesh resolutions have been considered, but here we show the results of the channel of dimensions $3\pi\delta \times 2\delta \times \frac{2}{3}\delta$ with $49 \times 33 \times 33$ cells resolution. Among the different buffer lengths tested, we show in Fig. 3 the result for a buffer region as long as $16\Delta x$, being Δx the cell length in stream-wise direction. The plots show the mean velocity profile (left panel) and the rms values of the stream-wise velocity (right panel). A good matching is found, proving that the methodology is effective. Finally the LES-AIR code is nested within the WRF model to reproduce a 5-h developing ABL, from 10 a.m. of August 25-th 2011, using a $2 \times 1 \times 2$ km domain, corresponding to a WRF cell size. In order to assess the performance of the LES-AIR the horizontally space-average of the quantities are considered. As an example the plots of the active scalars are shown in Fig. 4a, b. The WRF profiles are plotted in blue lines, the LES-AIR outputs in green. A good matching is found both for scalars and velocities components.

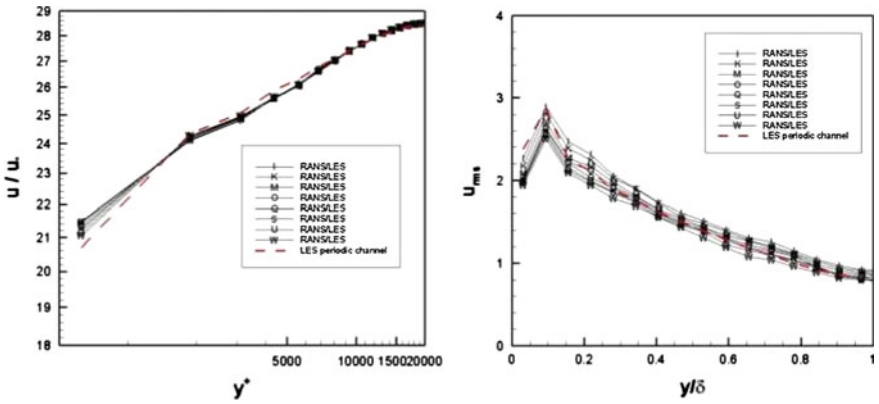

Fig. 3 Validation test results for the nesting procedure. In *red dashed line* there is the reference result from the periodic channel simulation, in *black lines* the quantities at different sections of the channel with the buffer region

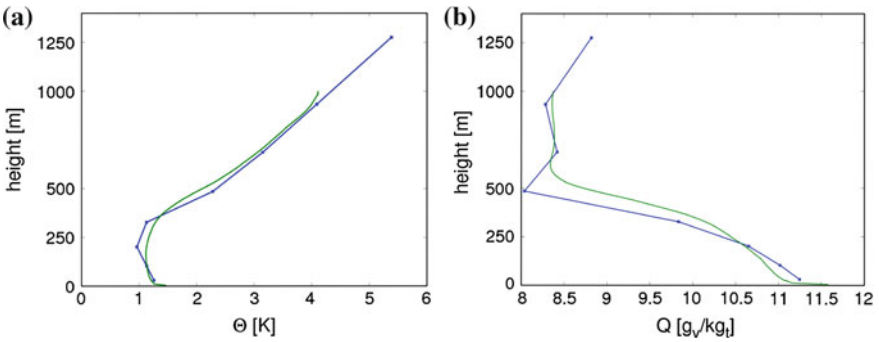

Fig. 4 **a** Validation of the nesting procedure with WRF output for θ. **b** Validation of the nesting procedure with WRF output for Q

4 Conclusions

LES-AIR, a numerical model for the analysis of pollutant dispersion at neighbour scale, is presented and validated. The validation test of the stratification effect due to both heat and humidity is firstly discussed. Experimental field data are properly elaborated considering the integral MOS relations, see for example [4], in order to compute the Monin-Obukhov fluxes to be used as BCs at the bottom layer of the LES domain. The model reproduces the main features of the atmospheric boundary layer during the complete daily cycle. Further a nesting procedure is proposed for those cases where a significant mesoscale wind is present in the area. The method is calibrated and validated in the case of the turbulent plane channel flow at Reynolds number comparable to those of atmospheric flows. As a final step the LES-AIR model is nested within a WRF domain. The vertical profiles of scalars and velocity in the LES domain are found to be in close agreement with the WRF model results, proving the effectiveness of the overall methodology here proposed and discussed.

The research has been partially supported by CINFAI through the project RITMARE.

References

1. Arya, S.P.: Introduction to Micrometeorology, 2nd edn. Academic Press, San Diego (2001)
2. Businger, J.A., Wyngaard, J.C., Izumi, Y., Bradley, E.F.: Flux-profile relationships in the atmospheric surface layer. J. Atmos. Sci. **28**, 181–189 (1971)
3. Cabot, W., Moin, P.: Approximate wall boundary conditions in the large-eddy simulation of high Reynolds number flows. Flow Turbul. Combust. **63**, 269 (2000)
4. Kumar, V., Svensson, G., Holstag, A.A.M., Meneveau, C., Parlange, M.B.: Impact of surface flux formulations and geostrophic forcing on large-eddy simulations of diurnal atmospheric boundary layer flow. J. Appl. Meteorol. Climatol. **49**, 1496–1516 (2010)

5. Moeng, C.H., Dudhia, J., Klemp, J.B., Sullivan, P.: Examining two-way grid nesting for large eddy simulation of the PBL using the WRF model. Mon. Weather Rev. **135**(6), 2295 (2007)
6. Skamarock, W.C., Klemp, J.B., Dudhia, J., Gill, D.O., Barker, D.M., Duda, M.G., Huang, X.Y., Wang, W., Powers, J.G.: A description of the advanced research WRF version 3. NCAR Technical Note (2008)

Large-Eddy Simulation of Turbulent Flow Over an Array of Wall-Mounted Cubic Obstacles

Mohammad Saeedi and Bing-Chen Wang

1 Introduction

The massively developing urban areas with different buildings in proximity of each other, makes it an important topic to study wind engineering to understand the mechanism of flow-structure interactions. To this purpose, extensive experimental studies have been conducted to investigate the turbulent flow around wall-mounted obstacles and buildings. Lim et al. [1] studied the turbulent flow over a cubic bluff body in a wind tunnel experiment. They showed that the generally accepted assumption of Reynolds-number independency for bluff bodies submerged in thick boundary layers was not always valid. Wang and Zhou [2] conducted wind tunnel experiments using hot-wire anemometry and particle-image velocimetry to analyze the wake region of a square cylinder of different aspect ratios. They characterized the wake region by the interaction of the tip, base and spanwise vortices.

Traditionally, numerical studies heavily relied on the Reynolds-averaged Navier-Stokes (RANS) approach, which however, cannot provide detailed temporal and spatial information. Lien and Yee [3] studied turbulent flow over an array of three-dimensional buildings using the k-ε models. They could obtain good agreement with the experimental results for the mean velocities but underpredicted the turbulent kinetic energy (TKE) above the buildings. With the fast development of computational technology, high-resolution numerical simulations have become more and more accessible. Cheng et al. [4] compared the large-eddy simulation (LES) and RANS approach in simulating the turbulent flow over a matrix of cubes at a relatively low Reynolds number. They showed the better performance of LES especially in prediction of the Reynolds stress and spanwise mean velocity. Although there have

M. Saeedi (✉) · B.-C. Wang
Department of Mechanical Engineering, University of Manitoba,
Winnipeg, MB R3T 5V6, Canada
e-mail: umsaeedi@cc.umanitoba.ca

B.-C. Wang
e-mail: BingChen.Wang@ad.umanitoba.ca

J. Fröhlich et al. (eds.), *Direct and Large-Eddy Simulation IX*,
ERCOFTAC Series 20, DOI 10.1007/978-3-319-14448-1_57

been some studies based on direct numerical simulation (DNS) of flow around bluff bodies, conducting a DNS over an array of obstacles at a high Reynolds number of practical interest can be prohibitively expensive due to the demand for high-resolution mesh near a large number of solid surfaces. Furthermore, detailed flow information at the finest Kolmogorov scales obtained from DNS is not always necessary in engineering practice. In view of this, LES can be an optimum tool for unsteady simulation of turbulent flows and investigation of detailed flow structures over an idealized urban area.

In this research, we perform a high-resolution LES over an array of 3-D wall-mounted obstacles and conduct a comparative study of different inlet boundary conditions. Three SGS stress models have been tested and the obtained numerical results are validated against available experimental data to compare the predictive performances of the SGS stress models.

2 Simulation Set-Up and Numerical Schemes

The simulation is to reproduce the experiment of Brown et al. [5] conducted at the U.S. Environmental Protection Agency's (EPA) meteorological wind tunnel. In this experiment, a regular array of 77 (7 rows by 11 columns) cubes with side-length of $h = 15\,\text{cm}$ were immersed in an emulated neutrally stratified atmospheric boundary layer. The cubes were strictly aligned with a uniform spacing of h in the streamwise and spanwise directions. The Reynolds number based on the cube side and mean freestream velocity was 30,000. Mean and turbulent velocities along the center line plane (plane of symmetry) were measured using a high resolution pulsed-wire anemometer.

The numerical simulations were performed using an in-house code developed using the FORTRAN 90/95 programming language, and fully-parallelized using the message passing interface (MPI) library. The code is based on a fully implicit fractional step method and fully conservative finite difference discretization scheme based on a staggered grid arrangement. Numerical simulations were conducted on a local 252-core computer cluster. In total, 45,000 CPU hours have been spent to perform each simulation.

Figure 1 shows the schematic view of the array of cubes and the coordinate system. Given the fact that the flow domain is symmetric in the spanwise direction, only the

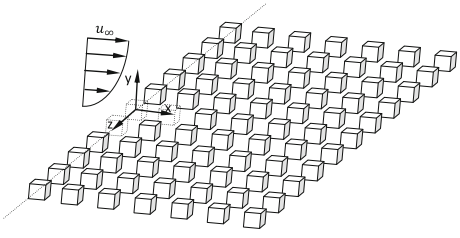

Fig. 1 Schematic of the array of 7×11 wall-mounted *cubes* (the origin of the x-coordinate is at the windward face of the *first row*)

central column (7×1 cubes) has been considered with a periodic boundary condition applied to the spanwise direction following the approach of Lien and Yee [3]. The upper boundary is $5.3h$ away from lower wall. In total, $1000 \times 112 \times 128$ grid-points are used to discretize the domain in the streamwise, vertical and spanwise directions, respectively, such that the lowest value of y^+ at the first cell off the solid surfaces is 1.2.

2.1 Boundary Conditions

No slip boundary condition is used for all the solid surfaces and periodic boundary condition has been applied to the domain boundaries in spanwise direction. Neumann boundary condition is applied to the outlet boundary and slip condition is considered for the upper boundary. One of the major challenges for this problem is to prescribe a realistic inlet boundary condition that would allow LES to reproduce precisely the wind-tunnel experiment of Brown et al. [5]. The mean velocity profile at the inlet is considered to follow the power-law profile given by

$$u = u_\infty \left(\frac{y}{0.15}\right)^{0.16} \quad \text{with} \quad u_\infty = 3 \text{ m/s}. \tag{1}$$

Since the purpose of the original experiment was to simulate a deep rough-wall atmospheric boundary layer, the approaching flow has an exceptionally high turbulence level. In fact the lowest turbulence intensity at the inlet and above the cubes is approximately 10 %. In order to reproduce the high turbulence level using LES, four methods have been tested for modeling the inlet boundary, which include: (A) prescribing mean profile with no fluctuations, (B) using a turbulent plane channel flow simulation as a precursor, (C) using a solid grid at the inlet plane of the domain, and (D) using a solid grid at the inlet plane with superimposed random fluctuations in regions above the cubes. In method D, random numbers are superimposed in regions above the cubes (for $x/h > 3$ and $y/h > 1.35$) based on the approach of method C. The superposition is implemented at the beginning of consecutive time-windows. The duration of each time-window is 0.03 s which is 60 % of the time required for the mean flow to travel one cube side. The random fluctuations generated at each step, are correlated to the previously imposed fluctuations through a linear relationship and then imposed to the flow. In order to evaluate the performances of these four inlet boundary condition methods, the profiles of the streamwise RMS velocity predicted by LES at a typical point ($x/h = 9.5$) are compared against the experimental data. As evident in Fig. 2, method A cannot generate any turbulence above the cubes. As an improvement, method B can generate turbulence above the cubes but it is still significantly under the high turbulence level measured in the experiment. Although the approach for method C is drastically different than that for method B, its performance is not considerably different from method B. Based on the observation that methods A, B and C all fail to reproduce the high turbulence level above the cubes, we propose method D, which is able to reproduce the highest turbulence level above

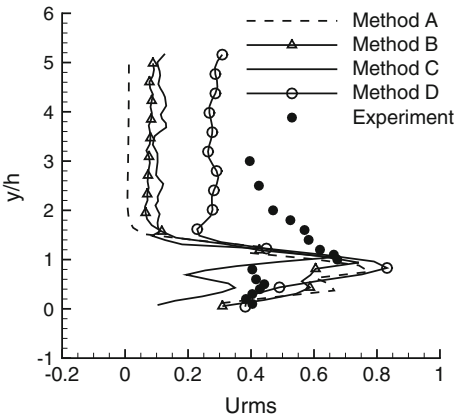

Fig. 2 Effects of 4 different inlet conditions on the streamwise RMS velocity level at the location $x/h = 9.5$ and $z/h = 0$

the cubes (closest to the measured value). The results reported in this paper is based on method D.

2.2 Subgrid-Scale Models

Three subgrid-scale (SGS) models are used for conducting the simulations. The modeling equations for the SGS stresses are briefly described as follows. The first model is the conventional dynamic Smagorinsky model (DSM) [6], which expresses the SGS stress tensor as

$$\tau_{ij}^* \stackrel{\text{def}}{=} \tau_{ij} - \frac{\tau_{kk}}{3}\delta_{ij} = -2C_s\bar{\Delta}^2|\bar{S}_{ij}|\bar{S}_{ij}, \tag{2}$$

where $\bar{S}_{ij} \stackrel{\text{def}}{=} (\partial\bar{u}_i/\partial x_j + \partial\bar{u}_j/\partial x_i)/2$ is the resolved strain rate tensor, $|\bar{S}_{ij}|$ is the norm of $\bar{S}_{ij}$, δ_{ij} is the Kronecker delta, and an asterisk denotes the trace free form of a tensor.

The second model is the dynamic two parameter mixed model (DTPMM) of Morinishi and Vasilyev [7] which calculates the SGS stress as

$$\tau_{ij}^* = -2C_s\bar{\Delta}^2|\bar{S}_{ij}|\bar{S}_{ij} + C_L L_{ij}^*, \tag{3}$$

in which L_{ij} is the resolved Leonard type stress defined as $L_{ij} \stackrel{\text{def}}{=} \widetilde{\bar{u}_i\bar{u}_j} - \tilde{\bar{u}}_i\tilde{\bar{u}}_j$.

The third model is the dynamic non-linear model (DNM) proposed by Wang and Bergstrom [8], viz.

$$\tau_{ij}^* = -C_S\beta_{ij} - C_W\gamma_{ij} - C_N\eta_{ij}, \tag{4}$$

where the base tensors are defined as $\beta_{ij} \stackrel{\text{def}}{=} 2\bar{\Delta}^2|\bar{S}|\bar{S}_{ij}$, $\gamma_{ij} \stackrel{\text{def}}{=} 4\bar{\Delta}^2(\bar{S}_{ik}\bar{\Omega}_{kj} + \bar{S}_{jk}\bar{\Omega}_{ki})$ and $\eta_{ij} \stackrel{\text{def}}{=} 4\bar{\Delta}^2(\bar{S}_{ik}\bar{S}_{kj} - \bar{S}_{mn}\bar{S}_{nm}\delta_{ij}/3)$. Here, $\bar{\Omega}_{ij} \stackrel{\text{def}}{=} (\partial\bar{u}_i/\partial x_j - \partial\bar{u}_j/\partial x_i)/2$ is the resolved rotation rate tensor.

3 Results and Discussions

Figure 3 shows the mean streamwise velocity profile above the rooftop and inside the canyon of the array, at $x/h = 8.5$ and $x/h = 9.5$, respectively. The general trends of the numerical prediction and experimental measurement are similar. In terms of the prediction of $\langle \bar{u} \rangle$, no significant effect is observed arising from using different SGS models. As shown in Fig. 3, in the street canyon, LES slightly overpredicts the magnitude of the negative velocity (corresponding to the recirculation flow). In Fig. 4, the RMS profiles of the streamwise velocity are shown at $x/h = 8.5$ and $x/h = 9.5$. At both locations, the maximum turbulence activity occurs around the cube rooftop ($y/h \approx 1$). This peak value in the resolved TKE is the result of the strong shear production at the rooftop of the cube. The u_{rms} around the cube rooftop is fairly well captured by all numerical simulations, however, the turbulence level above the cube is under-predicted by numerical simulations and it decays quickly

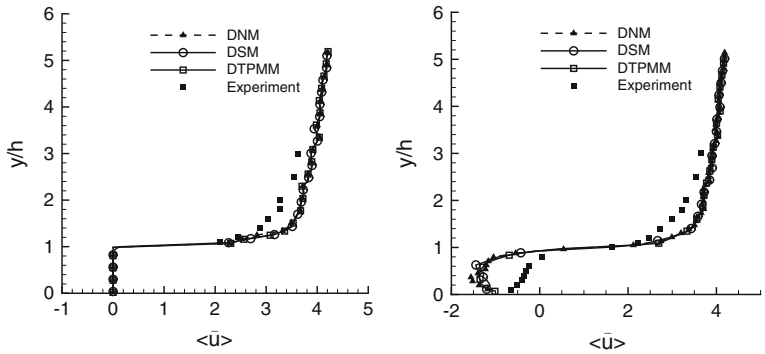

Fig. 3 Profiles of the mean streamwise velocity above the rooftop (*left*, $x/h = 8.5$) and inside the canyon (*right*, $x/h = 9.5$) of the array in the central plane of the domain ($z/h = 0$)

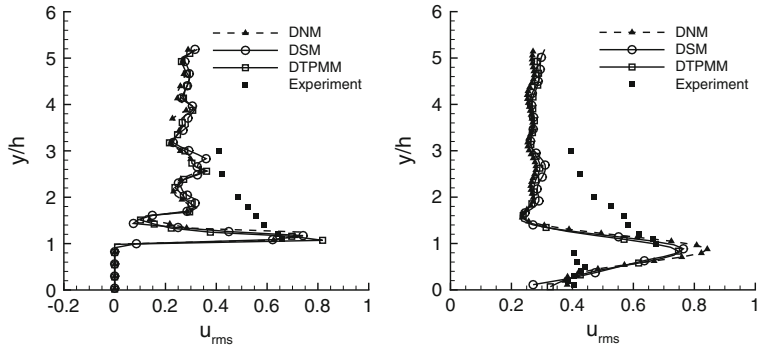

Fig. 4 Profiles of the streamwise RMS velocity above the rooftop (*left*, $x/h = 8.5$) and inside the canyon (*right*, $x/h = 9.5$) of the array in the central plane of the domain ($z/h = 0$)

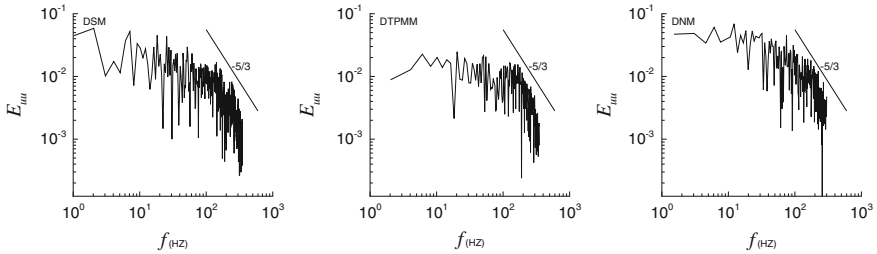

Fig. 5 Temporal energy spectra for streamwise velocity obtained from simulations with three SGS models at $x/h = 5.5$ and $y/h = 1.0$, in the central plane of the domain ($z/h = 0$)

as the vertical distance from the rooftop increases. Figure 5 shows the streamwise energy spectra at $x/h = 5.5$ and $y/h = 1.0$ obtained from simulations with three SGS models. From the figure, it is evident that simulations based on all three SGS stress models have been able to capture the inertial subrange. Furthermore, a perusal of three subfigures indicates that the resolved streamwise TKE predicted by the DNM is the largest at all frequencies. This shows that when DNM is used as the SGS stress model, higher values of kinetic energy have been captured at this special location.

4 Conclusion

Large-eddy simulation of turbulent flow over an array of wall-mounted cubic obstacles at Re = 30000 has been conducted using three SGS models. In order to reproduce the exceptionally high turbulence level (with a minimum turbulence intensity of 10 %) of the neutrally stratified atmospheric boundary layer simulated in the wind tunnel, four methods have been tested to model the inlet boundary condition. It is observed that use of different inlet conditions can significantly affect the streamwise turbulence intensity (u_{rms}) profile. The proposed method based on mounting a solid grid at the inlet and superimposing correlated random fluctuations in regions above the cubes is effective in generating sustained high turbulence levels. Time averaged first- and second-order flow statistics do not show sensitivity towards the SGS models tested. With respect to the temporal energy spectra of the streamwise velocity at a typical canyon location, the results from simulations with different SGS models are also similar, however, the DTPMM shows the lowest predicted energy level and the DNM shows the highest predicted level.

References

1. Lim, H.C., Castro, I.P., Hoxey, R.P.: Bluff bodies in deep turbulent boundary layers: Reynolds-number issues. J. Fluid Mech. **571**, 97–118 (2007)
2. Wang, H.F., Zhou, Y.: The finite-length square cylinder near wake. J. Fluid Mech. **638**, 453–490 (2009)

3. Lien, F.-S., Yee, E.: Numerical modelling of the turbulent flow developing within and over a 3-D building array. Part I: a high-resolution Reynolds-averaged Navier-Stokes approach. Bound.-Layer Meteorol. **112**, 427–466 (2004)
4. Cheng, Y., Lien, F., Yee, E., Sinclair, R.: A comparison of large eddy simulations with a standard k-ε Reynolds-averaged Navier-Stokes model for the prediction of a fully developed turbulent flow over a matrix of cubes. J. Wind Eng. Ind. Aero. **91**, 1301–1328 (2003)
5. Brown, M.J., Lawson, R.E., DeCroix, D.S., Lee, R.L.: Comparison of centerline velocity measurements obtained around 2D and 3D building arrays in a wind tunnel. Report LA-UR-01-4138, Los Alamos National Laboratory (2001)
6. Lilly, D.K.: A proposed modification of the Germano subgrid-scale closure method. Phys. Fluids A **4**, 633–635 (1992)
7. Morinishi, Y., Vasilyev, O.V.: A recommended modification to the dynamic two-parameter mixed subgrid scale model for large eddy simulation of wall bounded turbulent flow. Phys. Fluids **13**, 3400–3410 (2001)
8. Wang, B.-C., Bergstrom, D.: A dynamic nonlinear subgrid-scale stress model. Phys. Fluids **17**, 035109 (2005)

Direct Numerical Simulation of the 3D Stratified Separated Viscous Fluid Flows

P.V. Matyushin and V.A. Gushchin

1 Introduction

The investigation of the fundamental features of the 3D separated flows of the stratified fluid around a horizontally moving blunt body is very complex problem which solved with difficulty and which give us also some insight on the real atmospheric flows around the hills and the mountains.

Direct numerical simulation (DNS) of the linearly stratified viscous fluid flows around a sphere and a 2D square cylinder on supercomputers on the basis of the Navier-Stokes equations in the Boussinesq approximation (including the diffusion equation for the stratified component (salt)) gives us opportunity to better understand the complex transformations of the vortex structures of the wake with changing of the main non-dimensional parameters: Reynolds $Re = Ud/\nu$ and internal Froude $Fr = U/(N \cdot d)$ numbers, where U is the scalar of the body velocity, d is the vertical size of the body, ν is the kinematical viscosity, N is the buoyancy frequency; the dimensionless density $\rho = (1 - x/(2C) + S)$ where x is a vertical Cartesian coordinate, $C = \Lambda/d$, $\Lambda = g/N^2$ is the buoyancy scale, S is a dimensionless perturbation of salinity.

The existing experimental data give us opportunity to confirm the results of our simulation at some values of Re and Fr. In the experiments [3, 9] the 2D internal waves structure in the vertical plane and the 3D vortex structure of the sphere wake are observed. Using DNS the full 3D vortex structures of the flow (the 3D internal waves and the 3D sphere wake) can be observed (see Figs. 1 and 2).

P.V. Matyushin (✉) · V.A. Gushchin
Institute for Computer Aided Design of the Russian Academy of Sciences,
Moscow, Russia
e-mail: pmatyushin@mail.ru

V.A. Gushchin
e-mail: gushchin@icad.org.ru

J. Fröhlich et al. (eds.), *Direct and Large-Eddy Simulation IX*,
ERCOFTAC Series 20, DOI 10.1007/978-3-319-14448-1_58

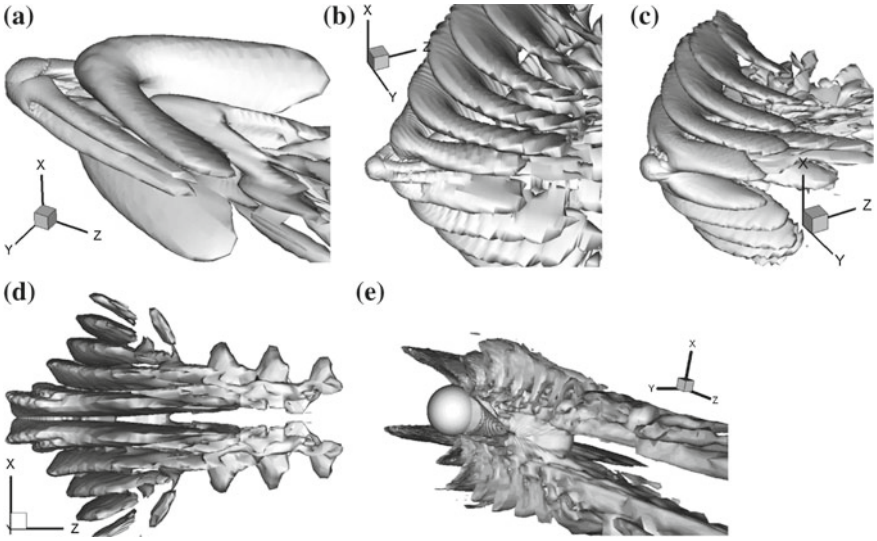

Fig. 1 The vortex structures in the stratified fluid around a moving sphere at $Re = 100$: **a**–**e** $Fr = 1$, 0.8, 0.5, 0.2, 0.08; **a**–**e** The isosurfaces of $\beta = 0.02$; 0.005; 0.02; 0.02; 0.005

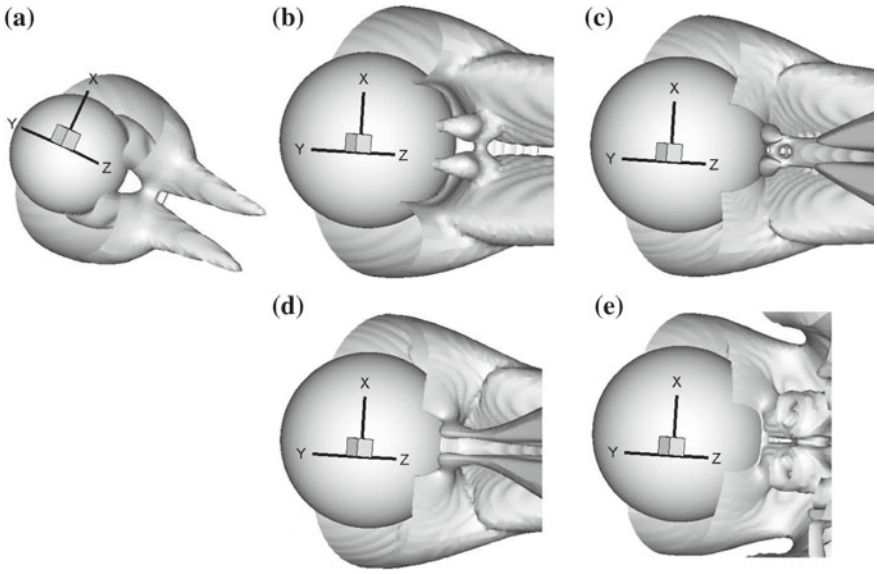

Fig. 2 Vortex structures of the sphere wake at $Re = 100$: **a**–**e** $Fr = 2$, 1, 0.7, 0.6, 0.35; **a**–**e** Isosurfaces of $\beta = 0.15$, 0.1, 0.087, 0.087, 0.087

2 Numerical Method SMIF

For solving of the Navier-Stokes equations the Splitting on physical factors Method for Incompressible Fluid flows (SMIF) with hybrid explicit finite difference scheme (second-order accuracy in space, minimum scheme viscosity and dispersion, capable for work in wide range of Re and Fr and monotonous) based on Modified Central Difference Scheme (MCDS) and Modified Upwind Difference Scheme (MUDS) with special switch condition depending on the velocity sign and the signs of the first and second differences of transferred functions has been developed and successfully applied [1, 4]. The Poisson equation for the pressure has been solved by the Diagonal Preconditioned Conjugate Gradients Method.

3 The Visualization of the 3D Vortex Structures

For the visualization of the 3D vortex structures in the fluid flows the isosurfaces of β have been drawing (see Figs. 1 and 2), where β is the imaginary part of the complex-conjugate eigen-values of the velocity gradient tensor **G**.

4 The Classification of Flow Regimes Around a Sphere

The following classification of viscous fluid flow regimes around sphere at $Re \leq 500$ [8, 10] has been obtained by SMIF: (I) $Fr > 10$ the homogeneous case [5–7]; (II) $1.5 \leq Fr \leq 10$ the quasi-homogeneous case (with four additional threads connected with the vortex sheet (VSh) surrounding the sphere, Figs. 1a and 2a); (III) $0.9 < Fr < 1.5$—the non-axisymmetric attached vortex in the recirculation zone (**RZ**) (Figs. 1a and 2b); (IV) $0.6 < Fr \leq 0.9$ the two symmetric vortex loops in **RZ** (Figs. 1b and 2c); (V) $0.4 \leq Fr \leq 0.6$ the absence of **RZ** (Figs. 1c and 2d); (VI) $0.25 < Fr < 0.4$ a new **RZ** (Fig. 2e); (VII) $Fr \leq 0.25$—the two vertical vortices in new RZ (bounded by the internal waves (**IWs**)) (Figs. 1d, e). At $Fr \leq 0.3$, $Re > 120$ a periodical generation of the vortex loops (facing left or right) has been observed. The corresponding Strouhal numbers $0.19 < St = fd/U < 0.24$ (where f is the frequency of shedding) and horizontal and vertical separation angles are in a good agreement with the experiment [9]. The drag coefficients also correspond to experimental values. The interesting transformation of the four main threads (at $Fr = 1$, Fig. 1a) into the high gradient sheets of density near the sphere pole (before the sphere) (at $Fr = 0.08$, Fig. 1e) is shown at Fig. 1.

At $Re = 100$ with decreasing of Fr (from 10 to 2) the vortex ring in **RZ** is deformed in an oval (Fig. 2a). At the vertical plane the part of fluid is supplied in **RZ**. Then this fluid goes through the core of the vortex oval and is emitted downstream at the horizontal plane. The 3D instantaneous stream lines which are going near the sphere surface go around this vortex oval and form the four vortex threads (Fig. 2a).

At $Fr < 1.5$ the big initial vertical flattening of the flow prevent the vortex formation mechanisms typical for the homogeneous fluid [7]. At $Fr < 1.5$ the new vortex formation mechanisms (which are typical for the stratified fluid) are realised with increasing of Re. With decreasing of Fr the fluid structures around the sphere are slowly flattened both along the vertical axis X and along the line Z of the sphere motion (the length of the internal waves in the vertical plane is $\lambda/d = 2\pi \cdot Fr$).

At $0.9 < Fr < 1.5$ the vortex oval in **RZ** has been transformed into the quasi-rectangle with two shot vertical vortex tubes (Fig. 2b). With decreasing of Fr the thickness of the horizontal tubes of this quasi-rectangle in the vertical plane $X - Z$ is diminishing up to zero and the flow in **RZ** is redirected in the streamwise direction. Thus this quasi-rectangle is transformed into the system of the two symmetric vortex loops (Fig. 2c, d). It means that the wave processes destroy the rectangular vortex in **RZ**. With following decreasing of Fr starting from $Fr = 0.4$ a new recirculation zone is generated from the nearest wave crest on axis Z (Fig. 2e).

5 The Classification of 2D Flow Regimes Around a Cylinder

The following classification of stratified viscous fluid flow regimes around a 2D square cylinder (moving along the horizontal axis X, $\rho = (1 - y/(2C) + S)$) has been obtained by SMIF at $Re < 200$ (Fig. 3): (**HC**) $Fr > 20$ a steady symmetrical **RZ** with length L_0 (the homogeneous case); (**1RZ**) a steady symmetrical **RZ** with length $L < L_0$ and **IWs**; (**V**) a procession of the vortices in the wake; (**2RZ**) two steady symmetrical **RZs** before and after the square cylinder (the boundary between **1RZ** and **2RZ** flow regimes—at $Fr = 0.45$); (**BZ**) a steady symmetrical **RZ** (or blocking zone (**BZ**) with the length L_b) before the square cylinder (Fig. 4a), **IWs** and the high gradient sheet of density are forming on axis X after the cylinder (L_b is rapidly increasing with decreasing of Fr); (**2RZU**) a procession of the vortices in the wake (bounded by **IWs**); (**2RZS**) an unsteadiness inside **RZ** (with steady symmetric boundaries) and the symmetric field of **IWs** (the boundary between **2RZU** and **2RZS** flow regimes—at $Fr = 0.37$). The classification at Fig. 3 is based on the stream lines patterns corresponding to the steady state flow (stationary with a constant value of drag coefficient C_d or unstationary periodical with constant value of the amplitude of oscillation of $C_d(t)$) after a pulse start of the cylinder at $t = 0.0$.

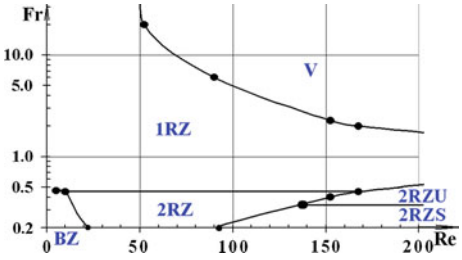

Fig. 3 The classification of the regimes of the 2D stratified viscous fluid flows around a square cylinder obtained by the numerical method SMIF

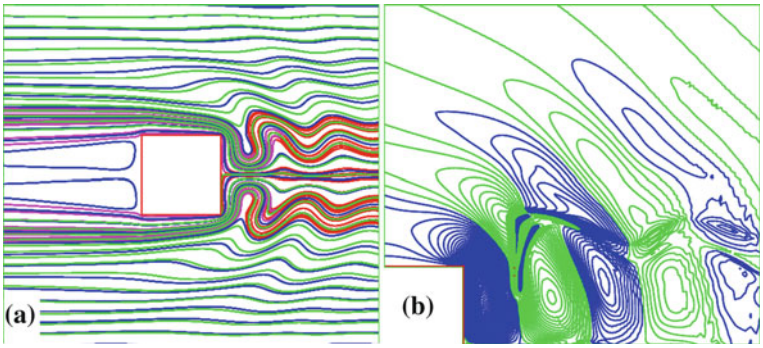

Fig. 4 Stream lines (**a**) and isolines of $S_x = \delta\rho/\delta x$ (**b**) (with step 1.17×10^{-4}) around a square cylinder ($d = 2.24$ cm, $T_b = 6.29$ s^{-1}) at $Fr = 0.1$, $Re = 50$, $C = 440$ at time $T = 575 \times T_b$ (the *darker* isolines correspond to negative S)

The classification at Fig. 3 is more close to experimental one from [2] at $Re < 200$ and more complex then this classification. The flow regimes **2RZU** and **2RZS** are combined in [2] in the flow regime C_M (**Multiple centerline structures**). At the same time the classification at Fig. 3 is slightly more simple then experimental one from [12].

At [2, 11, 12] at $Fr < 0.37$, $Re > 30$ the two downstream wavy horizontal streaks (lines) are observed in the wake in the shadowgraphs (Fig. 4b). These two lines (the hanging high gradient sheet of density) are started from two vortices clearly seen at Fig. 4a after the square cylinder at $Fr = 0.1$, $Re = 50$. After a pulse start of the cylinder at $t = 0.0$ these vortices have been separated from the cylinder angels and shifted slightly downstream. These two downstream wavy horizontal lines separate the wake from the outer flow. These lines are the share layers in the velocity field (Fig. 4a).

Acknowledgments This work has been supported by Russian Foundation for Basic Research (grants No. 11-01-00764), by the grants from the Presidium of RAS and the Department of Mathematical Sciences of RAS.

References

1. Belotserkovskii, O.M., Gushchin, V.A., Konshin, V.N.: Splitting method for studying stratified fluid flows with free surfaces. Comput. Math. Math. Phys. **27**, 594–609 (1987)
2. Boyer, D.L., Davies, P.A., Fernando, H.J.S., Zhang, X.: Linearly stratified flow past a horizontal circular cylinder. Philos. Trans. R. Soc. Lond. Series A: Math. Phys. Sci. **328**(1601), 501–528 (1989)
3. Chomaz, J.M., Bonneton, P., Hopfinger, E.J.: The structure of the near wake of a sphere moving horizontally in a stratified fluid. J. Fluid Mech. **254**, 1–21 (1993)
4. Gushchin, V.A., Konshin, V.N.: Computational aspects of the splitting method for incompressible flow with a free surface. J. Comput. Fluids **21**(3), 345–353 (1992)

5. Gushchin, V.A., Kostomarov, A.V., Matyushin, P.V., Pavlyukova, E.R.: Direct numerical simulation of the transitional separated fluid flows around a sphere and a circular cylinder. J. Wind Eng. Ind. Aerodyn. **90**(4-5), 341–358 (2002)
6. Gushchin, V.A., Kostomarov, A.V., Matyushin, P.V.: 3D visualization of the separated fluid flows. J. Visual. **7**(2), 143–150 (2004)
7. Gushchin, V.A., Matyushin, P.V.: Vortex formation mechanisms in the wake behind a sphere for $200 < Re < 380$. Fluid Dyn. **41**(5), 795–809 (2006)
8. Gushchin, V.A., Matyushin, P.V.: Numerical simulation and visualization of vortical structure transformation in the flow past a sphere at an increasing degree of stratification. Comput. Math. Math. Phys. **51**(2), 251–263 (2011)
9. Lin, Q., Lindberg, W.R., Boyer, D.L., Fernando, H.J.S.: Stratified flow past a sphere. J. Fluid Mech. **240**, 315–354 (1992)
10. Matyushin, P.V., Gushchin, V.A.: Transformation of vortex structures in the wake of a sphere moving in the stratified fluid with decreasing of internal Froude number. J. Phys.: Conf. Ser. **318**, 062017 (2011)
11. Mitkin, V.V., Chashechkin, Yu.D.: Transformation of hanging discontinuities into vortex systems in a stratified flow behind a cylinder. Fluid Dyn. **42**(1), 12–23 (2007)
12. Voeikov, I.V., Chashechkin, Yu.D.: Formation of discontinuities in the wake of a cylinder in a stratified flow. Fluid Dyn. **28**(1), 14–18 (1993)

Part XI
Rotating Turbulence

Effects of Rotation on the Oscillatory Flow Over Ripples

D.G.E. Grigoriadis and V. Armenio

Abstract Large-eddy simulations (LES) of oscillating turbulent boundary layers, over a rippled bed, subjected to frame rotation are presented. This flow is archetypal of a bottom-ocean, tidally driven boundary layer developing over sand dunes. A forcing-type immersed boundary method (IBM) is used to represent the solid bed and the filtered structure function model for the sub-grid stresses. Three different rotation patterns were examined, each one corresponding to different geographic latitudes. The effect of ripples was found to significantly modify the elliptical patterns and the phase of the Ekman layers generating between the ripple crests.

1 Introduction

The unidirectional turbulent oscillatory flow over a flat bed has been studied experimentally by Jensen et al. [4] and numerically [3, 6]. Recently, [5] studied the effect of rotation on the flow over a flat bed revealing interesting flow patterns depending on the latitude considered. In the present study, we aim to further extend the analysis by including bed-modulation effects by means of introducing ripples along the bed. The main objective of the present work is to study the effect of bed modulation on the generated flow patterns under the influence of external flow-oscillation and rotation. These interactions and the associated generation of coherent structures are expected to play a significant role on sediment-related phenomena.

Following the study of Salon and Armenio [5], we consider three different rotation rates representative of conditions respectively occurring in the polar case (PL), in a

D.G.E. Grigoriadis (✉)
Computational Sciences Laboratory UCY-CompSci, Department of Mechanical and Manufacturing Engineering, NIREAS International Water Research Center, University of Cyprus, Nicosia, Cyprus
e-mail: grigoria@ucy.ac.cy

V. Armenio
Dipartimento di Ingegneria e Architettura, Universitá di Trieste, Piazzale Europa 1, 34127 Trieste, Italy
e-mail: armenio@dica.units.it

J. Fröhlich et al. (eds.), *Direct and Large-Eddy Simulation IX*,
ERCOFTAC Series 20, DOI 10.1007/978-3-319-14448-1_59

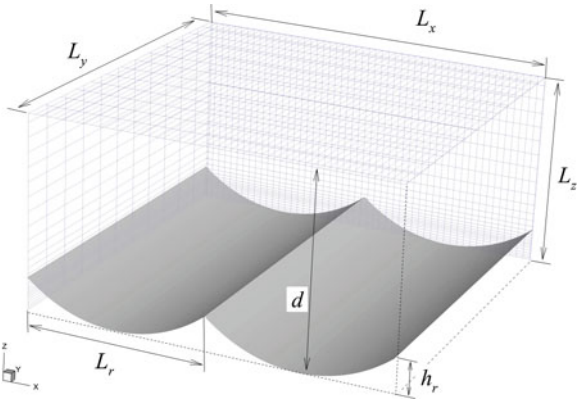

Fig. 1 Computational domain and grid for the flow over the ripples. Every tenth computational *line* is shown

mid-latitude case (ML) and in a quasi-equatorial case (QE). Further, results will be presented for the oscillatory flow over ripples of different heights.

The filtered Navier-Stokes equations are integrated using a time-splitting scheme for the temporal discretization and a second order accurate finite-differences approximation on orthogonal grid for the spatial discretization. The rippled bed is represented using the immersed boundary method on Cartesian grids. The oscillatory flow is generated by imposing an oscillating external pressure gradient and the subgrid-scale momentum fluxes are parameterized using the filtered structure function model [1].

2 Governing Equations and Simulation Set-Up

The incompressible oscillatory flow over the ripples (Fig. 1) is generated by an external pressure gradient associated to a free stream current of amplitude U_o and angular frequency ω as,

$$u_o(t) = U_o\,(\sin(\omega t)) \tag{1}$$

The characteristic length scales which can be used to non-dimensionalise the problem are either the Stokes length $\delta_s = \sqrt{2\nu/\omega}$ or the the amplitude of the orbital motion $\alpha_o = U_o/\omega$. Using these parameters, the relevant Reynolds numbers become, $Re_{\delta_s} = \frac{U_o \delta_s}{\nu}$ and $Re_\alpha = \frac{U_o \alpha_o}{\nu}$ with $Re_{\delta_s} = \sqrt{2 Re_\alpha}$. The resulting non-dimensional set of equations describing the problem then become,

$$\frac{\partial \overline{u}_i}{\partial x_i} = 0 \tag{2}$$

$$\frac{\partial \overline{u}_i}{\partial t} + \frac{\partial \overline{u}_i \overline{u}_j}{\partial x_j} = -\left(\frac{\Delta P}{\Delta x}\right)_t - \frac{\partial \overline{p}}{\partial x_i} + \frac{1}{Re_\alpha}\frac{\partial {\overline{u}_i}^2}{\partial x_j \partial x_j} - \frac{\partial \tau_{ij}}{\partial x_j} + \varepsilon_{imn} Ro_{m,\alpha}[\sin(t)\delta_{n1} - \overline{u}_n] + f_{u,i} \tag{3}$$

The last term of Eq. 3 is the immersed boundary forcing term which is used to represent the effect of solid boundaries in the computational domain (details in [2, 3]). The first term in the right hand side $(\Delta P/\Delta x)_t = \omega U_o \cos(\omega t)$ is the pressure gradient generating the external flow and ε_{imn} is the Levi-Civita tensor. Rotation effects are included by the non-dimensional rotation parameter $Ro_{m,\alpha}$ along direction m, expressing the ratio of Coriolis to inertial acceleration,

$$Ro_{m,\alpha} = \frac{f_m}{\omega} = \frac{f_m \alpha}{U_o} \tag{4}$$

i.e. the inverse of Rossby number [5]. In case the calculation is performed with respect to the Stokes length δ_s, the relevant Reynolds and rotation parameters in Eq. 3 should be substituted by Re_{δ_s} and $Ro_{m,\delta_s} = \frac{f_m \delta_s}{U_o} = \frac{2 Ro_{m,\alpha}}{Re_{\delta_s}}$.

3 Results

In order to validate our numerical method, we first considered the oscillatory flow over a flat bed without frame rotation. This case corresponds to the experimental case "Case 8" reported by Jensen et al. [4] at $Re_{\delta_s} = 1{,}790$. A numerical resolution of $96 \times 96 \times 320$ cells was used in a computational domain of $50\delta_s \times 25\delta_s \times 60\delta_s$ along the streamwise, spanwise and wall-normal directions respectively. Periodic boundary conditions have been used along the streamwise and spanwise directions. The bed itself was modelled using the IBM method. Figure 2 shows the comparison

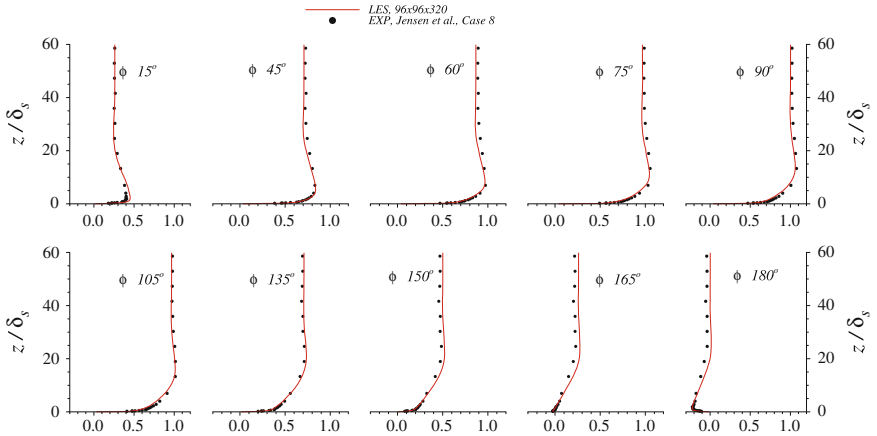

Fig. 2 Numerical validation for the oscillatory flow over a flat bed without rotation. Comparison between the predicted LES velocity profiles for the mean streamwise velocity at various phases of the cycle. *Symbols* experimental measurements from "Case 8" of Jensen et al. [4] and *lines* present LES results using $96 \times 96 \times 320$ cells

Table 1 Summary of computational cases considered at $Re_{\delta_s} = 1790$, $Re_\alpha = 1.6 \times 10^6$

Case	ϕ	f_y/ω	f_z/ω	Ro_{y,δ_s}	Ro_{z,δ_s}
PL	90	0	1.047	0	1.170×10^{-3}
ML	45	0.735	0.735	8.215×10^{-3}	8.215×10^{-3}
QE	5	1.024	0.090	1.144×10^{-3}	1.005×10^{-3}

between the present LES results and the reference experimental data. Overall, an excellent agreement was found.

As a second validation, we considered the case of an oscillatory boundary layer over a flat bed, under several rotation rates as shown in Table 1. These cases correspond to the LES cases presented by Salon and Armenio [5] at $Re_{\delta_s} = 1{,}790$. Figure 3 presents the comparison between the present study and the reported wall-resolved LES data in [5]. An excellent overall agreement was found with respect to the variation of the mean velocity field between the two studies. Depending on the axes of rotation, the flow exhibits elliptical patterns between the streamwise and the spanwise velocity components as shown in Fig. 3.

The flow field developing over the sand dunes was investigated for the same cases and the same parameters as those shown in Table 1. The rippled bed consisted of successive circular arcs of length $L_r = 50\delta_s$, height $h_r = 4\delta_s$ and radius or curvature $r = 80.125\delta_s$ leading to sharp crests as shown in Fig. 1. The computational domain included two ripples and extended to $100\delta_s \times 50\delta_s \times 60\delta_s$. A numerical resolution of $256 \times 128 \times 256$ cells was used along the streamwise, spanwise and vertical direction. A total of 16 cycles were computed and statistical phase averaging was performed over the last eight cycles.

Figure 4 shows the variation of the elliptical patterns developing over the trough, for various distances from the wall. Compared with the flat wall case (full symbols), these patterns are still anti-clockwise but become significantly distorted by the presence of ripples. For all cases, the amplitude of streamwise velocity oscillation was

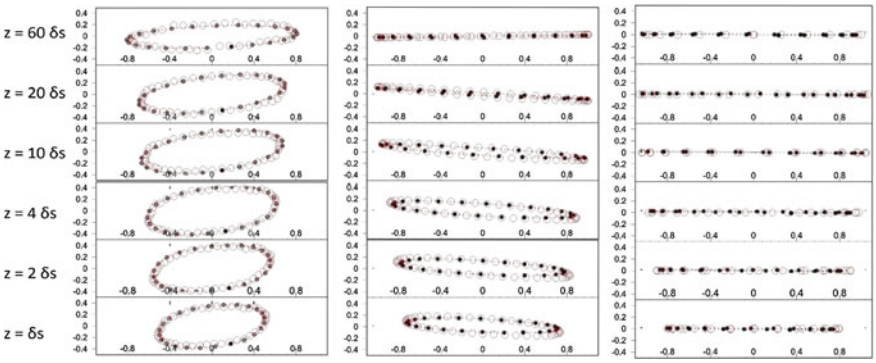

Fig. 3 Mean streamwise velocity component versus spanwise component for three different rotation patterns (*open symbols*) against previously reported data from Salon and Armenio [5] (*full symbols*) at various distances from the bottom wall. *Left* Case PL, *middle* Case ML, *right* Case QE from Table 1

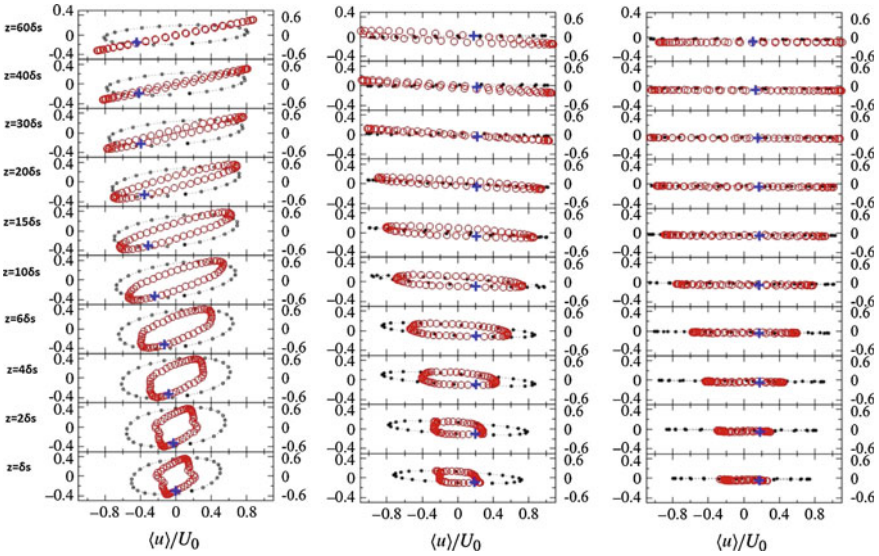

Fig. 4 Mean streamwise velocity component versus spanwise component for three different rotation patterns for the flow over a rippled bed (*open symbols*, *right axis*) against previously reported data for the flow over a flat bed from Salon and Armenio [5] (*full symbols*, *left axis*). Results are shown for several cases at the trough location $x = L_r/2$, at various distances from the bottom wall. The *cross symbol* corresponds to $\omega t = 0°$ and time runs anticlockwise along the path. *Left* Case PL, *middle* Case ML, *right* Case QE from Table 1

found to attenuate at the trough close to the bed, up to a distance of 10–15δ_s. For the height of the ripples considered, very close to the bed ($O(\delta_s)$) the variation of the streamwise velocity component was found to be smaller by a factor of ≈2.5.

The spanwise component of velocity on the other hand, was found to oscillate with larger amplitudes due to the ripples. Especially for the polar and the mid-latitude cases PL and ML, the existence of ripples was found to increase the amplitude of oscillation of the spanwise velocity component by almost 50 %.

The shape of these elliptical patterns was found to depend very weakly on the streamwise location along the ripple with very similar patterns recorded for various downstream locations. However, the phase of Ekman layer was found to be modified by the ripples. For cases with strong elliptical patterns (e.g. case PL), the Ekman profiles at the trough were found to always lag with respect to the profiles along the lee and stoss sides of the ripples.

4 Conclusions

Large eddy simulations of the oscillatory flow over sharp, fixed ripples subjected to frame rotation have been presented. The objective of the present work was to perform a preliminary study on the effect of rotation on the elliptical velocity patterns over the

bed. It was found that the presence of ripples significantly increases the momentum transfer to the spanwise direction, by generating stronger velocity oscillations along the spanwise direction. Additionally, a phase shift was clearly noticed between the Ekman layers forming at the trough and the lee and stoss sides of the ripples. Combined, these two effects can be expected to significantly modify sediment transport and promote asymmetries along the ripples of erodible beds.

References

1. Ducros, F.D., Comte, P.C., Lesieur, M.: Large-eddy simulation of transition to turbulence in a boundary layer developing spatially over a flat plate. J. Fluid Mech. **326**, 1–36 (1996)
2. Grigoriadis, D.G.E., Balaras, E., Dimas, A.A.: Large-eddy simulations of unidirectional water flow over dunes. J. Geophys. Res. **114**, F02022 (2009)
3. Grigoriadis, D.G.E., Balaras, E., Dimas, A.A.: Large-eddy simulation of wave turbulent boundary layer over rippled bed. Coast. Eng. **60**, 174–189 (2012)
4. Jensen, B.L., Sumer B.M., Fredsøe, J.: Turbulent oscillatory boundary layers at high Reynolds numbers. J. Fluid Mech. **206**, 265–297 (1989)
5. Salon, S., Armenio, V.: A numerical investigation of the turbulent Stokes-Ekman bottom boundary layer. J. Fluid Mech. **684**, 316–352 (2011)
6. Salon, S., Armenio, V., Crise, A.: A numerical investigation of the Stokes boundary layer in the turbulent regime. J. Fluid Mech. **570**, 253–296 (2007)

Numerical Simulations of a Middle Gap Turbulent Taylor-Couette-Poiseuille Flow

R. Oguic, S. Viazzo and S. Poncet

1 Introduction

Turbulent flows in an opened Taylor-Couette system with an axial throughflow is studied here by the means of large eddy simulations. The ultimate industrial application is the effective cooling of the rotor-stator gap of an electrical motor. The recent review of Fénot et al. [4] pointed out the lack of reliable data in such configurations for the hydrodynamic fields and most of all for the thermal one. Among others, Nouri and Whitelaw [6] and Escudier and Gouldson [3] provided detailed velocity measurements in very elongated middle-gap cavities. In a recent paper, Poncet et al. [7] used a second-order turbulence model assuming the flow as being steady and axisymmetric, whose results compared quite well with the ones of [3]. Little is known about the near-wall turbulent structures when an axial Poiseuille is superimposed. We can cite the numerical work of Chung and Sung [2], who highlighted the destabilization of the near-wall turbulent structures due to the rotation of the inner wall giving rise to an increase of sweep and ejection events. The main objective of the present work is to validate the present LES approach against reliable data available in the literature [2, 6], which can be seen as a first step towards the simulation of the real flow conditions.

R. Oguic · S. Viazzo · S. Poncet (✉)
Laboratoire M2P2 UMR 7340 CNRS, Aix-Marseille Université,
Marseilles, France
e-mail: poncet@l3m.univ-mrs.fr

R. Oguic
e-mail: oguic@l3m.univ-mrs.fr

S. Viazzo
e-mail: viazzo@l3m.univ-mrs.fr

J. Fröhlich et al. (eds.), *Direct and Large-Eddy Simulation IX*,
ERCOFTAC Series 20, DOI 10.1007/978-3-319-14448-1_60

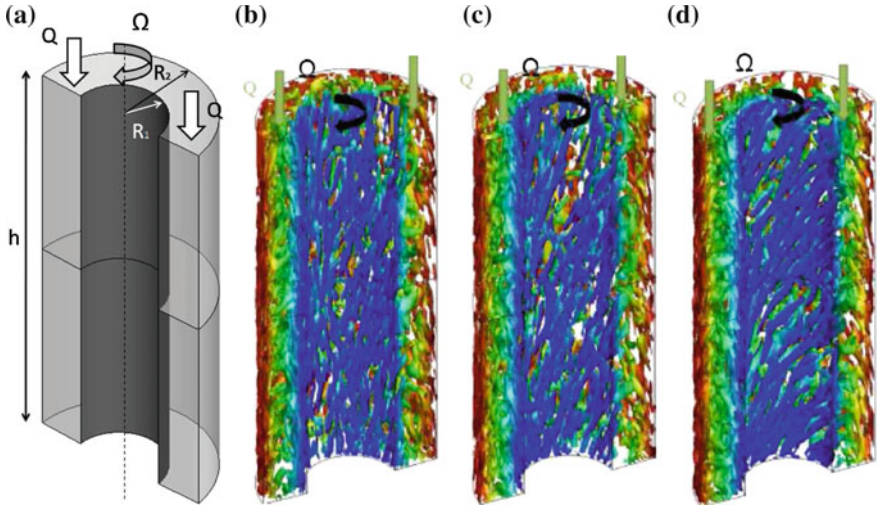

Fig. 1 **a** Schematic representation of the Taylor-Couette-Poiseuille system with relevant notations; isosurfaces of the Q-criterion ($Q = 0.5$) *colored* by the radial position for **b** $N = 0.2145$, **c** $N = 0.429$ and **d** $N = 0.858$

2 Geometrical Configuration and Flow Parameters

The fluid is confined between two concentric cylinders of height h (see Fig. 1). The inner cylinder of radius R_1 is rotating at the rate Ω, while the outer one of radius R_2 is stationary. The cavity may be characterized by two geometrical parameters: its aspect ratio $\Gamma = h/(R_2 - R_1)$ and its radius ratio $\eta = R_1/R_2$, fixed here to 9 and 0.5 respectively. An axial throughflow is imposed within the gap at a constant inlet axial velocity W_m. The hydrodynamic fields are governed by the rotational and bulk Reynolds numbers defined as $Re_\Omega = \Omega R_1(R_2 - R_1)/\nu$ and $Re_Q = 2W_m(R_2 - R_1)/\nu = 8{,}900$ (ν the fluid kinematic viscosity). The rotational Reynolds number may vary such that the rotation parameter $N = \Omega R_1/W_m$ will take the values 0.2145, 0.429 and 0.858.

3 Numerical Method

The numerical method is based on the work of Abide and Viazzo [1], who developed a 2D compact fourth-order projection decomposition method in Cartesian coordinates. It has been recently validated in the case of turbulent rotor-stator flows in cylindrical coordinates by Viazzo et al. [8]. The time advancement is second order accurate and based on the explicit Adams-Bashforth scheme for the convective terms and an implicit backward Euler scheme for the viscous ones. The derivatives are

approximated using fourth order compact formula in the radial and axial directions. The time splitting scheme is an improved projection method ensuring the incompressibility at each time step. The projection decomposition method is based on a direct non-overlapping multidomain Helmholtz/Poisson solver, which provides the solution of each Helmholtz/Poisson problem. The multidomain solver ensures the continuity of the solution and its first normal derivative across the conforming interface using an influence matrix technique. Conservation equations are solved using a Fourier approximation in the homogeneous tangential direction. The problem is thus reduced at each time step to a set of two-dimensional Helmholtz equations. Periodic boundary conditions are applied in the axial and circumferential directions and no-slip boundary conditions are imposed on the walls. A dynamic Smagorinsky model is used as subgrid-scale modelling.

All the numerical details used in the present work are summed in Table 1 and compared to the LES calculations of Chung and Sung [2]. It is noticeable that the domain is decomposed into 2 subdomains in the axial direction. In order to save computational resources, the solution is calculated by assuming a $\pi/2$-periodicity, though the grid resolutions are given for a π-periodicity to enable direct comparisons with [2]. After reaching the statistical convergence (about 2,000 s of computed physical time), the mean and rms quantities are sampled the last 80 s in each case and averaged both in the tangential and axial directions. All the calculations have been performed on the M2P2 cluster composed of 2 xeon quadcore 3 GHz.

Table 1 Numerical details and mean flow parameters

Parameters	[2]	Present	[2]	Present	[2]	Present
N	0.2145	0.2145	0.429	0.429	0.858	0.858
Δz_i^+	22.95	21.36	16.8	15.87	9.93	9.31
Δz_o^+	–	19.4	–	13.41	–	7.05
Δr_i^+	0.27	0.47	0.3	0.33	0.35	0.63
Δr_o^+	0.23	0.43	0.24	0.45	0.26	0.47
$(R_1\Delta\theta)^+$	8.01	7.34	8.8	8.22	10.4	9.7
$(R_2\Delta\theta)^+$	13.86	13.33	14.34	13.9	15.8	14.7
(N_θ, N_z)	(128, 128)	(128, 130)	(128, 192)	(128, 194)	(128, 384)	(128, 386)
$\delta t(s)$	–	9×10^{-3}	–	7×10^{-3}	–	4×10^{-3}
CFL	–	0.2	–	0.22	–	0.25
CPU time	–	5.2 (s/it)	–	9 (s/it)	–	25.5 (s/it)
$C_{f,i}$	8.91×10^{-3}	8.91×10^{-3}	9.86×10^{-3}	1.08×10^{-2}	1.2×10^{-2}	1.58×10^{-2}
$C_{f,o}$	–	7.44×10^{-3}	–	8.05×10^{-3}	–	9.05×10^{-3}
$Re_{\tau,i}$	163.21	149.53	179.24	167.52	211.85	197.51
$Re_{\tau,o}$	141.19	135.8	146.1	141.6	160.91	149.71

The number of mesh points N_r in the radial direction is fixed to 65 in all calculations. Comparisons with the LES of [2]

4 Results

The present LES results are compared to the velocity measurements of Nouri and Whitelaw [6] and to the LES of Chung and Sung [2] for three values of the rotation parameters $N = 0.2145$, 0.429 and 0.858.

4.1 Flow Structures

To highlight the presence of near-wall structures, Fig. 1b–d present isovalues of the Q-criterion colored as a function of the radius. Whatever the value of the rotation parameter N, coherent structures are well aligned with the axial flow along the stator. Rotation of the inner cylinder tilts the coherent structures appearing as spiral rolls and forming a negative angle (as they roll up in the opposite sense of the rotor) with the axial direction. These spirals are not observed in the LES results of Chung and Sung [2] for $N = 0.429$.

4.2 Mean Flow Field

Figure 2 shows the radial distribution of the mean axial and tangential velocity components normalized respectively by W_m and ΩR_1. The axial velocity is weakly influenced by the rotation parameter N and the profile resembles the turbulent Poiseuille profile usually observed in pipe flows. The tangential velocity profile is similar to the Batchelor profile observed in interdisk rotor-stator flows with two thin boundary layers developed on each disk separated by a central region, where V_θ slightly decreases with the radius. The present results are in good agreement with the experimental data of Nouri and Whitelaw [6] for $N = 0.429$ and improve the previous ones of [2]. The variation of V_θ with $1/r$ is recovered confirming that the angular momentum is almost constant along a radius. The average friction coefficients C_f and the friction Reynolds numbers Re_τ obtained along both cylinders compare very favorably to the LES results of Chung and Sung [2] as listed in Table 1.

4.3 Turbulent Flow Field

The radial variations of the $R_{\theta\theta}$ and R_{rz} components of the Reynolds stress tensor normalized by W_m^2 are displayed in Fig. 2. Velocity fluctuations are particularly higher for the tangential component with very intense peak values close to the walls. For the two other normal components (not shown here), the same behavior is observed with almost constant turbulence intensities within the gap, which vanish towards the cylinders. As expected, increasing the rotation parameter N (i.e. the rotation rate Ω)

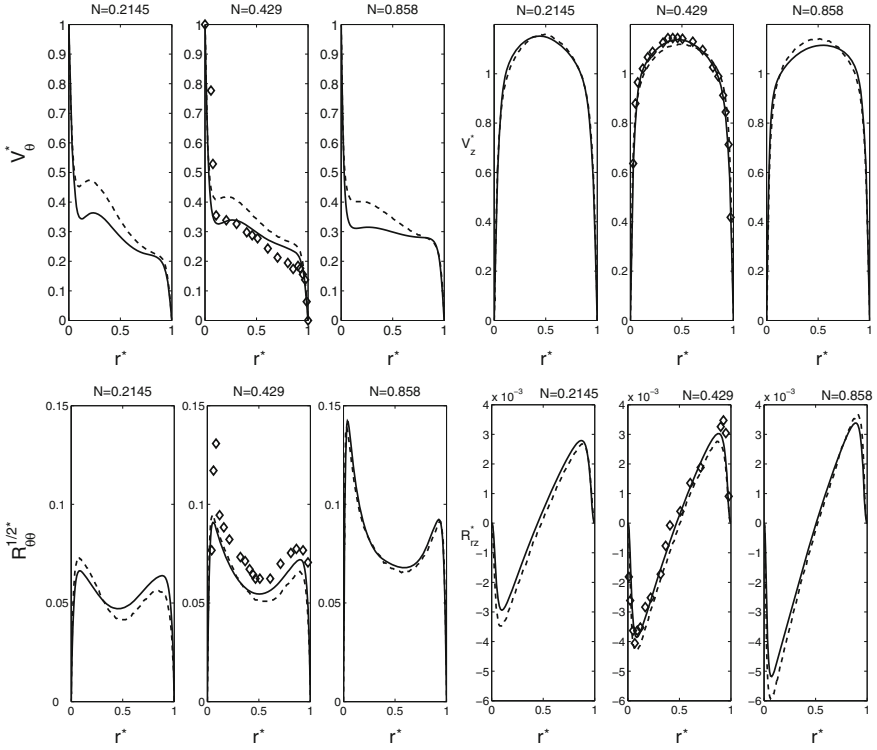

Fig. 2 Radial distributions of the mean tangential and axial velocity components and of the two components of the Reynolds stress tensor for the three values of N. Present LES (*straight lines*), LES of Chung and Sung [2] (*dashed lines*) and measurements of Nouri and Whitelaw [6] (*symbols*)

induces higher turbulence levels especially for the radial and tangential components. Furthermore, the distributions of the normal components are asymmetric, which may be attributed to the destabilizing effect of the centrifugal force. The R_{rz} shear component of the Reynolds stress tensor is shown in Fig. 2. When N increases, the shear stresses increase in strength too. A good quantitative agreement has been obtained between our present LES results and the data of Nouri and Whitelaw [6]. It slightly improves the LES results of [2] highlighting the importance of the high order schemes.

Figure 3 presents the anisotropy invariant map for the Reynolds stress tensor. It is noticeable that the present LES results respect the realizability diagram of Lumley [5]. As expected, turbulence is mainly at two-component close to the cylinders and tends to the isotropic state within the center of the gap. There is only a weak effect of the rotation parameter, the flow getting more isotropic in the center region for high N values. Our results and the ones of [2] do not support their conclusions about a "disk-like" state at mid-radius. Even if the third invariant gets weakly negative, all the normal components of the Reynolds stress tensor are indeed all of the same order.

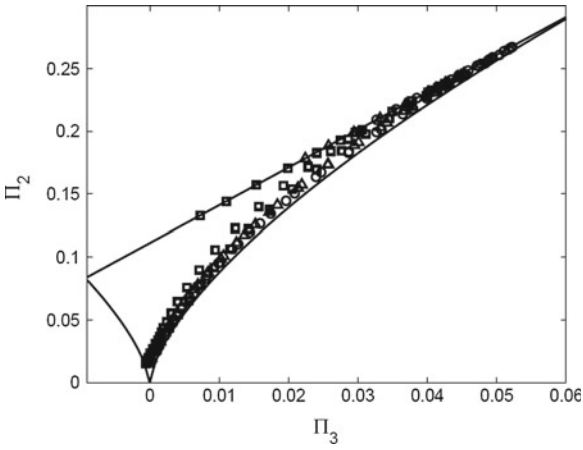

Fig. 3 Anisotropy invariant map for the Reynolds stress tensor: $N = 0.2145$ (*circles*), $N = 0.429$ (*triangles*) and $N = 0.858$ (*squares*)

5 Conclusion

The LES code developed by Viazzo et al. [8] has been extended here to its multidomain version using the methodology described in [1]. This new approach has been fully validated against the velocity measurements of Nouri and Whitelaw [6] and the numerical results of Chung and Sung [2] in an opened Taylor-Couette system with an axial throughflow. Near-wall structures appearing as elongated spiral rolls are observed along the inner cylinder. A very good agreement has been obtained for both the mean and turbulent fields and for the three values of the rotation parameter considered highlighting the importance of the order of the spatial schemes. Some numerical developments are still required to simulate the whole problem of the effective cooling in the rotor-stator gap of an electrical motor.

References

1. Abide, S., Viazzo, S.: A 2D compact fourth-order projection decomposition method. J. Comput. Phys. **206**, 252–276 (2005)
2. Chung, S.Y., Sung, H.J.: Large-eddy simulation of turbulent flow in a concentric annulus with rotation of an inner cylinder. Int. J. Heat Fluid Flow **26**, 191–203 (2005)
3. Escudier, M.P., Gouldson, I.W.: Concentric annular flow with centerbody rotation of a Newtonian and a shear-thinning liquid. Int. J. Heat Fluid Flow **16**, 156–162 (1995)
4. Fénot, M., Bertin, Y., Dorignac, E., Lalizel, G.: A review of heat transfer between concentric rotating cylinders with or without axial flow. Int. J. Therm. Sci. **50**, 1138–1155 (2011)
5. Lumley, J.L.: Computational modeling of turbulent flows. Adv. Appl. Mech. **18**, 123–176 (1978)
6. Nouri, J.M., Whitelaw, J.H.: Flow of Newtonian and non-Newtonian fluids in a concentric annulus with rotation of the inner cylinder. J. Fluid Eng. **116**, 821–827 (1994)
7. Poncet, S., Haddadi, S., Viazzo, S.: Numerical modeling of fluid flow and heat transfer in a narrow Taylor-Couette-Poiseuille system. Int. J. Heat Fluid Flow **32**(1), 128–144 (2011)
8. Viazzo, S., Poncet, S., Serre, E., Randriamampianina, A., Bontoux, P.: High-order large eddy simulations of confined rotor-stator flows. Flow Turbul. Combust. **88**(1–2), 63–75 (2012)

Effect of Span-Wise Resolution for LES of Flow Over a Rotating Cylinder at High Reynolds Number

S. Rolfo and A. Revell

1 Introduction

Recently there has been some renewed interest in the three-dimensional flow around a rotating circular cylinder at high Reynolds number, due partly to investigation into potential energy savings available for maritime propulsion. Motivated by work with Prandtl [11], Flettner successfully demonstrated that large vertical rotating cylinders on ships could be used to generate a propulsive force via the Magnus effect. Though initially dropped in favour of the low-cost fuel of the time, modern day emphasis on the reduction of emissions has resurrected this technology.

Many numerical studies have been conducted in order to investigate the flow physics of a rotating cylinder, though they have generally addressed Reynolds number far lower than those encountered by Flettner rotors; e.g. $\mathrm{Re} = 200$ [10] and $\mathrm{Re} = 300$ [4], where the focus is on instability and transition analysis for different spin ratios α, defined as the ratio between cylinder tangential wall velocity u_{θ_W} and the undisturbed velocity U_∞. More recently studies have been conducted at higher Reynolds numbers using Unsteady Reynolds Averaged Navier-Stokes (URANS) approaches; e.g. 8×10^5 [3] and 5×10^6 [8]. However the lack of experimental data for such flow regimes limits the degree of confidence that one can attain, and the predictive accuracy of these results is thus not fully assessed. Furthermore it is difficult to gain insight into the flow physics without some form of turbulent scale resolution.

S. Rolfo (✉)
STFC Daresbury Lab, Warrington, UK
e-mail: stefano.rolfo@stfc.ac.uk

A. Revell
School of MACE, The University of Manchester, Manchester, UK
e-mail: alistair.revell@manchester.ac.uk

J. Fröhlich et al. (eds.), *Direct and Large-Eddy Simulation IX*,
ERCOFTAC Series 20, DOI 10.1007/978-3-319-14448-1_61

Indeed the Large Eddy Simulation (LES) study of [2] for flow around a stationary circular cylinder at $\mathrm{Re} = 1.4 \times 10^5$ clearly demonstrates the challenges faced by this case even without rotation; a strong dependence was observed on mesh resolution and domain extent, in particular in the span-wise direction. It is perhaps then unsurprising that there is only one instance [7] of the application of LES to the rotating cylinder at high Reynolds number (same as [2]).

To the authors' knowledge there are no instances of reliable wall-resolved LES applied to the flow around a static or rotating cylinder for Reynolds greater than 140,000. This study aims to investigate the feasibility of LES for higher Reynolds number flows (fixed at 5×10^5 for this work) and a spin ratio $0 \leq \alpha \leq 5$, in order to approach the operating conditions of a Flettner rotor ($\mathrm{Re} \geq 1 \times 10^6$) and to provide insight into the relevant turbulent flow field.

2 Test Case Definition

The geometry under consideration is sketched in Fig. 1 along with relevant dimensions. Two different two-dimensional meshes have been created for extrusion: the first mesh (M1) has 284 points around the cylinder circumference and a total of 83,000 cells, while the second (M2) is refined to 424 and 160,000 respectively. Mesh M1 has been subjected to three extrusions in the span-wise direction, whilst maintaining a uniform resolution: $0.5D$ with 32 cells, $1D$ with 64 and $2D$ with 128. The resulting total mesh sizes range from 2.5 m up to 10.5 m cells. Compared to the finest mesh used in [2], mesh M2 has double the number of points in the span-wise direction, and over 50 % more in each plane.

Calculations have been performed using *Code_Saturne*, an open-source CFD code developed by EDF R&D [1], extensively optimised for High Performing Computing as described by [5]. A dynamic procedure has been employed for the evaluation of the Smagorinsky constant [6], with minimization following Lilly [9].

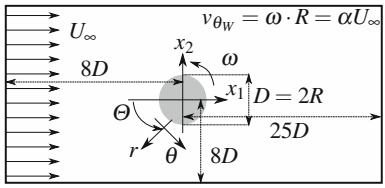

Fig. 1 Geometry definition of a rotating *cylinder* enclosed in a *rectangular* domain

3 Results

Table 1 summarises calculations performed thus far for both the static case ($\alpha = 0$) and the rotating case ($\alpha = 5$); reporting force coefficients, their variance and the Strouhal number, St, of the vortex shedding. Strouhal numbers for the $\alpha = 5$ case are currently not fully averaged but substantial deviations from tabulated values are not anticipated. By way of initial validation of our method, we first consider the static case. Results reported in Table 1 for the $\alpha = 0$ case are reported to fall well within the range of the experimental values summarised in [12]. The agreement is also clear from Fig. 2, which reports the comparison with experimentally reported pressure coefficient profiles at various Reynolds numbers in the same range as the current numerical work. As expected around the front of the cylinder, where the flow is laminar, there is no significant difference observed with either Reynolds or mesh resolution. Figure 3 reports skin friction coefficient and resolved turbulent kinetic energy for both meshes. At $\theta = 90°$, the flow is seen to become turbulent, and separates at $\theta = 104°$ for mesh M1 and $\theta = 100°$ for M2. Note that in Figs. 2 and 3

Table 1 Summary of calculations for $\alpha = 0$ and $\alpha = 5$ for each *Mesh#-Span* (Z/D)

$\alpha = 0$	*M1-0.5*	*M1-1.0*	*M1-2.0*	*M2-1.0*
C_D	0.3021	0.2933	0.2843	0.3961
C'_D	0.0298	0.0207	0.0141	0.0312
C_L	−0.0017	−0.0016	0.0018	0.0168
C'_L	0.1592	0.1158	0.0818	0.1759
St	0.35	0.35	0.35	0.22
$\alpha = 5$	*M1-0.5*	*M1-1.0*	*M1-2.0*	*M2-1.0*
C_D	0.3638	0.3509	0.3926	0.2777
C'_D	0.1162	0.1785	0.2208	0.1268
C_L	−15.416	−14.035	−12.926	−13.357
C'_L	0.4517	0.6208	0.6218	0.3024
St	≈0.15	≈0.13	≈0.13	≈ 0.10

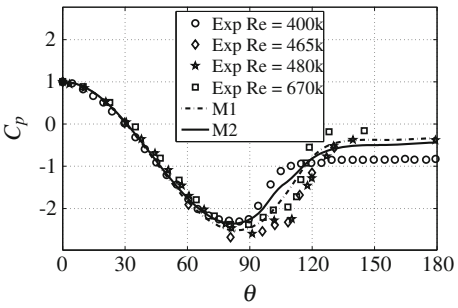

Fig. 2 Average C_p along wall: $\alpha = 0$

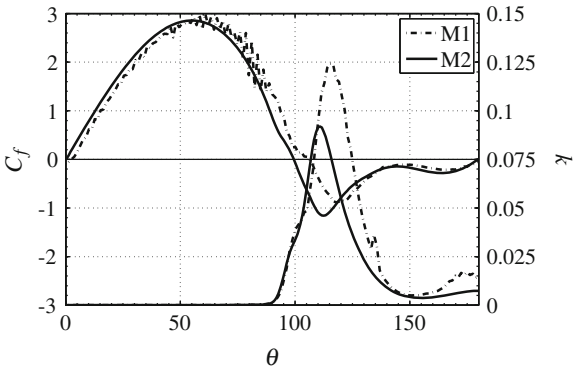

Fig. 3 Average C_f and k along wall: $\alpha = 0$

only one profile is reported for M1, since there was no substantial difference between the three span- wise extrusion lengths. Experimental results for Re $\geq 465k$ indicate a small kink in the pressure coefficient in the region $100° < \theta < 110°$, which is reported to be associated with boundary layer transition [12]. It is noted from Fig. 2 that a similar kink is observed with M2 in the same region, while results from M1 don't appear to capture this feature. While agreement with C_p levels in the region beyond $\theta = 100°$ is not perfect, there is acknowledged variation in experimental values at these Reynolds, which prevents an assessment of absolute error.

Results for the static case using M1 indicate a low influence of span-wise extent; values of C_D for all three extrusions fall within a 6 % interval, while in each case $St = 0.35$ and lift is virtually unchanged. In contrast, fluctuating force coefficients are seen to decrease by half with span-wise extent, demonstrating a dependency which warrants some further investigation. However, the weak dependency of mean values on the span is also supported by the 2D contours of the resolved normal stress, $\tau_{11} = \langle u_1 u_1 \rangle - \langle u_1 \rangle \langle u_1 \rangle$ (see Fig. 4). Additional refinement of the two-dimensional slice is shown to have a significant effect; M2 indicates a 30 % higher value of C_D than

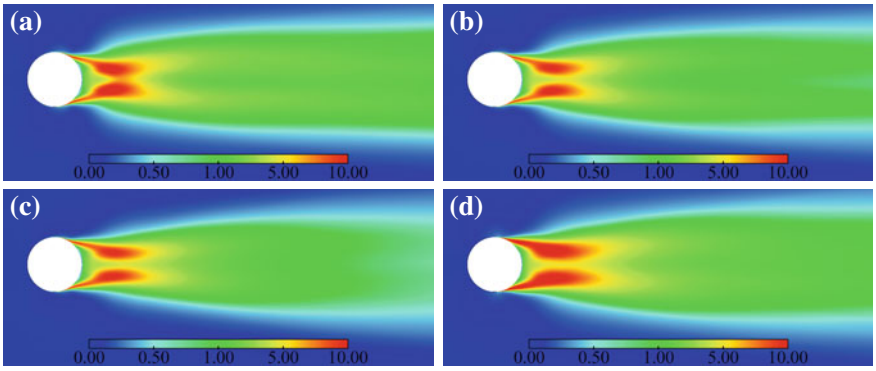

Fig. 4 Contours of τ_{11} at $\alpha = 0$: **a** *M1-0.5*, **b** *M1-1.0*, **c** *M1-2.0D*, **d** *M2-2.0D*

M1, while St is 40 % lower. This clearly indicates a need for further investigation Returning to Table 1, the principal effect of the rotation is an increase of the lift generation with the increase of the rotation rate α. This is focus and motivation of this work, though it should be reminded that aerodynamic benefit is offset by the additional power required to spin the cylinder. The mean flow streamlines from mesh M1-1.0 are provided in Fig. 5 for both static and rotating cases. The mechanism for the additional lift force is clearly evidenced by the large pressure gradient across the cylinder. The aft flow recirculation has all but disappeared and flow separation is rotated 90° around the cylinder.

The influence of span-wise resolution for the case $\alpha = 5$ appears to be slightly stronger than for the static case. Values of C_D and C_L vary by 11 and 16 % respectively, while rms values of the same coefficients vary by 50–100 %. We also note that all forces increase with spanwise extent, while for the static case they decrease. Further investigation is required to fully understand the implications of these findings. In particular it is felt that a further refinement of the 2D plane is necessary, before proceeding to investigate span-wise extent at this resolution.

Figure 6 presents the variation of resolved turbulent kinetic energy in the wall normal direction at locations around the cylinder. It is interesting to note that, in contrast with the static case, a turbulent boundary layer is present around the entire cylinder. For $\alpha = 0$, the transition point is clearly observed to occur in the region $90° < \Theta < 100°$ and is followed by a rapid increase in turbulence, which quickly spreads away from the wall in the region $100° < \Theta < 120°$. In contrast, when

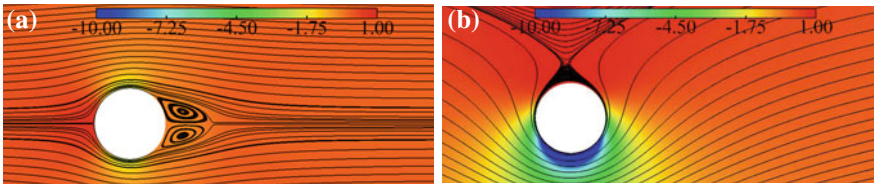

Fig. 5 Pressure coefficient and streamlines for *M1-1.0* at **a** $\alpha = 0$, **b** $\alpha = 5$

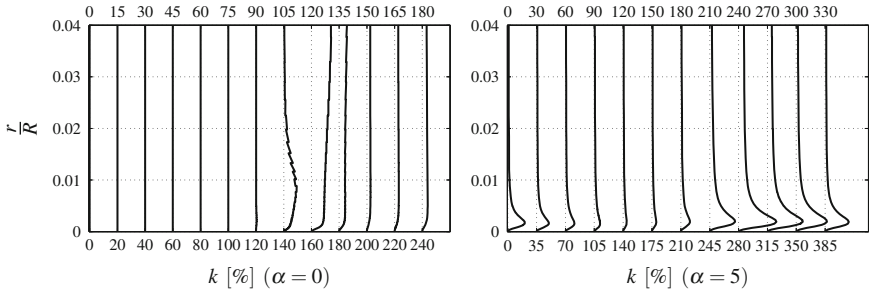

Fig. 6 Dimensionless turbulent kinetic energy profiles $k/U_\infty^2 \times 100$ (angular position along *top*)

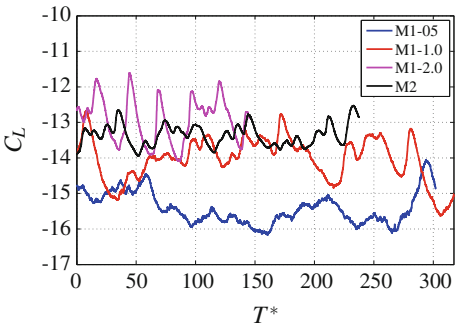

Fig. 7 Lift coefficient time history

$\alpha = 5$, the profiles appear to indicate that turbulence remains confined to an attached boundary layer, with a peak of k located very close to the wall.

Figure 7 compares the time evolution of lift coefficient $\alpha = 5$ for all meshes, where non-dimensional time is $T^* = T\ U_\infty / D$. While magnitude of lift decreases with span extent, fluctuations increase, as discussed above. There is reasonable agreement between both meshes when span is $z/D = 1$. In all cases bar the smallest extent, significant variation between maximum and minimum lift occurs, which warrants further investigation in order to derive understanding of the associated flow mechanism.

Figure 8 displays turbulent structures present at two time instances during the calculation on mesh M2. Iso-surfaces of the Q-criteria are coloured by positive/negative components of vorticity in the y-direction. The first and second snapshots correspond to instances of maximum and minimum lift respectively. The formation of a pair of counter-rotating structures is observed to occur periodically during the simulation. These structures wrap around the front and the lower part of the cylinder against the

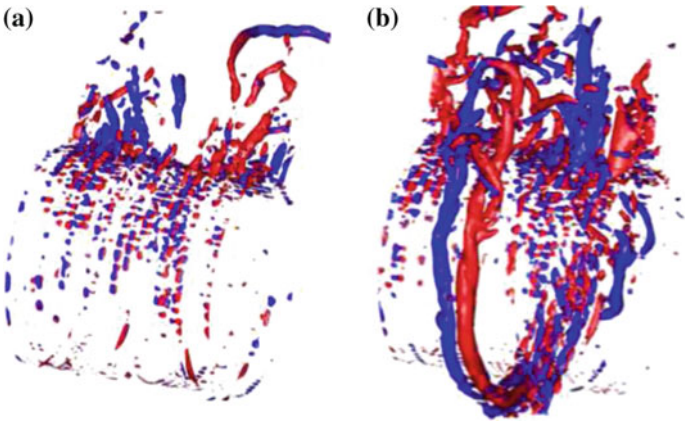

Fig. 8 Snapshot at **a** max and **b** min lift

direction of rotation, and upon reaching a critical size, they appear to detach from the cylinder at a point in time associated with low levels of lift generation. The ensuing periods are generally absent of the observed coherent structures and coincide with occurrences of maximum lift. The investigation of these structures is ongoing.

4 Conclusions

This work presents an investigation of the flow around a cylinder at high Reynolds number for both static and rotating cylinder. preliminary findings indicate that for the static case a span-wise extension equal to $1D$ appears to be sufficient to capture the mean flow features, although this does not appear to hold for the spinning case. Furthermore, a mesh refinement of the cross-plane indicates that the coarser mesh is insufficient to capture correctly the generation and distribution of turbulence for both static and rotating cases. Only with the finer mesh did the boundary layer appear to be qualitatively correct, compared to limited experimental data.

The investigation of features at $\alpha = 5$ has commenced, with the preliminary discovery of a link between the cyclic variation of lift force and the formation of a pair of counter-rotating structures in the lower and frontal part of the cylinder.

Further investigation is needed to (1) ensure the cross-plane resolution of mesh M2 is sufficient, and (2) to test span extent at this resolution compared to at coarse resolutions. Whilst retaining the same Reynolds number used here, calculations at higher values of α have been planned, as has an investigation into the potential lift augmentation offered with the presence of flat 'Thom disk' devices.

Acknowledgments The authors are grateful to UK Turbulence Consortium (UKTC) for providing additional computing time on UK National Supercomputing Service HeCTOR. The authors would like also to Prof B. Launder and Dr T. Craft for the continuous support received.

References

1. Archambeau, F., Mechitoua, N., Sakiz, M.: A finite volume method for the computation of turbulent incompressible flows—industrial applications. Int. J. Finite Vol. **1**, 1–62 (2004)
2. Breuer, M.: A challenging test case for large eddy simulation: high Reynolds number circular cylinder flow. Int. J. Heat Fluid Flow **21**, 648–654 (2000)
3. Craft, T., Iacovides H., Launder B.: Dynamic performance of Flettner rotors with and without Thom discs. In: Proceedings of the 7th Symposium on Turbulence and Shear Flow Phenomena, Ottawa (2011)
4. El Akoury, R., Braza, M., Perrin, R., Harran, G., Hoarau, Y.: The three-dimensional transition in the flow around a rotating cylinder. J. Fluid Mech. **607**, 0–11 (2008)
5. Fournier, Y., Bonelle, J., Moulinec, C., Shang, Z., Sunderland, A.G.: Optimizing code saturne for petascale computations. Comput. Fluids **45**, 1–12 (2011)
6. Germano, M., Piomelli, U., Moin, P., Cabot, W.H.: A dynamic subgrid-scale eddy viscosity model. Phys. Fluids A **3**, 1760–1765 (1991)

7. Karabelas, S.J.: Large eddy simulation of high-Reynolds number flow past a rotating cylinder. Int. J. Heat Fluid Flow **31**(4), 518–527 (2010)
8. Karabelas, S.J., Koumroglou, B.C., Argyropoulos, C.D., Markatos, N.C.: High Reynolds number turbulent flow past a rotating cylinder. Appl. Math. Model. **36**(1), 379–398 (2012)
9. Lilly, D.K.: A proposed modification of the Germano subgrid-scale closure method. Phys. Fluids A **4**(3), 633 (1992)
10. Mittal, S., Kumar, B.: Flow past a rotating cylinder. J. Fluid Mech. **76**, 303–334 (2003)
11. Prandtl, L.: The magnus effect and wind-powered ships. Naturwissenschaften **13**, 93–108 (1925)
12. Zdravkovich, M.: Flow Around Circular Cylinders: Fundamentals. Oxford University Press, Oxford (1997)

Part XII
Reactive Flows and Combustion

LES of Turbulence-Radiation Interaction in Plane Reacting and Inert Mixing Layers

Somnath Ghosh, Rainer Friedrich and Christian Stemmer

1 Introduction

It is the aim of this contribution to focus on the effect of thermal radiation on the turbulence structure rather than on the influence of turbulence on radiation. Concerning the prediction techniques for turbulence-radiation interaction (TRI), a very good compromise with respect to accuracy and cost is achieved by performing a large-eddy simulation (LES) of the flow field, applying the discrete ordinate method (DOM, [9]) to solve the radiative transfer equation (RTE) for an absorbing-emitting gas and to use the Statistical Narrow Band correlated-K (SNB-cK) model to account for the radiative properties of the gas. In [3], we followed this approach to investigate effects of radiation on supersonic turbulent channel flow with pure water vapour as working gas. The computations led to low optical thicknesses and hence weak effects of radiation on the turbulence structure. As a way to increase the optical thickness while keeping the Reynolds number fixed, we have adopted the procedure of Gupta et al. [4] which assumes a grey gas model with a Planck mean absorption coefficient which can be artificially increased.

When performing LES, the question arises whether subgrid-scale effects play a role in the filtered RTE. Roger et al. [10] performed DNS and concluded that neglecting subgrid-scale effects in the filtered RTE provides good results. Such effects have also been discarded by Amaya et al. [1]. Based on these findings and our aim to investigate fundamental effects of radiative heat transfer on the structure of turbulent mixing layers, we also neglect subgrid-scale effects on radiative emission and absorption in inert and reacting mixing layers.

S. Ghosh · R. Friedrich (✉) · C. Stemmer
Lehrstuhl Für Aerodynamik und Strömungsmechanik,
TU München, Munich, Germany
e-mail: r.friedrich@lrz.tum.de

S. Ghosh
e-mail: somnath.ghosh@aer.mw.tum.de

J. Fröhlich et al. (eds.), *Direct and Large-Eddy Simulation IX*,
ERCOFTAC Series 20, DOI 10.1007/978-3-319-14448-1_62

2 Basic Equations and Numerical Integration

The compressible Navier-Stokes equations for a multicomponent thermally radiating mixture of ideal gases are used to describe fluid flow and heat transfer by conduction, convection and radiation. Molecular transport coefficients are computed efficiently using the code EGLib [2], and polynomial expressions are applied to specify the temperature dependence of the specific heats. Reacting flow is modelled, using an infinitely fast global reaction and simplified diffusion mechanisms with constant Schmidt number. Species mass fractions are related to a mixture fraction via the Burke-Schumann relations. The radiative source term, $\frac{\partial q_{j,R}}{\partial x_j}$, in the energy equation (written in Cartesian coordinates) is obtained by integrating the radiative transfer equation (RTE, Eq. (1)) for a grey, emitting-absorbing gas over the solid angle Ω. The radiative intensity I depends on the direction $\mathbf{s}$ in which the energy propagates and on the location in space, $\mathbf{x}$. κ, I_b denote the frequency-integrated absorption coefficient and black body radiative intensity. The first and second term on the right-hand-side of the RTE describe the gain of radiative intensity by emission and the loss by absorption.

$$\frac{dI}{ds} = \kappa I_b - \kappa I, \quad \frac{\partial q_{j,R}}{\partial x_j} = 4\pi\kappa I_b - \kappa \int_{4\pi} I d\Omega = \underbrace{4\kappa_P \sigma T^4}_{emission} \underbrace{- \kappa \int_{4\pi} I d\Omega}_{absorption} \tag{1}$$

κ_P denotes Planck's mean absorption coefficient. σ is the Stefan-Boltzmann constant. The refractive index is assumed constant, equal to one. Following [4] we adopt the subsequent form for κ_P:

$$\kappa_P = C_k Y_{H_2O} \left[c_o + c_1 (A/T) + c_2 (A/T)^2 + c_3 (A/T)^3 + c_4 (A/T)^4 + c_5 (A/T)^5 \right]$$

The coefficients c_o–c_5 and A were taken from a radiation model suggested for water vapor [12]. The coefficient C_k allows for variation of κ_P independently of the other parameters. In our study, κ_P has been artificially increased by nearly an order of magnitude. Y_{H_2O} is the mass fraction of water vapour in both the inert and reacting flows. The convection and molecular transport terms in the flow equations are discretized, using the compact sixth-order scheme of [6]. A third-order low-storage Runge-Kutta scheme of [11] advances the solution in time. Our LES-approach which has been described and successfully tested against DNS data of inert compressible flow in [7] consists in defining an LES-grid and in filtering the high-order numerical solution explicitly at each time step using the composite filter, $(Q_N * G)$. G is a second order $Padé$ filter containing a parameter which allows to control the cutoff wavenumber, and Q_N is the approximate inverse of G, obtained from a van Cittert series which is truncated at $N = 5$. When chemical reaction takes place the filtered heat release term forms an extra closure problem. This is solved here in analogy to a

statistical model, see [8]. The three-dimensional RTE is integrated with the discrete ordinate method implemented in the code PRISSMA. This code uses finite-volume discretizations and a second-order Diamond mean flux scheme [5] to compute I along a line of sight. The flow field and the radiation field are directly coupled such that PRISSMA gets the filtered pressure and temperature fields at about every characteristic convective time interval and the compressible LES solver receives the radiative source term. We would like to point out, that we do not specifically denote LES variables with an overbar or a tilde. From now on, all flow variables are explicitly filtered space- and time-dependent quantities, unless otherwise stated. A variable with an overbar or a tilde represents a statistical average, while dashes and double-dashes denote Reynolds and Favre fluctuations.

3 Flow Configuration

Two cases of temporally evolving mixing layers are investigated. In the reacting case, the working fluid is a mixture of ideal gases where the low-speed stream consists of hydrogen and nitrogen and the high-speed stream of oxygen and nitrogen. Both streams are premixed in a way that the free-stream densities are the same and the stoichiometric mixture fraction is 0.3. In the inert case the low-speed stream consists of nitrogen at a temperature of 1,000 K and the high-speed stream is pure water vapour of 2,000 K, when radiation is turned off. The mixing layers are parametrized by a Reynolds number (based on vorticity thickness δ_ω), a convective Mach number M_c and an optical thickness τ_H, defined using Planck's mean absorption coefficient, κ_P:

$$Re_\omega = \frac{\rho_o \Delta u \delta_\omega}{\mu_o}, \qquad M_c = \frac{\Delta u}{c_1 + c_2}, \quad \tau_H = \int_0^H \kappa_P(y)dy, \qquad \kappa_P = \frac{\pi \kappa I_b}{\sigma T^4} \quad (2)$$

Δu is the velocity difference between high-speed stream (index 1) and low-speed stream (index 2) and c_1, c_2 are their sonic speeds. ρ_o, μ_o are averaged free-stream densities and viscosities, e.g. $\rho_o = (\rho_1 + \rho_2)/2$. H is the width of the computational domain in y-direction (across the streams). Table 1 lists the initial and final Reynolds numbers and the Mach numbers, together with the optical thicknesses of the mixing layers.

Table 1 Flow parameters of reacting and inert mixing layers with radiation

Flow	Re_{ω_o}	Re_{ω_f}	M_c	τ_H
Reacting	9,304 (9,304)	32,450 (32,449)	0.15 (0.15)	0.8
Inert	533 (533)	16,082 (15,754)	0.182 (0.178)	0.3

Values in brackets correspond to cases without radiation

The computational domain for inert flow of size $129 \times 180 \times 32$ in (x, y, z)-directions (stream-, cross- and spanwise) and measured in initial vorticity thicknesses, is discretized by $192 \times 288 \times 48$ points. The domain for reacting flow has the size $41.5 \times 21 \times 10.4$ in (x, y, z)-directions and is discretized by $192 \times 108 \times 48$ points. The mass, momentum and energy satisfy periodic boundary conditions in stream- and spanwise directions. In the end planes perpendicular to these directions, fully reflective boundary conditions (with zero emissivity) are imposed in the radiation code PRISSMA. In the cross-stream direction the flow variables satisfy non-reflective boundary conditions.

4 Results for Reacting and Inert Mixing Layers

We present a few statistical results of the reacting temporal mixing layer first, taken from self-similar states in which the momentum thickness grows at constant rate. When thermal radiation sets in, the growth rate increases. Due to heat of reaction the mean temperature of the mixing layer reaches a maximum value of 1,630 K (Fig. 1). Radiation reduces this peak value by 120 K. The temperature ratio of the two streams (upward/ downward streams: indices 2,1) is $T_2/T_1 = 2.03$. At initially constant pressure across the layer this guarantees equal densities on both sides. Thermal radiation causes an increase in mean density. The mean streamwise velocity remains practically unaffected by thermal radiation. The peak values of the RMS temperature fluctuations drop by 37 and 83 K, respectively, due to radiation (Fig. 2). Corresponding reductions are also noted in density fluctuations. On the other hand, pressure fluctuations increase. This points towards an increased activity of the fluctuating velocity field and shows up in the Reynolds stresses. Their peak values increase when radiation is included. In order to understand the decrease in temperature fluctuations (and hence also in density fluctuations) due to thermal radiation, we study the transport equation for the variance of the temperature fluctuations. It reads:

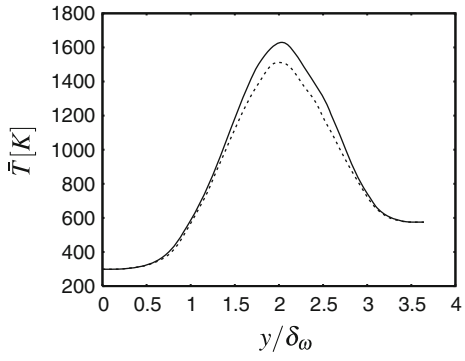

Fig. 1 Mean Temperature in reacting mixing layer. *Solid line* without radiation, *dashed line* with radiation

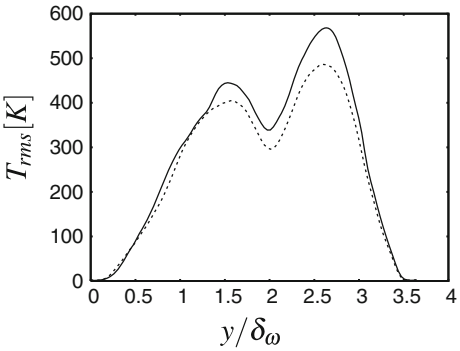

Fig. 2 RMS temperature fluctuations in reacting mixing layer. *Line* types as in Fig. 3

$$\frac{\partial\overline{\rho T''^2}}{\partial t}+\frac{\partial\widetilde{u}_j\overline{\rho T''^2}}{\partial x_j}=\underbrace{-2\overline{\rho u_j''T''}\frac{\partial\widetilde{T}}{\partial x_j}}_{Production}-\frac{\partial\overline{\rho u_j''T''^2}}{\partial x_j}\underbrace{-2\overline{\frac{T''}{C_p}\frac{\partial q_{j,R}}{\partial x_j}}}_{radiation}$$
$$\underbrace{-2\overline{\frac{T''}{C_p}\sum_{\alpha=1}^{N}h_\alpha\omega_\alpha}}_{Heat\ release}-2\overline{\frac{T''}{C_p}\frac{\partial T}{\partial x_j}\sum_{\alpha=1}^{N}\frac{\mu C_{p\alpha}}{Sc}\frac{\partial Y_\alpha}{\partial x_j}}+2\overline{\frac{T''}{C_p}\left(\frac{Dp}{Dt}+\tau_{ij}s_{ij}+\frac{\partial(\lambda\frac{\partial T}{\partial x_j})}{\partial x_j}\right)} \tag{3}$$

As known from inert non-radiating flow, the RHS of this equation contains production due to mean temperature gradient, turbulent diffusion and correlation between temperature fluctuation and the sum of pressure gradient, dissipation rate and divergence of conductive heat flux. When heat release, thermal radiation and energy transport by species diffusion play a role in the energy balance, extra correlations between temperature fluctuations and these mechanisms appear and control the behaviour of the temperature variance. In Fig. 3 we show profiles of three major source terms across

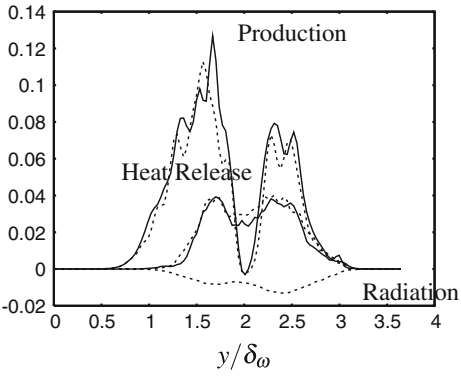

Fig. 3 Normalized source terms in the balance Eq. (3). *Line* types as in Fig. 3

the mixing layer, normalized with $\rho_o \Delta u T_o^2/\delta_\omega$. While the production term decreases under the effect of thermal radiation, the heat release term slightly increases. The important contribution to the reduced level of the temperature variance, however, is due to the interaction between temperature fluctuation and radiative source term.

The mean temperature of the inert mixing layer's hot side decreases due to thermal radiation (Fig. 4). At the same time all mean flow profiles are shifted towards the low-density side. It comes as a surprise, however, that the temperature and density fluctuations increase when radiation is included. Figure 5 presents the temperature fluctuations. The explanation for this contrasting behaviour is provided by the dominant source terms in Eq. (3). While the production of temperature fluctuations strongly increases, the interaction between temperature fluctuations and the radiative source term is very small (Fig. 6). Terms related to reaction and species diffusion do not appear.

The first author (S.G.) acknowledges the financial support received from Deutsche Forschungsgemeinschaft within the research project FR 478/25-1. We thank B. Cuenot and M. El Hafi for providing the code PRISSMA.

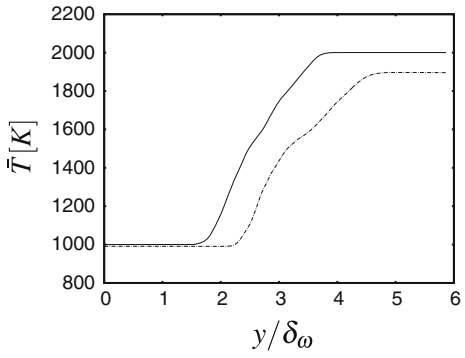

Fig. 4 Mean temperature in inert mixing layer. *Solid line* no radiation, -. - .- with grey gas, $\tau_H = 0.3$

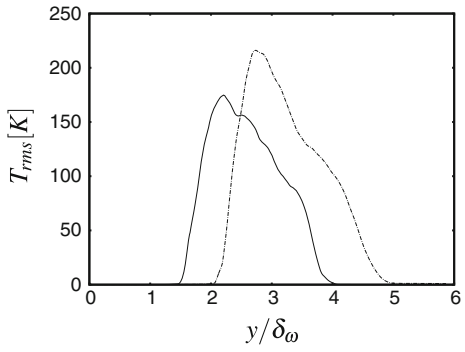

Fig. 5 RMS temperature fluctuations in inert mixing layer. *Line* types as in Fig. 4

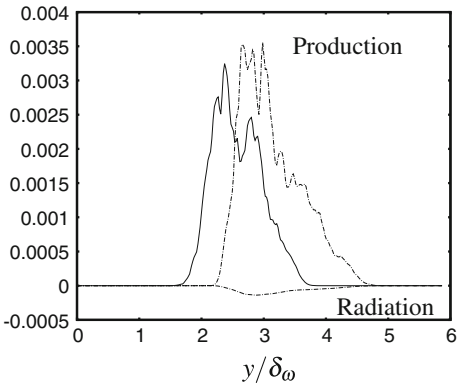

Fig. 6 Normalized source terms in the balance Eq. (3). *Line* types as in Fig. 4

References

1. Amaya, J., Collado, E., Cuenot, B., Poinsot, T.: Coupling LES, radiation and structure in gas turbine simulations. In: CTR, Proceedings of Summer Program, pp. 239–249 (2010)
2. Ern, A., Giovangigli, V.: Fast and accurate multicomponent transport property evaluation. J. Comput. Phys. **120**, 105–116 (1995)
3. Ghosh, S., Friedrich, R., Pfitzner, M., Cuenot, B., El Hafi, M.: Effects of radiative heat transfer on the structure of turbulent supersonic channel flow. J. Fluid Mech. **677**, 417–444 (2011). doi:10.1017/jfm.2011.92
4. Gupta, A., Modest, M.F., Haworth, D.C.: Large eddy simulation of turbulence-radiation interactions in a turbulent planar channel flow. J. Heat Transf. **131**, 061704 (2009)
5. Joseph, D., Hafi, M.El, Fournier, R., Cuenot, B.: Comparison of three spatial differencing schemes in discrete ordinates method using three-dimensional unstructured grids. Int. J. Therm. Sci. **44**, 851–864 (2005)
6. Lele, S.K.: Compact finite difference schemes with spectral-like resolution. J. Comput. Phys. **103**, 16–42 (1992)
7. Mathew, J., Lechner, R., Foysi, H., Sesterhenn, J., Friedrich, R.: An explicit filtering method for large-eddy simulation of compressible flows. Phys. Fluids **15**, 2279–2289 (2003)
8. Mahle I.: Direct and large-eddy simulation of inert and reacting compressible shear layers. Ph.D. thesis, Technical University of München (2007)
9. Modest, M.F.: Radiative Heat Transfer, 2nd edn. Academic Press, New York (2003)
10. Roger, M., Coelho, P.J., da Silva, C.B.: The influence of the non-resolved scales of thermal radiation in large eddy simulation of turbulent flows: a fundamental study. Int. J. Heat Mass Transf. **53**, 2897–2907 (2010)
11. Williamson, J.K.: Low-storage Runge-Kutta schemes. J. Comput. Phys. **35**, 48–56 (1980)
12. X. Sandia national laboratories combustion research facility, International Workshop on Measurements and Computation of Turbulent Nonpremixed Flames (2002)

A Priori Analysis of Dynamic Models for Large Eddy Simulations of Turbulent Premixed Combustion

D. Veynante , V. Moureau , M. Boileau and T. Schmitt

1 Introduction

Large eddy simulation (LES) gives access to unsteady flame behaviours as encountered during transient ignition [1], combustion instabilities [2] or cycle-to-cycle variations in internal combustion engine [3]. The unresolved flame/turbulence interactions is often modeled by algebraic expressions assuming an equilibrium between turbulence motions and flame surface [4–7]. A refined approach, adapted to transient situations, is to solve an additional balance equation for the flame surface density [3, 8] or the flame wrinkling factor [9].

Dynamic models automatically adjusting parameters during the simulation, appear as a promising alternative. However, while this approach is routinely used for unresolved transport since the pioneering work of Germano et al. [10], relatively few attempts have been made to develop dynamic combustion models [11–16]. The formulation of flame wrinkling factor dynamic models is investigated here. The wrinkling factor is a basic ingredient to describe interactions between flame fronts and turbulence motions in combustion models such as Level-Set [7, 14], Thickened Flame Model (TFLES) [5, 6] or algebraic flame surface density models [4]. Theoretical analysis are combined with a priori tests from a 2.6 billions cells, single step chemistry direct numerical simulation (DNS) of a lean premixed swirled turbulent flame (see [17] for details, Fig. 3 below visualizing an instantaneous iso-surface of the progress variable field).

D. Veynante (✉) · M. Boileau · T. Schmitt
Laboratoire EM2C, CNRS - Ecole Centrale Paris, Châtenay-Malabry, France
e-mail: denis.veynante@ecp.fr

V. Moureau
CORIA, CNRS, INSA et Université de Rouen, Saint-Étienne-du-Rouvray, France
e-mail: vincent.moureau@coria.fr

J. Fröhlich et al. (eds.), *Direct and Large-Eddy Simulation IX*,
ERCOFTAC Series 20, DOI 10.1007/978-3-319-14448-1_63

2 Theory and Modelling

The filtered reaction rate is written [11]:

$$\overline{\dot{\omega}(c)} = \Xi_\Delta W_\Delta(\widetilde{c}, \Delta) \tag{1}$$

where the progress variable c stands here for any quantity entering the reaction rate. $W_\Delta(\widetilde{c}, \Delta)$ is the resolved reaction rate, estimated from mass-weighted filtered quantities ($\widetilde{c}$). Δ is the LES filter size. The wrinkling factor Ξ_Δ measures the ratio of total to resolved flame surfaces in the filtering volume. Expression (1) holds as long as flame / turbulence interactions are described in terms of flame surface wrinkling factor or subgrid scale turbulent flame speed $S_T = \Xi_\Delta S_l$ where S_l is the laminar flame speed (flamelet assumption). Ξ_Δ may be modelled by the algebraic expression [5, 16], when $\Delta \geq \delta_l$:

$$\Xi_\Delta = \left(1 + \min\left[\max\left(\frac{\Delta}{\delta_l} - 1, 0\right), \Gamma\left(\frac{\Delta}{\delta_l}, \frac{u'_\Delta}{S_l}, Re_\Delta\right)\frac{u'_\Delta}{S_l}\right]\right)^\beta \tag{2}$$

The efficiency function Γ describes the ability of vortices to effectively wrinkle the flame front, β is the model parameter, u'_Δ and $Re_\Delta = u'_\Delta \Delta/\nu$ the subgrid scale turbulence intensity and Reynolds number, respectively, δ_l the laminar flame thickness, ν being the fresh gas kinematic viscosity. u'_Δ is extracted from DNS as:

$$u'_\Delta = \left[\frac{\int_\mathscr{V}\left(\overline{u^2 c_u} - \overline{u c_u}^2/\overline{c}_u\right) d\mathscr{V}}{\int_\mathscr{V} \overline{c}_u \, d\mathscr{V}}\right]^{1/2} \tag{3}$$

where u is the velocity vector, c_u the conditioning variable ($c_u = 1$ for $c \leq 0.04$, $c_u = 0$ elsewhere) and $\mathscr{V}$ the box volume, $\bar{\cdot}$ denoting the filtering operation. The threshold value is set as a compromise between the number of available fresh gas samples and the relevance of the estimation. Figure 1 displays u'_Δ/S_l and the wrinkling factor Ξ_Δ as a function of Δ/Δ_x where Δ_x is the mesh size, together with wrinkling factor modeling. Equation (2) predicts very well the Ξ_Δ increase with Δ, points below $\Delta/\Delta_x = 5$ having poor physical meaning ($\Delta \approx \delta_l$). Figure 1 also indicates that Eq. (2) is saturated and reduces to $(\Delta/\delta_l)^\beta$. The best fitting value, $\beta = 0.337$, gives a fractal dimension $D = \beta + 2 = 2.337$, in close agreement with the literature [18, 19].

The parameter β is dynamically determined by equating the reaction rate averaged over a given volume ($< \cdot >$), when evaluated at the LES-filter (Δ) and test-filter ($\widehat{\Delta}$) scales:

$$\left\langle \overbrace{\left(\frac{\Delta}{\delta_l}\right)^\beta W_\Delta(\widetilde{c}, \Delta)}^{\widehat{\ }} \right\rangle = \left\langle \left(\frac{\gamma\Delta}{\delta_l}\right)^\beta W_{\gamma\Delta}(\widetilde{\widetilde{c}}, \gamma\Delta) \right\rangle \tag{4}$$

where $\widetilde{\widetilde{c}}$ denotes a mass-weighted filtering at scale $\widehat{\Delta}$ of the filtered progress variable $\widetilde{c}$. $\gamma\Delta = (\Delta^2 + \widehat{\Delta}^2)^{1/2}$ is the effective filter size when combining LES and test Gaussian

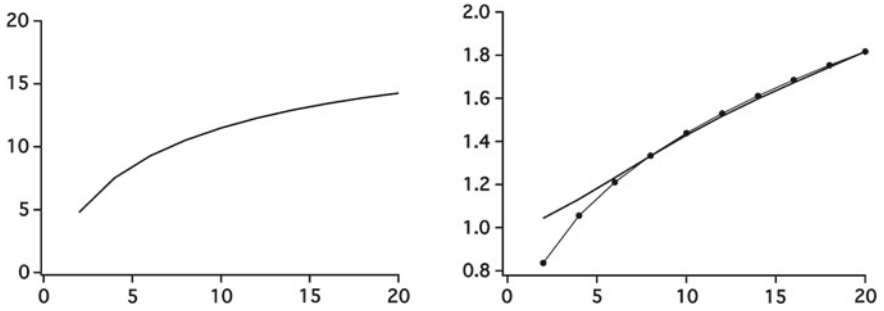

Fig. 1 Analysis of small part of the direct numerical simulation database (volume about $5.6 \times 6.3 \times 4.1$ mm^3). Mean sub-grid scale turbulence intensity, $\langle u'_\Delta \rangle / S_l$ ($S_l = 0.293$ m/s, *left*) and wrinkling factor $\langle \Xi_\Delta \rangle$ (*right*) are plotted as as a function of Δ/Δ_x. *Bold line* DNS ($\langle \Xi_\Delta \rangle = \langle |\overline{\nabla c}| \rangle / \langle |\nabla \overline{c}| \rangle$) ; *circles* Eq. (2) with $\beta = 0.337$; *thin lines* $\langle \Xi_\Delta \rangle = (\Delta/\delta_l)^{0.337}$

filters. Equation (4) then provides a relation to evaluate β. Two key requirements are considered: (i) to recover unity wrinkling factors ($\beta = 0$), when the flame wrinkling is fully resolved in simulations; (ii) to replace the averaging operation $< . >$ by a Gaussian filter, easier to implement for unstructured meshes and/or on massively parallel machines (diffusion operation). The best solution found is to recast Eq. (4) in terms of flame surfaces:

$$\left\langle \widehat{\left(\frac{\Delta}{\delta_l}\right)^\beta |\nabla \overline{c}|} \right\rangle = \left\langle \left(\frac{\gamma \Delta}{\delta_l}\right)^\beta |\nabla \widehat{\overline{c}}| \right\rangle \tag{5}$$

where $|\nabla \overline{c}|$, $\Xi_\Delta |\nabla \overline{c}|$, $|\nabla \widehat{\overline{c}}|$ and $\Xi_{\gamma\Delta} |\nabla \widehat{\overline{c}}|$ measure resolved and total flame surface densities at LES and test-filter scales, respectively. Unfortunately, Eq. (5) involves filtered quantities instead of Favre-filtered quantities that are solved for in LES. However, for infinitely thin flame fronts, $\overline{\rho c} = \overline{\rho c} = \rho_b \overline{c}$ and $\widehat{\overline{\rho}}\,\widetilde{\widetilde{c}} = \widehat{\overline{\rho c}} = \rho_b \widehat{\overline{c}}$, where ρ_b is the burnt gas density. These relations suggest, in agreement with DNS data (not shown here), to approximate β, assumed to be uniform over the averaging volume, as:

$$\beta \approx \frac{\ln\left(\left\langle \widehat{|\nabla \overline{\rho c}|} \right\rangle / \left\langle |\nabla \widehat{\overline{\rho}}\,\widetilde{\widetilde{c}}| \right\rangle\right)}{\ln(\gamma)} \approx \frac{\ln\left(\left\langle \widehat{|\nabla \overline{c}|} \right\rangle / \left\langle |\nabla \widehat{\overline{c}}| \right\rangle\right)}{\ln(\gamma)}, \tag{6}$$

3 A Priori Test Results

Figure 2 compares the filtered reaction rate predicted by the TFLES model, writing $W_\Delta = \dot{\omega}(\widetilde{c})/F$ where $F = \sqrt{\Delta^2 + \delta_l^2}/\delta_l$ is the thickening factor, to the reaction rate extracted from DNS. The agreement is very good (correlation coefficient of about

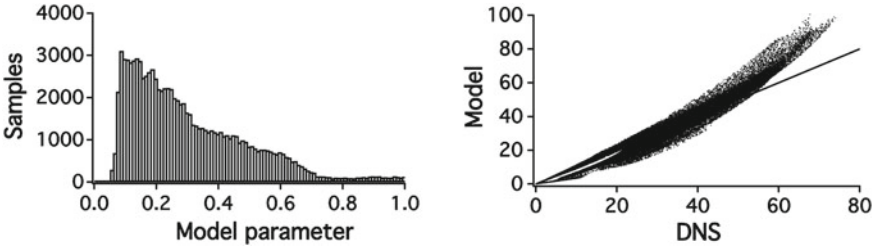

Fig. 2 *Left* distribution of the parameter β; *Right* TFLES modeled reaction rate as a function of the filtered reaction rate $\langle\overline{\dot{\omega}(c)}\rangle$ extracted from DNS. 95306 samples are displayed from the same DNS part as in Fig. 1

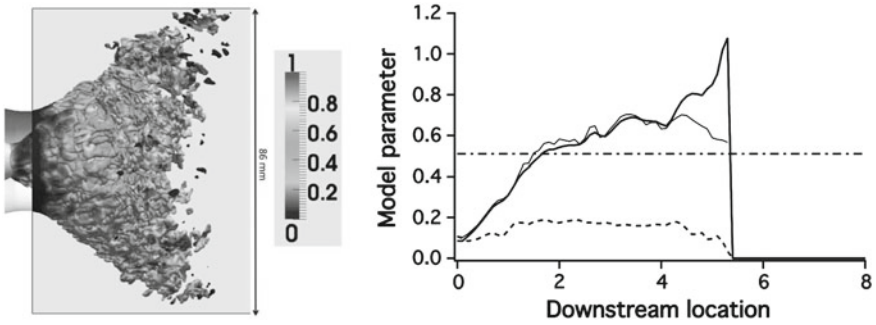

Fig. 3 *Left* instantaneous view of $c = 0.8$ isosurface coloured by the model parameter β. *Right* evolution of β with the downstream location (cm). *Bold line* mean β values; *dashed line* β-RMS; *thin line* β estimated using transverse slices of 1 mm thickness as averaging volume ($< \cdot >$); *dotted-dashed line* global β value (averaging $< \cdot >$ over the computational domain). *Filter size* $\Delta = 10\Delta_x$, where Δ_x is the mesh size, test-filter size $\widehat{\Delta} = 1.5\Delta$, "averaging" Gaussian filter size $\Delta_m = 3\Delta$, $\delta_l = 3.4\Delta_x$

0.99) even if the model slightly underestimates (respectively overestimates) low (large) reaction rate values. The corresponding distribution of the model parameter confirms that β cannot be assumed uniform and provides further justification for a dynamic formalism.

Figure 3 displays an instantaneous β field (left) as well as the evolution of mean and RMS β values with the downstream direction (right) as extracted from the full DNS database (2.6 billion cells). The mean parameter value, starting from $\beta \approx 0.1$ at the burner inlet, increases up to $\beta \approx 0.6$ at $x = 2$ cm, as the flame is progressively wrinkled by turbulence and convected downstream. Then, β is roughly constant for $2 \leq x \leq 4$ cm, denoting the equilibrium between turbulence motions and flame surface. In the last phase ($4 \leq x \leq 5.5$ cm), β strongly increases which can be associated with the formation of flame pockets. The RMS of β is roughly constant and about 0.2. The "1-D β-values", computed using transverse slices of 1 mm thickness in the downstream direction as averaging volume $\langle\cdot\rangle$ (i.e. β depends only on time t and downstream coordinate x), are very similar up to $x \approx 4$ cm. The discrepancies

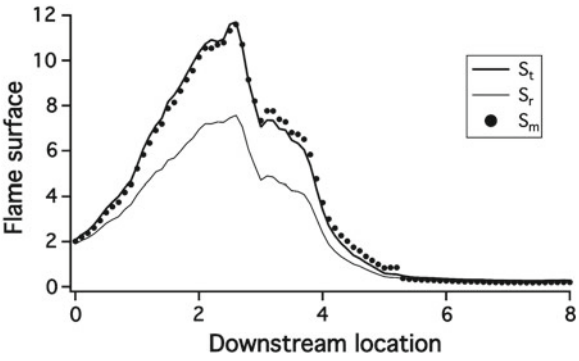

Fig. 4 Total (S_t), resolved (S_r) and modeled, $S_m(x) = (\Delta/\delta_l)^{\beta_m(x)} S_r(x)$, flame surfaces (cm^2) over transversal slices of 1 mm thickness as a function of the downstream location x (cm). $\beta_m(x)$ is the mean parameter value displayed in Fig. 3 (*right*)

observed downstream are due to flame pockets: mean β-values are conditioned on the flame front while "1-D β" are smoothed by the averaging volume, and correspond to very low flame surfaces (see Fig. 4). The global parameter value ($\beta \approx 0.51$), evaluated by volume-averaging over the computational domain, overestimates the front wrinkling factors during the development phase of the flame ($x \leq 2$ cm), while being in fair agreement with mean local values when the flame / turbulence equilibrium is reached. Note also that β evolves rather smoothly and would be compatible with numerical simulations.

Figure 4 displays the downstream evolution of the total (S_t), resolved (S_r) and modeled (S_m) flame surfaces. As expected, the resolved flame surface is lower than the total flame surface by about 30 %, while the total flame surface is very well recovered, validating the dynamic fractal-like model.

Acknowledgments The authors warmly acknowledge the support of the Center for Turbulence Research (CTR) at Stanford University (USA) during the 2012 Summer Program. Computational time was provided by GENCI (Grand Equipement National de Calcul Intensif) under the allocation x2012026880 at IDRIS (CNRS) and by PRACE in the MS-COMB project at TGCC (CEA).

References

1. Boileau, M., Staffelbach, G., Cuenot, B., Poinsot, T., Bérat, C.: LES of an ignition sequence in a gas turbine engine. Combust. Flame **154**(1–2), 2–22 (2008)
2. Menon, S., Jou, W.H.: Large eddy simulations of combustion instability in an axisymmetric ramjet combustor. Combust. Sci. Technol. **75**(1–3), 53–72 (1991)
3. Richard, S., Colin, O., Vermorel, O., Benkenida, A., Angelberger, C., Veynante, D.: Towards large eddy simulation of combustion in spark ignition engines. Proc. Combust. Inst. **31**(2), 3059–3066 (2007)
4. Boger, M., Veynante, D., Boughanem, H., Trouvé, A.: Direct numerical simulation analysis of flame surface density concept for large eddy simulation of turbulent premixed combustion. Proc. Combust. Inst. **27**, 917–925 (1998)
5. Charlette, F., Meneveau, C., Veynante, D.: A power-law flame wrinkling model for LES of premixed turbulent combustion. part I: non-dynamic formulation and initial tests. Combust. Flame **131**(1/2), 159–180 (2002)

6. Colin, O., Ducros, F., Veynante, D., Poinsot, T.: A thickened flame model for large eddy simulations of turbulent premixed combustion. Phys. Fluids A **12**(7), 1843–1863 (2000)
7. Pitsch, H.: Large-eddy simulation of turbulent combustion. Annu. Rev. Fluid Mech. **38**, 453–482 (2006)
8. Hawkes, E.R., Cant, S.R.: A flame surface density approach to large eddy simulation of premixed turbulent combustion. Proc. Combust. Inst. **28**, 51–58 (2000)
9. Weller, H.G., Tabor, G., Gosman, A.D., Fureby, C.: Application of a flame-wrinkling LES combustion model to a turbulent mixing layer. Proc. Combust. Inst. **27**, 899–907 (1998)
10. Germano, M., Piomelli, U., Moin, P., Cabot, W.H.: A dynamic subgrid-scale eddy viscosity model. Phys. Fluids A **3**(7), 1760–1765 (1991)
11. Charlette, F., Meneveau, C., Veynante, D.: A power-law flame wrinkling model for LES of premixed turbulent combustion. part II: dynamic formulation. Combust. Flame **131**(1/2), 181–197 (2002)
12. Hawkes, E.R., Chatakonda, O., Kolla, H., Kerstein, A.R., Chen. J.H.: A petascale direct numerical simulation study of the modelling of flame wrinkling for large-eddy simulations in intense turbulence. Combust. Flame **159**(8):2690–2703 (2012) ISSN 0010–2180. doi:10.1016/j.combustflame.2011.11.020
13. Knikker, R., Veynante, D., Meneveau, C.: A dynamic flame surface density model for large eddy simulation of turbulent premixed combustion. Phys. Fluids **16**(11), L91–L94 (2004)
14. Knudsen, E., Pitsch, H.: A dynamic model for the turbulent burning velocity for large eddy simulation of premixed combustion. Combust. Flame **154**, 740–760 (2008)
15. Wang, G., Boileau, M., Veynante, D.: Implementation of a dynamic thickened flame model for large eddy simulations of turbulent premixed combustion. Combust. Flame **158**(11), 2199–2213 (2011)
16. Wang, G., Boileau, M., Veynante, D., Truffin, K.: Large eddy simulation of a growing turbulent premixed flame kernel using a dynamic flame surface density model. Combust. Flame **159**(8), 2742–2754 (2012)
17. Moureau, V., Domingo, P., Vervisch, L.: From large-eddy simulation to direct numerical simulation of a lean premixed swirl flame: filtered laminar flame-pdf modeling. Combust. Flame **158**(7), 1340–1357 (2011)
18. Gouldin, F.C.: An application of fractals to modeling premixed turbulent flames. Combust. Flame **68**(3), 249–266 (1987)
19. Kerstein, A.R.: Fractal dimension of turbulent premixed flames. Combust. Sci. Technol. **60** (4–6), 441–445 (1988)

Lagrangian Analysis of Mixing and Soot Transport in a Turbulent Jet Flame

A. Attili, F. Bisetti, M.E. Mueller and H. Pitsch

1 Introduction

Soot particles are formed during rich combustion of fossil fuels in technical devices such as internal combustion engines, jet engines, and coal burners [1]. The carbon mass tied up in particulates is a combustion inefficiency since the full chemical potential of the fuel is not realized via complete conversion of carbon to carbon dioxide. Soot particles are also recognized as an important cause of health complications such as pulmonary conditions and cancer [2, 3]. Over the past few years, a few detailed simulation studies on soot formation in turbulent flames have been performed. These studies describe soot formation in turbulent ethylene-air counterflow diffusion flames [4], flame weakening, flame extinction, and soot leakage across the flame in a two-dimensional convection-driven turbulent wall-flame [5], soot-flame interaction and soot transport in a temporally evolving jet [6, 7], and formation and early evolution of soot in a two-dimensional turbulent *n*-heptane/air flame [8]. In the present paper, an analysis of soot formation and growth, based on a detailed numerical simulation of an *n*-heptane/air turbulent nonpremixed jet flame, is presented. Rather than the semi-empirical approach [9, 10] used in previous work

A. Attili (✉) · F. Bisetti
King Abdullah University of Science and Technology,
Thuwal, Kingdom of Saudi Arabia
e-mail: antonio.attili@kaust.edu.sa

F. Bisetti
e-mail: fabrizio.bisetti@kaust.edu.sa

M.E. Mueller
Princeton University, Princeton, USA
e-mail: muellerm@princeton.edu

H. Pitsch
RWTH Aachen University, Aachen, Germany
e-mail: h.pitsch@itv.rwth-aachen.de

J. Fröhlich et al. (eds.), *Direct and Large-Eddy Simulation IX*,
ERCOFTAC Series 20, DOI 10.1007/978-3-319-14448-1_64

[4, 6, 7], state-of-the-art chemistry and soot models [11–13], employed before only in a two-dimensional case [8], are used in a three-dimensional turbulent jet flame.

2 Physical Models, Numerical Methods, and Configuration

The gas phase hydrodynamics and combustion are modeled with the reactive, unsteady Navier-Stokes equations in the low Mach number limit. The transport of species mass fractions is described with a mixture averaged diffusion model. Combustion is modeled using a finite rate chemistry approach with 47 species and 290 reactions [14].

Soot particles and aggregates are described by their volume (V) and surface area (S) [12, 15]. A moment method in which equations are solved only for a few moments of the number density function (NDF) is adopted in the present work. The moments of the bivariate NDF are defined as $M_{x,y} = \sum_i V_i^x S_i^y N_i$. $M_{x,y}$ is the moment of order x for volume and y for surface, and V_i, S_i, and N_i are the volume, surface area, and number density of a soot aggregate belonging to size class i. As for all moment methods, the rate of change of a given moment depends on additional moments, and a closure scheme is necessary. Seven statistical moments of the bivariate distribution are transported and the Hybrid Method of Moments (HMOM) closure [13] is used. HMOM combines the interpolative closure of the Method of Moments with Interpolative Closure [12, 16] with a single delta function conceptually borrowed from the Direct Quadrature Method of Moments [17]. Closure is described by

$$M_{x,y} = N_0 V_0^x S_0^y + \exp\left(\sum_{r=0}^{R}\sum_{k=0}^{r} a_{r,k} x^k y^{r-k}\right) = N_0 V_0^x S_0^y + M'_{x,y}, \qquad (1)$$

where $a_{r,k}$ are the interpolation coefficients, obtained using available moments up to order R, and V_0 and S_0 are the volume and surface of the nucleated spherical soot particles. The first term of the equation describes the population of the smaller spherical incipient particles and models the contribution to the moments with a delta function fixed in phase space at a size corresponding to two naphthalene dimers ($V_0 = \pi d_0^3/6$, where $d_0 = 0.98$ nm). The second term in Eq. 1 describes the contribution to the moments of larger soot aggregates. Six statistical moments ($R = 2$) are used to describe the soot population, in addition to the weight of the delta function N_0.

The soot model considers several physical and chemical processes. The details of the functional form of soot source terms in the context of the HMOM closure are described by Mueller et al. [12, 13]. Nucleation occurs from the collision of two PAH dimers. A dimer is a molecular cluster composed of two PAH molecules. The rate of formation of dimers is assumed to be equal to the rate of self-collision of naphthalene molecules in the gas phase weighted by a sticking coefficient [11]. Collision

rates between soot particles are formulated to be valid from the free molecular (small collision diameter) to the continuum regime (large collision diameter). Growth by surface reactions is described by the H-abstraction/C_2H_2-addition (HACA) mechanism [18]. Oxidation of soot particles with OH and O_2 leads to the loss of soot mass and number density of the small particles.

The configuration selected for the study is a temporally evolving plane jet of diluted *n*-heptane and air. The region between the fuel and oxidizer is modeled as a layer with the equilibrium stoichiometric composition. This layer mimics the pilot usually employed in experimental studies of jet flames. The initial velocity field in the jet core is obtained with a simulation of a fully developed turbulent channel at Reynold number $\mathrm{Re}_\tau = 390$. Periodic boundary condition are applied in the y (streamwise) and z (spanwise) directions. In the x direction (normal to the average flame sheet), open boundary conditions are prescribed in order to allow mass outflow generated by combustion.

The gas velocity and reactive scalar fields are solved with a conventional finite-difference scheme [19]. The system of advection-reaction equations for soot moments is solved with a Lagrangian particle scheme [15, 20–22].

Table 1 shows the main physical and numerical parameters for the configuration. It is worth noting that while the simulation is fully resolved for turbulence and chemistry, it cannot be considered a direct numerical simulation for the soot dynamics due to the assumptions in the models, i.e. statistical treatment and closure of soot population dynamics, and the high Schmidt number of the moments.

Table 1 Simulation parameters

Jet centerline initial velocity U_c (m/s)	8.74
Coflow velocity (m/s)	−8.74
Initial jet width H (mm)	15
Jet Reynolds number $Re = \Delta U H/\nu$	15000
Fuel stream (jet core)	15 % *n*-heptane and 85 % nitrogen
Oxidizer stream	21 % oxygen and 79 % nitrogen
Initial fuel (oxidizer) temperature (K)	400 (800)
Domain size $L_x \times L_y \times L_z$ (mm)	$105 \times 94 \times 47$
Simulation time (ms)	21
Grid points $N_x \times N_y \times N_z$	$1024 \times 1024 \times 512$
Lagrangian notional particles	≈1 Billion
$\delta x = \delta y = \delta z$ (μm)	91
Kolmogorov scale (minimum) (μm)	100
OH layer thickness (minimum)	$\approx 10\delta x$

3 Results

Figure 1 shows the number density and mass fraction of soot in mixture fraction space at several time instants, from the initial phase of the jet development up to the late time solution. The flame is located approximately at the value $Z = 0.15$ in mixture fraction space. Figure 2 displays statistics of the soot number density and mass fraction growth at time $t = 20$ ms. Soot grows mainly in the region $0.3 < Z < 0.5$, it is oxidized in the region $0.15 < Z < 0.3$, and source terms approach zero for $Z > 0.6$. The negative value of the mean growth of number density for $Z > 0.3$ is related to the dominant role of coagulation with respect to nucleation.

In the first phase of the jet development, soot is concentrated mainly near the flame surface. Up to 1 ms, soot number density grows quickly in the region $0.2 < Z < 0.5$ in mixture fraction space due to available soot precursors. Then, coagulation starts

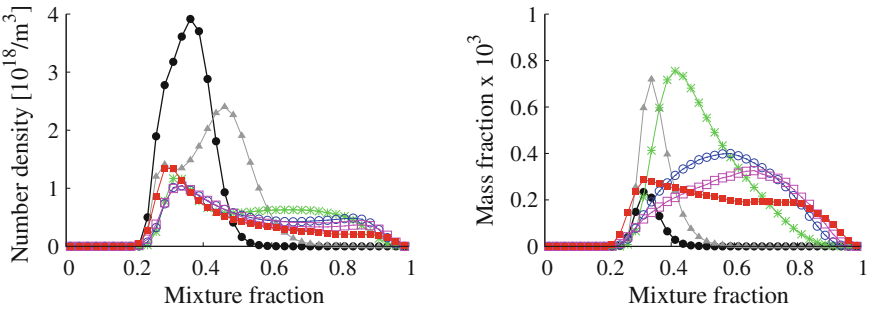

Fig. 1 Mean number density (*left*) and mean mass fraction of soot (*right*), conditioned on mixture fraction, at several time instants: 1 ms (*filled circles*, *black*), 2 ms (*triangles*, *gray*), 6 ms (*stars*, *green*), 8 ms (*open circles*, *blue*), 10 ms (*open squares*, *purple*), and the late time solution at 20 ms (*filled squares*, *red*)

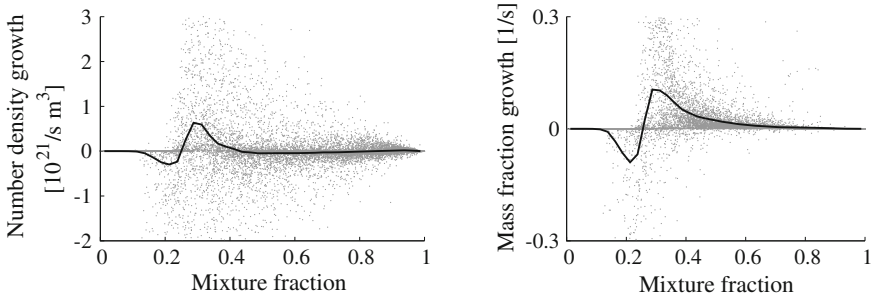

Fig. 2 Soot number density (*left*) and mass fraction (*right*) growth at time $t = 20$ ms. Every point represents a Lagrangian particle and the time derivative is computed on the Lagrangian trajectory. Only a small fraction of the entire set of particles is shown. *Lines* indicates the mean soot number density and mass fraction growth conditioned on mixture fraction

to dominate, and the number density decreases. Meanwhile, turbulent fluctuations, originating from the break-up of the Kelvin-Helmholtz structures and the production by mean shear, induce significant drift of particles in mixture fraction space. At late time, soot is present in the entire fuel-rich side of the mixture fraction space. On the lean side, i.e. $Z < 0.2$, the amount of soot is negligible for the entire duration of the simulation. This is the consequence of two different phenomena: (i) soot, which is generated in the region $0.3 < Z < 0.5$, tends to move preferentially toward richer mixtures. From the analysis of Lagrangian trajectories in mixture fraction space, it is observed that only 6 % of the notional particles that experienced some soot growth cross the threshold $Z = 0.2$ and (ii) when soot is transported toward leaner mixture, oxidation becomes dominant and consumes all of the soot mass. Oxidation is solely responsible for the negative growth of soot mass that appears in Fig. 2 for $0.15 < Z < 0.25$.

Mass fraction of soot grows quickly in time up to 5 ms, reaching a peak value at $Z = 0.4$. From the analysis of Fig. 2, it is evident that significant soot formation happens mainly in the region $0.25 < Z < 0.5$. Therefore, the wide range of mixture fractions (in particular for $Z > 0.5$) at which soot is present is due to differential diffusion between soot and mixture fraction and not to soot formation or growth at large mixture fraction values.

Lagrangian statistics are the most appropriate tool to study the evolution of soot during its movement in physical and mixture fraction space. Figure 3 shows probability density functions of the Lagrangian time derivative of mixture fraction conditioned on mixture fraction. This time derivative characterizes the movement of soot in mixture fraction space. The conditional mean is also reported at several time instants. The PDFs shows large exponential tails with values much larger than the root mean square (not shown), a signature of the intermittent nature of the turbulent field. Two distinct phase can be identified: up to 10 ms the mean is positive

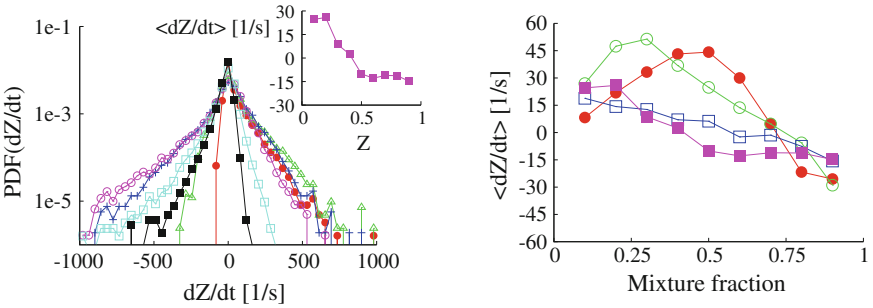

Fig. 3 *Left* PDFs of Lagrangian time derivative of mixture fraction conditioned on several value of mixture fraction at time $t = 20$ ms. $Z = 0.1$ (*red*, *filled circles*), 0.2 (*green*, *triangles*), 0.4 (*dark blue*, *plus*), 0.6 (*purple*, *open circles*), 0.8 (*light blue*, *open squares*), 0.9 (*black*, *filled squares*). *Inset* mean value for the distributions shown in the main figure. *Right* the mean value at different time instants: 5 ms (*red*, *filled circles*), 10 ms (*green*, *open circles*), 15 ms (*blue*, *open squares*), 20 ms (*purple*, *filled squares*)

for mixture fraction $Z < 0.7$ and it is negative for $Z > 0.7$, while at later times the sign changes at $Z \approx 0.5$. Positive values correspond to movement towards rich mixtures. It is interesting to observe that large amounts of soot appears at very high mixture fractions $Z > 0.7$, even if the mean Lagrangian derivative is negative for $Z > 0.4$. Therefore, it is possible to conclude that the large amount of soot at high mixture fraction values is due to turbulent fluctuations whose overall effects cannot be captured considering only the mean mixing process.

Acknowledgments We wish to acknowledge valuable support from KAUST Supercomputing Laboratory and the financial support by Saudi Aramco.

References

1. Bockhorn, H.: Soot Formation in Combustion. Springer, New York (1994)
2. Donaldson, K., Tran, L., Jimenez, L.A., Duffin, R., Newby, D.E., Mills, N., MacNee, W., Stone, V.: Combustion-derived nanoparticles: a review of their toxicology following inhalation exposure. Part. Fibre Toxicol. **2**(10), 1–14 (2005)
3. Lighty, J.S., Veranth, J.M., Sarofim, A.F.: Combustion aerosols: factors governing their size and composition and implications to human health. J. Air Waste Manage. Assoc. **50**, 1565–1618 (2000)
4. Yoo, C.S., Im, H.G.: Transient soot dynamics in turbulent nonpremixed ethylene air counterflow flames. Proc. Combust. Inst. **31**, 701–708 (2007)
5. Narayanan, P., Trouvé, A.: Radiation-driven flame weakening effects in sooting turbulent diffusion flames. Proc. Combust. Inst. **32**, 1481–1489 (2009)
6. Lignell, D.O., Chen, J.H., Smith, P.J.: Three-dimensional direct numerical simulation of soot formation and transport in a temporally evolving nonpremixed ethylene jet flame. Combust. Flame **155**, 316–333 (2008)
7. Lignell, D.O., Chen, J.H., Smith, P.J., Lu, T., Law, C.K.: The effect of flame structure on soot formation and transport in turbulent nonpremixed flames using direct numerical simulation. Combust. Flame **151**, 2–28 (2007)
8. Bisetti, F., Blanquart, G., Mueller, M.E., Pitsch, H.: On the formation and early evolution of soot in turbulent nonpremixed flames. Combust. Flame **159**(1), 317–335 (2012)
9. Leung, K.M., Lindstedt, R.P., Jones, W.P.: A simplified reaction mechanism for soot formation in nonpremixed flames. Combust. Flame **87**, 289–305 (1991)
10. Moss, J.B., Stewart, C.D., Syed, K.J.: Flowfield modelling of soot formation at elevated pressure. Proc. Combust. Inst. **22**, 413–423 (1988)
11. Blanquart, G., Pitsch, H.: A joint volume-surface-hydrogen multi-variate model for soot formation. In: Bockhorn, H., D'Anna, A., Sarofim, A.F., Wang, H. (eds.) Combustion Generated Fine Carbonaceous Particles, pp. 437–463. KIT Scientific Publishing, Karlsruhe (2009)
12. Mueller, M.E., Blanquart, G., Pitsch, H.: A joint volume-surface model of soot aggregation with the method of moments. Proc. Combust. Inst. **32**(1), 785–792 (2009)
13. Mueller, M.E., Blanquart, G., Pitsch, H.: Hybrid method of moments for modeling soot formation and growth. Combust. Flame **156**(6), 1143–1155 (2009)
14. Blanquart, G., Pepiot-Desjardins, P., Pitsch, H.: Chemical mechanism for high temperature combustion of engine relevant fuels with emphasis on soot precursors. Combust. Flame **156**(3), 588–607 (2009)
15. Attili, A., Bisetti, F., Mueller, M.E., Pitsch, H.: Formation, growth, and transport of soot in a three-dimensional turbulent non-premixed jet flame. Combust. Flame (2014, in press)
16. Frenklach, M.: Method of moments with interpolative closure. Chem. Eng. Sci. **57**(12), 2229–2239 (2002)

17. Marchisio, D.L., Fox, R.O.: Solution of population balance equations using the direct quadrature method of moments. J. Aerosol Sci. **36**(1), 43–73 (2005)
18. Frenklach, M., Wang, H.: Detailed modeling of soot particle nucleation and growth. In: Symposium (International) on Combustion, vol. 23, pp. 1559–1566. Elsevier, London (1991)
19. Desjardins, O., Blanquart, G., Balarac, G., Pitsch, H.: High order conservative finite difference scheme for variable density low mach number turbulent flows. J. Comput. Phys. **227**, 7125–7159 (2008)
20. Attili, A., Bisetti, F., Mueller, M.E.: DNS of soot formation and growth in turbulent nonpremixed flames: Damköhler number effects and Lagrangian statistics of soot transport. In: Proceedings of the Summer Program Center for Turbulence Research, NASA AMES—Stanford University (2012)
21. Attili, A., Bisetti, F.: Application of a robust and efficient lagrangian particle scheme to soot transport in turbulent flames. Comput. Fluids **84**, 164–175 (2013)
22. Koumoutsakos, P.: Multiscale flow simulations using particles. Annu. Rev. Fluid Mech. **37**, 457–487 (2005)

The Influence of Differential Diffusion in Turbulent Oxygen Enhanced Methane Flames

F. Dietzsch, C. Hasse, G. Fru and D. Thévenin

1 Introduction

For conventional combustion processes one of the most common oxidizers is air, mainly because it is cheap and readily available compared to other oxidizers. However, flames where the amount of O_2 is successively increased gain gradually more popularity for industrial applications. These so called oxy-fuel flames have certain advantages compared to conventional air flames, e.g. an increased thermal efficiency, increased flame stability and reduced NOx emissions [1].
Several aspects of oxygen enhanced combustion have been studied in previous works. In [2] the authors investigated the influence of oxy-fuel conditions on gas and particle radiation characteristics. Krishnan et al. [3] put the focus on radiation properties of ethane diffusion flames, varying the amount of oxygen up to pure oxygen. The modeling of radiation of oxygen enhanced coal combustion was investigated in [4]. A numerical study of NO formation including detailed chemistry and transport properties of an oxygen enriched methane diffusion flame was done by [5]. Several configurations, concerning different levels of O_2 enrichment, stretch rates and kinetic mechanisms were investigated by [6]. Turbulent oxygen enhanced coal combustion was investigated in [7] using the LES approach. From an

F. Dietzsch (✉) · C. Hasse
TU Bergakademie Freiberg, Chair of Numerical Thermo-Fluid Dynamics,
Freiberg, Germany
e-mail: Felix.Dietzsch@vtc.tu-freiberg.de

C. Hasse
e-mail: Christian.Hasse@vtc.tu-freiberg.de

G. Fru · D. Thévenin
Institute of Fluid Dynamics and Thermodynamics, Otto-von-Guericke
University Magdeburg, Magdeburg, Germany
e-mail: gordon.fru@ovgu.de

D. Thévenin
e-mail: dominique.thevenin@ovgu.de

J. Fröhlich et al. (eds.), *Direct and Large-Eddy Simulation IX*,
ERCOFTAC Series 20, DOI 10.1007/978-3-319-14448-1_65

experimental point of view [8] analyzed the combustion characteristics and flame length of turbulent oxy-fuel flames using pure methane as fuel. However, to the best knowledge of the authors there exists no publication that explicitly addresses the influence of differential diffusion in turbulent oxygen enhanced methane flames.

2 Diffusion Flux Modelling

Taking into account both, a proper model for the species transport and thermal diffusion the diffusive mass flux velocity is described by

$$\mathbf{j}_i = \rho\, \mathbf{u}_i \mathrm{Y}_i \quad with \quad \mathbf{u}_i = \mathbf{u}_{\mathrm{D},i} + \mathbf{u}_{\mathrm{T},i} + \mathbf{u}_{\mathrm{C}}, \tag{1}$$

where ρ denotes density, $\mathbf{u}_i$ is the diffusion velocity and Y_i is the species mass fraction of species i. As shown in (1) the diffusion velocity is split up into an ordinary diffusion velocity ($\mathbf{u}_{\mathrm{D},i}$), a thermo-diffusion velocity ($\mathbf{u}_{\mathrm{T},i}$) and a possible correction velocity ($\mathbf{u}_{\mathrm{C}}$), which ensures $\mathbf{u}_{\mathrm{C}} = \sum_{i=1}^{N} \mathbf{u}_i \mathrm{Y}_i = 0$, depending on the employed model. Available models are listed in Table 1. All of these models require the evaluation of the diffusion driving force d_i, which in general is a function of the mole fraction gradient ($\nabla \mathrm{X}_i$), the pressure gradient and demixing due to buoyancy. Details about the evaluation of d_i, the binary diffusion coefficient $\mathscr{D}_{\mathrm{ik}}$ and the diffusion matrix D_{ik} can be found in [9–11].

The diffusive mass flux is directly linked to the species transport and energy conservation equation by

$$\frac{\partial}{\partial t}(\rho \mathrm{Y}_i) + \nabla \cdot (\rho \mathbf{v} \mathrm{Y}_i) = -\nabla \cdot \mathbf{j}_i + \dot{\omega}_i \tag{2}$$

$$\frac{\partial}{\partial t}(\rho e) + \nabla \cdot (\rho \mathbf{v} e) = -\nabla \cdot (q + \Pi \mathbf{v}) + \sum_{i=1}^{N_s} \rho \mathrm{Y}_i (\mathbf{v} + \mathbf{u}_{\mathrm{D},i})\, \mathbf{F}_i \tag{3}$$

where $\dot{\omega}_i$ denotes the chemical source term of species i, Π is the viscous stress tensor, q describes the heat flux due to diffusive and radiative phenomena and $\mathbf{F}_i$ is

Table 1 Models for the species diffusion velocity $\mathbf{u}_{\mathrm{D},i}$

($\mathbf{u}_{\mathrm{C}} = 0$)	Non-conservative ($\mathbf{u}_{\mathrm{C}} \neq 0$)
Multi-component: $\mathbf{u}_{\mathrm{D},i} = -\frac{1}{\mathrm{X_i}} \sum_{\mathrm{k} \neq i}^{N_s} \mathrm{D_{ik}}\, \mathrm{d_k}$	Mixture-averaged: $\mathbf{u}_{\mathrm{D},i} = -\frac{1}{\mathrm{X_i}} \frac{1 - \mathrm{Y_i}}{\sum_{i \neq k} X_{\mathrm{k}} / \mathscr{D}_{\mathrm{ik}}}\, \mathrm{d}_i$
Lewis unity: $\mathbf{u}_{\mathrm{D},i} = -\frac{1}{\mathrm{X_i}} \frac{\lambda}{\rho\, c_p}\, \mathrm{d}_i$	Lewis non-unity: $\mathbf{u}_{\mathrm{D},i} = -\frac{1}{\mathrm{X_i}} \frac{\lambda}{\rho\, c_p\, \mathrm{Le}_i}\, \mathrm{d}_i$

the external force per unit mass acting on the ith species. For a detailed description of how these terms are computed it is referred to [12, 13].

3 Description of the Numerical Method

The code used for the numerical analysis is called Parcomb3D and was originally described in [14]. It is an explicit direct numerical simulation (DNS) code that solves the fully compressible, multi-component, reactive Navier-Stokes equations. A sixth order explicit finite-difference scheme (skew-symmetric [15]) is used for spatial discretization and a fourth order Runge-Kutta scheme is used for time integration. Boundaries are treated with the extended Navier-Stokes Characteristic Boundary Conditions (NSCBC) as described in [16, 17]. In order to evaluate the previously mentioned coefficients for the computation of the diffusive transport the code is linked to the EGlib library [12]. For the initialization of the turbulent flow field Parcomb3D uses a technique as described in [18] in conjunction with a Passot-Pouquet spectrum.

A chemical mechanism involving 29 species and 141 reactions [19] is used to describe the combustion of methane in an oxygen enhanced environment. Therefore, a laminar counter-diffusion configuration as shown in Fig. 1 is ignited in a one dimensional domain, whereas the initial temperature of both fuel and oxidizer are set to 300 K. The initial mass fractions of methane and oxygen are set to $Y_{CH_4} = 0.5$ and $Y_{O_2} = 0.9$ and an appropriate nitrogen complement is added in order to fulfill $\sum_{i=1}^{N_s} Y_i = 1$. Boundary conditions are both set to outlet conditions.For the turbulent flame case the ignition is still performed in one dimension but the configuration is altered according to Fig. 2. After a stable burning flame has established the solution is extended to the second dimension and superimposed by a pseudo-turbulent, time decaying velocity field. For the turbulent flame case all boundary conditions are set

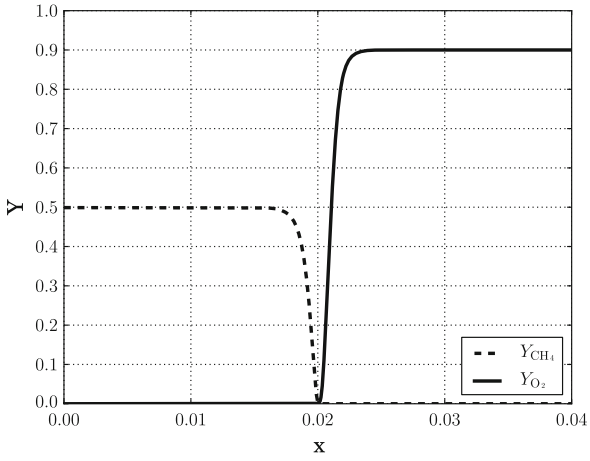

Fig. 1 Initial setup for the laminar counter-diffusion setup

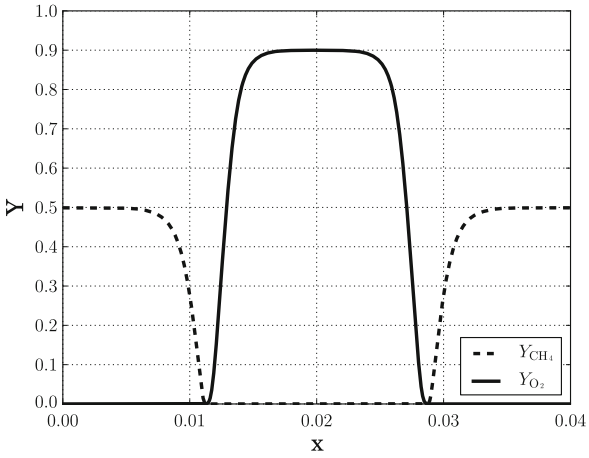

Fig. 2 Initial setup for the turbulent counter-diffusion setup

to be periodic. The domain used for both laminar and turbulent flame simulations has a size of 4 cm, 4×4 cm respectively, and is discretized by 1,200 grid points in each direction. According to Table 1 the Lewis-unity and Lewis non-unity approaches are used to account for species diffusion. In case of the Lewis non-unity approach Lewis numbers are obtained by running one simulation using the mixture-averaged approach and averaging over the domain. Throughout the simulations these Lewis numbers are kept constant.

$$\mathrm{Le}_i = \frac{\lambda}{\rho\, c_p\, D_i^{\mathrm{M}}} \tag{4}$$

4 Results and Discussion

Comparing first the laminar flame setups (see Fig. 3) it becomes clear that both oxygen enhancement and differential diffusion have a strong influence on the flame structure. In Fig. 3a for example temperature profiles for oxygen enhanced combustion are much broader than for air combustion. In addition, if differential diffusion is considered, the shift in position of the peak temperature is more distinct compared to the air case. Similar conclusions can be drawn while looking at Fig. 3b. To analyze the influence of differential diffusion in an oxygen enhanced environment more closely the elemental mass fractions for C and H are plotted against mixture fraction in Fig. 4

$$F_C = \frac{Z_C - Z_{C,2}}{Z_{C,1} - Z_{C,2}} \qquad F_H = \frac{Z_H - Z_{H,2}}{Z_{H,1} - Z_{H,2}} \tag{5}$$

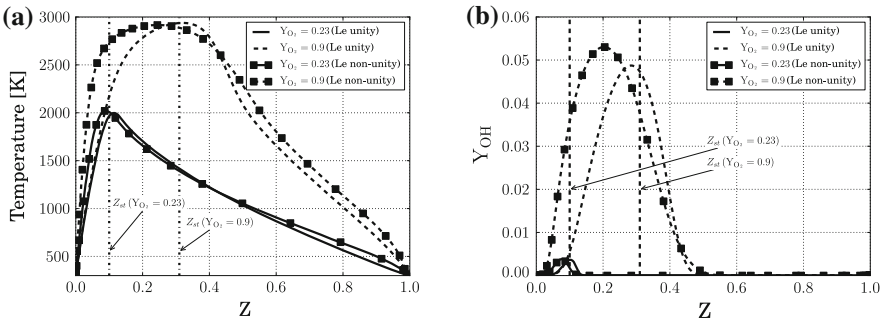

Fig. 3 **a** Comparison of temperature profiles for air and oxygen enhanced combustion for different transport models. **b** Comparison of OH mass fraction profiles for air and oxygen enhanced combustion for different transport models

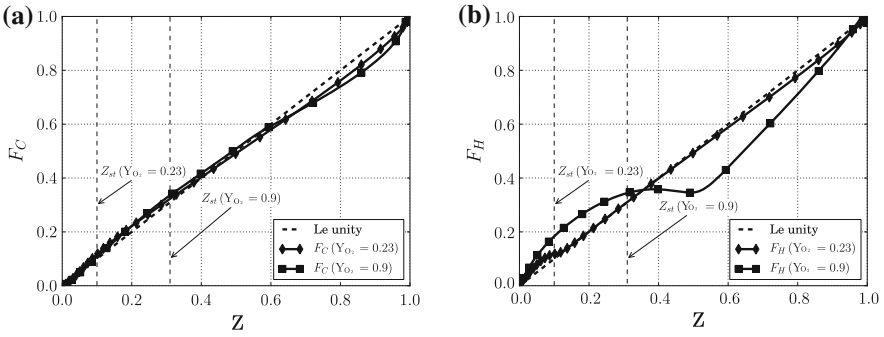

Fig. 4 **a** Mass fraction of C for air and oxygen enhanced combustion. **b** Mass fraction of H for air and oxygen enhanced combustion

where subscripts 1 and 2 denote pure fuel and oxidizer respectively. For laminar flames Fig. 4 demonstrates the importance of the transport model for oxygen enhanced methane combustion. While for conventional air combustion deviations from the Lewis unity transport model are almost negligible, differential diffusion strongly effects the species transport in oxygen enhanced environments.

For a turbulent setup, the burning regime completely changes because the flame front is highly wrinkled by the flow field and both turbulent and diffusive transport become important. As an example Fig. 5 shows elemental mass fractions for C and H in a turbulent counter-diffusion flame ($Re_t \approx 250$). While the general trend (Fig. 5a) looks similar for the laminar and turbulent case a zoomed plot (Fig. 5b) reveals that in regions not affected by the flame zone the turbulent transport clearly dominates transport processes and the scatter of C and H mass fractions is moving towards the line of equal diffusivities.

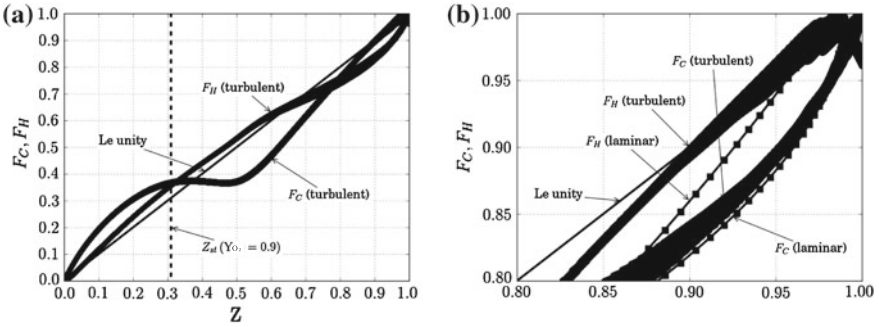

Fig. 5 **a** Mass fraction of C and H for turbulent, oxygen enhanced combustion. **b** Comparison of turbulent and laminar results for C and H mass fractions for oxygen enhanced combustion (zoomed plot).

5 Concluding Remarks

While for standard methane air combustion the Lewis unity transport model is sufficient, differential diffusion has to be considered for oxygen enhanced methane combustion. In flame regions where the laminar-diffusive transport is dominating, clear deviations between differential diffusion and the equal diffusivities assumption can be observed. On the other hand for turbulent flame regimes it is possible to distinguish between regions of equal diffusivities (turbulent transport is dominant) and zones where differential diffusion should be considered.

References

1. Baukal, C.E.: Oxygen-enhanced combustion. CRC. (1998)
2. Andersson, K., Johansson, R., Johnsson, F.: Thermal radiation in oxy-fuel flames. Int. J. Greenhouse Gas Control **5**, S58–S65 (2011)
3. Krishnan, S.S., Saini, M.K., Zheng, Y., Gore, J.P.: Radiation properties of oxygen-enhanced normal and inverse diffusion flames. J. Heat Transfer **134**(2), 022701 (2012)
4. Krishnamoorthy, G., Sami, M., Orsino, S., Perera, A., Shahnam, M., Huckaby, E.D.: Radiation modelling in oxy-fuel combustion scenarios. Int. J. Comput. Fluid Dyn. **24**, 69–82 (2010)
5. Sung, C.J., Law, C.K.: Dominant chemistry and physical factors affecting no formation and control in oxy-fuel burning. Proc. Combust. Inst. **27**(1), 1411–1418 (1998)
6. Cheng, Z., Wehrmeyer, J.A., Pitz, R.W.: Experimental and numerical studies of opposed jet oxygen-enhanced methane diffusion flames. Combust. Sci. Technol. **178**(12), 2145–2163 (2006)
7. Edge, P., Gubba, S.R., Ma, L., Porter, R., Pourkashanian, M., Williams, A.: LES modelling of air and oxy-fuel pulverised coal combustion-impact on flame properties. Proc. Combust. Inst. **33**(2), 2709–2716 (2011)
8. Kim, H.K., Kim, Y., Lee, S.M., Ahn, K.Y.: Studies on combustion characteristics and flame length of turbulent oxy-fuel flames. Energy Fuels **21**(3), 1459–1467 (2007)
9. Ern, A., Giovangigli, V.: Fast and accurate multicomponent transport property evaluation. J. Comput. Phys. **120**, 105–116 (1995)

10. Hirschfelder, J.O., Bird, R.B., Curtiss, C.F.: The Molecular Theory of Gases and Liquids. Wiley, Hoboken (1954)
11. Kee, R.J., Dixon-Lewis, G., Warnatz, J., Coltrin, M.E., Miller, J.A., Moffat, H.K.: A Fortran computer code package for the evaluation of gas-phase, multicomponent transport properties. Sandia National Laboratories Report SAND86-8246B (1988)
12. Ern, A., Giovangigli EGLIB, V.: A general-purpose fortran library for multicomponent transport property evaluation. User manual version 3.4 (2004)
13. Laverdant, A.: Notice dutilisation du programme SIDER (PARCOMB3D). Technical Report RT 2/13635 DEFA, The French Aerospace Lab., ONERA (2008)
14. Thévenin, D., Behrendt, F., Maas, U., Przywara, B., Warnatz, J.: Development of a parallel direct simulation code to investigate reactive flows. Comput. Fluids **25**(5), 485–496 (1996)
15. Honein, A.E., Moin, P.: Higher entropy conservation and numerical stability of compressible turbulence simulations. J. Comput. Phys. **201**(2), 531–545 (2004)
16. Baum, M., Poinsot, T., Thévenin, D.: Accurate boundary-conditions for multicomponent reactive flows. J. Comput. Phys. **116**(2), 247–261 (1995)
17. Poinsot, T.J., Lele, S.K.: Boundary conditions for direct simulations of compressible viscous flows. J. Comput. Phys. (ISSN 0021–9991), **101**, 104–129 (1992)
18. Kraichnan, R.H.: Diffusion by a random velocity field. Phys. Fluids **13**(1), 22–31 (1970)
19. Lindstedt, R.P., Meyer, M.P.: A dimensionally reduced reaction mechanism for methanol oxidation. Proc. Combust. Inst. **29**(1), 1395–1402 (2002)

Application of Flamelet Generated Manifolds Approach with Heat Loss Inclusion to a Turbulent High-Pressure Premixed Confined Jet Flame

A. Donini, S.M. Martin, R.J.M. Bastiaans, J.A. van Oijen and L.P.H. de Goey

1 Introduction

A predominant part of the world energy demand is obtained by the combustion of fossil fuels. In this framework, gas turbine combustion is the most important energy conversion method today. This is because using gas turbines, large scale, high efficiency, low cost and low emission energy production is possible. For these types of engines, low NOx emissions can be achieved by very lean premixed combustion systems. This type of combustion requires special attention to the balance between emissions, flame stability and completeness of combustion. In the present paper a computational analysis of a high pressure confined premixed turbulent methane/air jet flame is presented.

In this scope, chemistry is reduced by the use of the Flamelet Generated Manifold (FGM) method [1], and the fluid flow is modeled in an LES and RANS context. The elevated pressures in combination with high flow velocities and heat loss to the walls demand a superior attention on the modeling, since thinner flames generate stiffer solutions.

A generic lab scale gas-turbine like burner for high-pressure (5 bar) high-velocity (40 m/s at the inlet) preheated jet is used for validation. Turbulent, lean premixed flames of different fuels (methane, methane/hydrogen) have previously been studied in this axis-symmetric gas turbine combustor [2, 3]. This research attempts to apply the FGM chemistry reduction method coupled with LES and RANS models, in order to predict the evolution and description of the mentioned turbulent jet flame in high pressure (and high Reynolds number) flow conditions, including the important effect of heat loss by conduction to the walls.

A. Donini (✉) · R.J.M. Bastiaans · J.A. van Oijen · L.P.H. de Goey
Eindhoven University of Technology, Eindhoven, The Netherlands
e-mail: A.Donini@tue.nl

S.M. Martin
Eagle Flight Research Center, Embry-Riddle Aeronautical University, Daytona Beach, FL, USA

J. Fröhlich et al. (eds.), *Direct and Large-Eddy Simulation IX*,
ERCOFTAC Series 20, DOI 10.1007/978-3-319-14448-1_66

2 Flamelet Generated Manifolds—Heat Loss and Turbulence Effects Inclusion

Flamelet Generated Manifolds (FGM) [1] is a chemistry reduction method that combines the advantages of chemistry reduction and flamelet models. The approach is based on the idea that the most important aspects of the internal structure of the flame fronts should be taken into account. In the FGM technique the course of the reaction is defined in terms of a few control variables, for which transport equations are solved during run-time. The flamelet system is computed in a pre-processing stage, and a FGM with all the information about combustion chemistry is stored in a tabulated form. To this purpose a laminar flamelet database is generated from a one-dimensional flamelet calculation performed with full kinetics and detailed transport. In this study we consider fully premixed methane/air combustion at high pressure conditions (5 bar) with lean equivalence ratio and pre-heated inlet.

The enthalpy is not conserved throughout the domain because of heat loss to the walls of combustion chamber. In order to take this into account in the tabulation process, the laminar flamelets have to be solved for different values of enthalpy [1], introducing enthalpy (h) as a control variable. This procedure might be done in different ways, but the most straightforward are: (1) decreasing the enthalpy of the free flamelets simply diminishing the inlet temperature, (2) calculation of burner-stabilized flamelets, and therefore imposing a certain increasing amount of heat loss to the burner. It has been proven that the choice of the enthalpy-decrease method for the tabulation procedure has negligible influence on the final result [1]. The enthalpy levels of the manifold data along the single flamelets are shown in Fig. 1a.

Chemistry is represented by the GRImech 3.0 mechanism [4] which contains 325 elementary reactions between 53 species. A unity Lewis number assumption is chosen during the calculation of the flamelets, and a result of this assumption

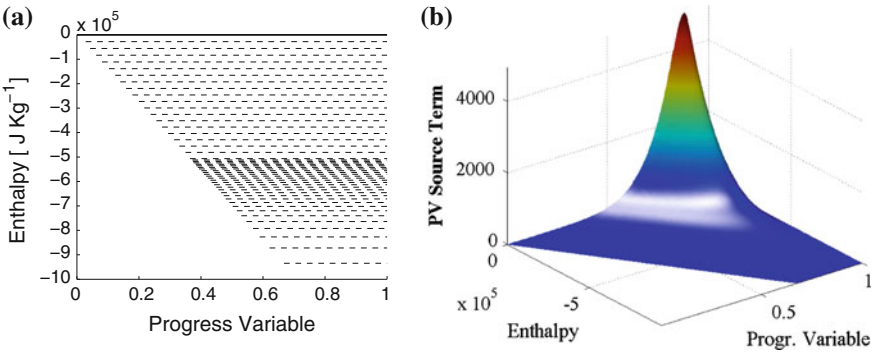

Fig. 1 **a** Enthalpy along the flamelets composing the manifold.The reaction progress variable is scaled between zero (fresh mixture) and one (exhaust gas). Enthalpy is set to zero at the inlet conditions for practical convenience. **b** Representation of the manifold: progress variable source term [kg m^{-3} s^{-1}] in the laminar case, as function of progress variable and enthalpy

is directly visible in Fig. 1a; in fact the enthalpy levels are constant throughout the distinct flamelets, because of the even balance between mass and heat diffusion along the flamelet. The chemistry data obtained by the tabulation procedure is rearranged through a coordinate transform. The tabulated data is then directly retrievable as a function of progress variable and control variable. An overview of the resulting manifold can be seen in Fig. 1b, where the progress variable source term is represented as a function of the progress variable and enthalpy. This dataset is stored in memory and linked to the CFD code. The turbulence-chemistry interaction is taken into account by describing variables in a stochastic way. Locally a variable is described by a Probability Density Function (PDF) defining the probability of occurrence of a certain state. This is therefore accounted for by convolution of the laminar database using a β-function shaped PDF [5]. The β-pdf shape has the advantage of including singularities near the end points while being simple to compute. The integration operation generates an increase of the dimension of the manifold, which will finally reach the number of three dimensions for the present case. The final dimensions for the manifold are: mean progress variable, enthalpy and variance of the progress variable.

During run-time the CFD code must solve conservation equations for the progress variable and enthalpy, together with the momentum and continuity equations. For the calculation of the variance of the progress variable c_{var} a suitable, and often used, model is the gradient-based model as described in [5, 6]:

$$c_{var} = \frac{a^2 \Delta_k^2}{12} \left(\frac{\partial \tilde{c}}{\partial x_k} \right)^2, \tag{1}$$

where a is assumed to be constant. The parameter Δ_k is the filter width, which is considered to be the grid resolution in the present study. This has to be handled with care, in order to avoid zones in the domain where $\Delta_k > \delta_{th}$, with δ_{th} the flame thermal thickness. In this case $a = 1.4$ is used, following [7].

3 Geometry, Scales and Numerical Methods

The geometry consists essentially in a cylindrical confinement. The jet has a diameter $d = 25$ mm and the combustor a diameter of $d_c = 75$ mm, providing flame stabilization by recirculation of hot combustion products. The overall length of the chamber is $22d$. The simulations presented in this paper are performed with an inlet velocity of $v_{in} = 40$ m/s, inlet temperature of 623 K, CH_4 with an equivalence ratio of $\phi = 0.5$ and $p = 5$ bar. The corresponding Reynolds number calculated with the inlet diameter is roughly 100,000. The inlet velocity profile is chosen to be parabolic in order to take account of the presence of the walls, and the velocity profile is therefore set in order to conserve the mass flow rate. Heat losses to the walls are imposed by enforcing a temperature T_w to the walls.

This geometry was selected and extensively analyzed experimentally by [2, 3], where flame structures were determined with Laser Induced Fluorescence measurements of the OH radical. The overall accuracy of the measurement with this method

is estimated to be approximately within ±7 % on the flame height, and ±10 % on the flame brush thickness.

A consideration about the scales involved in the flow and combustion process of the present case must be made in order to ensure the respect of the flamelet hypothesis [8, 9]. An approximation of the turbulent length scales gives an estimate value for the Kolmogorov scale of $\eta \approx 0.02$ mm. In relation to the chemistry, the flame thickness can be calculated based on the highest value of the temperature gradient along the flamelet, from the chemistry database. A reaction layer thickness can also be calculated based on the integral consumption term of the fuel. Considering the flamelet at inlet conditions, therefore without heat loss, the reaction layer thickness can be estimated as $\delta_r = 0.008$ mm. These values confirm the assumption of falling within the thin reaction zone regime with the present simulations.

The solver used for the simulations is Ansys-CFX 14.0 [10], coupled with the above described three-dimensional FGM implementation. The approach used for turbulence is LES with dynamic sub-grid model [11] and RANS with the two equations RNG $k - \varepsilon$ model. The solver chosen for the computations of this work is incompressible. The 3D mesh used consists of 3,407,868 hexahedral elements over 3,478,067 nodes, distributed with a consistent refinement in the flame region.

4 Results

An overview of the profile and behavior of the reacting flow in the burner is represented in Fig. 2, where an instantaneous LES iso-contour of the progress variable is shown colored as a function of the mean progress variable source term in order to reveal the flame location. With the intent of evaluating the difference between standard simulations which do not include heat loss, a comparison is performed. Profiles of axial velocity and temperature are respectively shown in Fig. 3, plotted in the center plane at different distances from the inlet. The major effect of heat loss on the flame behavior is clearly visible from this comparison.

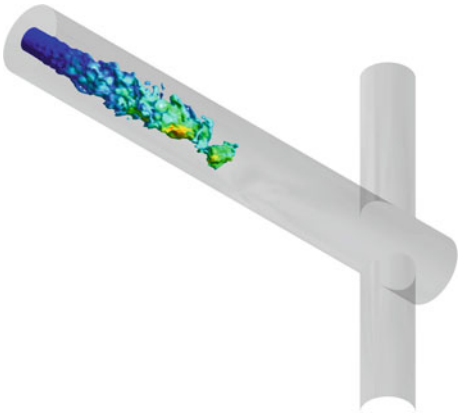

Fig. 2 Overview of the domain by means of a time snapshot of the LES simulation with heat loss. The flame here is represented by an iso-surface of progress variable ($\tilde{c} = 0.5$), and colored as function of its source term

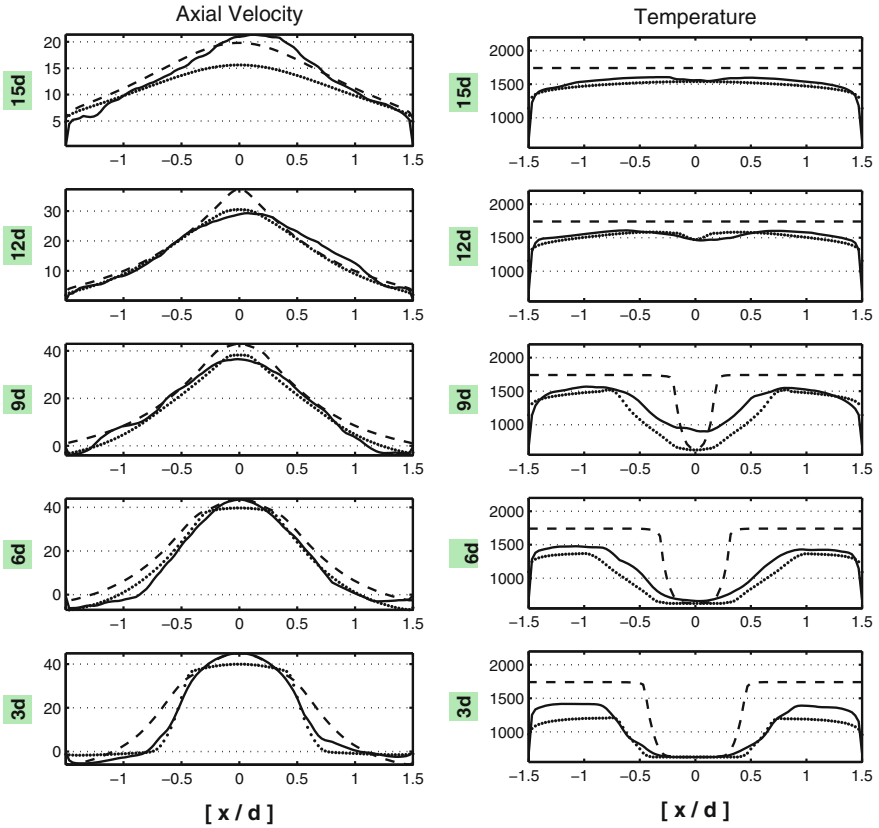

Fig. 3 Axial velocity [ms^{-1}] and temperature [K] comparison at different distances from the inlet. *Solid lines* are representing time-averaged LES results with heat loss inclusion, *dotted lines* are RANS with heat loss and *dashed lines* are RANS without heat loss

In the experiments of [2] a most probable flame front contour is obtained by processing the OH signal intensity gradient. A comparison of this experimental values with LES averaged results (with heat loss) reveals a difference in the flame height of +4.9 %, while in the RANS (with heat loss) simulations this difference increases to +13.5 %.This relatively small difference can be explained by the absence of turbulence at the inlet in the simulations. In the experiments of [2] it is in fact shown how the inlet turbulence shortens the flame slightly in the present geometry.

5 Conclusions

The chemistry reduction method FGM is coupled with LES and RANS turbulence models, in order to predict the evolution and description of a turbulent jet flame in high pressure conditions, including the important effect of heat loss to the walls.

The method is shown to capture in a coherent way the combustion features, leading to a representative prediction of the flame shape and height. The inclusion of heat loss plays a major role on the flame shape and velocity profiles, indicating a considerable difference on the prediction of the recirculation zones. Furthermore, the use of FGM as a combustion model shows that combustion features in gas turbine conditions can be reproduced with a reasonable computational effort. The simulation time of the cases performed with heat loss in this paper is on the order of 60 CPU-hours for RANS, and roughly 7,000 CPU-hours for LES. This notably low calculation time is due to the use of the FGM reduction model, allowing us to perform broader and more detailed investigations in future works.

Acknowledgments The authors would like to acknowledge Daniele Salvatore, for providing the test data.

References

1. van Oijen, J.A., de Goey, L.P.H.: Modelling of premixed laminar flames using flamelet-generated manifolds. Combust. Sci. Technol. **161**(1), 113–137 (2000)
2. Daniele, S., Jansohn, P., Mantzaras, J., Boulouchos, K.: Turbulent flame speed for syngas at gas turbine relevant conditions. Proc. Combust. Inst. **33** (2010)
3. Griebel, P., Siewert, P., Jansohn, P.: Flame characteristics of turbulent lean premixed methane/air flames at high pressure: turbulent flame speed and flame brush thickness. Proc. Combust. Inst. **31**, 3083–3090 (2007)
4. Smith, G.P., Golden, D.M., Frenklach, M., Moriarty, N.W., Eiteneer, B., Goldenberg, M., Bowman, C.T., Hanson, R.K., Song, S., Gardiner, W.C., Lissianski, V.V., Qin, Z.: Gri-Mech 3.0. http://www.me.berkeley.edu/gri-mech/
5. Vreman, A., van Oijen, J.A., de Goey, L.P.H., Bastiaans, R.J.M.: Subgrid scale modeling in large-eddy simulation of turbulent combustion using premixed flamelet chemistry. Flow Turbul. Combust. **82**(4), 511–535 (2009)
6. Donini, A., Martin, S.M., Bastiaans, R.J.M., van Oijen, J.A., de Goey, L.P.H.: Numerical simulations of a premixed turbulent confined jet using the flamelet generated manifold approach with heat loss inclusion. In: Proceedings of the ASME Turbo Expo, GT2013-94363 (2013)
7. Cardoso de Souza, T., Bastiaans, R.J.M., Geurts, B., de Goey, L.P.H.: LES and RANS of premixed combustion in gas-turbine like combustor using the flamelet generated manifold approach. In: Proceedings of the ASME Turbo Expo, GT2011-46355 (2011)
8. Peters, N.: Reducing mechanisms. In: Smooke, M.D. (ed.) Reduced Kinetic Mechanisms and Asymptotic Approximations for Methane-Air Flames, pp. 48–67. Springer, Berlin (1991)
9. Peters, N.: Laminar flamelet concepts in turbulent combustion. Proc. Combust. Inst. **21**, 1231–1250 (1986)
10. Ansys CFX software, fluid dynamics program. http://www.ansys.com
11. Germano, M., Piomelli, U., Moin, P., Cabot, W.H.: A dynamic subgrid-scale eddy viscosity model. Phys. Fluids **4**, 1760–1765 (1991)

Direct Numerical Simulations of Turbulent H_2-Air Pre-mixtures and Analysis Towards Safety-Relevant Ignition Prediction

Gordon Fru, Dominique Thévenin and Detlev Markus

1 Introduction

The energy requested to obtain a stable ignition in a turbulent gas mixture has been investigated extensively during many decades [1], mostly through experiments or reduced (zero- or one-dimensional) simulation models [2]. A quantitative numerical investigation requires in principle an excellent description of the flow (as obtained by Direct Numerical Simulation, DNS) coupled to an accurate description of all relevant chemical, diffusive and thermodynamic processes. This leads to extremely high requirements in terms of computing time, so that only few such studies can be found in the literature. Baum and Pointsot considered this situation for homogeneous mixtures, but were forced to carry out two-dimensional computations in order to obtain acceptable computing times [3]. More recently, three- (respectively two-) dimensional DNS with simplified (respectively detailed) chemistry of ignition processes in inhomogeneous mixtures and/or with thermal stratification can also be found (see, e.g., [4] and references therein). There is, therefore, an obvious need to pursue and extend these investigations, since it is expected that kinetic effects will highly influence the ignition process.

The present study relies exclusively on DNS with detailed chemical and transport models to investigate hotspot ignition events in turbulent premixed flame kernels burning hydrogen. Configurations where successful ignition or misfire is obtained in the absence of any external flow are afterwards perturbed by adding turbulent

G. Fru (✉) · D. Thévenin
Institute of Fluid Dynamics and Thermodynamics, University Magdeburg, Magdeburg, Germany
e-mail: gordon.fru@ovgu.de

D. Thévenin
e-mail: thevenin@ovgu.de

D. Markus
Physikalisch-Technische Bundesanstalt (PTB), Braunschweig, Germany
e-mail: detlev.markus@ptb.de

J. Fröhlich et al. (eds.), *Direct and Large-Eddy Simulation IX*,
ERCOFTAC Series 20, DOI 10.1007/978-3-319-14448-1_67

fluctuations of increasing intensity. The impact of turbulence is quantified in a statistically meaningful manner by repeating these DNS simulations, leading to independent realizations.

2 Numerical Details and Configuration

The DNS code *parcomb* is employed to solve the set of compressible reacting flow transport equations for mass, momentum, total energy and species using a sixth-order central differencing scheme on a Cartesian grid. An explicit fourth-order Runge-Kutta time integrator is adopted. The simulated domain is a cube of side length $L = 1.6\,\text{cm}$ discretized with a uniform grid spacing of $20\,\mu\text{m}$. The extended non-reflecting Navier-Stokes Characteristic Boundary Conditions are applied along all open faces. Further generic details of the solver are contained in [5].

We consider perfectly spherical hot kernels with initial temperature T_0 and radius R_0, initialized within a laminar stoichiometric H_2-air mixture under atmospheric conditions (see Fig. 1a). A 9 species, 37 reaction chemical scheme is used [6]. The initial mixture composition consists of the mass fractions $Y_{H_2} = 0.0291$, $Y_{O_2} = 0.233$ and $Y_{N_2} = 0.738$ at $T_u = 300\,\text{K}$. All remaining mass fractions are set to zero.

The initial system is then superimposed with a homogeneous time-decaying isotropic turbulent field at $t = 0$, generated using a digital filtering technique [5, 7]. The integral length scale (l_t) and mixture viscosity (ν) are both kept constant at $1.27\,\text{mm}$ and $1.74 \times 10^{-5}\,\text{m}^2/\text{s}$, respectively. Thirteen turbulence levels have been simulated, ultimately spanning a wide range in turbulence intensities

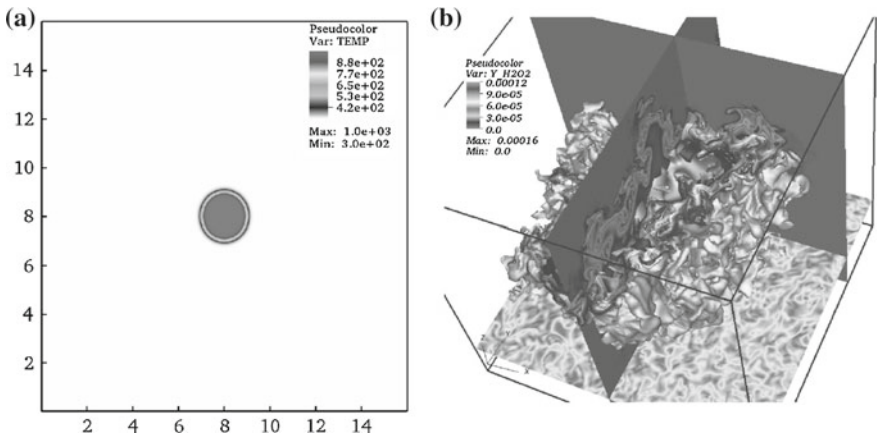

Fig. 1 **a** Slice of the initially perfectly spherical hot kernel at $T_0 = 1{,}000\,\text{K}$ within the computational domain ($L = 1.6\,\text{cm}$) at $t = 0$, showing the temperature field. **b** Exemplary turbulent flame structure at $t/\tau = 2.0$ showing a heavily wrinkled instantaneous isosurface of temperature colored by H_2O_2 radical and x-velocity field (*lower slide*) after a successful ignition event ($\text{Re}_t = 328$)

($0.63 \leq u'/s_L \leq 7.5$) and turbulent Reynolds numbers $\mathrm{Re}_t = u' l_t/\nu$ ($37 \leq \mathrm{Re}_t \leq 438$). Statistics are obtained for up to sixty realizations for some u'/s_L values. As will be shown shortly, a sufficiently rich DNS database might be needed to rule out spurious effects and to obtain a safer confidence interval for ignition probability of such flammable mixtures.

Typical computing time vary between 20 days (3D) and less than half a day (2D) on a local Linux-cluster in a single-user mode until ignition or misfire.

3 Results: Turbulent Ignition Probability

The turbulent flame structure is exemplified in Fig. 1b, where an instantaneous isosurface of H_2O_2 radical at $t = 2.0\tau$ (where τ is the turbulent time) is shown, revealing the heavily wrinkled flame front at $\mathrm{Re}_t = 328$ after a successful ignition event. Depending on the turbulent intensity, but also on T_0 and R_0, two scenarios emerge. Consider the ($T_0 = 1,000$ K, $R_0 = 1.0$ mm) pair in Fig. 2a that always ignites under laminar conditions. A similar situation occurs for mild turbulence levels, as exemplified by the time history of maximum temperature for the laminar and first fifteen turbulent realizations in Fig. 3a. A successful ignition is recorded for all cases without exception. We also note that the mean ignition delay ($\tau_{mean} = 0.253$ ms) for the turbulent realizations is higher than the unperturbed ignition delay ($\tau_0 = 0.215$ ms) by 18 %. For established reaction fronts, turbulence promotes burning velocities [8]. At the same time, turbulence also increases the rate of heat loss from the hot kernel to the surrounding cold mixture, hence delaying and possibly preventing ignition. This is the dominant effect modulating the ignition delay here, as observed as well in experimental works [9]. However, this observation is different from that found in non-premixed or non-homogeneous mixtures [10, 11] and applies only to perfectly homogeneous pre-mixtures in terms of composition.

Ultimately, a stronger turbulent environment can modify the initial conditions so rapidly that a misfire is observed (see Figs. 2c and 3c). In such a case, the turbulent

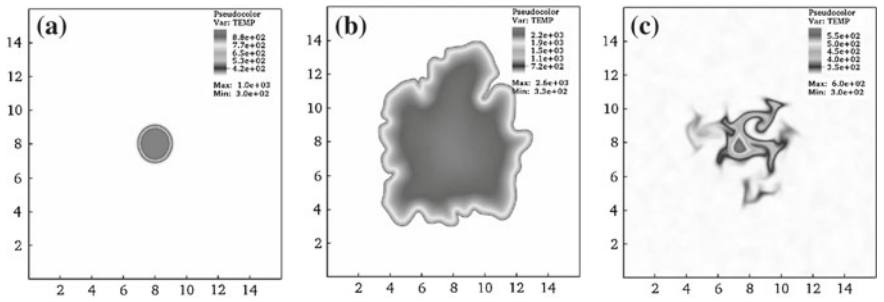

Fig. 2 **a** Initial setup ($t/\tau_t = 0.0$), **b** successful ignition ($u'/s_L = 5.0$, $t/\tau_t = 1.6$), **c** misfired event ($u'/s_L = 7.50$, $t/\tau_t = 1.6$)

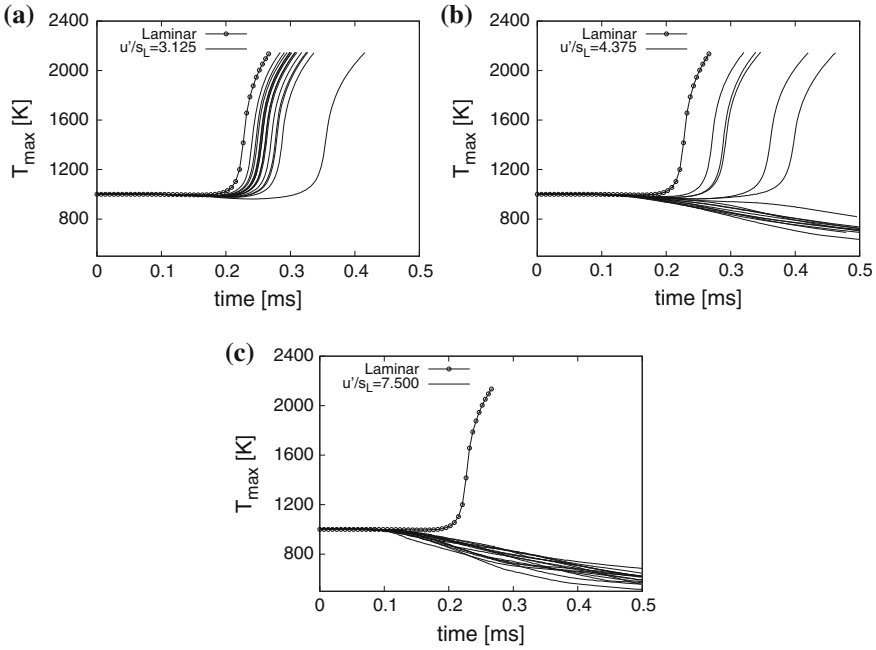

Fig. 3 **a** Mild turbulence level ($\mathrm{Re}_t = 182$), **b** intermediate turbulence level ($\mathrm{Re}_t = 255$), **c** strong turbulence level ($\mathrm{Re}_t = 438$)

intensity is so intense that enhanced mixing of hot pockets with the cold mixture supersedes chemical reaction, ultimately cooling down the entire system and leading to a complete quenching. Turbulence removes rapidly the initial thermal stratification, which, if present, could have enabled the hot pockets to ignite earlier [4]. The intermediary cases, such as the cases in Fig. 2b (for which we happen to obtain a successful ignition) trade between these two extremes, with ignition occurring still later (compared to the laminar case) but with a decreasing probability, as shown in Fig. 3b. As a whole, the probability of successful ignition events is found to decrease monotonically and almost linearly with u'/s_L when this value exceed roughly 3.125, until getting a systematic misfire.

4 Results: Logistic Regression Statistics

Considering ignition events as a kind of sensitivity experiment, where the goal is to measure the critical level of a stimulus that produces a certain result in a test sample, then a regression technique [12] can be employed to analyze the statistics. In practical cases, the stimulus could be the spark energy, energy density, charge, etc. as is the case in ignition experiments using electric discharge. In the case at hand,

the stimulus level for the ith test is denoted by x_i, where x could be the initial hot kernel temperature, T_0, radius, R_0 or imposed turbulence intensity, u'/s_L. Here, the test sample is the H_2-air mixture and the result y_i is a binary outcome—ignition (=1) or misfire (=0). All the x_i and y_i for the n test samples are collectively represented by a likelihood function

$$L = \prod_{i=1}^{n} P_i(x_i)^{y_i}[1 - P_i(x_i)]^{1-y_i} \tag{1}$$

The ignition probability $P_i(x_i)$ is represented by a parametric logistic distribution function:

$$P_i(x_i) = 1/[1 + \exp(-\beta_0 - \beta_1 x_i)] \tag{2}$$

Here, β_0 and β_1 are parameters estimated by maximizing L in Eq. 1. For a two-sided interval, the lower (LCL) and upper (UCL) confidence limits for the $100(1-\alpha/2)$ % confidence interval for the percentile x_q can be calculated using

$$\text{UCL/LCL} = x_q \pm Z_{\alpha/2}\sqrt{(\sigma_{00} - 2x_q\,\sigma_{01} + x_q^2\,\sigma_{11})/\beta_1^2}. \tag{3}$$

In Eq. 3, σ_{00} and σ_{11} are the variances and σ_{01} is the co-variance of β_0 and β_1, $Z_{\alpha/2} = 100(1-\alpha/2)$th percentile from a standard cumulative Gaussian distribution and $\alpha = (1 - \text{confidence level})$.

The outcome of this analysis is a cumulative probability distribution of the n ignition tests and a confidence envelope on the probability of ignition versus the considered stimulus, x. As an example, the logistic probability distribution and a 95 % confidence envelope (i.e., $\alpha = 1-0.95 = 0.05$) for two turbulence intensities are plotted in Fig. 4a ($u'/s_L = 0.625$), and Fig. 4b ($u'/s_L = 2.5$) as a function of R_0. From these profiles, a clear shift to the right is observable with increasing turbulence intensity. In both cases, a safety margin is clearly established and could then be employed as a modeling guideline in the development of practical systems and regulations

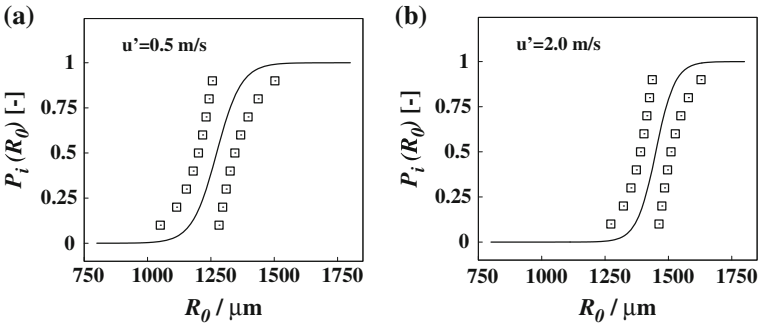

Fig. 4 **a** Ignition probability for $u'/s_L = 0.625$. **b** Ignition probability for $u'/s_L = 2.5$

[13, 14]. Such a statistical method, therefore, offers a suitable platform on which DNS and experimental findings can be compared quantitatively.

5 Concluding Remarks

Parametric Direct Numerical Simulations of atmospheric H_2-air pre-mixtures under stoichiometric conditions have been performed to characterize the influence of varying the turbulent Reynolds number on hotspot-induced ignition. It is observed that all spherical kernels with initial temperature and radius greater than a critical value will lead to a successful ignition and an established flame in a mild turbulent environment (typically below $u'/s_L \leq 3.125$). For all cases considered, the mean ignition delay in a turbulent flow is always larger than the laminar one. At the other extreme, a misfire appears to be inevitable for $u'/s_L \geq 7.5$. The principal physical phenomenon modulating the induction time under turbulent conditions is the concurrence between transport processes and chemical reactions. By repeating the DNS realizations up to sixty times, the probability of successful ignition events is found to decrease almost linearly with u'/s_L when this value exceeds roughly 3.125, until obtaining a systematic misfire. Preliminary probing of the DNS data with the help of the logistic regression statistical approach hints to a potentially suitable means of directly comparing experimental and simulated results of ignitable setups. This possibility, if tried and proven, could prove beneficial in varying a broad range of parameters not accessible to experiments, which could eventually lead to safety-relevant calibrations and regulations for practical devices and systems. This is ongoing work. Future studies will equally focus on the possible influence of composition and temperature inhomogeneities on the ignition probability. Additionally, more complex fuels like ethylene and diethyl ether will be considered, which are highly relevant for practical safety issues.

Acknowledgments The financial support of the German Research Foundation (DFG) within the research group *FOR1447* ("Physicochemical-based Models for the Prediction of safety-relevant Ignition Processes") is gratefully acknowledged.

References

1. Lewis, B., von Elbe, G.: Combustion, Flames and Explosions of Gases, 3rd edn. Academic Press Inc., New York (1987)
2. Horstmann, T., Leuckel, W., Maurer, B., Maas, U.: Influence of turbulent flow conditions on the ignition of flammable gas/mixtures. Process Saf. Prog. **20**(3), 215–224 (2001)
3. Baum, M., Poinsot, T.: Effect of mean flow on premixed flame ignition. Combust. Sci. Technol. **106**, 19–39 (1995)
4. Yoo, C., Lu, T., Chen, J.H., Law, C.K.: Direct numerical simulations of ignition of a lean n-heptane/air mixture with temperature inhomogeneities at constant volume: parametric study. Combust. Flame **158**(9), 1727–1741 (2011)

5. Fru, G., Janiga, G., Thévenin, D.: Impact of volume viscosity on the structure of turbulent premixed flames in the thin reaction zone regime. Flow Turbul. Combust. **88**(4), 451–478 (2012)
6. Maas, U., Warnatz, J.: Ignition processes in hydrogen-oxygen mixtures. Combust. Flame **74**, 53–69 (1988)
7. Klein, M., Chakraborty, N., Cant, R.: Effects of turbulence on self-sustained combustion in premixed flame kernels: a direct numerical simulation (dns) study. Flow Turbul. Combust. **81**, 583–607 (2008)
8. Fru, G., Thévenin, D., Janiga, G.: Impact of turbulence intensity and equivalence ratio on the burning rate of premixed methane-air flames. Energies **4**(6), 878–893 (2011)
9. Ballal, D., Lefebvre, A.: Ignition and flame quenching in flowing gaseous mixtures. Proc. R. Soc. Lond. A. **357**, 163–181 (1977)
10. Hilbert, R., Thévenin, D.: Autoignition of turbulent non-premixed flames investigated using direct numerical simulations. Combust. Flame **128**(1–2), 22–37 (2002)
11. Chakraborty, N., Mastorakos, E., Cant, S.: Effects of turbulence on spark ignition in inhomogeneous mixtures: a direct numerical simulation (DNS) study. Combust. Sci. Technol. **179**, 293–317 (2007)
12. Hosmer, D., Lemeshow, S.: Applied Logistic Regression. Wiley, New York (1989)
13. Langer, T., Markus, D., Lienesch, F., Maas, U.: Streamer discharges caused by high-frequency voltage leading to ignition of hydrogen/air mixtures. Combust. Sci. Techol. **182**, 1718–1734 (2010)
14. Eckhoff, R., Ngo, M., Olsen, W.: On the minimum ignition energy (MIE) for propane/air. J. Hazard. Mater. **175**, 293–297 (2010)

Large-Eddy-Simulation of High-Frequency Flame Dynamics in Perfect Premix Combustors with Elevated Inlet Temperatures

Mathieu Zellhuber and Wolfgang Polifke

1 Introduction and Motivation

Sequential combustion is a promising concept for stationary gas turbines to achieve high thermodynamic efficiency and low NOx emission levels over wide load ranges [1]. The burner design and the combustion regime in such combustors differ significantly from typical swirl combustors, as the flame stabilisation is ensured by auto-ignition due to the high oxidiser inlet temperatures. Thus the flame is likely to react differently to acoustic perturbations, with corresponding consequences for thermoacoustic stability of such combustors. In the scope of the present work, high-frequency flame dynamics are of special interest, i.e. the feedback between the flame and acoustic modes with transverse velocity components and thus wavelengths of the order of the combustor height.

Possible thermoacoustic feedback mechanisms for such a case are indicated in Fig. 1. In practical configurations, the fuel typically penetrates the oxidiser stream as a jet-in-cross flow configuration. Coherent mixture modulations might therefore lead to a feedback. In addition, flame wrinkling, density variations, and a periodic displacement of the flame by acoustic velocity can also cause a thermoacoustic coupling. The displacement effect has been identified recently by Schwing et al. [5] and Méry et al. [4]. The model proposed in [5] was extended by Zellhuber et al. [9]. Furthermore, the heat release rate can also be altered through the sensitivity of chemical reaction rates to changes in acoustic pressure, see the authors' previous publications [6, 8].

The topic is investigated using Large Eddy Simulations (LES) of an acoustically excited model combustor with high inlet temperatures. In order to reduce the physical

M. Zellhuber (✉) · W. Polifke
Lehrstuhl für Thermodynamik, TU München, 85747 Garching, Germany
e-mail: zellhuber@td.mw.tum.de

W. Polifke
e-mail: polifke@td.mw.tum.de

J. Fröhlich et al. (eds.), *Direct and Large-Eddy Simulation IX*,
ERCOFTAC Series 20, DOI 10.1007/978-3-319-14448-1_68

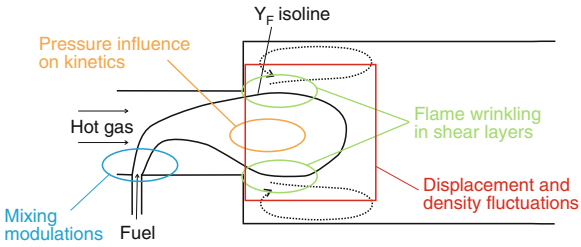

Fig. 1 Illustration of thermoacoustic mechanisms in practical combustor

complexity, a perfect premix configuration is considered here. The same setup has been studied by the authors in [7], but without accounting for the pressure sensitivity of the chemical kinetics. This previous study allowed to make qualitative observations of the flame wrinkling and the displacement, as well as to quantify the overall thermoacoustic feedback. In the present work, the pressure sensitivity is also considered and analytical models for non-compact flame transfer functions are proposed and verified using the LES data.

2 Combustion Modelling and Implementation

The simulation methodology targets combustion processes in industrial applications. Hence, special focus was put on the computational efficiency. The method used is based on a progress variable approach, using detailed tabulated chemistry data, together with a stochastic fields ansatz, in order to account for the turbulence-chemistry interaction at the subgrid level. The method, as it is applied for multi-stream mixing cases, was described by Kulkarni et al. [2, 3].

The progress variable definition and the mathematical details of the stochastic fields ansatz for the perfect premix case are given by the authors in [7]. In the present work, the physical complexity is further increased by taking additionally into account the pressure sensitivity. Therefore, the combustion model is extended by a pressure sensitivity factor φ_p, introduced in previous kinetic studies [6, 8]. This non-dimensional factor quantifies the deviations of the progress variable source term $\dot{\omega}_c'$ when acoustic pressure variations appear. By doing this, the state change caused by an acoustic wave is assumed to be isentropic. Detailed evolutions of this factor can be found in [6, 8] for different types of progress variable definitions. It is generally observed that the factor is positive and approximately constant over the duration of the ignition process. In order to ease the implementation, it is assumed to take on a constant value of $\varphi_p = 5$.

Figure 2 shows the implementation of the stochastic fields ansatz in the commercial solver Fluent 13, including the extension with respect to the pressure sensitivity of the kinetics. A total of $N = 8$ stochastic fields is used here, and a stochastic transport equation is solved for each field (inner loop in the figure). The reaction source term $\dot{\omega}_{c,chem}^{(n)}$ in the n'th field is recovered from chemistry tables generated

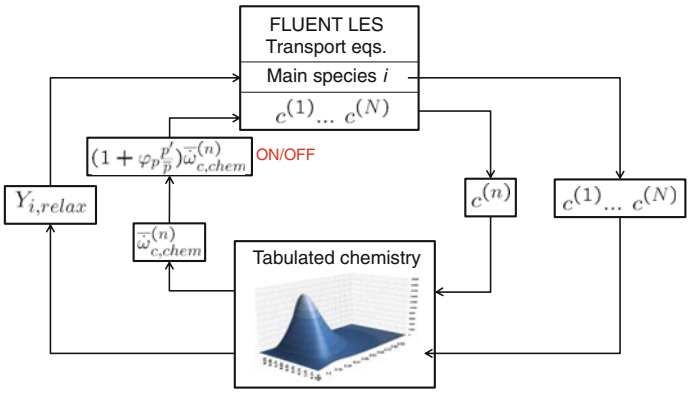

Fig. 2 Implementation of stochastic fields ansatz for progress variable

offline, and is then modified depending on the local acoustic pressure deviation p'. The outer loop in Fig. 2 describes the coupling between stochastic and non-stochastic transport equations. A target value for the main species mass fractions is obtained from a convolution over all fields and the use of chemistry tables. This allows to derive a chemical source term for the non-stochastic transport equations for species and enthalpy, as explicated in [7].

The simulated configuration is subjected to an acoustic excitation at a frequency of 3838 Hz, applied via momentum source terms in transverse direction at the combustor walls. In response, the first transverse mode in the combustion chamber develops. Since the flame cannot be considered as acoustically compact, a local analysis of flame dynamics is performed via frequency filtering of variable time series at individual grid points located in the central symmetry plane.

3 Simulation Results

Oscillations of relevant flow parameters at the excitation frequency are characterised via harmonic analysis. Processing the velocity and pressure signals allows for instance to recover the acoustic mode shape. With respect to thermoacoustic stability, it is of interest to study combustion-related flow variables. Figure 3 shows e.g. a plot of phase distributions of the heat release rate oscillations, i.e. the phase shift of the local heat release rate in comparison to the pressure signal at a reference point located just a bit downstream of the burner exit, see Fig. 3. Regions outside the flame are masked by a luminosity filter proportional to the amplitude of heat release rate fluctuations.

The phase distribution allows an interpretation of the flame movement. The rainbow pattern observed in the shear layer downstream of the burner exit is indicative of intense flame wrinkling. Further downstream, the wrinkles dissipate and the phase distribution shows two constant phase regions within each shear layer, shifted by

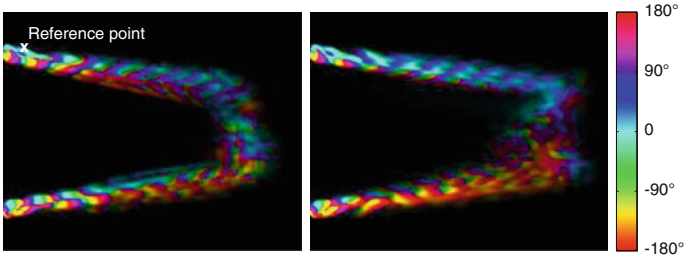

Fig. 3 Planar distributions of phase of heat release rate oscillations without (*left*) and with (*right*) pressure sensitivity

180° with respect to each other. These regions are particularly pronounced in the simulation run without pressure sensitivity and are caused by a periodic transverse displacement of the flame caused by the acoustic displacement, as observed previously [4, 5]. A more detailed discussion of various aspects of flame displacement can be found in [7, 9].

The heat release rate fluctuations linked to density and pressure sensitivity are further overlaid on the heat release phase distributions. Both effects scale with the local acoustic pressure, and lead therefore to signals with 0° and 180° phase in the upper and lower shear layer, respectively. As a consequence, one can observe for the upper shear layer a slight dominance of bluish colors (0° phase) in the case without pressure sensitivity, which is far more pronounced when the pressure sensitivity is added. This way, one can interpret the phase plots and recognise the thermoacoustic feedback mechanisms introduced earlier.

By combining real-valued oscillation signals of pressure and heat release rate one can retrieve information on thermoacoustic coupling intensity, by calculating the local Rayleigh index ri over the oscillation period T: $\mathrm{ri}(\mathbf{x}) = \int_0^T p'(\mathbf{x}, t)\dot{q}'(\mathbf{x}, t)dt$.

The result for the case without pressure sensitivity has already been discussed by the authors in [7]. Adding the sensitivity leads to larger regions with positive feedback, i.e. $\mathrm{ri} > 0$, due to the direct proportionality to the acoustic pressure, as can be seen in Fig. 4. Negative coupling then only appears very close to the burner

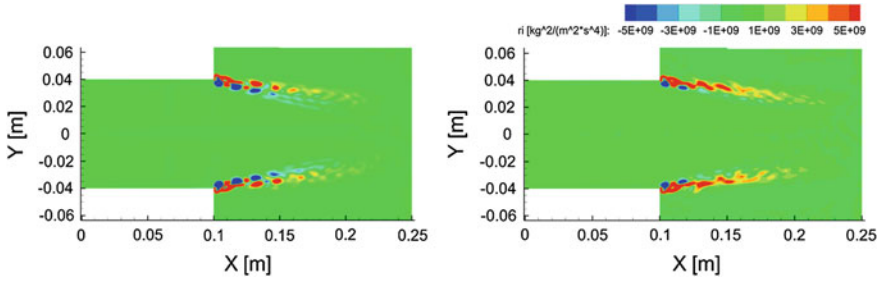

Fig. 4 Distributions of Rayleigh index without (*left*) and with (*right*) pressure sensitivity

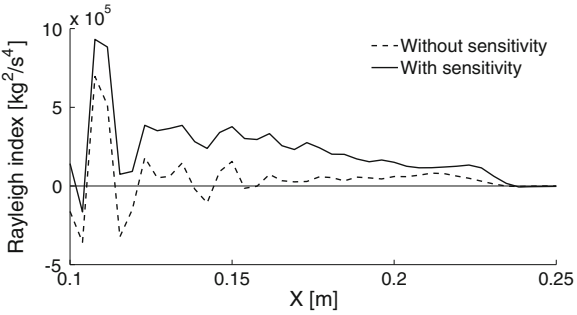

Fig. 5 Comparison of axial Rayleigh index distributions computed with LES

exit. This result can be further illustrated by axial profiles of the Rayleigh index. Therefore, the domain is split into thin observation windows stretching over the entire combustor height. Through an area integration of the local Rayleigh index in each window i, one obtains integral Rayleigh index values $\mathrm{RI}_{LES,i}$ that are plotted along the combustor in Fig. 5. Here, one can observe that the addition of the pressure sensitivity leads to a significant increase in the total thermoacoustic feedback.

4 Modelling of Heat Release Rate Modulations

The following non-compact, complex flame transfer functions are proposed for the feedback contributions linked to density, displacement, and pressure sensitivity:

$$\text{Density:} \quad \left.\frac{\dot{q}'(\mathbf{x},t)}{\bar{\dot{q}}(\mathbf{x})}\right|_{\rho,mod} = \frac{1}{\gamma}\frac{p'(\mathbf{x},t)}{\overline{p}(\mathbf{x})} \tag{1}$$

$$\text{Pressure sensitivity:} \quad \left.\frac{\dot{q}'(\mathbf{x},t)}{\bar{\dot{q}}(\mathbf{x})}\right|_{\varphi_p,mod} = \varphi_p\frac{p'(\mathbf{x},t)}{\overline{p}(\mathbf{x})} \tag{2}$$

$$\text{Displacement:} \quad \left.\frac{\dot{q}'(\mathbf{x},t)}{\bar{\dot{q}}(\mathbf{x})}\right|_{\Delta,mod} = -\frac{1}{i\omega}\frac{\mathbf{u}'(\mathbf{x},t)\cdot\nabla\bar{\dot{q}}(\mathbf{x})}{\bar{\dot{q}}(\mathbf{x})} \tag{3}$$

The first two model formulations are derived by considering an acoustic state change as isentropic and using the definition of the pressure sensitivity factor. Equation 3 follows from a theoretical description of the displacement effect, which is explicated by the authors in [9]. Modelled Rayleigh index values can be calculated for each of these effects and their sum is compared to the LES results, as shown in Fig. 6. The model formulations do not include fluctuations due to flame wrinkling and thus cannot reproduce the alternating behaviour observed in the upstream region. The wrinkling contributions do however cancel out to a large extent when integrating

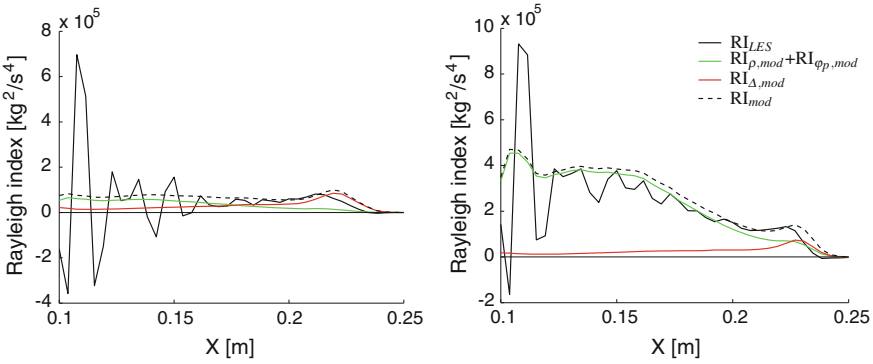

Fig. 6 Simulated and modelled axial Rayleigh index distributions—*left* $\varphi_p = 0$, *right* $\varphi_p = 5$

over the entire combustor length, and hence the model ansatz delivers a satisfying prediction of the total thermoacoustic feedback produced by the flame in response to a transverse acoustic mode.

5 Summary and Outlook

Acoustically excited LES of a model reheat combustor are conducted under perfect premix conditions. In comparison to previous publications, the combustion model is extended to take into consideration an additional thermoacoustic feedback mechanism, linked to the pressure sensitivity of reaction kinetics. The flame dynamics are characterized via a harmonic analysis of local heat release rate fluctuations, which allows to discern between the different feedback mechanisms. The pressure sensitivity adds a significant positive coupling contribution. Analytical model formulations are proposed for three coupling mechanisms to predict the respective feedback levels. Their sum allows a prediction of the total feedback computed by the LES, using only the mean heat release rate distribution and the acoustic mode shape. The feedback models can thus be used in straightforward manner in industrial development processes, e.g. in acoustic wave equation calculations using finite element methods.

This work demonstrates how LES can be used in an industrial environment as an auxiliary development tool, which allows to gain a physical understanding of complex processes, from which analytical descriptions can be derived. In the future, similar investigations have to be conducted for technical premix combustors and the results be validated against experimental data.

Acknowledgments The authors acknowledge the financial support by Alstom Power and the State of Bavaria in the framework of the research initiative KW21 II (sub-project BY13GV).

References

1. Joos, F., Brunner, P., Schulte-Werning, B., Syed, K., Eroglu, A.: Development of the sequential combustion system for the ABB GT24/GT26 gas turbine family. In: Proceedings of ASME Turbo Expo 96-GT-315 (1996)
2. Kulkarni, R., Polifke, W.: LES of Delft-Jet-In-Hot-Coflow (DJHC) with tabulated chemistry and stochastic fields combustion model. Fuel Proc. Techol. **107**, 138–146 (2013)
3. Kulkarni, R., Zellhuber, M., Polifke, W.: LES based investigation of autoignition in turbulent co-flow configurations. Combust. Theor. Model. **17**(2), 224–259 (2013)
4. Méry, Y., Hakim, L., Scouflaire, P., Vingert, L., Ducruix, S., Candel, S.: Experimental study of the combustion-acoustics coupling in liquid rocket engine high-frequency instabilities. In: Proceedings of AAAF-ESA-CNES Space Propulsion (2012)
5. Schwing, J., Grimm, F., Sattelmayer, T.: A model for the thermo-acoustic feedback of transverse acoustic modes and periodic oscillations in flame position in cylindrical flame tubes. In: Proceedings of ASME Turbo Expo GT2012-68775 (2012)
6. Zellhuber, M., Bellucci, V., Schuermans, B., Polifke, W.: Modelling the impact of acoustic pressure waves on auto-ignition flame dynamics. In: Proceedings of the European Combustion Meeting (2011)
7. Zellhuber, M., Meraner, C., Kulkarni, R., Schuermans, B., Polifke, W.: LES of flame response to transverse acoustic excitation in a model reheat combustor. J. Eng. Gas Turbines Power **135**(091508), 1–9 (2013)
8. Zellhuber, M., Schuermans, B., Polifke, W.: Impact of acoustic pressure on auto-ignition and heat release. Combust. Theor. Model. **18**(1), 1–31 (2014)
9. Zellhuber, M., Schwing, J., Schuermans, B., Sattelmayer, T., Polifke, W.: Experimental and numerical investigation of thermoacoustic sources related to high-frequency instabilities. Int. J. Spray Combust. Dyn. **6**(1), 1–34 (2014)

Direct Numerical Simulation of Hydrogen-Carbon Monoxide Turbulent Premixed Flame

F. Battista, F. Picano, G. Troiani and C.M. Casciola

1 Introduction

Environmental issues and new regulations for pollutant emissions lead to consider alternative fuels for the new generation of power generators such as hydrogen, syngas, green diesel, or biodiesel. In this context, a deeper understanding of the interaction between turbulent structures and chemical kinetics is needed to design burner optimized for these fuels.

A mixture of hydrogen-carbon monoxide (CO/H_2 50–50 %) and air is here considered as a model for syngas flames.

Several recent works in literature deal with the syngas combustion both in laminar case [3, 4] and in the turbulent regime [7] with the main purpose to provide the evaluation of the laminar/turbulent flame speed at different conditions, e.g. equivalence ratio, hydrogen or third body, namely nitrogen or carbon-dioxide concentration, and, thermodynamics conditions.

Bouvet et al. [3] address the combustion of syngas in Bunsen flame configuration at laminar regime. OH chemilumiscence and Schlieren imaging methodology have been used to extract the laminar flame speed in a wide range of equivalence ratio

F. Battista (✉) · C.M. Casciola
Department of Mechanical and Aerospace Engineering, La Sapienza University,
via Eudossiana 18, 00184 Rome, Italy
e-mail: francesco.battista@uniroma1.it

C.M. Casciola
e-mail: carlomassimo.casciola@uniroma1.it

F. Picano
Linné Flow Centre, KTH Mechanics, Osquars Backe 18, 100 44 Stockholm, Sweden
e-mail: picano@mech.kth.se

G. Troiani
Sustainable Combustion Laboratory, ENEA CR Casaccia, via Anguillarese 301,
00123 Rome, Italy
e-mail: guido.troiani@enea.it

J. Fröhlich et al. (eds.), *Direct and Large-Eddy Simulation IX*,
ERCOFTAC Series 20, DOI 10.1007/978-3-319-14448-1_69

and mixture composition, namely $0.3 < \phi < 1.2$ and $1\,\% < \%H_2 < 100\,\%$. Other experimental measurements on the laminar flame speed diluted with N_2 and CO_2 are provided in [4], besides the flame stability is addressed for different nitrogen and carbon-dioxide. It has been shown that increasing the N_2 and CO_2 concentration the laminar burning velocity decreases due to the lower heat release and greater heat capacity. The presence of CO tends to stabilize the flame while the opposite effects is induced by the H_2.

The experimental measurements of burning velocity have been performed also in the turbulent regime by Liu et al. [7]. They measured the laminar and turbulent flame speed at different environmental pressure on a spherical flame configuration, observing as the pressure increases the instability of the flame whose surface is characterized by classical cellular structures.

The aim of the present work is to investigate the effect of the presence of CO on the hydrogen thermo-diffusive instabilities in turbulent conditions via Direct Numerical Simulation (DNS).

We will show that the presence of CO with respect to pure H_2/Air flames reduces both local quenching and local temperature peaks that control pollutant production.

2 Numerical Method

The algorithm discretizes in a cylindrical domain the Low-Mach number formulation of the Navier-Stokes equations which describe a reactive flow at low Mach number with arbitrary density variations, neglecting acoustics effects.

Spatial discretization is based on second order central finite differences in conservative form on a staggered grid. Concerning scalars, the convective terms of the reaction-advection-diffusion equations are discretized by a bounded central difference scheme designed to avoid spurious oscillations. A low-storage third order Runge-Kutta scheme is employed for temporal integration.

A fully turbulent velocity inlet is enforced at the inflow section (unsteady Dirichlet condition) using a cross-sectional plane of a periodic turbulent pipe flow of a companion DNS. A convective outflow condition at the outlet and a traction-free condition at the side boundary have been adopted to mimic an open environment surrounding the flame, see [1, 8] for additional details.

A chemical kinetics scheme with 10 species and 24 reactions is employed [9] for the combustion of H_2/CO.

The DNS reproduces a premixed Bunsen burner with a diameter-based Reynolds number $Re_D = U_0 D/\nu_\infty = 6,000$, with U_0 the bulk velocity and D the diameter. The parameters of the simulation correspond to a lean premixed Bunsen flame at $\phi = 0.4$. The heat capacity ratio is fixed at $\gamma = c_p/c_v = 1.33$, while a temperature dependent viscosity is used, $\mu \propto \sqrt{T}$. Binary diffusion coefficients of all species are calculated with respect to the gaseous nitrogen which is the abundant species in Air flames.

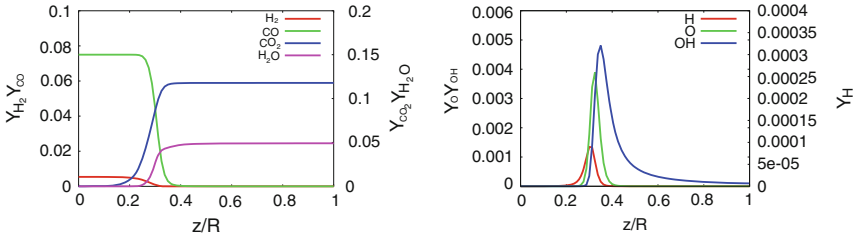

Fig. 1 One-dimensional profiles of reactants and products mass concentration (*left panel*) and significant radicals mass concentration (*right panel*)

The computational domain, $[\theta_{max} \times R_{max} \times Z_{max}] = [2\pi \times 6.2D \times 7D]$, is discretized by $N_\theta \times N_r \times N_z = 128 \times 201 \times 560$ nodes with radial mesh stretching for accurate resolution of the shear layer and of the instantaneous flame front ($4-5$ points within the instantaneous flame thickness), see [1, 2] for details and tests. It is noteworthy to highlight that the flame thickness is here defined as the inverse of the temperature gradient across the lame front, $\delta_L = (T_b - T_u) \,/\, \nabla T|_{max}$, where $T_{b/u}$ is the temperature of the burned/unburned gases, which is the most stringent flame thickness definition.

In Fig. 1 the One dimensional premixed plane flame is reported. In particular in the left panel the burning fuel mass concentration profiles, namely CO and H_2 and the products mass concentration profiles, namely CO_2 and H_2O are provided; in the right panel the main radicals of the present chemical reaction are shown, e.g. atomic hydrogen and oxygen and OH. The 1D simulation reproduces a laminar premixed plane flame with the same inlet conditions of the 3D one. It is performed by the same algorithm of the 3D simulation providing a validation of the chemical kinetics and the main parameters describing a premixed flame: unstretched flame thickness δ_L, flame speed S_L, and adiabatic temperature T_{ad}.

3 Results and Discussion

A qualitative description of the instantaneous fields provides interesting hints concerning the interaction between turbulence and chemistry showing also the presence of the thermo-diffusive instabilities (typical effects induced by the non-unity fuel Lewis number Le). Indeed, the flame front consists of by super-burning where the local temperature exceeds the adiabatic one T_{ab} and quenched regions with temperature lower than T_{ad}, but with vanishing reactants. Similar findings have been observed experimentally in [5] and numerically in [6]

The most-left panel of Fig. 2 shows the temperature-based instantaneous progress variable field $c_T = T - T_u/(T_{ad} - T_u)$, the OH mass concentration is shown in the middle panel and the most-right panel reports the CO_2 mass concentrations.

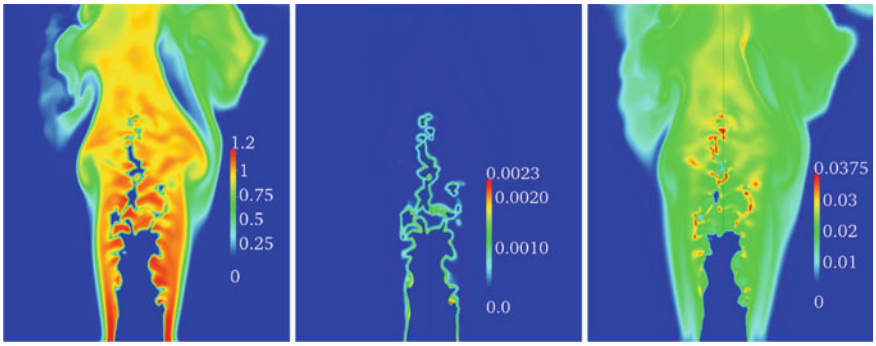

Fig. 2 Instantaneous slice of hydrogen/carbon-monoxide/air turbulent premixed flame: progress variable c_T (*left panel*), *OH* mass concentration (*middle panel*) and CO_2 mass concentration (*right panel*)

Regions of the flame front convex towards the burned gases—the so-called gullies—typically present higher curvature than the bulges, where the convexity is towards the fresh gas [5]. In the bulges c_T is significantly larger than unity, with values up to 1.2 (super-adiabaticity), while sub-adiabatic conditions, $c_T < 1$ occur in gullies. This behavior is common to the pure hydrogen premixed turbulent flame, see Fig. 3 and is related to the well-known thermo-diffusive instability [5, 6].

These phenomena are usually observed in pure hydrogen lean flame, and are a direct consequence of the diffusivity of molecular hydrogen exceeding the thermal diffusivity of the mixture ($Le \ll 1$). In bulges, reactants diffuse towards burnt gases faster than heat towards fresh gases, so their concentration is larger in the bulges

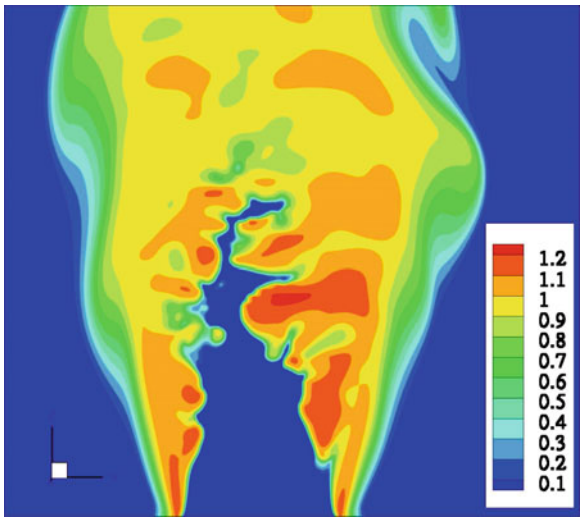

Fig. 3 Instantaneous 2D snapshot of the progress variable based on the temperature $c_T = T - T_u/(T_{ad} - T_u)$ of pure hydrogen/air premixed turbulent flame with the same equivalence ratio of the hydrogen/carbon-monoxide/air flame

and almost null in the gullies, causing there an unstable condition [2] which leads to instantaneous local quenching.

Even though similar phenomena occur in the syngas flame the local quenching, observed in the gullies of pure hydrogen flames, are not present when the carbon-monoxide is added to the reactants. Though the gullies are still characterized by a lack of hydrogen, the oxidation of the carbon monoxide is able to keep the temperature high enough to support the OH production and the overall reaction rate. A qualitative evidence of this phenomenon is provided in the most-right panel of Fig. 2 representing the CO_2 concentration which peaks in the gullies.

The qualitative analysis here reported shows how the local quenching phenomena are reduced by the presence of CO in the fuel mixture with respect to pure H_2/Air flames.

In order to deeper characterize, the correlation between the flame front geometry and species concentration is addressed. The local flame curvature is employed to describe the geometry of the flame front. It is defined as the divergence of the normal unity vector n along the flame front $k = \nabla \cdot n$, with $n = \nabla c_T / |\nabla c_T|$. The intensity of the turbulent combustion process is inferred looking at the fluctuation of the mass concentration of a generic ith species with respect to the corresponding laminar condition. Specifically, it is defined as the difference between the actual turbulent concentration and its value in the laminar planar case at a corresponding value of c_T. It is noteworthy to stress that negative/positive curvatures correspond to bulges/gullies.

Figure 4 shows the joint probability density function of the two quantities above described for the H radical (left panel) that is considered a marker of combustion for hydrogen as the OH, and CO_2 (right panel). The negative correlation between the H concentration fluctuation and the curvature k demonstrates that higher concentration with respect to laminar conditions (positive fluctuations) occur more frequently in bulges (negative curvatures) than in the gullies. This behavior suggests that the reaction rate for hydrogen peaks in bulges, being H a marker for hydrogen

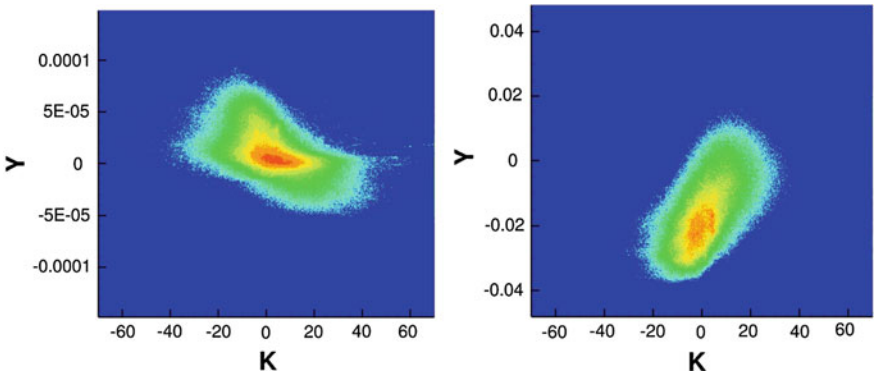

Fig. 4 Joint probability function of curvature k and concentration fluctuation respect to the unstretched configuration Y of H radical (*left panel*), and carbon dioxide, CO_2 (*right panel*)

combustion. Observing the joint-pdf for carbon-dioxide, the opposite correlation is found. Positive fluctuation of CO_2 concentration correlates with positive curvatures denoting a more intense CO oxidation in the gullies region than the laminar plane flame.

From the previous discussion, we conclude that the presence of CO in a Hydrogen/Air mixture mitigates the thermo-diffusive instabilities reducing thermal fluctuations, local quenching and the super-adiabatic temperature peaks. Last feature is expected to reduce emissions of NOx which are mainly formed in the highest temperature spots.

References

1. Battista, F., Picano, F., Troiani, G., Casciola, C.M.: Intermittent features of inertial particle distributions in turbulent premixed flames. Phys. Fluids **23**(12), 123304 (2011)
2. Baum, M., Poinsot, T.J., Haworth, D.C., Darabiha, N.: Direct numerical simulation of h2/o2/n2 flames with complex chemistry in two-dimensional turbulent flows. J. Fluid Mech. **281**, 1–32 (1994)
3. Bouvet, N., Chauveau, C., Gökalp, I., Lee, S.-Y., Santoro, R.J.: Characterization of syngas laminar flames using the Bunsen burner configuration. Int. J. Hydrogen Energy **36**(1), 992–1005 (2011)
4. Burbano, H.J., Pareja, J., Amell, A.A.: Laminar burning velocities and flame stability analysis of H_2/CO/air mixtures with dilution of N_2 and CO_2. Int. J. Hydrogen Energy **36**(4), 3232–3242 (2011)
5. Chen, Y.C., Bilger, R.W.: Experimental investigation of three-dimensional flame-front structure in premixed turbulent combustion: II. lean hydrogen/air bunsen flames. Combust. Flame **138**(1), 155–174 (2004)
6. Im, H.G., Chen, J.H.: Preferential diffusion effects on the burning rate of interacting turbulent premixed hydrogen-air flames. Combust. Flame **131**(3), 246–258 (2002)
7. Liu, C.C., Shy, S.S., Chiu, C.W., Peng, M.W., Chung, H.J.: Hydrogen/carbon monoxide syngas burning rates measurements in high-pressure quiescent and turbulent environment. Int. J. Hydrogen Energy **36**(14), 8595–8603 (2011)
8. Picano, F., Battista, F., Troiani, G., Casciola, C.M.: Dynamics of PIV seeding particles in turbulent premixed flames. Exp. Fluids 1–14 (2010)
9. Saxena, P., Williams, F.A.: Testing a small detailed chemical-kinetic mechanism for the combustion of hydrogen and carbon monoxide. Combust. Flame **145**(1), 316–323 (2006)

Part XIII
Magnetohydrodynamics

Helical Turbulence in Fluids and MHD

R. Marino, J. Baerenzung, P.D. Mininni, A. Pouquet, C. Rorai, D. Rosenberg and J. Stawarz

Perhaps because turbulence is central to a variety of applications for atmospheric and oceanic flows, as well as engineering, and yet remains largely unsolved, high-performance computing plays a central role, on par with observations and experiments, for progressing in our detailed understanding of such flows. These approaches are complementary, and both direct numerical simulations (DNS) and large eddy simulations (LES) give a large amount of information, in particular for small scale statistics where intermittent events occur, although Reynolds numbers in DNS remain small compared to those encountered in geophysical and astrophysical flows.

Turbulence is sometimes viewed as the solution of last resort, as the *deus ex machina* that will make us move from a contradiction between, say, observations

R. Marino · A. Pouquet (✉) · J. Stawarz
NCAR, P.O. Box 3000, Boulder, USA
e-mail: pouquet@ucar.edu

R. Marino
e-mail: marino@ucar.edu

J. Stawarz
e-mail: stawarz@ucar.edu

J. Baerenzung
I.C. Dynamics of Complex System, 14476 Postdam, Germany
e-mail: baeren@voila.fr

P.D. Mininni
Department FíSica, Ciencias Exactas Y Naturales, UBA, Buenos Aires, Argentina
e-mail: mininni@df.uba.ar

C. Rorai
Nordita, Roslagstullsbacken 23, Stockholm, Sweden
e-mail: ceciliarorai@gmail.com

D. Rosenberg
National Center for Computational Science, Oak Ridge National Laboratory,
Oakridge, USA
e-mail: d7r@ornl.gov

J. Fröhlich et al. (eds.), *Direct and Large-Eddy Simulation IX*,
ERCOFTAC Series 20, DOI 10.1007/978-3-319-14448-1_70

and theory, and a self-consistent view of the object at hand. For example, in the interstellar medium, the tenuous and cold gas ($T_0 \sim 10\,\mathrm{K}$) between the stars, there are molecules that are observed at frequencies corresponding to temperatures 10 times the mean: how is that possible? But turbulent flows are known to develop intermittency, i.e. leading through nonlinear mode coupling to strong sparsely distributed coherent structures. These structures (vortex filaments and columns, density layers, vorticity and current sheets in a plasma) are known to dissipate energy, themselves or in their vicinity, so the local temperature can be increased substantially, sufficiently so to populate higher-energy atomic and molecular lines that radiate at the proper (observed) frequency; examples in combustion may be given as well. Similarly, making rain from small particle seeds, using linear theory, takes days when in reality a few hours are sufficient, thanks to the intense acceleration due to strong events in a turbulent fluid such as the atmosphere. Examples abound of applications where turbulence plays a role insofar as it affects the distribution of events at small scale, such as phyto- and zoo-plankton in the ocean, wetlands, pollutants in the atmosphere, or diapycnal mixing in the ocean, related to the breaking of internal waves as they impinge on bottom topography.

Turbulent flows are complex, with interactions between waves and nonlinear eddies of varying relative intensities at different spatio-temporal scales. From a more fundamental point of view, the breaking of mirror-symmetry as measured for example by helicity (velocity $\mathbf{u}$-vorticity $\boldsymbol{\omega} = \nabla \times \mathbf{u}$ correlations) is one of the main ingredient in the emergence of large-scale magnetic fields in planets, stars, galaxies and beyond, in the so-called dynamo problem and it may also affect the evolution of super-cell storms into tornadoes [1], or that of hurricanes, because of the linkage associated with the secondary circulation.

1 Turbulence: A Multi-scale Problem

To paraphrase Kolmogorov, it can be said that in the absence of a theory of turbulence, one has to rely on data, experimental, observational and numerical to formulate simplifying hypotheses. Progress in our understanding of turbulent flows and multi-scale non-linear phenomena has been made over the last fifty years: one can think for example of (i) the Lorenz attractor and the inherent lack of predictability of turbulent flows which limits for example the temporal span of weather predictions; (ii) solitons—when there is a balance between nonlinear steepening and dispersion, and more generally, (iii) the role of coherent structures in the dynamics and statistics of turbulent flows; (iv) the immense progress in metrology and in the speed of computers that finally allow for an exploration of three-dimensional (3D) flows, at least for simple geometries; (v) the realization that under the constraints of more than one invariant in the ideal (non-dissipative) case, excitation can move to large scales, such as for the Navier-Stokes equations in two dimensions (2D), or magnetic helicity in 3D, and that statistical mechanics is able to predict large-scale structures as in the case of the oval or of the jets in the atmosphere of planets like Jupiter; (vi) numerical and phenomenological modeling and regularization techniques; (vii) weak turbulence

in the presence of waves due for example to imposed rotation, stratification or strong magnetic fields: the statistical problem can be closed naturally under the assumption of a small ratio between the wave period and the eddy turn-over time (although the theory is non-uniform in scale and breaks down at some scale) [2]; (viii) fractal boundaries, as in clouds, and self-organized criticality, as in avalanches; and (ix) intermittency and anomalous exponents of structure functions (i.e., the cascade is not entirely self-similar and gives rise to intense localized structures), a problem solved theoretically for the Burgers equation (a one dimensional, compressible model), and for the advection of a passive tracer by a random field.

Intermittency is due to memory effects, in time and space (as a trace of initial conditions or forcing); in the former case, so-called "1/f" noise has been observed in a variety of turbulent flows. Intermittency is one impediment to the functioning of wind farms, as such events occur without warning and with strong variations of wind speeds. In fact, not only is intermittency measured in Probability Distribution Functions (PDFs) of velocity gradients through non-Gaussian wings, but it is also present in the temperature and velocity fields in shear flows, n the atmosphere (see, e.g., [3]) and in direct numerical simulations of the Boussinesq equations (see [4] and references therein). Heavy tails for the velocity PDFs are observed as well in the Solar Wind [5, 6]. They can be associated with the interactions of eddies and waves [4], and intermittent bursts were also found for an intermediate value of the interaction parameter in magnetohydrodynamic (MHD) in the quasi-static limit, at low magnetic Reynolds number and high imposed uniform magnetic field.

2 The Role of Helicity in Turbulent Flows and its Modeling

An important statistical quantity to consider is the kinetic helicity, $H_V = \langle \mathbf{u} \cdot \boldsymbol{\omega} \rangle$, or in relative terms $\sigma_V(\mathbf{x}) = \cos[\mathbf{u}(\mathbf{x}), \boldsymbol{\omega}(\mathbf{x})]$, with $|\sigma_v| \leq 1$; relative helicity in spectral space is defined as $\Sigma_V(k) = H_V(k)/[kE_V(k)]$, with again $|\Sigma_V(k)| \leq 1$; $E_V(k)$ and $H_V(k)$ are the energy and helicity Fourier spectra. Note that helicity is a pseudo-scalar (it changes sign when going from a right-handed to a left-handed frame of reference), and that it is not definite positive; helicity is the first step away from an isotropic flow although the velocity correlation function is still expressed in terms of the modulus of the wavenumber. It refers to the linkage of vortex lines, or to their twist [7]. Helicity has been measured in the atmosphere in hurricanes as well as in the Planetary Boundary Layer [8]. In hydrology, it is associated with the secondary flows in river bends or at the confluence of two rivers. Furthermore, isopycnal surfaces develop a non-cartesian topology when one deals, as in the oceans, with a non-linear equation of state relating temperature, density and salinity.

In homogeneous isotropic turbulence, helicity can be created point-wise, through alignment of vorticity and pressure gradient or shear. However, when volume-integrated, it is globally an invariant of the ideal equations of motion in the absence of dissipation. Since in the incompressible case these equations are quadratic, helicity is conserved for each individual triadic interaction.

Because of this so-called detailed conservation, one can use as a model of helical flows the restriction of the entire dynamics to the interactions between a certain subset of waves. In [10] it was shown that, when performing a decomposition of the flow on the eigenvectors of the curl operator (circularly $\pm$ polarized waves) and further restricting nonlinear interactions to be of one sign only (say, +), then total helicity is positive (H^+), and an inverse cascade of energy together with a direct cascade of helicity was observed. Three remarks at this stage are in order: (a) Kraichnan already noticed in 1973 that these subsets are subdominant and the overall energy cascade will be to small scales; (b) the inverse cascade obtained numerically in [10] gives a straightforward explanation to the fact that, when observing the total energy transfer in the general case, it has an averaged value that is positive, corresponding to direct transfer, but it has strong excursions of both signs; and (c) such a dual cascade with one-signed helicity was already observed in rotating flows with a Beltrami fully helical ($\sigma_V = +1$) forcing, the direct cascade being dominated by one-signed helicity together with an inverse cascade of energy toward large scales [11].

In this case of reduced interactions, there are two positive invariants ($E_V = \langle|\mathbf{u}^2|\rangle/2$ and H^+), the latter weighing the small scales more than the energy. The situation is clearly similar to that of 2D fluids, where the second invariant is enstrophy $Z = \langle|\boldsymbol{\omega}^2|\rangle$, and for which regularity of the fluid can be proven for all times. In fact, it was shown recently in [12] that in the reduced helical case, regularity obtains as well. Can that result be used for the full-fledged Navier-Stokes case? One can remark that if relative helicity in homogeneous isotropic turbulence decays with scale ($\Sigma(k) \sim 1/k$), a fact compatible with the recovery of the symmetries of the equations at small scale (recall that the Fourier spectra of both the energy and helicity follow a $k^{-5/3}$ law), nevertheless locally vortex filaments prevail at the beginning of the dissipative range and are fully helical: velocity and vorticity are aligned (or anti-aligned), a feature commonly used for detecting the filaments using wavelets. Assuming these vortices are very strong and dominate their environment, one can recover the velocity field through the Biot-Savart law, using for example the Localized Induction Approximation that is known to lead to smooth behavior since it can be mapped into the Nonlinear Schrödinger equation [13].

2.1 The Rotating Stratified Case

The invariance of helicity carries on to the rotating case, where it can be shown to play an important role in the energy redistribution among scales [14]. In Fig. 1 (top) is shown a Perspective Volume Rendering (PVR) of the energy transfer (left) and helicity (right) for a computation on a grid of 1536^3 points [11]; the Reynolds number is 5,100 and the Rossby number (measuring the ratio of the inertial period f to the eddy turn-over time τ_{nl}) is 0.06. The strong vertical columns are fully helical and shrouded by a sea of vortex filaments; it is clear that most of the energy transfer, both positive and negative, takes place in the vicinity of these columns.

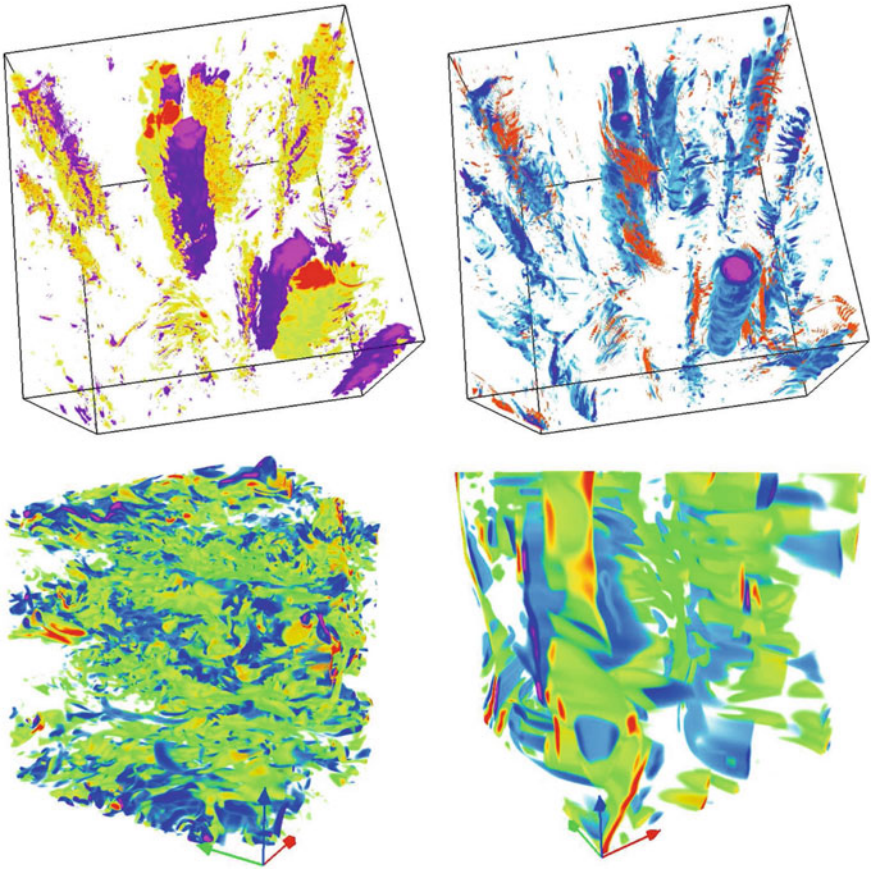

Fig. 1 *Top* Perspective volume rendering (PVR) of energy flux (*left*) and helicity (*right*) for a DNS flow with Rossby and Reynolds numbers $Ro = U_0/[L_0 f] = 0.06$, $Re = U_0 L_0/\nu$ =5,100, with U_0, L_0 characteristic velocity and length scale; f is twice the rotation rate and ν the viscosity; tri-periodic grid of 1536^3 points. Note the strong transfer in the vicinity of the helical columnar structures. *Bottom* PVR of helicity in forced rotating stratified turbulence for $Fr = 1/[N\tau_{nl}]$ respectively equal to 0.1, $N/f = 4$ (*left*) and $Fr = 0.025$, $N/f = 2$ (*right*), where $Fr = 1/[N\tau_{nl}]$ is the Froude number [9]. DNS on grids of 512^3 points, with Reynolds number of 10^4. Note the more turbulent aspect of the flow at higher Froude number for which the Ozmidov scale $L_{oz} \sim [\varepsilon/N^3]^{1/2}$ at which isotropy recovers is resolved., with $\varepsilon \equiv \dot{E}$ the energy dissipation rate

In the stratified case, helicity is not conserved any longer. In Fig. 2 is shown the temporal growth of relative helicity (left) and the spectral relative helicity at the final time of the computation (right), for a run with a Reynolds and Froude number of respectively 2×10^4 and 0.03 (solid line) or 0.1 (dashed line), using grids of 2048^3 points (the Froude number is the ratio of the Brunt-Väisälä frequency N to the eddy turn-over time). Even though σ_V remains small (of the order of 10 %), its growth is steady, and similar for both runs. Scale by scale, it is constant at large scale, and decays rapidly at small scale; the break between these two behaviors takes place at

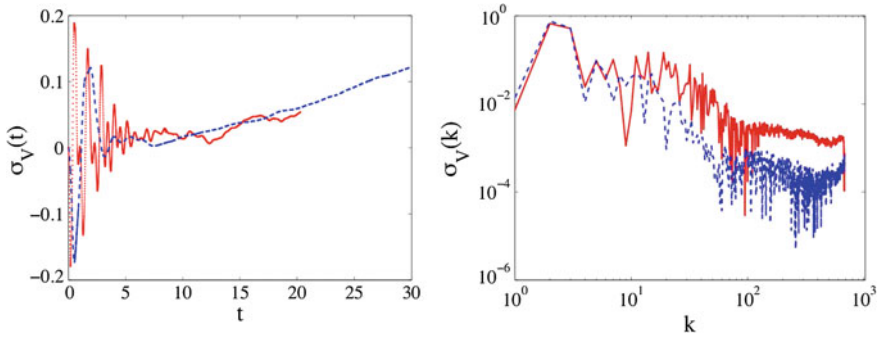

Fig. 2 Temporal (*left*) and spectral (*right*) variation of relative helicity in forced stratified turbulence for Froude numbers equal to 0.1 (*dashed line*) and 0.03 (*solid line*); grids of 2048^3 points, Reynolds number of 2×10^4 [4]. Note the steady growth, and the flat spectrum at large scale, as observed in the atmosphere [8]

the so-called buoyancy scale $L_B = U_0/N$ which is a rough measure of the thickness of the stratified layers in the vertical direction in which gravity acts.

Finally, in the presence of both rotation and stratification, it was shown in [15] that for quasi-geostrophic flows (for which there is a balance between pressure gradient, Coriolis and gravity forces), helicity can be produced by the flow through the correlation of vertical velocity gradients and buoyancy (temperature or density fluctuations). This creation of helicity was recently observed numerically as well [9], including in the turbulent regime. The resulting helicity is shown in Fig. 1 (bottom) for two flows; note that at a given Reynolds and Rossby number, the flow is more turbulent when the Froude number is larger, as expected. The governing parameter is in fact the so-called buoyancy Reynolds number $\mathscr{R}_B = ReFr^2$, respectively ≈ 9 and ≈ 100 for the two flows in the Figure. For $\mathscr{R}_B \approx 1$, the Ozmidov scale L_{oz} at which isotropy recovers is comparable to the Kolmogorov (dissipative) scale, and for $\mathscr{R}_B > 1$, a Kolmogorov spectrum is expected at scales smaller than L_{oz}.

2.2 Modeling of Helical Flows

Helicity may well play a role in the small-scale dynamics of turbulent flows in a variety of contexts, and it may be advantageous to incorporate its effect in LES. There are several ways the effect of helicity in turbulent flows can be modeled. The need for such specific modeling has been recognized early [16], in part due to an analogy with flows that are coupled to a magnetic field. Taking the MHD approximation in which the displacement current is neglected for sub-luminal velocities, one can show that the volume-integrated cross-correlation between the velocity and the magnetic field **b** (in units of Alfvén velocity), H_C, and the magnetic helicity (correlations between magnetic induction and magnetic potential), H_M, are ideal invariants. It is also known that the kinetic helicity contained in the small scales is a source of large-scale growth

for the magnetic field (see also §2.3). The identical effect does not exist in the purely hydrodynamical case, as shown using the renormalization group, unless the small scales are anisotropic [17]. It is also known that, in channel flows, one has to adjust the Smagorinsky constant C_S in LES runs in order to take into account a less-efficient energy transfer, an observation which could be attributed to the fact that the streaks that develop in such flows are helical.

An alternative is to take a standard value for C_S and introduce specific helical models. In [16] (see also [18] for the MHD case), a Direct Interaction Approximation is used to compute modeling of rotating flows and pipe flows, having in mind the idea that the energy cascade to small scales is less efficient in the presence of helicity since the Lamb vector $\mathbf{u} \times \boldsymbol{\omega}$ is weakened. Note that it has been shown more recently using a combination of DNS and LES that the onset of decay of helical turbulence is postponed but that, once established, it takes place at the same rate as in the non-helical case in the absence of waves. However, with rotation (and with stratification), the decay of energy becomes slower, and when helicity is also present in these rotating stratified flows, the decay is slower again; namely, for a so-called box-limited flow, one observe decays of t^{-2}, t^{-1} and $t^{-1/3}$ respectively [19, 20].

Other helical models have been devised recently [21–24]. For example, in [23], it is shown by assuming a Kolmogorov spectrum valid in the absence of rotation that the classical Smagorinsky model underestimates energy and helicity dissipation by 40 %, although numerically the effect seems smaller.

In [21, 22], the modeling is done based on the EDQNM (Eddy Damped Quasi Normal Markovian) closure. One arrives at a formulation of eddy viscosity and eddy noise which, in addition to the traditional expressions, specify contributions, stemming from the helicity of the flow, for the eddy viscosity and for the eddy noise. Unsurprisingly, the helicity spectrum is much better described when using this helical subgrid scale model [22]; but one can remark that the growth rate of the total energy in the inverse cascade in rotating flows is also better estimated using this helical model. Finally, it has also been found that sub-grid helicity dissipation is responsible for observed asymmetries in the joint Probability Distribution Functions of the invariants of the vorticity gradient tensor, an asymmetry attributed to the geometry of twisted vortex tubes [24].

2.3 The Case of Magnetohydrodynamics

It has been known for a long time that in MHD, small-scale helicity acts as a destabilizing factor of large-scale magnetic fields (the so-called alpha effect). The role of magnetic helicity $H_M = \langle \mathbf{A} \cdot \mathbf{b} \rangle$ (with $\mathbf{b} = \nabla \times \mathbf{A}$, $\mathbf{A}$ being the magnetic potential) is far from being understood. The dynamics of magnetic helicity has brought some unexpected results recently [26, 27]: its Fourier spectrum follows a law which is much steeper ($\sim k^{-3.3}$) that what dimensional analysis predicts ($\sim k^{-2}$), steep enough that nonlocal effects between widely separated scales may play a role as well. This is interpreted in [27] as being due to a scale-by-scale equilibrium between a

quasi-equipartition between energy (kinetic and magnetic) and helicity (kinetic and magnetic as well). To progress in the detailed study of magnetic helicity, one has to envisage using rather large resolutions. In aiding in the computations of such runs, one can implement simple devices to gain some computing time. One such method is tested here, the idea being very simple: use the results of a previously computed ideal run to start the dissipative run. How much can be gained without measurable changes to the overall statistics of the flow?

Under the assumption of universality (i.e. of independence of statistical results on initial conditions and forcing), turbulent flows have properties that are determined by (i) the nonlinear terms, and (ii) the dissipation and forcing terms. In the absence of the latter ($\nu = 0,\ \eta = 0,\ \mathbf{F} = 0$), long-time dynamics yields in the simplest case an equipartition among Fourier modes; but at intermediate times, before the grid resolution is reached by the data, and at intermediate scales, it has been shown both for fluid (Euler) flows and for MHD that turbulent dynamics (say, vortex sheets and a Kolmogorov spectrum) are obtained. In other words, the ideal flow has the characteristics of a turbulent flow, as postulated e.g. by Kraichnan. Thus, one can take the run performed in the ideal case (no dissipation) to start the run with dissipation and observe the evolution towards a decaying turbulent flow and the destabilization of the ideal coherent structures in reconnecting events.

Preliminary results (see Fig. 3) indicate the following. All runs have close to identical statistics, including for the energy spectra, except in the smallest scales for the extreme case of starting the decay run with the ideal data at $t = 2$. The energy decay rate and the ratio of magnetic to kinetic energy as a function of time cannot be distinguished (after a transient) between the various initial conditions; differences

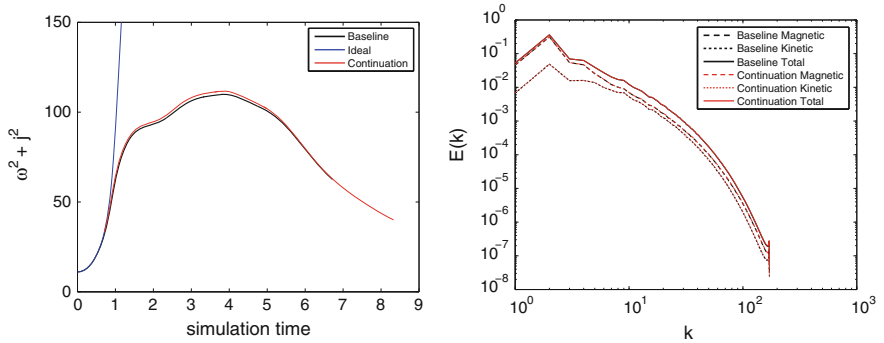

Fig. 3 MHD turbulence, DNS on grids of 512^3 points with in blue, an ideal run (zero viscosity ν and magnetic resistivity η), and in black a decay run starting from the same large-scale random initial conditions. The other runs are started from the ideal state at various times, between 0.7 (*thin line*), just before the inflection point in the dissipative case, and up to 2.0 (*dashed line*) when the current in the ideal case has already reached a very large value [25]. All runs have unit magnetic Prandtl number ($\nu = \eta$). *Left* Total enstrophy $\langle\omega^2\rangle + \langle J^2\rangle$, $\boldsymbol{\omega}$ and $\mathbf{J}$ being the vorticity and the current density. *Right* Kinetic (small dash), magnetic (*long dash*) and total (*solid line*) energy spectra for the same dissipative runs as in Fig. 3, and with the same line code. The overall statistics of the decay runs are close to identical, yet all are progressively less costly to compute

are noticeable, though, when examining the temporal evolution of the total enstrophy $\langle\omega^2\rangle + \langle J^2\rangle$, given the large initial values, although the peak occurs for all runs at $t \approx 4$, and the later temporal evolutions are identical. We can thus conclude that this will allow for a measurable savings, of the order of 20 %, when computing at very high resolution, provided one has already examined the ideal phase. Of course, similar savings can be obtained starting with data from lower resolution runs, as has been done in several instances (see e.g. [25] for the ideal MHD case using a code imposing the symmetries of the so-called Taylor-Green flow generalized to MHD, leading to an equivalent resolution grid of 6144^3 points). One of the central question concerns magnetic reconnection, and the destabilization of ideal structures when dissipation is introduced: what happens to the rotational quasi-discontinuities observed in the ideal case [25]? Does the lack of universality observed in decaying MHD flows in [28] persist at higher Reynolds numbers?

3 Concluding Remarks

Helicity may be an important aspect of turbulence. It can lead to an inverse cascade of energy [10, 11] and it is at the origin of an instability through the so-called AKA (anisotropic Kinetic Alpha) effect [17] as may occur in hurricanes [1]. Helicity is also created in the presence of rotation and stratification [9, 15] and it can be modeled using new transport coefficients [16, 22, 23]. However, being able to unravel the different dynamical ranges in the presence of rotation, stratification and helicity may require substantial CPU resources. Hybrid parallelization using a combination of MPI and OpenMP [29]. Using a general purpose community code for fluids and MHD, with a pseudo-spectral algorithm and explicit time-stepping, linear scaling is found up to 98,000 processors on cubic grids of up to 6144^3 points, allowing for so-called hero runs of turbulence with spectral accuracy. For example, a grid of 12144^3 points for rotating stratified flows may allow to resolve three ranges ($L_B \leq \ell \leq L_F$, $L_{oz} \leq \ell \leq L_B$ and $L_{diss} \leq \ell \leq L_{oz}$, where L_{diss} is the dissipation scale. Such a run will be feasible, at a cost, in a couple of years and could serve as a data base for testing both phenomenological concepts of the interactions of nonlinear eddies and waves in stratified turbulence, and for developing anisotropic LES for such flows.

Acknowledgments Color figures available upon request. Work supported by NSF/CMG-1025183, NCAR/ASD, NSF ASC090050 & TG-PHY100029, and DOE DE-AC05-00OR22725.

References

1. Levina, G., Montgomery, M.: A first examination of the helical nature of tropical cyclogenesis. Dokl. Earth Sci. **434**, 1285–1289 (2010)
2. Newell, A.C., Zakharov, V.E.: The role of the generalized Phillips spectrum in wave turbulence. Phys. Lett. A **372**, 4230–4233 (2008)

3. Lenschow, D.H., Lothon, M., Mayor, S., Sullivan, P.P., Canut, G.: A comparison of higher-order vertical velocity moments in the convective boundary layer from lidar with in situ measurements and large-eddy simulation. Bound. Layer Meteor. **143**, 107–123 (2012)
4. Rorai, C., Mininni, P.D. and Pouquet, A.: Turbulence comes in bursts in stably stratified flows. Phys. Rev. E to appear. arXiv:1308:6564 (2014)
5. Marino, R., Sorriso-Valvo, L., Carbone, V., Veltri, P., Noullez, A., Bruno, R.: The magnetohydrodynamic turbulent cascade in the ecliptic solar wind: study of Ulysses data. Planet. Space Sci. **59**, 592–597 (2011)
6. Marino, R., Sorriso-Valvo, L., D'Amicis, R., Carbone, V., Bruno, R., Veltri, P.: On the occurrence of the third-order scaling in high latitude solar wind. Astrophys. J. **750**, 41 (2012)
7. Moffatt, H.K., Tsinober, E.: Helicity in laminar and turbulent flow. Annu. Rev. Fluid Mech. **24**, 281–312 (1992)
8. Koprov, B.M., Koprov, V.M., Ponomarev, V.M., Chkhetiani, O.G.: Experimental studies of turbulent helicity and its spectrum in the atmospheric boundary layer. Dokl. Phys. **50**, 419–422 (2005)
9. Marino, R., Mininni, P.D., Rosenberg, D., Pouquet, A.: Emergence of helicity in rotating stratified turbulence. Phys. Rev. E **87**, 033016 (2013)
10. Biferale, L., Musacchio, S., Toschi, F.: Inverse energy cascade in three-dimensional isotropic turbulence. Phys. Rev. Lett. **108**, 164501 (2012)
11. Mininni, P., Pouquet, A.: Rotating helical turbulence. Part I. Global evolution and spectral behavior. Phys. Fluids **22**, 035105 (2010)
12. Biferale, L., Titi, E.S.: On the global regularity of a helical-decimated version of the 3D Navier-Stokes equations. J. Stat. Phys. **151**, 1089–1098 (2013)
13. Ricca, R.L.: Momenta of a vortex tangle by structural complexity analysis. Physica D **237**, 2223–2227 (2008)
14. Pouquet, A., Mininni, P.D.: The interplay between helicity and rotation in turbulence: implications for scaling laws and small-scale dynamics. Phil. Trans. Roy. Soc. **368**, 1635–1662 (2010)
15. Hide, R.: A note on helicity. Geophys. Astrophys. Fluid Dyn. **7**, 157–161 (1976)
16. Yokoi, N., Yoshizawa, A.: Statistical analysis of the effects of helicity in inhomogeneous turbulence. Phys. Fluids **A5**, 464–477 (1993)
17. Frisch, U., She, Z.S., Sulem, P.L.: Large-scale flow driven by the anisotropic kinetic alpha effect. Physica D **28**, 382–392 (1987)
18. Yokoi, N.: Cross helicity and related dynamo. Geo. Astro. Fluid Dyn. **107**, 114–184 (2013)
19. Rorai, C., Rosenberg, D., Pouquet, A., Mininni, P.D.: Helicity dynamics in stratified turbulence in the absence of forcing. Phys. Rev. E **87**, 063007 (2013)
20. Teitelbaum, T., Mininni, P.D.: Effect of helicity and rotation on the free decay of turbulent flows. Phys. Rev. Lett. **103**, 014501 (2009)
21. Baerenzung, J., Politano, H., Ponty, Y., Pouquet, A.: Spectral modeling of turbulent flows and the role of helicity. Phys. Rev. E **77**, 046303 (2008)
22. Baerenzung, J., Mininni, P., Pouquet, A., Rosenberg, D.: Spectral modeling of turbulent flows and the role of helicity in the presence of rotation. J. Atmos. Sci. **68**, 2757–2770 (2011)
23. Li, Y., Meneveau, C., Chen, S., Eyink, G.L.: Subgrid-scale modeling of helicity and energy dissipation in helical turbulence. Phys. Rev. E **74**, 026310 (2006)
24. Li, Y.: Geometrical statistics and vortex structures in helical and nonhelical turbulences. Phys. Fluids **22**, 035101 (2010)
25. Brachet, M.-E., Bustamante, M., Krstulovic, G., Mininni, P.D., Pouquet, A., Rosenberg, D.: Ideal dynamics of three-dimensional MHD flows implementing the Taylor-Green symmetries. Phys. Rev. E **87**, 013110 (2013)
26. Mininni, P.D., Pouquet, A.: Finite dissipation and intermittency in MHD. Phys. Rev. E **80**, 025401 (2009)
27. Müller, W.C., Malapaka, S.K.: Role of helicities for the dynamics of turbulent magnetic fields. Geophys. Astrophys. Fluid Dyn. **107**, 93–100 (2013)

28. Lee, E., Brachet, M.E., Pouquet, A., Mininni, P.D., Rosenberg, D.: On the lack of universality in decaying magnetohydrodynamic turbulence. Phys. Rev. E **81**, 016318 (2010)
29. Mininni, P.D., Rosenberg, D., Reddy, R., Pouquet, A.: A hybrid MPI-OpenMP scheme for scalable parallel pseudospectral computations for fluid turbulence. Parallel Comput. **37**, 316–326 (2011)

Linear Instability Analysis of 3D Magnetohydrodynamic Flow by Direct Numerical Simulation

I. Grants and G. Gerbeth

1 Introduction

Direct numerical simulation (DNS) is normally used to study turbulent flows. Though, it may be also very useful for linear instability analysis of complex laminar flows. Given an essentially three-dimensional basic flow the number of coupled active degrees of freedom may easily exceed 10^5. Calculation of the full spectrum is hardly possible if meaningful in such cases. Only a few leading modes are needed for the linear instability analysis. Iteration techniques such as Arnold iteration may be used to find an isolated eigenvalue. A separate effort, however, is then needed to verify that this eigenvalue really has the maximum real part.

Our study demonstrates that the linear instability problem can be effectively solved by means of DNS. The most straight-forward approach would be to calculate the transient equations long enough to ensure that only the leading eigenmode survives. There is, however, a more efficient way to find few leading eigenvalues and eigenmodes [3]. This method approximates $n + 1$ equidistant flow 'snapshot' by n modes that vary exponentially in time. We describe the numerical implementation of this method coupled with DNS and demonstrate it on an example of a three-dimensional magnetohydrodynamic flow. This flow models melt motion in the Czochralski crystal growth process with a horizontal magnetic field (HMF) [4].

I. Grants (✉) · G. Gerbeth
Helmholtz-Zentrum Dresden-Rossendorf, P.O. Box 510119,
01314 Dresden, Germany
e-mail: i.grants@hzdr.de

G. Gerbeth
e-mail: g.gerbeth@hzdr.de

J. Fröhlich et al. (eds.), *Direct and Large-Eddy Simulation IX*,
ERCOFTAC Series 20, DOI 10.1007/978-3-319-14448-1_71

2 Problem Formulation

Let us consider a liquid metal flow in a closed electrically insulating rotating cylinder heated from below in a transverse (horizontal) magnetic field. The height and diameter of the cylinder is $2H_0$ and $2R_0$, respectively. Temperature difference between the bottom and top is ΔT. The cylinder rotates around its axis with the angular velocity Ω. Induction of the horizontal field is B. Material properties of the liquid are: kinematic viscosity ν, electric conductivity σ, density ρ, thermal expansion coefficient β and temperature diffusivity κ. The magnetic field of the induced currents is neglected assuming small magnetic Reynolds number $\sigma\mu\Omega R_0^2 \ll 1$, where μ is the magnetic permeability of the liquid. The dimensionless problem for velocity $\mathbf{v}$, pressure P, temperature T, electric current $\mathbf{j}$, potential φ is

$$\frac{\partial \mathbf{v}}{\partial t} + (\mathbf{v}\nabla)\mathbf{v} = \nabla^2\mathbf{v} - \nabla P + GrT\mathbf{e}_z + Ha^2\mathbf{j}\times\mathbf{B}, \tag{1}$$

$$\frac{\partial T}{\partial t} + (\mathbf{v}\nabla)T = \frac{\nabla^2 T}{Pr}, \tag{2}$$

$$\mathbf{j} = -\nabla\varphi + \mathbf{v}\times\mathbf{B}, \tag{3}$$

$$\nabla\cdot\mathbf{v} = 0, \quad \nabla\cdot\mathbf{j} = 0, \tag{4}$$

with boundary conditions

$$\mathbf{v}|_S = Re\, r\mathbf{e}_\phi, \tag{5}$$

$$\left.\frac{\partial\varphi}{\partial r}\right|_{r=1} = 0, \quad \left.\frac{\partial\varphi}{\partial z}\right|_{z=\pm Z} = -Re\, r\cos(\phi), \tag{6}$$

$$T|_{z=\pm Z} = \mp 0.5, \quad \left.\frac{\partial T}{\partial r}\right|_{r=1} = 0. \tag{7}$$

The expression of the applied magnetic field in cylindrical coordinate system is

$$\mathbf{B} = (\cos(\phi), -\sin(\phi), 0)\,.$$

The problem is governed by five dimensionless parameters summarized in Table 1. The Prandtl number is fixed $Pr = 0.025$ in this study. Solution of (1–4) is three-dimensional for $Re > 0$ and $Ha > 0$ because the HMF breaks the rotational symmetry.

Table 1 Governing dimensionless parameters

Parameter	Definition	Range or value
Grashof number	$Gr = \beta g \Delta T R_0^3 \nu^{-2}$	$[0{:}7 \times 10^6]$
Hartmann number	$Ha = \sigma^{1/2} (\rho \nu)^{-1/2} R_0 B$	[0:1200]
Reynolds number	$Re = \Omega R_0^2 \nu^{-1}$	2,000
Prandtl number	$Pr = \nu \kappa^{-1}$	0.025
Aspect ratio	$Z = H_0 R_0^{-1}$	[0.25:1]

3 Numerical Implementation

We solve this problem numerically by a spectral DNS code [4]. Each of the flow variables is decomposed in normal azimuthal modes in form $u^m(r, z, t)\mathrm{e}^{\mathrm{i}m\phi}$ that are further expressed by Chebyshev polynomials

$$u^m(r, z, t) = \sum_{i=0}^{I} \sum_{j=0}^{J} u^m_{ij}(t) T_i(z/Z) T_{2j+p}(r). \tag{8}$$

This expression has a certain r-symmetry described by value of p that may be either $p = 0$ (for v_z, P, T, φ at even m and for v_ϕ, v_r at odd m) or $p = 1$ otherwise. Equations (1–4) are advanced in time by second order implicit scheme. That reduces the problem to repeated solution of two-dimensional Helmholtz type equations for separate azimuthal modes. This is accomplished by numerical separation of variables [2]. The divergence-free condition is enforced by solving the Poisson's equation for the pressure. The non-linear and magnetic force terms are calculated on an expanded mesh of nodal values ('3/2' rule). Conversion between coefficient presentation (8) and nodal values is accomplished by the fast Fourier transform (FFT). The spatial resolution is between 33^3 and 43^3.

4 Leading Eigenvalue Search

Solving the linear instability problem means finding conditions when the real part of the leading eigenvalue of the linearized equations (1–4) around their basic stationary solution turns to zero. The core problem, thus, is the leading eigenvalue search. Since the basic solution of (1–7) is generally three-dimensional, the azimuthal modes do not decouple and the number of active degrees of freedom is $N = 3 \times 33^3 > 10^5$. The method [3] has been developed for computing leading eigenvalues and eigenvectors of large asymmetric matrices. This matrix itself, however, needs not to be explicitly given. Instead, the method processes $n + 1$ consecutive state of the associated dynamical system. These 'snapshots' can be calculated by DNS provided that the flow remains close enough to the basic solution.

The basic solution is first approached integrating (1–4) in time. A few more time-steps are then completed with an added random body force. Its amplitude is adjusted so to cause small perturbation in the order of 10^{-3} of the base flow. The perturbed flow is further integrated in time to provide input of 'snapshots'. Time delay between them is an arbitrary numerical parameter that ranges between 20 and 200 time steps in the current study. The DNS produced 'snapshots' contain also the basic stationary solution itself. That poses no additional difficulty because the method [3] extracts the basic solution as an eigenmode with (near) zero eigenvalue and the largest weight. That means, particularly, that the initial accuracy of the basic solution needs not to be better than the amplitude of the perturbation.

The method [3] may be implemented on the basis of the linear algebra package LAPACK. First, an orthonormal basis is constructed of all but the final vector ('snapshot') by ZGEQLF and ZUNGQL routine calls. Then a translation matrix from the input vectors to the orthonormal basis is evaluated. This step involves matrix inversion. Given the translation matrix, the coefficients are calculated, that express the final 'snapshot' in the series by the n preceding ones. These coefficients allow to find n eigenmodes and their complex growth-rates by solving nth order algebraic equation [3]. The roots are found by transforming this equation to a low order eigenvalue problem [5]. Number of modes is $n = 7$ in the current study.

Spurious eigenvalues may often be produced by this method and, therefore, an extensive testing may be needed. Our tests controlled how much the leading eigenvalue changed with one set of 'snapshots' to the next. The eigenvalue search was stopped when this variation was less than 10^{-5} in relative terms. A separate test controlled whether the leading eigenmode had the largest weight (beyond the zero-eigenvalue mode representing the basic solution).

5 Results

The liquid rotates as a solid body in case of no HMF. As the field strength is increased, the HMF induces magnetic force that opposes the rotation. The differential rotation and, thus, the secondary flow increases with HMF until the bulk ceases to rotate. Let us denote the corresponding field strength by Ha_s. It may be shown [4] that Ha_s scales as

$$Ha_s \propto Re^{1/4}. \tag{9}$$

This scaling follows from the integral magnetic and viscous force balance in the almost rigidly rotating regime (at $Ha \ll Ha_s$) and it is confirmed numerically [4]. For $Ha \gg Ha_s$ the flow develops characteristic magnetic boundary layers of $O(Ha^{-1})$ thickness at the field facing part of the side wall. Boundary layers of $O(Ha^{-1/2})$ thickness form at the field-parallel walls [4].

Figure 1 shows the critical Grashof number as a function of HMF strength in either rotating or stationary container. In both cases the strong HMF ($Ha \gg Ha_s$)

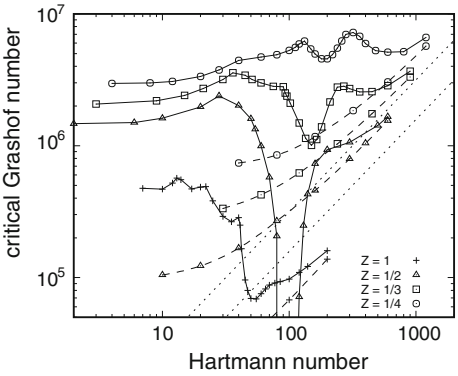

Fig. 1 The critical temperature difference versus the HMF strength in cylinders of variable height as given in the legend. The rotation rate is $Re = 2{,}000$ (*solid lines*) or $Re = 0$ (*dashed lines*). *Dotted lines* display the asymptotic high field results in a channel [1] for $Z = 1/2$ and 1/4

results converged with each other and agreed reasonably with the instability results in a rectangular channel [1].

In case of a rotating container there was a range of intermediate Hartmann numbers around $Ha \approx Ha_s$ where the HMF had a destabilizing action. An extreme manifestation of it caused instability of an isothermal flow ($Z = 1/2$, $Ha \in [86 : 115]$). Figure 2 explores this phenomenon for variable Z at $Re = 2000$. An instability 'island' is formed in the parameter space as shown in Fig. 3a. It is centered around $Z = 0.6$ and $Ha \approx 50/Z$. The critical mode had a form of the field-aligned roll slightly tilted by the rotation (Fig. 3b).

The leading eigenvalue had zero imaginary part in all cases displayed in Figs. 2 and 3. That means 'exchange of stabilities' where the basic stationary solution is replaced with another stationary solution. The new solution had a broken vertical symmetry. In contrary to the basic solution it had non-zero electric potential drop along the axis that may be easily detected experimentally. Expectedly, this new solution experiences secondary instability at some higher rotation rate. However, we observed no signs of such instability for rotation rates as high as $Re = 10^4$ ($Z = 0.625$) and the corresponding $Ha_s = 5^{1/4}80 \approx 120$ evaluated from (9).

Although the snapshot method [3] is developed for complex matrices it is not restricted to spectral solutions. To demonstrate that, we applied it with real-valued

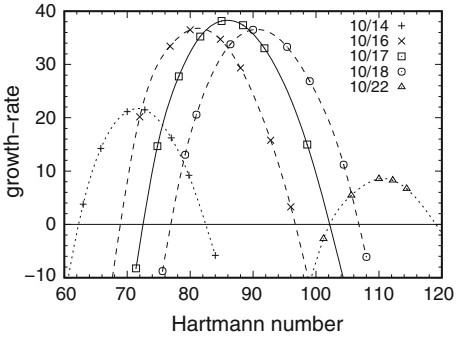

Fig. 2 Growth-rate of the most unstable mode versus Ha at a fixed $Re = 2{,}000$, $Gr = 0$ and aspect ratio Z indicated in the legend

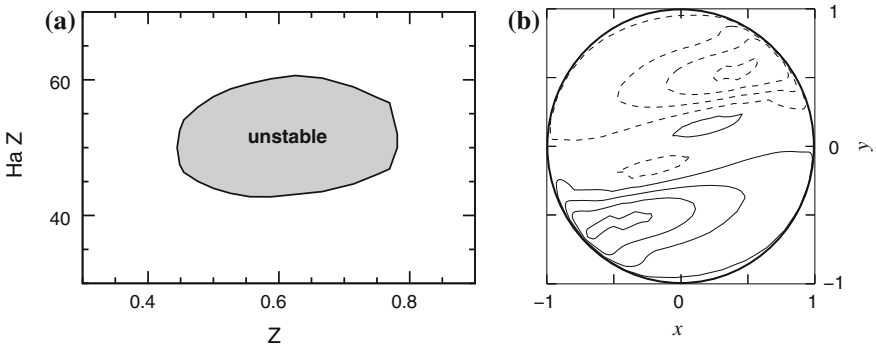

Fig. 3 **a** Isothermal instability island at $Re = 2{,}000$; **b** axial velocity of the critical isothermal mode at the mid-plane for $Re = 2{,}000$, $Z = 0.625$. *Dashed lines* correspond to negative values

snapshots representing our solution on the collocation mesh. The corresponding critical Grashof number and absolute value of frequency of instability stayed unchanged in limits of accuracy of the method. The eigenvalues with non-zero imaginary part appeared in conjugate couples that practically means loss of the sign of the frequency. This sign describes direction of propagation of the mode (direction of the rotation in our case).

6 Summary

The snapshot method [3] with DNS is an efficient and powerful tool for the linear instability analysis for complex flows. It may be easily implemented and it requires little additional numerical effort. The basic solution may be retained in the DNS-produced snapshots. It appears as a zero eigenvalue mode in the decomposition which is easily recognized. The method is not restricted to spectral solutions that provide complex input. Only the sign of frequency is lost if nodal values of the flow are used as the input.

The rotating Rayleigh-Bénard cell is first stabilized by the horizontal magnetic field at $Ha \ll Ha_s$. At $Ha \approx Ha_s$ the instability is promoted causing even the isothermal flow onset in a range of aspect ratios around $Z \approx 0.6$ and $Ha \approx 50/Z$ for rotation rates $Re > 1{,}800$. This instability leads to a new stationary solution which remains stable for rotation rates as high as $Re \approx 10^4$. High performance computing is likely required to observe the secondary instability.

References

1. Burr, U., Müller, U.: Rayleigh-Bénard convection in liquid metal layers under the influence of a horizontal magnetic field. J. Fluid Mech. **453**, 345–369 (2002)
2. Canuto, C., Hussaini, M.Y., Quarteroni, A., Zang, T.A.: Spectral methods in fluid dynamics. Springer, Berlin (1988)
3. Goldhirsch, I., Orszag, S.A., Maulik, B.K.: An efficient method for computing leading eigenvalues and eigenvectors of large asymmetric matrices. J. Sci. Comput. **2**, 33–58 (1987)
4. Grants, I., Gerbeth, G.: Rayleigh-Bénard instability of Czochralski configuration in a transverse magnetic field. J. Cryst. Growth **358**, 43–50 (2012)
5. Press, W.H., Teukolsky, S.A., Vetterling, W.T., Flannery, B.P.: Numerical recipes. Cambridge University Press, Cambridge (1992)

Numerical Study of Turbulent Pipe Flow with Transverse Magnetic Field Using a Spectral/Finite Element Solver

X. Dechamps, M. Rasquin, K.E. Jansen and G. Degrez

1 Introduction

The study of duct flow for electrically conducting liquid metal fluids exposed to an externally applied magnetic field is acknowledged to be a good approach for a better understanding of the fundamental properties of magnetohydrodynamic (MHD) turbulence. This fundamental type of flow is frequent in industrial processes such as the casting/stirring of steel or the Czochralski process used to obtain single crystals of semiconductors [1, 2].

The experimental study of the MHD pipe flow began in 1937 with Hartmann [3]. In the 60s–70s, numerous experiments [4–6] were conducted on several configurations (non conductive wall or with finite conductivity—transverse or longitudinal magnetic field). In the late 90s and early 2000s, numerical results began to appear [7–9]. Finally, in 2008, additional experimental results were obtained [10] for a Reynolds number $Re_b = 11{,}300$. In contrast, much more results were obtained in the case of a flow inside a rectangular/square duct. This is linked with the greater choice of the electrical conductivity of the walls. A combination of electrically conducting/non-conducting walls puts forward instability processes that do not occur (or not so easily) in the case of the pipe flow.

X. Dechamps (✉) · G. Degrez
Department of Aero-Thermo-Mechanics, Université Libre de Bruxelles, Brussels, Belgium
e-mail: xavier.dechamps@ulb.ac.be

G. Degrez
e-mail: gerard.degrez@ulb.ac.be

M. Rasquin
Argonne Leadership Computing Facility, Argonne National Laboratory, Argonne, IL, USA
e-mail: mrasquin@alcf.anl.gov

K.E. Jansen
Department of Aerospace Engineering, University of Colorado Boulder, Boulder, CO, USA
e-mail: jansenke@colorado.edu

J. Fröhlich et al. (eds.), *Direct and Large-Eddy Simulation IX*,
ERCOFTAC Series 20, DOI 10.1007/978-3-319-14448-1_72

In this work, additional numerical results are analysed to improve the knowledge of MHD turbulence inside circular pipes subject to an external transverse uniform magnetic field. The following sections will detail the physical model, its numerical representation as well as the numerical results obtained for a Reynolds number $Re_b = 8{,}000$ and a Hartmann number $0 \leq Ha \leq 100$.

2 Physical Model

This work is concerned with the unsteady and incompressible flow of an electrically conducting and Newtonian fluid (i.e. a liquid metal) inside a pipe of circular cross-section and diameter $d = 2R$ (see Fig. 1). An external, constant and uniform magnetic field $\mathbf{B} = B\,\mathbf{e}_x$ is applied along the transverse direction x ($\theta = 0$). The wall of the cylinder is solid, smooth and electrically insulating. A periodicity is imposed between the inlet ($z = 0$) and the outlet ($z = L_z$) of the domain.

Under the flow conditions specified later, we observe that the magnetic Reynolds number $Re_m = \mu_0 \sigma U_b d \ll 1$ where μ_0 denotes the magnetic permeability of vacuum, σ the electrical conductivity of the fluid and U_b the mean streamwise velocity. Under this condition, the inductionless form of the MHD equations described by the set of Eqs. (1)–(4) can be used. The validity of this model has been confirmed in numerous works (see e.g. [2, 11]). Additionally, numerical results of Knaepen et al. [12] show that no significant deviations are observed for $Re_m \leq 1$ between the inductionless model and the full set of MHD equations. In the set of inductionless MHD equations, ρ is the density, ν the kinematic viscosity and σ the electrical conductivity of the fluid. The unknowns of the problem are the components of the velocity field $\mathbf{u} = (u_z, u_r, u_\theta)$, pressure p and the scalar potential ϕ. This set of equations is accompanied by boundary conditions on the velocity field $\mathbf{u}(z, r = R, \theta) = 0$ and $\frac{\partial \phi}{\partial n}(z, r = R, \theta) = 0$ where n stands for the external normal to the wall. Regularity conditions are imposed on the axis for velocity, pressure and electric potential.

$$R_{cont} = \nabla \cdot \mathbf{u} = 0 \tag{1}$$

$$\mathbf{R}_{mom} = \frac{\partial \mathbf{u}}{\partial t} + (\mathbf{u} \cdot \nabla)\,\mathbf{u} + \nabla p - \nu \nabla^2 \mathbf{u} - \frac{\mathbf{J} \times \mathbf{B}}{\rho} = 0 \tag{2}$$

$$R_{charge} = \nabla^2 \phi - \nabla \cdot (\mathbf{u} \times \mathbf{B}) = 0 \tag{3}$$

$$\mathbf{J} = \sigma\,(-\nabla \phi + (\mathbf{u} \times \mathbf{B})) \tag{4}$$

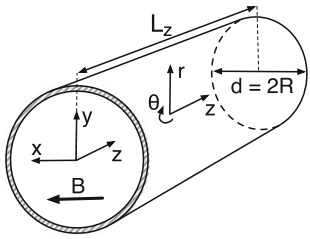

Fig. 1 Geometry of the domain and definition of the axes

3 Numerical Method

The numerical solver is an extension to liquid metal MHD problems of the in-house hybrid Spectral/Finite Element Large-Eddy Simulation (SFELES). The main assumption in SFELES relies on a direction of periodicity in the flow and can simulate 3D flows associated with complex planar or axisymmetric geometries. In the present case, the cylindrical coordinates are used. The spatial discretization in SFELES is split into two different methods. First, a stabilized finite element method (linear interpolation on triangular elements FEM) is used in 2D meridional planes. The stabilization of the 2D finite element method is ensured by the traditional Streamline Upwind Petrov-Galerkin (SUPG) and Pressure-Stabilized Petrov-Galerkin (PSPG) formulations. Then, a collocated spectral method describes the problem in the azimuthal direction. This means that the unknowns $\mathbf{q} = \{u_z, u_r, u_\theta, p, \phi\}$ are written under the following form

$$\mathbf{q}(z, r, \theta, t) = \frac{1}{N} \sum_{k=-\frac{N}{2}+1}^{\frac{N}{2}-1} \hat{\mathbf{q}}_k(z, r, t)\, e^{Ik\frac{2\pi}{\theta_{max}}\theta} \tag{5}$$

where I is the imaginary number, k is the wave number and θ_{max} is the maximal azimuthal coordinate of the domain in the direction of periodicity. Moreover, because of the real-valued nature of the flow, the mathematical property $\hat{q}_{-k} = [q]_k^*$ is used and divides by two the number of Fourier modes to be solved. The non-linear terms are treated through a pseudo-spectral approach with the 2/3 dealiasing rule. This leads to a decoupling of the discretized equations for each Fourier mode $\hat{\mathbf{q}}_k(z, r, t)$ in Eq. (5). For each time step, a set of independent 2D linear systems are solved in Fourier space. The time integration is split into 2 different schemes: an implicit one (Crank-Nicolson) for all the linear terms and an explicit one (Adams-Bashforth or Runge-Kutta) for the right-hand side coupling terms. The increment in time of the solution $\delta\hat{\mathbf{q}}_k = \hat{\mathbf{q}}_k^{n+1} - \hat{\mathbf{q}}_k^n$ is then computed during each time step by solving

$$\underbrace{\left(\frac{M_k}{\Delta t} + \frac{L_k}{2}\right)}_{A_k} \delta\hat{\mathbf{q}}_k = \underbrace{-L_k\hat{\mathbf{q}}_k^n - \sum_{s=1}^{S-1} \beta_s \hat{C}_k^s}_{b_k} \tag{6}$$

where M_k, L_k and $\hat{C}_k$ are respectively the matrices resulting from the time-derivative dependent terms, the linear terms and the vectors resulting from the pseudo-spectral approach of all the non-linear terms and β_s are coefficients specific to the explicit temporal integration scheme.

4 Numerical Results

This section develops the numerical results obtained for a hydrodynamic Reynolds number $Re_b = u_b\, d/\nu = 8{,}000$ based on bulk velocity and pipe diameter and a Hartmann number $0 \leq Ha = BR\sqrt{\sigma/\rho\nu} \leq 100$. A forcing term in the z-momentum equation ensures a constant Re_b. The length of the pipe was set to $L_z = 5d$. The simulation parameters are reported in Table 1. All the following results were obtained by averaging in time over 100 convection time units and along the axial direction.

The mean axial velocity component u_z profiles (adimensionalized by the value on the axis) are represented in Fig. 2 as a function of the radial coordinate (adimensionalized by the radius of the pipe). Turbulent ($Ha \leq 10$) and laminar ($Ha \geq 15$) regimes are clearly distinct. The case $Ha = 10$ is slightly less rounded than the purely hydrodynamic flow. In the direction parallel to **B**, the laminar velocity profiles are flattened and the typical size of the Hartmann layer scales like $\mathcal{O}(Ha^{-1})$. In the direction perpendicular to **B**, the Hartmann number do not influence as much the velocity profiles as in the previous direction. The root-mean square of the axial velocity component $u^+_{z,rms}$ are represented in Fig. 3. The profiles are adimensionalized by the corresponding friction velocity u_τ for each Hartmann number.

Table 1 Mean flow configurations for the numerical simulations

Ha$= BR\sqrt{\sigma/\rho\nu}$ [a]	0	5	10	15	20	30	100
Re$_b = u_b\, d/\nu$ [b]	8,000	8,000	8,000	8,000	8,000	8,000	8,000
Re$_\tau = u_\tau\, d/\nu$ [b]	517	510.5	494.8	421	477.2	572.7	1015.7

[a] Hartmann number with B the applied magnetic field, R the radius of the pipe, σ the electrical conductivity of the fluid, ρ the density of the fluid and ν the kinematic viscosity of the fluid.
[b] Hydrodynamic Reynolds numbers with d the diameter of the pipe, u_b the average velocity and u_τ the wall shear velocity defined by the wall shear stress $\tau_w = \rho u_\tau^2$

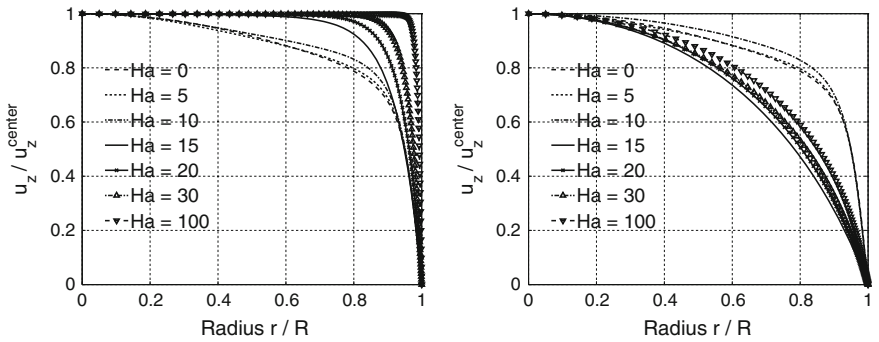

Fig. 2 Average axial velocity profile normalized by the core velocity in a direction parallel (*left*) and perpendicular (*right*) to **B**

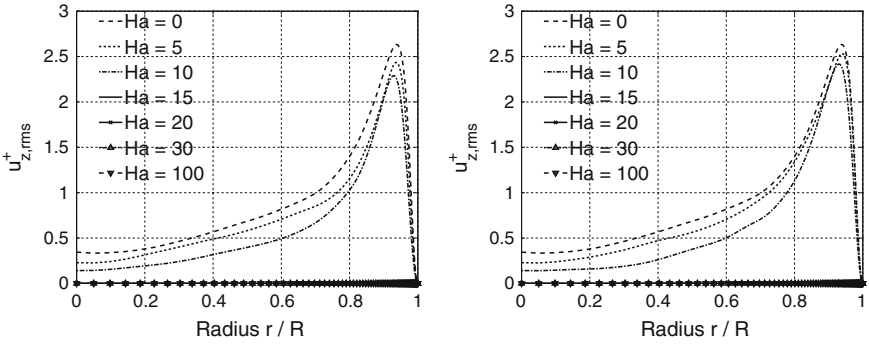

Fig. 3 Axial velocity fluctuations in a direction parallel (*left*) and perpendicular (*right*) to **B**. The results were adimensionalized by the corresponding friction velocity u_τ

The damping effect of the magnetic field on turbulence is clearly visible. This attenuation of the fluctuations is more noticeable in the direction parallel to the magnetic field. One main advantage of the FEM is the ability to compute *a posteriori* the energy budget. The viscous and Joule dissipations are shown respectively in Figs. 4 and 5. A general observation is the appearance of peaks of dissipation in the Hartmann layers. These peaks are more important for high Hartmann numbers because of the narrowing Hartmann layer. In contrast, the evolution of the dissipations is smooth in the Roberts layers. The global skin friction coefficient $C_f = \tau_w/\rho u_b^2/2$ is shown in Fig. 6 as a function of the ratio Ha/Re_b. A very good agreement is observed between the present results and the other numerical / experimental values obtained for other

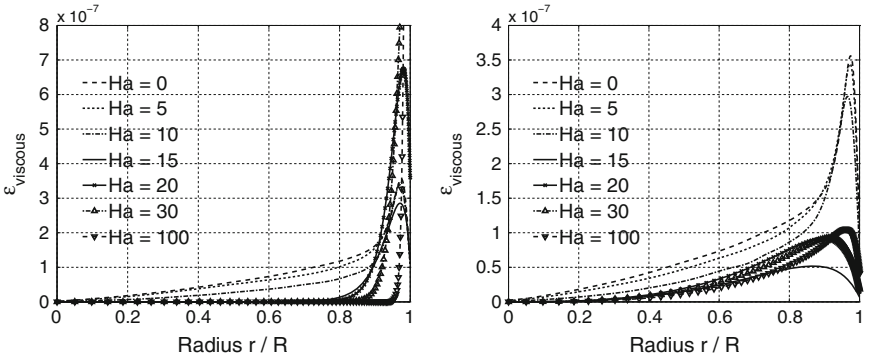

Fig. 4 Average viscous dissipation in a direction parallel (*left*) and perpendicular (*right*) to **B**

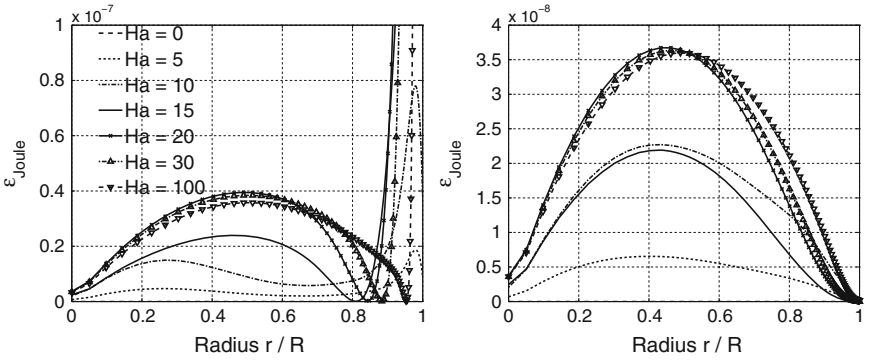

Fig. 5 Average Joule dissipation in a direction parallel (*left*) and perpendicular (*right*) to **B**

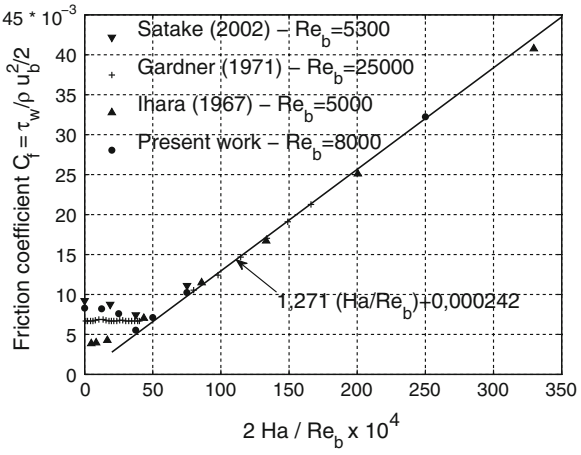

Fig. 6 Skin friction coefficient $C_f = \tau_w/\rho u_b^2/2$ as a function of the ratio Ha/Re

Reynolds numbers. The laminar results fits with a line of higher slope than the theoretical value of $3\pi/8$ found by Shercliff. This discrepancy between theoretical and numerical/experimental slope was also observed by Loeffler et al. [5, 6].

References

1. Davidson, P.: Ann. Rev. Fluid Mech. **31**(1), 273–300 (1999)
2. Davidson, P.: An introduction to Magnetohydrodynamics. Cambridge University Press, Cambridge (2001)
3. Hartmann, J.: Det Kongelige Danske Videnskabernes Selskab. Mathematisk-Fysiske Medd. **XV**(6),1–28 (1937)
4. Ihara, S., Tajima, K., Matsushima, A.: J. Appl. Mech. **34**(1), 29–36 (1967)
5. Loeffler, A., Maciulaitis, A., Hoff, M.: Phys. Fluids **12**, 2445 (1969)
6. Gardner, R., Lykoudis, P.: J. Fluid Mech. **47**(1), 737–764 (1971)

7. Ji, H., Gardner, R.: Int. J. Heat Mass Transfer **40**(8), 1839–1851 (1997)
8. Barrett, K.: Int. J. Numer. Methods Eng. **50**(8), 1893–1906 (2001)
9. Satake, S., Kunugi, T., Smolentsev, S.: JTurb **3**(1), 020 (2002)
10. Takeuchi, J., Satake, S., Morley, N., Kunugi, T., Yokomine, T., Abdou, M.: Fusion Eng. Des. **83**(7–9), 1082–1086 (2008)
11. Müller, U., Bühler, U.: Magnetofluiddynamics in Channels and Containers. Springer, Berlin (2001)
12. Knaepen, B., Kassinos, S., Carati, D.: J. Fluid Mech. **513**, 199–220 (2004)

On Turbulence Generation and Mixing in the Wake of Magnetic Obstacles: A DNS Study

Saša Kenjereš

1 Introduction

The flow of electrically conducting fluids with an internal blockage, can be divided into two major categories: flows past solid internal obstacles (bluff bodies) subjected to an external uniform magnetic field, and flows locally influenced by imposed steady and non-uniform magnetic fields (so called magnetic obstacles), [1–3]. The aim of the present work is to study the instantaneous and long-term averaged flow and heat transfer features of a three-dimensional MHD flow past different magnetic dipole configurations in a channel with electrically and thermally insulated horizontal walls, over a range of working parameters. These include different combinations of magnetic dipoles (one-, two- or three-permanent magnets), and different values of the electromagnetic interaction parameter ($0 \leq \mathrm{N} \leq 50$), but a fixed inflow (laminar) condition of $\mathrm{Re} = 10^3$.

2 Mathematical Formulation

The motion and heat transfer of an electrically conducting fluid subjected to an external magnetic field can be described by conservation equations of mass, momentum, energy, electric current density and magnetic field, as follows:

$$\nabla \cdot \mathbf{v} = 0, \quad \nabla \cdot \mathbf{b} = 0, \quad \nabla \cdot \mathbf{j} = 0, \tag{1}$$

S. Kenjereš (✉)
Transport Phenomena Section, Department of Chemical Engineering,
Faculty of Applied Sciences and J.M. Burgers Centre for Fluid Dynamics,
Delft University of Technology, Julianalaan 136, 2628 BL Delft, The Netherlands
e-mail: s.kenjeres@tudelft.nl

J. Fröhlich et al. (eds.), *Direct and Large-Eddy Simulation IX*,
ERCOFTAC Series 20, DOI 10.1007/978-3-319-14448-1_73

$$\rho\left[\frac{\partial \mathbf{v}}{\partial t}+(\mathbf{v}\cdot\nabla)\,\mathbf{v}\right]=-\nabla p+\mu\nabla^2\mathbf{v}+\mathbf{j}\times\mathbf{b}, \tag{2}$$

$$\mathbf{j}=\sigma\left(-\nabla\phi+\mathbf{v}\times\mathbf{b}\right), \quad \nabla^2\phi=\nabla\cdot(\mathbf{v}\times\mathbf{b}), \tag{3}$$

$$\rho\left[\frac{\partial \theta}{\partial t}+(\mathbf{v}\cdot\nabla)\,\theta\right]=a\nabla^2\theta, \tag{4}$$

where $\mathbf{v}$ is the velocity, $\mathbf{b}$ is the magnetic field, $\mathbf{j}$ is the electric current density, p is the pressure, ϕ is the electric potential, θ the temperature. The fluid properties, the density (ρ), the dynamic viscosity (μ), the thermal diffusivity (a), the electric conductivity (σ), are all assumed to be constant. The last term in the momentum equation (Eq. 2) represents the Lorentz force ($\mathbf{f^L}=\mathbf{j}\times\mathbf{b}$). The electric current density equation is obtained from Ohm's Law in the moving frame of reference, Eq. 3. Taking the divergence of Ohm's Law, the equation for electric potential is obtained, Eq. 3. In the thermal energy equation, Eq. 4, the viscous dissipation and Joule heating contributions are neglected. Note that there is the one-way coupling between the velocity and the imposed magnetic field (i.e. the imposed magnetic field spatial distributions are not influenced by changes in the velocity field). In contrast to that, there is the two-way coupling between the velocity and electric potential, which gives a spatial and temporal variation of the generated Lorentz force.

The typical non-dimensional parameters that fully determine the flow, heat transfer and electromagnetic interactions are the Reynolds number ($\mathrm{Re}=\mathrm{V_0H_0}/\nu$), the Prandtl number ($\mathrm{Pr}=\nu/a$) and the interaction parameter ($\mathrm{N}=\dfrac{\sigma|b_0|^2\mathrm{H_0}}{\rho\mathrm{V_0}}$), where $|b_0|$ is the magnetic dipole strength. Note that the Hartmann number can be easily obtained as $\mathrm{Ha}=(\mathrm{Re\ N})^{1/2}$.

3 Numerical Method

The system of equations Eqs. 1–4 is discretised by using a finite volume Navier-Stokes solver for general non-orthogonal structured geometries. The Cartesian vector and tensor components in the non-staggered grid arrangements are applied, i.e. all variables are located in the centers of hexahedral control volumes (CVs). The SIMPLE algorithm is used for coupling between velocity and pressure fields. The diffusive terms of both momentum and thermal energy equations are discretised by a second-order central differencing scheme (CDS). This scheme is also used for the convective terms of the momentum equation. The convective term of the thermal energy equation is discretised by a total-variation-diminishing scheme (TVD)

with the min-mod flux limiter. The time integration is performed by a fully-implicit second-order scheme that employs three consecutive time steps.

4 Results

4.1 The Setup, Initial and Boundary Conditions

We investigated a channel flow configuration, with a specific aspect ratio of $L : H : D = 1 : 0.02 : 0.3$, where L is length (in the x-direction), H is the vertical distance between walls (in the z-direction), and, D is depth (in the y-direction). The fully developed parabolic inlet is imposed in the vertical inlet plane (x $= 0$), with characteristic Reynolds number of Re $= 10^3$. The horizontal and vertical walls are assumed to be both electrically and thermally insulated. The inlet temperature distribution obeys a delta distribution, i.e. $\theta^* = 0$, for $0 \leq y < (D/2 - D_\theta/2)$ and $(D/2 + D_\theta/2) < y \leq D$, and $\theta^* = 1$ for $(D/2 - D_\theta/2) \leq y \leq (D/2 + D_\theta)/2)$. Here $\theta^* = \theta/\Delta\theta = 1$, and $D_\theta = 0.04$. The temperature is assumed to be a passive scalar. The convective outlet boundary conditions are applied for all variables at the exit of the flow domain. Along the side boundaries, a free-slip boundary condition is applied for the velocity and the zero-gradient boundary conditions for the electric potential and temperature. Different combinations of magnetic dipoles arrangements that include a single-, two- and three-magnetic dipoles cases are investigated. The numerical mesh is designed in a such way that the magnetic dipoles and the near-wall regions are very well resolved (up to the Kolmogorov length-scales). In total, approximately 7.5×10^6 control volumes are employed in the entire simulation domain.

The galinstan (eutectic alloy of Gallium) is selected as a working fluid, because of its high electric conductivity ($\sigma = 3.4 \times 10^6$ S/m) and its potentials to be used in experimental investigations. It is also a low Prandt fluid with Pr $= 0.022$. The typical values of the non-dimensional parameters investigated in this study are Re $= 10^3$, $0 \leq$ N ≤ 50 and $0 \leq$ Ha ≤ 225.

4.2 Flow and Heat Transfer

To give an overall impression of the flow and heat transfer for different arrangements of the magnetic-dipoles, the contours of the instantaneous vertical vorticity (ω_z) and of the temperature in the central horizontal plane (z/H $= 0.5$) are shown in Figs. 1 and 2. It can be seen how the incoming laminar flow, starts to be deflected by the locally imposed magnetic field, which generates strong shear and a rapid transition towards the turbulent state takes place, Fig. 1. By shifting the location of the magnetic dipoles, a localized flow acceleration or de-acceleration can be easily achieved,

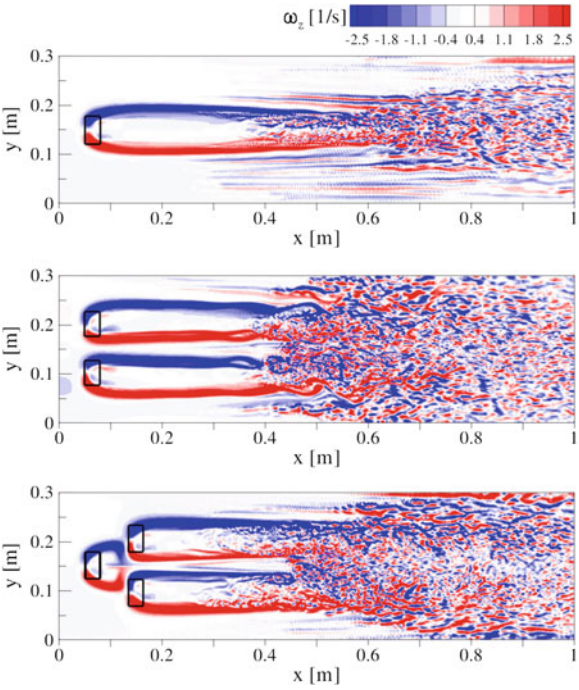

Fig. 1 Contours of the instantaneous vertical vorticity component (ω_z) in the central horizontal plane in a channel flow of a conductor subjected to localized magnetic fields, $\mathrm{Re} = 10^3$, $\mathrm{N} = 10$. The locations of the different magnetic dipoles (permanent magnets) are represented by *black rectangles*

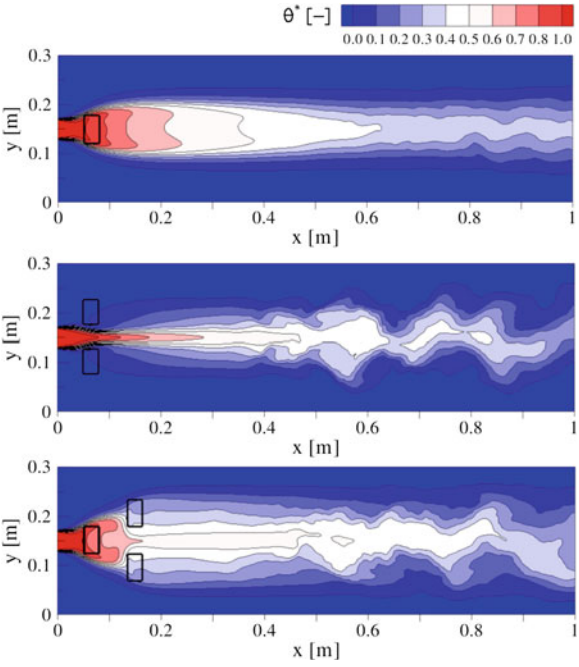

Fig. 2 Same as in Fig. 1, but now contours of the instantaneous passive scalar (temperature)

resulting in even more dramatic turbulent mixing in the wakes. The spanwise spreading of the temperature is illustrated in Fig. 2. It can be seen that the significant changes in the spatial distribution of temperature for different arrangements of the magnetic dipoles are observed. The sequence of events can be listed as follows. The initial deflection (for one- and three-magnetic dipoles) or focusing (for two-magnetic dipoles) of the incoming profiles is clearly observed in the approaching phase. This is then followed by an initialization of the Kelvin-Helmholtz instabilities (as also seen in Fig. 1) and finally, by generation of the distinct vortex-shedding phenomena in the far-wake regions, Fig. 2. The long-term time averaged central profiles of the streamwise velocity and of the turbulence kinetic energy, extracted along the central line of the central horizontal plane (z/H = 0.5), are shown in Fig. 3. The mean streamwise velocity exhibits a full range of different behaviors—from slightly or significantly pronounced recirculative regions, for the one- or three-magnetic dipoles, respectively, to the situation where this recirculation is totally absent (for the two-magnetic obstacles case). Despite the big differences in the streamwise velocity profiles, the turbulence kinetic energy profiles indicate a gradual intensification of the energy of the velocity fluctuations in the far wake regions, confirming that the flow undergoes a transition between the initial laminar and developed turbulence state. Similar conclusions can be derived also from the temperature and its variance profiles, shown in Fig. 4. Despite the fact the temperature is a passive scalar, huge differences between the turbulence kinetic energy and temperature variance profiles are observed. This is consequence of the low Prandtl value. The temporal spectra of the electric potential at characteristic monitoring points along the domain centerline, for a single-magnetic dipole case with N = 5, are shown in Fig. 5. The distinct frequencies can be identi-

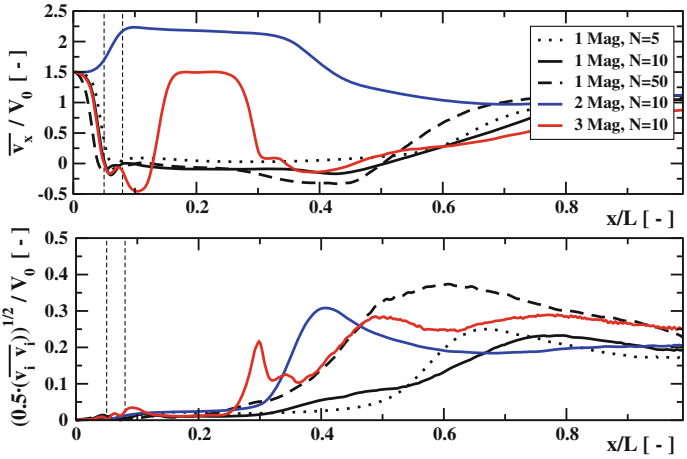

Fig. 3 Profiles of the long-term averaged non-dimensional streamwise velocity ($\overline{v_x}/V_0$) and of the non-dimensional turbulent kinetic energy (TKE) in the central horizontal (z/H = 0.5) plane and along y = 0.15 line for all considered situations

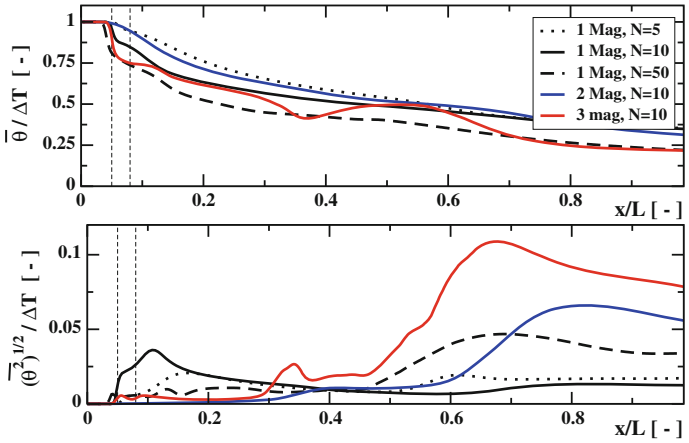

Fig. 4 Same as in the Fig. 3, but now profiles of the non-dimensional temperature and temperature variance

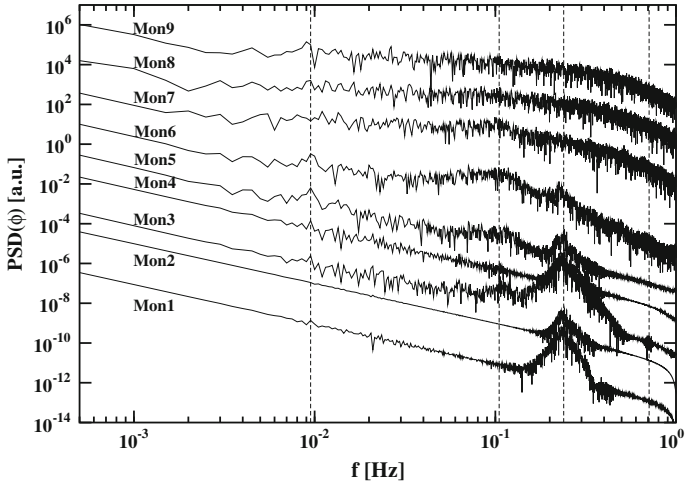

Fig. 5 Temporal spectra of the electric potential at characteristic monitoring locations (*Mon1–Mon9*) along the *central horizontal line* for a single magnet configuration and N = 5. The *vertical dash lines* indicate typical distinct frequencies

fied, confirming the vortex shedding phenomenon in the near-wake of the magnetic obstacle. Farther downstream, the absence of distinct peaks and a smooth spectra portray established turbulent regime.

5 Conclusions

It is demonstrated that application of the localized magnetic fields can be potentially very powerful method for flow and heat transfer control. By tailoring the different arrangements of the magnetic dipoles, significant flow and heat transfer enhancement or suppression can be obtained.

References

1. Cuevas, S., Smolentsev, S., Abdou, M.A.: On the flow past a magnetic obstacle. J. Fluid Mech. **553**, 227–252 (2006)
2. Votyakov, E.V., Kolesnikov, Yu., Andreev, O., Zienicke, E., Thess, A.: Structure of the wake of a magnetic obstacle. Phys. Rev. Lett. **98**(144504), 1–4 (2007)
3. Kenjereš, S., ten Cate, S., Voesenek, C.J.: Vortical structures and turbulent bursts behind magnetic obstacles in transitional flow regimes. Int. J. Heat Fluid Flow **32**(3), 510–528 (2011)

Simulation of Instabilities in Liquid Metal Batteries

N. Weber, V. Galindo, T. Weier, F. Stefani and T. Wondrak

1 Introduction

Liquid metal batteries, i.e. batteries in which both electrodes as well as the electrolyte are in the liquid state (Fig. 1) are usable for grid-scale energy storage and have received considerable attention recently [4, 5]. A current and comprehensive account focusing on their applicability in future large scale storage systems is provided by Bradwell [1, 2], earlier investigations of the technology were oriented on smaller units and thermally regenerative electrochemical systems, see, e.g., [3].

A battery with fully liquid active interior has a number of advantages: when densities are chosen properly, the battery is self-assembling due to stable stratification. Liquid-liquid interfaces allow for very fast kinetics and thereby rapid charging and discharging. Structure-less (liquid) electrodes are insusceptible to aging providing nearly unlimited cyclability. Liquid metal batteries may be built from abundant and cheap feed-stock [1, 2]. NaS and ZEBRA batteries share several of the advantages mentioned above, but require large initial investments due to their complicated construction, which is mainly dictated by the fragile ceramic electrolyte. In any case, scalability is a key enabler for cheap grid storage and ease of scale-up is one of the main underlying assumptions of liquid metal battery development. However, large electrode areas and high current densities imply large total current per cell and it is here where Magnetohydrodynamics (MHD) comes into play.

Aluminum reduction cells—which are often mentioned to have sparked the idea for large scale energy storage using liquid metals, see, e.g., [1, 2]—suffer from an interfacial instability which puts a constraint on the minimum electrolyte thickness. While this limitation has also to be considered, our focus here is on another kind of instability, which limits the upper size of liquid metal batteries and is known in astrophysics under the label Tayler instability (TI) [8]. In our context, the TI is a kink-type

N. Weber (✉) · V. Galindo · T. Weier · F. Stefani · T. Wondrak
Department of Magnetohydrodynamics, Helmholtz-Zentrum Dresden-Rossendorf, Dresden, Germany
e-mail: norbert.weber@hzdr.de

J. Fröhlich et al. (eds.), *Direct and Large-Eddy Simulation IX*,
ERCOFTAC Series 20, DOI 10.1007/978-3-319-14448-1_74

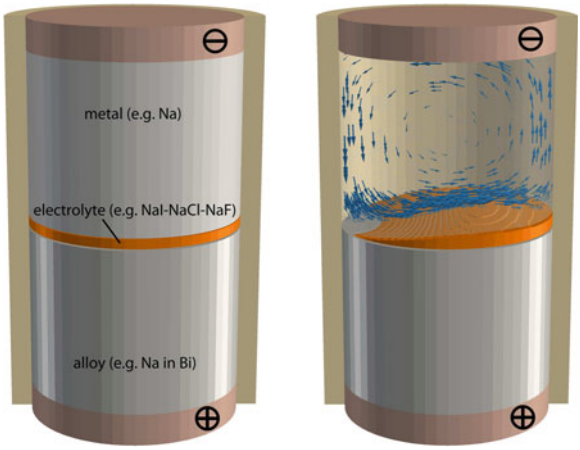

Fig. 1 Sketch of a liquid metal battery with typical interior (*left*) and the fluid flow induced by the TI. The TI will appear first in the better conducting fluid, which is the anode. A slow flow may increase reaction rates, while strong flows may short-circuit the battery

(i.e. non-axisymmetric) instability that occurs if the current through a column of liquid metal exceeds some critical value in the order of kA, depending on the material properties. If this current threshold is exceeded, the TI leads to some stirring of the battery interior (Fig. 1) which possibly could destroy the stable density stratification and short-circuit the electrodes. Due to its potentially dramatic consequences, the TI should definitely be avoided during liquid metal battery operation. Numerical simulation of the TI in incompressible fluids was already carried out at Leibniz-Institut für Astrophysik Potsdam (AIP) [6], but the model can not reach the low magnetic Prandtl numbers typical for liquid metals. To allow a comprehensive analysis of critical currents and transient effects of the TI in liquid metal batteries, a 3D MHD solver was developed [9]. Results are compared with experimental data [7]. In this paper, the focus will be on the implementation in the open CFD library OpenFOAM®.

2 Governing Equations

In this section we outline the governing equations of the model as described in more detail in [9]. With the fluid initially at rest, the only possible choice for a characteristic velocity scale is the Alfvén velocity $v_A = B_0(\mu_0\rho)^{1/2}$, which is proportional to the magnetic induction B_0 caused by the imposed battery current. In a non-dimensional form, with L, v_A, B_0, L/v_A, ρv_A^2 and $\sigma v_A B_0$ being the distance, velocity, magnetic induction, time, pressure and current density scale, respectively, we obtain the Navier-Stokes equation (NSE)

$$\frac{\partial \mathbf{u}}{\partial t} + (\mathbf{u}\cdot\nabla)\,\mathbf{u} = -\nabla p + \frac{1}{Re_A}\nabla^2\mathbf{u} + \frac{Ha^2}{Re_A}\mathbf{J}\times\mathbf{B} \tag{1}$$

describing the fluid flow, where L is a characteristic length, ρ is the density, ν is the dynamic viscosity, σ is the electric conductivity, μ_0 is the vacuum permeability, $Re_A = v_A L/\nu$ and $Ha = B_0 L\sqrt{\sigma/(\rho\nu)}$ is the Hartmann number.

The Lorentz force $\mathbf{f}_L = \mathbf{J} \times \mathbf{B}$ is the source of the flow. The (high) current density $\mathbf{J}_0$, applied to, or provided by the battery induces a magnetic field $\mathbf{B}_0$. The fluid flow itself induces a (small) current density $\mathbf{j}$ and thus a (small) magnetic field $\mathbf{b}$, neither of which can be neglected since they are multiplied with a large current or magnetic field: $\mathbf{f}_L = (\mathbf{J}_0+\mathbf{j}) \times (\mathbf{B}_0+\mathbf{b})$. Using Ohm's law $\mathbf{j} = (-\nabla\varphi+\mathbf{u}\times\mathbf{B})$ and Kirchhoff's circuit law $\nabla \cdot \mathbf{J} = 0$, with $\varphi = \phi - J_0\, z$ as the perturbed electric potential (scale $v_A B_0 L$), we obtain

$$\nabla^2\varphi = \nabla \cdot (\mathbf{u} \times \mathbf{B})\,. \tag{2}$$

This Poisson equation is—in addition to the NSE—the second equation which has to be solved. Knowing the induced current, we can now compute the induced magnetic field via Biot-Savart's law

$$\mathbf{b}(\mathbf{r}) = \frac{1}{4\pi} \int dV' \, \frac{\mathbf{j}(\mathbf{r}') \times (\mathbf{r} - \mathbf{r}')}{|\mathbf{r} - \mathbf{r}'|^3}. \tag{3}$$

For a given grid cell, the currents at all other cells have to be added to obtain the induced field. This step is the most time consuming calculation in our code.

3 Numerical Implementation

We implement the model in the open source CFD library OpenFOAM®, based on the solver `pimpleFoam` for incompressible flows. We do transient simulations, using the PISO algorithm, together with Rhie-Chow interpolation for solving the NSE. Before entering the main calculation loop, we define additional fields and compute the static magnetic field $\mathbf{B}_0$ in `createFields.H`. For each iteration, we calculate the time step, based on an appropriated Courant number (see bellow), followed by the PISO predictor and corrector step. With the (not yet correct) velocity we compute the current density $\mathbf{j} = \mathbf{u} \times \mathbf{B}$ on the cell faces and solve the Poisson equation for the electric potential, in close analogy to the pressure corrector step of the PISO algorithm. We update the current density and compute Biot-Savart's integral.

As mentioned above, the Alfvén velocity is the characteristic velocity scale of our problem. With the latter, we compute a new defined Alfvén Courant number, in analogy to the hydrodynamic Courant number, defined in `CourantNo.H`. The Alfvén Courant number is typically more than 100 times higher than the hydrodynamic one. Finally, without losing accuracy, the Alfvén Courant number can be chosen slightly greater than one. The resulting error is also discussed in [9].

We split the Lorentz force into a velocity dependent and an independent part. We include the first part in `UEqn`, while we interpolate and reconstruct the latter one—together with the pressure gradient—in the predictor step of the PISO algorithm.

The goal of this approach is to avoid fluctuations due to strong body forces or pressure gradients. It was implemented e.g. in `buoyantBoussinesqPimpleFoam` as proposed by Zhang and Zhao [10]. In the corrector step, the velocity-independent Lorentz force is interpolated to the cell faces and added to the velocity flux term.

The most time consuming calculation is the Biot-Savart integral. For the MPI parallelisation of Biot-Savart's law, we use the UPstream library of OpenFOAM®. Each processor has to compute a complete b-field, but only with a local current field. At the end, these fields are exchanged and summed up by the master processor. In the case, that the number of cells treated by each processor is not the same, the number of cells is exchanged to reserve the appropriate memory. The Biot-Savart computation is carried out every nth time step, producing a small error as described in [9].

Besides of the MPI parallelisation of Biot-Savart's law, we implemented also the computation on a separate mesh. While the NSE should be solved on a very fine grid, Biot-Savart's law may be computed on a much coarser mesh (cell length / $L \approx 0.06$), without significant loss of information. For the current we use only the fine mesh and sum up it's contribution to the coarse b-mesh. Finally, the coarse b-mesh is interpolated to a fine b-mesh with the method `interpolate` of `meshToMesh.H`. We obtained the best results with simple mapping of the values. An interpolation smoothed the b-field, which resulted in lower growth rates of the TI.

4 Error Estimation

We do simulations in a cuboid geometry with the apect ratio of $H/(2L) = 1.25$. Figure 2 shows the typical growth behaviour of the TI. Exceeding the critical current, the TI will grow exponentially until reaching saturation. Regarding liquid metal

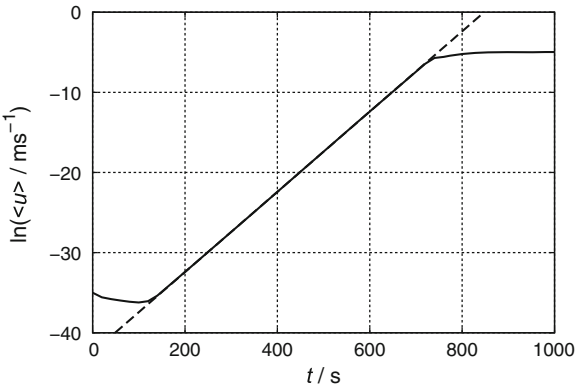

Fig. 2 Exceeding the critical current I_{cr}, the TI develops an eigenfield, which grows exponentially for a few minutes until reaching saturation. The growth rate of the TI is represented by the slope of the *black line*

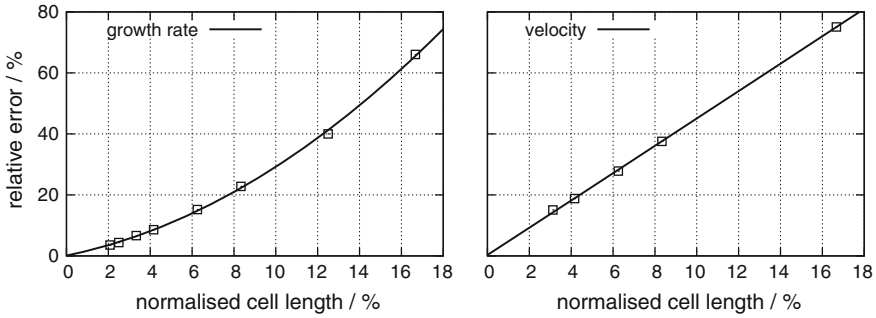

Fig. 3 Refining the calculation grid, the growth rate of the TI as well as the velocities increase. The best estimated growth rate and saturated velocity is Richardson extrapolated from the simulation results. Based on that value, the relative error for different meshes is computed (growth rate *left*, saturated velocity *right*)

batteries, the most important errors are those of the growth rate and the saturated mean flow velocity. Besides of time and Biot-Savart's calculation step, the largest error will be induced by the finite grid [9], which we refine as many times as possible and do a Richardson extrapolation to obtain the best estimated value. We use this value to compute the relative error for different meshes. Computing on an Intel® quad core processor, Fig. 3 gives an idea of possible mesh refinement. Of course, the determination of growth rates takes less time than those of the mean velocities at the saturated state and depends also on the applied current.

5 Results

In the following we will show some results of the simulation corresponding to the geometry used in an experimental setup, conducted by Seilmayer et al. [7]. To a vertical tube ($d = 100\,\text{mm}$, $h = 750\,\text{mm}$), filled with the eutectic GaInSn ($\sigma = 3.29 \cdot 10^6$ S/m, $\rho = 6403$ kg/m^3, $\eta = 3.4 \cdot 10^{-7}$ m^2/s), a current is applied between top and bottom. The growth rate of the magnetic field b_z, induced by the TI, is measured, for which we obtain a very good agreement with the simulation (Fig. 4). The simulated spatial wave length of the convection cells ($\lambda = 121$ mm) matches well the theoretical value of $\lambda = 127$ mm for the infinite cylinder (Fig. 5).

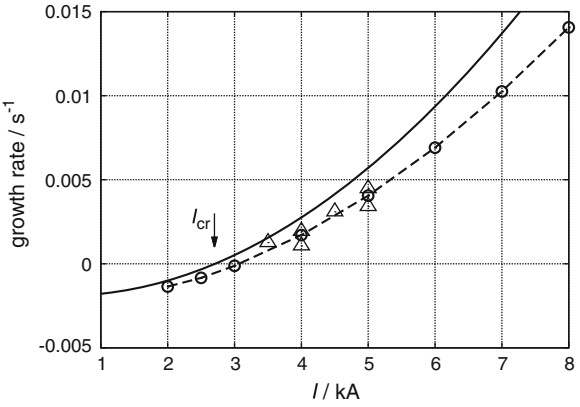

Fig. 4 The figure shows the growth rate as measured by Seilmayer et al. [7] (*triangles*), the values for the infinite long *cylinder* [6] (*black line*) and the simulated ones. Our values (for the finite *cylinder*) fit very well the experimental data

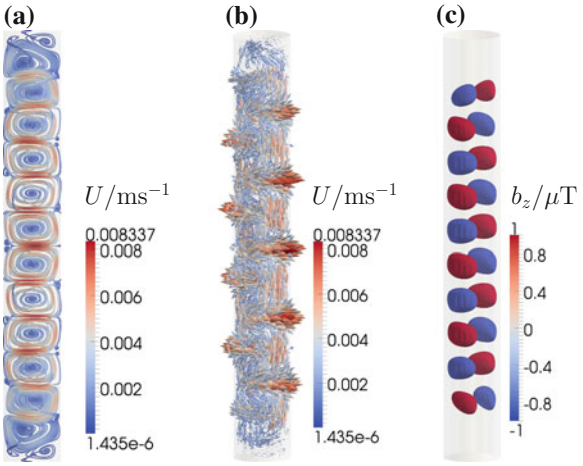

Fig. 5 Flow field of the TI in a *cylinder* filled with GaInSn. **a** Shows streamlines and **b** vectors of the saturated velocity field for $I = 10$ kA, **c** displays contours of the axial induced magnetic field b_z

References

1. Bradwell, D.J.: Liquid metal batteries: ambipolar electrolysis and alkaline earth electroalloying cells. Ph.D. thesis, MIT (2011)
2. Bradwell, D.J., Kim, H., Sirk, A.H.C., Sadoway, D.R.: Magnesium-antimony liquid metal battery for stationary energy storage. J. Am. Chem. Soc. **134**, 1895–1897 (2012)
3. Crouthamel, C., Recht, H.: Regenerative EMF Cells. American Chemical Society, Washington, DC (1967)
4. Huggins, R.E.: Energy Storage. Springer Science+Business Media, New York (2010)

5. Kim, H., Boysen, D.A., Newhouse, J.M., Spatocco, B.L., Chung, B., Burke, P.J., Bradwell, D.J., Jiang, K., Tomaszowska, A.A., Wang, K., Wei, W., Ortiz, L.A., Barriga, S.A., Poizeau, S.M., Sadoway, D.R.: Liquid metal batteries: past, present, and future. Chem. Rev. **113**, 2075–2099 (2013)
6. Rüdiger, G., Gellert, M., Schultz, M., Strassmeier, K.G., Stefani, F., Gundrum, T., Seilmayer, M., Gerbeth, G.: Critical fields and growth rates of the Tayler instability as probed by a columnar gallium experiment. Astrophys. J. **755**, 181 (2012)
7. Seilmayer, M., Stefani, F., Gundrum, T., Weier, T., Gerbeth, G., Gellert, M., Rüdiger, G.: Experimental evidence for a transient Tayler instability in a cylindrical liquid-metal column. Phys. Rev. Lett. **108**, 244501 (2012)
8. Stefani, F., Weier, T., Gundrum, T., Gerbeth, G.: How to circumvent the size limitation of liquid metal batteries due to the Tayler instability. Energ. Convers. Manage. **52**, 2982–2986 (2011)
9. Weber, N., Galindo, V., Stefani, F., Weier, T., Wondrak, T.: Numerical simulation of the Tayler instability in liquid metals. New J. Phys. **15**, 043034 (2013)
10. Zhang, S., Zhao, X.: General formulations for Rhie-Chow interpolation. In: ASME 2004 Heat Transfer/Fluids Engineering Summer Conference (2004)

Part XIV
Multiphase Flows

DNS and LES of Two-Phase Flows with Cavitation

S. Hickel

1 Introduction

We report on the numerical modeling and simulations of compressible two-phase flows that involve phase transition between the liquid and gaseous state of the fluid. Cavitation refers to the process of formation and implosion of vapor cavities within the liquid phase due to a change in pressure. Vapor cavities usually form in technical devices when the liquid is accelerated such that, by Bernoulli's principle, the static pressure falls sufficiently far below the vapor saturation pressure, or when sufficiently strong expansion waves propagate into an already preconditioned low-pressure region. When these vapor bubbles are then advected into regions where the static pressure of the surrounding liquid is above the vapor-saturation pressure, sudden re-condensation occurs, which is accompanied by a rapid acceleration of the surrounding liquid. Once all vapor is consumed, the fluids inertia leads to a strong compression of the liquid towards a focal point. This "water-hammer" effect can lead to peak pressures of several thousand bars and the emission of strong shock waves. The repeated vigorous collapse of vapor cavities is a source of noise and vibrations, and can even lead to severe structural damage of solid surfaces, so-called cavitation erosion. Cavitation erosion is one of the major reasons for premature failure of technical devices involving the processing of liquids, such as marine propellers, automotive fuel injection nozzles, liquid-rocket engine cooling channels and turbo-pump inducers. On the other hand, the effects of cavitation are exploited in industrial surface-cleaning applications and in medical applications, such as the shock wave lithotripsy.

Numerical simulations of cavitating flows must solve complex multiphysics and multiscale problems in a consistent way. Compressibility of both the liquid phase and the gaseous phase plays a decisive role. High grid resolution and very large numbers of time steps are required: Length and time scales of bubble collapses are in the

S. Hickel (✉)
Institute of Aerodynamics and Fluid Mechanics, Technische Universität München, Munich, Germany
e-mail: sh@tum.de

J. Fröhlich et al. (eds.), *Direct and Large-Eddy Simulation IX*,
ERCOFTAC Series 20, DOI 10.1007/978-3-319-14448-1_75

range of micrometers and nanoseconds whereas the typical scales of hydrodynamic flow features in technical devices are centimeters and milliseconds. Another major challenge is the accurate simultaneous representation of the dynamics of phase interfaces, phase change, strong shock waves and turbulence at low Mach numbers in a compressible fluid.

We numerically study cavitation on two very different scales. Controlling cavitation damage requires a better understanding of the underlying fundamental bubble-collapse processes. As a first step, the high-speed dynamics of cavitation bubbles is studied in well resolved simulations with a sharp-interface numerical model [1, 2] on a micro scale. The underlying assumption of the employed evaporation/condensation model is that phase change occurs in thermal non-equilibrium and that the associated timescale is larger than that of the wave dynamics described by the interfacial Riemann problem.

Direct interface resolving simulations are however intractable for real world technical applications, such as turbulent flows involving cavitation clouds with millions of vapor bubbles and a wide range of time and length scales. For this reason, we developed a coarse grained model for large-eddy simulation (LES) of turbulent two-phase flows with cavitation [3, 4]. In LES, vapor bubbles constitute sub-grid scales that have to be modeled accordingly. On the grid scale, we solve the compressible Navier-Stokes equations for a homogeneous mixture of liquid and vapor. Infinitely fast and isentropic phase change is assumed and macroscopic effects are lumped into the constitutive relations for the homogeneous cell averaged fluid. This macroscopic model is applied to realistic technical problems [4, 5] and to more generic flows to study the interaction of cavitation and turbulence [6].

2 Cavitation-Bubble Dynamics Near Walls

High-speed photography gives a first insight into the bubble dynamics during the collapse [7, 8] and shows two fundamental phenomena during the non-spherical cavitation bubble collapse process: the development of high-speed jets and the release of shock-waves upon final bubble collapse. Both, the impact of shock waves and of high-speed jets on a surface can lead to material erosion. A precise determination of peak pressures at the wall and its association with the initial bubble configuration and evolution is beyond current experimental capabilities, but can be obtained from detailed numerical simulations.

2.1 Sharp-Interface Non-Equilibrium Model

Our sharp-interface non-equilibrium model [1, 2] is intended for very detailed direct numerical simulations (DNS). The computational domain Ω is divided by the phase interface $\Gamma(t)$ into two different sub-domains $\Omega_l(t)$ and $\Omega_v(t)$. The volume $\Omega_l(t)$

accounts for the region occupied by the liquid state and $\Omega_v(t)$ refers to the region occupied by the gaseous state. We integrate the compressible Navier-Stokes equations separately for each fluid phase on the respective sub-domain by a standard finite volume scheme on a three-dimensional Cartesian grid. For the vapor domain, the pressure is determined from an ideal gas equation of state (EOS), and for water like liquids are modeled, for example, by Tait's equation of state.

The standard finite volume scheme is modified in grid cells that are cut by the interface $\Gamma(t)$ in such a way that only the cell volume and face fractions that belong to the respective subdomain contribute to the finite-volume flux balance. The geometry of the moving and strongly deforming liquid-vapor interface (cell-face apertures, volume fractions and interface area) is reconstructed from a level-set field, which is advected with the local fluid velocity and describes the signed distance of any point from the immersed interface [9]. The zero level-set contour represents the interface between the two fluids.

The solutions for the two sub-domains are strongly coupled through an interface interaction term $\mathbf{X}$, that enters the finite-volume flux balances and accounts for the mass, momentum and energy transfer between liquid and vapor. We apply a thermal non-equilibrium assumption to model the phase change at the interface. That is, during the phase-change process, the pressure is in equilibrium and the temperature has a discontinuity at the phase interface. The model of Schrage [10] is used for computing the rate of evaporation and condensation, and a two-fluid Riemann problem is solved in interface-normal direction for the interface pressure. From the solution of the two-material Riemann problem, the interface pressure p_I and the interface normal velocity u_I^* serve to compute the pressure interaction term

$$\mathbf{X}_v^p = -\mathbf{X}_l^p = \begin{pmatrix} 0 \\ p_I \Delta\Gamma \ (\mathbf{n} \cdot \hat{i}) \\ p_I \Delta\Gamma \ (\mathbf{n} \cdot \hat{j}) \\ p_I \Delta\Gamma \ (\mathbf{n} \cdot \hat{k}) \\ p_I \Delta\Gamma \ u_I^* \end{pmatrix} . \tag{1}$$

The mass transfer term is given by

$$\mathbf{X}_v^t = -\mathbf{X}_l^t = \begin{pmatrix} \dot{m} \ \Delta\Gamma \\ \dot{m} \ \Delta\Gamma \ (\mathbf{v} \cdot \hat{i}) \\ \dot{m} \ \Delta\Gamma \ (\mathbf{v} \cdot \hat{j}) \\ \dot{m} \ \Delta\Gamma \ (\mathbf{v} \cdot \hat{k}) \\ \dot{m} \ \Delta\Gamma \left(e_v + \frac{1}{2} |\mathbf{v}|^2\right) + p_I \ \Delta q^* \ \Delta\Gamma \end{pmatrix} , \tag{2}$$

where $\mathbf{v}$ is the velocity of the liquid at the interface in case of evaporation and the velocity of the vapor in case of condensation, respectively. $\Delta q^* = \dot{m}/\rho_l$ is the phase-change induced velocity and $\dot{m}$ the phase-change rate proposed in Ref. [10]

$$\dot{m} = \frac{\lambda}{\sqrt{2\pi R_v}} \left(\frac{p_{sat}(T_l)}{\sqrt{T_l}} - \frac{p_v}{\sqrt{T_v}} \right) , \tag{3}$$

where R_v is the specific gas constant in the vapor phase, λ is the accommodation coefficient for evaporation or condensation, T_v and T_l are the temperatures of vapor and liquid at the phase interface, p_v is the actual vapor pressure at the interface, and p_{sat} is the equilibrium saturation pressure.

2.2 Vapor-Bubble collapse simulations

With this model, three different configurations of spherical cavitation bubbles are investigated: a detached bubble, a bubble cut by the wall in its lower hemisphere, and one cut by the wall in its upper hemisphere. As shown in Fig. 1, the initial bubble radius is 400 μm and we consider three different wall positions A, B and C. We take advantage of symmetries and compute only one quarter of the bubble and results are mirrored on the (X-Y)- and (Y-Z)-plane for visualization. The grid spacing is equidistant in the bubble region with 100 computational cells over the initial bubble radius. Grid stretching is applied in the far-field. Outlet boundary conditions are imposed at $x, y, z = 10$ mm. Both fluids have a common temperature of 293.0 K, which is the saturation temperature corresponding to the initial vapor pressure of 0.0234 bar. Initial liquid pressure is 100 bar and the accommodation coefficient is taken as $\lambda = 0.01$.

For all configurations, the vapor bubble shrinks slowly during the initial period. The rapid stage of the bubble collapse starts with the development of a cavity, followed by the formation of a liquid jet. Two fundamentally different scenarios at the early stages of bubble collapse can be found. For a detached bubble or a bubble cut in the lower hemisphere, the collapse is initiated at the top of the bubble. A fast liquid re-entrant jet develops and penetrates through the bubble in wall-normal direction (Fig. 2a, b). For an attached bubble cut in the upper hemisphere, the collapse is initiated between wall and interface and a liquid jet develops radially towards the bubble center (Fig. 2c). The appearance of a secondary jet can be observed for

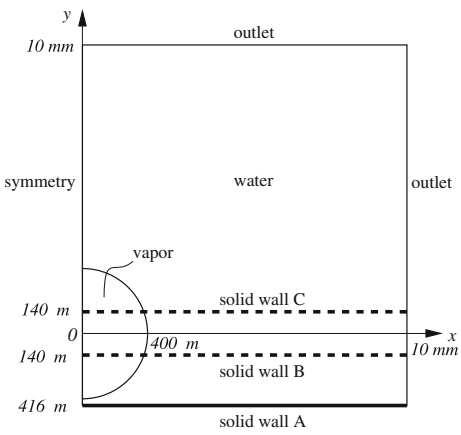

Fig. 1 Sketch of the bubble-collapse problem

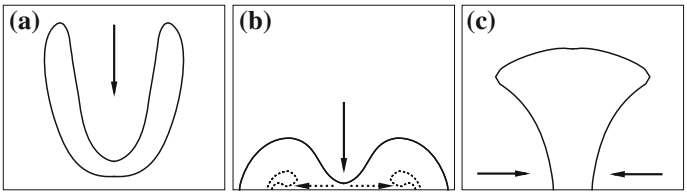

Fig. 2 Liquid jets during vapor bubble collapse near a wall (frame size in μm): **a** Wall-normal re-entrant jet for configuration A, **b** primary wall-normal re-entrant jet (*solid line*) and secondary wall-parallel outward pointing jet (*dashed line*) for configuration B, and **c** wall-parallel inward pointing jet for configuration C. *Arrows* indicate the jet direction

configuration B, where the wall normal re-entrant jet is deflected at the wall and interacts with the remaining bubble ring (Fig. 2b, dashed lines). This secondary jet is radially symmetric and develops from the symmetry axis outwards in wall-parallel direction. For configuration A no secondary jet develops as the residual bubble ring is not attached to the wall.

Figure 3 shows a three-dimensional visualization of the bubble shape during the stage where the three different liquid jets are developed. The first occurrence of extreme pressure magnitudes coincides with jet breakdown. For cases A and B with a wall-normal re-entrant jet, the observed maximum wall pressures are of comparable magnitude of about 100 times the liquid's initial pressure. Slightly larger values for the detached bubble can be attributed to a larger jet velocity. Looking at wall-parallel radial jets, one has to distinguish between the outward-pointing secondary jet of configuration B and the inward pointing primary jet of configuration C. In the latter case, the liquid is gradually compressed while being transported towards the symmetry axis, where maximum pressure occurs. The maximum pressure after inward-pointing, wall-parallel jet breakdown is about six times larger than that for a wall-normal jet. For the outward-running, wall-parallel secondary jet of configuration B, very low pressure is observed inside the jet as an expansion of the liquid further decreases the pressure of the high-velocity jet. After the jet breaks down, the liquid pressure increases, but remains significantly smaller than for the inward-pointing jet.

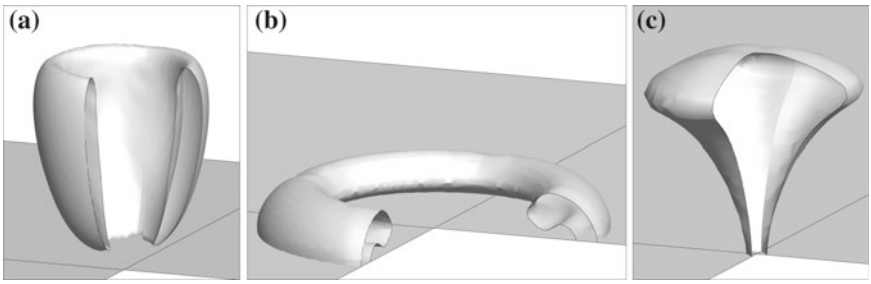

Fig. 3 Cuts through an iso-surface of the zero level-set (interface) showing the shape of the bubble during the late stage of the liquid jets for configurations A, B and C

During the final stage of the bubble collapse, two different scenarios occur. For cases A and C, the residual vapor bubble is detached after jet breakdown. Thus, the maximum pressure due to final bubble collapse occurs away from the wall. The emitted shock waves impinge on the wall with reduced magnitude, and the wall pressures do not reach the levels observed during jet breakdown. A different scenario is observed for configuration B. After primary and secondary jet breakdown, a residual vapor ring remains at the wall. This ring is surrounded by high pressure liquid, which initiates the final collapse radially towards the symmetry axis. The liquid is compressed towards the center region resulting in large pressure with a maximum at the symmetry axis of about 400 times the initial ambient pressure.

3 Cavitation in Turbulent Flows

Coherent turbulence structures play an important role in the cavitation process in wall bounded and free shear flows. High negative pressure peaks associated with turbulent eddies can lead to cavitation inception. Vice versa, cavitation can generate and enhance vorticity, but also trigger vortex break-up. Arndt [11] gives a nice review of this complex interaction. Most technical applications involve turbulent flows for which direct numerical simulations are intractable. To address real world technical applications and fundamental questions related to the mutual interaction of turbulence and cavitation and the resulting modulation of turbulence due to phase change, we developed a coarse grained model for large-eddy simulations (LES) of turbulent two-phase flows with cavitation.

3.1 Thermodynamic Equilibrium Model

LES is based on scale separation into represented and unrepresentable scales, which is usually achieved through filtering the governing equations. The same paradigm can be applied to two phase flows. Applying a top hat filter that is consistent with a finite-volume discretization method to a cavitation cloud yields a cell averaged state vector that represents the mean density $\overline{\rho}$, mean momentum $\overline{\rho\mathbf{u}}$ and mean energy $\overline{\rho E}$. Accordingly, the coarse grained Navier-Stokes equations need then to be closed by constitutive relations for the mean pressure $\overline{p}$ and mean viscosity $\overline{\mu}$ of the homogenized (that is, volume-averaged) fluid.

As we consider cavitating flows with phase change, this homogenized fluid can be either pure liquid ($\alpha = 1$), pure vapor ($\alpha = 1$) or a mixture of liquid and gaseous state ($0 < \alpha < 1$) with a vapor volume fraction α. For facilitate the reconstruction of the state within the volume of a computational cell we assume that phase changes are infinitely fast and isentropic, which is justified if the numerical timestep is large compared to the time scale of phase change. Furthermore, we assume mechanical equilibrium and we do not attempt to reconstruct the shape of the liquid-vapor interface. This means that the effect of surface tension on the vapor pressure is neglected.

With these assumptions, the densities of liquid and vapor in cells that contain both phases ($0 < \alpha < 1$) are $\rho_l = \rho_{l,sat}$ and $\rho_v = \rho_{v,sat}$, and we can compute the vapor volume fraction from

$$\alpha = \begin{cases} 0 & , \quad \overline{\rho} \geq \rho_{l,sat} \\ \frac{\rho_{l,sat} - \overline{\rho}}{\rho_{l,sat} - \rho_{v,sat}} & , \quad \rho_{l,sat} > \overline{\rho} \geq \rho_{v,sat} \\ 1 & , \quad \rho_{v,sat} > \overline{\rho} \end{cases} \tag{4}$$

Once the vapor volume fraction is known, an equation of state can be derived and the mean pressure and temperature can be computed. Note that the equilibrium pressure p_{sat} and densities $\rho_{l,sat}$ and $\rho_{v,sat}$ at the saturation point generally depend on temperature, which requires an iterative procedure. An example of a barotropic equation of state (EOS) for water and water vapor is given in Ref. [4]. Alternatively, tabulated EOS-data can be used for more complex fluids, such as Diesel fuel.

The dynamics of wall-bounded turbulence is strongly influenced by viscous stresses. As the dynamic viscosities of liquid and vapor usually differ by several orders of magnitude, the chosen model for the viscosity of the homogenized two-phase fluid is of particular importance. In bubbly flows, the surface tension at the phase boundaries can increase the resistance against deformation substantially. For this reason we combine a straightforward linear blending of the viscosities of liquid and vapor with Einstein's [12] law for suspensions of rigid particles, which leads to

$$\overline{\mu} = (1 - \alpha)(1 + 2.5\alpha)\mu_l + \alpha\mu_v \tag{5}$$

for the volume averaged viscosity of the cell-averaged two-phase fluid [13].

3.2 LES of Cavitation in a Micro Channel

In the following we briefly report on LES of the turbulent cavitating flow in a micro-channel at two different operating points. The investigated geometry is characteristic for throttle valves found in fuel injection systems. The geometric properties of the considered micro-channel and the investigated operating points are specified in Fig. 4. This geometry and modifications thereof have been extensively examined experimentally at different operating conditions [14, 15].

The governing equations are the compressible Navier-Stokes equations for a homogeneous mixture of liquid and vapor, and we use a tabulated barotropic equation of state for the test oil Shell V1404. The system is solved by a finite-volume method on adaptive, locally refined Cartesian grids and an explicit 3rd-order accurate Runge-Kutta method for time integration. Complex geometric shapes are represented by a conservative immersed boundary method [16] that follows a similar approach as the sharp interface model for two-phase flows. The effect of non-represented turbulent flow scales (subgrid-scales, SGS) is accounted for by an implicit modeling methodology based on the adaptive local deconvolution method (ALDM, [3, 4, 17]), which yields an SGS energy transfer that is consistent with turbulence theory.

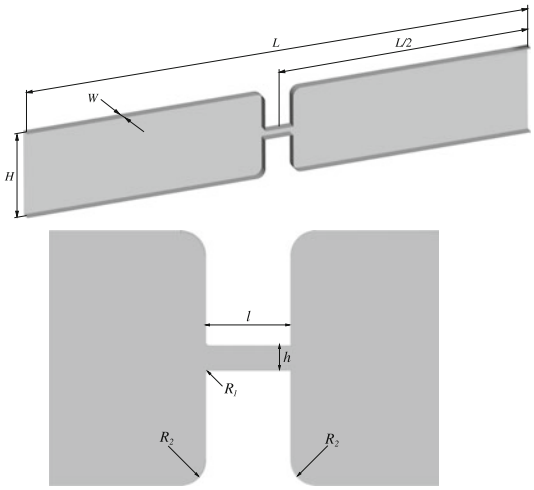

Property	Value [$\times 10^{-3}$ m]
L	18.0
l	1.0
H	3.0
h, W	0.3
R_1	0.04
R_2	0.4

OP	$\dot{m}$ [kg/s]	U_B [m/s]	p_{out} [Pa]
A	0.01450	19.310	115×10^5
B	0.01508	20.078	55×10^5

Fig. 4 Micro-channel geometry and investigated operating points (OP)

At the inflow boundary a bi-parabolic velocity profile with bulk velocity U_B is specified. At the outflow boundary condition we set a fixed static pressure p_{out}. The block structured adaptive Cartesian grid consists of roughly 31×10^6 cells. The resolution at the wall in the micro-channel is approximately 1×10^{-6} m in order to resolve the velocity gradient at the wall.

Figure 5 shows instantaneous snapshots of λ_2 iso-surfaces (upper row) and iso-surfaces of 10 % vapor volume fraction (lower row) for both operating points.

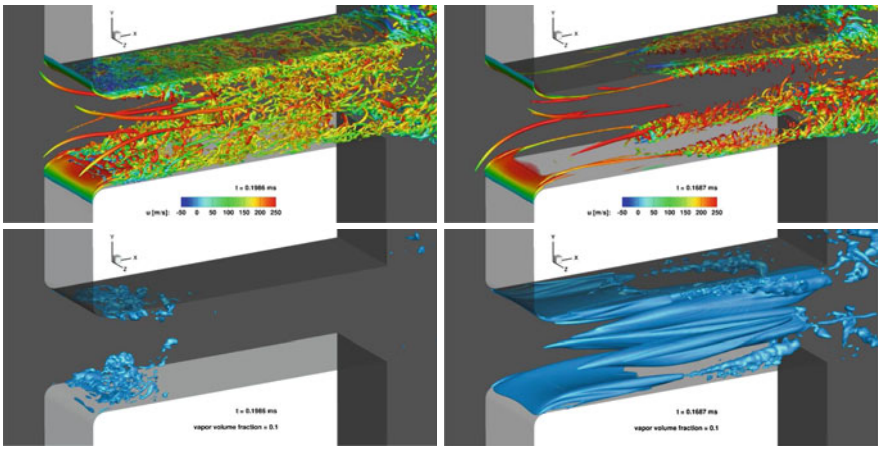

Operating point A Operating point B

Fig. 5 Instantaneous snapshots of the flow field in a throttle valve: λ_2 iso-surfaces colored by the streamwise velocity (*top pictures*) and corresponding cavitation structures visualized by a vapor volume fraction of 10 % (*bottom pictures*)

These visualizations already show that phase change alters the properties of turbulence considerably. The flow field at operating point A is highly instationary. The flow separates at the throttle inlet and forms a recirculation zone. The initially laminar duct flow undergoes sudden bypass transition within the shear layer between the bulk flow and the separation bubble. The resulting transitional and turbulent vortices are the main source of cavitation. We observe that the generated vapor cavities shed with a frequency of approximately 300 kHz.

At operating point B the back pressure has been reduced, which results in a more stationary behavior compared to operating point A. Stable sheet cavitation due to inertia effects is observed at the throttle inlet. Cavitation is also observed in the corner vortices. The λ_2 iso-surface indicates that the flow remains laminar throughout the first half of the throttle. Transition to turbulence is observed first at the corner vortices, which start to break up half way down the throttle valve. Furthermore, large cavitating vortex cores are present in the center of the throttle valve. These vortices originate from Görtler instability of the boundary layer in the chamber upstream of the throttle.

4 Summary

A first step towards controlling the cavitation damage requires to fully understand the underlying fundamental bubble-collapse mechanisms. For this purpose, generic configurations with spherical bubbles have been investigated by direct numerical simulations with a sharp-interface non-equilibrium model. Results for the collapse of a spherical vapor bubble close to a solid wall have been discussed for three different bubble–wall configurations. The major challenge for such numerical investigations is to accurately reproduce the dynamics of the interface between liquid and vapor during the entire collapse process, including the high-speed dynamics of the late stages, where compressibility of both phases plays a decisive role. Due to the very small timescales, liquid and vapor are in non-equilibrium at the interface, which has to be taken into account by a numerical model. Our numerical sharp-interface method copes with these problems by coupling both phases with a conservative interface-interaction term that includes a non-equilibrium phase-change model.

Direct interface resolving simulations are intractable for real world technical applications such as turbulent flows involving cavitation clouds with millions of vapor bubbles and a wide range of time and length scales. With our thermodynamic equilibrium model for large-eddy simulations, we solve the coarse grained Navier-Stokes equations for a homogenized, cell-averaged fluid that can represent pure liquid, pure vapor and arbitrary mixtures of liquid and vapor. For deriving an appropriate equation of state, we assume that the characteristic time scale of phase change is much smaller than the numerical time step and that phase change is isentropic and in mechanical equilibrium at the saturation pressure.

This thermodynamic equilibrium model has been applied in LES of real world technical applications. Results for the cavitating flow in a throttle valve typical for

fuel injection systems have been presented. We also use this model in fundamental research that contributes to the better understanding of the mutual interaction of turbulence and cavitation.

References

1. Lauer, E., Hu, X.Y., Hickel, S., Adams, N.A.: Numerical modelling and investigation of symmetric and asymmetric cavitation bubble dynamics. Comput. Fluids **69**, 1–19 (2012)
2. Lauer, E., Hu, X.Y., Hickel, S., Adams, N.A.: Numerical investigation of collapsing cavity arrays. Phys. Fluids **24**, 052104 (2012)
3. Hickel, S.: Implicit subgrid-scale modeling for large eddy simulation of compressible flows and shock turbulence interaction (2012)
4. Hickel, S., Mihatsch, M., Schmidt S.J.: Implicit large eddy simulation of cavitation in micro channel flows. In: WIMRC 3rd International Cavitation Forum, ISBN: 978-0-9570404-1-0 (2011)
5. Egerer, C.P., Hickel, S., Schmidt, S.J., Adams, N.A.: Analysis of turbulent cavitating flow in a micro-channel. In: 14th European Turbulence Conference, Lyon, France (2013)
6. Egerer, C.P., Hickel, S., Schmidt, S.J., Adams, N.A.: Implicit large-eddy simulation of cavitation in a turbulent shear layer. In: Ohl, C.-D., Klaseboer, E., Ohl, S.W., Gong, S.W., Khoo B.C. (eds.) Proceedings of the Eighth International Symposium on Cavitation (CAV 2012), ISBN: 978-981-07-2826-7 (2012)
7. Lindau, O., Lauterborn, W.: Cinematographic observation of the collapse and rebound of a laser-produced cavitation bubble near a wall. J. Fluid Mech. **479**, 327–348 (2003)
8. Tomita, Y., Shima, A.: Mechanisms of impulsive pressure generation and damage pit formation by bubble collapse. J. Fluid Mech. **169**, 535–564 (1986)
9. Fedkiw, R., Aslam, T., Merriman, B., Osher, S.: A non-oscillatory Eulerian approach to interfaces in multimaterial flows (the ghost fluid method). J. Comput. Phys. **152**, 457–492 (1999)
10. Schrage, R.W.: A theoretical study of interphase mass transfer. Columbia University Press, New York (1953)
11. Arndt, R.E.A.: Cavitation in vortical flows. Annu. Rev. Fluid Mech. **34**, 143–175 (2002)
12. Einstein, A.: Eine neue Bestimmung der Moleküldimensionen. Section 2: Berechnung des Reibungskoeffizienten einer Flüssigkeit, in welcher sehr viele kleine Kugeln in regelloser Verteilung suspendiert sind. Annalen der Physik, IV, 297–306 (1906)
13. Beattie, D., Whalley, P.: A simple two-phase frictional pressure drop calculation method. Int. J. Multiph. Flow **8**, 83–87 (1962)
14. Iben, U., Morozov, A., Winklhofer, E., Wolf, F.: Laser-pulse interferometry applied to high-pressure fluid flow in micro channels. Exp. Fluids **50**, 597–611 (2011)
15. Winklhofer, E., Kull, E., Kelz, E., Morozov, A.: Comprehensive hydraulic and flow field documentation in model throttle experiments under cavitation conditions. In: Ineichen, B. (ed.) Proceedings of the 17th ILASS-Europe, Zurich, Switzerland (2001)
16. Meyer, M., Devesa, A., Hickel, S., Adams, N.A.: A conservative immersed interface method for large-eddy simulation of incompressible flows. J. Comput. Phys. **229**, 6300–6317 (2010)
17. Hickel, S., Adams, N.A., Domaradzki, J.A.: An adaptive local deconvolution method for implicit LES. J. Comput. Phys. **213**, 413–436 (2006)

Four-Way Coupled LES Predictions of Dense Particle-Laden Flows in Horizontal Smooth and Rough Pipes

M. Alletto and M. Breuer

1 Introduction

Turbulent disperse multiphase flows play an important role in many technical applications such as the transport of powders in pneumatic conveying systems. The transport of particles is governed by many physical effects. First of all the continuous flow is in general in the turbulent regime at moderate or high Re. Thus an adequate prediction requires either statistical turbulence models based on RANS or more advanced techniques such as LES. Since in the majority of flows considered complex phenomena such as curved streamlines, secondary flows and transition are involved, the latter is preferred in the present study. The continuous flow provides the basis to determine the fluid dynamic forces such as the drag force and the lift forces due to velocity shear or rotation. Furthermore, the particle motion is strongly influenced by inter-particle collisions. Even for overall dilute two-phase flows, locally high particle concentrations may appear due to the effect of gravity, turbophoresis or the known accumulation of particles in low vorticity regions. These phenomena require to take inter-particle collisions by four-way coupled predictions into account. Last but not least the interaction of the particles with walls plays a dominant role, especially for rough walls. Wall roughness is known to have a significant influence on particle-laden wall-bounded flows. It directly affects the particulate phase due to collisions with rough surfaces and thus needs to be modeled adequately.

In the present contribution all issues mentioned above are incorporated in a four-way coupled Euler-Lagrange LES methodology and applied to the pneumatic conveying of particles through smooth and rough horizontal pipes in the turbulent regime.

M. Alletto · M. Breuer (✉)
Department of Fluid Mechanics, Helmut-Schmidt-Universität Hamburg, Hamburg, Germany
e-mail: breuer@hsu-hh.de

M. Alletto
e-mail: alletto@hsu-hh.de

J. Fröhlich et al. (eds.), *Direct and Large-Eddy Simulation IX*,
ERCOFTAC Series 20, DOI 10.1007/978-3-319-14448-1_76

Two mass loadings (polydisperse) are considered. The secondary flow structures observed in the pipe cross-section are analyzed. The outcome confirms recently published experimental results [2] that the secondary flow is of second kind.

2 Computational Methodology

The continuous phase is simulated in the Eulerian frame of reference using LES. The code is based on a standard 3-D finite-volume method for arbitrary non-orthogonal and block-structured grids. The discretization is of second-order accuracy in space and time. Different subgrid-scale and wall-models can be applied. To take the influence of the particle on the fluid motion into account (two-way coupling), the particle-source-in-cell (PSIC) method is used.

For the particulate phase a huge number of individual particles are tracked throughout the computational domain in a Lagrangian frame of reference taking drag, lift, gravity and buoyancy forces in Newton's second law into account. In order to enable efficient tracking of millions of particles on a block-structured curvilinear grid, the particle tracking is carried out in *c-space* [5] rather than in p-space which possesses the advantage that no search of the particle's new position is required leading to a very fast algorithm.

For tiny particles with a relaxation time of the same order as the smallest fluid time scales the unresolved scales in LES become important for the particle motion. To consider the effect of the subgrid scales, the stochastic model by Pozorski and Apte [8] is applied, where the subgrid-scale kinetic energy is estimated with the help of the scale similarity approach. To account for the rotation of the spherical particles around three Cartesian axes, Newton's second law for the angular momentum is considered.

In contrast to many previous studies relying on statistical particle-particle collision models, in the present investigation a deterministic algorithm is applied for handling the collisions (four-way coupling). The procedure is split into two stages: First, particles are moved based on the equation of motion without inter-particle interactions. Second, the occurrence of collisions during the first stage is examined by a very efficient two-step algorithm [3] for all particles. If a collision is found, the velocities of the collision pair are replaced by the post-collision ones without changing their position. The velocity changes during the collision are predicted by assuming an inelastic collision process of hard spheres including Coulomb's friction leading to either sliding or non-sliding collisions.

The collisions of particles with solid walls is governed by the same relations as long as the wall is ideally smooth. In order to mimic the effect of technically relevant rough walls on the particulate phase, Breuer et al. [4] recently suggested a sandgrain roughness model taking a minimum of measured or empirically determined physical quantities into account. Following Nikuradse's idea a sandgrain roughness model was proposed for the disperse phase in which the wall is covered by a densely packed layer of sand grains idealized by spheres of constant radii. Based on geometric

considerations relying on generally used roughness parameters such as the mean roughness R_z, the local inclination of the wall is determined allowing to predict the inelastic collision of the particle with the rough wall. The sandgrain model also takes the shadow effect into account leading to asymmetric probability density functions of the wall inclination angles, where the mean normal vector is turned towards the incoming particle trajectory [4].

3 Setup and Results

The present applications are concerned with the pneumatic conveying in horizontal pipe flows. Huber and Sommerfeld [6] carried out measurements in 5 m long horizontal glass and steel pipes with a vdiameter $d_{\text{pipe}} = 80\,\text{mm}$. Based on the superficial gas elocity ($U_b = 24\,\text{m/s}$) of the air at standard ambient conditions a Reynolds number of $\text{Re} = U_b\, d_{\text{pipe}}/\nu = 120{,}000$ results. After a certain development length of about $50\, d_{\text{pipe}}$ the flow is assumed to be fully developed. Hence, in the simulations periodic boundary conditions are applied. The computational domain has an extension of $6 d_{\text{pipe}}$ and is discretized by 3×10^7 cells. The wall model of Schumann [9] is applied for the continuous flow.

The particles are spherical glass beads ($\rho_p = 2{,}500\,\text{kg/m}^3$) with a size distribution ranging between about 1.5–98 μm and a number mean diameter of about 40 μm. Experimentally a mass loading of $\eta = 30\,\%$ was investigated [6]. The roughness height for the steel pipe is set to $R_z = 10\,\mu\text{m}$ and the constant describing the surface finishing is given by $C_{\text{Surface}} = 3$ (see Breuer et al. [4]). Two different mass loadings are considered in the simulations: First the statistics computed with a mass loading of $\eta = 30\,\%$ are compared with the experiments of Huber and Sommerfeld [6] to validate the methodology. After that, the origin of the secondary flow observed in the present simulations for both mass loadings η is explained exemplary by means of the computations performed at $\eta = 70\,\%$. Note that a very detailed validation against experiments and DNS and a comprehensive analysis on the appearances of secondary flows in horizontal particle-laden pipe flows can be found in [1].

Figure 1 depicts the simulated mean particle velocity for the glass and the steel pipe compared with the experiments [6]. Obviously, good agreement is found for both cases. Furthermore, it is evident that the wall roughness of the steel pipe leads to a reduction of the influence of the gravitational settling. In case of the glass pipe the mean particle velocity profile shows a strong asymmetry between the lower and upper half of the cross-section due to momentum loss during the wall collisions of the particles settling down at the bottom part of the pipe. Furthermore, the fluid is additionally decelerated at the bottom part due to the highly concentrated particles in this region. Due to the shadow effect in case of the steel pipe the roughness leads to a redistribution of the particle streamwise momentum towards the wall-normal direction. This effect is responsible for a resuspension of the particles and hence to a reduction of the particle concentration in the vicinity of the bottom wall (Fig. 2). This again causes a reduction of the force exerted by the particles on the fluid against the

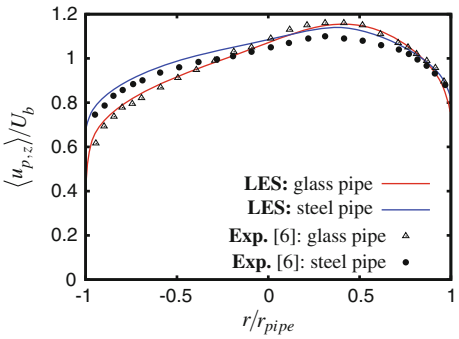

Fig. 1 Mean particle velocity along a *vertical line* for the glass (smooth) and the steel pipe (with roughness)

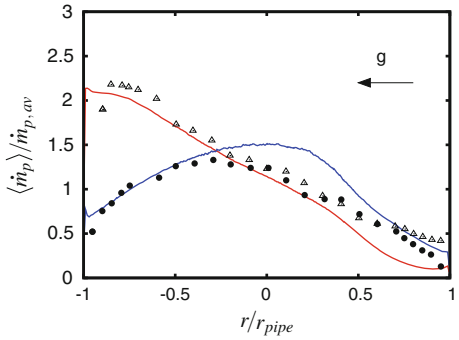

Fig. 2 Mean particle mass flux along a *vertical line* for the glass (smooth) and the steel pipe (with roughness)

mean flow direction in the bottom part of the tube compared with the smooth pipe and hence via the mutual interaction between the particles and the fluid to a higher mean particle velocity near the bottom wall.

Figure 2 shows the mean particle mass flux in streamwise direction at the midplane parallel to the axis of gravity. It is evident that the wall roughness has a drastic effect on this particle statistic. For the smooth wall the particle mass flux near the bottom wall is very high due to the influence of the gravity. For the steel pipe, however, the particles streamwise momentum is redistributed towards the wall-normal direction due to the shadow effect [4, 7]. Hence, after a wall impact the particles acquire a steeper trajectory towards the pipe center since in a pipe the wall-normal vector points towards the pipe center. Consequently, the particles tend to accumulate in this region (focusing effect). Also for the mean particle mass flux good agreement is found between the simulation and the experiment for both cases.

The projected streamlines of the averaged flow field in the pipe cross-section ($\eta = 70\,\%$) are shown in Fig. 3 for the smooth glass pipe and in Fig. 4 for the rough steel pipe. The colormap displays the fluid velocity component against the gravitational acceleration. It is evident that for both cases two rotating cells develop. The fluid flows upstream along the symmetry line. Then it deflects to the left and right in order to circulate downstream along both side walls building a closed vortex. The intensity of the secondary flow in the glass pipe is in the order of 2 % of the

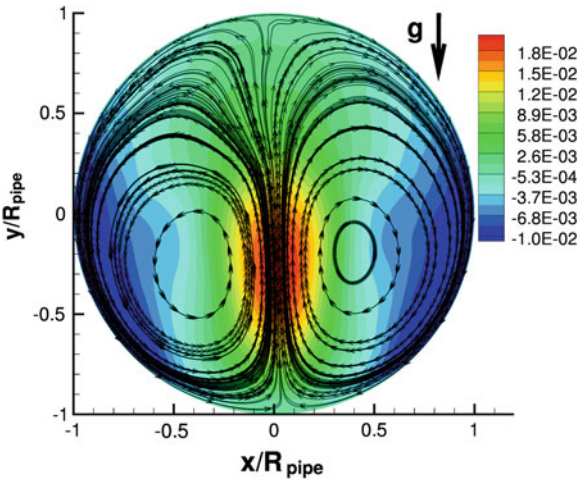

Fig. 3 Projected streamlines for the smooth glass pipe ($\eta = 70\,\%$)

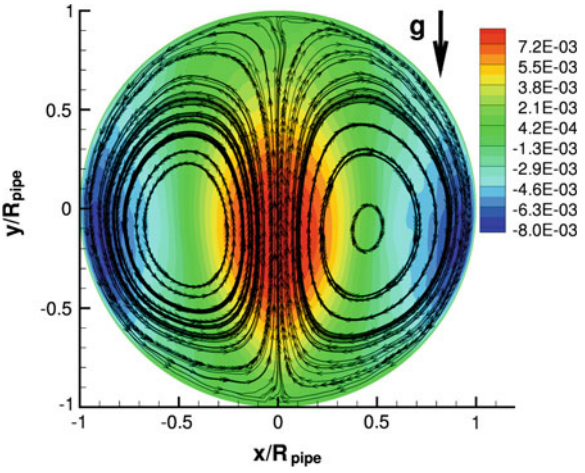

Fig. 4 Projected streamlines for the rough steel pipe ($\eta = 70\,\%$)

bulk velocity and 1 % in the steel pipe. Note that a very similar flow structure can be found in the experiments of Belt et al. [2].

Two reasons for the development of a secondary flow in a circular pipe cross-section can be found [2]: (i) The particles are directly driving the secondary flow via the two-way coupling yielding a secondary flow of first kind or (ii) the particles inhomogeneously attenuate the turbulence leading to an anisotropy in the Reynolds stresses which gives rise to a secondary flow of second kind. In order to exclude that the developing secondary flow is of first kind, the direction and magnitude of the force exerted by the particle on the fluid (time-averaged) is displayed in Fig. 5 for the glass pipe and in Fig. 6 for the steel pipe. The colormap represents the magnitude of the force. It is evident that for both glass and steel pipe the particles decelerate

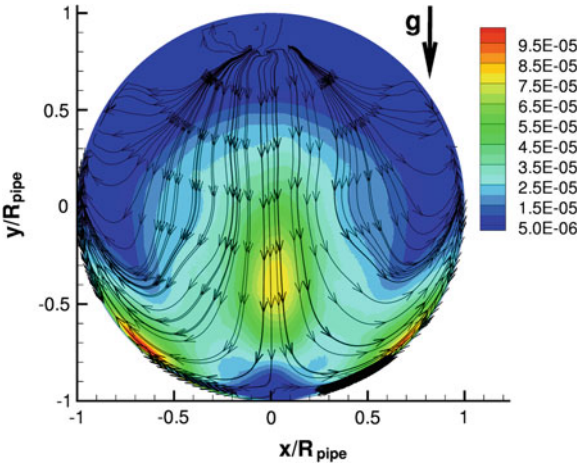

Fig. 5 Mean direction and magnitude of the force exerted by the particles on the fluid, glass pipe ($\eta = 70\,\%$)

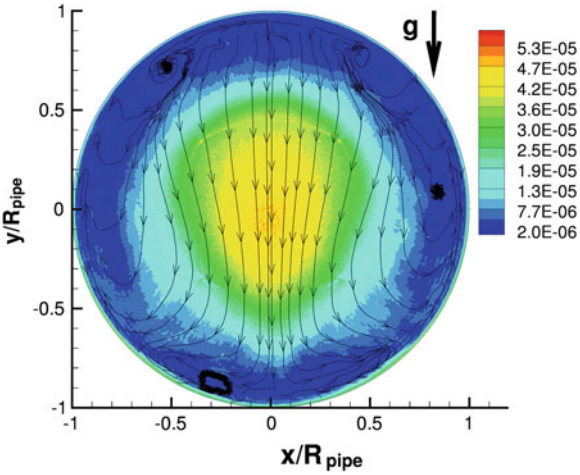

Fig. 6 Mean direction and magnitude of the force exerted by the particles on the fluid, rough steel pipe ($\eta = 70\,\%$)

the fluid in most regions of the pipe cross-section, i.e., the particles are driven by the secondary flow and not the other way round. Hence, the secondary flow of first kind can be excluded.

Following the analysis of Belt et al. [2] and also Alletto and Breuer [1] the gradient of the circumferential Reynolds stress $\langle u'_\theta u'_\theta \rangle$ can be identified as the driving force of the secondary flow. In order to explain the difference in magnitude of the secondary flow between the two investigated pipes, the circumferential Reynolds stress for the glass pipe (Fig. 7) and steel pipe (Fig. 8) is shown. In case of the glass pipe the particles accumulate in the bottom part of the cross-section (concentration contours not shown for the sake of brevity) and hence, the turbulence is more attenuated in this region compared to the top part of the pipe (see Fig. 7). This leads to a gradient of

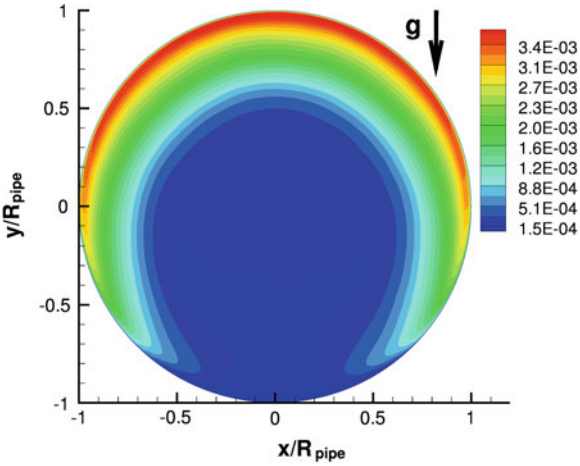

Fig. 7 Mean circumferential Reynolds stress $\langle u'_\theta u'_\theta \rangle$, smooth glass pipe

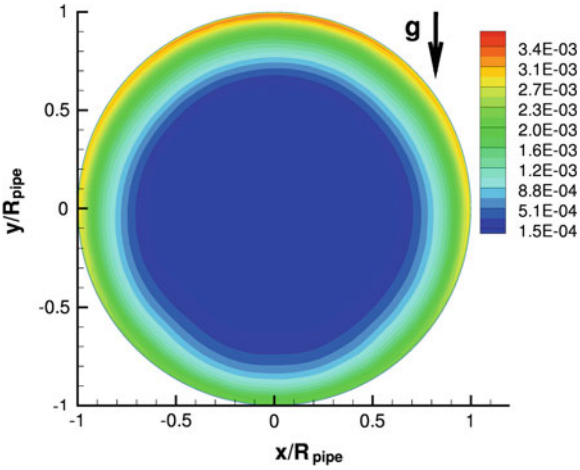

Fig. 8 Mean circumferential Reynolds stress $\langle u'_\theta u'_\theta \rangle$, rough steel pipe

the circumferential Reynolds stress in circumferential direction near the wall which pushes the flow towards the bottom part of the pipe. Due to continuity reasons in the center the fluid flows upwards. The same effect can be found for the steel pipe but not as pronounced as in the glass pipe since the particle are resuspended by the shadow effect and hence accumulate near the pipe center. Nevertheless, turbulence is still more strongly attenuated in the bottom part of the pipe than in the top part leading to a gradient of $\langle u'_\theta u'_\theta \rangle$ in circumferential direction at the wall (Fig. 8) which drives the flow.

4 Conclusions

Secondary flow structures in turbulent flows through horizontal glass and steel pipes were investigated numerically based on a four-way coupled LES. The results were found to be in good agreement with the reference data [6]. Contrary to previous investigations [6, 7] the two-cell secondary flow structure (glass pipe: 2 % U_b; steel pipe: 1 % U_b) is identified to be of the second kind, i.e., driven by the anisotropy of the Reynolds stresses being in line with recently published experimental results [2].

References

1. Alletto, M., Breuer, M.: Prediction of turbulent particle-laden flow in horizontal smooth and rough pipes inducing secondary flow. Int. J. Multiph. Flow **55**, 80–98 (2013)
2. Belt, R.J., Daalmans, A.C.L.M., Portela, L.M.: Experimental study of particle-driven secondary flow in turbulent pipe flows. J. Fluid Mech. **709**, 1–36 (2012)
3. Breuer, M., Alletto, M.: Efficient simulation of particle-laden turbulent flows with high mass loadings using LES. Int. J. Heat Fluid Flow **35**, 2–12 (2012)
4. Breuer, M., Alletto, M., Langfeldt, F.: Sandgrain roughness model for rough walls within Eulerian-Lagrangian predictions of turb. flows. Int. J. Multiph. Flow **43**, 157–175 (2012)
5. Breuer, M., Baytekin, H.T., Matida, E.A.: Prediction of aerosol deposition in 90 degrees bends using LES and an efficient Lagrangian tracking method. J. Aerosol Sci. **37**(11), 1407–1428 (2006)
6. Huber, N., Sommerfeld, M.: Modelling and numerical calculation of dilute-phase pneumatic conveying in pipe systems. Powder Technol. **99**, 90–101 (1998)
7. Lain, S., Sommerfeld, M.: Numerical calculation of pneumatic conveying in horizontal channels and pipes: detailed analysis of conveying behavior. Int. J. Multiph. Flow **39**, 105–120 (2012)
8. Pozorski, J., Apte, S.V.: Filtered particle tracking in isotropic turbulence and stochastic modeling of subgrid-scale dispersion. Int. J. Multiph. Flow **35**, 118–128 (2009)
9. Schumann, U.: Subgrid-scale model for finite difference simulations of turbulent flows in plane channels and annuli. J. Comput. Phys. **18**, 376–404 (1975)

Biomass Pyrolysis in DNS of Turbulent Particle-Laden Flow

E. Russo, J.G.M. Kuerten and B.J. Geurts

1 Introduction

Biomass is important for co-firing in coal power plants thereby reducing CO_2 emissions. Modeling the combustion of biomass involves various physical and chemical processes, which take place successively and even simultaneously [1, 2]. An important step in biomass combustion is pyrolysis, in which virgin biomass is converted into char. In this paper a point-particle model for the pyrolysis of biomass particles based on Haseli [3] is developed, which is coupled to a direct numerical simulation of the turbulent flow of gas in a channel with heated walls, using two-way coupling of mass, momentum and energy. We do not model combustion and gasification of biomass, but focus on pyrolysis, in particular on the effect of particle-gas interaction on the conversion time, i.e. the time needed to convert biomass into char. This is the first attempt in modeling the pyrolysis of biomass in a 3D flow framework. Gas-particle interaction affects the conversion time, which shows a characteristic dependence on particle size and concentration as shown in the results presented in this paper. In the following, the model of the biomass pyrolysis and of the gas with details on the way the two phases are coupled are introduced.

2 Biomass Pyrolysis Model

The model by Haseli [3] distinguishes four stages in biomass pyrolysis. This model was approximated by a set of ordinary differential equations for each of the four stages. This reduction in complexity rests on an assumed quadratic dependence

E. Russo (✉) · J.G.M. Kuerten · B.J. Geurts
Eindhoven University of Technology, Eindhoven, The Netherlands
e-mail: e.russo@tue.nl

J.G.M. Kuerten · B.J. Geurts
Faculty EEMCS, University of Twente, Enschede, The Netherlands

J. Fröhlich et al. (eds.), *Direct and Large-Eddy Simulation IX*,
ERCOFTAC Series 20, DOI 10.1007/978-3-319-14448-1_77

of the temperature on the radial coordinate, which is an accurate representation [3] and enables coupling to DNS. We sketch the main aspects of the model next; full details will be provided in an upcoming paper.

1. In the first stage the virgin biomass particle is heated by the surrounding gas and the walls. Because of this heat flux, the initially assumed constant temperature inside the particle changes and the particle can be divided in two regions separated by a thermal front. In the inner region the temperature is still at the initial value, while in the outer region the temperature increases. The model assumes spherical symmetry, so that a one-dimensional problem remains, described by the heat equation:

$$\frac{\partial T}{\partial t} = \alpha_b \frac{1}{r^2} \frac{\partial}{\partial r} \left(r^2 \frac{\partial T}{\partial r} \right), \tag{1}$$

   where T is the temperature, α_b the thermal diffusivity of the biomass and r the radial coordinate. Haseli [3] validated this simplified model against comprehensive models and experimental results, showing that the model gives accurate predictions. Therefore, at the surface of the particle the heat flux is homogeneous and is the sum of the convective flux from the surrounding gas to the particle and the radiative flux from the wall: $\dot{q} = h(T_g - T_s) + \sigma\varepsilon(T_w^4 - T_s^4)$, with h the heat transfer coefficient, σ the Stefan-Boltzmann constant, ε the emissivity of the particle and T_g, T_w and T_s the temperature of the gas at the particle location, the wall and the particle surface, respectively. At the thermal front, the temperature equals the initial value and $\dot{q}$ equals zero. Approximating the temperature profile by a parabolic function of r, the heat equation can be simplified to an ordinary differential equation for the temperature at the surface.
2. The second stage is the pre-pyrolysis phase, in which the thermal front has reached the center of the particle. It is described by (1), the same boundary condition at the particle surface and a symmetry boundary condition at the particle center. The assumption of a parabolic temperature profile inside the particle again leads to an ordinary differential equation for $T_s(t)$.
3. In the third stage T_s reaches the pyrolysis temperature T_p, pyrolysis starts and a char front moves from the surface towards the center of the particle. The particle is again divided into two regions separated by the interface at which pyrolysis occurs at position r_c. We assume parabolic temperature profiles in both regions:

$$T_B(r) = \phi_2(r - r_c)^2 + \phi_1(r_c - r) + \phi_0 \quad \text{for} \quad 0 \geq r \geq r_c \tag{2}$$

$$T_C(r) = \psi_2(r - r_c)^2 + \psi_1(r - r_c) + \psi_0 \quad \text{for} \quad r_c \geq r \geq R. \tag{3}$$

   The heat equation (1) applies in both regions, but with α_b replaced by α_c, the thermal diffusivity of char, for $r_c \geq r \geq R$. At the char front the temperature is equal to the pyrolysis temperature and the heat flux is discontinuous across the pyrolysis interface, incorporating the specific enthalpy of pyrolysis which is given to volatiles. From the boundary conditions all coefficients in (2) and (3) can be expressed in terms of ϕ_1. In this paper we also consider the heat exchange

between the volatiles released during pyrolysis and the char, when the volatiles travel to the particle surface. Therefore, the governing Eq. (1) in the char region becomes:

$$\frac{\partial T}{\partial t} = (1-\omega)\,\dot{m}\alpha_{vol}\frac{\partial T}{\partial r} + \alpha_c \frac{1}{r^2}\frac{\partial}{\partial r}\left(r^2\frac{\partial T}{\partial r}\right), \tag{4}$$

where $\alpha_{vol} = c_{vol}/(\rho_c c_c)$ and $\omega = \rho_c/\rho_b$, with ρ_c the char density, c_{vol} and c_c the volatiles and char heat capacities, respectively. Integration of the heat equation over the char region and over the remaining virgin biomass region leads to two ordinary differential equations coupling the key variables. The third governing equation in this phase is $dv_c/dt = r_c$, which is the definition of the char-front velocity. The three equations together constitute a set of coupled ordinary differential equations for the variables T_s, ϕ_1 and v_c. In the first and last part of stage 3, the small size of the char and biomass region makes the set of equations stiff. This has been solved by using approximate analytical solutions in the beginning and end of stage 3.

4. The fourth stage or the post-pyrolysis stage is similar to the pre-pyrolysis stage with biomass properties replaced by char properties. In this stage the char is only allowed to be heated up, we do not include combustion of char.

In all four stages of the process, the heat flux to a particle is not only dependent on time through its dependence on T_s, but also by the dependence of T_g on time, e.g., due to motion of the particle in the non-uniform gas temperature field in the domain and due to explicit changes in the gas temperature with time.

If a particle is thick enough, pyrolysis can start before the thermal front in stage 1 reaches the center of the particle. In such a case the particle is divided in three regions and quadratic temperature profiles are assumed in all three.

Since particles are small and have a much higher mass density than the gas phase, we assume that the drag force is the only relevant force between the two phases [4]. For each particle, the following equation of motion is solved:

$$\frac{d\mathbf{v}_i}{dt} = (\mathbf{u}\,(\mathbf{x}_i, t) - \mathbf{v}_i)\left(\frac{\left(1 + 0.15Re_p^{0.687}\right)}{\tau_p} + \frac{1}{m_i}\frac{dm_i}{dt}\right), \tag{5}$$

in which the Stokes force and the acceleration due to change in mass of the particle are taken into account. The mass rate of change $dm_i/dt = 4\pi r_c^2(\rho_b - \rho_c)v_c$ is computed from the velocity of the char front, which is one of the variables in the set of equations of the particle in stage 3. In (5) $\mathbf{v}_i$ is the velocity of particle i, $\mathbf{u}\,(\mathbf{x}_i, t)$ the velocity of the gas at location $\mathbf{x}_i$ of the particle, $Re_p = \mid \mathbf{v}_i - \mathbf{u}(\mathbf{x}_i, t) \mid d_i/\nu$ the Reynolds number of the particle, $\tau_p = \rho_i d_i^2/18\mu_g$ the particle relaxation time with d_i the particle diameter, ρ_i the time-dependent mass density of the particle, and μ_g the dynamic viscosity of the gas.

3 Carrier Phase

The carrier phase of the channel flow consists of air. The compressible Navier-Stokes equations are solved with a second-order accurate finite volume method. Because of the two-way coupling, some extra terms are present in the Navier-Stokes equations. In this way the contribution of a particle to the gas equations is added to the control volume in which the particle is present. The particle-gas interaction does not change the total mass, momentum and energy of the system. Integration in time is performed using the same four-stage second-order accurate Runge-Kutta method for the gas phase and the particles.

The channel geometry has a size of $4\pi H$ in streamwise direction and $2\pi H$ in spanwise direction, where H is half the channel height (see Fig. 1). The mesh is uniform in the periodic directions (streamwise and spanwise) and clustering is adopted near the walls. At the walls the no-slip condition is adopted and the temperature is kept fixed. For the particles, periodic conditions are applied in the homogeneous flow directions. If a particle approaches a wall within a distance of its radius, elastic collision without heat transfer is applied.

Simulations are performed at Reynolds number $Re_\tau = 150$, based on friction velocity and half the channel height. The flow is initialized by a fully developed turbulent velocity and temperature field obtained from a previous simulation without particles. The initial particle distribution is random and homogeneous. The initial particle velocity is equal to the gas velocity at the particle location. The initial particle temperature is 300 K.

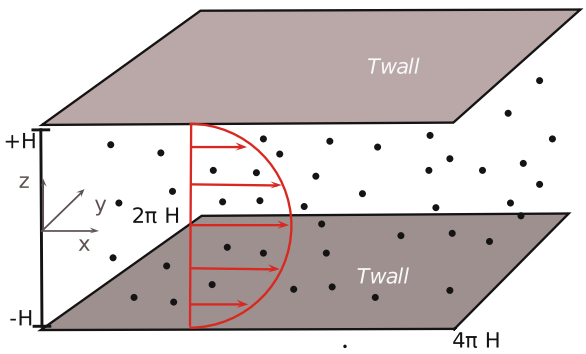

Fig. 1 Geometry of the channel

4 Pyrolysis Conversion Time

The analysis of the dependency of the conversion time on the particle volume fraction and the particle size was performed by means of numerical simulations.

We performed simulations with different numbers of particles in order to analyze the pyrolysis conversion time as a function of the particle volume fraction. The diameter of all particles was 0.7 mm. The initial gas temperature was 1,400 K. The particle Stokes number changes from 40 to 5 during pyrolysis. The results show that the heating-up time increases with increasing volume fraction. The two-way particle-gas interaction affects the gas temperature because of the convective heat exchange: more particles extract more heat from the gas compared to simulations with fewer particles. This results in a slower particle heating up and increases the mean particle pyrolysis conversion time, as shown in Fig. 2.

In order to investigate the effect of particle size on the conversion time, we performed simulations with constant volume fraction and varying particle diameter. The volume fraction (2.55×10^{-4}) is in the range where particle collisions can be ignored but two-way coupling is relevant [5]. The initial gas temperature in these simulations was taken 1,200 K. Without two-way coupling the gas temperature would remain constant and the conversion time would increase linearly with the diameter of the particles. Due to two-way coupling the gas temperature is time dependent and the particle conversion time shows a more than linear dependence on particle diameter, see Fig. 3.

In practical applications of co-firing of biomass and coal, the probability density function of biomass particle diameter follows a Rosin-Rammler distribution [6]. In Fig. 4 the distribution of torrefied beech wood is shown. We used this size

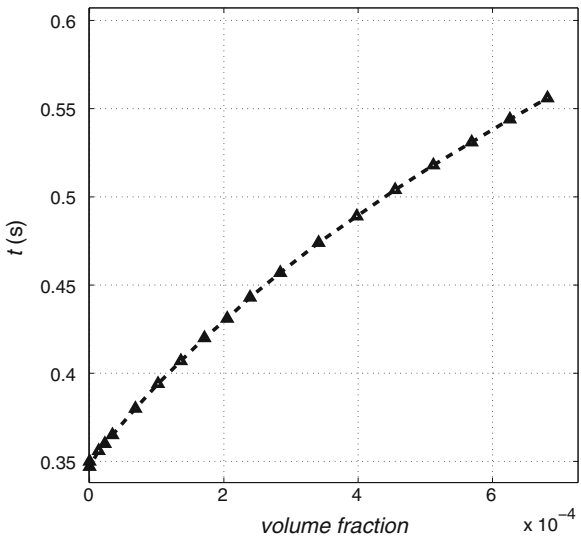

Fig. 2 Conversion time for different volume fractions with particle diameter 0.7 mm

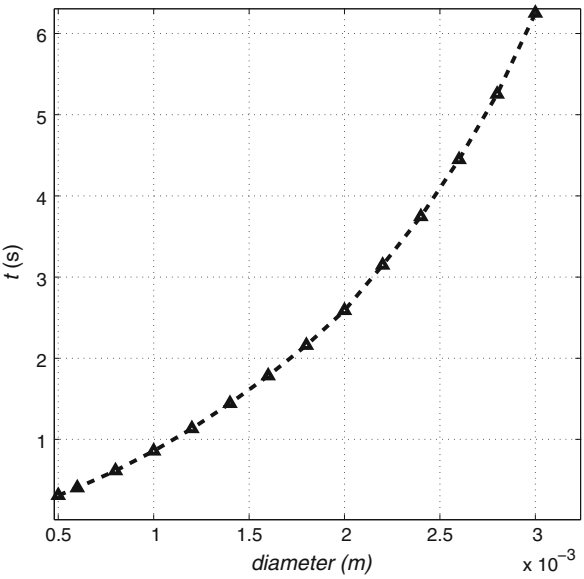

Fig. 3 Conversion time versus particle diameter at constant volume fraction

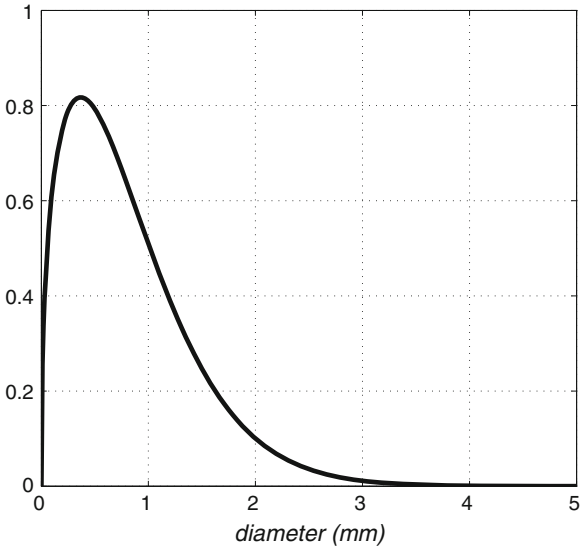

Fig. 4 Rosin-Rammler size distribution of torrefied beech wood

distribution but truncated at 3 mm. For larger particles the point-particle assumption is less accurate. It can be observed that only few particles are larger than 3 mm. Very small particles require a very small time step in our explicit time-integration method. Therefore, we also bounded the size distribution from below. We performed four simulations in which the cut-off of the particle size pdf was set at 0.5, 0.3, 0.2 and 0.15 mm in order to investigate whether it is possible to disregard very small

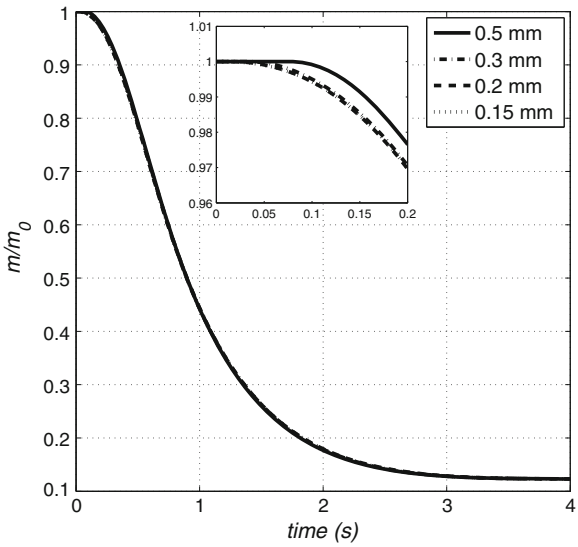

Fig. 5 Biomass mass versus time at different cut-off values

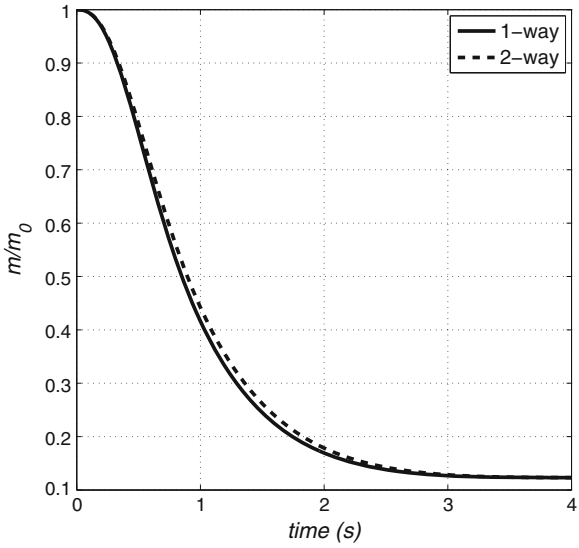

Fig. 6 Biomass mass loss: 1-way and 2-way coupling

particles without noticeably influencing the results. The volume fraction of biomass is 6×10^{-5}.

In the absence of very small particles the pyrolysis and therefore the particle mass loss starts somewhat later, as Fig. 5 shows for an initial gas temperature of 1,200 K. The results show that a cut-off at 0.2 mm or less hardly influences the results. According to [5], the volume fraction used is in the one-way coupling range, where the coupling terms in the momentum equation can be ignored. The results in Fig. 6

demonstrate that the same holds for the coupling terms in the gas temperature equation, as the differences between one-way coupled and two-way coupled simulations are small.

Acknowledgments This research is supported by the Dutch Technology Foundation STW, applied-science division of NWO (Netherlands Organization for Scientific Research), and the Technology Program of the Ministry of Economic Affairs of the Netherlands.

References

1. Haseli, Y., van Oijen, J.A., de Goey, L.P.H.: Modeling biomass particle pyrolysis with temperature-dependent heat of reactions. J. Anal. Appl. Pyrol. **90**, 140–154 (2011)
2. Haseli, Y., van Oijen, J.A., de Goey, L.P.H.: Numerical study of the conversion time of single pyrolyzing biomass particles at high heating conditions. Chem. Eng. J. **169**, 299–312 (2011)
3. Haseli, Y., van Oijen, J.A., de Goey, L.P.H.: Predicting the pyrolysis of single biomass particles based on a time and space integral method. J. Anal. Appl. Pyrol. **96**, 126–138 (2012)
4. Armenio, V., Fiorotto, V.: The importance of the forces acting on particles in turbulent flows. Phys. Fluids **13**, 2437 (2001)
5. Elghobashi, S.: On predicting particle-laden turbulent flows. Appl. Sci. Res. **52**, 309–329 (1994)
6. Rosin, P., Rammler, E.: The laws governing the fineness of powdered coal. J. Inst. Fuel **7**, 29–36 (1933)

Modulation of Isotropic Turbulence by Resolved and Non-resolved Spherical Particles

A.H. Abdelsamie and D. Thévenin

1 Introduction

The main objective of the current study is to investigate the effect of either non-resolved (point particles) or fully resolved particles on a field of isotropic, either stationary or decaying turbulence using direct numerical simulation (DNS), clarifying how those different settings influence the turbulence statistics. This work can help answering some of the questions raised by Lucci et al. [12] and Abdelsamie and Lee [1]. The first group concluded that it is not correct at all to investigate two-way coupling using stationary turbulence; the second showed that using a point-force approach with a Stokes number, St, larger than unity, both stationary and decaying turbulence lead to the same qualitative trends. The non-resolved particles, with diameter (d) smaller than the Kolmogorov length scale (η), are tracked using a point approach, whereas the fully resolved particles, with a diameter larger than the Kolmogorov length scale, are tracked using an Immersed Boundary Method. Two different collision models have been tested in the fully resolved case; the hard sphere model (HSM) and the velocity barrier model (VBM).

The results reveal that decaying and stationary turbulence lead to different findings when considering fully resolved particles ($\mathrm{St} \gg 1$). On the other hand, the point-force approach ($\mathrm{St} > 1$) leads to the same trends with either decaying or stationary turbulence. The employed collision models impacts noticeably the small scale statistics, particularly turbulence kinetic energy dissipation rate. On the other hand, large scale statistics are only slightly modified. Therefore, a close look at the small-scale statistics appears to be essential when developing and testing models for four-way coupling.

A.H. Abdelsamie (✉) · D. Thévenin
Otto von Guericke University of Magdeburg, Magdeburg, Germany
e-mail: abouelmagd.abdelsamie@ovgu.de

D. Thévenin
e-mail: thevenin@ovgu.de

J. Fröhlich et al. (eds.), *Direct and Large-Eddy Simulation IX*,
ERCOFTAC Series 20, DOI 10.1007/978-3-319-14448-1_78

2 Mathematical Approaches

In the present study, an Eulerian-Lagrangian approach is used to represent the coupled dynamics of fluid and particles. We consider solid spherical particles with diameters either larger or smaller than the Kolmogorov length scale, dispersed in an incompressible isotropic flow. Therefore, the governing equations for the carrier-phase are the Navier-Stokes equations,

$$\frac{\partial u_i}{\partial t} = rhs_i + f_i, \tag{1}$$

$$rhs_i = -\frac{\partial}{\partial x_i}\left(\frac{p}{\rho} + \frac{1}{2}u_j u_j\right) + \varepsilon_{ijk} u_j \omega_k + \nu \frac{\partial^2 u_i}{\partial x_j \, \partial x_j}, \tag{2}$$

and the fluid continuity equation,

$$\frac{\partial u_i}{\partial x_i} = 0. \tag{3}$$

Here, the alternating tensor ε_{ijk} represents the cross product between the fluid velocity u and vorticity ω, p is the fluid pressure, ρ and ν are the fluid density and kinematic viscosity, respectively. The last term in Eq. (1), f, is a force term in Eulerian space (g_h) which represents the action of solid spheres upon the fluid converted from the Lagrangian space (S_m) force, F, either in point force approach,

$$f(x) = \sum_{m=1}^{N_p} F(X^m)\delta_h(x - X^m) \quad \forall\, x \in g_h,\ X^m \in S_m, \tag{4}$$

or in fully resolved approach,

$$f(x) = \sum_{m=1}^{N_p} \sum_{l=1}^{N_L} F(X^m)\, \delta_h(x - X_l^m)\, \Delta V_l^m \quad \forall\, x \in g_h,\ X_l^m \in S_m, \tag{5}$$

using a 3-point approximation of the Dirac delta function [12, 16], δ_h, where N_p, N_L are the number of the released particles and uniformly distributed points over the sphere surface (in fully resolved approach) that are used to transfer the point forces to the fluid, respectively. Every point force, in fully resolved approach, has an associated discrete volume ΔV_l^m, which was proposed in [18] in order to formulate a volume force at each Lagrangian force point instead of a singular force as introduced in the original IBM in [15]. The motion of the non-resolved particles is impacted in the current study only by Stokes drag force, considering that the particle to fluid density ratio is high ($\rho_p/\rho \sim 800$). Therefore, Saffman and Magnus lift forces can be neglected,

$$\frac{\partial U_i^m}{\partial t} = \frac{\tilde{u}_i - U_i^m}{\tau_p}. \tag{6}$$

For the fully resolved solid sphere particles moving in incompressible fluid and simulated with immersed boundary, the conservation equations of linear and angular momentum shown in [12, 18] are used, neglecting gravity,

$$V_c^m \left(\rho_p^m - \rho\right) \frac{d\mathrm{U}^m}{dt} = -\rho \sum_{l=1}^{N_L} \mathrm{F}(X_l^m) \Delta V_l^m, \tag{7}$$

$$I_c^m \frac{d\Omega^m}{dt} = -\rho \sum_{l=1}^{N_L} \left(X_l^m - X_c^m\right) \times \mathrm{F}(X_l^m) \Delta V_l^m + \rho \frac{d}{dt} \int_{S_m} \left[\left(x - X_c^m\right) \times \mathrm{u}\right] dx, \tag{8}$$

where I_c^m, X_c^m and X_l^m are the m-th particle moment of inertia, center position and location of the distributed points over each particle that describe particle surface [12], respectively. The variables U^m, Ω^m, ρ_p and V_c^m are the particle translational velocity, rotational velocity, density and volume, respectively. In Eq. (6), $\tilde{u}$ is the fluid velocity at the particle location, which is obtained by a fourth-order Lagrange interpolation.

2.1 Particle-Particle Interaction

Particle-particle interaction (collision) has been considered in the fully resolved case in order to avoid unphysical particle overlapping and penetration. Two different models have been used and tested: velocity barrier model (VBM [6]),

$$B_U^{(m,j)} = \begin{cases} -\frac{V_{ref}}{d_p} \left[\frac{d_R^2 - d_{(m,j)}^2}{d_R^2 - d_p^2}\right]^2 \left(X_p^m - X_p^j\right), & \text{if } d_{(m,j)} < d_R, \\ 0, & \text{elsewhere,} \end{cases} \tag{9}$$

and the hard sphere model (HSM [5, 11]),

$$m_p^m (\mathbf{U}^m(1) - \mathbf{U}^m(0)) = \mathbf{J}, \tag{10}$$

$$m_p^j (\mathbf{U}^j(1) - \mathbf{U}^j(0)) = -\mathbf{J}, \tag{11}$$

$$I_p^m (\Omega^m(1) - \Omega^j(0)) = d_p^m \, \mathbf{n} \times \mathbf{J}, \tag{12}$$

$$I_p^j (\Omega^m(1) - \Omega^j(0)) = d_p^j \, \mathbf{n} \times (-\mathbf{J}), \tag{13}$$

where $B_U^{(m,j)}$ is velocity barrier added to the particle velocity before advection, while d_R and $d_{(m,j)} = |X_p^m - X_p^j|$ are prescribed and actual distance between m and j particle centers, respectively. For HSM, $\mathbf{U}(0)$, $\mathbf{U}(1)$, $\Omega(0)$ and $\Omega(1)$ are the particle's transitional and rotational velocity vectors of the particle before and after the collision, respectively. In Eqs. (10–13) $\mathbf{J}$ and $\mathbf{n}$ are the impulsive force exerted on the particles and the normal vector parallel to the center line between two particles.

2.2 Numerical Schemes

Numerically, the main difference between the point force and fully resolved particles is how to obtain the force, f in Eq. (1). In the point force approach, the force in Lagrangian space (S_m) is computed from the particle acceleration (Eq. 6) times particle mass. Another solution is needed for fully resolved particles. Following [18], a general discretization can be written as:

$$\frac{u_i^{n+1} - u_i^n}{\Delta t} = rhs_i^{n+1/2} + f_i^{n+1/2} \quad \forall\, x \in g_h, \tag{14}$$

and f is computed in Lagrangian space as follows:

$$F^{n+1/2} = \frac{\mathrm{U}^d - \widetilde{\mathrm{U}}^{*n}}{\Delta t} \quad \forall\, X \in S_m, \tag{15}$$

$$\widetilde{\mathrm{U}}^{*n}(X_l^m) = \sum_{g_h} \left[\mathrm{u}^n(x) + \Delta t \left(rhs^{n+1/2}(x) \right) \right] \delta_h \left(x - X_l^m \right) \Delta x^3 \tag{16}$$

where U^d is the desired particle velocity,

$$\mathrm{U}^d(X_l^m) = \mathrm{U}^m + \Omega_p^m \times \left(X_l^m - x_p^m \right). \tag{17}$$

A pseudo-spectral algorithm is used in the present work to solve the Navier-Stokes equation, instead of a finite difference method like that used by Lucci et al. [12, 18]. It is thus possible to obtain a high-accuracy solution, but this leads to new challenges for combining with IBM [13, 14]. In the pseudo-spectral algorithm all the dependent variables are expanded in a Fourier series over a periodic domain, $L^3 = (2\pi)^3$. The time-advancing scheme for fluid and particle equations is a third-order, three-stage Runge-Kutta scheme.

The 3-point approximation of the delta function, δ, is used to interpolate variables (u, rhs) from Eulerian to Lagrangian spaces, Eq. (16), and to interpolate force, F, from Lagrangian to Eulerian spaces, Eqs. (4) and (5). The results discussed below have been collected over 128^3 grid points for flows with Taylor micro-scale Reynolds number, $\mathrm{R}_\lambda = 60$, Kolmogorov length scale, $\eta = 0.025$, Kolmogorov time scale, $\tau_k = 0.042$, integral length scale, $\Lambda = 1.006$ and large eddy turn overtime scale,

$\tau_\Lambda = 0.409$. All these quantities are dimensionless. The flow field was generated by stationary isotropic flow code, and then it is used as an initial field for both stationary and decaying turbulence. The particles are injected, initially, with the same velocity as the surrounding flow.

3 Results

In this section the modulation of turbulence due to the presence of solid particles is discussed comparing the point force approach and the fully resolved approach.

3.1 Point Force Approach (Non-resolved Particles)

Figure 1a–c show the modulation of the turbulence kinetic energy, q^2, and its dissipation rate, ε, versus St for stationary turbulence. Additionally, the modulation of the turbulence kinetic energy and its dissipation rate in decaying turbulence,

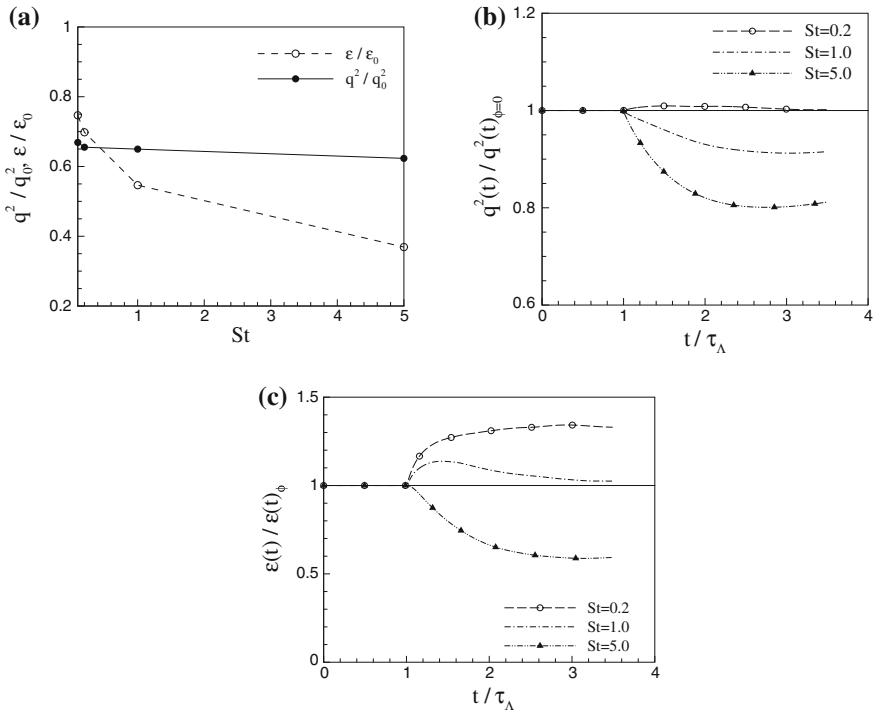

Fig. 1 **a** Average stationary turbulence kinetic energy and its dissipation rate modulation, **b** temporal decaying turbulence kinetic energy modulation, **c** temporal decaying turbulence kinetic energy dissipation rate modulation

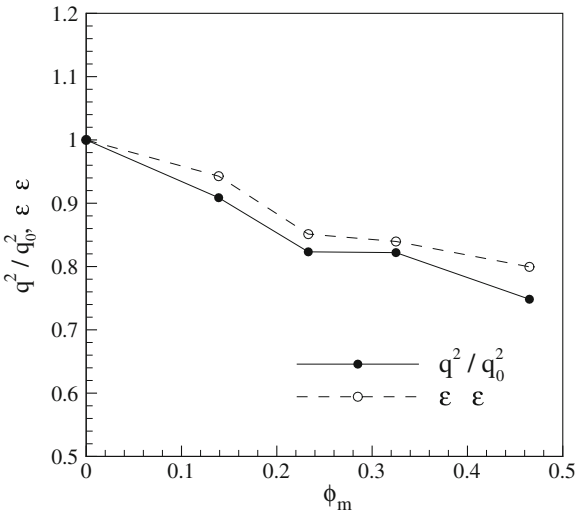

Fig. 2 Average stationary turbulence kinetic energy and its dissipation rate modulation

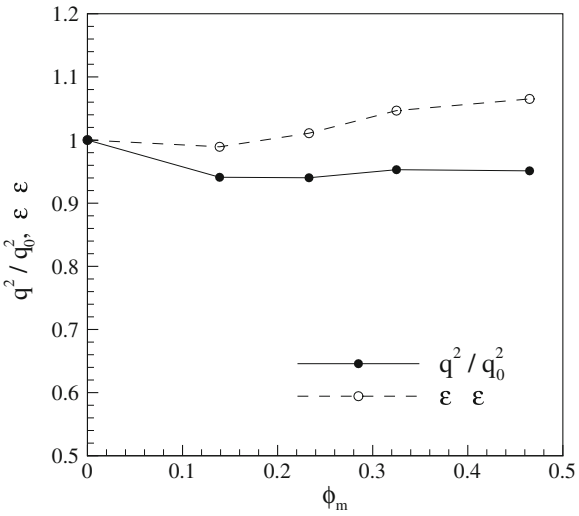

Fig. 3 Average decaying turbulence kinetic energy and its dissipation rate modulation

respectively, are shown for a constant mass loading, $\phi_m = 0.4$. The quantities in Fig. 1 are all normalized with the averaged turbulence quantities (q_0^2 and ε_0) obtained for one-way simulations (without particles). For decaying turbulence, the normalization relies on the temporal value obtained without particles ($q^2(t)_{\phi=0}$ and $\varepsilon(t)_{\phi=0}$). In these figures the kinetic energy and dissipation rate modulation are qualitatively similar considering either stationary or decaying turbulence as long as St ≥ 1. These observations are consistent with observations from the literature [1, 2, 4, 7–10, 17].

3.2 Fully Resolved Approach

The particles considered with the fully resolved approach are always with $\mathrm{St} \gg 1$ and $d/\eta \gg 1$: $35 \leq \mathrm{St} \leq 120$, $1.5 \leq \rho_p/\rho \leq 5$, $d/\eta = 20$, $N_L = 1{,}200$ and $N_p = 350$. At the opposite of the results found with the point force approach, stationary and decaying turbulence lead now to different modulation behaviors. Figures 2 and 3 show the time average of kinetic energy and its dissipation rate in stationary and decaying turbulence, respectively. In stationary turbulence, the kinetic energy and dissipation rate decrease monotonically with particle mass loading (Fig. 2). On the other hand, in decaying turbulence the kinetic energy decreases only slightly with mass loading before remaining quite constant, whereas the dissipation rate increases monotonically with mass loading (Fig. 3). We attribute the enhancement in decaying turbulence dissipation rate to the local enhancement in turbulence small scale structure (at a size of the order of particle diameter), which is due to the presence of the particles and thus increases with mass loading. This local turbulence enhancement cannot expand up to a global enhancement in stationary turbulence because of the artificial force added to keep turbulence stationary (further details and a spectrum analysis can be found in [3]).

Figures 2 and 3 were obtained from simulation using VBM to prevent particle overlapping. Changing now the collision model to HSM, the turbulence large scale quantities are not much changed, as it can be seen from Fig. 4, which shows the temporal turbulence kinetic energy modulation with HSM and VBM compared to that without particles ($\phi_m = 0.00$). However, the turbulence kinetic energy dissipation rate (a small scale property), shows a high sensitivity to the collision model (Fig. 5). For all cases considered up to now, HSM and VBM show qualitatively the same modulation trend, but lead to noticeable quantitative differences for small-scale properties.

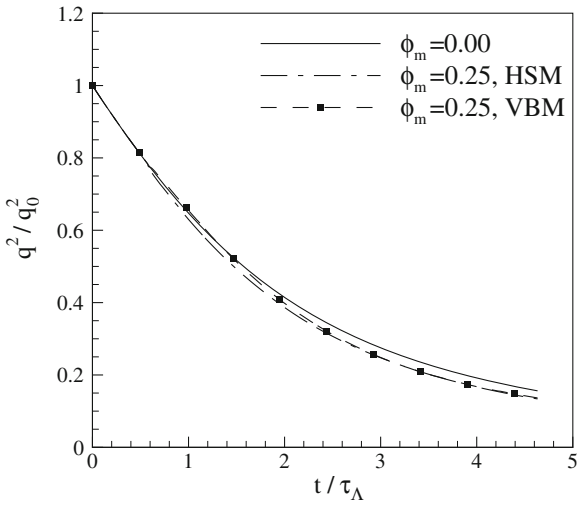

Fig. 4 Effect of collision model (*HSM* or *VBM*) on the temporal decaying turbulence kinetic energy

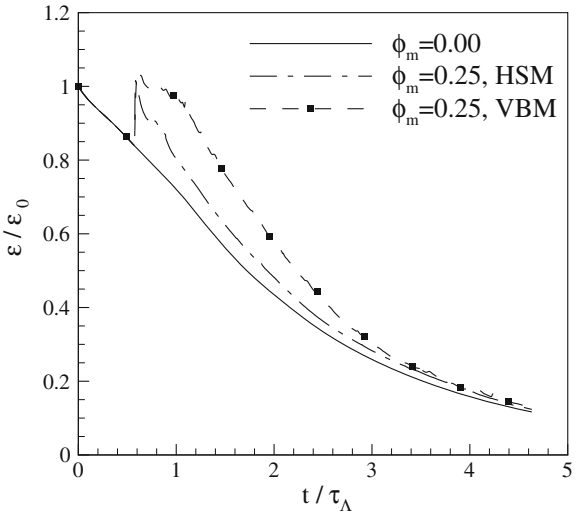

Fig. 5 Effect of collision model (*HSM* or *VBM*) on the temporal decaying turbulence kinetic energy dissipation rate

4 Conclusions

Considering fully resolved particles in the simulation, decaying and stationary turbulence lead to different evolutions of the key turbulence properties. On the other hand, decaying and stationary turbulence lead to identical qualitative trends when modeling particles with a point-force approach. These discrepancies and the connected issue of the particle's Stokes number must be elucidated in further studies. The collision model needed to avoid artificial particle overlapping shows a significant effect on the small-scale turbulence statistics, particularly on the dissipation rate. Therefore, it appears to be particularly important to check small-scale turbulence properties when developing and testing models suitable for four-way coupling simulations.

Acknowledgments The authors would like to thank Prof. C. Lee for his recommendations and discussions about spectral methods. The help of Dr. G. Janiga and Dr. G. Fru concerning post-processing is gratefully acknowledged.

References

1. Abdelsamie, A.H., Lee, C.: Decaying versus stationary turbulence in particles-laden isotropic turbulence: turbulence modulation mechanism. Phys. Fluids **24**, 015106 (2012)
2. Abdelsamie, A.H., Lee, C.: Decaying versus stationary turbulence in particle-laden isotropic turbulence: heavy particle statistics modifications. Phys. Fluids **25**, 033303 (2013)
3. Abdelsamie, A.H., Chittipotula, T., Lee, C., Thévenin, D.: Stationary and decaying turbulence modulation by finite size fully resolved particles. In: 8th International Conference on Multiphase Flow, Jeju, Korea, (2013)

4. Boivin, M., Simonin, O., Squires, K.D.: Direct numerical simulation of turbulence modulation by particles in isotropic turbulence. J. Fluid Mech. **375**, 235–263 (1998)
5. Crowe, C., Sommerfeld, M., Tsuji, Y.: Multiphase Flows with Droplets and Particles. CRC, Boca Raton (1998)
6. Dance, S.L., Climent, E., Maxey, M.R.: Collision barrier effects on the bulk flow in a random suspension. Phys. Fluids **16**, 828–831 (2004)
7. Druzhinin, O.A., Elghobashi, S.: On the decay rate of isotropic turbulence laden with microparticles. Phys. Fluids **11**, 602–610 (1999)
8. Druzhinin, O.A.: The influence of particle inertia on the two-way coupling and modification of isotropic turbulence by microparticles. Phys. Fluids **13**, 3738–3755 (2001)
9. Elghobashi, S., Truesdell, G.C.: On the two-way interaction between homogeneous turbulence and dispersed solid particles. I: Turbulence modification. Phys. Fluids A **5**, 1790–1801 (1993)
10. Ferrante, A., Elghobashi, S.: On the physical mechanisms of two-way coupling in particle laden isotropic turbulence. Phys. Fluids **15**, 315–329 (2003)
11. Kempe, T., Fröhlich, J.: Collision modelling for the interface resolved simulation of spherical particles in viscous fluids. J. Fluid Mech. **709**, 445–489 (2012)
12. Lucci, F., Ferrante, A., Elghobashi, S.: Modulation of isotropic turbulence by particles of taylor length-scale size. J. Fluid Mech. **650**, 5–55 (2010)
13. Mohd-Yusof, J.: Combined Immersed-Boundary/B-spline Methods for Simulations of Flow in Complex Geometries. CTR Annual Research Briefs, Stanford Univ., pp. 317–327 (1997)
14. Mohd-Yusof, J.: Development of Immersed Boundary Methods for Complex Geometries. CTR Annual Research Briefs, Stanford Univ., pp. 325–336 (1998)
15. Peskin, C.: The immersed boundary method. Acta Numer. **11**, 1–39 (2002)
16. Roma, A., Peskin, C., Berger, M.: An adaptive version of the immersed boundary method. J. Comput. Phys. **153**, 509–534 (1999)
17. Sundaram. S., Collins, L. R.: A numerical study of the modulation of isotropic turbulence by suspended particles. J. Fluid Mech. **379**, 105–143 (1999)
18. Uhlmann, M.: An immersed boundary method with direct forcing for the simulation of particulate flows. J. Comput. Phys. **209**, 448–476 (2005)

A Hybrid Stochastic-Deconvolution Model for LES of Particle-Laden Flow

W.R. Michałek, J.G.M. Kuerten, J.C.H. Zeegers, R. Liew, J. Pozorski and B.J. Geurts

1 Introduction

In recent years numerical simulation methods have been developed for the study of particle-laden turbulent flows. For large numbers of small particles the details of the flow around each particle cannot be resolved, and a point-particle approach has to be adopted, in which correlations for the forces exerted by the fluid on a particle are used [1]. In direct numerical simulation (DNS) all scales of the fluid flow are resolved. Large-eddy simulation (LES) can be performed at higher Reynolds numbers because in LES only the larger eddies are resolved. The absence of the small scales in the flow requires a sub-grid scale (SGS) model for the fluid.

The missing scales in LES affect the motion of small particles present in the flow and can only be neglected when the particle relaxation time is large compared to the Kolmogorov time scale and to the time scales of the smallest resolved scales. The missing effect of SGS on the particles leads to discrepancies in the prediction of turbulent dispersion and of turbophoresis [3].

The influence of the missing SGS can be modeled by an SGS model for particles. Two types of SGS models have been developed in the past. The first type is a

W.R. Michałek (✉) · J.G.M. Kuerten
Department of Mechanical Engineering, Eindhoven University of Technology, Eindhoven, The Netherlands
e-mail: w.michalek@tue.nl

J.G.M. Kuerten
e-mail: j.g.m.kuerten@tue.nl

J.C.H. Zeegers · R. Liew · B.J. Geurts
Department of Applied Physics, Eindhoven University of Technology, Eindhoven, The Netherlands

J. Pozorski
Institute of Fluid-Flow Machinery, Polish Academy of Sciences, Gdańsk, Poland

B.J. Geurts · J.G.M. Kuerten
Faculty EEMCS, University of Twente, Enschede, The Netherlands

J. Fröhlich et al. (eds.), *Direct and Large-Eddy Simulation IX*,
ERCOFTAC Series 20, DOI 10.1007/978-3-319-14448-1_79

stochastic model for the unresolved scales [5]. The second type of SGS models is based on approximate deconvolution. The deconvolution of the filtered fluid velocity in LES allows to recover the energy up to the smallest resolved scales [3]. The SGS model for particles based on ADM improves the prediction of statistical particle quantities substantially in channel flow at lower Reynolds numbers. However, at higher Reynolds numbers the improvement is less satisfactory [4].

In 2012, Geurts and Kuerten [2] investigated ideal stochastic forcing of particles in LES of particle-laden channel flow in which the drag force exerted by the fluid on the particles is the only relevant force. The investigation was based on the results of DNS of particle-laden turbulent channel flow at Reynolds numbers: $\mathrm{Re}_\tau = 150$, 395, and 950 and for different particle sizes corresponding to a range of Stokes numbers, i.e., particle relaxation time in wall units, $\mathrm{St} = 0.2$, 1, 5 and 25. They decomposed the fluid velocity $\mathbf{u}$ at the particle position into two contributions: the known deconvolution of the filtered fluid velocity ($\mathbf{u}^*$) and $\delta\mathbf{u}^* = \mathbf{u} - \mathbf{u}^*$, which needs to be modeled. Hence, the particle equation of motion can be written as:

$$\frac{d\mathbf{v}}{dt} = \frac{\mathbf{u}^*(\mathbf{x}, t) - \mathbf{v}}{\tau_p} + \frac{\delta\mathbf{u}^*}{\tau_p}, \tag{1}$$

where $\mathbf{v}$ is the particle velocity and τ_p the particle relaxation time. The first term on the right-hand side involves particle SGS based on ADM [3, 4]. The second term requires additional modeling. The statistical properties of $\delta\mathbf{u}^*$, like the root-mean square (RMS) are basically identical for all investigated Stokes numbers [2].

2 Governing Equations and Numerical Methods

The results of the *a priori* [2] analysis are used to develop a SGS model for particles, which is a combination of ADM and a stochastic model. This model is tested on LES of particle-laden channel flow at Reynolds number $\mathrm{Re}_\tau = 950$ based on the shear velocity $\mathbf{u}_\tau$ and half the channel height H. An Eulerian-Lagrangian approach is used for the fluid and for point particles one-way coupled to the fluid.

Since, the ADM is used as the SGS model for the fluid, the incompressible Navier-Stokes equation is solved in the following rotational form:

$$\frac{\partial\overline{\mathbf{u}}}{\partial t} + \overline{\omega^* \times \mathbf{u}^*} + \nabla\overline{P} = \nu\Delta\overline{\mathbf{u}} + \mathbf{F} - \chi(I - Q_N G)\overline{\mathbf{u}}, \tag{2}$$

where

$$u_i^* = Q_N\overline{u}_i = \sum_{k=0}^{5}(I - G)^k\overline{u}_i \tag{3}$$

and $\overline{u}_i = G * u_i$ is the filtered velocity with filter kernel G. The vorticity field of the deconvolved velocity is denoted by $\omega^* = \nabla \times \mathbf{u}^*$ and $\overline{P} = \overline{p}/\rho_f + \frac{1}{2}\overline{\mathbf{u}}^2$ with

p the fluctuating part of the pressure, ρ_f the fluid mass density, and $\mathbf{F}$ is the driving force per unit mass in the streamwise direction parallel to the walls of the channel, constant in time and space. The filtered velocity field satisfies the continuity equation for incompressible flow: $\nabla \cdot \overline{\mathbf{u}} = 0$.

Lagrangian tracking of particles is performed by numerically integrating the equation: $d\mathbf{x}(t)/dt = \mathbf{v}$, together with Eq. (1). A solution of the Langevin equation

$$\frac{d\delta\mathbf{u}^*}{dt} = -\frac{\delta\mathbf{u}^*}{\tau} + Cw(t), \tag{4}$$

is taken as the model for the stochastic part in Eq. (1) [5]. Here τ is the Lagrangian correlation time of $\delta\mathbf{u}^*$, $C = \delta\mathbf{u}^*_{rms}\sqrt{2/\tau}$ and $w(t)$ is Gaussian white noise of unit variance. Both $C = \delta\mathbf{u}^*_{rms}$ and τ follow from the *a priori* analysis [2]. The basic hybrid stochastic-deconvolution model presented above does not satisfy the well-mixed condition [6]. Therefore, an extension of the model is proposed to retain an initial uniform distribution of passive particles at later times. The well-mixed condition can be satisfied similarly as Thomson proposed [6]. It leads to an extra term in the stochastic equation for the wall-normal component of δu_y^*:

$$\frac{d\delta u_y^*}{dt} = -\frac{\delta u_y^*}{\tau} + Cw(t) + f(St)\frac{d(\sigma_y^*)^2}{dy}\left(1 + \frac{1}{2}\frac{(\delta u_y^*)^2}{(\sigma_y^*)^2}\right), \tag{5}$$

where y is the wall-normal coordinate and σ_y^* is the RMS of δu_y^* obtained from the *a priori* results [2]. The extra term is multiplied with a function of the Stokes number $f(\mathrm{St})$ to have the possibility to attenuate the effect of the well-mixed term for larger Stokes numbers if necessary. This function should be between 0 and 1. To satisfy the well-mixed condition for passive particles, $f(0)$ should be equal to 1.

The initial state of the particles is a random uniform distribution with the particle velocity equal to the fluid velocity at the particle position and the initial value of $\delta\mathbf{u}^*$ chosen randomly from a Gaussian distribution with the same RMS as obtained in the *a priori* results. The diameters of the particles are chosen in such a way that the corresponding Stokes numbers are equal to: 0.2, 0.4, 0.7, 1, 1.5, 2, 3, 4, 5, 6, 8, and 25. For each size, 64,000 particles are tracked. Statistical results of the particles are averaged over the two homogeneous directions and over time in the statistically steady state and presented as functions of the wall-normal coordinate.

3 Results

Figure 1 shows the wall-normal component of $\delta\mathbf{u}^*_{rms}$ as a function of the wall-normal coordinate in wall units y^+. The differences between the *a priori* results for the four different Stokes numbers are small, but clearly visible [2]. A good agreement between *a priori* and *a posteriori* results for $\delta u^*_{y,rms}$ means that the hybrid stochastic-deconvolution model works well and yields the correct statistical results for $\delta\mathbf{u}^*$.

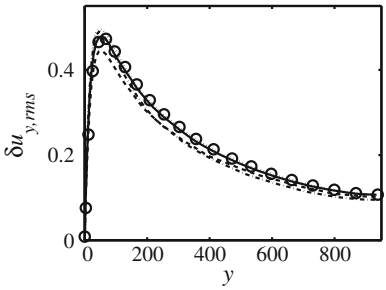

Fig. 1 $\delta u^*_{y,rms}$ as a function of the wall-normal coordinate in wall units for $\mathrm{Re}_\tau = 950$; *dotted a priori* $\mathrm{St} = 0.2$, *solid a priori* $\mathrm{St} = 1$, *dashed a priori* $\mathrm{St} = 5$, *dashed-dotted a priori* $St = 25$, ∘ *a posteriori* $\mathrm{St} = 1$ with $f(1) = 0.6$

In spite of the weak dependence of $\delta \mathbf{u}^*_{rms}$ on Stokes number, it turned out that small deviations in C in Eq. (4) result in significant changes in the statistical particle results, especially in the prediction of particle concentration. Therefore, we used the separate *a priori* results for each Stokes number.

In general, all statistical particle velocity properties are similar or slightly improved by the use of the hybrid stochastic-deconvolution model (Eq. (4)) in comparison to the results of the SGS model for the particles with only the ADM in the particle equation of motion. For the biggest particles considered here ($\mathrm{St} = 25$) also the prediction of the particle concentration is very accurate. However, the turbophoresis effect is strongly overpredicted for smaller particles, especially with $\mathrm{St} \leq 1$.

The stochastic model does not satisfy the well-mixed condition [6] and it results in overprediction of the particle concentration close to the wall. Moreover, for inertial particles with small Stokes numbers and especially for passive particles, which follow the fluid flow exactly, the use of the stochastic model to generate the unfiltered fluid velocity at the particle position results in a continuous increase in particle concentration near the walls, in contrast with the DNS results.

The concentration results for $\mathrm{St} = 0.2$ are in a very good agreement with the DNS results when the well-mixed term is added to the basic hybrid model and $f(0.2) = 1$. However, the situation is different in case of larger particles. Figure 2 shows the

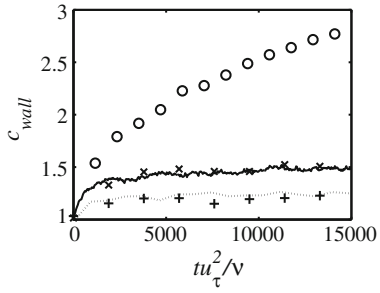

Fig. 2 The particle concentration close to the walls as a function of time in wall units, t^+, for $\mathrm{St} = 1$; *solid* DNS, *dotted* LES with ADM for particles, ∘ LES with ADM and stochastic model for particles, + LES with ADM and stochastic model with the well-mixed term for particles, x LES with ADM and stochastic model with $f(1) = 0.6$ for particles

particle concentration close to the walls for particles with St = 1 as a function of time in wall units $t^+ = tu_\tau{}^2/\nu$, for the results with Eq. (5). The effect of the extra term is indeed a decrease of the particle concentration close to the walls. We find that only for passive particles and inertial particles with $St \ll 1$ the prediction of the particle concentration close to the walls is in close agreement with DNS results. For larger particles the decrease of the concentration close to the walls is too large. This underestimation increases with increasing Stokes number and the extra term is only required for smaller particles and should be reduced in magnitude for inert particles. Therefore, we propose to multiply the extra term with a function of Stokes number, $f(\mathrm{St})$, which equals 1 for St = 0 and monotonically decreases to zero. Figure 2 shows that a very good agreement with the DNS results is obtained if $f(1) = 0.6$.

For larger particles, we chose the optimum values of $f(\mathrm{St})$ which give the best agreement in the statistically steady state. Figure 3 shows the results of this investigation which are well described by $f(\mathrm{St}) = \exp(-\mathrm{St}/2)$.

The phenomenon of turbophoresis and all quantities related to it are caused by the mean relative particle velocity in the wall-normal direction, which is a consequence of the inhomogeneity of the turbulence. Figure 4 presents the mean relative particle velocity as a function of the distance from the wall in wall units, y^+, for St = 1. The addition of the stochastic model in the particle equation of motion that includes the well-mixed term for particles results in a significant improvement of the mean relative particle velocity. The stochastic model has no influence on the streamwise particle velocity (mean and RMS). However, the stochastic model improves the RMS

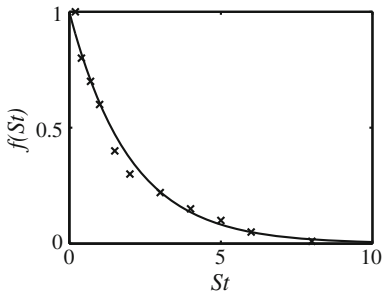

Fig. 3 The optimum values of $f(\mathrm{St})$ (*markers*) and a general trend (*solid*)

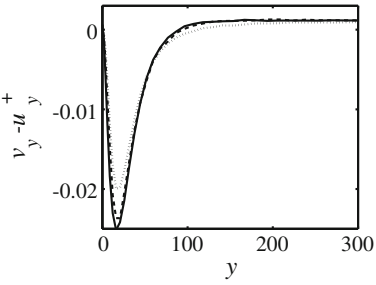

Fig. 4 The mean relative particle velocity as a function of y^+ for St = 1; *solid* DNS, *dotted* LES with ADM for particles, *dashed* LES with ADM and stochastic model with $f(1) = 0.6$ for particles

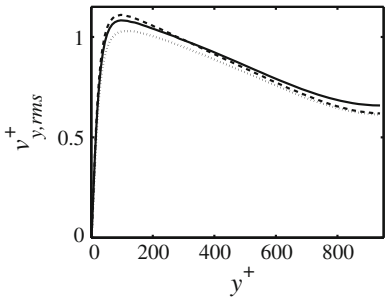

Fig. 5 The RMS of the wall-normal particle velocity as a function of the wall-normal coordinate in wall units for St = 1; *solid* DNS, *dotted* LES with ADM for particles, *dashed* LES with ADM and stochastic model with $f(1) = 0.6$ for particles

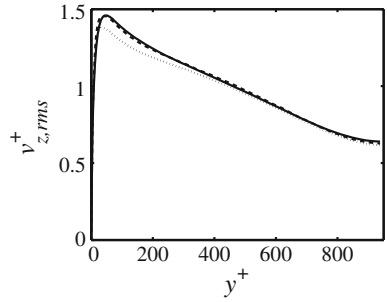

Fig. 6 The RMS of the spanwise particle velocity as a function of the wall-normal coordinate in wall units for St = 1; *solid* DNS, *dotted* LES with ADM for particles, *dashed* LES with ADM and stochastic model with $f(1) = 0.6$ for particles

of the wall-normal and spanwise particle velocity. Figures 5 and 6 show the RMS of the wall-normal and spanwise particle velocity respectively as a function of the distance from the wall in wall units, y^+, for St = 1. The well-mixed term does not affect the results for the streamwise and spanwise particle velocity and the influence on the wall-normal component is barely visible.

The results for other Stokes numbers are very similar. In all cases the hybrid model shows a better agreement with DNS results for the wall-normal and spanwise particle velocity fluctuations compared to simulations in which only the ADM is applied in the particle equation of motion.

4 Conclusions and Discussion

We developed a hybrid stochastic-deconvolution model for the particle equation of motion in LES of particle-laden turbulent flow. The coefficients in the stochastic part of the model are based on *a priori* results of DNS of the same flow.

For particles with small Stokes number an important requirement is that the stochastic model satisfies the well-mixed condition, but for larger particles the inclusion of the well-mixed term in the model deteriorates the results. The proposed a Stokes-number dependent well-mixed term yields good agreement between LES and DNS results for all Stokes numbers.

Acknowledgments This research is supported by the Dutch Technology Foundation STW, applied-science division of NWO (Netherlands Organisation for Scientific Research), and the Technology Program of the Ministry of Economic Affairs of the Netherlands. This work was sponsored by the Stichting Nationale Computerfaciliteiten (National Computing Facilities Foundation, NCF) for the use of supercomputer facilities, with Financial support from the Nederlandse Organisatie voor Wetenschappelijk Onderzoek, NWO. We thank the DEISA Consortium (www.deisa.eu), co-funded through the EU FP6 project RI-031513 and the FP7 project RI-222919, for support within the DEISA Extreme Computing Initiative.

References

1. Elghobashi, S.: On predicting particle-laden turbulent flows. Appl. Sci. Res. **52**, 309–329 (1994)
2. Geurts, B.J., Kuerten, J.G.M.: Ideal stochastic forcing for the motion of particles in large-eddy simulation extracted from direct numerical simulation of turbulent channel flow. Phys. Fluids **24**, 081702 (2012)
3. Kuerten, J.G.M.: Subgrid modeling in particle-laden channel flow. Phys. Fluids **18**, 025108 (2006)
4. Michałek, W.R., Liew, R., Kuerten, J.G.M., Zeegers, J.C.H.: LES of droplet-laden non-isothermal channel flow. J. Phys. Conf. Ser. **318**, 042056 (2011)
5. Simonin, O., Deutsch, E., Minier, J.P.: Eulerian prediction of the fluid/particle correlated motion in turbulent two-phase flows. Appl. Sci. Res. **51**, 275–283 (1993)
6. Thomson, D.J.: Criteria for the selection of stochastic models of particle trajectories in turbulent flows. J. Fluid Mech. **180**, 529–556 (1987)

Direct Numerical Simulation of a Compressible Multiphase Flow Through the Eulerian Approach

M. Cerminara, L.C. Berselli, T. Esposti Ongaro and M.V. Salvetti

1 Introduction

This work is part of a long-term project concerning modeling, simulation and analysis of particle-laden turbulent plumes, motivated by the study of the injection of ash plumes in the atmosphere during explosive volcanic eruptions. Ash plumes represent indeed one of the major volcanic hazards, since they can produce widespread pyroclastic fallout in the surrounding inhabited regions, endanger aviation and convect fine particles in the stratosphere, potentially affecting climate. Volcanic plumes are characterized by the ejection of a mixture of gases and polydisperse particles (ranging in diameter from a few microns to tens of millimetres) at high velocity (100–300 m/s) and temperature (900–1,100 °C), resulting in an equivalent Reynolds number exceeding 10^7 (at typical vent diameters of 10–100 m) [10]. Estimates of the particle concentration in the plume [11] suggest that particle volume fraction decreases rapidly above the vent by the concurrent effect of adiabatic expansion of hot gases and turbulent entrainment of air, down to values below 10^{-3}, at which plume density becomes lower than atmospheric density.

To simulate such phenomenon by means of a fluid dynamic model, Direct Numerical Simulation (DNS) and a Lagrangian description of particles are beyond our

M. Cerminara
Scuola Normale Superiore di Pisa, Pisa, Italy
e-mail: matteo.cerminara@sns.it

L.C. Berselli (✉)
Dip. di Matematica, Università di Pisa, Pisa, Italy
e-mail: berselli@dma.unipi.it

T.E. Ongaro
Istituto Nazionale di Geofisica e Vulcanologia, Sezione di Pisa, Pisa, Italy
e-mail: ongaro@pi.ingv.it

M.V. Salvetti
Dip. di Ing. Civile e Industriale, Università di Pisa, Pisa, Italy
e-mail: mv.salvetti@ing.unipi.it

J. Fröhlich et al. (eds.), *Direct and Large-Eddy Simulation IX*,
ERCOFTAC Series 20, DOI 10.1007/978-3-319-14448-1_80

current computational capabilities. Following [9], we therefore describe the eruptive mixture by adopting a multiphase flow approach, i.e., solid particles are treated as continuous, interpenetrating fluids (phases) characterized by specific rheological properties. For each phase, the Eulerian multiphase balance equations of mass, momentum and energy are considered. A Large Eddy Simulation (LES) framework, requiring the specification of sub-grid closure terms, is used to account for turbulence. Even by adopting such an approach, however, the description of a large number of Eulerian phases is still extremely computationally costly and has not allowed, so far, to perform reliable multiphase LES of volcanic plumes.

The aim of the present work is to formulate a faster, Eulerian multiphase flow model able to describe the most relevant non-equilibrium behaviour of volcanic mixtures (such as the effect of the grain-size distribution on mixing and entrainment, particle clustering and preferential concentration of particles by turbulence) while keeping the computational cost as low as possible, in order to achieve a sufficient resolution to perform reliable LES at the full volcanic scale.

In Sect. 2, we discuss a hierarchy of multiphase flow models, their potential and limits. Among them, a quasi-equilibrium model based on a first-order asymptotic expansion of model equations in powers of τ_s (the particle equilibrium time, [2]) is preferred in the context of volcanic plume simulations. Section 3 focuses on the capability of such models to describe gas-particle homogeneous and isotropic turbulence in compressible regime. Finally, we discuss the properties of the Favre-filtered models and the a-priori estimates of sub-grid terms, which is preliminary to the formulation of a closure model for LES of volcanic plumes.

2 Eulerian Multiphase Flow Models

In order to use Eulerian models, we first discuss the physical constraints that characterized volcanic plumes. (1) Grain size distribution can be discretized into a finite number of particulate classes. (2) Particles are heavy, i.e., $\hat{\rho}_s/\hat{\rho}_g \gg 1$ ($\hat{\rho}_s \approx 400$–$3{,}000\ \mathrm{kg/m^3}$), where the hat denotes the density of the phase material. (3) Each class can be described as a continuum (Eulerian approach), i.e., the mean free path is much smaller than, say, the numerical grid size). (4) Low concentration: particle volume fraction $\varepsilon_s = V_s/V < 10^{-3}$. Under such conditions, particles can be considered as non-interacting (pressure-less) or weakly-interacting (small pressure term). As a consequence of 2 and 4, the bulk densities ($\rho_g = (1-\varepsilon_s)\hat{\rho}_g$ and $\rho_s = \varepsilon_s\hat{\rho}_s$) can be of the same order of magnitude (about $1\ \mathrm{kg/m^3}$ or less).

Following the same approach described in [1], we can build a hierarchy of models based on the ratio between a particle characteristic equilibrium time τ_s and a characteristic time of the fluid flow τ_η (which can be the Kolmogorov time in the case of developed turbulent flows, or a large eddy turnover time).

Moreover, to simplify our analysis, we will assume in the following that the flow is iso-entropic (i.e., we neglect the initial explosive phase, which affects only the first hundreds of metres above the vent), and we consider a barotropic model,

thus avoiding to solve the full energy equation. This approach is widely used in atmospheric and plume models and verified by experiments [6, 11].

Barotropic Eulerian-Eulerian model: For small relative Reynolds number, $\rho_g|\mathbf{u}_s - \mathbf{u}_g|d_s/\mu < 1$ (where d_s is the particle's diameter, μ and ρ are gas density and dynamic viscosity and $\mathbf{u}_g$ and $\mathbf{u}_s$ are the gas and solid phase velocities) the drag force between the gas and a solid phase can be expressed by the Stokes law $\mathbf{f}_d = \rho_s(\mathbf{u}_s - \mathbf{u}_g)/\tau_s$ and particle relaxation time is defined by $\tau_s = \hat{\rho}_s d_s^2/18\,\mu$.

When τ_s is of the same order of magnitude as τ_η, the fully coupled multiphase flow equations must be considered. For a two-phase (monodisperse) mixture, the system of mass and momentum balance equations reads:

$$\partial_t \rho_g + \nabla \cdot (\rho_g \mathbf{u}_g) = 0, \qquad \partial_t \rho_s + \nabla \cdot (\rho_s \mathbf{u}_s) = 0, \tag{1}$$

$$\partial_t (\rho_g \mathbf{u}_g) + \nabla \cdot (\rho_g \mathbf{u}_g \otimes \mathbf{u}_g + p_g\, \mathrm{I}) - \nabla \cdot \sigma = \tfrac{\rho_s}{\tau_s}(\mathbf{u}_s - \mathbf{u}_g) + \rho_g \mathbf{g}, \tag{2}$$

$$\partial_t (\rho_s \mathbf{u}_s) + \nabla \cdot (\rho_s \mathbf{u}_\mathbf{s} \otimes \mathbf{u}_\mathbf{s} + p_s\, \mathrm{I}) - \nabla \cdot \pi = -\tfrac{\rho_s}{\tau_s}(\mathbf{u}_s - \mathbf{u}_g) + \rho_s \mathbf{g}, \tag{3}$$

where the subscripts g and s represent the gas and solid phase, respectively, the pressure terms p_s and p_g are given by the barotropic model as $p = p_0(\rho/\rho_0)^\gamma$ (but the exponent γ may be different), $\pi = \mu_s \rho_s \nabla^{sym}\mathbf{u}_s$, $\sigma = \mu\left(\nabla^{Sym}\mathbf{u}_g - \frac{2}{3}\nabla \cdot \mathbf{u}_g\, \mathrm{I}\right)$ and γ (γ_s) is the specific heat ratio of the gaseous (solid) phase. Here $\mathbf{g}$ is the gravitational acceleration, which has not been considered in the following simulations.

Fast Eulerian model: for smaller (but non negligible) τ_s, it is possible to insert a first-order approximation of the particle velocity into the Eulerian-Eulerian equations: $\mathbf{u}_s = \mathbf{u}_g - \tau_s \mathbf{a}_g$, where $\mathbf{a}_g = \frac{D}{Dt}(\mathbf{u}_g) - \mathbf{g}$ is the gas phase acceleration (cf. [2]).

This allows to reduce the number of model equations to one single momentum equation for the mixture plus N equations for mass conservation. By assuming also local thermal equilibrium, we get the following system, again written for a two-phase mixture for the sake of simplicity (here $\rho_m \equiv \rho_g + \rho_s$):

$$\partial_t \rho_g + \nabla \cdot (\rho_g \mathbf{u}_g) = 0, \qquad \partial_t \rho_s + \nabla \cdot (\rho_s \mathbf{u}_s) = 0, \tag{4}$$

$$\partial_t (\rho_m \mathbf{u}_g) + \nabla \cdot (\rho_m \mathbf{u}_g \otimes \mathbf{u}_g + p\mathrm{I}) - \nabla \cdot \sigma = \rho_m \mathbf{g} + \tau_s \nabla \cdot (\rho_s \mathbf{a}_g)\mathbf{u}_g. \tag{5}$$

Dusty Gas model: Finally, when τ_s is negligible, the fast Eulerian model reduces to the so-called dusty-gas model [5], in which all phases have the same velocity. As predicted by the theory, preliminary simulations carried out for turbulent plumes have shown that the dusty-gas model is not capable of reproducing preferential concentration and the effect of particle inertia on turbulent mixing. Therefore, such a model does not appear to be well suited to our purposes, and, hence, the results of the dusty-gas model will not be shown herein.

We implemented these models into OpenFOAM®. Since the flow density is varying in time and space due to the presence of particles, we adopted a robust numerical scheme to simultaneously treat compressibility, buoyancy effects, and turbulent dispersal dynamics, which is based on a segregated solution algorithm [3], with

an adaptive time-stepping. Since we limit our analysis to moderate $\mathrm{Ma}_{\mathrm{rms}}$ (up to 0.6), we do not need shock-capturing schemes. Here $(\cdot)_{\mathrm{rms}}$ stands for root mean square.

3 Numerical Results

As a first step for the appraisal of the considered models, we performed numerical tests by performing DNS of decaying homogeneous isotropic turbulence as reported in [4, 7]. We consider an initial solenoidal velocity field with spectrum $E(k) \propto (k/k_0)^4 \exp\big(-2\,(k/k_0)^2\big)$, $k_0 = 2$ and viscosity $\mu \simeq 0.00239$ to have the Taylor microscale $\lambda = 1/2$, $Re_\lambda = 50$ and that the Kolmogorov scale η remains bigger than the mesh-size: $\eta/\Delta x \geq 2.0$. The initial velocity field is identical for both the gas and the solid, the Stokes number at $t = 0$ is $St = 0.02$, the specific-heat ratios are $\gamma = 1.4$ and $\gamma_s = 1$ and the solid phase viscosity $\mu_s = 10^{-8}$. Since $\rho_s = \rho_g = 1$, the inertial forces of particles are significant in the flow dynamics.

To validate our simulations in the single-phase case, we compared the energy spectrum obtained with our code with the one computed by an eighth order scheme [8]. The comparison is made after one large-eddy turnover time at $\mathrm{Ma}_{\mathrm{rms}} = 0.2$, we find the L^2 norm of the difference between the two spectra is 4.0×10^{-4}. This validates the accuracy of our numerical solver in the single-phase case.

As in [4], we keep the same velocity field in all simulations and modified the initial homogeneous pressure field in order to modify the Mach number. In the single-phase case we used $\mathrm{Ma}_{\mathrm{rms}} = 0.2,\ 0.5$. In the gas-particle case, we keep the same velocity and pressure fields, modifying in this way the non dimensional parameters. In particular the equivalent Reynolds number doubles because the mixture bulk density moves from $\rho_g = 1$ to $\rho_g + \rho_s = 2$, while the equivalent Mach number increases of a factor $\simeq 1.4$ because the speed of sound of the mixture decreases.

Comparison of the two Eulerian models: Fig. 1 shows the time evolution of kinetic energy and enstrophy obtained in the single-phase case (NSE) and in the two-phase one by the barotropic Eulerian and fast Eulerian models respectively. We first observe

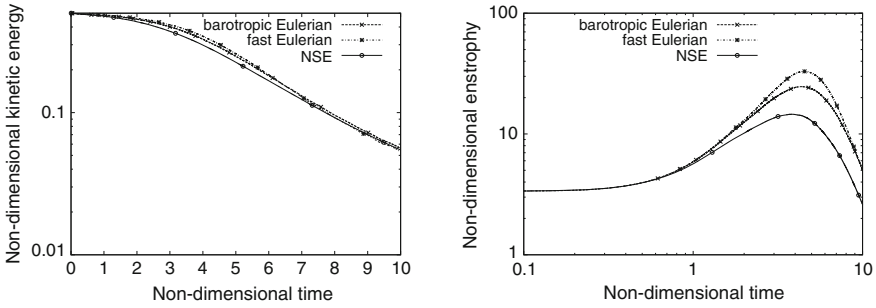

Fig. 1 Turbulence global properties evolution: kinetic energy (*left*) and enstrophy (*right*)

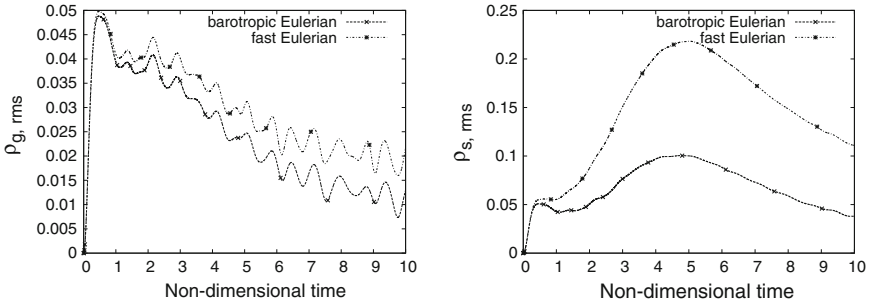

Fig. 2 Density fluctuations $\sqrt{\langle(\rho - \langle\rho\rangle)^2\rangle}$: gaseous phase ρ_g (*left*), solid phase ρ_s (*right*)

that, as expected because of the doubled Re, the vorticity and the energy are larger than in the single-phase case. Next, we observe that in our codes the Fast Eulerian model is less diffusive than the Eulerian one (the enstrophy becomes larger and the turbulent dissipation is more efficient, cf. [4]). In Fig. 2 we report the evolution of the density fluctuations, for both the solid and gaseous phases. We find that the presence of a massive solid phase increases the density fluctuation (the Mach number is modified by the presence of a solid phase), and that in the Fast Eulerian model the preferential concentration of the solid particles is stronger than in the Eulerian simulation (the latter being more diffusive than the former). These differences between the two models are quite surprising since for the values of the Stokes number of the considered particles they are expected to give close results. A possible cause may be a difference in the treatment of source term in the two Eulerian models. In particular, the Stokes coupling between the two phases has been treated explicitly in the Eulerian model, probably underestimating its fluctuations. This will be further investigated in future works.

A priori tests: Moving forward, we use the DNS results to evaluate the SGS terms which would arise in LES. To filter model equations, we have defined a Favre filter $\tilde{}$, $\breve{}$, for each phase so that: $\overline{\rho_g \psi} = \overline{\rho_g}\tilde{\psi}$ and $\overline{\rho_s \psi} = \overline{\rho_s}\breve{\psi}$. Using these filters in our models we get new sub-grid terms, which are evaluated on the DNS results.

In the barotropic Eulerian model, the SGS terms different from zero are:

$$\mathrm{E}_1 = \nabla \cdot \tau, \quad \mathrm{E}_2 = \nabla \cdot \theta, \quad \mathrm{E}_3 = \overline{\rho_s}(\breve{\mathbf{u}}_g - \tilde{\mathbf{u}}_g)/\tau_s, \quad \mathrm{E}_4 = a\nabla(\overline{\rho_g^{\gamma}} - \overline{\rho_g}^{\gamma}),$$

where $a = p_0/\rho_0^{\gamma}$, $\tau = \bar{\rho}_g(\widetilde{\mathbf{u}_g \otimes \mathbf{u}_g} - \tilde{\mathbf{u}}_g \otimes \tilde{\mathbf{u}}_g)$, and $\theta = \bar{\rho}_s(\widetilde{\mathbf{u}_s \otimes \mathbf{u}_s} - \breve{\mathbf{u}}_s \otimes \breve{\mathbf{u}}_s)$. The subgrid terms E_1 and E_2 represent the divergence of the classical SGS stress tensor for the gas and the solid phases respectively, while E_3 represents the SGS effects on the Stokes drag acting on the particles and E_4 the barotropic pressure SGS term. Figure 2 shows the time evolution of the r.m.s. of E_i in semi-log scale. The filtering is made by a top hat filter with radius $\delta = \sqrt{2}h$.

We observe that the subgrid term related with the barotropic pressure is significantly smaller than the others. Hence, in addition to the terms present in the

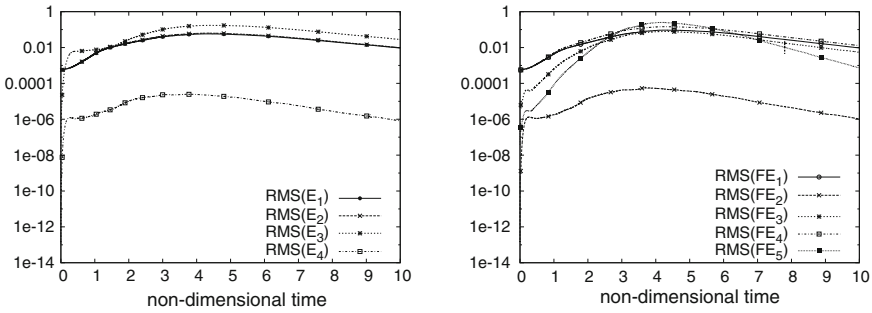

Fig. 3 Barotropic eulerian: evolution of the RMS of E_i at Mach = 0.35 (*left*), barotropic fast eulerian: evolution of the RMS of FE_i at Mach = 0.28 (*right*)

mono-phase case, also the Stokes force of interaction between the two phases is of the same order of magnitude and requires LES modeling (Fig. 3).

In the case of the Fast Eulerian model, different terms comes out from the Favre filtering operation. In particular, we have:

$$\mathrm{FE}_1 = \nabla \cdot \bar{\rho}_g(\widetilde{\mathbf{u}_g \otimes \mathbf{u}_g} - \tilde{\mathbf{u}}_g \otimes \tilde{\mathbf{u}}_g),$$
$$\mathrm{FE}_2 = \overline{p} - p_0(\overline{\rho}_g/\rho_0)^\gamma,$$
$$\mathrm{FE}_3 = \partial_t(\overline{\rho}_s(\breve{\mathbf{u}}_g - \tilde{\mathbf{u}}_g)),$$
$$\mathrm{FE}_4 = \nabla \cdot \bar{\rho}_g(\mathbf{u}_g \breve{\otimes} \mathbf{u}_g - \tilde{\mathbf{u}}_g \otimes \tilde{\mathbf{u}}_g), \mathrm{FE}_5 = \tau_S \left[\overline{\nabla \cdot (\rho_s \mathbf{a}_g)\mathbf{u}_g} - \nabla \cdot (\overline{\rho}_s \tilde{\mathbf{a}}_g)\tilde{\mathbf{u}}_g\right]$$

As in the other case the subgrid term related with the barotropic pressure is significantly smaller than the others. The other terms require LES modeling and we can observe that they are of the same order of magnitude of the relevant terms appearing in the Eulerian case.

References

1. Balachandar, S., Eaton, J.K.: Turbulent dispersed multiphase flow. Ann. Rev. Fluid Mech. **42**, 111–133 (2010)
2. Ferry, J., Balachandar, S.: A fast Eulerian method for disperse two-phase flow int. J. Multiph. Flow **27**, 1199–1226 (2001)
3. Demirdzic, I., Lilek, Z., Peric, M.: A collocated finite volume method for predicting flows at all speeds. Int. J. Numer. Meth. Fluids **16**, 1029–1050 (1993)
4. Garnier, E., Mossi, M., Sagaut, P., Comte, P., Deville, M.: On the use of shock-capturing schemes for large-eddy simulation. J. Comput. Phys. **153**, 273–311 (1999)
5. Marble, F.E.: Dynamics of dusty gases. Ann. Rev. Fluid Mech. **2**, 397–446 (1970)
6. Morton, B.R., Taylor, G., Turner, J.S.: Turbulent gravitational convection from maintained and instantaneous sources. Proc. R. Soc. Lond. A **234**, 1–23 (1956)
7. Lesieur, M., Métais, O., Comte, P.: Large-Eddy Simulations of Turbulence. Cambridge University Press, New York (2005)

8. Pirozzoli, S., Grasso, F.: Direct numerical simulations of isotropic compressible turbulence: influence of compressibility on dynamics and structures. Phys. Fluids **16**, 4386 (2004)
9. Esposti Ongaro, T., Cavazzoni, C., Erbacci, G., Neri, A., Salvetti, M.V.: A parallel multiphase flow code for the 3D simulation of explosive volcanic eruptions. Par. Comp. **33**, 541–560 (2007)
10. Valentine, G. A.: Eruption column physics. From Magma to Tephra: Modelling Physical Processes of Explosive Volcanic Eruptions (eds.). Elsevier, New York, pp.91–136 (2001)
11. Woods, A.W.: The fluid dynamics and thermodynamics of eruption columns. Bull. Volcanol. **50**, 169–193 (1988)

DNS of Turbulent Bubbly Downflow with a Coupled Level-Set/Volume-of-Fluid Method

M. Kwakkel, W.-P. Breugem and B.J. Boersma

1 Introduction

Turbulent bubbly and droplet-laden flows are abundant in industry and nature. Examples are bubble column reactors [1], spray combustion systems [2] and rain clouds [3]. The interaction between the bubbles/droplets and the surrounding turbulent carrier flow is complex and still not well understood, in particular when the bubbles/droplets have a finite-size (relative to the Kolmogorov scale) and when the bubble/droplet volume concentration is not dilute [4, 5]. Visibility constraints hamper optical measurements of the velocity field inside dense two-phase flows. Direct Numerical Simulation (DNS) provides an alternative to obtain detailed insight in the structure and dynamics of such flows. Though DNS of turbulent two-phase flows is computationally demanding, it is currently getting in reach because of the ever increasing computing power and the development of efficient numerical methods. Recent DNS studies on turbulent bubbly flow in a vertical plane channel have been reported by Lu and Tryggvason [6–8] and Bolotnov et al. [9]. In the present DNS study we consider the same flow geometry with a turbulent *down*flow.

Popular methods for DNS of flows laden with finite-size and deformable bubbles are front-tracking and front-capturing methods. In front-tracking methods marker

M. Kwakkel · W.-P. Breugem (✉)
Laboratory for Aero and Hydrodynamics, Delft University of Technology,
Leeghwaterstraat 21, 2628 Delft, The Netherlands
e-mail: w.p.breugem@tudelft.nl

M. Kwakkel
e-mail: m.kwakkel@tudelft.nl

B.J. Boersma
Process & Energy Department, Delft University of Technology,
Leeghwaterstraat, 2628 Delft, The Netherlands
e-mail: b.j.boersma@tudelft.nl

J. Fröhlich et al. (eds.), *Direct and Large-Eddy Simulation IX*,
ERCOFTAC Series 20, DOI 10.1007/978-3-319-14448-1_81

particles are used for an explicit discrete approximation of the bubble interface [10]. In front-capturing methods the interface is implicitly represented by either an iso-surface of a smooth phase indicator (Level-Set) function or by the local volume fraction of the dispersed phase (Volume-of-Fluid function) [11, 12]. Changes in the interface topology are automatically dealt with in front-capturing methods, while front-tracking methods require regular re-meshing of the marker particles on the interface. Front-capturing methods seem therefore to be better suited when coalescence and break-up events are frequent [13].

For the present DNS study we make use of the multiple marker Coupled Level-Set/Volume-of-Fluid (CLSVOF) method of Coyajee and Boersma [14] and modified by Kwakkel et al. [15, 16], based on the original CLSVOF method introduced by Sussman and Puckett [17]. The CLSVOF method combines the sharp interface representation of the Level-Set method with the mass-conserving interface representation of the Volume-of-Fluid method. Recently, the method was extended with a coalescence/break-up module [16] based on the film-drainage model of Zhang and Law [18]. The aim of the present study is to determine the applicability of the CLSVOF method to DNS of turbulent bubbly down flow in a vertical plane channel laden with $O(10^3)$ deformable bubbles. Coalescence and break-up of bubbles is currently not taken into account.

The reason to study turbulent bubbly down flow in a vertical plane channel is that both experimental and numerical data is available for comparison. Lu and Tryggvason [6] were the first to perform DNS of this flow geometry with help of a finite-volume/front-tracking method. They considered cases of up to 72 bubbles (corresponding to a bubble volume fraction of 6 %) with the undeformed bubble diameter equal to $d^+ \equiv \rho_l d\, u_\tau/\mu_l = 31.8$ (i.e., finite-size bubbles) at a friction Reynolds number $Re_\tau \equiv \rho_l h\, u_\tau/\mu_l = 127.3$ (based on the wall friction velocity u_τ and the half-channel height h). The Morton and Eötvös numbers were chosen such that the bubbles remained nearly spherical. The liquid/bubble mass density ratio was 10 and the dynamic viscosity ratio taken equal to 1, which is rather low. The simulation results showed that a lift force acts on the bubbles that drives them towards the core of the channel, thus leaving the wall regions bubble-free. This process keeps on going until the core of the channel is in hydrostatic equilibrium and the bubble distribution is nearly uniform. At statistical equilibrium the mean liquid and bubble velocity profiles are almost uniform in the core region of the channel with the mean liquid velocity profile exhibiting a slight peak near the walls. These results for the mean velocity profiles and the mean bubble volume fraction are in qualitative agreement with previously reported experiments [19–22].

Different from the study of Lu and Tryggvason [6] in the present study we consider air bubbles in water with a much higher water/air mass density and viscosity ratio. However, as will be discussed later the high mass density ratio chosen in our study is probably responsible for numerical instabilities. The remainder of this paper is organized as follows. In the next section the governing equations and details of the numerical method are given. The subsequent section deals with the simulation setup and some preliminary results are presented. Finally, the conclusions are given.

2 Governing Equations and Numerical Method

The governing equations are the incompressible Navier-Stokes equations for both the liquid and the bubble phase:

$$\nabla \cdot \mathbf{u} = 0\,, \tag{1}$$

$$\frac{\partial \mathbf{u}}{\partial t} + \nabla \cdot \mathbf{uu} = -\frac{1}{\rho}\nabla p + \frac{1}{\rho}\nabla \cdot \left(\mu\left(\nabla \mathbf{u} + \nabla \mathbf{u}^T\right)\right) + \mathbf{g}\,, \tag{2}$$

where $\mathbf{g}$ is the gravitational acceleration. These equations have be solved subject to the following conditions on a bubble interface:

$$[\mathbf{u}]_\Gamma = \mathbf{0}\,, \tag{3}$$

$$\left[-p\mathbf{n} + \mu\left(\nabla \mathbf{u} + \nabla \mathbf{u}^T\right)\right]_\Gamma = -\sigma\kappa_\Gamma \mathbf{n}\,, \tag{4}$$

where the brackets denote the jump of the respective quantity over the interface Γ (from the liquid to the bubble phase), $\mathbf{n}$ is the unit normal pointing into the bubble phase, $\kappa_\Gamma \equiv -\nabla \cdot \mathbf{n}$ is the interface curvature and σ is the surface tension coefficient. In our CLSVOF method the viscosity is regularized over the interface and consequently Eq. (4) can be simplified to [23]: $[p\mathbf{n}]_\Gamma = \sigma\kappa_\Gamma \mathbf{n}$.

In the CLSVOF method the variation in density and viscosity over an interface is computed from the Level-Set (LS) function ϕ, defined as the signed distance to the interface. Assuming that the two phases are immiscible, the following equation holds for the location of the interface ($\phi = 0$):

$$\frac{\partial \phi}{\partial t} + \nabla \cdot \mathbf{u}\phi = 0\,. \tag{5}$$

The LS function yields a sharp representation of the interface, though it is well-known that it is not mass-conserving. For that reason we combine it with the Volume-of-Fluid (VOF) method, which is mass-conserving by construction though its interface representation is diffuse. In the VOF method the following mass conservation law is solved for the bubble volume fraction ψ:

$$\frac{\partial \psi}{\partial t} + \nabla \cdot \mathbf{u}\psi = 0\,. \tag{6}$$

In the CLSVOF method both Eqs. (5) and (6) are solved. At every time step the new LS function is then corrected for mass conservation with help of the computed VOF function. Next, the corrected LS function is reinitialized to obtain the correct distribution of the LS function around a bubble interface. Because of the correction for mass conservation, the LS function is non-smooth and hence we make use of the VOF function to compute the interface curvature from a second-order accurate

height-function method. More details of the CLSVOF method can be found elsewhere [14–16, 24].

The above set of equations is solved with a finite-volume method on a fully staggered and uniform Cartesian grid. A second-order accurate pressure-correction method is used to integrate the Navier-Stokes equations in time. Spatial gradients are discretized with help of the second-order accurate central-differencing scheme. The Poisson equation for the correction pressure in the pressure-correction method is solved with an Incomplete Cholesky preconditioned Conjugate Gradient (ICCG) method, where the preconditioning has been extended with a deflation method for reason of computational efficiency [15]. For the advection of the LS and VOF functions a second-order accurate conservative operator split advection scheme is used. More details on the numerical method can be found in [14–16, 24].

3 Simulation Setup and Results

The flow geometry is a vertical plane channel containing 384 air bubbles dispersed in water. The number of air bubbles remains constant throughout the simulation (no coalescence). The channel dimensions are $6h \times 4h \times 2h$ in the streamwise (x), spanwise (y), and wall-normal (z) direction, respectively. The friction Reynolds number is set to $Re_\tau = 180$. The flow is directed downwards and pressure-driven. The undeformed bubble diameter is $d = 0.2h$ or $d^+ = 36$. The bubble volume fraction is approximately 3.35 %. The air/water mass density ratio and the dynamic viscosity ratio are 1.225×10^{-3} and 0.018, respectively. The Froude number is set to $Fr \equiv u_\tau^2/gh = 0.0264$. The Weber number is $We \equiv \rho_l u_\tau^2 h/\sigma = 0.0888$.

The flow is resolved on a fully-staggered uniform Cartesian grid with $720 \times 480 \times 240$ cells, corresponding to a grid cell dimension $\Delta x^+ = 1.5$ and $d/\Delta x = 24$. Periodic boundary conditions are used in the streamwise and spanwise directions and the no-slip/no-penetration conditions for the walls. First, the simulation was run in the absence of bubbles (single-phase flow). After statistical convergence was achieved, the 384 bubbles were placed in the channel and the simulation was continued.

A snapshot of the bubble distribution and a cross-section of the flow is shown in Figs. 1 and 2 depicts a close-up of the flow around a few bubbles. Though the flow is not yet statistically converged, the bubbles tend to move towards the core of the channel as expected [6]. However, as mentioned in the introduction section, numerical instabilities are observed in the simulation. Occasionally very large upward velocities are observed *within* some bubbles, whereas all bubbles are expected to be dragged downwards along with the flow. The flow field is still divergence-free, but due to the artificially high velocities inside some bubbles the time step becomes occasionally very small to satisfy the CFL time step criterion for numerical stability. The observed numerical instabilities appear to originate from an inconsistency in the spatial discretisation of the advection of momentum and the advection of mass, which becomes apparent when the mass density ratio is very large. While the advective terms in the equations for the LS and VOF functions are discretized in conservative form, the

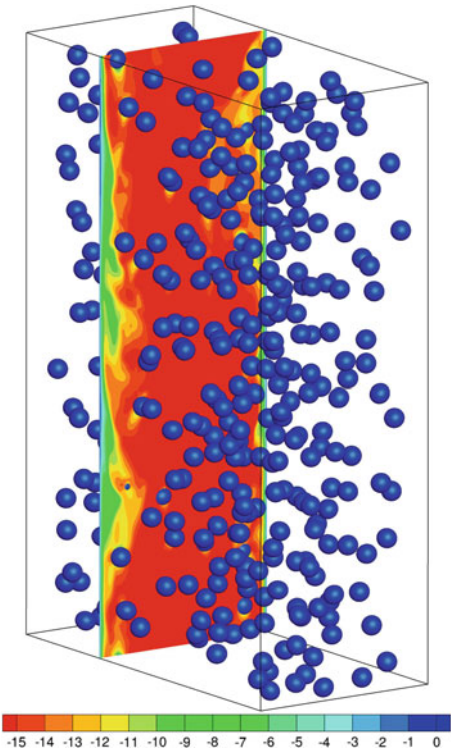

Fig. 1 Instantaneous bubble distribution and streamwise velocity (normalised with u_τ) in a plane perpendicular to the channel walls

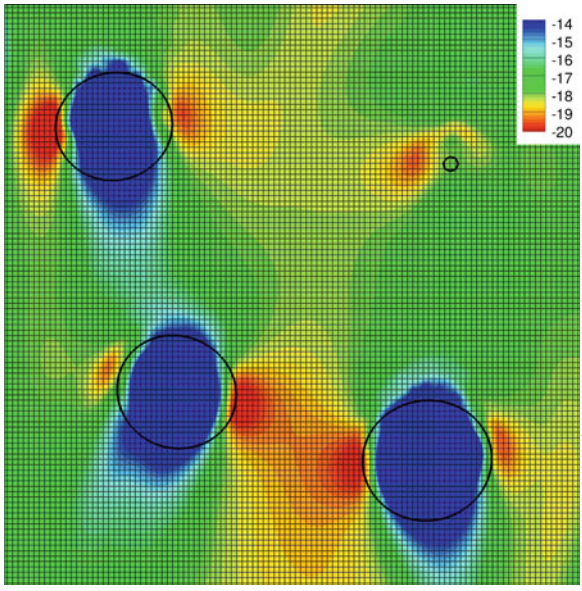

Fig. 2 Close-up of velocity field around a few bubbles in plane shown in Fig. 1. *Grid lines* indicate the resolution with which the flow is resolved

advective term in the momentum equation (i.e., the second term on the left-hand side of Eq. (2)) is discretized in non-conservative form. Consequently, small errors in the position of the interface (LS function) can result in spurious interfacial momentum transfer when the mass density ratio is high [25]. In recent literature a few remedies have been proposed to improve the coupling of the mass and momentum transport [25–27], which we plan to investigate in more detail in future.

4 Conclusions

The CLSVOF method has been applied to DNS of a turbulent bubbly downflow in a vertical plane channel. The flow contained 384 air bubbles dispersed in water. Numerical instabilities have been observed, probably caused by the high water/air mass density ratio. This problem can presumably be solved by improving the coupling of the LS/VOF and momentum fields.

References

1. Mudde, R.F.: Gravity-driven bubbly flows. Annu. Rev. Fluid Mech. **37**, 393–423 (2005)
2. Serignano, W.A.: Fluid Dynamics and Transport of Droplets and Sprays. Cambridge University Press, Cambridge (1999)
3. Shaw, R.A.: Particle-turbulence interactions in atmospheric clouds. Annu. Rev. Fluid Mech. **35**, 183–227 (2003)
4. Balachandar, S., Eaton, J.K.: Turbulent dispersed multiphase flow. Annu. Rev. Fluid Mech. **42**, 111–133 (2010)
5. Tryggvason, G., Thomas, S., Lu, J., Aboulhasanzadeh, B.: Multiscale issues in DNS of multiphase flows. Acta. Math. Sci. **30**(2), 551–562 (2010)
6. Lu, J., Tryggvason, G.: Numerical study of turbulent bubbly downflows in a vertical channel. Phys. Fluids **18**(10), 103302 (2006)
7. Lu, J., Tryggvason, G.: Effect of bubble size in turbulent bubbly downflow in a vertical channel. Chem. Eng. Sci. **62**, 3008–3018 (2007)
8. Lu, J., Tryggvason, G.: Effect of bubble deformability in turbulent bubbly upflow in a vertical channel. Phys. Fluids **20**(4), 040701 (2008)
9. Bolotnov, I.A., Jansen, K.E., Drew, D.A., Oberai, A.A., Lahey, R.T., Podowski, M.Z.: Detached direct numerical simulations of turbulent two-phase bubbly channel flow. Int. J. Multiph. Flow **37**(6), 647–659 (2011)
10. Tryggvason, G., Bunner, B., Esmaeeli, A., Juric, D., Al-Rawahi, N., Tauber, W., Han, J., Nas, S., Jan, Y.J.: A front-tracking method for the computations of multiphase flow. J. Comput. Phys. **169**(2), 708–759 (2001)
11. Scardovelli, R., Zaleski, S.: Direct numerical simulation of free-surface and interfacial flow. Ann. Rev. Fluid Mech. **31**, 567–603 (1999)
12. Osher, S., Fedkiw, R.P.: Level set methods: an overview and some recent results. J. Comput. Phys. **169**(2), 463–502 (2001)
13. Tryggvason, G., Esmaeeli, A., Lu, J., Biswas, S.: Direct numerical simulations of gas/liquid multiphase flows. Fluid Dyn. Res. **38**(9), 660–681 (2006)
14. Coyajee, E., Boersma, B.J.: Numerical simulation of drop impact on a liquid-liquid interface with a multiple marker front-capturing method. J. Comput. Phys. **228**, 4444–4467 (2009)

15. Kwakkel, M., Breugem, W.-P., Boersma, B.J.: An efficient multiple marker front-capturing method for two-phase flows. Comput. Fluids **63**, 47–56 (2012)
16. Kwakkel, M., Breugem, W.P., Boersma, B.J.: Extension of a CLSVOF method for droplet-laden flows with a coalescence/break-up model. J. Comput. Phys., revision under review (2013)
17. Sussman, M., Puckett, E.G.: A coupled level-set and volume-of-fluid method for computing 3D and axisymmetric incompressible two-phase flows. J. Comput. Phys. **162**, 301–337 (2000)
18. Zhang, P., Law, C.K.: An analysis of head-on droplet collision with large deformation in gaseous medium. Phys. Fluids **23**(4), 042102 (2011)
19. Ishii, M., Paranjape, S.S., Kim, S., Sun, X.: Interfacial structures and interfacial area transport in downward two-phase bubbly flow. Int. J. Multiph. Flow **30**, 779–801 (2004)
20. Hibiki, T., Goda, H., Kim, S., Ishii, M., Uhle, J.: Structure of vertical downward bubbly flow. Int. J. Heat Mass Transf. **47**, 1847–1862 (2004)
21. Sun, X., Paranjape, S., Ishii, M., Uhle, J.: LDA measurement in airwater downward flow. Exp. Therm. Fluid Sci. **28**(4), 317–328 (2004)
22. Sun, X., Paranjape, S., Kim, S., Goda, H., Ishii, M., Kelly, J.M.: Local liquid velocity in vertical air-water downward flow. J. Fluids Eng. **126**(4), 539–545 (2004)
23. Kang, M., Fedkiw, R.P., Liu, X.-D.: A boundary condition capturing method for multiphase incompressible flow. J. Sci. Comput. **15**, 323–360 (2000)
24. Coyajee, E.: A front-capturing method for the numerical simulation of dispersed two-phase flow. Ph.D. thesis, Delft University of Technology (2007)
25. Desjardins, O., Moureau, V.: Methods for multiphase flows with high density ratio. In: Center for Turbulence Research—Proceedings of the Summer Program 2010, pp. 313–322 (2010)
26. Rudman, M.: A volume-tracking method for incompressible multifluid flows with large density variations. Int. J. Numer. Meth. Fluids **28**, 357–378 (1998)
27. Raessi, M., Pitsch, H.: Consistent mass and momentum transport for simulating incompressible interfacial flows with large density ratios using the level set method. Comput. Fluids **63**, 70–81 (2012)

Particle-Laden Turbulent Channel Flow with Wall-Roughness

B. Milici, M. De Marchis, G. Sardina and E. Napoli

1 Introduction

Turbulent flows transporting a dispersed-phase are found in many environmental applications and engineering devices. Particle-laden flows are characterized by several peculiar phenomenologies such as preferential particle concentration and turbulence modulation of the carrier-phase due to the presence of the inertial particles [1].

Preferential particle concentration appears in the form of small-scale clustering and turbophoresis. Small-scale clustering consists of loss of spatial homogeneity of the particle distribution due to the combination between particle inertia and turbulent fluctuations. On the other hand, turbophoresis is the turbulence-induced particle accumulation towards to the wall, for a review of this phenomenology see [2]. It is important to underline that while small-scale clustering occurs in both homogeneous and inhomogeneous flows, turbophoresis is a distinctive feature of particle dispersion in wall-bounded flows. Despite this two processes are separately addressed commonly they occur simultaneously in wall bounded flows, where they form different aspects of the same process as described in [3]. The main parameter that controls inertial particle dynamics in turbulent flows is the so-called Stokes number, that is the ratio between the particle relaxation time τ_p and a characteristic time of the turbulent flow. Usually, the small-scale clustering is controlled by the Kolmogorov Stokes number St_η, based on the smallest characteristic turbulence time scale, while the turbophoresis is influenced by the viscous Stokes number $St^+ = \tau_p \nu / U_\tau^2$ where ν is the kinematic viscosity and U_τ is the friction velocity. In particular, the maximum

B. Milici · M. De Marchis · G. Sardina (✉)
Facoltà di Ingegneria, Architettura E Delle Scienze Motorie,
Università Degli Studi di Enna "Kore", Enna, Italy
e-mail: gaetano.sardina@unikore.it

E. Napoli
Dipartimento di Ingegneria Civile, Ambientale E Aerospaziale,
Università Degli Studi di Palermo, Palermo, Italy

J. Fröhlich et al. (eds.), *Direct and Large-Eddy Simulation IX*,
ERCOFTAC Series 20, DOI 10.1007/978-3-319-14448-1_82

wall accumulation is reached by particles characterized by $St^+ \approx 25$, at least in flat wall configurations.

Turbulent flows of engineering and environmental interest are frequently bounded by solid irregular rough walls. Nevertheless, to the best knowledge of the authors, the study of small-scale clustering and turbophoresis, deeply investigated in the last years by means of Direct Numerical Simulations, has been usually focused on turbulent channel and pipe flows with flat and regular walls. On the other hand, experimental and numerical researches of turbulent flow over irregular rough surfaces were mainly focused on the understanding of the effects of the roughness on the mean current, while the interaction between the irregularities and the dispersed particle was neglected. The main effect of a rough wall on the turbulent flow consists on the downward shift of the streamwise mean velocity profile in the log region, while it is not clear how can modify the interaction between the dispersed-phase and the carrier-phase. In this paper, we want to explore this issue, analysing the effects of rough walls on the particle dynamics in turbulent channel flows especially in terms of preferential particle wall accumulation.

2 Description of Numerical Method

The turbulent channel flow is studied using the DNS approach. The Navier-Stokes and continuity equations are resolved using a finite-volume numerical code PANORMUS [4]. The numerical model, which is second-order accurate both in time and space, uses the explicit Adams-Bashforth method for the time advancement of the solution, while the fractional-step technique is used to overcome the pressure-velocity decoupling typical of incompressible flows. To accelerate the convergence of the pressure Poisson equation, a line-SOR technique in conjunction with a multigrid V-cycle accelerator is used (details on the numerical procedure can be found in [5]). The numerical simulations are performed using structured boundary-fitted grids. Periodic boundary conditions are imposed in both the streamwise and spanwise directions, while the no-slip condition is enforced at the walls.

The inertial particles are evolved in a Lagrangian framework. We introduce the following simplifying hypothesis: every particle is assumed to be a rigid sphere with diameter smaller than the Kolmogorov turbulence scale and with density ratio respect to the fluid order 1,000, gravity is neglected. Under this assumption the particle motion equation reads:

$$\frac{\mathrm{d}\mathbf{v}^p}{\mathrm{d}t} = \frac{\mathbf{u}(\mathbf{x}^p(t), t) - \mathbf{v}^p}{St}; \frac{\mathrm{d}\mathbf{x}^p}{\mathrm{d}t} = \mathbf{v}^p \tag{1}$$

where $\mathbf{v}^p$ and $\mathbf{x}^p$ denote velocity and position of the p^{th} particle, respectively. The Stokes number St is defined as the ratio between the particle response time $\tau_p = \rho_p\, d_p^2/(18\rho\nu)$, with d_p the particle diameter and ρ_p its density, ρ is the fluid density and the integral time scale h/U_τ, where h is the channel half-height. The interpolation

of the fluid velocity at particle position $\mathbf{u}(\mathbf{x}^p(t), t)$ is based on the use of the Taylor expansion of the fluid velocity function u_i^f about the fluid node closest to the particle position up to the order of accuracy required by the DNS solver. The numerical integration of positions and velocities is performed with the Adam-Bashforth scheme of the carrier phase. We consider the particles to be very diluted to neglect two-way coupling effects on the carrier phase and particle collisions. The interaction between the dispersed phase and the solid walls of the channel are modeled as elastic rebounds occurring when the particle surface hits the wall. In the rough case, the application of the same methodology requires some preliminary evaluations in terms of the identification of the collision plane. In this paper a simple, but robust, procedure is used taking into account for the specific irregular shape of the boundary, designed in order to univocally identified the collision plane.

Two DNS were performed at friction Reynolds number $Re_\tau = 180$ differing just for the rough level of the walls with fixed pressure gradient. The size of the computational domain is $4\pi h \times 4\pi h/3 \times 2h$ in streamwise, spanwise and wall-normal directions, with a resolution of $256 \times 128 \times 128$ grid points for both flat and rough simulations. One simulation involves classical completely flat wall while in the other 2D irregular roughness was set considering superimposition of sinusoidal functions with random amplitudes given by:

$$r(x_1) = \sum_{i=1}^{n} A_n \sin\left(\frac{2n\pi x_1}{L/2}\right) \tag{2}$$

where x_1 is the streamwise coordinate, $r(x_1)$ is the wall distance from the flat reference surface, L is the channel length, n is the number of sinusoidal functions, A_n and $L/2n$ are the amplitude and the wavelength of the n-th function, respectively. In Fig. 1 a 3D representation of the rough walls is shown, it was obtained considering four different wavelenghts.

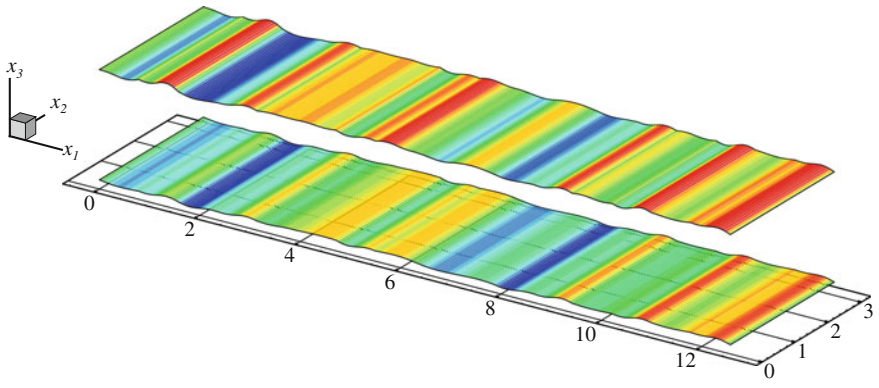

Fig. 1 3D plot of the channel domains for the 2D irregular roughness

Six particle populations are evolved differing for the Stokes number $St^+ = 0.5$, 1, 5, 10, 25, 50 for both flat and rough configurations.

3 Results

The comparison between the particle distribution obtained in flat and rough walls is shown. The mean normal profiles of particle concentration is shown in figure. The particle concentration $C^* = C/C_0$ is defined as the number of particles per unit volume and normalized with the bulk concentration C_0 that it is the total number of particles divided the total volume of the channel. The wall normal coordinate is normalized in inner units z^+. Purely fluid particles $St^+ = 0$, not shown here, are characterized by a uniform mean particle concentration so that $C^* = 1$. In the left panel of Fig. 2, for the flat case, the particles with finite inertia show a value of normalized concentration in the viscous region that is almost 300 times the value of the uniform distribution. These is a signature of the turbophoretic phenomenology consisting in the preferential particle accumulation in the wall region. In the center of the channel the concentration is below its bulk value. Particles with Stokes number 25 exhibit a strong level of concentration in the viscous region $z^+ < 5$ and the smallest value of concentration in the channel centerline, the ratio between the wall and the center concentration is more than 10^4. Particles with Stokes numbers $St^+ = 10$ and $St^+ = 50$ share the same wall and centerline concentration. These results are in agreement with previous DNS results at the same friction Reynolds number in the flat case and similar values of the Stokes number [3]. In the right panel of Fig. 2, the particle concentration for the rough channel is shown for the different particle populations. As can be qualitatively observed in the instantaneous snapshot in the bottom panel of Fig. 3, the large inertial particles tend to avoid the slow flow regions close to the wall, this brings to the total disappearance of the preferential

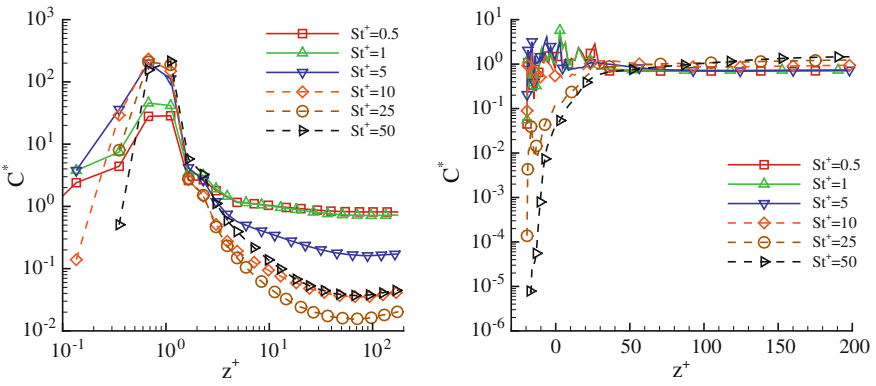

Fig. 2 Mean normalized particle concentration versus wall-normal coordinate z^+ for the different particle populations. *Left panel* flat simulation. *Right panel* rough simulation

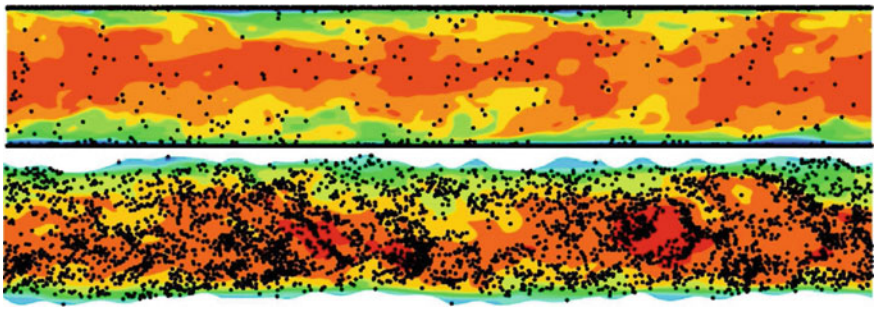

Fig. 3 Wall-normal slices of an instantaneous configuration of the streamwise velocity field (*contours*) and particles (*black dots*) with $St^+ = 25$ for the flat (*upper panel*) and the rough (*right panel*) cases in the buffer layer ($z^+ = 15$)

wall accumulation and an increase of the centerline concentration, almost the double for $St^+ = 50$, where the concentration profile monotonically increases along the wall-normal coordinate moving from the wall to the channel centerline. The particle depletion in the wall regions increase monotonically with the Stokes number, for the heaviest particles the wall-concentration is of the order of 10^{-5} with respect to the Lagrangian fluid tracers. A very small amount of turbophoresis is found for the lightest particles. We highlight that the concentration profiles are in the fully developed steady state for the particles removing all the transient accumulating process and are characterized by statistical invariance in time. Figure 4 shows an horizontal plane in

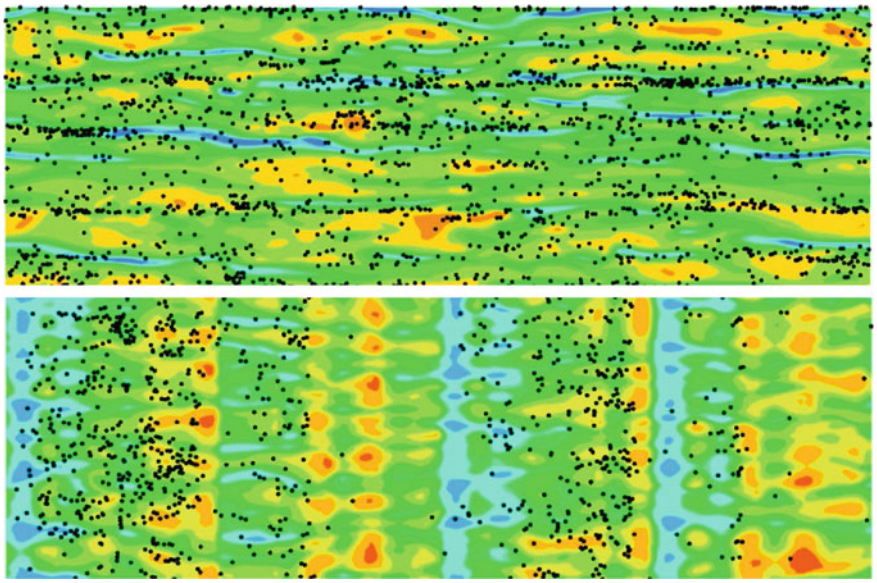

Fig. 4 Wall-parallel slice of an instantaneous configuration of the streamwise velocity field (*contours*) and particles (*black dots*) with $St^+ = 25$ for the flat (*top*) and the rough (*bottom*) cases

the buffer layer ($z^+ = 15$) where there is the peak of turbulent kinetic energy and the instantaneous velocity field is characterized by the presence of high and low streaks typical of wall turbulence for the flat case.

In agreement with previous studies, Fig. 4 shows that when a flat wall is considered the particles tend to avoid the high speed regions (sweeps events/red zones) and preferentially sample the low speed regions (ejection events/blue zones). The inertial particles tend to create very long and straight structures aligned with the long quasi-streamwise flow vortical structures. On the contrary, these long quasi-streamwise structures are not present in the rough case (lower panel of Fig. 4) and the particles distribute nonhomogeneously and collect into filaments separated by empty regions, this evidence was already shown in wavy walls [6].

4 Conclusions

The effects of irregular wall roughness on particles laden turbulent flows have been addressed by means of DNS of low-Reynolds-number turbulent channel flow coupled with Lagrangian particle tracking of a large number of passive particles to examine the dispersion process and preferential concentration in the near-wall region (turbophoresis), in connection with the dynamics of the wall turbulent structures. We performed DNS in two computational domains: a standard channel flow geometry between two flat walls and a channel in which both the upper and lower walls of the channel have been roughened through the superimposition of sinusoidal functions having four different wavelengths and random amplitudes. Coherently with literature findings of standard turbulent channel flow seeded with inertial particles particle preferential accumulation and turbophoretic effects dominate in the flat wall case, whereas in the rough channel, where the wall roughness clearly affects the turbulent flow field in the viscous region and in the buffer layer with a direct dependence on the roughness height, the particles tend to avoid the slow velocity regions close to the wall and accumulate slightly farther away from the wall.

References

1. Balachandar, S., Eaton, J.K.: Turbulent dispersed multiphase flow. Ann. Rev. Fluid Mech. **42**, 111–133 (2010)
2. Soldati, A., Marchioli, C.: Physics and modelling of turbulent particle deposition and entrainment: Review of a systematic study. Int. J. Mult. Flow **35**, 827–839 (2009)
3. Sardina, G., Schlatter, P., Brandt, L., Picano, F., Casciola, C.M.: Wall accumulation and spatial localization in particle-laden wall flows. J. Fluid Mech. **699**, 50–78 (2012)
4. Napoli, E., Armenio, V., De Marchis, M.: The effect of the slope of irregularly distributed roughness elements on turbulent wall-bounded flows. J. Fluid Mech. **613**, 385–394 (2008)

5. De Marchis, M., Napoli, E., Armenio, V.: Turbulence structures over irregular rough surfaces. J. of Turbul. **11**(3), 1–32 (2010)
6. Marchioli, C., Armenio, V., Salvetti, M.V., Soldati, A.: Mechanisms for deposition and resuspension of heavy particles in turbulent flow over wavy interfaces. Phys. Fluids **18**, 025102–025102 (2006)

Direct Numerical Simulation of Bed-Load Transport of Finite-Size Spherical Particles in a Turbulent Channel Flow

B. Vowinckel, T. Kempe, J. Fröhlich and V. Nikora

1 Introduction

Bed-load transport in particle-laden flows is an important process in many environmental, civil engineering, and industrial applications. The particle transport mechanisms are complex and often involve highly organised structures such as multi-scale 2D and 3D bedforms moving with different speeds. The predictive capabilities for bed-load, currently available to engineers and researchers, are very limited due to lack of fundamental knowledge of these mechanisms. The presented study employs particle-resolving DNS of mobile sediment transported over a rough bed, extending the previous work of the authors in [10] by using a larger domain. For a systematic investigation of the key mechanisms, the sediment supply and the mobility are varied. These are characterized by the void fraction and the Shields parameter

$$\Theta = \frac{u_\tau^2}{\rho' \, g \, D}, \tag{1}$$

respectively. Here, u_τ is the friction velocity, g the gravitational acceleration, D the particle diameter, and $\rho' = (\rho_p - \rho_f)/\rho_f$ the relative submerged particle density with ρ_p the particle density and ρ_f the fluid density. The Shields parameter was first

B. Vowinckel (✉) · T. Kempe · J. Fröhlich
Institute of Fluid Mechanics, Tu Dresden, Dresden, Germany
e-mail: bernhard.vowinckel@tu-dresden.de

T. Kempe
e-mail: tobias.kempe@tu-dresden.de

J. Fröhlich
e-mail: jochen.froehlich@tu-dresden.de

V. Nikora
Institute of Environmental Fluid Mechanics, The University of Aberdeen,
Aberdeen, Scotland, UK
e-mail: v.nikora@abdn.ac.uk

J. Fröhlich et al. (eds.), *Direct and Large-Eddy Simulation IX*,
ERCOFTAC Series 20, DOI 10.1007/978-3-319-14448-1_83

derived in the framework of an experimental analysis of incipient motion to quantify the mobility of a multidisperse sediment on the basis of a statistical approach [8]. It compares the average frictional force to the gravitational forces inhibiting the mobilisation of a particle embedded in a sediment packing.

2 Description of Numerical Method

For the continuous phase, the unsteady three-dimensional Navier-Stokes equations for incompressible fluids

$$\frac{\partial \mathbf{u}}{\partial t} + (\mathbf{u} \cdot \nabla)\mathbf{u} = \frac{1}{\rho_f}\nabla p + \nu_f \nabla^2 \mathbf{u}, \;\; \nabla \cdot \mathbf{u} = 0 \tag{2}$$

are solved as described in [3], where $\mathbf{u}$ is the velocity vector, t time, p pressure, and ν_f the constant kinematic viscosity. The disperse phase is represented by an enhanced immersed boundary method [3]. For particle contact, the adaptive collision model (ACM) proposed in [4] was used. It accounts for all relevant mechanisms that have to be modelled during the collision process: short-range lubrication forces, normal forces during surface contact, and tangential forces due to friction between particles. It was validated in great detail for single collisions. Previous investigations showed that for bed-load transport the collision model is important for the formation of large-scale structures and suggested that the ACM yields realistic results that are in agreement with experiments [9, 10].

3 Computational Setup

An open channel flow is considered with a computational domain $L_x \times (H + H_{sed}) \times L_z$ in streamwise, vertical, and spanwise direction, respectively, with H the channel height and H_{sed} the sediment height as defined below. Periodic boundary conditions are applied in $x-$ and $z-$direction, a free-slip condition at the top, and a no-slip condition at the bottom and the particle surfaces. The numerical and physical parameters are summarized in Table 1. The bottom of the channel is roughened by one layer of 13,500 fixed mono-disperse particles which are arranged in a hexagonal pattern. In the reference run (case: *Ref*) particles of the same number and of the same diameter were released on top of this sediment bed. The restitution coefficient $e = -u_{p,out}/u_{p,in}$ for these is $e = 0.97$ as used in [9, 10]. The Shields parameter is

Table 1 Common values of simulation parameters

Re_b	Re_τ	D^+	D/Δ_x	H/D	L_x/H	L_z/H	N_{tot}
2,941	193	21	22.2	9	24	6	1.4×10^9

slightly above the threshold of initiation of motion based on [8]. The friction velocity u_τ is defined by extrapolating the linear profile of the total shear stress of an unladen flow down to $y = 0$, while the origin of the vertical coordinate y is at the top of two layers of fixed spheres [11]. This location is maintained if part of the spheres are mobile. It excludes stresses taken up by the sediment bed from the analysis. The resulting friction Reynolds number is $Re_\tau = 193$ and the particle Reynolds number is $D^+ = D\,u_\tau/\nu_f = 21$. The resolution of the equidistant, Cartesian grid is set to $D/\Delta_x = 22.2$ to guarantee proper resolution of the viscous effects. This results in a total amount of $N_{tot} = 1.4 \times 10^9$ grid cells.

Subsequently, the key parameters mentioned above were varied to elucidate their effect on bed-load transport. In the case *FewPart*, the number of mobile particles is reduced by 50 % to 6,750 particles. In the case *LowSh*, the specific density of the particles of the reference run was increased by 57 % to obtain a Shields parameter well below the threshold of sediment motion. The three simulations of particle-laden flows were initialized in the same way by releasing the mobile particles at some elevation above the fixed bed. Afterwards, the simulations were run until an equilibrium between erosion and deposition was obtained. This was verified by a statistical analysis of the particle properties presented in [11]. For each simulation, statistical data was gathered for more than 200 bulk units $\tau_b = H/U_b$.

4 Results and Discussion

In the three cases considered, distinctly different particle patterns are observed (Fig. 1). The reference run (Fig. 1a) produces two dunes with their major axis in spanwise direction. The dunes have an undulating shape in the average and travel on the surface of a layer of inactive particles. This phenomenology is similar to the in field and experiments [1]. Reducing the mass loading results in streamwise aligned, inactive ridges that extend over the entire computational domain (Fig. 1b) being related to secondary currents in form of counter-rotating vortices that further stabilise the particle pattern [6, 10]. Heavy particles form a closed, lower stage plane bed with only a few particles being eroded (Fig. 1c).

The observed particle patterns are directly reflected in the two-point correlation

$$R_{uu}(r_x) = \frac{\langle u'(x)\,u'(x+r_x)\rangle_{x,z,t}}{\sqrt{\langle u'(x)u'(x)\rangle_{x,z,t}\,\langle u'(x+r_x)u'(x+r_x)\rangle_{x,z,t}}} \tag{3}$$

in the streamwise direction of the fluid phase in the near-wall region ($y = 0.5D$), with $u'(x, y, z, t) = u(x, y, z, t) - \langle u\rangle_{x,z,t}(y)$ the fluid fluctuation with respect to the average in horizontal directions and time and r_x the correlation length in the x-direction (Fig. 2). The local maximum of R_{uu} at $r_x = 12H$ of the reference run reflects the statistically averaged distance of the two dunes and coincides with half the domain size. To which extent this value depends on the domain size is an open issue but would require larger calculations. For the case *FewPart*, R_{uu} decays to

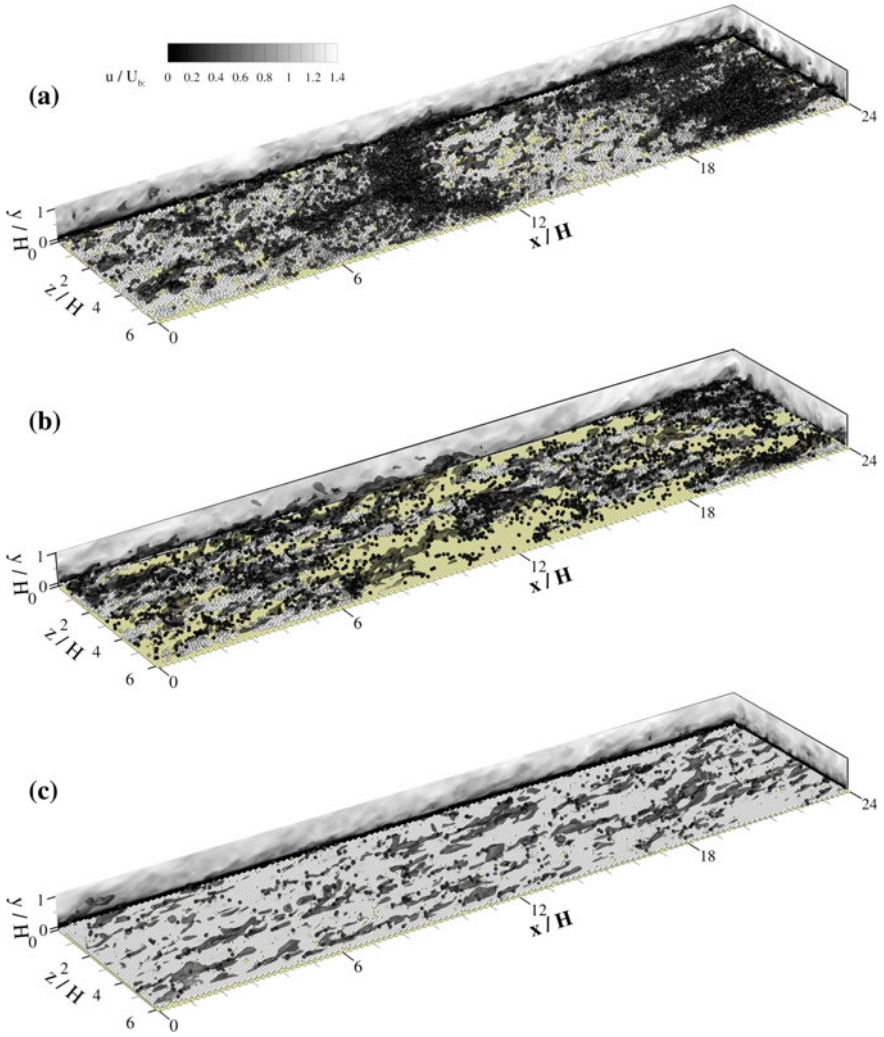

Fig. 1 **a** Instantaneous particle distribution of the reference run (*Ref*). Contour plot of u/U_b on the sides of the domain, 3d-iso-surfaces of fluid fluctuations with $u'/U_b = -0.3$ inside the domain. Particle colours: *grey* fixed, *white* $|\mathbf{u}_p| < 1.5u_\tau$, *black* $|\mathbf{u}_p| > 1.5u_\tau$. **b** Same as Fig. 1a, but for case *FewPart*. **c** Same as Fig. 1a, but for case *LowSh*

a value lower than zero, which indicates that the streamwise extent of the ridges exceeds 50 % of the streamwise domain length. Note, however, that these particle structures are very stable and could theoretically extend to an infinite size. In fact, field observations report ridges several kilometers long [1]. The particle pattern of *LowSh* with only a low fraction of active particles, is similar to the large-scale behavior of natural streams with a high submergence H/D and, hence, a negligible mass loading [7]. The corresponding two-point correlation decays to zero after roughly $6H$.

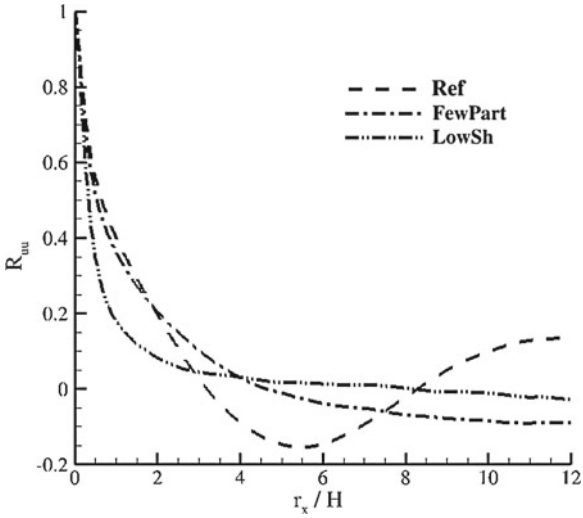

Fig. 2 Two-point correlation function of the fluid in phase in the streamwise direction at $y = 0.5D$

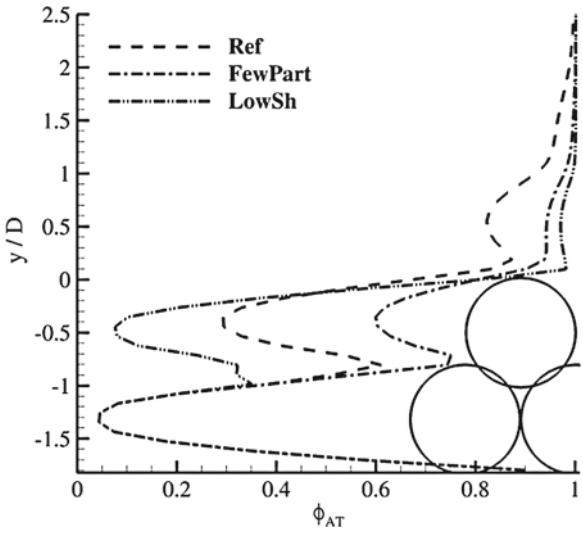

Fig. 3 Time-space porosity of the sediment bed in the near wall region

As reported in [11], the wall-normal profiles of the the streamwise velocity component of the fluid phase reveal a deceleration of the fluid in the near wall region as a function of the porosity. This deceleration is compensated by an accelerated outer flow, where the influence of the particles becomes negligible. The corresponding porosity [5] $\phi_{AT}(y) = \langle \gamma \rangle_{x,z,t}(y)$ is reported in Fig. 3 where γ is a clipping function equal to 1 in the fluid and 0 inside a particle. The profiles of ϕ_{AT} collapse for $y/D < -1$ as this is the region of the fixed bed. The peak $y/D \approx -0.4$ corresponds to the inactive particles trapped in the plane bed (case *Ref* and *LowSh*) or the ridges (case *FewPart*). From the value of this peak one can derive its counterpart,

the amount of particles constituting the bed-load. In the reference run, 26 % of a full layer are active and form the dune-like structures. Reducing the number of particles also decreases the number of active particles. Only 8 % of a full layer travel within the troughs between the ridges eroding the inactive structures at different locations. Despite the low value of Θ in *LowSh*, more than 3 % of the mobile particles are active.

The wall-normal velocity fluctuations presented in [11] show that the value of the Reynolds shear stress $\langle u'v' \rangle$ increases with the number of eroded particles. Hence, active particles generate turbulent fluctuations that contribute to the mechanisms of bed-load transport.

5 Conclusion

Highly-resolved simulations of three flows with sediment transport were performed and the resulting particle structures were investigated by two-point correlations of the fluid velocity and the porosity of the disperse phase. A channel flow with a high mass loading of light particles produced dunes with a distance of about $12H$. Reducing the mass loading leads to ridges with a large streamwise extent. Decreasing the mobility forms a closed bed and the coherent structures in the flow become similar to those of a flow over a rough wall. Further analysis of the data is underway.

Acknowledgments The present work is funded by the German Research Foundation (DFG) via the project FR 1593/5-1. The authors gratefully acknowledge the Gauss Centre for Supercomputing (GCS) for providing computing time for a GCS Large Scale Project on the GCS share of the supercomputer JUQUEEN at Jülich Supercomputing Centre (JSC).

References

1. Allen, J.L.R.: Sedimentary structures: their character and physical basis. Elsevier, New York (1982)
2. Dietrich, W.E., Kirchner, J.W., Ikeda, H., Iseya, F.: Sediment supply and the development of the coarse surface-layer in gravel-bedded rivers. Nature **340**(6230), 215–217, 1 (1989)
3. Kempe, T., Fröhlich, J.: An improved immersed boundary method with direct forcing or the simulation of particle laden flows. J. Comput. Phys. **231**, 3663–3684 (2012a)
4. Kempe, T., Fröhlich, J.: Collision modeling for the interface-resolved simulation of spherical particles in viscous fluids. J. Fluid Mech. **709**, 445–489 (2012b)
5. Nikora, V., Ballio, F., Coleman, S., Prokrajac, D.: Spatially-averaged flows over mobile rough beds: definitions, averaging theorems, and conservation equations. J. Hydraul. Eng. (2013). doi:10.1061/(ASCE)HY.1943-7900.0000738
6. Shvidchenko, A.B., Pender, G.: Macroturbulent structure of open-channel flow over gravel beds. Water Resour. Res. **37**(3), 709–719 (2001)
7. Sukhodolov, A.N., Nikora, V.: Bursting and flow kinematics in natural streams. In: Murillo, R. (ed.) River Flow 2012: International Conference on Fluvial Hydraulics, pp. 113–120. ISBN 978-0-415-62129-8 (2012)
8. Shields, A.: Anwendung der Ähnlichkeitsmechanik und der Turbulenzforschung auf die Geschiebebewegung. Ph.D. thesis, Mitteilungen der Preußischen Versuchsanstalt für Wasserbau und Schiffbau, Berlin (1936)

9. Vowinckel, B., Kempe, T., Fröhlich, J.: Impact of collision models on particle transport in open channel flow. In: Proceedings of 7th International Symposium TSFP, Ottawa, Canada (2011)
10. Vowinckel, B., Kempe, T., Fröhlich, J., Nikora, V.: Numerical simulation of sediment transport in open channel flow. In: Murillo, R. (ed.) River Flow 2012: International Conference on Fluvial Hydraulics, pp. 507–514. ISBN 978-0-415-62129-8 (2012)
11. Vowinckel, B., Kempe, T., Fröhlich, J.: Particle-resolving simulations of bed-load sediment transport. In: Proceedings of 8th International Conference on Multiphase Flow, paper No. 792 (2013)

An Inhomogeneous Stochastic Model for Subgrid-Scale Particle Dispersion in LES

M. Knorps and J. Pozorski

1 Introduction

Turbulent flows with small particles are of interest both for physicists and engineers: the dispersed phase is involved in a range of phenomena (including preferential concentration, agglomeration, and wall deposition) that are important in particle separators, combustion chambers, etc. From the numerical standpoint, even in the simplest point-particle approach with the one-way momentum coupling, adopted here, the direct numerical simulation (DNS) reveals to be overly expensive beyond relatively low Reynolds numbers and simple geometries. Yet, DNS can be very useful for model validation and this is also the case of the present work. We focus on the Eulerian-Lagrangian approach with the flow equations solved from the large-eddy simulation (LES) and heavy particles tracked in such a smoothed velocity field. The LES becomes particularly well suited when the prediction of instantaneous flow structures is crucial for the particulate phase. The subgrid scales (SGS) may have an impact on the motion of particles, specially those of lower inertia. This issue is called here the SGS particle dispersion. Several classes of models have been proposed, including the approximate deconvolution [5] or stochastic diffusion [2, 8, 9]. The latter approach is further developed and tested here, accounting both for a possible anisotropy of the diffusion term and inhomogeneity of the drift term.

The carrier phase is described by the incompressible Navier–Stokes equations. Heavy ($\rho_p/\rho_f \gg 1$), point-particles are treated in the Lagrangian way:

$$\frac{d\mathbf{x}_p}{dt} = \mathbf{V_p}\,, \quad \frac{d\mathbf{V_p}}{dt} = f_D \frac{\mathbf{U}^* - \mathbf{V_p}}{\tau_p}\,. \tag{1}$$

where only the drag force is retained, $\tau_p = (\rho_p/\rho_f)d_p^2/(18\nu_f)$ is the particle momentum relaxation time and $f_D = \mathcal{O}(1)$ is a semi-empirical drag correction factor.

M. Knorps · J. Pozorski (✉)
Institute of Fluid-Flow Machinery, Polish Academy of Sciences, Gdansk, Poland
e-mail: jp@imp.gda.pl

J. Fröhlich et al. (eds.), *Direct and Large-Eddy Simulation IX*,
ERCOFTAC Series 20, DOI 10.1007/978-3-319-14448-1_84

2 Subgrid Scale Particle Dispersion Modelling

In Eq. (1), the fluid velocity along particle trajectories, denoted by $(\cdot)^*$, can be decomposed into the filtered part and the SGS contribution:

$$\mathbf{U}^* = \overline{\mathbf{U}}^* + \mathbf{u}^* \tag{2}$$

where $\overline{\mathbf{U}}^* = \overline{\mathbf{U}}(\mathbf{x}_p, t)$ is interpolated from the LES mesh and the residual contribution $\mathbf{u}^*$ may need a separate model. SGS dispersion may be neglected for large-inertia particles, or long-time dispersion from the point source.

In cases where SGS contribution can change the behaviour of the dispersed phase (e.g., the wall-deposition rate), we choose a stochastic analogue of advection-diffusion equation, namely the Langevin equation [8]. Recently, we have proposed an extension of the model to the anisotropic formulation, accounting also for possible correlations among SGS velocity components [4, 9].

$$d\mathbf{u}^* = -\frac{\mathbf{u}^*}{\tau_{sg}}\, dt + \boldsymbol{\sigma} \cdot d\mathbf{W}, \tag{3}$$

where $d\mathbf{W}$ is a vector of independent increments of the Wiener process, $\boldsymbol{\sigma}$ is a diffusion matrix, τ_{sg} is a characteristic timescale of SGS velocity seen by particles and also the autocorrelation time of the resulting stochastic process. The model, Eq. (3), has been proposed by analogy to turbulent dispersion in RANS. However, given the instantaneous character of LES and the statistical character of RANS, the analogies are not complete. The model parameters that need to be estimated are τ_{sg} and $\boldsymbol{\sigma}$; their choice comes from the statistical description of the smallest scales.

We implicitly assume that the SGS turbulent energy along particle trajectories is equal to that of fluid, which is not completely true because particles tend to segregate in the flow and the concentration patterns depend on vorticity field and the particle Stokes numbers. Arguably, we choose the parameters τ_{sg} and $\boldsymbol{\sigma}$ to conserve the SGS kinetic energy. As a first estimation, we take the Lagrangian time scales of SGS motions "seen" by the particle, τ_{sg}, as equal to the Eulerian time scales of fluid and computed from:

$$\tau_{sg} = C_{sg}\overline{\Delta}/\sigma_{sg}\ . \tag{4}$$

Here, $\sigma_{sg} = \sqrt{2k_{sg}/3}$ is the relevant velocity scale, k_{sg} is the SGS kinetic energy and $\overline{\Delta}$ is the width of LES filter. The model constant $C_{sg} = \mathcal{O}(1)$ accounts for the uncertainty concerning the time scale of the SGS velocity autocorrelation.

The diffusivity tensor $\boldsymbol{\sigma}$ is defined here in the form adjusted to the channel flow, with only the cross-correlation of streamwise (x) and wall-normal (y) velocity:

$$\sigma = \sqrt{\frac{2}{\tau_{sg}}} \begin{bmatrix} \sqrt{(\overline{u_x^2} - \overline{u_x u_y}/\overline{u_y^2})} & 0 & 0 \\ \overline{u_x u_y}/\sqrt{\overline{u_y^2}} & \sqrt{\overline{u_y^2}} & 0 \\ 0 & 0 & \sqrt{\overline{u_y^2}} \end{bmatrix}, \tag{5}$$

where $\overline{u_i^2}$ and $\overline{u_i u_j}$ are variances and covariances of SGS velocities, respectively. The formulation (5) accounts for anisotropy of near-wall turbulence and the effects of correlation between SGS velocities [9].

Another issue is the estimation of the residual scales from LES. To include the SGS velocity correlations, we retrieve them from a Yoshizawa-like formula (6), where $\overline{(\cdot)}$ is the basic LES filter and $\widehat{(\cdot)}$ is the second, wider filter [9]

$$\overline{u_i u_j} = C_I \overline{\Delta}^2 |\overline{S}|^2 = \frac{\widehat{\overline{U_i}\,\overline{U_j}} - \widehat{\overline{U_i}}\,\widehat{\overline{U_j}}\rangle}{\langle \overline{\Delta}^2 |\overline{S}|^2} - \widehat{\overline{\Delta}^2}\,|\widehat{\overline{S}}|^2\rangle \overline{\Delta}^2 |\overline{S}|^2. \tag{6}$$

Figure 1 shows the evaluation of SGS shear stress computed from filtered DNS field and compared with LES results obtained with Eq. (6).

We found that the model proposed in Eq. (3) improves the particle statistics, such as the r.m.s. fluctuating velocity, specially in the near-wall regions. Yet, we are still not quite satisfied with the particle concentration profiles in the wall-normal directions [4, 9]. In a related work [6], a hybrid deconvolution-stochastic SGS dispersion model is proposed. There, an attempt to improve the particle concentration is done with the gradients of turbulence intensity; however, it seems that the use of an adjustable constant (sensitized to particle inertia) is still necessary.

In the present work, we continue on the path of systematic developments, following the exact formulation of the deterministic drift terms that account for non-homogeneity of fluid velocity statistics. Such terms are shown to appear both in RANS [7] and in LES [2] settings. Consequently, a proposed model for the SGS fluid velocity at particle position $\mathbf{u}^*$, has the form:

$$d\mathbf{u}^* = \left(-(\mathbf{u}\cdot\nabla)\overline{\mathbf{U}} + \nabla\cdot\boldsymbol{\tau}\right)^* dt - \frac{\mathbf{u}^*}{\tau_{sg}}\, dt + \boldsymbol{\sigma}\cdot d\mathbf{W}, \tag{7}$$

where $\boldsymbol{\tau}$ is the SGS stress tensor. In the following, the first expression on the right-hand-side will be referred to as "deterministic terms"; they appear in the derivation of the equation for the SGS fluid velocity at particle position (see [2]).

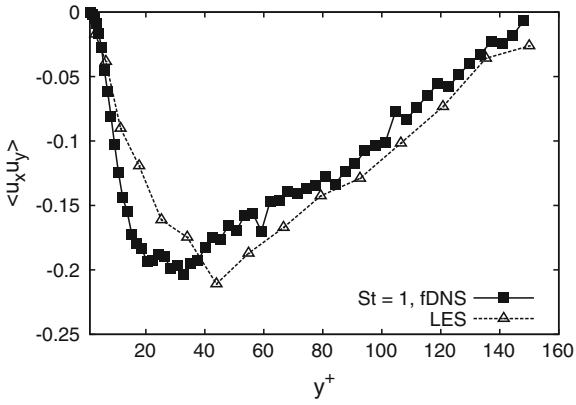

Fig. 1 The SGS shear stress (covariance of wall-normal and streamwise velocity) in channel flow: 'LES': evaluation from Eq. (6), 'fDNS': data from filtered DNS field of the same filter size as LES

3 Results for Channel Flow

A suitable geometry for testing the importance of the "deterministic terms" in Eq. (7) is a channel. We use a pseudo-spectral DNS/LES code (courtesy of J.G.M. Kuerten). The flow is periodic in the streamwise (x) and spanwise (z) directions; the wall-normal nodes (y) are distributed according to Chebyshev polynomials. The channel size is $4\pi \times 2 \times 2\pi$. For the dispersed phase, 2nd order Lagrange interpolation of fluid velocity at particles is used and 2nd order R-K scheme is applied to solve Eq. (1). Whenever "filtered DNS" is used, we apply a box filter with coarsening factors $4 \times 4 \times 2$. The LES grid is the same as filtered DNS. The Reynolds number based on the friction velocity is $Re_\tau = 150$. Four classes of heavy particles are tracked ($St = \tau_p/\tau_f = 1, 5, 25, 125$) with 100,000 particles in each class.

To assess the possible influence of the deterministic terms, we compute them directly from filtered DNS ('fDNS'). Figure 2a shows component-by-component contributions of these terms in Eq. (7), normalised with u_τ^3/ν. The most significant components are derivatives of SGS stress tensor in wall-normal and streamwise directions and $(\mathbf{u} \cdot \nabla)\overline{U}_x$, which is expected, since the gradients of streamwise velocities are the strongest at the walls. These data show some resemblance to the results of [1]

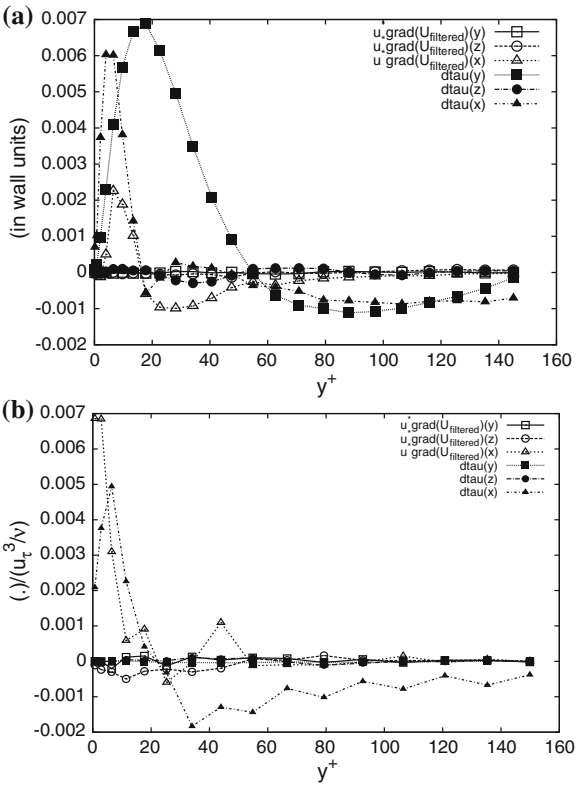

Fig. 2 **a** Deterministic terms in Eq. (7) obtained from filtered DNS. **b** Deterministic terms in Eq. (7) computed by LES using Eq. (6)

and [3] considering evaluation of the so-called stochastic forcing. We think that they may be partially reintroduced to SGS models by "deterministic terms". Figure 2b shows the LES results of the terms of interest, obtained with Eq. (6). The qualitative agreement of the overall effect (summing up the terms in streamwise direction) is good, although the question of the underprediction of $(\mathbf{u} \cdot \nabla)\overline{U}_y$ remains.

Another important issue concerning stochastic SGS model is the Lagrangian relaxation time of $\mathbf{u}^*$. The previously used basic formula (Eq. 4), with the user-chosen constant C_{sg}, showed non-physical behaviour at the walls (see Fig. 3a; here $C_{sg} = 0.1$). That might have been due to the fact that according to this model:

$$\lim_{y^+ \to 0} \tau^*_{sg} = \lim_{y^+ \to 0} C_{sg} \frac{\overline{\Delta}}{\sqrt{2/3 C_I \overline{\Delta}^2 |\overline{S}|^2}} = \infty, \tag{8}$$

because $\lim_{y^+ \to 0} |\overline{S}| = const$ and $\lim_{y^+ \to 0} C_I = 0$.

We propose to evaluate τ_{sg} with the van Driest damping formula (Eq. 9):

$$\tau_{sg}(y^+, St) = [1 - \exp(-y^+/25)] C^0_{sg}(St) \overline{\Delta}/\sigma_{sg} \tag{9}$$

The problem of adjusting τ_{sg} is non-trivial and was considered in [6].

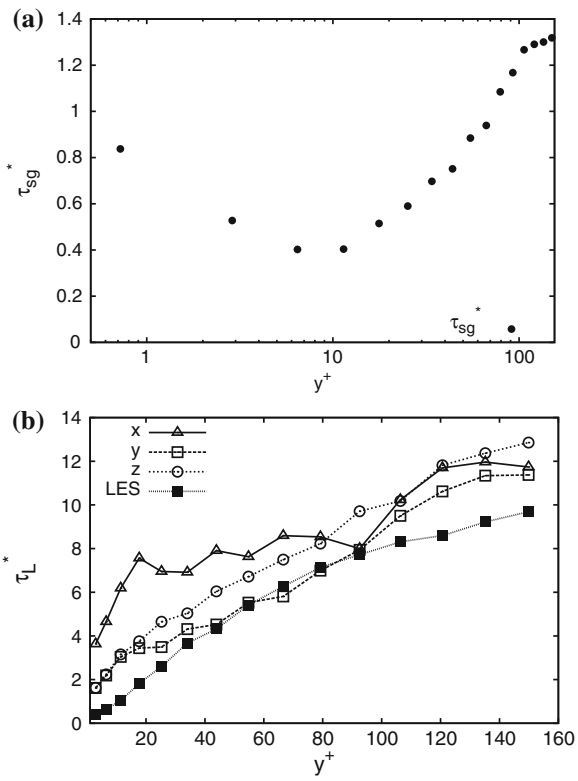

Fig. 3 **a** The SGS time scale computed in LES and based on (4); $C_{sg} = 0.1$. **b** The SGS time scale computed in LES with (9); best fit $C_0 = 0.26$

To obtain the constant C_{sg}^0 in Eq. (9) for different St, we compute time-scales T_{ii} of fluid velocity at particle positions, defined as times for which the autocorrelation function decays to $1/e$. As shown in Fig. 4, for the time scales T_{ii} (no sum over i) some difference between components is observed, although no clear dependence of T_{ii} on St is stated. The clarification comes with the computations of C_{sg}^0.

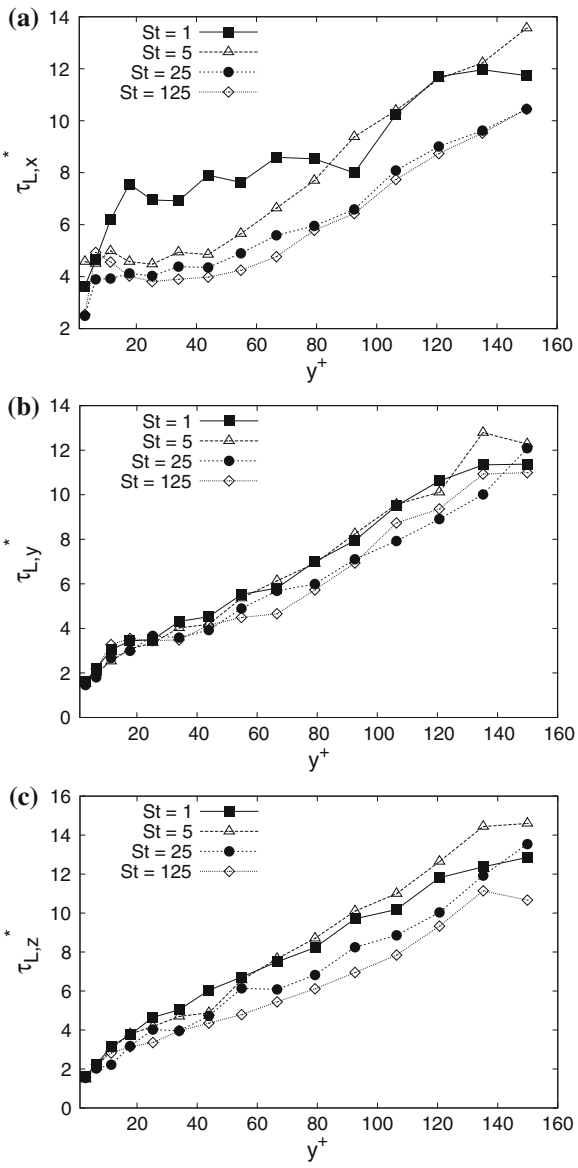

Fig. 4 Autocorrelation time scale of SGS fluid velocity at particle position in: **a** streamwise, **b** wall-normal, **c** spanwise direction; for $St = 1, 5, 25, 125$

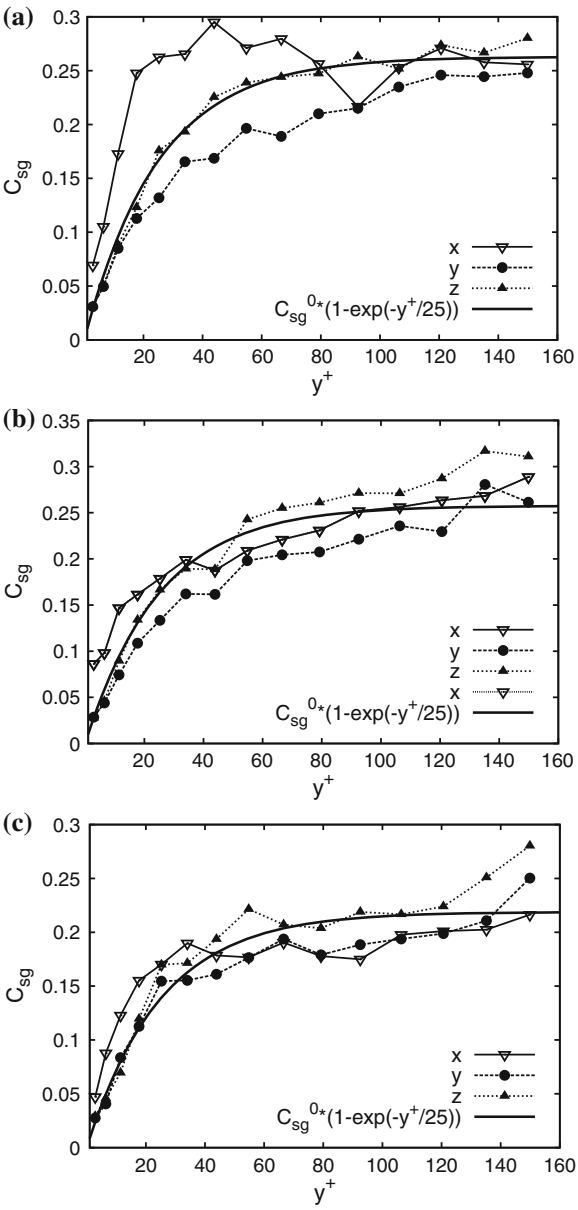

Fig. 5 Constant in model (4) as a function of the distance from the wall compared with best fit of function $C_{sg}^0(St)$ $(1-\exp(-y^+/25))$; **a** $St = 1$, **b** $St = 5$, **c** $St = 25$

The best fit (in the least-squares sense) of the parameter C_{sg}^0 in Eq. (9) is computed. The damping function with mean value of C_{sg}^0 for each St is shown in Fig. 5. An acceptable agreement with the theoretical results obtained from a priori computations $C_{sg} = T_{ii}/[\overline{\Delta}/\sqrt{(2/3)k_{sg}}]$ is noticed. The parameter C_{sg}^0 depends on the particle size.

4 Summary

We considered anisotropic formulation of stochastic model based on Langevin equation for SGS fluid velocity at particle position. We shown the importance of the deterministic terms for the channel flow. The resemblance of these terms to the filtering error introduced to fluid velocity at particle position was brought up, and the method of modelling was shown. Another focus of this paper was on the SGS relaxation time. It was shown that previous model enhanced with damping function estimates τ_{sg} better, although still an a priori model constant is needed.

Acknowledgments We would like to thank Prof. J.G.M. Kuerten (TU/e, the Netherlands) for the kind permission to use his spectral code for DNS and LES of channel flow. The work has been funded by the National Science Centre (NCN, Poland) through the research project 2011/03/B/ST8/05677. We also acknowledge the COST Action MP0806 'Particles in Turbulence'.

References

1. Bianco, F., Chibbaro, S., Marchioli, C., Salvetti, M.V., Soldati, A.: Intrinsic filtering errors of Lagrangian particle tracking in LES flow fields. Phys. Fluids **24** (2012). doi:10.1063/1.3701378
2. Fede, P., Simonin, O., Villedieu, P., Squires, K.D.: Stochastic modelling of the turbulent subgrid fluid velocity along inertial particle trajectories. In: Summer Program, Center for Turbulence Research, Stanford University, 247–258 (2006)
3. Geurts, B.J., Kuerten, J.G.M.: Ideal stochastic forcing for the motion of particles in large-eddy simulation extracted from direct numerical simulation of turbulent channel flow. Phys. Fluids **24** (2012). doi:10.1063/1.4745857
4. Knorps, M., Pozorski, J.: A priori analysis of an anisotropic subfilter model for heavy-particle dispersion. J. Turbul., submitted (2013)
5. Kuerten, J.G.M.: Subgrid modelling in particle-laden channel flow. Phys. Fluids **18** (2006) doi:10.1063/1.2176589
6. Michalek, W.R., Kuerten, J.G.M., Liew, R., Zeegers, J.C.H., Pozorski, J., Geurts, B.J.: A hybrid deconvolution stochastic model for LES of particle-laden flow. DLES **9** (2013)
7. Minier, J.P., Peirano, E.: The PDF approach to turbulent polydispersed two-phase flows. Phys. Rep. **352**, 1–214 (2001)
8. Pozorski, J., Apte, S.V.: Filtered particle tracking in isotropic turbulence and stochastic modelling of subgrid- scale dispersion. Int. J. Multiph. Flow **35**, 118–128 (2009)
9. Pozorski, J., Knorps, M., Minier, J.-P., Kuerten, J.G.M.: Anisotropic stochastic dispersion model for LES of particle-laden turbulent flows. In: Engineering Turbulence Modelling and Measurements 9, Thessaloniki, Greece, 6–8 June 2012

LES of the Ranque-Hilsch Vortex Tube

W.R. Michałek, J.G.M. Kuerten, J.C.H. Zeegers and R. Liew

1 Introduction

The Ranque-Hilsch vortex tube (RHVT) is a device without any moving parts in which pressurized inlet gas is separated into a hot peripheral and a cold inner stream [1]. The RHVT is commonly used in industry although the nature of the energy separation is not well understood.

The first theories for the energy separation were published shortly after the invention of the RHVT [2–5]. The secondary circulation inside the RHVT was mentioned in several publications [2, 6]. Ahlborn et al. [7] proposed a closed loop system and suggested a heat pump mechanism transferring energy in the RHVT. Liew et al. measured wobbling [8] of the vortex and proposed a new theory [9] for the mechanism of energy separation and a model that matches the measurements well. Many numerical investigations on the RHVT were conducted in two- and three-dimensional domains. Only Kazantseva et al. [10] reported precession of the axial vortex.

The high swirl conditions of the flow in the RHVT allow us to expect good capabilities for droplet separation. The expansion of the tangentially introduced gas in the vortex chamber leads to a temperature drop and condensation of droplets. The gas acceleration and a large swirl cause the movement of droplets towards the wall. Thus, the main goals of this research are the investigation and improvement of the separation rate by droplet-laden large-eddy simulation (LES) of the RHVT utilizing ANSYS FLUENT. The results of the LES will be validated by comparison with the results of laser Doppler anemometry (LDA) measurements of particle velocity, concentration and size in the RHVT.

W.R. Michałek (✉) · J.G.M. Kuerten
Department of Mechanical Engineering,
Eindhoven University of Technology, Eindhoven, The Netherlands
e-mail: w.michalek@tue.nl

J.C.H. Zeegers · R. Liew
Department of Applied Physics, Eindhoven University of Technology,
Eindhoven, The Netherlands

J. Fröhlich et al. (eds.), *Direct and Large-Eddy Simulation IX*,
ERCOFTAC Series 20, DOI 10.1007/978-3-319-14448-1_85

2 Equations, Numerical Methods, Mesh and Setup

The Euler-Lagrange approach was used to solve the particle-laden flow. For the fluid, the momentum, energy and the continuity equation are solved. The trajectories of particles are solved by integration of the particle equation of motion, $\frac{d\mathbf{u}}{dt} = F_D(\mathbf{u}-\mathbf{v})$, where $F_D(\mathbf{u}-\mathbf{v})$ is the drag force per unit particle mass with $\mathbf{v}$ the particle velocity, $\mathbf{u}$ the fluid velocity at the particle position, and $F_D = 3\mu C_D Re/4\rho_p d_p^2$, with μ the molecular viscosity of the fluid, ρ_p the particle mass density, d_p the particle diameter, $\mathrm{Re}_p = \rho d_p|\mathbf{v}-\mathbf{u}|/\mu$ the relative Reynolds number with ρ the fluid mass density and C_D is the drag coefficient.

In order to avoid too large restrictions on the time step, the coupled pressure-based solver was chosen for the RHVT flow simulation. This is possible since there are no shocks in the flow. The second-order accurate bounded central-differencing method was used as the discretization scheme for the momentum equations. A second-order method is used to interpolate the pressure at the cell faces. The least squares cell-based method was chosen to calculate gradients and derivatives. The second-order upwind scheme is used to estimate the values of density and energy at cell faces, and a second-order implicit method for integration in time.

The geometry of the RHVT is presented in Fig. 1 and is similar to the one in the experiment. The domain contains a vortex chamber with eight tangential inlet slots. The diameters of the vortex tube and the vortex chamber are equal to 20 and 40 mm respectively, the total length 500 mm. Two outlets are present on the opposite sides of the RHVT. The cold outlet diameter is equal to 15 mm and the hot outlet dimensions are: $r_{in} = 17$ and $r_{out} = 20$ mm.

Figure 2 shows the section of the mesh through the vortex chamber. Since $\delta r^+ > 30$ at the wall, standard wall functions are used. The total number of cells equals 3, 223, 596 and the number of cells in the tangential and radial directions are respectively 112 and 122.

The fluid inlet and outlet boundary conditions are presented in Table 1 and these values correspond to the values measured in the experiments. The mass flux is defined at the hot outlet and inlet and at the cold outlet only the pressure and backflow temperature, so the total mass in the system can vary in time. At the walls no-slip adiabatic conditions are applied.

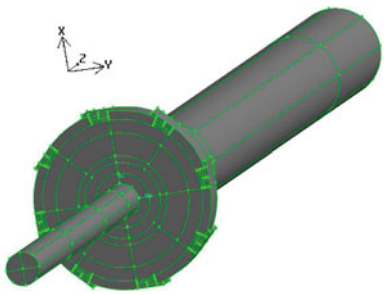

Fig. 1 Isometric view of the domain

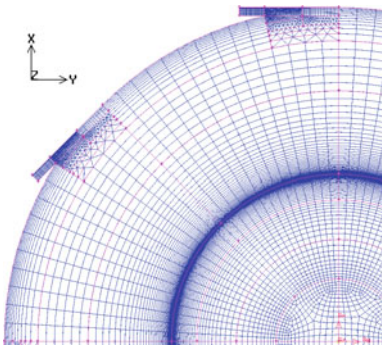

Fig. 2 Computational grid

Table 1 Boundary conditions for a mass flow equal to 200 m_n^3/h

Type of boundary	Total pressure (bar)	Total temperature (K)	Mass flux (g/s)
Inlet	4.64	299	70.0
Hot outlet	1.82	319	45.5
Cold outlet	1.42	263	24.5

Particles with four diameters were injected ($d_p = 0.5$, 1, 1.5, and 2.5 μm) at 8 points each rotated by 45°. The injection point position is 0.1 mm from the inlet symmetry point. The initial particle velocity is equal to the mean fluid velocity at the injection point. At the walls, particles are trapped, at the outlets particles escape.

3 Fluid Results

A good agreement between experimental data by Liew et al. [8, 9] and results of the $k - \varepsilon$ turbulence model with the density-based solver can be seen in Fig. 3, where the Mach number is presented as a function of the radial coordinate at $z = 7$ mm (in the middle of the vortex chamber).

All results of the density-based solver are axially symmetric in the whole domain. This implies that the center of the vortex coincides with the axis. The final solution of the density based solver was used as the initial state for the pressure-based solver.

As can be seen in Fig. 4 the steady solution of the pressure-based solver is not axi-symmetric. This figure shows the mean tangential fluid velocity component as a function of the axial coordinate at three different locations for the two solvers. The center of the vortex does not coincide with the axis, especially in the range of axial coordinates between 100 and 300 mm and this implies wobbling of the vortex. Apart from the presence of oscillations, the swirl velocity is damped more strongly. The asymmetric character of the flow field disappears when in transient simulation.

The LES was started with the initial condition obtained with the $k - \varepsilon$ model and the coupled pressure-based solver. A steady state of turbulence was obtained after 30 ms. The time averaged quantities of the fluid were collected through 50 ms.

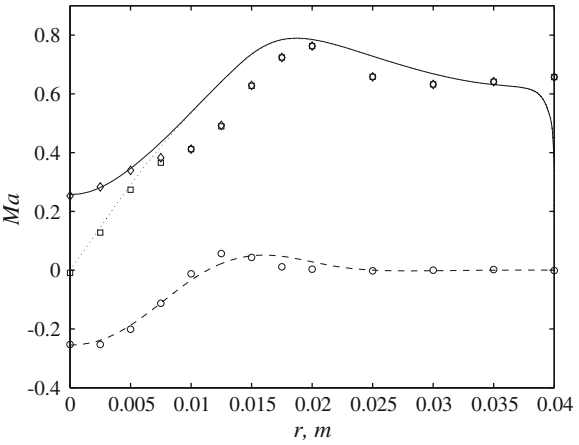

Fig. 3 Mach number as a function of the radial coordiate at $z = 7$ mm; *dashed* LES, axial component of the Mach number; *dotted* LES, tangential component of the Mach number; *solid* LES, total Mach number; *circles* experiment, axial component of the Mach number; *squares* experiment, tangential component of the Mach number; *diamonds* experiment, total Mach number

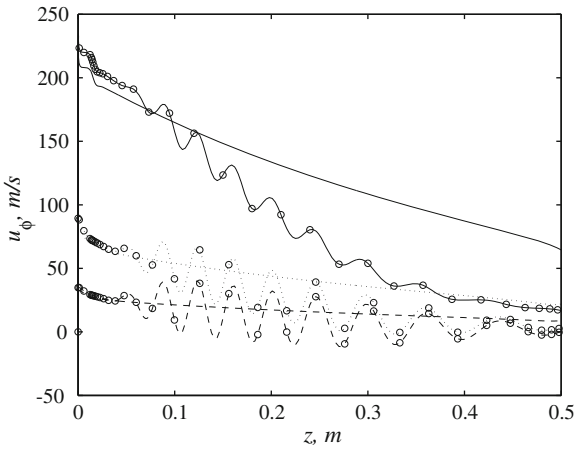

Fig. 4 Mean tangential fluid velocity as a function of the axial coordinate obtained with the $k - \varepsilon$ model at $y = 0$; *solid* $z = 16$ and $r = 0$ mm; *dotted* $r = 2$ mm; *dashed* $r = 5$ mm; *lines with circles* coupled pressure-based solver; *lines without circles* density based solver

Positive values of the axial fluid velocity are found in the peripheral area of the vortex tube and negative values in the core. A "camel hump" in the axial velocity profile (the maximum negative axial velocity is distanced from the axis) can be noticed, especially between $z = 200$ and $z = 350$ mm. Moreover, in the last 100 mm of the vortex tube the mean axial velocity equals zero. The presence of the stagnation point at the axis implies that a further elongation of the vortex tube will not increase the energy separation.

Figure 5 shows a contour plot of the mean tangential fluid velocity in a half cross section of the domain. In the vortex chamber between $r = 20$ and $r = 40$ mm a free vortex occurs. A forced vortex is present in the inner part of the vortex chamber and

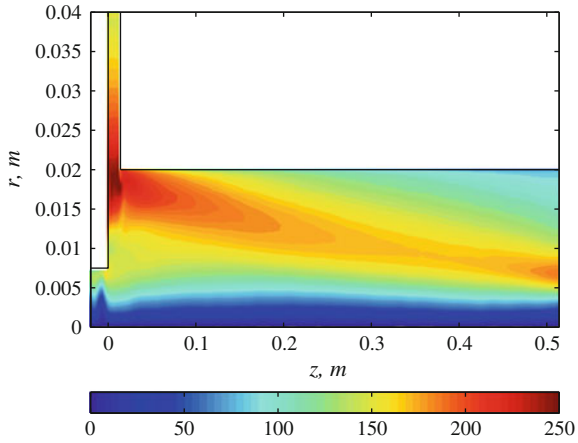

Fig. 5 Contour plot of the mean tangential fluid velocity [m/s] in a half cross section of the RHVT domain

in the beginning of the vortex tube (up to $z = 50$ mm). At further axial coordinates, the forced vortex is turning into a Rankine vortex due to the presence of the wall.

4 Particle Results

Particles were injected in the statistically steady state. A steady state of particle concentration was obtained after 20 ms. The particle time statistics were collected through the next 30 ms. The four sizes of particles considered allow us to investigate the behavior of different types of particles. The smallest particles considered are present along the whole length of the vortex tube. This can be seen in Fig. 6, where the decimal logarithm of the particle concentration is presented in a contour plot in a half cross section of the RHVT domain for $d_p = 0.5\,\mu$m. The second smallest

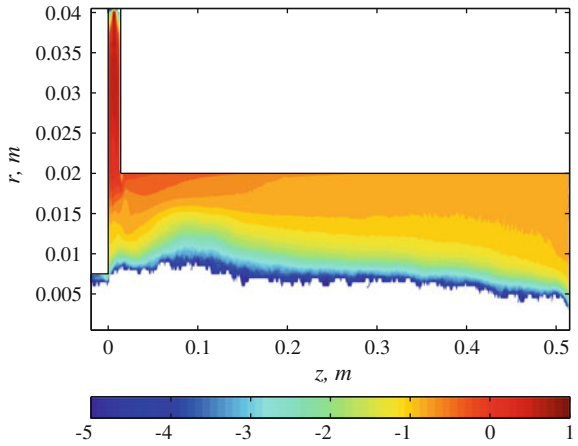

Fig. 6 Contour plot of the decimal logarithm of the particle concentration in a half cross section of the RHVT domain for $d_p = 0.5\,\mu$m

particles considered are also present in the whole length of the vortex tube, but the particle concentration after half of the tube length is very low. Particles with $d_p = 1.5\,\mu\text{m}$ are not present in the second half of the tube and with $d_p = 2.5\,\mu\text{m}$ are mainly present in the vortex chamber.

The smallest particles considered are good tracers while the largest particles are prevented to enter the vortex tube by the centrifugal force. The behavior of the particles can be characterized by their ability to migrate towards the wall. This can be visualized by the number of particles colliding with the wall per unit axial distance as a function of the axial coordinate and this is shown in Figs. 7 and 8 for the smallest and largest particles. The number of the smallest particles leaving the computational domain through the hot outlet is significant in comparison to the total amount of particles trapped at the wall. Some of the particles leave the domain through the cold outlet or are trapped at the cold outlet tube wall. The next larger particles behave in a similar way, but more particles are trapped by the wall. All particles

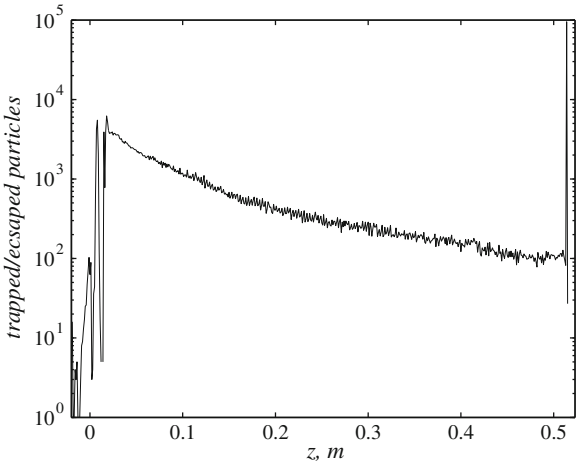

Fig. 7 Number of trapped/escaped particle per 1 mm as a function of the axial coordinate for $d_p = 0.5\,\mu\text{m}$

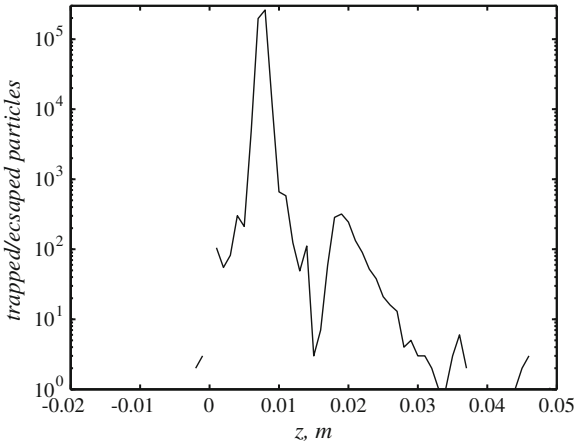

Fig. 8 Number of trapped/escaped particle per 1 mm as a function of the axial coordinate for $d_p = 2.5\,\mu\text{m}$

with $d_p = 1.5\,\mu\text{m}$ are collected at the wall of the vortex chamber or within the first 150 mm of the vortex tube. The vast majority of the largest particles considered is collected at the vortex chamber wall.

The mean axial and tangential particle velocity appear independent of particle size and is almost identical to the fluid velocity. In contrast, the mean radial particle velocity depends on the particle size. Figure 9 shows the mean radial particle velocity as a function of the radial coordinate at $z = 35$ mm. The profile of the mean radial particle velocity appears particle size independent for $r < 17\,\text{mm}$. From this radius outward, the mean radial velocity increases with the size of the particle due to the increasing effect of the centrifugal force. For all quantities except the axial velocity, the instantaneous result is similar to the time averaged result. However, the instantaneous axial velocity presented in Fig. 10 illustrates a non-uniformity in the axial direction which disappears after time averaging.

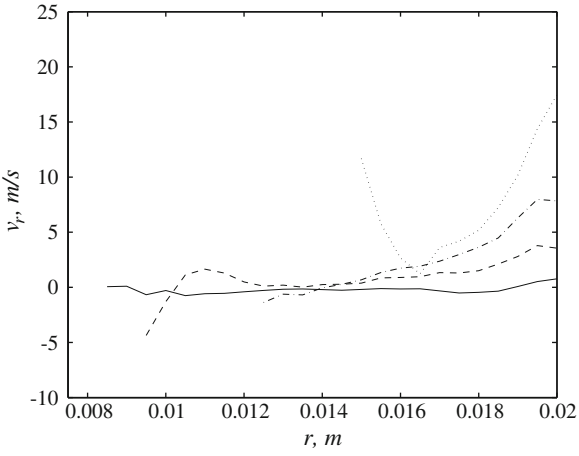

Fig. 9 Mean radial particle velocity as a function of the radial coordinate at $z = 35\,\text{mm}$; *solid* $d_p = 0.5\,\mu\text{m}$; *dashed* $d_p = 1.0\,\mu\text{m}$; *dashed-dotted* $d_p = 1.5\,\mu\text{m}$; *dotted* $d_p = 2.5\,\mu\text{m}$

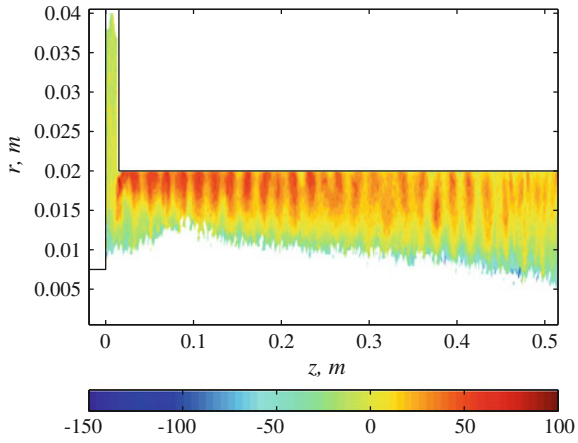

Fig. 10 Contour plot of the instantaneous axial particle velocity [m/s] in a half cross section of the RHVT domain for $d_p = 0.5\,\mu\text{m}$

5 Discussion

The good agreement in velocities between this numerical work and earlier performed experiments indicates that the fluid flow is properly solved in FLUENT. The particle-laden LES allows us to assess the capability of the RHVT as a particle separator. The RHVT is a particle separator for particles larger than 1.5 μm. The flow through the cold outlet has a much smaller particle concentration than the inflow. However, to investigate the real situation, the implementation of phase changes is crucial. Condensation is mainly present in the vortex chamber and in the beginning of the tube. Evaporation occurs in the rest of the vortex tube. Condensation enhances the separation and evaporation deteriorates the separation of the smaller particles. In future work evaporation and condensation models will be implemented.

Acknowledgments This research is supported by the Dutch Technology Foundation STW.

References

1. Ranque, G.J.: Methods and apparatus for obtaining from a fluid under pressure two outputs of fluid at different temperatures. U.S. Patent No. 1,952,281 (1934)
2. Fulton, C.D.: Ranque's tube. J. ARSE Refrig. Eng. *58*, 473–479 (1950)
3. Hilsch, R.: The use of expansion of gases in a centrifugal filed as a cooling process. Rev. Sci. Instrum. **18**(2), 108–113 (1947)
4. Kassner, R., Knoerschild, E.: Friction laws and energy transfer in circular flow. Wright-Patterson Air Force Base. Technical Report No. F-TR-2198-ND, Ohio (1948)
5. Kurosaka, M.: Acoustic streaming in swirling flow and the Ranque-Hilsch (vortex-tube) effect. J. Fluid Mech. **124**, 139–172 (1982)
6. Gao, C.M., Bosschaart, K.J., Zeegers, J.C.H., de Waele, A.T.A.M.: Experimental study on a simple Ranque-Hilsch vortex tube. Cryogenics **45**(3), 173 (2005)
7. Ahlborn, B., Keller, J.U., Rebhan, E.: The heat pump in a vortex tube. J. Non-Equilib. Thermodyn. **23**, 159–165 (1998)
8. Liew, R., Zeegers, J.C.H., Kuerten, J.G.M., Michałek, W.R.: 3D velocimetry and droplet sizing in the Ranque-Hilsch vortex tube. Exp. Fluids **54**, 1416 (2013)
9. Liew, R., Zeegers, J.C.H., Kuerten, J.G.M., Michałek, W.R.: Maxwell's demon in the Ranque-Hilsch vortex tube. Phys. Rev. Lett. **109**, 054503 (2012)
10. Kazantseva, O.V., Piralishvili, S.A., Fuzeeva, A.A.: Numerical simulation of swirling flows in vortex tubes. High Temp. **43**(4), 608–613 (2005)

Direct Numerical Simulation of Heat Transfer in Colliding Droplets by a Coupled Level Set and Volume of Fluid Method

N. Talebanfard and B.J. Boersma

1 Introduction

Study of heat and mass transfer in droplets is of importance in a range of industrial applications; modeling fuel droplets in internal combustion engines and cavitation are examples of such applications. For numerical modeling of simple multiphase problems with moving boundaries, it is possible to use adaptive mesh or variable grid spacing. In these methods re-meshing the whole domain or a part of it, is required every time step. This makes these methods computationally expensive and therefore not the best solution for more complicated problems such as evaporation or collision with large topological changes of disperse phase. These methods have been used in a number of studies such as [1] on mass transfer from a falling droplet using finite element method in a Lagrangian framework and study of [2] on interface tracking in merging and breakup by using moving mesh. Adaptive mesh has been used in a number of studies, an adaptive unstructured volume remeshing for simulation of multiphase flow is used in [3]. A local adaptive mesh for capturing interface curvature is used in [4] for simulation while [5] used an adaptive mesh redistribution for incompressible mixture flows and [6] studied multiphase flows by using moving mesh interface tracking with adaptive meshing. For more complicated problems other methods such as boundary integral, marker particle methods, front capturing, front tracking methods or a combination of them can be used on a fixed grid. Gilmanov and Acharya [7] proposed a hybrid method for flow and heat transfer on deformable objects using immersed boundary method for the moving boundaries and material point method for movements of the object. Deshpande and Zimmerman [8] has simulated interfacial mass transfer by droplet dynamics using the level set method.

N. Talebanfard (✉) · B.J. Boersma
Process and Energy Department, Delft University of Technology,
Leeghwaterstraat 44, 2628 CA Delft, The Netherlands
e-mail: n.talebanfard@tudelft.nl

B.J. Boersma
e-mail: b.j.boersma@tudelft.nl

J. Fröhlich et al. (eds.), *Direct and Large-Eddy Simulation IX*,
ERCOFTAC Series 20, DOI 10.1007/978-3-319-14448-1_86

Tanguy et al. [9] has proposed a level set method for vaporizing two-phase flows. Level set is employed to capture interface accurately. A coupled level set and volume of fluid method was introduced by [10] in which a level set function is taking care of accurate computing the location of interface and a VOF function is responsible for volume and mass conservation with a common marker function in the whole domain. The method was improved by [11] by adding separate marker functions for each interface in the domain preventing numerical coalescence in the solution. Kwakkel et al. [12] studied droplet-laden flows by a CLSVOF method with local markers for every unconnected object in the domain which results in reduction in computation time significantly. The break up and coalescence of droplets is also considered by applying a film drainage model. In this paper a coupled level set and volume of fluid method is used to model heat transfer in colliding droplets in merging and bouncing regimes.

2 Computational Approach

In the range of velocities interested to us we can assume the flows to be incompressible. A staggered grid is used such that the velocity components are placed at faces of the cells and the scalars such as temperature, pressure, level set and volume of fluid denoted as T, P, ϕ and ψ respectively are located at the center of each cell. The governing equations for flow are conservation of mass, conservation of momentum and the energy equation as follows:

$$\nabla \cdot \mathbf{u} = 0 \tag{1}$$

$$\frac{\partial \mathbf{u}}{\partial t} + \nabla \cdot \mathbf{u}\mathbf{u} = -\frac{1}{\rho}\nabla p + \frac{1}{\rho}\nabla \cdot \left(\mu \left(\nabla \mathbf{u} + \nabla \mathbf{u}^T\right)\right) + \mathbf{g} \tag{2}$$

$$\frac{\partial T}{\partial t} + \nabla \cdot (T\mathbf{u}) = \frac{k}{\rho c_p}\nabla^2 T \tag{3}$$

In which $\mathbf{u}$ is the velocity vector, μ, denotes the viscosity, ρ is the density, k is the thermal conductivity and c_p denotes the heat capacity. Stress and velocity are assumed continuous over the interface by the following conditions:

$$[\mathbf{u}]_\Gamma = 0 \tag{4}$$

$$\left[-p\mathbf{n} + \mu\left(\nabla \mathbf{u} + \nabla \mathbf{u}^T\right) \cdot \mathbf{n}\right]_\Gamma = -\sigma \kappa_\Gamma \mathbf{n} \tag{5}$$

where $[.]_\Gamma$ represents a jump across the interface, $\mathbf{n}$ denotes the interface normal vector, κ is the magnitude of the interface curvature, and σ is the surface tension coefficient. Thermophysical properties such as density and viscosity are defined

by the one-field formulation in the whole domain using the level set function as a criterion to determine which phase properties should be used. Level set function takes zero at the interface, positive values in the liquid phase and negative values in the gas phase. Subscripts 0 and 1 denote the gas phase and the liquid phase respectively.

$$\rho = \rho_0 (1 - H(\phi)) + \rho_1 H(\phi) \tag{6}$$

$$\mu = \mu_0 (1 - H(\phi)) + \mu_1 H(\phi) \tag{7}$$

$$H_\alpha(\phi) = \begin{cases} 0 & if \quad \phi < -\alpha \\ \frac{1}{2}\left(1 + \frac{\phi}{\alpha} + \frac{1}{\pi}\sin\left(\frac{\pi\phi}{\alpha}\right)\right) & if \quad |\phi| \leq \alpha \\ 1 & if \quad \phi > \alpha \end{cases} \tag{8}$$

In which $H(\phi)$ is 1 in the droplets and zero elsewhere. The viscosity is regularized by replacing $H(\phi)$ by $H_\alpha(\phi)$, in which $\alpha = \frac{3}{2}h$, and h is the mesh width. Using the regularized viscosity the velocity gradients become continuous at the interface and there will be no jump condition for velocity. The level set method and volume of fluid method are combined to develop a mass conserving method for capturing accurate interfaces. In this method the level set function locates the interface accurately while the volume of fluid method takes care of mass and volume conservation. The level set and volume of fluid functions are separately advected in time using the velocity field from the previous time step and then the level set function is reinitialized to remain a distance function of the advected volume of fluid function. The numerical approach to solve the Navier-Stokes equations is the same as in [11].

$$\frac{\partial \phi}{\partial t} + \nabla \cdot (\mathbf{u}\phi) = 0 \tag{9}$$

$$\frac{\partial \psi}{\partial t} + \nabla \cdot (\mathbf{u}\psi) = 0 \tag{10}$$

3 Results and Discussions

The computational domain is a rectangular box in which a fixed uniform grid is defined. The velocity boundary conditions for the normal velocity component to each face is the Neumann boundary condition and for other components is the symmetry boundary condition. Pressure is assumed to be zero at all boundaries. The two droplets approach with equal initial velocity. Simulations are performed for three different configuration of droplets. The multiple marker concept and the interface level set of droplets is shown in Figs. 1 and 2. The markers carrying the droplets are defined locally in the computational domain which results in less memory consumption. According to the type of collision these markers will change into a larger marker if the droplets merge into one droplet and if they breakup after collision a new marker

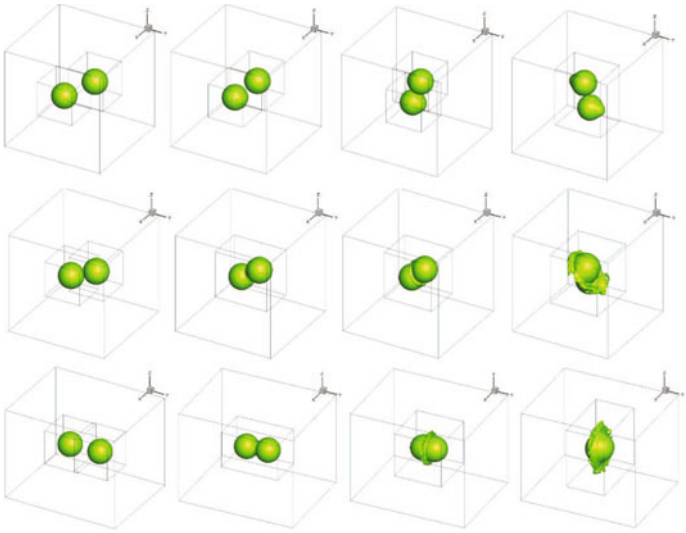

Fig. 1 Level set of droplets surface in time for three different configurations for We = 1.33

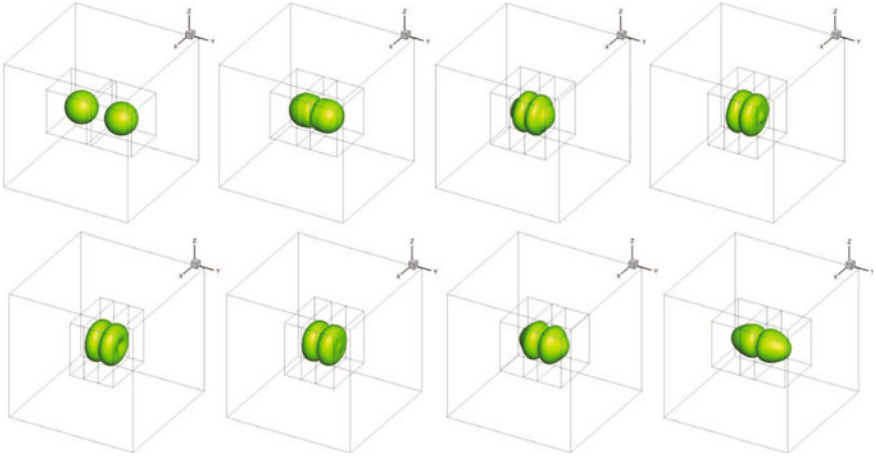

Fig. 2 Level set of bouncing droplets surface in time for We = 0.0149

is introduced for each separated volume. Figures 3 and 4 show the development of temperature in the droplets and the ambient fluid in time.

Using the average surface temperature and the normal temperature gradient at the surface, the average Nusselt number is calculated by the following equation and the effect of deformation on heat transfer rate is investigated.

$$Nu_m = \frac{1}{A(T_{s,m} - T_\infty)} \int \nabla T \cdot n dA \tag{11}$$

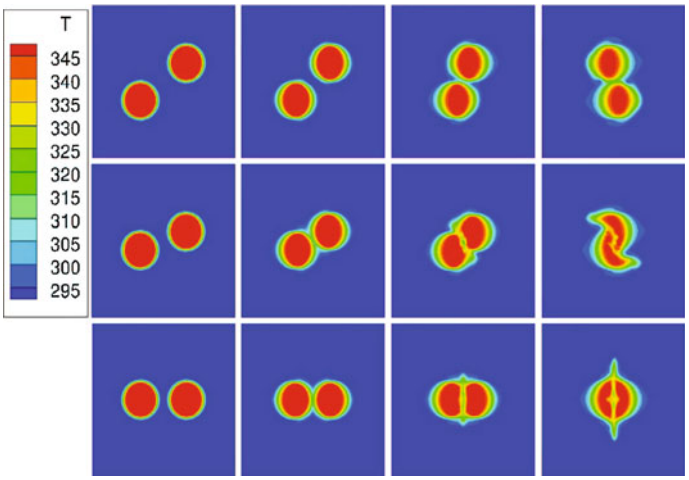

Fig. 3 Temperature distribution in time for three different configurations for We = 1.33

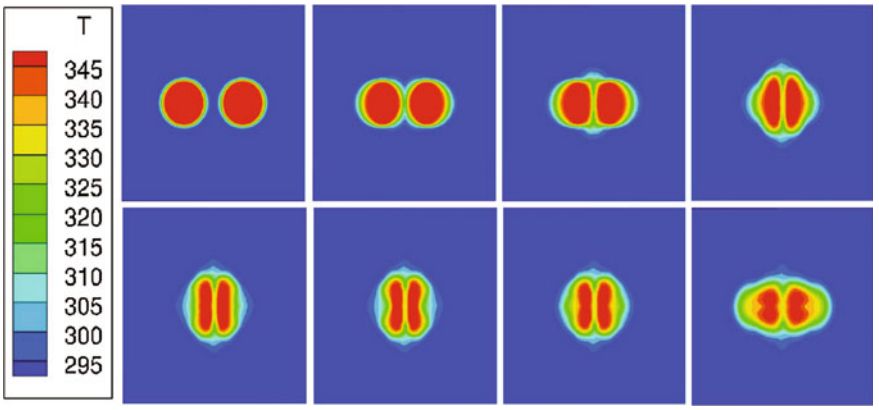

Fig. 4 Temperature distribution in time for bouncing droplets for We = 0.0149

In which $n = \frac{\nabla\varphi}{|\nabla\varphi|}$, $T_{s,m}$ is the average surface temperature, $T_\infty = 293.15\,\mathrm{K}$ is the initial ambient temperature and droplets are initially at 350 K.

In Fig. 5a the effect of Weber number on heat transfer rate when the center of droplets are distanced a radius is shown. As it is observed in the graph the Nusselt number is generally higher for higher Weber number. According to the definition of the Weber number the higher it is means the more important is the effect of inertia comparing to surface tension. In lower surface tension the droplets can rupture faster due to collision or just because of the inertia of the surrounding flow, providing larger surface in contact with the flow which can result in higher heat transfer rate.

Figure 5b shows the variation of Nusselt number in time for different configuration of approaching droplets. Comparing the head-on collision with the tangent case, one

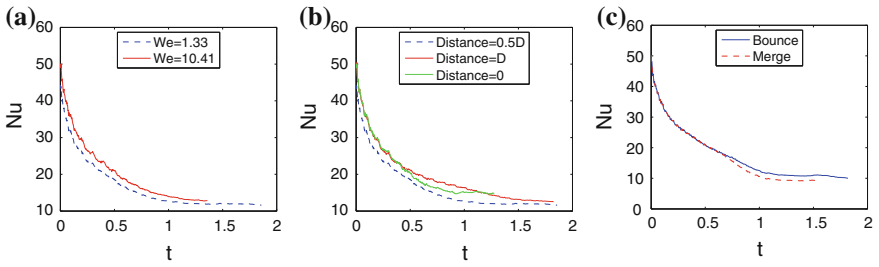

Fig. 5 **a**Variation of Nu in time for different We numbers. **b** Effect of droplets distance on Nusselt number. **c** Nu in bouncing and merging droplets

can observe that Nusselt is almost the same before droplets touch, but after they contact in case of head-on collision Nusselt number decreases due to reduction in heat transfer surface until $t = 1\,\mathrm{s}$, at this point contact surface of droplets expands forming some thin volume of splashes from which heat can be transferred easily so the Nusselt number increases and exceeds the Nusselt number of tangent droplets at $t = 1.2\,\mathrm{s}$. In case of droplets center with distance of r, the Nusselt number is generally lower than other cases, it seems that the distance between the droplets should be either too short to make a thin layer of ambient fluid which escapes when the two drops approach or should be large enough such that they do not affect the inertia of one another.

In bouncing and merging cases for head-on collision as shown in Fig. 5c the Nusselt number has the same amount during approach and contact time. If droplets start merging after collision the Nusselt number decreases while a higher Nusselt number is observed for bouncing droplets. The reason is the surface from which heat transfer can occur is larger in bouncing case.

References

1. Petera, J., Weatherley, L.R.: Modelling of mass transfer from falling droplets. Chem. Eng. Sci. **56**, 4929–4947 (2001)
2. Quan, S., Lou, J., Schmidt, D.P.: Modeling merging and breakup in the moving mesh interface tracking method for multiphase flow simulations. J. Comput. Phys. **228**, 2660–2675 (2009)
3. Anderson, A., Zheng, X., Cristini, V.: Adaptive unstructured volume remeshing I: the method. J. Comput. Phys. **208**, 616–625 (2005)
4. Quan, S., Schmidt, D.P.: A moving mesh interface tracking method for 3D incompressible two-phase flows. J. Comput. Phys. **221**, 761–780 (2007)
5. Tan, Z., Lim, K.M., Khoo, B.C.: An adaptive mesh redistribution method for the incompressible mixture flows using phase-field model. J. Comput. Phys. **225**, 1137–1158 (2007)
6. Quan, S.: Simulations of multiphase flows with multiple length scales using moving mesh interface tracking with adaptive meshing. J. Comput. Phys. **230**, 5430–5448 (2011)
7. Gilmanov, A., Acharya, S.: A computational strategy for simulating heat transfer and flow past deformable objects. Int. J. Heat Mass Transf. **51**, 4415–4426 (2008)

8. Deshpande, K.B., Zimmerman, W.B.: Simulation of interfacial mass transfer by droplet dynamics using the level set method. Chem. Eng. Sci. **61**, 6486–6498 (2006)
9. Tanguy, S., Mnard, T., Berlemont, A.: A level set method for vaporizing two-phase flows. J. Comput. Phys. **221**, 837–853 (2007)
10. Sussman, M., Puckett, E.G.: A coupled level set and volume-of-fluid method for computing 3D and axisymmetric incompressible two-phase flows. J. Comput. Phys. **162**, 301–337 (2000)
11. Coyajee, E., Boersma, B.J.: Numerical simulation of drop impact on a liquid–liquid interface with a multiple marker front-capturing method. J. Comput. Phys. **228**, 4444–4467 (2009)
12. Kwakkel, M., Breugem, W.-P., Boersma, B.J.: An efficient multiple marker front-capturing method for two-phase flows. Comput. Fluids **63**, 47–56 (2012)

On the Numerical Modeling of Active Flow Control for Aerodynamics Applications and Its Impact on the Pressure Field

M. El-Alti, P. Kjellgren and L. Davidson

1 Introduction

The modeling of flow control is generally applied as a time-varying boundary condition at the slot position. In vehicle aerodynamics, the flow is assumed to be incompressible; however active flow control produces pressure waves that propagate instantly throughout the computational domain. It has been found that when using incompressible finite volume methods, the pressure field in the whole domain is oscillating. Most of the drag on a truck is caused by the wake behind the trailer, which is called the base drag. It is introduced by the sharp edges on the rear end where the flow naturally separates. This effect gives rise to a large low pressure region and thus increases the pressure difference between the front and back. An effective way to increase the pressure on the back is to introduce angled flaps. The idea is to increase the base pressure by attaching the flow onto the flap surface again. The attachment is done using active flow control (AFC). The idea of using flaps and re-attaching the separated flow is in line with successful research on tilt-rotor aircrafts and trucks done by the authors in [1, 2]. We use a simplified truck model in our simulations. The truck is simplified as a rectangular bluff body with a typical width ($w = 2.6\,\mathrm{m}$, y direction) and length ($l = 13.0\,\mathrm{m}$) relevant for a real truck. The height (the z direction) is $H = 0.2\,\mathrm{m}$, i.e. the domain is three-dimensional (Fig. 1). The truck is mounted with angled flaps on the rear end in which the oscillating synthetic jet actuators are placed. The actuators are modeled as a time-varying boundary condition at the slot. The Reynolds number is reduced to 200,000 by increasing the viscosity to $\mu = 3.25 \times 10^{-4}$.

M. El-Alti (✉) · P. Kjellgren · L. Davidson
Division of Fluid Dynamics, Department of Applied Mechanics,
Chalmers University of Technology, 412 96 Göteborg, Sweden
e-mail: mohammad.el-alti@chalmers.se

J. Fröhlich et al. (eds.), *Direct and Large-Eddy Simulation IX*,
ERCOFTAC Series 20, DOI 10.1007/978-3-319-14448-1_87

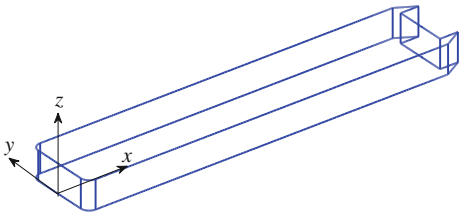

Fig. 1 Simplified truck model. Inlet at $x = -12$ w; outlet at $x = 30$ w; side walls at $y = -8.5$ w and $y = 8.5$ w. The width of the truck is denoted by w (y direction)

2 CFD Codes

2.1 Numerical Method

The modeled actuator is very narrow and the maximum excitation velocity is about 110 % of the free-stream velocity. The actuation frequency is also much higher than the Strouhal frequency of the wake. Thus fine resolution is needed both in space and time. Therefore, in order to make an accurate prediction of the turbulent flow, large-eddy simulation is used. The filtered Navier-Stokes equations read

$$\frac{\partial \bar{u}_i}{\partial t} + \frac{\partial}{\partial x_j}\left(\bar{u}_i \bar{u}_j\right) = -\frac{1}{\rho}\frac{\partial \bar{p}}{\partial x_i} + \nu \frac{\partial^2 \bar{u}_i}{\partial x_j \partial x_j} - \frac{\partial \tau_{ij}}{\partial x_j} \tag{1}$$

The Smagorinsky model for the sub-grid scales is used with the Smagorinsky constant $C_S = 0.25$, in the near wall region, the turbulence is resovled and the filter width is reduced using Van Driest damping function. The temporal discretization is the explicit four-step Runge-Kutta scheme for the convection terms and the Crank-Nicholson method for the diffusion terms. The forcing is modeled as a transient velocity inlet and the governing variables are the slot width, the velocity (both magnitude and direction) and the frequency. The RMS momentum from the slot is defined as

$$J_{RMS} = \int \rho u_{RMS}^2 \, dh = \rho u_{RMS}^2 \Delta h, \quad C_{(\mu,RMS)} = \frac{J_{RMS}}{w\frac{1}{2}\rho u_\infty^2} = \frac{u_{RMS}^2 \Delta h}{w\frac{1}{2}u_\infty^2} \tag{2}$$

Δh is the effective slot width. From Eq. 2 the velocity (assuming purely sinusoidal) in the slot is given and the non-dimensional forcing frequency is given by

$$u_{RMS} = \sqrt{\frac{C_{(\mu,RMS)}\, w\, u_\infty^2}{2\Delta h}}, \quad u(t) = \sqrt{2} u_{RMS} \sin(2\pi F t), \quad F^+ = \frac{F \cdot X_{TE}}{U_\infty} \tag{3}$$

where X_{TE} is the distance from the slot to the trailing edge of the flap. In our simulations with Fluent, Star-CCM+ and compressible Star-CCM+, we chose the segregated

Table 1 The boundary conditions in the different codes

Boundary	FlowPhys	Fluent	Star-CCM+	Compressible Star-CCM+
Inlet	Velocity	Velocity	Velocity	Far-stream inlet
Outlet	Weak	Pressure $P_s = 0.0$	Pressure $P_s = 0.0$	Far-stream inlet
Side walls (y)	Weak	Slip wall	Slip wall	Slip Wall
Side walls (z)	Slip wall	Slip wall	Slip wall	Slip wall

pressure solver. In Fluent we also chose the Non-Iterative Time Marching scheme (NITA) for the pressure-velocity coupling. In compressible STAR-CCM+, the coupled solver was used to provide a steady initial solution. The settings are identical in the codes but the convection scheme in both Star-CCM+ codes were bounded central difference (CD) with 5 % upwind. The proper setting and procedure followed best practice and guidelines provided by CD-ADAPCO [3]. The inhouse and commercial FlowPhys ver. 2.0a software has a semi-implicit, fractional step finite element solver which was used in the simulations. The convection scheme in FlowPhys was pure CD.

The boundary conditions used are described in Table 1. The inlet flow is modeled as an inlet boundary condition (BC) with prescribed constant free-stream velocity, $U_\infty = 25$ m/s, in all codes but the STAR-CCM+ compressible code, where the inlet is a far-stream inlet BC with a prescribed Mach number, pressure and temperature. The outlet BC in FlowPhys is a weak outlet, in Fluent and STAR-CCM+ it is a pressure outlet with prescribed pressure $P_{outlet} = 0$ and in STAR-CCM+ a compressible far-stream inlet BC with prescribed Mach number, pressure and temperature is used. The side-walls are prescribed frictionless walls, i.e. slip BC. The AFC slot was implemented using a user subroutine and functions which were compiled and set on the slot boundaries.

3 Results

This section starts with a time series of the pressure field in the computational domain. The relevant time instants are when the forcing (AFC) i.e. the velocity at the slot, is (1) zero, (2) minimum (suction stroke) and (3) the subsequent occasion when the slot velocity is zero.

3.1 RMS of Drag

The RMS values of drag is shown in Table 2. The RMS of drag is reduced in FlowPhys and increased in the other three codes. The compressible code shows an increase in RMS of the forced case by 34 % which is the highest RMS values.

Table 2 RMS values of drag for the different codes

CFD code	$RMS\ C_{D,AFC\ OFF}$	$RMS\ C_{D,AFC\ ON}$	$\Delta RMSC_{D,reduc}(\%)$
FlowPhys v2.0	0.085	0.071	16
Fluent v13.0	0.090	0.098	−9
CCM+ v6.06	0.081	0.107	−31
CCM+ v6.06 comp	0.086	0.1149	−34

3.2 Pressure Probes

The pressure was monitored far downstream ($X_{far} = (20, 6, 6, 0.26\,\mathrm{w})$) away from the truck. Figure 2 plots the relative pressure at X_{far} to the reference pressure at a predefined location. The time is normalized and all signals start when forcing is initiated. The fluctuation frequency is constrained to the actuation frequency, and there is a phase shift between the forcing and the pressure fluctuation. The compressible code however shows much lower fluctuations in pressure. To investigate if these fluctuations occur not only close to the forcing boundary conditions (i.e. the slot), we

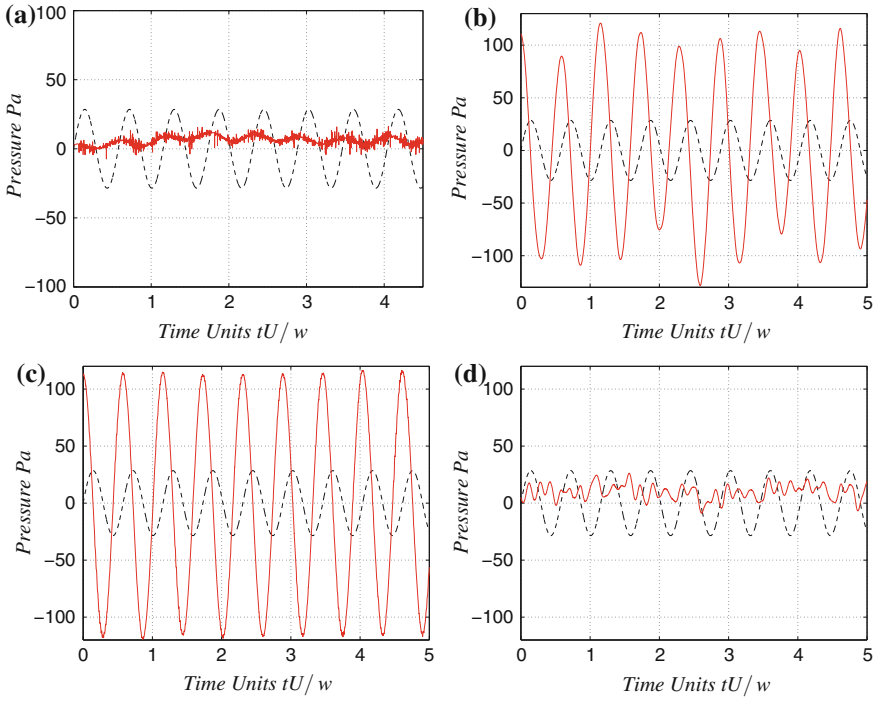

Fig. 2 Time history of pressure at X_{far} in the different codes. *Dashed black line* inlet velocity at the flow, *red solid line* pressure at X_{far}. **a** FlowPhys v2.0a, **b** ANSYS Fluent v13.0, **c** STAR-CCM+ incompressible, **d** STAR-CCM+ v6.06 compressible

monitored the pressure far away from the forcing. The incompressible FVM codes show high pressure fluctuations, even though the monitored point is far downstream of the forcing. The variations are between −100 and 100 Pa. The fluctuations in the incompressible FVM codes are thus present in the whole domain. FlowPhys and the compressible code have much more stable pressure.

3.3 Time Series of the Pressure Field

This section discusses the pressure at three different time instants in the forcing period. The times when the pressure is close to maximum, zero and minimum occur at zero, minimal and second zero forcing in the forcing suction period. The differences between the codes are remarkable, see Fig. 3. FlowPhys and STAR-CCM+

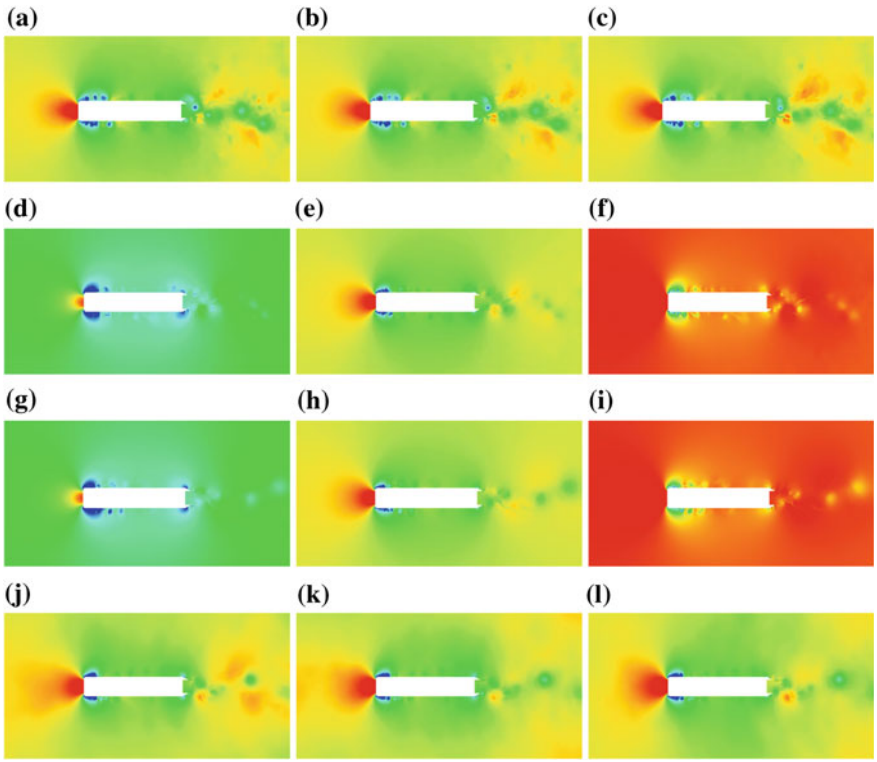

Fig. 3 Time series of the pressure field in the $x - y$ plane around the truck in different codes, $red > 200 Pa$, $blue < -500 Pa$ and identical colorbar for all figures. **a** FlowPhys: 1st zero AFC, **b** FlowPhys: min AFC, **c** FlowPhys: 2nd zero AFC, **d** Fluent: 1st zero AFC, **e** Fluent: min AFC, **f** Fluent: 2nd zero AFC, **g** CCM: 1st zero AFC, **h** CCM: min AFC, **i** CCM: 2nd zero AFC, **j** CCM compressible, **k** CCM compressible, **l** CCM compressible

compressible show stable pressure fields at all three time instants. Both Fluent and STAR-CCM+, i.e. the incompressible FVM codes, show large differences in pressure in the whole domain at the three time instants.

4 Discussion and Conclusions

The results obtained emphasize the sensitivity of the FVM incompressible codes to abrupt changes in pressure elsewhere in the domain. The forcing in the AFC is a prescribed velocity on a small slot at the boundary, and it is found that it makes the pressure in the whole domain oscillate. The pressure oscillation frequency is constrained to the forcing frequency. In unsteady simulations, when the aerodynamic drag is the target result, it is essential to predict the pressure field correctly during the entire time history. The reason for the oscillations in incompressible FVM codes is basically explained from the equations. The incompressible Navier-Stokes is parabolic-elliptic and thus each change in pressure is propagated through the entire domain, whereas, in the compressible Navier-Stokes, the pressure waves are resolved and the equation is of a hyperbolic-parabolic type. The explanation for the stable pressure field in the FEM code is probably the natural or weak outlet boundary condition; the pressure is not prescribed at the outlet boundary as in FVM pressure outlet. This is an advantage of the FEM codes compared with FVM codes, considering abrupt pressure changes. When using FVM for AFC in configuration similar to the present case, the compressible solver should be considered.

Acknowledgments This work is supported by the Swedish Agency of Innovation Systems (VINNOVA), Volvo 3P, SKAB and CD-ADAPCO. Financial support by SNIC (the Swedish National Infrastructure for Computing) for computer time at C3SE (Chalmers Centre for Computational Science and Engineering) is gratefully acknowledged.

References

1. El-Alti M., Kjellgren P., Davidson L.: On the Download Alleviation for the XV-15 Wing by Active Flow Control Using Large-eddy Simulation, ERCOFTAC workshop: Direct and Large-Eddy Simulation 7, Sept 8–10, Trieste, Italy (2008)
2. El-Alti, M., Kjellgren, P., Davidson, L.: Drag reduction of trucks by active flow control of the wake behind the trailer. In: 6th International Symposium on THMT, Rome, Italy (2009)
3. CD-adapco: Coupled Solver Best Practice, v6.06 (2011)